EVOLUTION OF EMISSION LINE GALAXIES

Thesis by

Irwin Kenneth Horowitz

In Partial Fulfillment of the Requirements

for the Degree of

Doctor of Philosophy

California Institute of Technology

Pasadena, California

1994

(Submitted 25 April 1994)

ACKNOWLEDGEMENTS

I suppose whenever you stay in one place for a long time, there ends up being a huge number of people whose lives have touched yours, therefore I would like to thank the following individuals for their assistance to me during the long, arduous task of completing this thesis. First, to my thesis advisor, Prof. Maarten Schmidt, who has provided extremely useful commentary on the progress of this program, and whose knowledge of the subject is exceeded only by his patience and his decency as a human being. I would also like to thank Dr. Donald Schneider for his frequent assistance in describing the details of the grism survey and the method of candidate selection which represents a fundamental aspect of this thesis, as well as for providing me with the reduced slit spectra from the grism survey that I have utilized in my analysis. In addition, I would like to thank Dr. Richard Burg for providing me with a list from his thesis of nearby CfA galaxies which showed strong [OIII]$\lambda\lambda$4959, 5007 emission as well as for providing me with vital followup information about the statistical properties of that sample.

Among the Caltech faculty, I would like to thank Prof. Jeremy Mould, who provided funds to help upgrade the Echelle Spectrograph for this project; Prof. Judy Cohen, for her dedication to improving the observing conditions at Palomar, and especially at the 60 inch telescope, as well as her efforts to improve the computing environment in Robinson; Prof. J. Bev Oke, who helped me with testing of the new grating mode of the Echelle Spectrograph; Profs. E. Sterl Phinney and Wallace S. W. Sargent, who asked insightful questions early on in this program and got me to think along alternative avenues; and lastly, Prof. Jim McCarthy, who as a graduate student, built a fabulous instrument for his thesis, and who had the forethought to design the Echelle Spectrograph to work in a long-slit, low resolution mode which was so useful for my observational program. In addition, Prof. McCarthy has been helpful on numerous occasions with some of the details of Fortran programming which

I required for this thesis.

I would like to thank the staff of Palomar Observatory, both on campus and on the mountain. I have enjoyed many conversations with the engineers in Robinson: Fred Harris, John Cromer, Hal Petrie and Earle Emery. I would also like to thank Mr. Gaston Araya, who machined the parts for upgrading the Echelle Spectrograph to his usual exacting standards. Thanks to Dr. Robert Brucato for all that he does in his position as the Assistant Director of Palomar. Thanks also to Ann Palfreyman, Lisle Hauck and Petra De La Cruz, for their efforts on behalf of the observatory. Thanks to the night assistants that I've had the pleasure of working with: Skip Staples, Jean Mueller, Dave Mendenhall, Will McKinley and Cynthia Brewer, and of course, Juan Carrasco, who made the nights that I spent with Prof. Schmidt and company on the 200 inch telescope so enjoyable. Thanks also to the engineering staff on the mountain: John Henning, Mike Doyle, and Dave Tennant, who received as in-depth an introduction into the workings of the Echelle Spectrograph as I did when this project was just starting out and who were frequently "instrumental" with last minute changes and problem solving, thus enabling me to acquire the data that I required to complete this thesis. And finally, to both Bob Thicksten and Merle Sweet, for their tireless efforts to keep the mountain running smoothly under occasionally adverse conditions (like the fire of '89!).

There are many post-docs and staff members here in Robinson that I would like to thank. Charlie Lawrence was extremely helpful to me during the year that Prof. Schmidt spent in Germany, assisting in many areas of this thesis. Thanks also to John Conway, Bob Goodrich, Jeff Kenney, Neill Reid and Michael Strauss for their friendship and assistance over the years. Additionally, I'd like to thank Michael Strauss and Basilio Santiago for providing me with helpful information on modelling the local flow field as well as with the data for correcting the CfA overdensity.

Thanks to the staff and postdocs of the Carnegie Institution of Washington,

especially Dr. Wendy Freedman, who provided me with the opportunity to work on an equally exciting project to measure the size of the universe (or at least our little corner of it!). Thanks to Todd Boroson who provided me with the table from John Salzer's thesis. Also thanks to Alan Dressler, Ian Thompson, Simon Morris, Barry Madore and Mario Mateo for their friendship and support over the years.

I would like to thank many of my fellow graduate students from over the years, both for their assistance when a confused computer neophyte had questions about Fortran programming or how a particular application works (like Figaro!) as well as for their friendship over the past seven years: Karl Stapelfeldt, Debbie Padgett, Steve Myers, Chuck Steidel, Alain Picard, Rich Rand, Christine Wilson, Helen Johnston, Chris Tinney, Joshua Roth, Michal Peri, Dave Thompson, Nick Weir, Thomas Herbig, Wenge Xu, Jose Navarro, Lin Yan, Will Deich, Todd Small, Tim Lynch, Angela Putney, Gautam Vasisht, Peter Bryant and Rachel Akeson. I would also like to thank those who managed to survive as my apartmentmates over the past seven years: Steinn Sigurdsson, James Cummings, Charles Morgan, Steve Sanders, John Feiler, Darrin Beigie, Paolo Coppi and Kevin Luster (Todd too!). I would like to thank the grad students from other departments that I've befriended over the years, including Julia Smith, Julie Moses, Patricia Schwartz, Jeff Hall and Chris Kochanek.

I'd like to thank the friends that I've made as a member of Caltech SEDS during my time here. These include Mark Adler, whose help as the treasurer was vital to the success of the 1989 SEDS International Conference which I chaired; Mark Looper and Rich Achterberg, my fellow "star-partiers"; John Wright, who isn't really a Caltech student, but it seems as though he's spent almost as much time here as I have; Phil Rosenthal, who didn't know how much of a con job I put over on him when he got involved in SEDS, but ended up running the whole shabang! Jeff Foust, who should have learned from Phil's example, but seems to have repeated it; and Sonny Arcilla, who taught me the valuable lesson that I didn't have to be in charge of Caltech SEDS

forever, and that it would do just fine without me. I would also like to thank the legions of friends that I've made worldwide as a result of my involvement in SEDS, from Canada to Great Britain, from Russia to Taiwan, as well as all over the United States.

Lastly, I'd like to thank the members of my family. Mom and Dad, you always maintained an environment in which the joy of learning far exceeded the occasional drudgery. To my sisters, Alaine and Robin, and my brother, Mitchell, who always created ever greater challenges for me to overcome as I grew up. As the youngest of the four of us, I constantly encountered teachers in school who expected nothing less than the best from me based on their experiences with each of you. Fortunately, I was generally able to deliver on those expectations! And finally, to my nieces and nephews, who give me hope for the future.

If I have overlooked anyone above (though I seem to have thanked everyone I've ever met here!), realize that such an omission was not intentional and I do apologize for the oversight.

For my parents

ABSTRACT

This thesis compares two samples of emission line galaxies, selected on the basis of the strength of their [OIII]$\lambda\lambda$4959, 5007 and/or Hβ λ4861 emission lines. The distant sample is drawn from the 4-Shooter transit survey undertaken by Schmidt, Schneider and Gunn (1994 and references therein), and consists of 370 galaxies with emission line equivalent widths in excess of 50Å and fluxes above well-defined wavelength-dependent limits. This survey consists of 6 narrow strips of the sky covering $\sim$ 62 square degrees. Each of these galaxies is classified by using line ratio diagnostics from the moderate resolution spectra taken to identify the emission line.

The nearby sample is taken from the first CfA Northern Sky Redshift Survey, and consists of 81 galaxies from Burg (1987) with [OIII]$\lambda\lambda$4959, 5007 EW$\geq$23.75Å and an additional 26 Seyfert galaxies from Edelson (1987). This sample is observed on the 1.5m Oscar Meyer telescope using the Echelle Spectrograph in a low-resolution, long slit mode (McCarthy, 1988). Each of the 107 galaxies is observed twice, along perpendicular axes over a wavelength range from 4350Å to 7200Å, which covers the emission lines of interest such as Hβ λ4861, [OIII]$\lambda\lambda$4959, 5007 and Hα λ6563. These data are used both to classify the 107 galaxies from their line ratio diagnostics as well as to model the spatial and spectral light distribution on the plane of the sky for a comparison of how each would appear in the distant survey as a function of redshift.

Maximum redshifts in both the nearby and the distant survey are determined for each CfA galaxy, and predicted number counts, based on both a no-evolution model as well as a model incorporating density evolution, are made from the corresponding ratio of accessible volumes in the two surveys. Corrections are made to the predicted counts to account for sample incompletenesses and the overdensity of the CfA survey relative to the average density of galaxies in the "local" universe. These predicted counts are compared to the observed counts from the distant survey for each object class. The results from this comparison are consistent with the no-evolution model for

emission line galaxies out to z$\sim$0.5, and do not support the conjecture (Broadhurst et al. 1988; Colless et al. 1990) that there is an evolving population of dwarf star-forming emission line galaxies.

Table of Contents

List of Figures

Chapter 1
Introduction

1.1 Scientific Motivation for this Work

Two of the most interesting and exciting topics of study in extragalactic astronomy today deal with the sources of unusual activity in galaxies and with the evolution of galaxies.

Galaxy activity is of interest since many of the most powerful physical processes known to exist in the universe are tied to this activity. The processes which give rise to this activity range from the formation of stars to the gravitational accretion of matter onto massive black holes, leading to the formation of an active galactic nucleus (AGN).

The interest in galaxy evolution is tied to the more fundamental questions of the origin, evolution and eventual fate of the universe as a whole. Determining how galaxies have evolved in the past, and observing how they appear at present can help to constrain various cosmological models used to describe the universe. In addition, the chemical evolution of galaxies is tied to their history of star formation.

Much of the current excitement in these areas is due to recent technical advances, both observationally, with the development of large-area linear detectors (CCDs) as well as in the theoretical domain, with the development of high-speed supercomputers which can rapidly model both the emission from active nuclei as well as the star formation histories within galaxies. They are also used to model the general evolution of galaxies in the universe.

1.2 Studies of Emission Line Galaxies

Galaxies display activity at various rates. In most, there is the slow, steady formation of stars, with one generation providing the seed material for the formation of the next generation. These galaxies show little difference from the norm, either spectroscopically or morphologically. A few galaxies produce massive bursts of star formation which last for only a short ($\sim$few$\times 10^7$ yr, Balzano 1983) period of time. During these outbursts, the hot, massive stars ionize the medium surrounding them, producing strong emission in narrow lines, which can be readily observed. Yet other galaxies show evidence of unusual activity in their nuclei, which has been conjectured to be caused by the accretion of matter onto massive ($\geq 1 \times 10^6 M_\odot$) black holes (Begelman, Blandford, and Rees 1984). Such objects tend to show a rich variety of emission features in their spectra. Sometimes, galaxies collide and merge, and in the process either set off a new phase of star formation or else feed a previously quiescent black hole in their center. Colliding galaxies are among the most luminous known to exist in the universe (Sanders et al. 1988).

Regardless of the source, one of the key results of galaxy activity is the presence of strong line emission in their optical spectra. This is due to the presence of a strong ultraviolet continuum, whether from hot stars or an active nucleus, which ionizes the gaseous medium of that galaxy. These emission lines help make the study of these objects more accessible, as they are readily observed even out to substantial redshifts. Indeed, even the study of the redshift distribution of galaxies is substantially simpler when one looks at emission line galaxies, since they are easier to detect and measure than galaxies which lack detectable line emission. This property makes these objects useful probes of the large-scale structure of the universe, assuming that emission line galaxies are good tracers of the underlying galaxy distribution. Based on the work of Longo (1991), nearby AGN do trace out some of the large-scale features of the local universe, such as the "Great Wall" (Geller and Huchra 1989).

There is a rich history of the study of such objects, going back to the pioneering work of Carl Seyfert in the early 1940s (Seyfert 1943), who studied six galaxies with strong nuclear emission and bright, point-like nuclei. More recent work on emission line galaxies comes from a number of surveys. Among these are the Markarian surveys (Markarian, Lipovetskii, and Stepanian 1981 and references therein), the Case-Western surveys (Pesch, Sanduleak, and Stephenson 1991 and references therein) and the University of Michegan-Tololo surveys (Smith, Aguirre, and Zemelman 1976; MacAlpine and Williams 1981 and references therein). Each of these is based on photographic data taken using Schmidt telescopes with an objective prism to give low-resolution spectra. These surveys cover large areas of the sky, and select candidate objects on the basis of having both/either a blue continuum and/or a detectable emission line, which, because of the accessible wavelength range for the photographic plates, is generally either Hβ λ4861, [OII]$\lambda\lambda$3726, 3729 or [OIII]$\lambda\lambda$4959, 5007.

The principle use of these surveys is that they provide large samples of different types of emission line/active galaxies. The properties of each type of galaxy can be measured and the underlying physics that gives rise to these properties can be studied (see, for example, Mazzarella and Balzano 1986 (MB86), for a summary of Markarian galaxies and Salzer 1989, Salzer et al. 1989a,b for UM-Tololo galaxies).

Due to the subjective nature of the selection criteria for these surveys (primarily a result of the visual inspection of the plates to detect candidate objects), statistical properties for the samples are difficult to quantify. This is because the definition of a complete sample of objects is a cumbersome task, and thus attempts to construct a luminosity function are hampered by the sample incompletenesses that are inherent in these surveys. According to MB86, "The non-uniformity of the limiting magnitude and the selection criterion indicate that the Markarian survey . . . can not be used to obtain reliable conclusions on the distribution and luminosity functions of the various types of AGN . . ." Similar statements can be made for the other surveys.

Studies of the space densities out to the limits of these surveys show no conclusive evidence for evolution of emission line galaxies, and are consistent with a "no evolution" model out to redshifts of $z \sim 0.1$. A recent study by Boroson, Salzer and Trotter (1993) of a sample of [OIII]$\lambda\lambda$4959, 5007-selected emission line galaxies shows that the space density of emission line galaxies is essentially identical at $z \sim 0.35$ and the present. This sample is based on a multi-band narrow filter search over 0.7 sq. degrees for low-luminosity Hα λ6563-selected galaxies, but is also sensitive to [OIII]$\lambda\lambda$4959, 5007-selected galaxies over a redshift range from $0.28 \leq z \leq 0.38$. They find 17 galaxies in that range, with a median m_{6600}=21.0, which corresponds to $M_B = -19.9$ ($H_0 = 75$) at z=0.35. For the 10 galaxies in the range $-20.4 \leq M_B \leq -19.5$, their space density is $\log \phi$=-3.67$\pm$0.16. Local determinations of the space density of emission line galaxies find comparable values (see Salzer 1989 and Wasilewski 1983), implying that there is no evolution of [OIII]$\lambda\lambda$4959, 5007-selected emission line galaxies with this range of absolute magnitude out to redshifts of z$\sim$0.35.

1.3 Evolution of Faint Field Galaxies

In addition to studies of emission line galaxies, there has been substantial work in the study of the evolution of faint ($b_j \sim 21$) field galaxies by several groups, including the Durham-AAO pencil beam survey of Broadhurst et al. (1988; BES), the Low Dispersion Survey Spectrograph (LDSS) survey of Colless et al. (1990) and work undertaken at Kitt Peak National Observatory (KPNO) by Koo and Kron (1987). A summary of this field is given in Koo and Kron (1992, KK92).

The study of faint field galaxies is of interest because these objects begin to sample a range in redshifts beyond z$\sim$ 0.1, where evolutionary effects might be expected to be observable. Amongst the more unexpected results from these studies are an excess in the number counts of faint galaxies over predictions for non-evolving models, redshift

distributions in accord with the predictions of a non-evolving model, a shift to bluer colors at fainter magnitudes and an increase in the frequency of line emission (KK92).

A number of researchers have found evidence for a steepening in the slope of the N(m) vs. m relation at very faint magnitudes (see, for example, Tyson 1988). In a strictly Euclidean universe, this relation should increase by a factor of four per magnitude, which represents the ratio of volumes for that interval. When this slope steepens beyond this value, it is generally interpreted to mean that the luminosity function of galaxies is changing at higher redshifts, such that there are more bright galaxies at those redshifts than in the "local" universe. This is either the result of there being a greater number of galaxies at those redshifts (for example, density evolution from mergers) or else that galaxies were intrinsically brighter in the past (luminosity evolution). Various evolutionary models, ranging from "non-evolving" scenarios to models with both/either luminosity and/or density evolution have been analyzed to explain the observations. These models make predictions for the number counts of faint galaxies in various filter passbands, which can be compared to the observations to determine the viability of the model.

A number of redshift surveys of nearby galaxies (Kirshner et al. 1978; Kirshner et al. 1983; Peterson et al. 1986; Metcalfe et al. 1989) are useful for computing the field galaxy luminosity function in the "local" universe, which can be compared to the derived LF of the faint surveys. Surveys of faint galaxy redshifts (BES; LDSS) result in distributions that are consistent with non-evolving models out to redshifts of $z\sim0.4$. These authors argue that since their number counts are steeper than permissable for such models, that some form of luminosity-dependent luminosity evolution is the cause. They propose a model whereby an intrinsically faint galaxy undergoing a burst of star formation would have a greater relative increase in its absolute magnitude and that these bursts are more frequent amongst these galaxies at redshifts $z>0.1$. However, KK92 argue that an alternative explanation might be that these

faint redshift surveys are biased against higher redshift objects. This is due primarily to the reduction in the surface brightness by a factor proportional to $(1+z)^{-4}$ which makes the high-z objects more difficult to detect. Other factors that KK92 claim could lead to this result include the fact that at such high redshifts, prominent spectral features like the 4000Å break move into the noisy red portion of the sky. Also, for emission line galaxies, the only common emission line readily observable in these surveys at z$\sim$0.5 is [OII]$\lambda\lambda$3726, 3729, as both Hβ λ4861 and [OIII]$\lambda\lambda$4959, 5007 have moved into the red spectral region.

Studies of the colors of galaxies show a progressive trend to bluer colors as one moves to fainter magnitudes. Median colors in the b_j-r_F system of Kron (1980) shift by 0.5 magnitudes blueward for galaxies fainter than B$\sim$22. This result is dramatically illustrated by the ultra-faint surveys of Tyson and Seitzer (1988) and Tyson (1988), who show as much as a one magnitude change in B_j-R of galaxies at their faint limits. However, others (for example Lilly et al. 1991) show a more gradual trend to bluer colors. This "blueing" of galaxy colors may be due to an increase in the proportion of intrinsically blue galaxies rather than a general trend of blue galaxies becoming bluer (KK92).

Both BES and LDSS state that there is a greater incidence of [OII]$\lambda\lambda$3726, 3729 emission in their samples at redshifts $z_{med} \sim 0.2$, ranging from a 40% to 100% increase in the fraction of galaxies with an equivalent width in this line $\geq$20Å as compared to the predictions of a non-evolving population using the sample of Peterson et al. (1986) for the "local" population. They argue that this supports their picture of enhanced bursts of star formation at z>0.1 for intrinsically faint galaxies. KK92 argue that the comparison to the Peterson et al. survey may not be applicable, since they don't necessarily contain similar galaxies. Indeed, they point out that a plot of the BES equivalent widths vs. z shows an *anti-correlation* with more strong-lined objects seen at z$\sim$ 0.15 than at z$\sim$ 0.3. This effect may be due to the correlation between

luminosity and redshift in the BES sample if fainter galaxies have intrinsically higher equivalent widths in [OII]$\lambda\lambda$3726, 3729. This last assumption is plausible based on the tendency of lower-luminosity galaxies to have bluer $U - B$ colors (Huchra 1977).

In KK92 and in Koo et al. (1993), an alternative model of galaxy evolution is presented in which their principle alteration to prior models is to separate out the different types of galaxies based on their intrinsic colors (early-type red elliptical and lenticular galaxies and late-type blue spirals and irregulars). They compute the "local" LF for each type separately through a non-negative least squares fit to the observed data and compare the predictions of these LFs for counts, colors and redshift distributions to the observations from faint surveys assuming no evolution. They get a remarkably good fit for each of these distributions from B$\leq$15 to B$\sim$24 for redshifts and B$\sim$26 for counts and colors, and their faint galaxy excess is red, not blue. Their fit still requires some mild luminosity evolution to account for their remaining deviations from the observed distributions.

1.4 Thesis Objectives

This thesis will examine the extent to which cosmological evolutionary effects are discernable between two samples of emission line galaxies, which have been selected on the basis of the fluxes and equivalent widths of their [OIII]$\lambda\lambda$4959, 5007 and Hβ λ4861 emission lines. In addition, statistical properties of the distant sample are derived.

The distant sample consists of 370 galaxies detected by Schmidt, Schneider and Gunn as a by-product of the 4-Shooter transit survey for high-redshift quasars. These galaxies are selected on the basis of an equivalent width in a detected emission line in excess of 50Å and a line flux above some wavelength-dependent limit, which corresponds to a set signal-to-noise limit. More detail on these objects can be found in Chapter 2.

The nearby sample consists of 107 galaxies selected from the CfA Northern Sky

Redshift Survey (Huchra et al. 1983). Of these, 81 objects have [OIII]$\lambda\lambda$4959, 5007 equivalent widths in excess of 23.75Å, based on the results of Burg (1987). The remaining 26 objects are classified as Seyfert galaxies, according to Edelson (1987), and have been included in this sample on the possibility that their combined Hβ λ4861 and [OIII]$\lambda\lambda$4959, 5007 strengths are sufficient for inclusion in the final sample. Chapter 3 of this work more fully discusses the details that went into the selection and observation of the CfA sample.

The analysis of the CfA data is described in Chapter 4, focusing on the details of how the comparison between the two samples is to be made. Chapter 5 compares the results for the two samples and discusses the relevance of those results to the issue of evolution in these types of galaxies.

Throughout this thesis, I shall assume the standard cosmological model, with a Hubble constant, $H_0 = 50$ km s^{-1}Mpc^{-1} and a deceleration parameter of $q_0 = 0.5$.

References

Balzano, V., 1983, *Ap. J.*, **268**, 602

Begelman, M., Blandford, R. and Rees, M., 1984, *Rev. Mod. Phys.*, **56**, 255

Boroson, T., Salzer, J. and Trotter, A., 1993, preprint

Broadhurst, T., Ellis, R. and Shanks, T., 1988, *MNRAS*, **235**, 827 (BES)

Burg, R., 1987, Ph. D. thesis, MIT, Cambridge, MA

Colless, M., Ellis, R., Taylor, K. and Hook, R., 1990, *MNRAS*, **205**, 1287 (LDSS)

Edelson, R., 1987, Ph. D. thesis, Caltech, Pasdena, CA

Geller, M. and Huchra, J., 1989, *Science*, **246**, 897

Huchra, J., 1977, *Ap. J. Suppl.*, **35**, 171

Huchra, J., Davis, M., Latham, D. and Tonry, J., 1983, *Ap. J. Suppl.*, **52**, 89

Kirshner, R., Oemler, A. and Schecter, P., 1978, *A. J.*, **83**, 1549

Kirshner, R., Oemler, A., Schecter, P. and Schectman, S., 1983, *A. J.*, **88**, 1285

Koo, D., Gronwall, C. and Bruzual, A., 1993, preprint

Koo, D. and Kron, R., 1987, *Observational Cosmology and Fundamental Physics*, ed. M Caffo, R. Fanti, G. Giacomelli and A. Renzini (Dordrecht: Kluwer), pp. 383-98

—, 1992, *Annu. Rev. Astron. Astrophys.*, **30**, 613 (KK92)

Kron, R., 1980, *Ap. J. Suppl.*, **43**, 305

Lilly, S., Cowie, L. and Gardner, J., 1991, *Ap. J.*, **369**, 79

Longo, M., 1991, *Ap. J. (Lett.)*, **372**, 59

MacAlpine, G., and Williams, G., 1981, *Ap. J. Suppl.*, **45**, 113

Markarian, B., Lipovetskii, V. and Stepanian, D., 1981, *Astrofizika*, **17**, 619

Mazzarella, J. and Balzano, V., 1986, *Ap. J. Suppl.*, **62**, 751 (MB86)

Metcalfe, N., Fong, R., Shanks, T. and Kilkenny, D., 1989, *MNRAS*, **236**, 207

Pesch, P. Sanduleak, N. and Stephenson, C., 1991, *Ap. J. Suppl.*, **76**, 1043

Peterson, B., Ellis, R., Efstathiou, G., Shanks, T., Bean, A., Fong, R. and Zen-Long, Z., 1986, *MNRAS*, **221**, 233

Salzer, J., 1989, *Ap. J.*, **347**, 152

Salzer, J., MacAlpine, G. and Boroson, T., 1989a, *Ap. J. Suppl.*, **70**, 447

—, 1989b, *Ap. J. Suppl.*, **70**, 479

Sanders, D., Soifer, B., Elias, J., Neugebauer, G., and Matthews, K., 1988, *Ap. J.*, **328**, 35

Seyfert, C., 1943, *Ap. J.*, **97**, 28

Smith, Aguirre and Zemelman, 1976, *Ap. J. Suppl.*, **32**, 217

Tyson, T., 1988, *A. J.*, **96**, 1

Tyson, T. and Seitzer, P., 1988, *Ap. J.*, **335**, 552

Wasilewski, A., 1983, *Ap. J.*, **272**, 68

Chapter 2
Transit Survey Sample

2.1 Survey Summary

The 4-Shooter transit survey of Schmidt, Schneider and Gunn (1986a,b; 1987a,b; 1988; 1989a,b; 1994; henceforth SSG) has resulted in a list of 1612 candidate emission line objects with 1760 lines detected (a number of objects are detected in two different lines). The transit survey consists of 6 strips of the sky, 8.5 arcminutes wide in declination by several hours long in right ascension. In transit mode, the telescope is stopped, and the CCDs are read out at the sidereal rate. Exposure times in transit mode are inversely proportional to $\cos\delta$. Each strip is observed twice, first in a direct imaging mode using Gunn g and i filters, to locate all of the objects that are observable above the noise limit in that strip, and then a second time using grisms to get low resolution slitless spectra for each of these objects. Additional details of the observing procedures and the data analysis can be found in the above referenced articles.

As a summary, every object in each of the strips is examined for the presence of emission lines in their slitless spectra. An object is flagged as a potential emission line candidate if at least one suspected line has both a signal-to-noise ratio in excess of some survey-specified limit as well as an equivalent width in excess of 50Å. Since the data are background limited, the signal-to-noise ratio is calculated from the following formula:

$$\frac{S}{N} = \frac{f_{line}(\lambda)R(\lambda)}{[Bd(d^2+w^2)^{1/2}]^{1/2}},$$

where $f_{line}(\lambda)$ is the line flux, $R(\lambda)$ is the response of the CCD as a function of wavelength, B is the sky brightness, d is the seeing FWHM and w represents the number of pixels that correspond to the typical line width in a quasar of 118Å. For a given $(S/N)_{lim}$, this translates into a line flux limit as a function of wavelength, which is shown in Figure 2–1. $(S/N)_{lim}$ is set to either 6.5 for both the IJ and the QR sub-surveys or 7 for the other four sub-surveys. The equivalent width is calculated by fitting a $2^{\underline{nd}}$ order polynomial to the data on both sides of the suspected emission line to estimate the continuum flux density under the line and comparing this to the measured line flux. Starting with an initial number of objects in each strip on the order of 100,000, a list with a few hundred candidates is created with $(S/N) \geq (S/N)_{lim}$ and EW$\geq$50Å in the emission line. These candidates are then observed using moderate resolution slit spectroscopy (both Double Spectrograph as well as the 4-Shooter) in order to determine the nature of the suspected emission line.

Of the 1612 suspected emission line objects in all 6 sub-surveys, 269 of them are quasars, found from one or more of the following lines in their spectra: Lyα λ1216; CIV λ1549; CIII]λ1909 or MgII λ2798. The survey detected a total of 665 low redshift galaxies. Of these, there are 295 galaxies detected solely on the basis of Hα λ6563 emission, and 284 that are detected in [OIII]$\lambda\lambda$4959, 5007 and/or Hβ λ4861. The remaining 86 galaxies are detected in both Hα λ6563 and [OIII]$\lambda\lambda$4959, 5007 and/or Hβ λ4861. Of the remaining objects, 92 have been rejected because they are either sub-structures in other galaxies (i.e., individual HII regions) or because they have been selected due to an interference effect from the grism spectrum overlapping with the spectrum of another object. 165 objects are nearby M stars, located in our own galaxy, whose complex spectra can mimic an emission line object. The remaining 421 objects show no emission at the expected wavelength.

Since the resolution of the slitless spectra is insufficient to separate out the galaxies detected primarily by [OIII]$\lambda\lambda$4959, 5007 from those detected primarily by Hβ λ4861,

all 370 objects are utilized to make up the distant sample for this thesis. An analysis of that sample shows that of the 24 objects whose primary emission feature at the suspected wavelength is Hβ λ4861, 23 of them are broad lined Seyfert 1 galaxies while the remaining object is catagorized as a Starburst galaxy (see below for the definitions of each class). The redshift range in these two emission lines for which the transit survey is sensitive runs up to $z \sim 0.5$.

2.2 Observations and Object Statistics

The transit survey consists of six strips in right ascension, covering a total of 62 square degrees on the sky. Table 2–1 gives a summary of the relevant parameters for each of the sub-surveys. The naming conventions used for each sub-survey are those adopted by SSG. The limiting line flux at 6100Å is given by $\log f_{\lambda}^{lim}(6100\text{Å})$. This is indicative of the typical depth reached by each survey. Both the MN and the QR sub-surveys are double-binned data, while the other four sub-surveys are triple-binned. The mean wavelength ($\bar{\lambda}$) is defined below.

Of the 1612 candidate emission line objects, 370 are detected by the emission of [OIII]$\lambda\lambda$4959, 5007 and/or Hβ λ4861. These objects are listed in Table 2–2, along with all of the relevant statistical quantities as derived by the transit survey. These include the measured signal-to-noise ratio as well as the line equivalent widths. The values for the redshifts are taken from the higher resolution slit spectra and are determined by fitting gaussian line profiles to both the [OIII]$\lambda\lambda$4959, 5007 and the Hβ λ4861 emission lines, using the FIGARO line fitting routine FIT (Zucker and Lawrence, 1988). Since the fitted wavelength residuals to these spectra are less than 1Å (SSG, 1987b), the errors in these redshifts are typically less than 0.0002.

For each sub-survey, a mean zero-redshift wavelength is calculated for the blend of Hβ λ4861 and [OIII]$\lambda\lambda$4959, 5007. The following formula is utilized to determine

the value of the mean zero-redshift wavelength:

$$\bar{\lambda} = \frac{1}{N} \sum_i \frac{\lambda_{bin,i}}{1 + z_{obs,i}}$$

where N is the total number of galaxies from that sample, λ_{bin} is the grism wavelength of the bin where the emission line was detected and z_{obs} is the observed redshift from the slit spectra. Figure 2–2 shows the histogram of values of the above expression for each sub-survey. This shows that the values tend to cluster around the expected range of wavelengths for a sample selected from Hβ λ4861 and [OIII]$\lambda\lambda$4959, 5007.

2.3 Statistical Properties of the Transit Survey Sample as a Whole

We can derive a number of statistical properties for this sample assuming that the galaxies are point sources (i.e., the optical extent is smaller than the aperture used by DPS in analyzing the grism data which is an incorrect assumption that is made here primarily for illustrative purposes and is not made for other parts of this thesis). For each galaxy, the observed luminosity in Hβ λ4861 + [OIII]$\lambda\lambda$4959, 5007 can be determined from:

$$\log L_{obs}(z_{obs}) = \log \left[4\pi A^2(z_{obs}) f_{obs}(z_{obs}) \right]$$

where the luminosity distance is given by (Schmidt and Green, 1986):

$$A(z) = \frac{2c}{H_0} \left\{ 1 + \frac{z}{\sqrt{1 + 2q_0 z} + 1} \right\} \left\{ \frac{z}{\sqrt{1 + 2q_0 z} + 1} \right\}.$$

2.3.1 Determination of Accessible Volume

We can derive a maximum redshift to which each galaxy would be observable in a particular sub-survey, using the observed line luminosity. This is accomplished by converting the line flux limit curves (Figure 2–1) into line luminosity limit curves. The above derived mean wavelength is utilized to determine the luminosity limits as a function of redshift for each sub-survey. Figure 2–3 shows this line luminosity limit vs. redshift diagram. The limiting luminosities are calculated using the following

formula:

$$\log L_{lim}(z_{bin}) = \log\left[4\pi A^2(z_{bin}) f_{lim}(z_{bin})\right]$$

where z_{bin} is given by:

$$z_{bin} = \frac{\lambda_{bin}}{\bar{\lambda}} - 1.$$

The accessible volume for each galaxy can be determined from these maximum redshifts, and therefore, a "luminosity function" can be generated for these emission line galaxies. This accessible volume is calculated from (Schmidt and Green, 1986):

$$\frac{dV}{dz} = \omega\left(\frac{c}{H_0}\right) A^2(z)(1+z)^{-3}(1+2q_0 z)^{-1/2}$$

giving (for $q_0 = 0.5$):

$$V_{max} - V_{min} = 4\omega\left(\frac{c}{H_0}\right)^3 \int_{z_{min}}^{z_{max}} \frac{[z - 2(1+z)^{1/2} + 2]}{(1+z)^{5/2}}\, dz,$$

whose solution is determined analytically (for $z_{min} = 0$):

$$V_{max} = 8\omega\left(\frac{c}{H_0}\right)^3 f(z_{max}),$$

where ω is the solid angle of the sub-survey in steradians and where

$$f(z) = \left(\frac{1}{1+z} - \frac{1}{(1+z)^{1/2}} - \frac{1}{3(1+z)^{3/2}} + \frac{1}{3}\right).$$

Following the procedure in Avni and Bahcall (1980), the accessible volume over all six sub-surveys is determined for each of the 370 galaxies in this sample:

$$V_a = 8\left(\frac{\pi}{180}\right)^2\left(\frac{c}{H_0}\right)^3 \sum_{j=1}^{N_{surveys}} \omega_j f(z_{max,j}),$$

where ω_j is the solid angle in square degrees for the j^{th} sub-survey. The space density for a given object is given by the inverse of this accessible volume. A plot of these space densities vs. observed line luminosities, binned to 0.4 dex (1 magnitude) in the log of the line luminosities, is shown in Figure 2–4. The error bars are determined by the Poisson statistics in each bin. A Schecter function gives a mediocre fit to this

data, as there is an apparent excess of objects with $40.6 \leq \log L \leq 41.0$ as well as too many objects at high luminosities to fit the exponential tail of the function. It should be remembered that this is not a true luminosity function, first since this is a plot of line luminosities, rather than continuum magnitudes and also because there exists an unknown distance-dependent bias on the measured line luminosities to each SSG galaxy due to the aperture used by DPS in analyzing the grism data.

2.3.2 Number-Redshift Relation for Distant Sample

The N(z) vs. z histogram of the SSG sample shows the typical dropoff at larger redshifts of a flux-limited sample (see Figure 2–5(a)). The dashed curve represents the expected number of objects at each redshift based on the assumption of no evolution. This is calculated by first determining the fraction of the total accessible volume for a given object that is enclosed by a given redshift interval, and then summing this over all 370 galaxies in the total sample. This can be expressed in the following manner:

$$N_{pred}(z) = \sum_{i=1}^{N} \frac{V_{e,i}(z)}{V_{a,i}},$$

where

$$V_{e,i}(z) = 8\left(\frac{\pi}{180}\right)^2 \left(\frac{c}{H_0}\right)^3 \sum_{j=1}^{N_{surveys}} \omega_j Min\Big\{ f(z+\frac{\Delta z}{2}) - f(z-\frac{\Delta z}{2}),$$
$$f(z_{max,j}) - Min\Big[f(z-\frac{\Delta z}{2}), f(z_{max,j})\Big]\Big\}.$$

For a given object in the j^{th} sub-survey, the minimum function leads to one of three possible solutions, depending on the relation between $z_{max,j}$ and $z \pm \frac{\Delta z}{2}$. These are:

$$\begin{aligned} Min &= 0 && z_{max,j} < z - \frac{\Delta z}{2} \\ &= f(z_{max,j}) - f(z-\frac{\Delta z}{2}) && z - \frac{\Delta z}{2} \leq z_{max,j} \leq z + \frac{\Delta z}{2} \\ &= f(z+\frac{\Delta z}{2}) - f(z-\frac{\Delta z}{2}) && z + \frac{\Delta z}{2} < z_{max,j}. \end{aligned}$$

For the first case, the galaxy has no enclosed volume at that redshift since its maximum redshift falls below the minimum redshift of that shell. The second case is that

in which the maximum redshift falls within the range of redshifts for that shell, while the last case is where the maximum redshift is beyond the maximum redshift of the shell, and thus all of the volume in that shell is enclosed by the object.

Figures 2–5(b)-(f) show the redshift distributions for each of the different classes of objects found in the distant sample. These classes are defined in Section 2.5. Some comments on these distributions include the fact that there are no observed Seyfert 1 galaxies for z<0.08. Only 6% of the HII galaxies have z>0.1. This is due to the definition used in this thesis for this class, which includes an absolute magnitude criterion. This result means that we are limited in the extent to which we can make a determination as to the extent of evolution in HII galaxies, since our distant sample is limited in redshift to z<0.1. The most striking feature in the distribution of Seyfert 2 galaxies is the peak at a redshift 0.18<z<0.20. Much of this signal is due to an apparent supercluster of galaxies located in the northern galactic hemisphere which form a 2-dimensional sheet on the plane of the sky (see section 2.4 and Figure 2–8). There is also a noticable deficit in both Starbursts and Seyfert 2s in the redshift range 0.10<z<0.12 which is reflected in the distribution of the total sample. Clearly there is evidence for large-scale structure in the distribution of emission line galaxies, which is further elaborated upon below in Section 2.4.

2.3.3 $\frac{V}{V_{max}}$ Tests for Distant Sample

A $\frac{V_e}{V_a}$ test on this sample gives a value of:

$$\frac{V_e}{V_a} = 0.61 \pm 0.015.$$

A $\frac{V}{V_{max}}$ test, in which each object is measured solely within the sub-survey in which it is discovered, gives a value of 0.59. The difference between the two values is due to the different flux limits of the six sub-surveys and the different number of objects from each sub-survey. The deeper sub-surveys, MN and QR, which have 208 of the 370 galaxies in the total sample between them, contain fainter galaxies which would

not be observable to as great a distance in the other four sub-surveys, and thus their $\frac{V}{V_{max}}$ is smaller than their $\frac{V_e}{V_a}$ values, thus accounting for this difference.

One reason why these values are different from the expected value of 0.5 for a complete, uniformly spaced sample (Schmidt, 1968), is that the aperture used by DPS to measure the light from each galaxy is smaller than the true extent of the galaxy. If, as is generally the case, portions of a galaxy's light have been excluded, then this would tend to bias both the $\frac{V_e}{V_a}$ as well as the $\frac{V}{V_{max}}$ results to higher values, as the true line luminosities are greater than what was measured, and thus both the limiting redshifts as well as V_{max} would increase.

2.3.4 Equivalent Width Distributions for Distant Sample

Plots of the equivalent width distribution, as a function of both line luminosity and redshift, are shown in Figures 2–6(a) and 2–6(b). The distribution with respect to line luminosity shows a correlation in which the low-luminosity galaxies have greater equivalent widths. In addition, there is an upper limit to the observed line luminosities of the distant sample of galaxies. There are no apparent correlations between equivalent width and redshift.

2.3.5 Determination of Continuum Magnitudes

A continuum magnitude for each SSG galaxy can be derived at the observed wavelength of the emission line from the following expression:

$$AB_{\bar{\lambda}(1+z_{obs})} = -2.5\log\left\{\frac{[\bar{\lambda}(1+z_{obs})]^2 f_\lambda^{line}}{c \cdot EW}\right\} - 48.6.$$

This, in turn, can be used to derive an absolute continuum magnitude beneath the line by using the observed luminosity distance, $A(z_{obs})$, and the formula for the distance modulus. In order to compare this absolute magnitude to the magnitudes used in the CfA survey, it is necessary to take into account the spectral slope of the continuum from a wavelength of $\bar{\lambda}$ to 4400Å. Assuming that the spectra go as $f_\nu \sim \nu^{-1}$, the correction amounts to $\sim +0.13$ magnitudes. The formula for the absolute magnitude

at 4400Å is:

$$M_{4400} = -2.5 \log\left\{\frac{[\bar{\lambda}(1+z_{obs})A(z_{obs})]^2 f_{\lambda}^{line}}{c \cdot EW}\right\} - 73.47.$$

Plots of the N(M) vs. M relation for the total sample, as well as each class of object, are given in Figure 2–7(a)-(f). As is seen in Figure 2–7(b), there are 18 objects in the distant sample which are more properly catagorized as low-luminosity quasars, based on the criterion M_B <-23, however, there are no differences being assumed between Seyfert 1 galaxies and low-luminosity quasars for the purposes of this thesis, and therefore, these eighteen objects will be classified as Seyfert 1 galaxies. Besides this point, the continuum magnitudes derived are consistent with values determined for local samples of emission line galaxies.

2.4 Spatial Distribution of SSG Galaxies

Figure 2–8 shows the three-dimensional distribution of the 370 emission line galaxies in the distant sample. The different symbols each represent a different sub-survey, and thus a different declination strip. As can be seen, there are several regions of clustering, as well as some regions of low-density, in the distribution. The Bootes void is visible at $\alpha \sim 14^h30^m$, z$\sim$0.05. One of the more prominent features would appear to be the "void" located at $12^h40^m \leq \alpha \leq 14^h40^m$, 0.24$\leq$ z $\leq$0.32. Another feature visible in this figure is the string of galaxies from $12^h00^m \leq \alpha \leq 13^h30^m$, z$\sim$0.18, which are mentioned above in the N(z) vs. z distributions as contributing to the overdensity in both the Sy2 as well as the total sample. These may represent a structure similar to the "Great Wall" pointed out by Geller and Huchra (1989).

Figure 2–9(a) and 2–9(b) show the N(z) vs. z distribution in the two galactic hemispheres. Figures 2–9(c) through 2–9(l) give the same distribution for different intervals of right ascension. Note that in Figure 2–9(j), there is evidence of the above mentioned "void" in the redshift distribution, with only one object detected between 0.24$\leq$z$\leq$0.32. A Poisson test using the existing data and observed redshift distribu-

tion demonstrate that this may be a robust feature in the large scale distribution of emission line galaxies, with the probability of such a distribution occuring randomly being under 1%. I believe that this is an area worthy of further investigation.

2.5 Diagnostics and Object Classification

Using the moderate resolution slit spectra from the distant sample, an attempt has been made to classify the nature of each of the emission line galaxies using line ratio diagnostics. The background of this field can be found in the papers of Baldwin, Phillips and Terlevich (1981, henceforth BPT) and Veilleux and Osterbrock (1987, henceforth VO), who utilize various combinations of line ratios to determine the source of the ionization in a given object. BPT relied mainly on the line ratios $\frac{[\mathrm{OII}]\lambda 3727}{[\mathrm{OIII}]\lambda 5007}$ and $\frac{[\mathrm{OIII}]\lambda 5007}{\mathrm{H}\beta\ \lambda 4861}$, since most high quality galaxy spectra at that time were in the blue spectral region. Due to the advent of red-sensitive CCD's as the primary detectors in modern spectrographs in the early 1980's, VO prefer a different set of line ratios. They developed a set of five criteria for the choice of acceptable line ratios. These are:

- Each ratio should be made up of strong lines that are easy to measure in typical spectra.
- Lines that are badly blended with other lines should be avoided because the somewhat subjective nature of the deblending procedure increases the uncertainty in the flux measurements of these lines.
- The wavelength separation between the two lines should be as small as possible so that the ratio is relatively insensitive to reddening and flux calibration.
- Ratios involving a line of only one element and an HI Balmer line should be preferred to those involving forbidden lines of different elements, because they are less abundance-sensitive.
- The lines should be in a region of the spectrum that is easily accessible with

present-day instruments. Among other considerations, lines in the ultraviolet should be avoided because of the low sensitivity of many CCDs at short wavelengths.

The best line ratios that satisfy these criteria include $\frac{[\mathrm{OIII}]\lambda 5007}{\mathrm{H}\beta\ \lambda 4861}$, $\frac{[\mathrm{NII}]\lambda 6583}{\mathrm{H}\alpha\ \lambda 6563}$, $\frac{[\mathrm{OI}]\lambda 6300}{\mathrm{H}\alpha\ \lambda 6563}$ and $\frac{[\mathrm{SII}]\lambda\lambda 6716,6731}{\mathrm{H}\alpha\ \lambda 6563}$. The $\frac{[\mathrm{NII}]\lambda 6583}{\mathrm{H}\alpha\ \lambda 6563}$ ratio does suffer from deblending problems to a certain extent, though in most instances, a sufficiently accurate deblending is possible to get an estimate of these line ratios. The $\frac{[\mathrm{OI}]\lambda 6300}{\mathrm{H}\alpha\ \lambda 6563}$ ratio is included because [OI]λ6300, which is generally emitted in the partially ionized zone surrounding AGN, is a reliable discriminator of the differences between power-law spectral sources and hot, thermal sources, even though it tends to be a fairly weak emission line in most objects.

VO showed that by plotting various combinations of these line ratios, it was possible to discriminate the mechanism responsible for the line emission. A brief summary of each type of object classified for this thesis is given below:

- **Seyfert 1 galaxies (Sy1)**: Sy1 galaxies are characterized by broad permitted lines ($\mathrm{v}_{FWHM} \gtrsim$1000 km/sec), such as H$\alpha$ λ6563 and narrower lines of forbidden transitions ($\mathrm{v}_{FWHM} \simeq$500 km/sec), such as [OIII]$\lambda\lambda$4959, 5007. The ionization source is believed to be an accreting, massive black hole in the galaxy center, which emits a very hard, power law continuum spectrum. They are strong X-ray sources, though they tend to have little or no radio emission (Elvis et al. 1978). Because of the large X-ray flux from the central engine, Sy1 galaxies have a large, partly ionized zone of hydrogen, where a number of low-ionization species can exist. Chief among these is [OI]λ6300. In general, due to the broad Balmer lines, Sy1 galaxies are fairly easy to classify. Note that for this thesis, I am not differentiating between Sy1 galaxies and QSOs, and indeed, several ($\sim$18) of the objects in the distant sample are bright enough to qualify as low-luminosity QSOs. With regards to the comparison to the CfA sample, this should

not adversely affect the results, as there is only one QSO which is bright enough to be observable to the CfA survey (3C 273), and it would lead to a no-evolution prediction of less than one quasar in the distant sample. As the number statistics are quite marginal, a statement about the evolution of quasars at low redshifts ($z \leq 0.5$) would be inappropriate.

- **Seyfert 2 galaxies (Sy2)**: Sy2 galaxies are very similar to the Sy1's, except for the lack of the broad emission lines. In Sy2's, one of the leading conjectures is that their central engine is obscured by dust in the accretion disk, and that the broad line region is therefore unobservable. Some of the evidence supporting this includes the work by Antonucci and Miller (1985), who observed broad emission in polarized light from the Sy2 nucleus NGC 1068. This has been interpreted as the reflected light scattered by electrons that have clear lines of sight to both the nucleus as well as the observer. Other evidence for this view comes from X-ray observations of a sample of Sy2 galaxies, showing strong absorption of the lower energy X-rays, but high energy fluxes that are comparable with Sy1 galaxies (Lawrence and Elvis 1982; Turner and Pounds 1989). Since the penetration depth of X-rays through dust is a strong function of the energy of those X-rays, this result is believed to be due to the absorption of the low energy X-rays by the dust torus. Therefore, there is evidence that Sy1 and Sy2 galaxies are both parts of the same family of objects, which are photoionized by a hard, power law source in their centers, and whose primary difference, the velocity width of permitted emission lines, is likely due to a geometric effect of whether or not the dusty accretion disk lies in our line of sight, thereby blocking the Broad Line Region (BLR) from our view. Sy2 galaxies are most readily recognized by the strength of their forbidden line emission, with, for example, $\frac{[\mathrm{OIII}]\lambda 5007}{\mathrm{H}\beta\ \lambda 4861} > 3$.

- **Low Ionization Nuclear Emission Line Regions (LINER's)**: LINER's have strong emission in low-ionization species, such as $[\mathrm{OI}]\lambda 6300$ and $[\mathrm{SII}]\lambda\lambda 6716, 6731$,

but they tend to have weaker [OIII]$\lambda\lambda$4959, 5007 emission than Sy2 galaxies, with $\frac{[\mathrm{OIII}]\lambda 5007}{\mathrm{H}\beta\ \lambda 4861}$ <3 (Heckman 1980). Because of this, LINERs are not expected to make up a significant portion of either sample for this thesis, which is based primarily on the strength of [OIII]$\lambda\lambda$4959, 5007. LINER's are suspected to be photoionized by a power-law source in their nucleus, similar to the source in Sy2 galaxies, but this is still uncertain.

- **HII Region galaxies (HII)**: HII galaxies have spectra similar to those found in the star-forming regions in our own galaxy, and are therefore believed to be caused by the formation of a large number of hot, OB stars. They tend to have strong [OIII]$\lambda\lambda$4959, 5007, but are weak in most of the other forbidden emission lines. These objects were first studied by Sargent and Searle (1970). French (1980) studied a sample of 14 galaxies, with the spectra of HII regions. 10 of these objects were of low-luminosity (M>-17, H_0 = 75 km sec^{-1} Mpc^{-1}), while the other four were bright (M≤-20). The bright galaxies were included for comparison purposes.
- **Starburst Galaxies (SBs)**: These objects are galaxies undergoing a substantial burst in star formation, with a preponderance of massive O and B stars which ionize the surrounding medium. These bursts tend to occur in the nuclei of the host galaxy. Spectroscopically, SBs appear similar to the HII Region galaxies, with strong [OIII]$\lambda\lambda$4959, 5007 and weaker in other forbidden lines. However, since they occur in larger galaxies, these objects tend to be more luminous.

Salzer et al. (1989b), in describing the properties of the emission line galaxies from the UM survey, classify star-forming galaxies into a number of different catagories. Their scheme is based on criteria that includes absolute magnitudes and sizes as well as the morphological appearances of the UM emission line galaxies and they minimize the extent to which line ratio diagnostics are used to classify those objects. This is so that they can examine the correlations of various line ratios with galaxy type. For this thesis, there is no detailed size or morphological information available for the

distant sample, and thus classification based on the line ratio analysis from the slit spectra is the only viable option. While other researchers may differentiate between a SB Galaxy and an HII galaxy based on a different set of criteria, such as morphology, for the purpose of this thesis, I am defining a SB Galaxy as having M_{4400} <-18, as measured by the grism survey. The calculation of the magnitude is shown in section 2.3.5. Objects which are fainter than this limit, which have the spectral signature of ionization from hot stars will be classified as HII Region Galaxies.

An analysis of the line ratios of the 370 galaxies in the SSG sample shows that 12% are Syl galaxies, 24% are Sy2 galaxies, 43% are Starbursts and 18% are HII galaxies while the remaining 3% are LINER's. Table 2–3 lists the classification and enumerates the measured line flux ratios for the logs of $\frac{[OII]\lambda 3727}{[OIII]\lambda 5007}$; $\frac{[OIII]\lambda 5007}{H\beta\ \lambda 4861}$; $\frac{[NII]\lambda 6583}{H\alpha\ \lambda 6563}$; $\frac{[SII]\lambda\lambda 6716,6731}{H\alpha\ \lambda 6563}$; and $\frac{[OI]\lambda 6300}{H\alpha\ \lambda 6563}$ for each object in the sample, as well as the ratio of $\frac{H\alpha\ \lambda 6563}{H\beta\ \lambda 4861}$. Reddening corrections are not made, in general because of great uncertainty in measuring the Balmer decrement in objects at higher redshifts, where Hα λ6563 is located in a noisy region of the spectrum. In addition, the various line ratios are plotted in Figures 2–10(a)-(d) (a la the plots in BPT and VO).

A difference to note between these plots and those of VO are that there is a clean separation between star-forming and active galaxies in the plots of VO, while in Figures 2–10 there is a greater degree of scatter which results in certain objects with line ratios that could be due either to star formation or to an active nucleus. The two principle reasons for this scatter are measurement uncertainties for the SSG spectra as well as the possibility that there truly are transitional objects which display both types of activity, but which were either not present or were ignored by VO in their paper. For the first issue, based on discussions that I have had with Dr. Charles Lawrence, the author of the line-fitting routine FIT, the range of uncertainty in the measurement of the line fluxes is as high as 100% for objects with weak emission lines, such as [OI]λ6300. In addition, since the typical 4-Shooter spectrum has a

resolution of 25Å, the [NII]$\lambda\lambda$6548, 6583 and Hα λ6563 lines were generally blended together, and the success in deblending these lines is, at times, questionable. Since Figures 2–10(b)-(d) all depend on the measurement of Hα λ6563, this deblending does cause additional uncertainty in the measurements of those line ratios. That said, the typical uncertainty in the logarithm of the line ratios is 0.1 to 0.2 for the SSG galaxies. As to the second possibility described above, VO used a sample that was intended to maximize the differences between ionization mechanisms, so that the suitability of their method would be best demonstrated. This would not deny the possibility that there are galaxies which display both types of photoionization, and as such, would occupy either the transition region between AGN and starbursts in these plots or else would appear to have AGN-like properties in certain line ratios (such as $\frac{[OI]\lambda 6300}{H\alpha\ \lambda 6563}$) while having starburst-like properties with other line ratios. Indeed, in Figures 2–10(b)-(d), there are several objects which appear to have strong $\frac{[OI]\lambda 6300}{H\alpha\ \lambda 6563}$, thus classifying them as Seyfert 2 galaxies, while their $\frac{[NII]\lambda 6583}{H\alpha\ \lambda 6563}$ or their $\frac{[SII]\lambda\lambda 6716,6731}{H\alpha\ \lambda 6563}$ ratios are too weak to be considered AGN (note that in all three plots, they would have identical values for the $\frac{[OIII]\lambda 5007}{H\beta\ \lambda 4861}$ ratio). It is the combination of these two effects which results in the overlap that is observed between AGN and star-forming galaxies in Figures 2–10(a)-(d).

The effect of this overlap on the results obtained in this thesis pertains to the issue of how accurate are the object classifications. Since I utilized the $\frac{[OI]\lambda 6300}{H\alpha\ \lambda 6563}$ line ratio as the primary criterion for active galaxies, if this ratio was overestimated for a particular object, then that object should be moved from the Seyfert 2 catagory into one of the star-forming catagories. It is unlikely that this ratio would be underestimated, which would result in a galaxy classified as a star-forming object being, in fact, an AGN. For that possibility, the spectra would have to have been too noisy to get a measurement of the [OI]λ6300 line flux, and in those cases, I generally relied on the other line ratios for object classification. As demonstrated in Chapter 5, the SSG

survey appears to underestimate the total predicted numbers of all galaxy types, particularly Seyfert galaxies, so if I misclassified one of the SSG galaxies as a Seyfert 2, then this underestimate would be exaggerated even further.

References

Antonucci, R. and Miller, J., 1985, *Ap. J.*, **297**, 621

Avni, Y. and Bahcall, J., 1980, *Ap. J.*, **235**, 694

Baldwin, J., Phillips, M. and Terlevich, R., 1981, *Publ. Ast. Soc. Pac.*, **93**, 5 (BPT)

Elvis, M., et al., 1978, *MNRAS*, **183**, 129

French, H., 1980, *Ap. J.*, **240**, 41

Heckman, T., 1980, *Astr. Ap.*, **87**, 152

Lawrence, A. and Elvis, M., 1982, *Ap. J.*, **256**, 410

Sargent, W. and Searle, L., 1970, *Ap. J. (Lett.)*, **162**, 155

Schmidt, M., 1968, *Ap. J.*, **151**, 393

Schmidt, M. and Green, R., 1986, *Ap. J.*, **305**, 68

Schmidt, M., Schneider, D. and Gunn, J., 1986a, *Ap. J.*, **306**, 411

—, 1986b, *Ap. J.*, **310**, 518

—, 1987a, *Ap. J. (Lett.)*, **316**, 1

—, 1987b, *Ap. J. (Lett.)*, **321**, 7

—, 1988, In *Astr. Soc. Pac. Conference Proceedings 2: Optical Surveys for Quasars*, ed. P. Osmer et al. (Brigham Young University:Provo), p. 87

—, 1989a, *A. J.*, **98**, 1507

—, 1989b, *A. J.*, **98**, 1951

—, 1994, *A. J.*, **107**, 1245

Turner, T. and Pounds, K., 1989, *MNRAS*, **240**, 833

Veilleux, S. and Osterbrock, D., 1987, *Ap. J. Suppl.*, **63**, 295 (VO)

Zucker, J. and Lawrence, C., 1988, FIT User's Manual, Caltech, Pasadena, CA

Table 2–1. Observational Parameters of Transit Survey Fields.

Survey Name	Right Ascension	Decl	Exp Time (sec)	Seeing FWHM (arc sec)	sec z	$\log f_\lambda^{lim}$ (6100Å)	Eff Area (sq. deg.)	$\bar{\lambda}$ (Å)
GH	$20^h45^m - 04^h45^m$	01°20'	34.8	1.80	1.18	-14.180	13.73	4969
IJ	$07^h00^m - 10^h25^m$	56°30'	62.6	2.20	1.09	-14.227	3.75	4976
KL	$11^h35^m - 16^h40^m$	38°00'	44.0	2.70	1.00	-14.108	7.83	4945
MN	$09^h05^m - 16^h50^m$	46°40'	50.5	1.65	1.11	-14.333	10.06	4987
OP	$21^h05^m - 04^h35^m$	02°20'	34.8	2.00	1.28	-14.101	14.58	4971
QR	$08^h05^m - 17^h15^m$	47°50'	51.6	1.65	1.05	-14.276	12.01	4985

Table 2–2. [OIII]$\lambda\lambda$4959, 5007 and Hβ λ4861 Galaxies from SSG Survey

Object	Rt Asc	Dec	λ_{bin}	z_{obs}	EW(Å)	S/N	$\log f_\lambda^{obs}$
0001+0214	00 01 02.3	+02 14 07	6195.5	0.232	2429.47	7.89	-14.185
0002+0118	00 02 01.1	+01 18 14	5343.0	0.086	279.58	9.95	-13.948
0004+0215	00 04 14.3	+02 15 15	5730.5	0.148	1323.81	20.11	-13.728
0007+0217	00 07 05.9	+02 17 37	5110.5	0.038	313.65	13.07	-13.799
0012+0219	00 12 36.1	+02 19 08	6815.5	0.362	432.81	7.92	-14.171
0028+0215	00 28 42.1	+02 15 33	5963.0	0.197	74.94	7.76	-14.166
0033+0220	00 33 22.6	+02 20 41	5730.5	0.154	146.64	7.07	-14.181
0036+0215	00 36 05.5	+02 15 22	6893.0	0.389	226.82	14.04	-13.882
0037+0119	00 37 12.2	+01 19 12	5265.5	0.065	1730.76	7.95	-14.022
0042+0218	00 42 02.5	+02 18 30	5885.5	0.185	63.59	7.83	-14.147
0047+0123	00 47 05.0	+01 23 42	5420.5	0.097	526.40	16.45	-13.745
0053+0221	00 53 00.2	+02 21 01	5808.0	0.164	359.93	10.69	-14.006
0055+0119	00 55 51.3	+01 19 32	5885.5	0.185	3217.80	7.50	-14.113
0100+0122	01 00 40.5	+01 22 36	5963.0	0.197	764.55	12.04	-13.926
0107+0213	01 07 47.9	+02 13 54	6660.5	0.347	361.87	8.66	-14.146
0116+0126A	01 16 50.9	+01 26 41	5420.5	0.087	107.55	8.16	-14.049
0116+0126B	01 16 51.0	+01 26 32	5343.0	0.088	64.46	22.21	-13.600
0116+0123	01 16 52.6	+01 23 39	5343.0	0.072	774.15	142.31	-12.793
0125+0222	01 25 25.8	+02 22 16	6583.0	0.334	86.24	14.00	-13.941
0128+0222	01 28 36.0	+02 22 00	5963.0	0.204	879.79	18.64	-13.786
0132+0221	01 32 47.9	+02 21 09	5188.0	0.046	407.12	7.43	-14.068
0134+0119	01 34 14.7	+01 19 48	5110.5	0.031	172.99	17.04	-13.652
0135+0119	01 35 22.4	+01 19 19	6660.5	0.333	1175.42	12.57	-13.928
0142+0123	01 42 08.7	+01 23 34	5885.5	0.175	162.14	8.68	-14.050
0142+0126	01 42 32.1	+01 26 51	5808.0	0.148	190.49	25.54	-13.567
0143+0121	01 43 38.8	+01 21 02	6118.0	0.231	155.32	23.61	-13.652
0146+0222	01 46 43.3	+02 22 24	5498.0	0.106	1388.33	22.41	-13.671
0148+0126	01 48 49.6	+01 26 59	5033.0	0.017	370.71	18.88	-13.592
0151+0124	01 51 34.7	+01 24 11	6428.0	0.312	94.39	8.00	-14.127
0157+0124	01 57 10.1	+01 24 38	5343.0	0.066	1852.51	9.12	-13.986
0159+0119	01 59 12.9	+01 19 37	5808.0	0.158	685.94	49.57	-13.279
0159+0219	01 59 31.4	+02 19 08	6660.5	0.336	355.11	33.80	-13.555
0201+0126	02 01 35.4	+01 26 40	5343.0	0.073	375.86	11.00	-13.905
0208+0218	02 08 22.1	+02 18 04	5033.0	0.023	305.74	10.01	-13.886
0208+0221	02 08 48.1	+02 21 59	5575.5	0.131	79.85	17.76	-13.780
0209+0120	02 09 23.4	+01 20 50	5188.0	0.044	185.32	8.94	-13.952
0211+0124	02 11 17.5	+01 24 57	6428.0	0.281	688.43	9.36	-14.059
0217+0124	02 17 15.9	+01 24 25	6428.0	0.290	186.24	8.97	-14.077
0218+0122	02 18 25.7	+01 22 24	6350.5	0.287	368.59	7.73	-14.138
0221+0217	02 21 01.6	+02 17 55	5033.0	0.029	62.34	19.52	-13.596
0222+0223	02 22 36.5	+02 23 07	6660.5	0.322	488.94	12.50	-13.987
0223+0125	02 23 57.3	+01 25 04	6428.0	0.284	129.50	10.20	-14.021
0231+0216	02 31 13.5	+02 16 17	6505.5	0.321	181.19	45.05	-13.436
0235+0121	02 35 35.2	+01 21 22	6738.0	0.394	70.93	19.95	-13.724
0235+0220	02 35 56.9	+02 20 53	5963.0	0.209	152.96	41.18	-13.441
0300+0221	03 00 21.1	+02 21 45	5420.5	0.088	643.14	11.68	-13.940
0302+0217	03 02 30.5	+02 17 16	5653.0	0.146	63.72	7.47	-14.159

Table 2–2. (cont.)

Object	Rt Asc	Dec	λ_{bin}	z_{obs}	EW(Å)	S/N	$\log f_\lambda^{obs}$
0303+0126	03 03 02.9	+01 26 13	5963.0	0.198	621.73	23.54	-13.635
0309+0223	03 09 04.4	+02 23 07	5033.0	0.020	823.75	112.87	-12.834
0311+0123	03 11 58.0	+01 23 46	5575.5	0.131	356.23	22.94	-13.612
0323+0219	03 23 55.0	+02 19 58	6428.0	0.276	453.59	14.11	-13.937
0324+0124	03 24 58.3	+01 24 05	5808.0	0.164	1396.22	15.43	-13.786
0340+0124	03 40 22.7	+01 24 32	6970.5	0.389	633.82	10.60	-13.968
0349+0126	03 49 29.8	+01 26 42	6583.0	0.322	560.64	8.47	-14.102
0404+0125	04 04 24.4	+01 25 37	5188.0	0.050	70.48	8.46	-13.976
0405+0226	04 05 28.2	+02 26 37	5343.0	0.091	316.83	9.15	-14.026
0419+0126	04 19 03.9	+01 26 01	5885.5	0.181	153.41	11.17	-13.940
0434+0133	04 34 57.2	+01 33 17	6505.5	0.294	1686.99	11.06	-13.986
0720+5620	07 20 07.9	+56 20 23	5420.5	0.087	146.28	9.93	-13.978
0735+5621	07 35 53.5	+56 21 53	5575.5	0.117	334.68	34.16	-13.453
0736+5621	07 36 06.4	+56 21 41	5808.0	0.177	269.12	6.80	-14.156
0804+5620	08 04 09.8	+56 20 59	7048.0	0.408	113.16	12.98	-13.899
0812+4744	08 12 40.7	+47 44 37	7082.0	0.430	90.79	6.71	-14.227
0817+5625	08 17 43.3	+56 25 36	5265.5	0.066	344.15	15.67	-13.741
0821+4749	08 21 58.3	+47 49 44	6152.0	0.231	1964.11	9.05	-14.133
0822+5622	08 22 50.2	+56 22 25	5420.5	0.089	120.69	6.74	-14.146
0823+5621	08 23 27.1	+56 21 09	5110.5	0.032	69.70	7.11	-14.041
0824+4749	08 24 53.0	+47 49 28	5480.3	0.097	307.41	10.55	-14.001
0825+5622	08 25 13.6	+56 22 40	6350.5	0.284	71.40	15.90	-13.846
0829+4745	08 29 26.6	+47 45 35	5273.7	0.050	724.41	25.32	-13.573
0850+5623	08 50 06.5	+56 23 25	7048.0	0.409	307.17	13.79	-13.872
0851+5628	08 51 28.2	+56 28 27	7048.0	0.442	134.24	19.32	-13.726
0851+5625	08 51 44.5	+56 25 21	5110.5	0.014	95.97	7.71	-14.006
0854+5622	08 54 51.6	+56 22 14	5265.5	0.066	750.63	9.96	-13.938
0855+5622	08 55 15.0	+56 22 54	5343.0	0.083	732.25	6.62	-14.135
0902+5622	09 02 29.1	+56 22 20	5188.0	0.047	98.17	18.40	-13.652
0904+5621	09 04 42.2	+56 21 45	5808.0	0.174	103.46	7.03	-14.142
0906+4750	09 06 20.7	+47 50 07	6513.7	0.297	1778.40	26.21	-13.670
0913+5628	09 13 30.3	+56 28 00	5265.5	0.072	108.41	8.46	-14.009
0913+4744	09 13 56.0	+47 44 51	6100.3	0.237	106.82	6.59	-14.270
0918+4634	09 18 33.1	+46 34 36	5170.3	0.041	78.00	8.14	-13.983
0920+5627	09 20 36.0	+56 27 44	7203.0	0.425	2709.72	8.83	-13.994
0922+4639	09 22 09.0	+46 39 25	5945.3	0.185	67.15	7.34	-14.157
0927+4640	09 27 41.4	+46 40 19	6772.0	0.350	206.36	7.40	-14.179
0929+4634	09 29 40.0	+46 34 45	6978.7	0.387	113.51	10.50	-13.998
0930+4633	09 30 55.3	+46 33 15	5790.3	0.152	225.73	19.32	-13.687
0930+4636	09 30 57.3	+46 36 32	5790.3	0.166	77.92	12.84	-13.864
0931+4640	09 31 31.9	+46 40 21	5222.0	0.047	200.42	12.11	-13.830
0933+4750	09 33 42.5	+47 50 17	5325.3	0.065	100.61	9.35	-14.020
0934+4637	09 34 01.7	+46 37 34	5325.3	0.066	2337.38	22.64	-13.592
0936+5623	09 36 50.1	+56 23 38	5963.0	0.191	1519.59	12.49	-13.920
0943+4638	09 43 46.7	+46 38 17	6152.0	0.225	182.31	23.83	-13.669
0944+5625	09 44 32.7	+56 25 09	6428.0	0.293	925.87	6.48	-14.232
0946+5627	09 46 30.8	+56 27 39	6350.5	0.280	541.34	7.49	-14.172

Table 2–2. (cont.)

Object	Rt Asc	Dec	λ_{bin}	z_{obs}	EW(Å)	S/N	$\log f_\lambda^{obs}$
0946+4636	09 46 34.5	+46 36 11	6513.7	0.307	798.99	8.52	-14.119
0947+4745	09 47 53.8	+47 45 46	6565.3	0.307	581.69	6.50	-14.273
0948+4750	09 48 14.5	+47 50 58	5118.7	0.023	753.61	14.48	-13.764
0948+4753	09 48 37.5	+47 53 17	6203.7	0.250	290.62	9.30	-14.123
0952+5628	09 52 53.2	+56 28 34	6428.0	0.284	321.58	19.39	-13.756
0955+4753	09 55 21.9	+47 53 16	6978.7	0.419	88.44	12.77	-13.958
0955+4747	09 55 51.7	+47 47 29	5325.3	0.067	1345.92	6.60	-14.171
0958+4746	09 58 00.9	+47 46 34	6978.7	0.393	123.63	11.49	-14.004
0959+4634	09 59 10.0	+46 34 49	5893.7	0.181	92.13	11.90	-13.928
1000+4753	10 00 37.9	+47 53 51	6668.7	0.334	206.61	7.97	-14.185
1004+4641	10 04 06.2	+46 41 02	5428.7	0.086	1127.74	15.09	-13.792
1004+4751	10 04 35.9	+47 51 16	5738.7	0.151	711.24	14.67	-13.863
1010+5624	10 10 44.0	+56 24 22	5343.0	0.070	377.10	15.91	-13.754
1010+4634	10 10 56.6	+46 34 45	6462.0	0.321	71.14	27.57	-13.610
1013+4637	10 13 03.4	+46 37 14	5945.3	0.187	126.44	9.08	-14.065
1015+4641A	10 15 10.8	+46 41 24	5377.0	0.080	229.85	69.76	-13.117
1015+4641B	10 15 11.1	+46 41 27	5377.0	0.079	872.69	172.75	-12.724
1015+4639	10 15 21.0	+46 39 18	5635.3	0.123	97.96	9.57	-14.011
1016+4747	10 16 27.5	+47 47 38	6720.3	0.341	624.83	7.69	-14.200
1016+5630	10 16 56.0	+56 30 37	6893.0	0.387	270.21	10.31	-13.975
1018+5631	10 18 18.5	+56 31 32	5343.0	0.046	94.39	7.95	-14.055
1019+4750	10 19 52.6	+47 50 06	5687.0	0.144	83.81	16.84	-13.809
1023+4748	10 23 37.4	+47 48 12	5738.7	0.151	146.41	10.32	-14.016
1024+4639	10 24 05.1	+46 39 53	5222.0	0.059	74.37	11.91	-13.837
1025+4749	10 25 50.0	+47 49 05	5170.3	0.051	72.59	7.59	-14.059
1028+4641	10 28 02.9	+46 41 41	5325.3	0.093	58.65	16.39	-13.733
1034+4636	10 34 03.5	+46 36 18	5842.0	0.174	856.79	13.77	-13.843
1038+4637	10 38 19.2	+46 37 46	6720.3	0.340	125.93	7.94	-14.151
1039+4754	10 39 28.8	+47 54 22	5428.7	0.090	125.43	6.84	-14.180
1040+4634	10 40 20.0	+46 34 43	5635.3	0.128	398.90	7.90	-14.095
1046+4752	10 46 52.3	+47 52 36	5325.3	0.062	700.75	9.83	-13.998
1050+4637A	10 50 17.0	+46 37 13	5170.3	0.038	339.70	11.03	-13.852
1050+4637B	10 50 24.3	+46 37 24	5377.0	0.086	52.07	7.39	-14.092
1052+4638	10 52 51.2	+46 38 17	5222.0	0.050	60.19	10.20	-13.905
1057+4635	10 57 12.8	+46 35 04	5583.7	0.126	242.58	13.72	-13.851
1058+4755	10 58 52.0	+47 55 27	5273.7	0.064	512.67	6.57	-14.159
1059+4749	10 59 01.8	+47 49 48	5635.3	0.121	82.38	6.55	-14.220
1059+4752	10 59 58.9	+47 52 32	5015.3	0.018	261.85	9.65	-13.915
1102+4641	11 02 51.0	+46 41 02	5015.3	0.006	2515.91	7.51	-13.989
1103+4636	11 03 36.2	+46 36 20	5222.0	0.053	145.81	10.61	-13.887
1105+4641	11 05 08.9	+46 41 01	6152.0	0.237	133.95	7.85	-14.151
1105+4636	11 05 58.1	+46 36 52	6410.3	0.279	1350.21	8.10	-14.142
1107+4754	11 07 01.0	+47 54 33	6565.3	0.315	84.90	10.62	-14.060
1108+4643	11 08 08.1	+46 43 15	5222.0	0.052	416.41	15.52	-13.722
1108+4749	11 08 36.0	+47 49 20	5325.3	0.070	180.45	21.44	-13.660
1109+4755	11 09 16.5	+47 55 13	5377.0	0.083	642.28	41.35	-13.389
1110+4642	11 10 37.0	+46 42 56	6823.7	0.372	209.26	9.04	-14.083

Table 2–2. (cont.)

Object	Rt Asc	Dec	λ_{bin}	z_{obs}	EW(Å)	S/N	$\log f_\lambda^{obs}$
1113+4643	11 13 13.3	+46 43 21	6255.3	0.248	221.84	10.85	-14.018
1114+4752	11 14 38.0	+47 52 16	7030.3	0.434	77.93	8.47	-14.134
1115+4637	11 15 45.7	+46 37 22	5222.0	0.043	750.84	13.06	-13.797
1117+4643	11 17 45.6	+46 43 22	6358.7	0.275	142.88	15.70	-13.858
1119+4750	11 19 33.9	+47 50 26	5377.0	0.076	174.37	16.72	-13.783
1120+4640	11 20 15.4	+46 40 05	7082.0	0.418	400.89	7.11	-14.170
1120+4636	11 20 38.2	+46 36 22	6203.7	0.235	777.58	9.12	-14.092
1122+4753	11 22 16.0	+47 53 59	5532.0	0.108	142.56	13.25	-13.906
1125+4639	11 25 01.2	+46 39 35	6255.3	0.271	98.75	7.31	-14.189
1128+4753	11 28 26.9	+47 53 31	5222.0	0.042	172.27	13.11	-13.840
1132+4755	11 32 02.4	+47 55 07	5532.0	0.103	116.71	7.16	-14.173
1140+4641	11 40 01.8	+46 41 13	5428.7	0.116	54.22	38.63	-13.384
1141+4752	11 41 06.6	+47 52 54	6048.7	0.208	954.78	17.07	-13.850
1144+4749	11 44 35.3	+47 49 39	5325.3	0.073	56.24	14.93	-13.817
1145+4638	11 45 09.7	+46 38 26	5738.7	0.150	954.78	15.80	-13.783
1149+4754	11 49 00.2	+47 54 46	5170.3	0.053	71.76	7.47	-14.066
1150+3756	11 50 14.7	+37 56 08	5110.5	0.038	179.73	10.96	-13.757
1150+4750	11 50 50.5	+47 50 21	5790.3	0.150	112.35	7.07	-14.175
1154+3754	11 54 09.1	+37 54 40	6660.5	0.339	188.62	7.66	-14.074
1155+4638	11 55 53.2	+46 38 37	6307.0	0.259	1916.78	8.75	-14.111
1157+4754	11 57 35.7	+47 54 00	5273.7	0.062	264.67	23.07	-13.614
1157+4753	11 57 43.7	+47 53 57	5687.0	0.132	106.55	12.46	-13.939
1200+4755	12 00 25.0	+47 55 53	5015.3	0.001	64.78	9.54	-13.920
1203+3801	12 03 02.6	+38 01 28	6195.5	0.245	3600.26	8.46	-14.032
1204+3755	12 04 26.6	+37 55 46	5885.5	0.187	85.89	22.58	-13.562
1206+4748	12 06 34.6	+47 48 48	5842.0	0.182	76.32	11.75	-13.964
1208+3754	12 08 25.4	+37 54 33	5265.5	0.065	146.95	7.45	-13.973
1211+3800	12 11 00.9	+38 00 39	6040.5	0.217	425.26	11.03	-13.899
1214+4636	12 14 25.1	+46 36 15	7133.7	0.402	84.23	7.03	-14.160
1214+3801	12 14 39.7	+38 01 38	4955.5	0.001	427.83	243.64	-12.356
1215+4755	12 15 48.2	+47 55 48	6100.3	0.221	701.10	9.18	-14.126
1216+4637	12 16 05.6	+46 37 47	6462.0	0.291	425.56	7.67	-14.165
1216+4753	12 16 58.7	+47 53 50	5945.3	0.183	328.72	6.55	-14.245
1217+4750	12 17 40.1	+47 50 25	5325.3	0.067	149.27	9.24	-14.025
1218+4640	12 18 26.9	+46 40 56	5687.0	0.123	160.15	12.57	-13.892
1219+4638A	12 19 40.4	+46 38 45	5893.7	0.185	108.56	10.14	-13.998
1219+4638B	12 19 42.4	+46 38 33	5842.0	0.185	103.76	9.39	-14.010
1220+4748	12 20 47.3	+47 48 43	5428.7	0.103	691.76	17.25	-13.778
1221+4752	12 21 21.1	+47 52 12	6565.3	0.307	546.08	24.99	-13.688
1221+4753	12 21 32.5	+47 53 44	5067.0	0.031	92.98	16.12	-13.707
1222+4754	12 22 17.7	+47 54 32	6720.3	0.368	65.82	7.97	-14.184
1224+3756	12 24 20.9	+37 56 38	5188.0	0.051	1082.45	40.56	-13.213
1227+3756	12 27 02.0	+37 56 20	6273.0	0.255	518.75	7.84	-14.067
1227+4749	12 27 57.9	+47 49 10	5893.7	0.181	356.13	6.67	-14.224
1229+4639	12 29 39.9	+46 39 09	5842.0	0.165	86.79	16.80	-13.757
1231+4748	12 31 43.5	+47 48 31	6462.0	0.292	295.34	8.99	-14.135
1233+4754	12 33 02.3	+47 54 12	5945.3	0.191	626.77	6.53	-14.247

Table 2–2. (cont.)

Object	Rt Asc	Dec	λ_{bin}	z_{obs}	EW(Å)	S/N	$\log f_\lambda^{obs}$
1233+4752	12 33 40.1	+47 52 08	6100.3	0.231	114.96	16.79	-13.864
1234+4752	12 34 40.0	+47 52 07	5377.0	0.080	213.18	8.80	-14.062
1237+4642	12 37 04.2	+46 42 13	5738.7	0.166	52.71	7.14	-14.128
1238+3757	12 38 03.8	+37 57 57	6505.5	0.320	149.99	12.22	-13.875
1238+3755	12 38 10.3	+37 55 43	5808.0	0.188	77.17	7.16	-14.051
1240+4641	12 40 40.3	+46 41 50	6565.3	0.315	3087.86	8.25	-14.133
1244+3800	12 44 04.3	+38 00 23	6815.5	0.365	699.15	8.06	-14.041
1245+4754	12 45 03.4	+47 54 13	5480.3	0.096	281.81	6.80	-14.191
1246+4636	12 46 44.2	+46 36 50	5480.3	0.089	572.67	7.27	-14.114
1246+4635	12 46 45.0	+46 35 52	5945.3	0.182	1002.71	11.25	-13.972
1247+4752	12 47 26.0	+47 52 53	5997.0	0.206	63.92	6.98	-14.232
1247+4641	12 47 30.3	+46 41 17	6203.7	0.237	540.36	10.28	-14.040
1247+4640	12 47 34.0	+46 40 59	6255.3	0.237	851.56	15.25	-13.870
1248+4752	12 48 30.7	+47 52 18	5067.0	0.030	133.86	16.25	-13.704
1251+4636	12 51 39.1	+46 36 28	5222.0	0.042	589.86	30.80	-13.424
1253+4635	12 53 14.3	+46 35 51	5222.0	0.049	241.94	13.32	-13.788
1253+4754	12 53 50.5	+47 54 53	6823.7	0.359	302.42	11.52	-14.018
1257+4643	12 57 47.1	+46 43 19	5170.3	0.038	473.07	6.97	-14.051
1300+3757	13 00 19.6	+37 57 42	5885.5	0.180	167.38	14.16	-13.765
1301+3801	13 01 00.5	+38 01 02	5343.0	0.086	368.81	11.73	-13.795
1301+4641	13 01 42.1	+46 41 15	6048.7	0.206	540.55	36.72	-13.474
1305+3756	13 05 09.4	+37 56 27	6583.0	0.332	98.94	7.93	-14.059
1309+4636	13 09 09.9	+46 36 16	7133.7	0.415	464.67	7.45	-14.135
1309+4640	13 09 53.7	+46 40 23	6617.0	0.329	195.21	8.81	-14.106
1310+3801	13 10 32.5	+38 01 07	5033.0	0.022	169.86	12.28	-13.683
1314+4638	13 14 08.2	+46 38 38	5480.3	0.100	450.33	21.93	-13.634
1316+3754	13 16 04.3	+37 54 23	5575.5	0.126	142.05	11.14	-13.853
1320+4750	13 20 32.1	+47 50 28	5428.7	0.092	132.59	6.56	-14.198
1321+3759	13 21 39.6	+37 59 14	6893.0	0.392	250.38	7.96	-14.013
1324+4635	13 24 29.9	+46 35 23	6823.7	0.362	623.12	23.04	-13.677
1324+4749	13 24 31.3	+47 49 01	5945.3	0.197	218.81	19.20	-13.779
1324+4637	13 24 55.7	+46 37 17	5893.7	0.179	77.34	7.22	-14.146
1325+4635	13 25 34.7	+46 35 11	5377.0	0.085	842.86	15.55	-13.769
1325+4639	13 25 56.0	+46 39 45	6048.7	0.222	145.15	6.96	-14.196
1326+4637	13 26 21.8	+46 37 47	5893.7	0.183	96.37	9.43	-14.030
1332+4748	13 32 25.5	+47 48 21	5273.7	0.061	133.26	7.22	-14.118
1335+4749	13 35 00.9	+47 49 39	6720.3	0.344	1846.57	7.08	-14.236
1340+4635	13 40 25.8	+46 35 49	5325.3	0.075	155.42	18.83	-13.672
1343+4753	13 43 04.4	+47 53 50	6978.7	0.399	166.94	10.57	-14.040
1348+4634	13 48 55.4	+46 34 23	5325.3	0.064	241.15	11.26	-13.896
1349+4749	13 49 38.2	+47 49 01	6823.7	0.355	182.51	10.19	-14.071
1353+4746	13 53 19.1	+47 46 37	6823.7	0.367	339.59	10.84	-14.044
1354+4749	13 54 32.2	+47 49 47	6100.3	0.216	548.72	8.52	-14.159
1357+4747	13 57 47.4	+47 47 28	6513.7	0.304	68.80	7.16	-14.234
1400+4638	14 00 10.5	+46 38 38	6100.3	0.237	70.37	13.52	-13.914
1401+3753	14 01 42.1	+37 53 12	6815.5	0.368	704.39	15.63	-13.753
1403+4634	14 03 07.7	+46 34 07	5893.7	0.183	569.61	70.26	-13.157

Table 2–2. (cont.)

Object	Rt Asc	Dec	λ_{bin}	z_{obs}	EW(Å)	S/N	$\log f_\lambda^{obs}$
1403+4635	14 03 42.6	+46 35 14	7082.0	0.457	144.56	7.44	-14.151
1406+4750	14 06 06.2	+47 50 22	6772.0	0.373	78.69	7.05	-14.238
1407+4748	14 07 26.1	+47 48 03	6048.7	0.217	328.73	10.62	-14.056
1410+4639	14 10 34.5	+46 39 50	6978.7	0.394	300.27	12.26	-13.931
1411+4753	14 11 51.2	+47 53 49	5015.3	0.008	296.62	61.14	-13.114
1412+4640	14 12 01.3	+46 40 49	5842.0	0.168	201.76	8.85	-14.035
1417+3752	14 17 52.4	+37 52 59	7203.0	0.479	56.84	15.81	-13.670
1419+4747	14 19 05.1	+47 47 43	5377.0	0.070	352.03	12.67	-13.903
1419+4638	14 19 55.4	+46 38 57	6978.7	0.419	120.94	15.19	-13.838
1420+4748	14 20 07.2	+47 48 02	6772.0	0.348	1246.90	6.52	-14.273
1420+4752	14 20 38.4	+47 52 55	5635.3	0.131	89.18	10.05	-14.034
1421+4749	14 21 36.6	+47 49 09	5325.3	0.072	75.30	20.45	-13.680
1423+4751	14 23 51.0	+47 51 09	5273.7	0.072	64.77	10.39	-13.960
1435+3753	14 35 33.1	+37 53 31	6505.5	0.335	61.69	10.43	-13.944
1435+3757	14 35 52.1	+37 57 50	6738.0	0.333	465.37	7.68	-14.070
1435+4635	14 35 52.2	+46 35 50	5325.3	0.073	110.90	8.91	-13.997
1436+4748	14 36 10.7	+47 48 40	7030.3	0.436	70.11	8.58	-14.128
1438+4634	14 38 02.7	+46 34 08	5325.3	0.074	66.11	15.02	-13.770
1439+4753	14 39 34.4	+47 53 17	5635.3	0.134	253.14	9.71	-14.049
1441+4635	14 41 38.7	+46 35 35	5067.0	0.010	64.54	23.74	-13.500
1442+4633A	14 42 11.0	+46 33 43	5738.7	0.150	979.41	8.37	-14.058
1442+4633B	14 42 55.4	+46 33 44	6462.0	0.289	2870.86	7.92	-14.151
1445+4746	14 45 59.1	+47 46 45	5480.3	0.081	243.48	6.68	-14.199
1446+3751	14 46 56.4	+37 51 02	5265.5	0.070	626.49	8.69	-13.906
1447+4634	14 47 21.2	+46 34 12	6048.7	0.200	470.88	10.46	-14.020
1448+4749	14 48 27.5	+47 49 59	5790.3	0.160	121.95	9.44	-14.050
1450+4747	14 50 37.7	+47 47 24	6823.7	0.359	99.04	8.62	-14.143
1451+4635	14 51 34.0	+46 35 12	5428.7	0.087	404.48	8.84	-14.025
1451+4748	14 51 45.6	+47 48 10	6513.7	0.300	68.89	6.92	-14.249
1452+3756	14 52 49.7	+37 56 14	5265.5	0.059	6123.27	15.31	-13.660
1452+4747	14 52 51.4	+47 47 49	5325.3	0.070	120.79	9.97	-13.992
1454+4748	14 54 19.8	+47 48 23	5583.7	0.125	171.12	8.71	-14.092
1454+4634	14 54 57.8	+46 34 33	6978.7	0.386	290.65	9.14	-14.058
1456+4635	14 56 22.1	+46 35 39	5170.3	0.037	69.75	8.24	-13.978
1459+4632	14 59 25.2	+46 32 40	5118.7	0.031	100.17	18.35	-13.621
1502+4639	15 02 12.8	+46 39 08	5377.0	0.078	55.82	13.76	-13.823
1504+4637	15 04 46.1	+46 37 18	6203.7	0.235	351.72	8.89	-14.103
1506+4633	15 06 18.7	+46 33 25	5480.3	0.095	109.71	31.50	-13.477
1506+4637	15 06 23.8	+46 37 27	6255.3	0.247	767.62	8.03	-14.148
1508+3750	15 08 46.0	+37 50 51	6583.0	0.334	780.06	8.69	-14.019
1510+3755	15 10 44.6	+37 55 27	5653.0	0.134	172.63	13.45	-13.775
1511+4632	15 11 30.1	+46 32 51	5170.3	0.039	301.32	13.50	-13.764
1516+4635	15 16 15.4	+46 35 58	5118.7	0.019	769.08	90.03	-12.931
1521+4751	15 21 18.0	+47 51 41	5377.0	0.078	260.85	10.67	-13.978
1522+3749	15 22 07.0	+37 49 30	5885.5	0.196	136.43	9.07	-13.958
1533+3756	15 33 56.5	+37 56 53	4878.0	0.020	440.73	18.06	-13.448
1534+4631	15 34 17.9	+46 31 03	5273.7	0.068	70.49	9.99	-13.929

Table 2–2. (cont.)

Object	Rt Asc	Dec	λ_{bin}	z_{obs}	EW(Å)	S/N	$\log f_\lambda^{obs}$
1534+4637	15 34 40.3	+46 37 23	6823.7	0.369	172.03	14.33	-13.883
1536+4636	15 36 05.3	+46 36 23	5170.3	0.038	140.59	7.66	-14.010
1538+4748	15 38 59.9	+47 48 33	6358.7	0.273	250.83	9.31	-14.124
1540+4633	15 40 29.1	+46 33 35	5687.0	0.129	116.02	7.77	-14.101
1543+4637	15 43 38.6	+46 37 21	6152.0	0.230	212.18	7.95	-14.146
1543+4632	15 43 55.3	+46 32 45	6565.3	0.232	1088.90	10.61	-14.024
1547+4635	15 47 26.1	+46 35 31	6100.3	0.220	237.17	9.82	-14.053
1549+4743	15 49 08.6	+47 43 58	6410.3	0.286	93.08	6.61	-14.273
1549+4630	15 49 35.4	+46 30 34	5428.7	0.097	96.77	23.32	-13.603
1551+4638	15 51 10.5	+46 38 01	5325.3	0.070	184.26	12.40	-13.854
1551+4747	15 51 33.8	+47 47 48	5635.3	0.128	1089.47	9.46	-14.060
1553+4632A	15 53 39.9	+46 32 43	5532.0	0.136	76.30	12.86	-13.870
1553+4632B	15 53 40.0	+46 32 41	5687.0	0.135	89.50	19.32	-13.705
1555+4635	15 55 54.6	+46 35 27	7030.3	0.406	221.32	9.00	-14.072
1605+4741	16 05 49.3	+47 41 37	5532.0	0.105	361.02	20.59	-13.714
1606+4746	16 06 21.6	+47 46 15	6307.0	0.260	116.92	8.20	-14.178
1607+4636	16 07 26.1	+46 36 15	5428.7	0.087	214.03	7.40	-14.102
1609+3752	16 09 00.3	+37 52 34	5498.0	0.096	233.68	8.03	-13.988
1613+4743	16 13 27.4	+47 43 54	5428.7	0.091	216.40	7.48	-14.141
1614+4635	16 14 20.3	+46 35 05	5480.3	0.097	700.65	13.23	-13.853
1614+4630	16 14 23.9	+46 30 17	5067.0	0.018	144.47	15.59	-13.682
1615+3752	16 15 28.2	+37 52 58	5110.5	0.037	73.06	17.26	-13.560
1616+4633	16 16 10.5	+46 33 34	5118.7	0.031	149.74	8.00	-13.982
1619+4635	16 19 20.1	+46 35 28	5997.0	0.194	1349.01	19.08	-13.753
1620+4743	16 20 21.7	+47 43 49	5118.7	0.019	401.53	31.98	-13.420
1622+4745	16 22 06.1	+47 45 57	5118.7	0.021	745.45	32.59	-13.412
1624+4634	16 24 35.8	+46 34 28	5687.0	0.132	173.63	10.54	-13.968
1625+4744	16 25 07.9	+47 44 26	6307.0	0.270	135.53	7.23	-14.233
1626+4742	16 26 24.3	+47 42 59	6255.3	0.262	93.57	41.07	-13.478
1629+4630	16 29 38.7	+46 30 07	5945.3	0.190	213.96	9.34	-14.053
1630+4633	16 30 52.2	+46 33 09	6203.7	0.250	123.32	8.13	-14.142
1638+4629	16 38 35.5	+46 29 11	5067.0	0.016	58.93	10.16	-13.868
1640+4630	16 40 01.0	+46 30 52	5790.3	0.150	92.24	8.95	-14.021
1646+4747	16 46 59.8	+47 47 40	6307.0	0.241	791.10	6.66	-14.268
1647+4743	16 47 33.6	+47 43 50	6048.7	0.205	383.53	21.15	-13.757
1704+4742	17 04 52.3	+47 42 11	5325.3	0.060	108.66	11.70	-13.923
1709+4741	17 09 52.1	+47 41 07	7030.3	0.322	545.10	8.88	-14.113
1710+4742	17 10 51.9	+47 42 34	5635.3	0.137	281.53	11.12	-13.990
2048+0128	20 48 00.6	+01 28 19	5265.5	0.060	469.45	8.38	-13.999
2055+0126	20 55 45.8	+01 26 21	5110.5	0.026	203.51	9.70	-13.896
2058+0122	20 58 27.7	+01 22 13	5265.5	0.068	532.91	32.59	-13.409
2106+0223	21 06 50.0	+02 23 25	5963.0	0.205	145.10	9.20	-14.092
2110+0223	21 10 16.8	+02 23 43	5653.0	0.148	57.61	10.73	-14.001
2114+0121	21 14 09.6	+01 21 53	5808.0	0.168	170.23	8.37	-14.052
2119+0219	21 19 26.0	+02 19 17	5730.5	0.160	61.69	8.15	-14.120
2122+0217	21 22 25.8	+02 17 55	6505.5	0.298	255.90	9.61	-14.108
2122+0128	21 22 28.1	+01 28 13	5110.5	0.048	1590.01	7.10	-14.032

Table 2–2. (cont.)

Object	Rt Asc	Dec	λ_{bin}	z_{obs}	EW(Å)	S/N	$\log f_\lambda^{obs}$
2125+0219	21 25 40.3	+02 19 25	6273.0	0.257	157.42	32.74	-13.569
2127+0217	21 27 55.9	+02 17 38	6815.5	0.368	807.10	9.28	-14.102
2128+0223	21 28 51.8	+02 23 45	5343.0	0.089	59.21	8.19	-14.074
2130+0220	21 30 41.6	+02 20 27	6118.0	0.228	194.63	11.29	-14.026
2138+0220	21 38 54.1	+02 20 04	6195.5	0.234	1275.29	8.16	-14.170
2141+0223	21 41 47.4	+02 23 28	5653.0	0.139	91.21	11.41	-13.975
2144+0222	21 44 32.9	+02 22 48	5730.5	0.156	749.07	7.64	-14.148
2145+0122	21 45 10.6	+01 22 15	6040.5	0.190	495.61	8.87	-14.075
2147+0218	21 47 00.5	+02 18 07	6118.0	0.223	196.43	7.51	-14.204
2204+0121	22 04 39.6	+01 21 01	5420.5	0.090	178.36	8.40	-14.037
2204+0217	22 04 40.0	+02 17 07	6660.5	0.333	125.85	9.68	-14.098
2207+0122	22 07 57.0	+01 22 20	5110.5	0.012	354.75	35.60	-13.332
2211+0119	22 11 36.7	+01 19 34	5885.5	0.183	91.51	8.45	-14.061
2213+0121	22 13 42.6	+01 21 18	5265.5	0.060	125.58	7.75	-14.033
2214+0216	22 14 51.8	+02 16 59	6505.5	0.314	61.13	7.39	-14.221
2220+0122	22 20 02.5	+01 22 49	5653.0	0.157	58.03	10.36	-13.961
2221+0125	22 21 37.1	+01 25 50	5343.0	0.069	329.22	7.76	-14.056
2229+0126	22 29 53.7	+01 26 31	5808.0	0.164	309.01	22.65	-13.619
2231+0217	22 31 13.6	+02 17 10	5808.0	0.150	85.20	7.44	-14.163
2232+0221	22 32 49.7	+02 21 15	6428.0	0.271	3124.80	6.96	-14.243
2233+0216	22 33 32.6	+02 16 46	6273.0	0.261	1772.21	7.00	-14.239
2245+0214	22 45 22.0	+02 14 43	5808.0	0.162	158.61	11.08	-13.991
2248+0125	22 48 37.5	+01 25 17	5498.0	0.090	805.94	9.91	-13.973
2251+0122	22 51 59.9	+01 22 38	5110.5	0.044	244.93	8.23	-13.968
2257+0221	22 57 00.4	+02 21 31	5188.0	0.047	91.99	34.49	-13.401
2316+0218	23 16 02.7	+02 18 35	5110.5	0.043	129.08	8.26	-13.998
2323+0125	23 23 28.1	+01 25 56	5575.5	0.124	254.94	7.46	-14.100
2328+0122	23 28 24.4	+01 22 47	5653.0	0.137	1283.77	8.41	-14.051
2330+0123	23 30 06.5	+01 23 48	5265.5	0.058	94.91	10.44	-13.903
2331+0121	23 31 05.0	+01 21 20	5885.5	0.190	113.01	10.99	-13.947
2335+0123	23 35 47.4	+01 23 28	5730.5	0.171	55.18	9.42	-14.001
2336+0219	23 36 46.5	+02 19 29	6273.0	0.251	65.72	8.10	-14.175
2342+0217	23 42 55.4	+02 17 53	5963.0	0.198	324.87	8.24	-14.140
2343+0219	23 43 54.5	+02 19 21	5963.0	0.190	163.05	9.90	-14.061
2345+0122	23 45 58.8	+01 22 22	5265.5	0.063	332.51	23.28	-13.555
2347+0125	23 47 05.6	+01 25 45	5343.0	0.072	61.22	10.98	-13.905
2347+0123	23 47 09.6	+01 23 20	5885.5	0.184	122.89	20.77	-13.671
2347+0124	23 47 22.3	+01 24 30	6738.0	0.358	174.09	7.17	-14.168
2348+0215	23 48 07.5	+02 15 28	5343.0		202.36	13.57	-13.855
2349+0214	23 49 14.5	+02 14 16	5265.5	0.052	65.25	11.52	-13.902
2351+0215	23 51 01.8	+02 15 09	6195.5	0.233	315.68	7.07	-14.233

Table 2–3. Emission Line Ratios for Galaxies from SSG Survey

Object	Type	$\log \frac{[OII]}{[OIII]}$	$\log \frac{[OIII]}{H\beta}$	$\log \frac{[NII]}{H\alpha}$	$\log \frac{[SII]}{H\alpha}$	$\log \frac{[OI]}{H\alpha}$	$\frac{H\alpha}{H\beta}$
0001+0214	SB		1.006		-1.060	-2.067	5.461
0002+0118	SB	-0.659	0.705	-0.923	-0.718	-1.694	2.951
0004+0215	SB		0.790	-1.576	-1.057	-1.714	5.685
0007+0217	HII		1.203	-1.938	-1.337	-3.480	16.437
0012+0219	SB	-0.141	0.513	-0.577	-0.766	-1.531	1.710
0028+0215	LINER		0.255	-0.796	-0.589	-1.243	5.177
0033+0220	SY2		0.719	-0.433	-0.453	-1.628	1.883
0036+0215	SY2		1.301				0.000
0037+0119	HII		0.727		-1.103		2.814
0042+0218	SY2			-0.595	-0.729	-1.275	
0047+0123	SB	-0.313	0.714	-1.152	-0.784	-1.390	4.228
0053+0221	SB		0.791	-2.050	-1.456	-2.041	3.882
0055+0119	HII		0.783	-2.057	-1.782	-2.027	4.125
0100+0122	SB	-0.546	0.675	-1.306	-0.863		3.091
0107+0213	SY2		1.632	0.064	-0.572	-0.320	23.465
0116+0126A	LINER		0.219	-0.476	-0.472	-1.029	3.134
0116+0126B	SB	0.145	0.261	-0.625	-0.508		3.836
0116+0123	SY2	-0.663	1.034	-0.654	-0.386	-0.767	3.518
0125+0222	SY1		-0.337	0.337	-0.242		0.101
0128+0222	SY2		0.684	-1.179	-0.861	-1.122	3.510
0132+0221	HII		0.819		-1.021	-1.826	5.287
0134+0119	HII		0.638	-1.036	-0.737		2.163
0135+0119	SB	-1.087	0.790	-1.055	-0.988	-1.618	3.497
0142+0123	SY2	-0.601	1.043	-0.313	-0.298	-0.855	4.115
0142+0126	SY2	-0.259	0.725	-0.176	-0.225	-0.975	4.075
0143+0121	SY1	-1.011	1.106	0.467	-0.173	-0.551	3.619
0146+0222	SB		0.900	-2.311	-1.440		3.870
0148+0126	HII		0.781	-1.596	-1.056		4.914
0151+0124	SY1	-0.519	0.678	-0.445	-0.579	-0.975	5.942
0157+0124	HII		0.784	-1.759	-1.351		2.666
0159+0119	SY2	-1.050	1.056	-0.440	-0.728	-0.972	4.510
0159+0219	SY2	-0.569	1.030	-0.213	-0.132	-0.902	3.182
0201+0126	HII		0.626	-1.790	-0.966	-1.680	3.271
0208+0218	HII		0.727		-0.901	-2.134	4.617
0208+0221	SY2		1.146	-0.197	-0.345	-1.070	7.770
0209+0120	HII		0.681	-2.630	-0.807	-2.055	6.809
0211+0124	SB	-2.165	0.679		-1.094	-1.119	2.410
0217+0124	LINER	0.134	0.209	-0.422	-0.501	-1.231	3.825
0218+0122	SB	-0.456	0.728	-0.944	-0.641	-1.611	2.998
0221+0217	SB		0.571	-1.220	-0.720	-1.896	4.766
0222+0223	SB	-1.007	0.945	-0.731	-0.777		3.082
0223+0125	SY2	-1.179	1.335	0.220	-0.429	-0.777	9.018
0231+0216	SY1	-0.424	0.739		-2.076	-1.481	5.758
0235+0121	SY1		-0.173	-0.367			2.336
0235+0220	SY1		1.456	0.056	-0.097	-0.155	5.174
0300+0221	SB		0.671	-1.905	-0.869	-1.453	3.522
0302+0217	LINER		0.125	0.344	-0.720		1.551

Table 2–3. (cont.)

Object	Type	$\log \frac{[OII]}{[OIII]}$	$\log \frac{[OIII]}{H\beta}$	$\log \frac{[NII]}{H\alpha}$	$\log \frac{[SII]}{H\alpha}$	$\log \frac{[OI]}{H\alpha}$	$\frac{H\alpha}{H\beta}$
0303+0126	SY1	-0.818	1.004	0.156	-0.666	-0.941	5.039
0309+0223	HII		0.815	-1.611	-1.206	-2.075	3.581
0311+0123	SB	-0.542	0.709	-1.332	-0.683	-1.540	4.212
0323+0219	SY1	-0.804	1.177	-0.177	-0.413	-0.739	5.431
0324+0124	SB		0.801		-1.022		4.047
0340+0124	SB	-1.005	0.862	-1.211	-1.072	-1.535	3.837
0349+0126	SY2	-1.169	1.100	-0.384	-0.654	-0.742	4.522
0404+0125	SB		0.296	-0.479	-1.115	-1.837	4.455
0405+0226	SB		0.845		-1.041	-1.366	6.003
0419+0126	SY2	-0.459	0.804	-0.433	-0.383	-1.018	4.818
0434+0133	SB	-1.016	0.840	-1.081	-0.903	-1.188	3.822
0720+5620	SB		0.926	-1.224	-0.389		7.783
0735+5621	SB		0.806	-1.272	-0.983	-1.527	6.264
0736+5621	SB		0.527	-0.792	-0.642	-1.417	5.705
0804+5620	SY1	-0.903	1.251				0.000
0812+4744	SY1		0.103	-0.960			0.715
0817+5625	SB		0.642	-2.170	-0.884	-1.742	3.731
0821+4749	SB		1.079		-0.213		3.339
0822+5622	SB		0.547	-1.183	-0.724	-1.478	6.029
0823+5621	HII		0.374		-0.631		3.652
0824+4749	SB		0.635		-0.751	-1.593	2.920
0825+5622	SY1	-0.554	0.256	0.745	0.070	-0.136	0.239
0829+4745	HII		0.865	-1.273	-1.059	-1.842	4.671
0850+5623	SY2	-0.585	0.848				0.000
0851+5628	SY1		0.559	-0.575		-0.117	3.474
0851+5625	HII		0.345		-0.909	-1.369	2.456
0854+5622	HII		0.966		-1.080		8.591
0855+5622	HII		0.818	-1.156	-0.680	-1.509	4.276
0902+5622	SY2		1.043	-0.649	-0.702	-0.745	4.579
0904+5621	SB		0.560	-0.909			3.416
0906+4750	SY2	-0.700	0.911	-1.046	-1.048	-1.118	4.297
0913+5628	SB		0.795	-1.634	-0.675		4.834
0913+4744	LINER	-0.361	0.465	-0.694	-0.545	-1.079	7.582
0918+4634	SY2		0.766	-0.887	-0.550	-1.394	5.432
0920+5627	SY2	-0.338	0.673				0.000
0922+4639	SY2		1.140	-0.096	-0.250	-0.626	10.881
0927+4640	SY2		1.018	-0.415	-0.079	-0.509	4.023
0929+4634	SY2	-1.098	0.778				8.938
0930+4633	SB		0.550	-1.289	-0.689	-1.792	3.506
0930+4636	SY1		-0.102		-0.856	-1.359	1.768
0931+4640	HII		0.705	-1.055	-0.948	-1.547	3.890
0933+4750	SB		0.674	-1.779	-1.358	-1.455	3.156
0934+4637	HII		0.843	-1.650	-1.106	-2.075	3.883
0936+5623	SB		0.493				0.610
0943+4638	SB		0.376		-0.837	-1.761	5.314
0944+5625	SB	-0.608	0.698		-0.945		2.242
0946+5627	SB	-0.778	0.786	-1.311	-0.949		2.419

Table 2–3. (cont.)

Object	Type	$\log \frac{[OII]}{[OIII]}$	$\log \frac{[OIII]}{H\beta}$	$\log \frac{[NII]}{H\alpha}$	$\log \frac{[SII]}{H\alpha}$	$\log \frac{[OI]}{H\alpha}$	$\frac{H\alpha}{H\beta}$
0946+4636	SB	-0.922	0.865				4.091
0947+4745	SB	-0.264	0.636		-0.887		3.188
0948+4750	HII		0.678	-1.186	-0.813	-1.888	3.000
0948+4753	SY2	-0.271	0.584	-1.265	-0.819	-1.167	3.538
0952+5628	SY2	-1.213	1.000	-0.322	-0.461	-0.931	2.484
0955+4753	SY1		-0.644	-1.175		-3.116	1.601
0955+4747	HII		0.845		-1.376		3.544
0958+4746	SY2	-1.045	1.840	-0.187	-0.838	-0.604	26.945
0959+4634	SY2			-0.198	-0.079	-0.771	
1000+4753	SB	-0.184	0.569	-0.999	-0.694	-1.723	3.270
1004+4641	HII		1.002		-1.024	-1.600	5.331
1004+4751	SB		0.770	-1.495	-1.098	-2.028	4.711
1010+5624	SB		0.638	-2.093	-0.986		4.635
1010+4634	SY1		-0.620	-1.698			1.801
1013+4637	SY2		0.760	0.398			1.766
1015+4641A	SB		0.548	-1.354	-0.893	-1.555	3.724
1015+4641B	SB		0.737	-1.350	-1.026	-2.206	3.444
1015+4639	SB		0.368	-0.819	-0.646	-1.287	5.081
1016+4747	SB	-0.513	0.722	-1.661	-0.930		3.485
1016+5630	SY2	-1.164	1.216		-0.534		9.873
1018+5631	SB		0.771		-0.429		9.936
1019+4750	SY2		0.690	0.321	0.323		1.672
1023+4748	SB		0.389	-0.582	-0.670	-1.417	3.874
1024+4639	SB		0.488	-1.172	-0.647	-1.566	3.418
1025+4749	SB		0.193		-0.552	-1.354	2.376
1028+4641	SY1		-0.229		-0.933	-2.079	3.214
1034+4636	SB		0.624		-0.569	-1.464	3.897
1038+4637	SY1	-0.517	0.569	-1.126	-0.885		13.151
1039+4754	SY2		0.758	-1.010	-0.682	-1.209	5.101
1040+4634	SB		0.575		-0.964	-1.719	4.003
1046+4752	HII		0.782	-1.350	-1.135	-1.732	3.123
1050+4637A	HII		0.700	-1.215	-0.774	-1.888	4.522
1050+4637B	SB		0.239	-0.521	-0.579		4.839
1052+4638	SB		0.451	-0.772	-0.552	-1.281	3.714
1057+4635	SB		0.630	-1.238	-0.760	-1.510	3.486
1058+4755	HII		0.926		-1.155	-2.102	8.443
1059+4749	SB		0.717	-1.914	-0.954	-1.352	4.586
1059+4752	HII		0.537	-1.731	-0.950	-1.859	4.561
1102+4641	HII						
1103+4636	HII		0.698	-1.033	-0.614	-1.612	5.208
1105+4641	SY2		1.229	-0.110	-0.468	-0.683	19.853
1105+4636	SB	-0.880	0.913		-0.744		3.477
1107+4754	SY1	-0.708	0.616	-0.353	-0.133	-0.154	1.596
1108+4643	HII		0.449	-0.952	-0.846		1.955
1108+4749	SB		0.717	-1.211	-0.934	-1.431	4.958
1109+4755	SB		0.692	-2.551	-0.904		4.684
1110+4642	LINER	-0.095	0.369	-0.882		-1.165	4.543

Table 2–3. (cont.)

Object	Type	$\log \frac{[OII]}{[OIII]}$	$\log \frac{[OIII]}{H\beta}$	$\log \frac{[NII]}{H\alpha}$	$\log \frac{[SII]}{H\alpha}$	$\log \frac{[OI]}{H\alpha}$	$\frac{H\alpha}{H\beta}$
1113+4643	SB		0.776				3.944
1114+4752	SY1		0.424	-0.975			4.674
1115+4637	HII		0.599				2.888
1117+4643	SY2		0.844	-0.178	-0.224		3.368
1119+4750	SB		0.588	-1.134	-0.645	-1.685	6.396
1120+4640	SB	-0.457	0.510	-0.317			1.779
1120+4636	SB	-0.466	0.755		-0.863		2.715
1122+4753	SB		0.711	-2.247	-0.745	-1.644	4.775
1125+4639	SY2	0.018			-1.027		
1128+4753	HII		0.671	-1.257	-0.872		2.944
1132+4755	SY2		0.539	-0.689	-0.530	-1.126	6.130
1140+4641	SY1		-0.450		-1.977		3.611
1141+4752	SB		0.856	-1.821	-1.068	-1.440	5.813
1144+4749	SY2			0.057	-0.364	-1.320	
1145+4638	SB		-0.022	-1.488	-1.025	-1.708	3.895
1149+4754	SB		0.638	-1.311	-0.589		4.411
1150+3756	HII		0.869	-1.166	-0.688	-1.173	6.914
1150+4750	SB		0.485	-0.742	-0.582	-1.472	5.702
1154+3754	SB	-0.544	0.467	-1.374	-0.700		5.181
1155+4638	SB	-0.692	0.728	-0.669	-0.963		3.041
1157+4754	SB		0.810		-0.793	-1.662	8.613
1157+4753	SY2		1.514	0.394	-0.154	-0.720	11.113
1200+4755	HII		0.434	-1.821	-0.763	-1.904	2.567
1203+3801	SB	-0.592	0.813		-0.517		3.078
1204+3755	SY1		-0.306	-1.362	-1.402	-1.723	2.400
1206+4748	SY1		0.239	-0.675	-0.378	-2.084	2.068
1208+3754	SB		0.820	-1.134	-0.716		6.744
1211+3800	SB	-0.417	0.582	-1.352	-0.977		3.575
1214+4636	SY2		0.949				0.000
1214+3801	HII		0.939		-1.449	-2.116	5.643
1215+4755	SB		0.847		-0.987		5.228
1216+4637	SB	-0.324	0.561		-0.699		2.997
1216+4753	SB		0.452	-0.670	-0.646		2.441
1217+4750	SB		0.575	-1.719	-0.630	-1.456	3.905
1218+4640	SY2		0.866	-1.267	-0.903	-1.209	10.276
1219+4638A	SY2		0.584	-0.704	-0.453	-1.246	5.115
1219+4638B	SY2		0.515	-0.648	-0.456	-1.466	6.569
1220+4748	SB		0.808	-1.666	-1.080	-1.889	4.606
1221+4752	SB	-1.024	0.732		-0.795	-1.317	2.865
1221+4753	SB		0.419	-1.346	-0.655	-1.802	3.642
1222+4754	SY1		-0.490	-0.048			0.994
1224+3756	HII		0.488		-1.241	-1.484	2.981
1227+3756	SB	-0.534	0.724		-0.742		3.623
1227+4749	SB		0.884	-1.503	-0.834	-1.549	5.985
1229+4639	SY2		1.303	-0.031	-0.447	-0.968	10.673
1231+4748	SB	-0.253	0.633		-0.689	-2.072	4.103
1233+4754	SB		0.853		-1.143	-1.320	4.253

Table 2–3. (cont.)

Object	Type	$\log \frac{[OII]}{[OIII]}$	$\log \frac{[OIII]}{H\beta}$	$\log \frac{[NII]}{H\alpha}$	$\log \frac{[SII]}{H\alpha}$	$\log \frac{[OI]}{H\alpha}$	$\frac{H\alpha}{H\beta}$
1233+4752	SY1		0.146		-0.767	-1.536	5.674
1234+4752	SB		0.676	-1.883	-0.701	-1.727	5.139
1237+4642	SY1		-0.789		-1.668		4.463
1238+3757	SY1	-0.742	0.832		-1.550		11.023
1238+3755	SY2			0.142	-0.251	-0.787	
1240+4641	SB		0.796		-1.032		3.692
1244+3800	SB	-0.412	0.552	-1.130	-0.804		2.979
1245+4754	SB		0.762	-2.062	-0.927		4.835
1246+4636	HII		0.972		-0.901		7.201
1246+4635	SB		0.730	-1.743			2.822
1247+4752	SY2		1.061	-0.774	-0.545	-0.847	21.099
1247+4641	SB		0.702		-0.699	-1.233	3.914
1247+4640	SB		0.882		-0.867		3.611
1248+4752	SY2		0.723		-0.729	-1.150	7.635
1251+4636	HII		0.892	-1.834	-0.970	-1.745	4.923
1253+4635	HII		0.539	-1.588	-0.825		2.746
1253+4754	SY2	-0.733	1.297	-0.929	-0.756		12.377
1257+4643	HII		0.615		-1.231		3.622
1300+3757	SY2		1.148	-0.134	-0.558	-1.145	4.787
1301+3801	SB		0.728		-0.968		3.751
1301+4641	SB		0.826		-0.929		4.403
1305+3756	SY2				-0.602		
1309+4636	SB	-0.435	0.581				2.122
1309+4640	LINER		0.410	-0.123	-0.722		2.062
1310+3801	HII		0.688		-0.834	-1.447	3.093
1314+4638	SB		0.732		-1.238		3.537
1316+3754	SB		0.453	-1.772	-0.603		3.943
1320+4750	SY2		0.965	-1.941	-0.695	-1.002	12.846
1321+3759	SY2	-0.511	1.028	-0.214	-0.169		3.733
1324+4635	SY2	-0.678	0.844	-0.368	-0.481		1.678
1324+4749	SY2		1.434	-1.941	-0.510	-0.798	16.893
1324+4637	SB		0.473	-0.983	-0.606	-1.058	6.433
1325+4635	HII		0.667		-1.255	-1.530	3.408
1325+4639	SB		0.431	-0.809	-0.514		7.584
1326+4637	SY2			0.682	-0.196		
1332+4748	SB		0.713	-1.769	-0.694		4.699
1335+4749	SB	-0.390	0.587		-0.624		2.610
1340+4635	?						
1343+4753	SB	-0.305	0.592	-1.593	-1.685	-1.330	3.035
1348+4634	HII		0.645	-1.054	-0.606		4.320
1349+4749	SY2		0.928		-1.137	-1.295	9.094
1353+4746	SY2	-0.547	1.230	-0.299	-0.455		6.044
1354+4749	SB	-0.710	0.665	-1.076	-0.591	-1.665	3.888
1357+4747	SY2	-0.722	1.080	-1.215	-0.550	-0.834	16.286
1400+4638	SY1		-0.268		-1.309	-2.415	2.932
1401+3753	SY2	-0.579	0.728			-0.960	4.042
1403+4634	SY2		1.206	-0.448	-0.402	-0.934	5.001

Table 2–3. (cont.)

Object	Type	$\log \frac{[OII]}{[OIII]}$	$\log \frac{[OIII]}{H\beta}$	$\log \frac{[NII]}{H\alpha}$	$\log \frac{[SII]}{H\alpha}$	$\log \frac{[OI]}{H\alpha}$	$\frac{H\alpha}{H\beta}$
1403+4635	SY1		-0.912				0.000
1406+4750	SY2	-0.823	1.812	-0.283		-0.823	57.556
1407+4748	SB	-0.378	0.631	-1.126	-0.665	-1.354	4.106
1410+4639	SY2		0.845				3.622
1411+4753	HII		0.590	-1.586	-0.889	-1.910	3.845
1412+4640	SB		0.591	-1.013	-0.605	-1.671	5.782
1417+3752	SY1		-0.603				0.000
1419+4747	HII		0.786	-1.536	-1.484		3.131
1419+4638	SY1		-0.516	-0.778			1.479
1420+4748	SB		0.791	-0.452	-0.404		2.125
1420+4752	SY1		0.409	-0.133	-0.611	-0.764	0.971
1421+4749	SB		0.560	-0.935	-0.896	-1.549	6.078
1423+4751	SB		0.436	-0.962	-0.690	-1.551	5.452
1435+3753	SY1	0.070	-0.540			-1.040	1.915
1435+3757	SY2	-0.743	1.136			-0.318	4.945
1435+4635	SB		0.643		-0.797	-1.204	4.173
1436+4748	SY1		0.248	-1.077			10.357
1438+4634	SB		0.585	-0.907	-0.735		5.229
1439+4753	SB		0.654	-1.046	-0.514	-1.791	4.922
1441+4635	SY2		0.889	-1.571	-0.701	-0.956	7.717
1442+4633A	HII		0.878		-0.926	-1.782	5.894
1442+4633B	SB		0.830				3.344
1445+4746	HII		0.575		-0.785	-2.036	3.772
1446+3751	HII		0.734		-0.925	-1.541	4.386
1447+4634	SB		0.793		-0.846		4.107
1448+4749	SB		0.450	-0.961	-0.774	-2.729	8.176
1450+4747	SY1		0.264	-1.774	-0.877		7.123
1451+4635	SY2		0.734		-1.103	-1.141	4.730
1451+4748	SY2	-0.318	0.624	-0.638	-0.846	-1.124	5.161
1452+3756	HII		1.032				5.765
1452+4747	SB		0.503	-3.125	-1.038		2.842
1454+4748	SB		0.327	-1.461	-0.576		2.989
1454+4634	SY2		0.977	0.355			1.846
1456+4635	SY2		0.701		-0.581	-1.232	5.055
1459+4632	HII		0.621		-0.636	-1.562	4.720
1502+4639	SY2		0.952	-0.390			20.314
1504+4637	SB		0.660		-0.581	-1.190	3.527
1506+4633	SY1		0.808	-0.343	-0.525	-1.132	4.467
1506+4637	SB		0.788		-0.748		1.888
1508+3750	SB	-0.383	0.631	-0.818	-0.950		3.469
1510+3755	SB		0.694		-0.803	-1.678	5.545
1511+4632	HII		0.685	-1.646	-0.834	-1.765	5.243
1516+4635	HII		0.730		-1.160	-3.348	3.422
1521+4751	SB		0.693	-1.825	-0.664	-1.436	6.212
1522+3749	SB		0.428	-1.433	-0.546	-1.619	4.996
1533+3756	HII		0.878		-1.467		2.988
1534+4631	SY2		0.561	-0.692	-0.553	-1.238	4.695

Table 2–3. (cont.)

Object	Type	$\log \frac{[OII]}{[OIII]}$	$\log \frac{[OIII]}{H\beta}$	$\log \frac{[NII]}{H\alpha}$	$\log \frac{[SII]}{H\alpha}$	$\log \frac{[OI]}{H\alpha}$	$\frac{H\alpha}{H\beta}$
1534+4637	SY2		0.927		-0.662	-0.640	4.979
1536+4636	HII		0.549	-1.174	-0.675	-2.801	3.301
1538+4748	SB	-0.282	0.403		-0.769	-2.018	4.796
1540+4633	SY2		0.650	-1.845	-0.581	-1.153	4.933
1543+4637	SB		0.472	-1.538	-0.990	-1.535	3.565
1543+4632	SB		0.812				4.297
1547+4635	SY2		0.748	-0.346	-0.404	-1.024	1.419
1549+4743	SY1	-0.391	0.254	-1.384	-0.635	-0.993	3.640
1549+4630	SB		0.654	-1.424	-0.592	-1.688	6.367
1551+4638	SY2		0.932	-0.953	-0.638	-0.822	6.199
1551+4747	HII		0.588		-1.893		2.314
1553+4632A	?		0.884				0.000
1553+4632B	SY2			0.316	-0.406	-0.152	
1555+4635	SY2		1.271				0.000
1605+4741	SB		0.770	-1.478	-0.628	-1.627	4.769
1606+4746	SB	-0.092	0.641	-1.055	-0.725	-1.728	3.550
1607+4636	SB		0.787	-1.265	-0.688	-1.553	7.281
1609+3752	SB		0.758		-0.747		3.899
1613+4743	SB		0.700		-0.574		3.343
1614+4635	HII		0.776	-1.916	-0.734	-1.713	3.443
1614+4630	HII			-2.324	-0.785		
1615+3752	SB		0.639	-1.069	-0.662	-1.744	4.008
1616+4633	HII		0.438		-0.713	-1.650	2.781
1619+4635	SB		0.886	-0.928	-0.738	-2.117	3.953
1620+4743	HII		0.622	-1.761	-0.936	-2.247	2.835
1622+4745	HII		0.790	-1.920	-1.057	-2.293	3.056
1624+4634	SB		0.910		-1.005	-1.785	7.812
1625+4744	SY1		0.172	-0.815	-0.924	-1.518	4.044
1626+4742	SY1		-0.152		-1.612	-2.147	3.149
1629+4630	SB		0.786			-1.339	3.116
1630+4633	SB		0.592		-0.792	-1.252	7.290
1638+4629	HII		1.183		-0.804		30.499
1640+4630	SY2		0.711	-0.406	-0.523	-0.963	4.402
1646+4747	SB	-0.928	0.789		-1.082		4.175
1647+4743	SY2		0.635	-1.168	-0.853	-1.331	4.898
1704+4742	LINER		0.350		-0.578	-1.122	2.192
1709+4741	SY2		0.954	-0.242			3.862
1710+4742	SB		0.810	-1.520	-0.922	-1.753	3.474
2048+0128	HII		0.908	-1.636	-1.409	-1.697	3.996
2055+0126	HII		0.725	-1.203	-0.860	-1.699	4.820
2058+0122	SB	-0.437	0.727	-1.157	-0.836	-1.577	3.967
2106+0223	LINER		0.416	-0.927	-0.700	-1.139	5.538
2110+0223	SY1		0.428		-0.520	-0.758	2.335
2114+0121	SY2		0.717	-0.602	-0.471		8.522
2119+0219	SY1		0.242	-2.183	-1.032	-1.599	6.124
2122+0217	SB	-0.684	0.428	-0.966	-1.022	-1.495	3.530
2122+0128	HII		1.209		-1.134		8.246

Table 2–3. (cont.)

Object	Type	$\log \frac{[OII]}{[OIII]}$	$\log \frac{[OIII]}{H\beta}$	$\log \frac{[NII]}{H\alpha}$	$\log \frac{[SII]}{H\alpha}$	$\log \frac{[OI]}{H\alpha}$	$\frac{H\alpha}{H\beta}$
2125+0219	SY2	-1.492	1.341	-0.637	-0.961	-1.088	10.519
2127+0217	SY2	-0.532	0.789	-0.950	-1.174	-1.416	2.308
2128+0223	SY2			-0.603	-0.554	-1.121	
2130+0220	SY2		0.904	0.166	-0.535	-0.461	2.491
2138+0220	SB		0.766	-1.907	-0.865		3.852
2141+0223	SY2		1.744	-0.577	-0.426	-0.481	29.215
2144+0222	SB		0.832		-1.185		3.136
2145+0122	SB		0.926		-0.783		5.228
2147+0218	SY2	-0.583	0.755	-0.721	-0.529	-0.947	4.083
2204+0121	SB		0.455	-0.961	-0.730	-1.515	5.205
2204+0217	SY2	-0.373	1.048	0.440	-0.069		1.183
2207+0122	HII		0.892	-1.407	-1.014		7.706
2211+0119	SY2		1.002	0.253	-0.099	-1.420	6.353
2213+0121	SB		0.748	-0.990	-0.591	-2.125	8.658
2214+0216	SY1		0.106	-0.472	-0.261		0.951
2220+0122	SY1		-0.093	0.122	-1.007	-0.852	0.713
2221+0125	HII		0.920	-2.132	-1.628	-1.620	7.854
2229+0126	SB	-0.422	0.620	-0.675	-0.715	-1.416	4.746
2231+0217	SY2			-0.241	-0.280	-0.649	
2232+0221	SB		0.784		-1.340		3.194
2233+0216	SY2	0.040	1.261	0.386			2.400
2245+0214	SY2		1.390	0.038	-0.337	-0.976	17.453
2248+0125	HII		0.801	-1.450	-0.987	-1.610	4.946
2251+0122	HII		0.831	-1.390	-0.713	-1.417	12.540
2257+0221	SY2		1.215	-1.175	-0.530	-1.188	14.050
2316+0218	HII		0.543	-1.073	-0.691	-1.440	4.835
2323+0125	SB		0.570	-0.777	-0.657	-1.645	5.355
2328+0122	HII		0.846		-0.922	-1.589	5.540
2330+0123	SB	0.122	0.598	-0.911	-0.691		4.140
2331+0121	SY1	-0.951	1.028	-0.662	-0.588	-0.960	5.805
2335+0123	SB		-0.486	-0.616	-1.114		2.530
2336+0219	SY1	0.134	1.447	-1.270	-1.034		31.985
2342+0217	SY2		0.755	-1.168	-0.728	-1.216	4.893
2343+0219	SB		0.716		-0.804	-1.423	3.614
2345+0122	SB		0.670	-1.821	-0.794	-1.833	4.500
2347+0125	SB		0.455	-1.129	-0.702		3.811
2347+0123	SY2	-1.040	1.489	0.078	0.226	-0.269	2.763
2347+0124	SY2		1.249			-1.467	20.155
2348+0215	SB			-1.070	-0.394	-0.606	
2349+0214	SB		0.477	-1.161	-0.508	-1.316	6.140
2351+0215	SB		0.629		-0.853		2.713

List of Figures for Chapter 2.

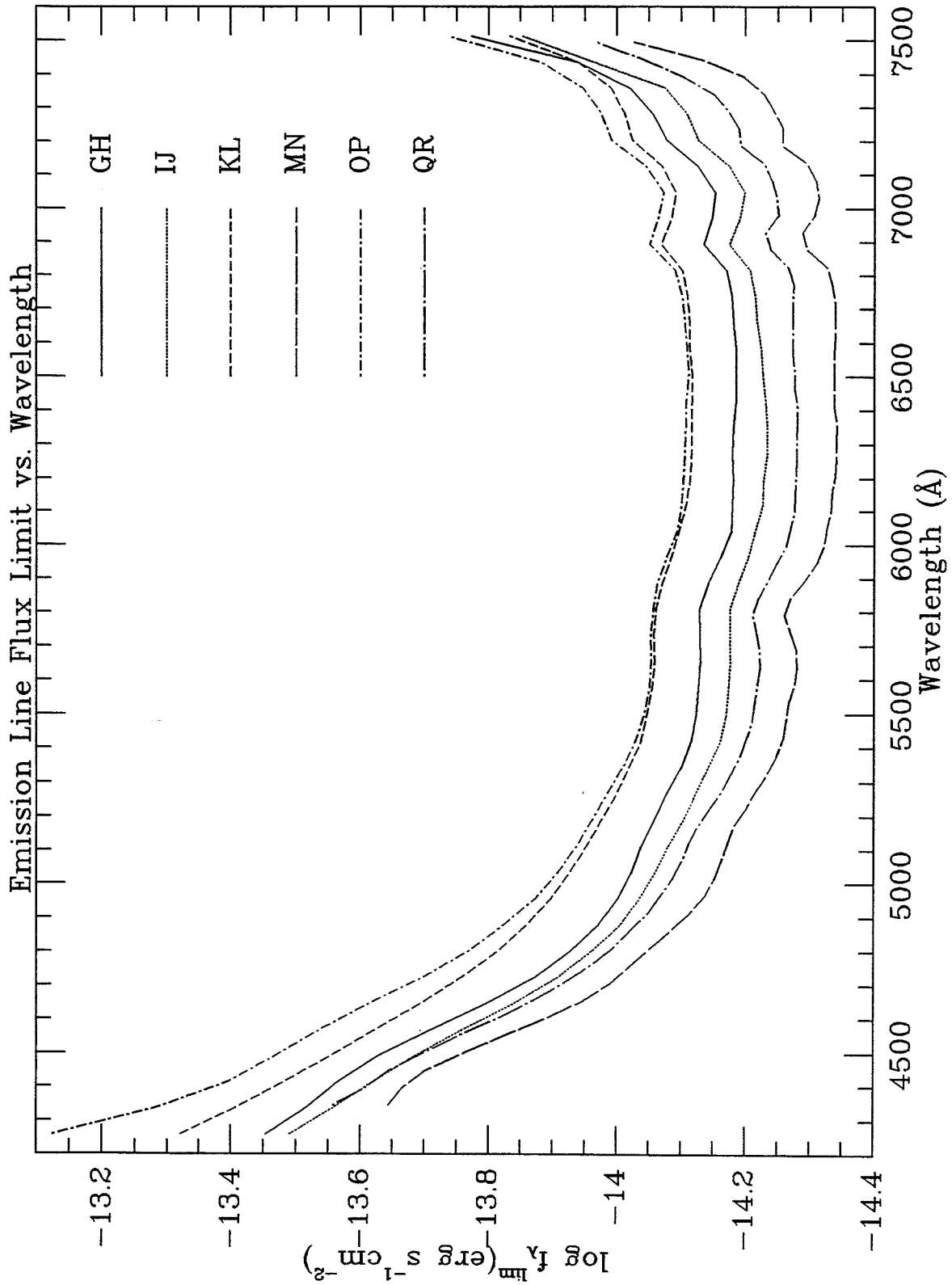
Emission Line Flux Limit vs. Wavelength
GH
IJ
KL
MN
OP
QR
log f_λ^{lim}(erg s^{-1}cm^{-2})
Wavelength (Å)
−13.2
−13.4
−13.6
−13.8
−14
−14.2
−14.4
4500
5000
5500
6000
6500
7000
7500

Figure 2–1

Mean Zero-redshift Wavelengths for Each of the Sub-surveys

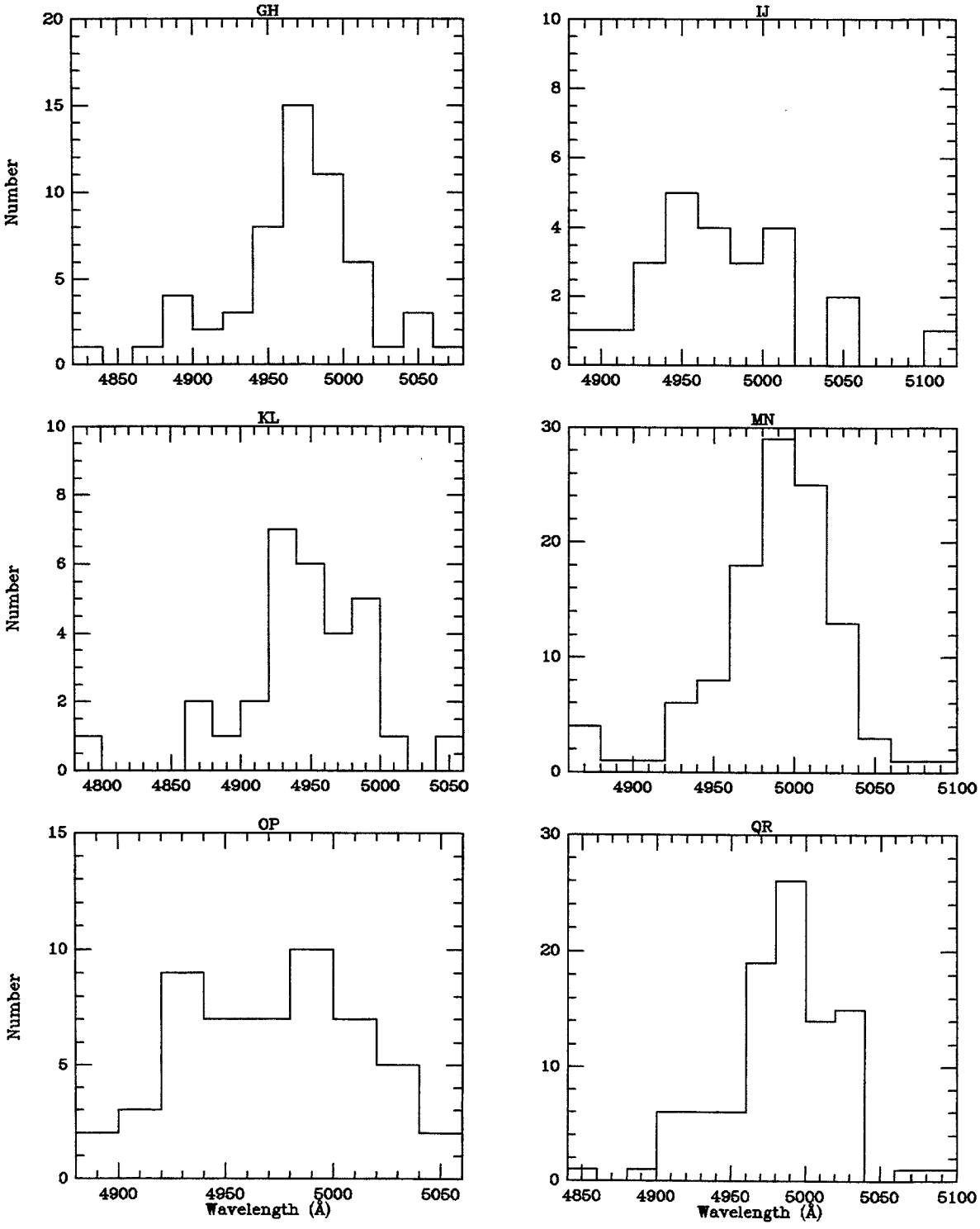

Figure 2–2 (a)-(f)

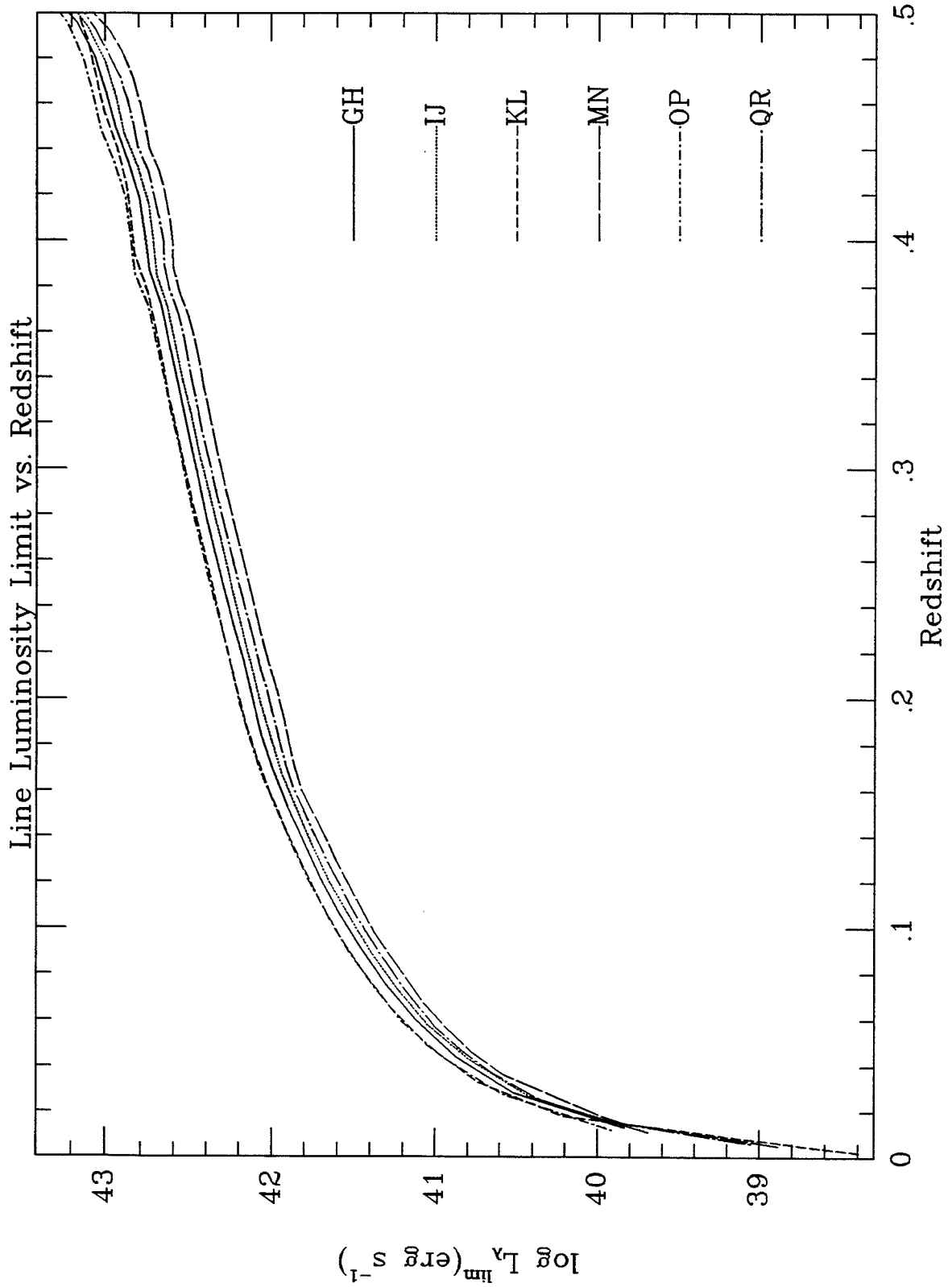
Line Luminosity Limit vs. Redshift
log L_λ^{lim}(erg s^{-1})
Redshift
GH
IJ
KL
MN
OP
QR
43
42
41
40
39
0
.1
.2
.3
.4
.5

Figure 2–3

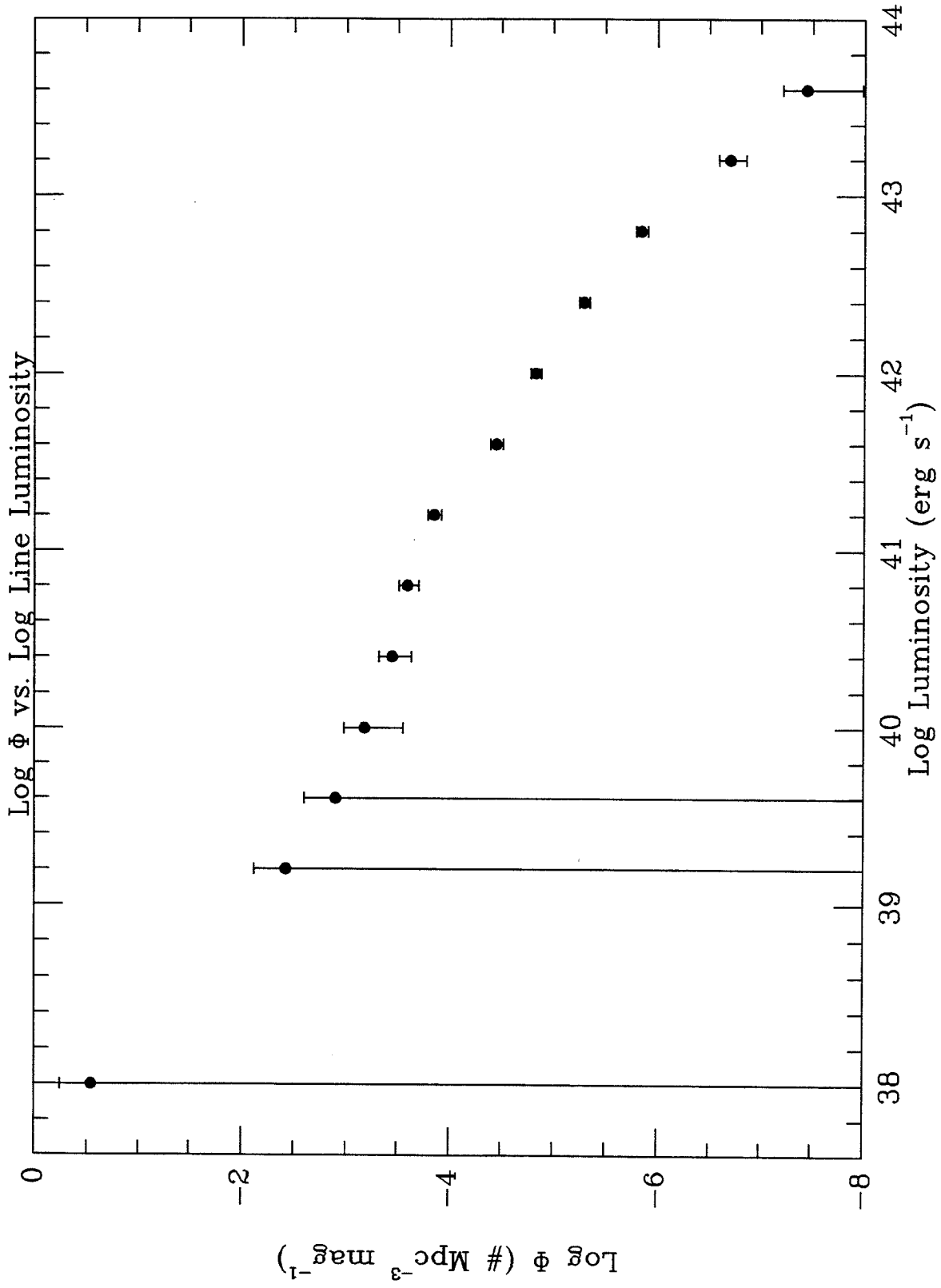
Log Φ vs. Log Line Luminosity
Log Φ (# Mpc^{-3} mag^{-1})
Log Luminosity (erg s^{-1})
0
−2
−4
−6
−8
38
39
40
41
42
43
44

Figure 2-4

N(z) vs. z Relation for Total Sample and Each Sub-class

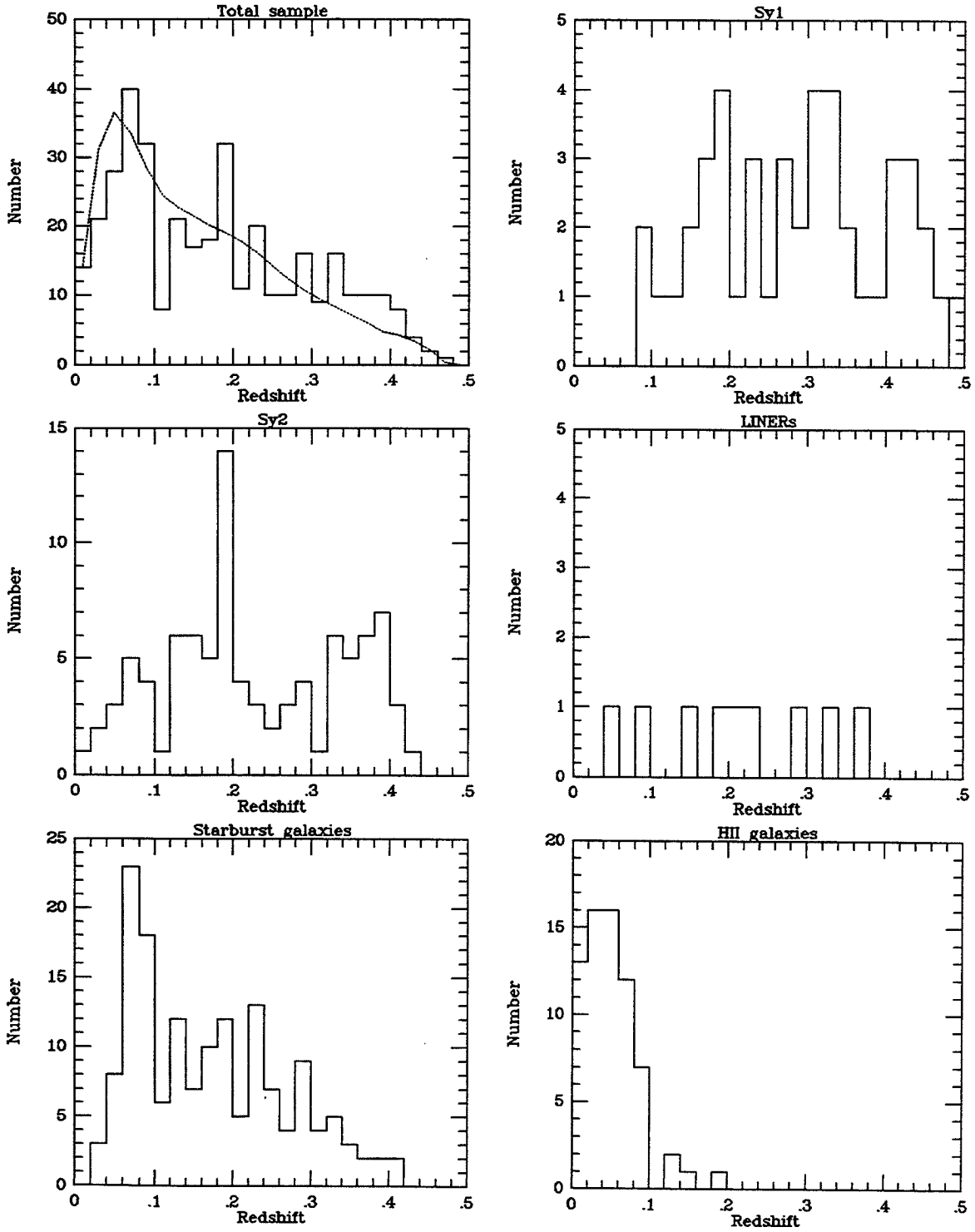

Figure 2–5 (a)-(f)

Log EW vs. Log Luminosity and Log EW vs. Redshift

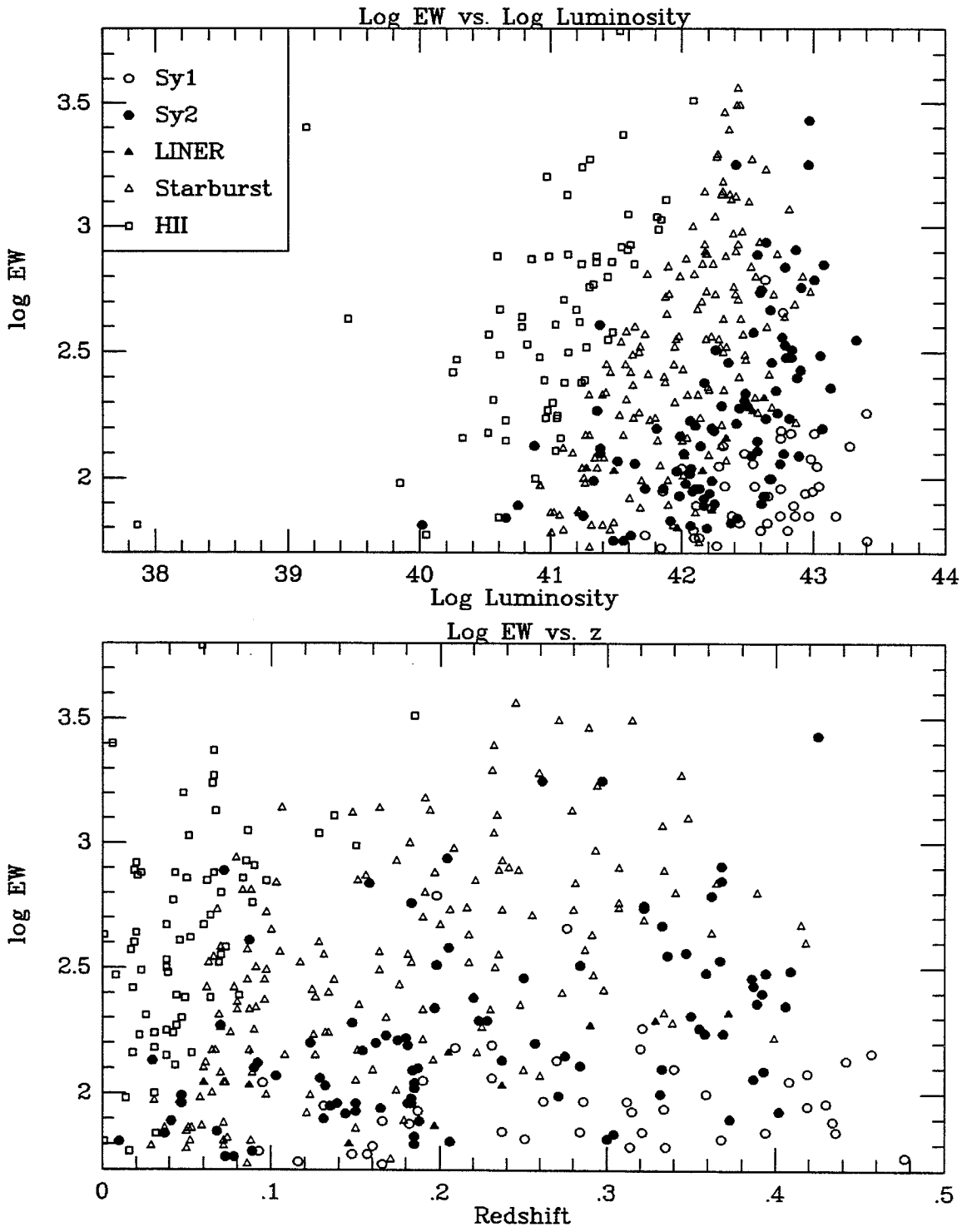

Figure 2-6 (a)-(b)

N(M) vs. M

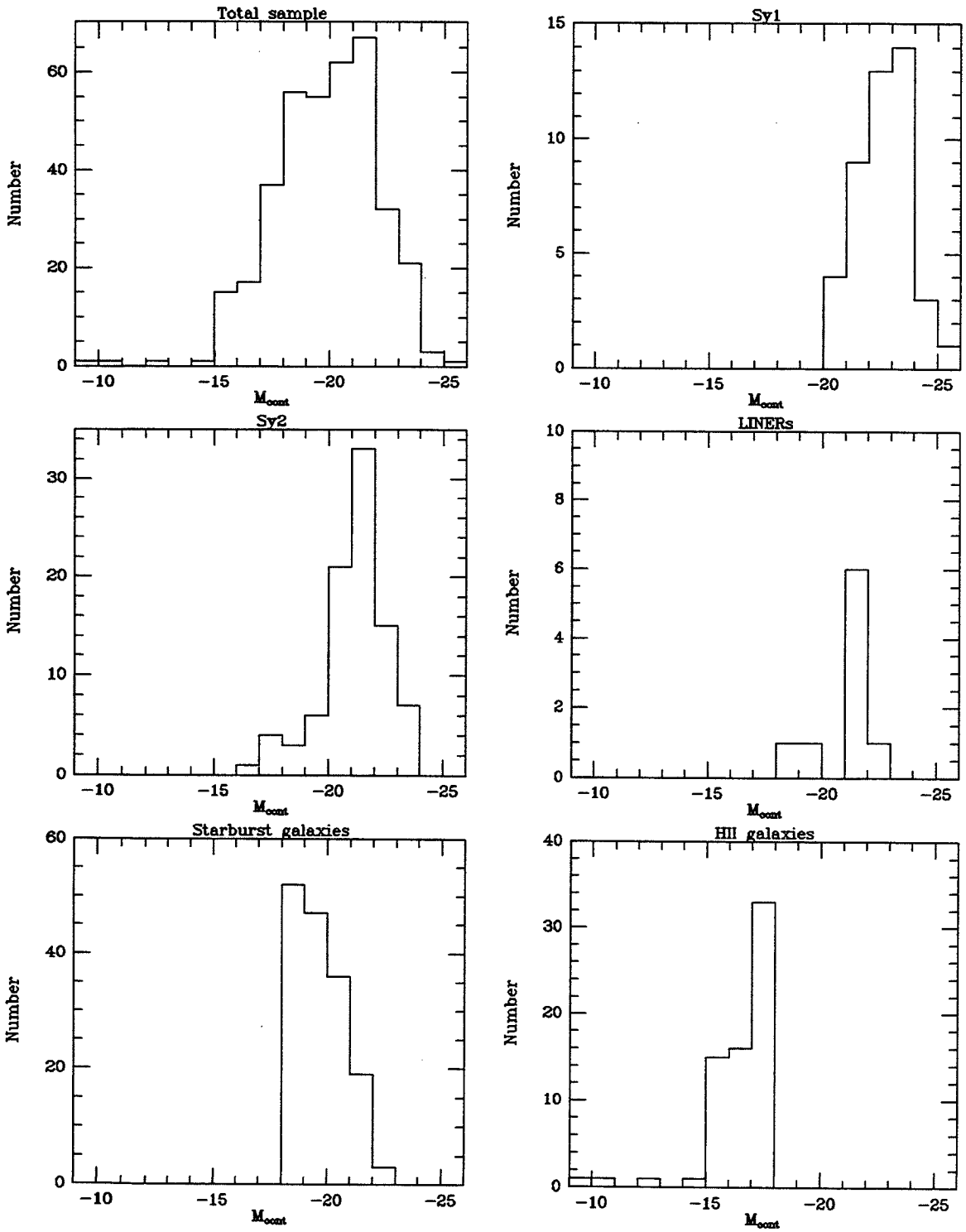

Figure 2–7 (a)-(f)

Spatial Distribution of SSG Galaxies

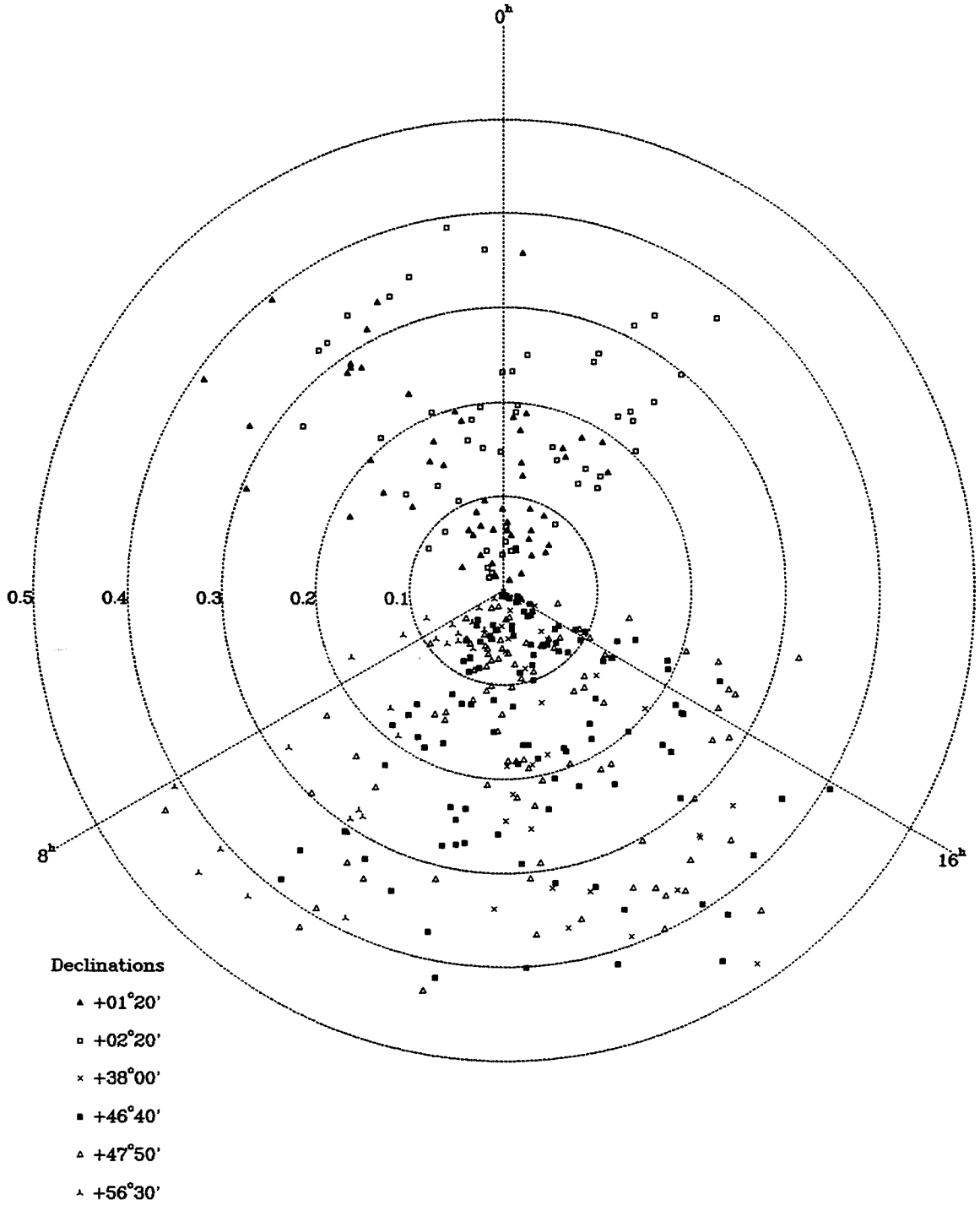

Figure 2–8

Redshift Distribution of SSG Galaxies as Function of RA

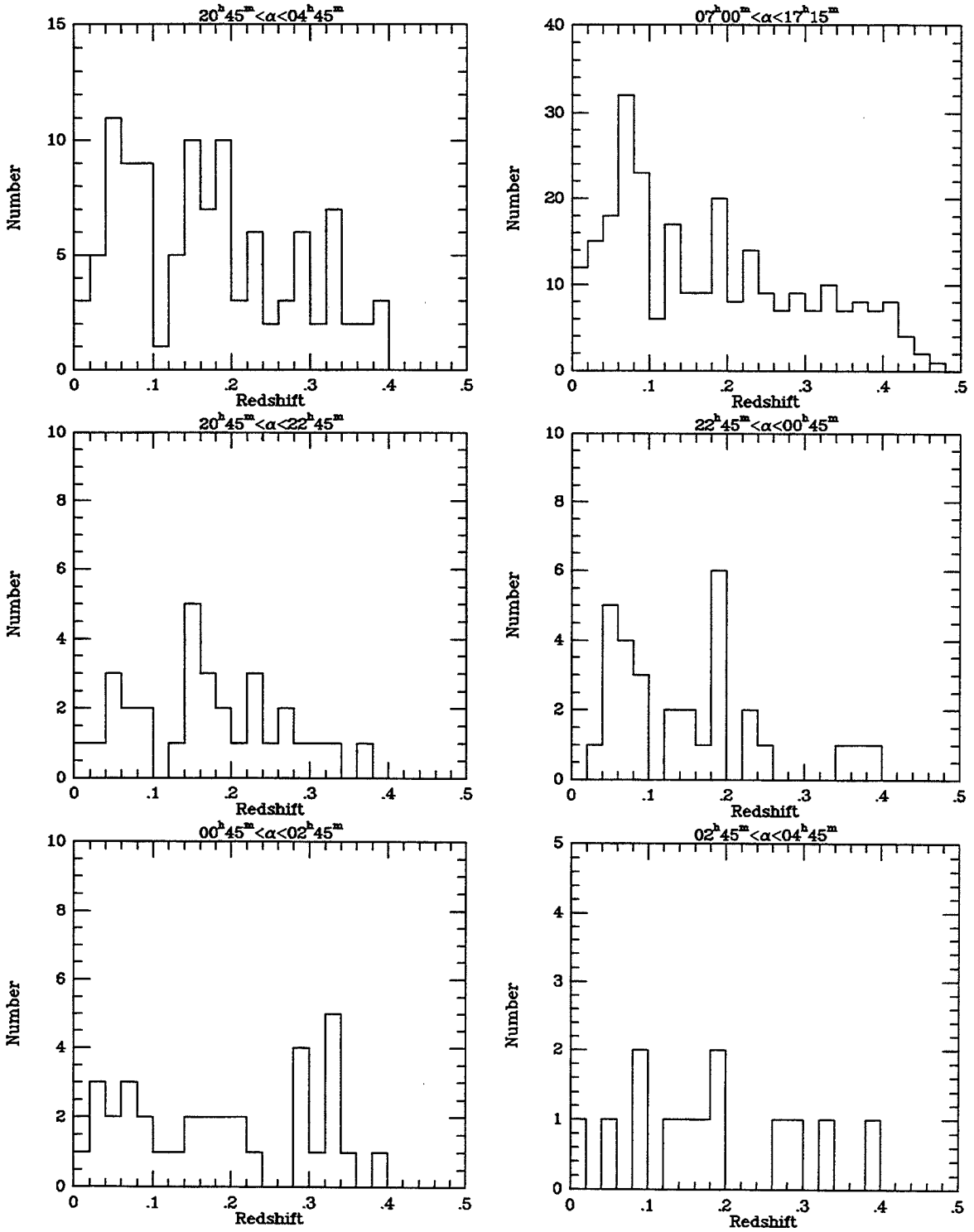

Figure 2–9 (a)-(f)

Redshift Distribution of SSG Galaxies as Function of RA (cont.)

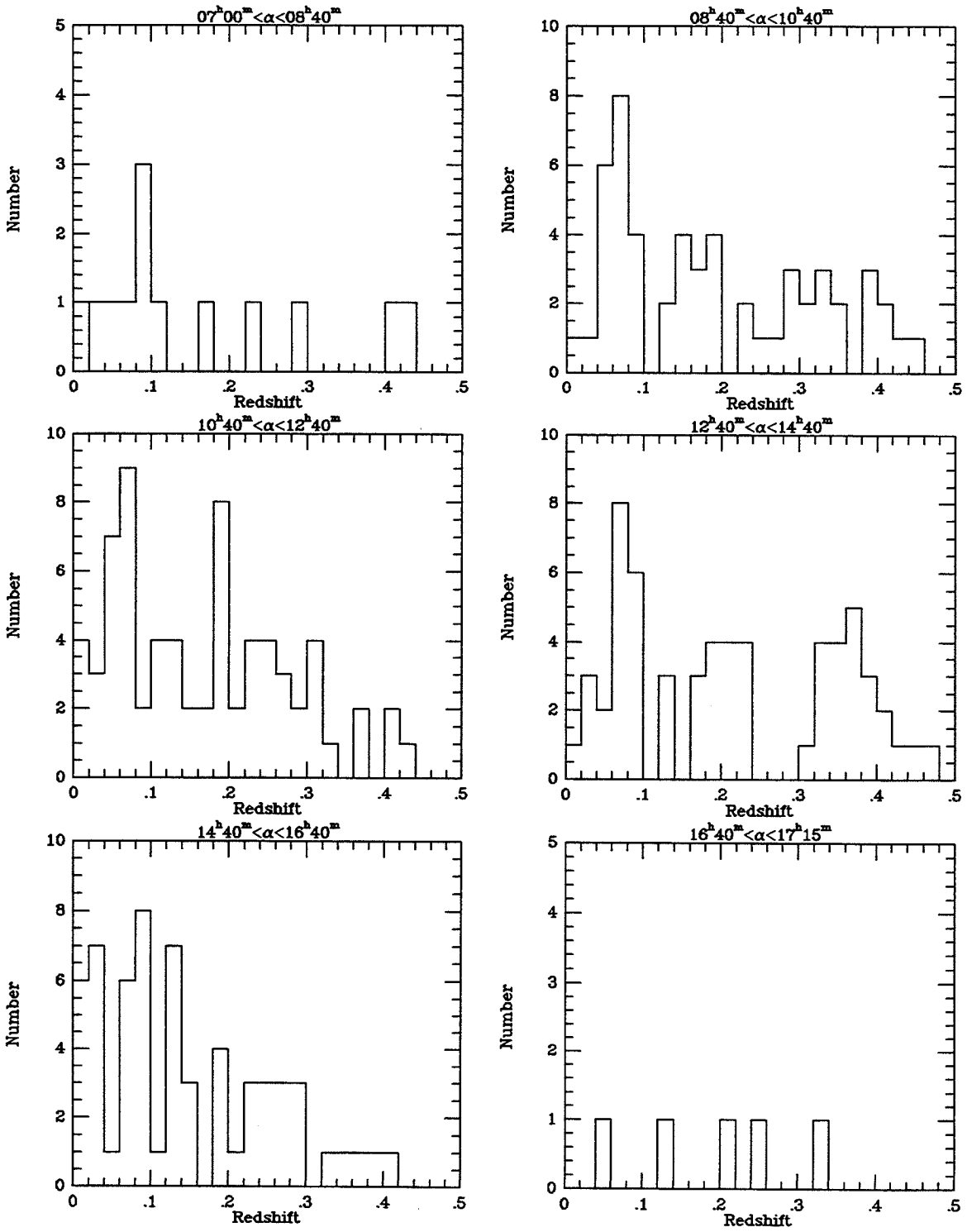

Figure 2–9 (g)-(l)

Line Ratio Diagnostics for SSG Galaxies

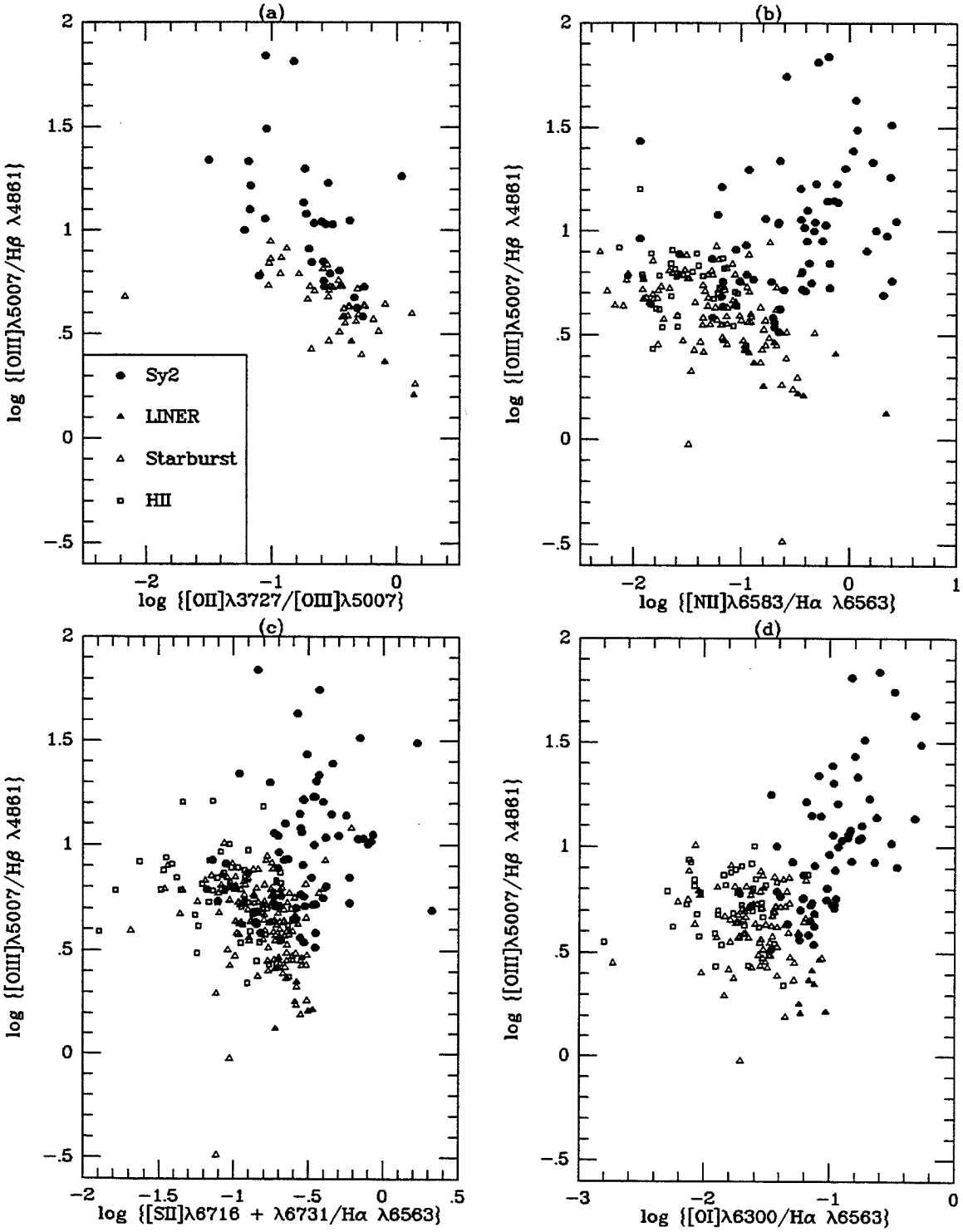

Figure 2–10 (a)-(d)

Chapter 3
The CfA Sample

3.1 Sample Selection

The selection of the nearby sample is based on the following criteria: First, a complete, well defined sample population of all types of galaxies is required, from which to create a subsample of emission line galaxies. This criterion is based on the desirability of minimizing any biases in the *a priori* selection of galaxy types as well as fulfilling the requirement of having a complete sample of nearby galaxies to ensure a proper statistical comparison to the distant sample. Second, the objects in this sample have to be bright enough to be observable using the Echelle Spectrograph on the Palomar sixty-inch (1.5m) telescope, as well as being visible from Palomar Observatory. This is due to the fact that access to the 1.5m telescope is much more readily available than access to other telescopes, both at Palomar and at other observatories. Finally, the sample of emission line galaxies needs to be large enough so that meaningful statistics can be determined and a comparison to the distant sample can be made.

A number of surveys of emission line galaxies have been undertaken in the recent past. Among these are the University of Michegan/Tololo surveys and the Case Western surveys. A summary of the relevant data on each survey is given in Table 3–1 (from Salzer 1987), with the additional data from the 4-Shooter transit survey. For each of the first two criteria given above, none of these samples would have been fully acceptable for work with this thesis. The selection of the candidate objects from

these objective prism survey plates is subjective in nature, thus making it difficult to effectively quantify the statistical limits that would apply. In addition, many of the objects in these surveys are extremely faint, and would have been exceedingly difficult to observe at the 1.5m telescope.

Therefore, it was decided to examine the first CfA Northern Sky Redshift Survey (Huchra et al. 1983) to see if an acceptable sample could be created. The advantages of the CfA survey are that all of the galaxies are fairly bright ($m_{zw} \leq 14.5$), and are thus readily observable and the survey has a reasonably well defined flux density limit (in terms of Zwicky magnitudes). The disadvantage in comparing to the SSG sample is that the CfA survey limits are in terms of broadband magnitudes, while the SSG survey is limited by the flux and equivalent width of the emission lines. In addition, there are over 2400 galaxies in the full CfA survey. Thus, it has been necessary to preselect a subsample of the galaxies in the CfA survey which are expected to show strong emission in Hβ λ4861 and/or [OIII]$\lambda\lambda$4959, 5007.

The sample that has been decided upon for observation has been taken from Burg (1987), who has supplied us with a list of 81 galaxies with [OIII]$\lambda\lambda$4959, 5007 equivalent widths in excess of 23.75Å. This list of objects is given in Table 3–2, along with relevant data for each galaxy. An additional 26 objects, all Seyfert galaxies, have been selected from Edelson (1987), on the premise that they would be observable to the transit survey if they have strong Hβ λ4861 emission. These objects are listed in Table 3–3. The classification of each galaxy is based on the observations taken at the P60 telescope (see chapter 4). Note that the galaxies 1345+3424 and IC 4397 in Table 3–3 are classified as a LINER and a Starburst, respectively, rather than as either a Sy1 or Sy2, based on these observations.

3.1.1 Could Compact HII Galaxies be Missed by CfA? How is CfA Defined?

The CfA survey is selected from the Catalog of Galaxies and Clusters of Galaxies

(CGCG, Zwicky 1961-8) and the Uppsala General Catalog (UGC, Nilson 1971). The CGCG is defined as all galaxies brighter than $m_{zw} = 15.5$ that are not point sources on 48" POSS plates, located north of $\delta = -3°$ but away from the obscuration of the galaxy. The UGC contains all galaxies larger than 1' as well as ALL galaxies brighter than $m_{zw} = 14.5$ (regardless of size) for $\delta > -2.5°$. All of the galaxies in both catalogs that are brighter than $m_{zw} = 14.5$, located either in the region $b > 40°$, $\delta > 0°$, or $b < -30°$, $\delta > -2.5°$ are included in the CfA survey.

According to Salzer (1987), the typical size of an HII galaxy is about 1 kpc, while the typical absolute blue magnitude is around -15.5. Thus, for such an object located at the limit of the CfA survey, it would have an angular diameter of:

$$\mu = m - M \sim 30$$

$$D = 10^{0.2(\mu+5)} = 10Mpc\,.$$

$$\theta = 2x10^5 \times \frac{d}{D} \sim 20''$$

At the plate scale of the Palomar Sky Survey (67"/mm), this corresponds to ~300 μm, which should have been easily detected by Zwicky in his galaxy search.

If HII galaxies exist which are much smaller than 1 kpc or more luminous than M_B ~-15.5 (and thus observable to greater distances), then the Palomar-Green survey (Schmidt and Green, 1983) should have detected these as UV-excess point sources. An examination of the work by Sargent and Searle (1970) based on a few of these objects, shows that a typical HII galaxy has a $(U-B) \sim -0.6$. The selection criterion of the PG survey is a $(U - B) \leq -0.4$. Therefore it is reasonable to assume that the PG survey is sensitive to this class of object and a quantitative analysis can be done based on the findings of this survey. Of the 36 non-Seyfert emission line galaxies discovered by the survey, only 10 objects are not included in the CGCG, and 9 of these 10 are too faint to have been included by Zwicky ($m_{zw}^{lim} = 15.5$). Thus only one object is bright enought to have been included in the CGCG (PG 0926+607). Since the CGCG covers approximately 20,000 sq. deg., and the area of the PG survey is

about $\frac{1}{2}$ of this, this suggests that Zwicky may have possibly missed 2 compact HII galaxies out of the 31,350 galaxies he cataloged. This is an incompleteness rate for this type of object of 0.006% for the CGCG. Therefore, out of the 2401 galaxies in the CfA, the statistics suggest that only 0.15 galaxies are missing in the CfA due to size constraints. Even if only $\frac{1}{2}$ of the HII galaxies have sufficient UV excesses, this results in an incompleteness of only 0.3 galaxies in the entire CfA survey.

3.2 Observations

Observations of the CfA sample of galaxies have been undertaken using the Palomar 1.5m telescope and the Echelle Spectrograph in a low-resolution, long slit mode (see McCarthy 1988 as well as the observing manual for the long slit mode, which has been included as Appendix A to this thesis). Each of the 107 galaxies in the sample is observed along two perpendicular position angles, which, when determined, are along the major and minor axes. The position angle of the major axis for each galaxy is determined from the UGC Catalog (Nilson 1971). For those objects that lack a measured position angle, observations are made at position angles of 45 and 135 degrees, so as to best minimize the effects of atmospheric dispersion. For each observation, a $1.''3$ wide $\times\, 6'$ long slit is utilized. Oke and Gunn (1983) spectrophotometric standard stars are observed using a slit that is 4" wide in order to minimize any vignetting effects. There is no order separating filter employed in the beam path, as the CCD detector utilized in the Echelle is insensitive to the second order blue light that is incident upon it. A 300 l/mm grating, blazed at 5000Å, is utilized, giving an effective wavelength range from 4350Å to 7200Å, with a dispersion of 3.567 Å/pixel. Typical observing times range from 300 to 1200 seconds for each position angle.

The data are reduced following the prescription for the reduction of long slit spectra given by Steidel in Vol. 2 of the FIGARO Manual. First, each spectrum is oriented so that the x-axis is parallel to the dispersion, going from blue to red, and

the y-axis is parallel to the position along the slit. The data then have the erase line subtracted off, and are converted into real numbers.

Each night's spectra are flat fielded according to standard methods. The flats are created from a series of four dome flats for each of the two slit widths. These dome flats are taken at the beginning of every night of observing. After cleaning off any obvious cosmic rays, each series is averaged to get a mean flat field for that slit for a given night. This averaged image is then corrected for the spectral output of the flat lamp by first extracting a spectrum from the entire flat field image and then fitting a $2^{\underline{nd}}$ order polynomial to the log of the observed mean counts as a function of wavelength and finally dividing the mean flat field by this log quadratic function. Lastly, the flat field is normalized to a mean count of 1.0 DN/pixel by dividing the image by the mean count over all of the pixels in the flat field image. All of the images (galaxy spectra, standard star spectra and arcs) are then divided by the appropriate flat field.

The images are rectified in the spatial direction by fitting a $3^{\underline{rd}}$ order polynomial curve to the wavelength-dependent centroid of the standard star spectrum using SDIST and then correcting all of the images using CDIST (two standard FIGARO routines). Following the spatial rectification, the images are then rectified in the direction of dispersion using the arc spectra, so as to line up the columns of the image with the dispersion. This two-stepped rectification process is needed so that a given column in the image would correspond to a particular wavelength, while a given row would correspond to a specific position along the slit. Following the rectification, the images are all cleaned of obvious cosmic ray hits using the routine CLEAN.

Wavelength calibrations are made by fitting the centroids of the He/Ne/Ar arcs to their laboratory wavelengths. The typical r.m.s. uncertainty in this calibration is $<$0.3Å. The spectra are all scrunched to cover a wavelength range from 4350Å to 7200Å. This sets the entire data set to a standard wavelength regime.

To flux calibrate a given night's spectra, it is necessary to determine the range of rows in the standard star spectrum which exceeds the sky background. An examination is made of the spatial cut (see Chapter 4 for definition) in order to determine this range. The counts from the standard star are then summed over that range of rows. Sky spectra on each side of the standard star are extracted and then a normalized sky spectrum is subtracted off of the standard star spectrum. This spectrum is then converted into a calibration curve, using the appropriate flux table.

A correction for atmospheric extinction is made using the Palomar extinction curves and the flux calibration is made row-by-row in the object spectra. This is done so as to maintain the spatial information along the slit, which is necessary during the later analysis of the data for the comparison to the SSG sample, rather than following the standard method of simply extracting the galaxy's spectrum along the slit. Finally, a correction is made for the atmospheric A bands around 6800Å.

3.3 Distance Determination to CfA Galaxies

In order to properly estimate the true distance to each of the 107 galaxies in the CfA sample, it is necessary to model the local flow field. The model chosen is solution $19G^2$ of the bi-infall model from Han and Mould (1990; HM90) and consists of terms which account for infall of the Local Group into both the Virgo supercluster as well as the "Great Attractor." In addition, further terms to account for the Perseus-Pisces supercluster are added into the model using solution 4 from Han and Mould (1992). With this model, it is possible to estimate a distance for a galaxy at a known position and heliocentric redshift. The values of the various parameters used in this model are given in Table 3–4.

First, a correction is made to the measured heliocentric velocities of the galaxies in the CfA sample to shift into the rest frame of the Local Group. This correction is 308 km/sec towards $(\ell^{II}, b^{II}) = (105, -7)$ (Yahil, Tammann and Sandage 1976).

The calculation of the predicted velocity in the Local Group frame is shown in the appendix to HM90, in which the linear infall velocity into each mass concentration is given by (from Peebles, 1976):

$$\mathbf{V}_V(\mathbf{r}_V) = W_V \left(\frac{r_V}{R_V}\right)^{-\gamma_V} \frac{\mathbf{r}_V}{R_V}$$
$$\mathbf{V}_{GA}(\mathbf{r}_{GA}) = W_{GA} \left(\frac{r_{GA}}{R_{GA}}\right)^{-\gamma_{GA}} \frac{\mathbf{r}_{GA}}{R_{GA}} ,$$
$$\mathbf{V}_{PP}(\mathbf{r}_{PP}) = W_{PP} \left(\frac{r_{PP}}{R_{PP}}\right)^{-\gamma_{PP}} \frac{\mathbf{r}_{PP}}{R_{PP}}$$

where $\gamma_V, W_V, \mathbf{r}_V$, and R_V are,respectively, the mass density distribution law, the amplitude of the Virgo infall measured at the local group, the distance vector from a field galaxy to the Virgo Cluster and the distance from the Local Group to Virgo. $\gamma_{GA}, W_{GA}, \mathbf{r}_{GA}$, and R_{GA} and $\gamma_{PP}, W_{PP}, \mathbf{r}_{PP}$, and R_{PP} are the corresponding values for the Great Attractor and Perseus-Pisces. The predicted velocity in the frame of the local group is given by:

$$V_{pred} = H_0 d - [\mathbf{V}_V(\mathbf{R}_V) - \mathbf{V}_V(\mathbf{r}_V)] \cdot \hat{\mathbf{d}} - [\mathbf{V}_{GA}(\mathbf{R}_{GA}) - \mathbf{V}_{GA}(\mathbf{r}_{GA})] \cdot \hat{\mathbf{d}}$$
$$- [\mathbf{V}_{PP}(\mathbf{R}_{PP}) - \mathbf{V}_{PP}(\mathbf{r}_{PP})] \cdot \hat{\mathbf{d}} - \mathbf{U} \cdot \hat{\mathbf{d}} ,$$

where the Hubble constant is given by:

$$R_V H_0 = V_0 + \mathbf{V}_V(\mathbf{R}_V) \cdot \hat{\mathbf{R}}_V + \mathbf{V}_{GA}(\mathbf{R}_{GA}) \cdot \hat{\mathbf{R}}_V + \mathbf{V}_{PP}(\mathbf{R}_{PP}) \cdot \hat{\mathbf{R}}_V$$
$$- \mathbf{V}_{GA}(\mathbf{R}_{GA} - \mathbf{R}_V) \cdot \hat{\mathbf{R}}_V - \mathbf{V}_{PP}(\mathbf{R}_{PP} - \mathbf{R}_V) \cdot \hat{\mathbf{R}}_V + \mathbf{U} \cdot \hat{\mathbf{R}}_\mathbf{V} .$$

It is thus possible to calculate the relation between the predicted velocity and "true" distance along a given line-of-sight for each of the CfA galaxies.

The results for each CfA galaxy are given in Table 3–5. For a few objects, the model distance falls in a "triple-valued" zone, where the "true" distance can take on three separate values due to infall into cluster cores. For these objects, I proceed with the analysis using each distance separately, rather than choosing, *a priori*, one of the three distances. This results in a range of accessible volumes for these galaxies within the limits of the CfA survey. These objects are denoted in Table 3–5 (and in the tables in Chapter 5) with an asterisk next to their name.

Using these model-derived "true" distances, along with their measured m_{zw} and the survey limit of m_{zw}=14.5, it is possible to determine the maximum distance to which each CfA galaxy would be observable in the CfA survey, and thus an accessible volume can be determined from:

$$V_a = \frac{\omega}{3} d^3$$

where ω=2.32 sr is the solid angle of the CfA survey. It is these volumes which are compared to the accessible volumes for each CfA galaxy in the distant survey (see Chapter 4) in order to predict the number counts for each class of emission line galaxy in the distant sample.

3.4 Physical Properties of the CfA Sample

Using the above distances and the observations, it is possible to measure a number of different absolute physical attributes for the galaxies in the nearby sample. These include the true sizes of the emission regions as well as the extent of the continuum emission. These are shown in Figure 3–1. These sizes are the FWZI sizes of these different regions. For some of these objects, these are upper limits on their sizes, as they are spatially unresolved in the spectra taken at the P60 telescope. Figure 3–2 gives the "luminosity function" for all 107 galaxies in the CfA sample, and is provided solely for illustrative purposes. Line ratio diagnostics are performed on the spectra taken for this thesis, and are presented in Figure 3–3(a)-(c). In both Figure 3–1 and Figure 3–3, the symbols are the same as those used in Chapter 2.

Figure 3–4 gives an histogram of the distributions of the rest-frame equivalent widths of both the SSG sample as well as the CfA sample. As is readily evident, there is a dearth of high equivalent width objects in the CfA sample, which is probably due to the selection criterion of the CfA being based on broad-band continuum magnitudes. High equivalent width objects tend to have low surface brightnesses, and are thus less likely to be included in surveys based on such criteria.

References

Han, M. and Mould, J., 1990, *Ap. J.*, **360**, 448

—, 1992, *Ap. J.*, **396**, 453

Huchra, J., Davis, M., Latham, D. and Tonry, J., 1983, *Ap. J. Suppl.*, **52**, 89

McCarthy, J., 1988, Ph. D. Thesis, California Institute of Technology, Pasadena

Nilson, P., 1971, *Uppsala General Catalogue of Galaxies*, Royal Society of Science of Uppsala, Uppsala

Oke, J. B. and Gunn, J., 1983, *Ap. J.*, **266**, 713

Peebles, J., 1976, *Ap. J.*, **205**, 318

Salzer, J., 1987, Ph. D. Thesis, University of Michegan, Ann Arbor

Schmidt, M. and Green, R., 1983, *Ap. J.*, **269**, 352

Yahil, A., Tammann, and Sandage, A., 1977, *Ap. J.*, **217**, 903

Zwicky, F., Herzog, E., Wild, P. and Kowal, C., 1961-68, *Catalogue of Galaxies and Clusters of Galaxies*, California Institute of Technology, Pasadena

Table 3–1. Summary of Objective Prism Surveys (from Salzer 1987)

Survey Name	Area (sq. deg.)	Number of ELGs	Density of ELGs (# per sq. deg.)	Completeness Limit (m_B)
Markarian (C)	15000	1500	0.10	15.2
Tololo (L)	1225	201	0.16	(15.0)†
UM (L)	667	349	0.52	16.5
Wasilewski (L)	825	96	0.18	15.0
Case (C+L)	532	381	0.72	16.0
POX (L)	205	51	0.25	(15.5)†
SBSSS (C+L)	48	233	4.65	(17.0)†
SSG (L)	62	665	10.73	(18.0)‡

C = Selected by Color; L = Selected by Emission-Lines

† Estimated Value

‡ AB(6100Å) magnitudes

Table 3–2. Burg's List of CfA Galaxies

Object Name	Rt Asc (h m s)	Decl (° ′ ″)	Mag m_{zw}	Helio Vel (km/sec)	Pos Angle	Equi Width (Å)	Type
0104+1625	01 04 43.0	+16 25 01	14.5	113	120	47.8	HII
0109+0104	01 08 56.4	+01 03 21	14.2	6809	136	37.2	SB
0141+0206	01 41 22.7	+02 05 54	14.0	5106	45	189.1	SY2
0152+0621	01 52 44.8	+06 22 00	14.5	5184	45	30.6	SY2
0157+2103	01 57 45.6	+21 02 45	14.1	3051	85	28.7	SB
NGC 1036	02 37 40.3	+19 05 00	13.5	773	5	29.6	HII
NGC 1068	02 40 06.5	-00 13 32	9.7	1093	70	49.5	SY2
NGC 2719A	08 57 07.4	+35 55 28	14.1	3197	133	131.3	SB
NGC 2820	09 17 43.7	+64 28 16	13.5	1581	59	285.0	SB
0940+0943	09 40 18.2	+09 41 56	13.7	3180	5?	87.7	SB
0948+0804	09 48 38.5	+08 03 43	14.4	491	155	68.6	HII
0954+1553	09 53 59.1	+15 52 34	14.3	4560	22	60.5	SB
1004+1036	10 04 40.1	+10 36 25	13.5	535	148	335.5	HII
NGC 3227	10 20 47.6	+20 07 00	11.75	1145	155	39.5	SY1
NGC 3239	10 22 23.3	+17 24 50	12.23	830	80?	374.9	SB
NGC 3264	10 29 08.6	+56 20 27	14.3	942	177	389.0	HII
1029+5439	10 29 22.2	+54 39 23	13.2	1390	45	53.7	SB
NGC 3310	10 35 40.3	+53 45 45	11.2	1018	45	27.3	LINER
1036+4811	10 36 47.4	+48 11 32	14.5	1505	45	39.1	SB
NGC 3362	10 42 15.2	+06 51 28	13.6	8322	90	36.9	SY2
NGC 3353	10 42 16.5	+56 13 20	13.47	935	45	233.5	SB
NGC 3395	10 47 02.3	+33 14 45	12.46	1634	50	62.1	LINER
NGC 3432	10 49 42.7	+36 53 05	11.94	619	38	125.4	SB
1049+2003	10 49 51.2	+20 03 26	14.2	1114	127	35.6	HII
NGC 3448	10 51 38.5	+54 34 23	12.42	1388	65	28.8	SB
1052+4959	10 52 05.5	+49 59 34	14.0	1427	35	98.2	SB
1058+4555	10 58 42.8	+45 55 25	14.1	8778	10	82.9	SY2

Table 3–2. (cont.)

Object Name	Rt Asc (h m s)	Decl (° ′ ″)	Mag m_{zw}	Helio Vel (km/sec)	Pos Angle	Equi Width (Å)	Type
1104+4400	11 04 00.7	+43 59 36	14.4	758	40	27.8	HII
IC 691	11 23 53.0	+59 25 47	14.2	1225	150	63.5	SB
IC 694	11 25 41.9	+58 50 00	12.6	3132	45	24.3	LINER
NGC 3741	11 33 25.2	+45 33 43	14.2	211	5	86.6	HII
NGC 3769	11 35 08.1	+48 09 39	12.71	761	152?	41.7	SB
NGC 3879	11 44 04.5	+69 39 35	13.5	1431	130	25.1	SB
1154+5327	11 54 14.4	+53 26 23	14.1	1066	175	36.3	HII
NGC 3991	11 54 56.3	+32 36 58	13.83	3204	33	24.2	SB
IC 755	11 58 36.5	+14 23 05	13.9	1501	145	25.8	SB
NGC 4051	12 00 35.9	+44 48 48	11.23	688	135	25.0	SY1
1202+3127	12 02 10.7	+31 27 16	14.0	7480	45	43.1	SY2
NGC 4108B	12 04 42.7	+67 30 50	14.5	2575	125	28.3	LINER
NGC 4151	12 08 00.9	+39 41 11	11.48	956	45?	203.7	SY1
NGC 4173	12 09 49.6	+29 29 05	13.7	1121	134	35.0	HII
1212+3614	12 12 32.3	+36 14 15	14.2	980	160	24.9	HII
NGC 4214	12 13 08.8	+36 36 19	10.38	298	160?	86.9	SB
NGC 4253	12 15 55.5	+30 05 27	13.7	3819	45	56.2	SY1
1216+0408	12 16 36.4	+04 08 07	14.5	1684	20?	268.9	HII
NGC 4388	12 23 14.8	+12 56 18	12.69	2538	92	224.2	SY2
1229+4007	12 29 34.3	+40 06 29	13.9	685	85?	40.2	HII
NGC 4509	12 30 39.0	+32 22 07	14.1	869	155	55.1	HII
1241+5510A	12 41 31.6	+55 10 10	14.5	4875	70?	30.6	SB
NGC 4656	12 41 32.0	+32 26 42	11.18	648	33	288.1	SB
NGC 4670	12 42 49.8	+27 23 58	13.44	1112	90	53.1	HII
NGC 4765	12 50 42.4	+04 44 10	12.9	706	80	34.7	HII
NGC 4861	12 56 40.3	+35 07 56	13.16	809	15	801.8	HII
NGC 5109	13 18 55.3	+57 54 16	13.6	2122	153	66.4	SB

Table 3–2. (cont.)

Object Name	Rt Asc (h m s)	Decl (° ′ ″)	Mag m_{zw}	Helio Vel (km/sec)	Pos Angle	Equi Width (Å)	Type
NGC 5107	13 19 09.0	+38 47 59	13.7	946	128	41.1	HII
1329+1122	13 29 55.4	+11 21 43	14.5	9590	40	23.9	LINER
NGC 5238	13 32 42.7	+51 52 09	14.2	254	160	36.7	HII
1333+6215	13 32 59.3	+62 14 58	14.1	3123	67	39.0	SB
NGC 5252	13 35 44.0	+04 47 43	14.5	6890	10	45.5	SY2
NGC 5256	13 36 14.7	+48 31 53	14.1	8353	45	125.8	LINER
NGC 5283	13 39 40.7	+67 55 33	14.3	2700	45	53.2	SY2
1407+4916	14 07 28.2	+49 16 33	14.4	1973	143	34.7	SB
NGC 5548	14 15 44.0	+25 22 01	13.54	5026	110	30.1	SY1
NGC 5674	14 31 22.3	+05 40 43	13.7	7442	45	30.6	SY2
1448+3547	14 48 55.1	+35 46 36	14.5	1176	58	202.8	HII
NGC 5789	14 54 29.1	+30 26 03	13.9	1804	45	191.7	SB
1501+1038	15 01 36.4	+10 37 59	14.0	10921	45	52.2	SY1
NGC 5899	15 13 15.0	+42 14 01	12.79	2549	18	32.3	SY2
NGC 5929	15 24 18.3	+41 50 43	14.0	2514	45	37.4	SY2
1604+4129	16 04 03.8	+41 28 40	13.6	1972	45	97.5	SB
NGC 7077	21 27 27.5	+02 11 39	14.3	1123	45?	25.6	HII
NGC 7241	22 13 26.1	+18 58 53	13.8	1434	20	66.2	SB
2237+0747	22 37 46.4	+07 47 37	14.3	7487	45	39.3	SY1
NGC 7464	22 59 24.7	+15 42 17	14.5	1795	45	47.2	SY2
NGC 7468	23 00 30.5	+16 20 00	14.0	2123	10?	31.1	SB
NGC 7469	23 00 44.4	+08 36 19	13.0	4846	125	35.7	SY1
NGC 7674	23 25 24.4	+08 30 06	13.6	8662	45	71.1	SY2
NGC 7682	23 26 30.2	+03 15 28	14.3	5147	45	85.2	SY2
NGC 7714	23 33 41.2	+01 52 42	13.1	2808	45?	54.3	SB
2354+1633	23 54 11.9	+16 32 09	14.5	1777	12	25.8	HII
NGC 7800	23 57 03.5	+14 31 46	13.4	1745	42	29.5	SB

Table 3–3. CfA Seyfert Galaxies from Edelson

Object Name	Rt Asc (h m s)	Decl (° ′ ″)	Mag m_{zw}	Helio Vel (km/sec)	Pos Angle	Type
0000+2141	00 00 35.5	+21 40 53	14.4	6608	105	SY2
0003+1955	00 03 45.1	+19 55 27	14.0	7688	45	SY1
0048+2908	00 48 52.9	+29 07 45	14.5	10781	45	SY1
0051+1225	00 50 57.9	+12 25 23	14.0	18205	45	SY1
0122+3153	01 22 42.7	+31 52 35	14.0	4654	32	SY1
NGC 863	02 12 00.6	-00 59 57	14.0	8061	45	SY1
NGC 1144	02 52 38.5	-00 23 07	13.6	8647	120?	SY2
NGC 3080	09 57 14.5	+13 17 02	14.5	10580	45	SY1
NGC 3079	09 58 35.4	+55 55 11	11.43	1101	165	SY2
NGC 3516	11 03 22.7	+72 50 25	12.86	2624	55?	SY1
NGC 3786	11 37 04.7	+32 11 13	13.5	2722	77	SY1
NGC 3982	11 53 52.3	+55 24 10	12.45	924	45	SY2
NGC 4235	12 14 35.7	+07 28 11	12.86	2343	48	SY1
1219+7535	12 19 33.5	+75 35 16	14.5	21413	45	SY1
1254+5709	12 54 05.0	+57 08 37	14.1	12300	10	SY1
NGC 5033	13 11 09.7	+36 51 30	10.85	861	170	SY1
1335+3925	13 35 28.3	+39 24 33	14.2	6023	45	SY2
NGC 5273	13 39 55.2	+35 54 18	12.71	1054	10	SY1
1345+3424	13 45 04.4	+34 23 57	14.5	4856	125	LINER
1351+6933	13 51 51.9	+69 33 13	14.5	9176	33	SY1
IC 4397	14 15 43.7	+26 38 45	14.2	4410	165	SB
1434+5901	14 34 58.0	+59 00 40	14.3	9392	45	SY1
NGC 5695	14 35 20.7	+36 47 13	13.9	4206	150	SY2
NGC 5940	15 28 51.1	+07 37 38	14.3	10172	45	SY1
NGC 6104	16 14 40.0	+35 49 46	14.1	8382	80?	SY1
NGC 7603	23 16 22.7	-00 01 48	14.4	8851	165	SY1

Table 3–4. Parameters for Tri-infall Distance Model.

Parameter	Virgo	Great Attractor	Perseus-Pisces
longitude (ℓ^{II})	283	309	130
latitude (b^{II})	85	18	-30
Hubble Distance (km/sec)	1422	4869	4798
W (Bulk Flow; km/sec)	197	400	115
γ	2	2	2

Table 3–5. Distances to CfA Galaxies

Object	m_{zw}	D_{obs} (Mpc)	V_{obs} (km/sec)	D_{max} (Mpc)	V_{max} (km/sec)	$\frac{V}{V_{max}}$	M_{zw}
0000+2141	14.40	113.3	1.3E+06	118.7	1.5E+06	0.87	-20.9
0003+1955	14.00	131.0	2.0E+06	164.9	4.0E+06	0.50	-21.6
0048+2908	14.50	181.5	5.3E+06	181.5	5.3E+06	1.00	-21.8
0051+1225	14.00	302.3	2.4E+07	380.6	4.9E+07	0.50	-23.4
0104+1625	14.50	4.2	6.6E+01	4.2	6.6E+01	1.00	-13.6
0109+0104	14.20	114.4	1.3E+06	131.3	2.0E+06	0.66	-21.1
0122+3153*	14.00	71.7	3.3E+05	90.3	6.5E+05	0.50	-20.3
0122+3153*	14.00	96.3	7.9E+05	121.2	1.6E+06	0.50	-20.9
0122+3153*	14.00	103.0	9.7E+05	129.6	1.9E+06	0.50	-21.1
0141+0206	14.00	85.0	5.4E+05	107.0	1.1E+06	0.50	-20.6
0152+0621	14.50	86.3	5.7E+05	86.3	5.7E+05	1.00	-20.2
0157+2103	14.10	49.3	1.1E+05	59.3	1.8E+05	0.58	-19.4
NGC 863	14.00	134.9	2.2E+06	169.9	4.3E+06	0.50	-21.7
NGC 1036	13.50	14.4	2.6E+03	22.8	1.0E+04	0.25	-17.3
NGC 1068	9.70	18.5	5.6E+03	168.3	4.2E+06	0.00	-21.6
NGC 1144	13.60	144.5	2.7E+06	218.7	9.3E+06	0.29	-22.2
NGC 2719A	14.10	60.6	2.0E+05	72.9	3.4E+05	0.58	-19.8
NGC 2820	13.50	34.1	3.5E+04	54.0	1.4E+05	0.25	-19.2
0940+0943	13.70	59.7	1.9E+05	86.3	5.7E+05	0.33	-20.2
0948+0804	14.40	8.7	5.8E+02	9.1	6.7E+02	0.87	-15.3
0954+1553	14.30	83.5	5.2E+05	91.5	6.8E+05	0.76	-20.3
NGC 3080	14.50	182.7	5.4E+06	182.7	5.4E+06	1.00	-21.8
NGC 3079	11.43	25.6	1.5E+04	105.1	1.0E+06	0.01	-20.6
1004+1036	13.50	9.1	6.7E+02	14.4	2.7E+03	0.25	-16.3
NGC 3227	11.75	21.0	8.2E+03	74.4	3.6E+05	0.02	-19.9
NGC 3239	12.23	13.5	2.2E+03	38.3	5.0E+04	0.04	-18.4
NGC 3264	14.30	22.5	1.0E+04	24.7	1.3E+04	0.76	-17.5
1029+5439	13.20	31.4	2.8E+04	57.2	1.7E+05	0.17	-19.3
NGC 3310	11.20	24.0	1.2E+04	109.6	1.2E+06	0.01	-20.7
1036+4811	14.50	33.6	3.4E+04	33.6	3.4E+04	1.00	-18.1
NGC 3362	13.60	146.4	2.8E+06	221.6	9.7E+06	0.29	-22.2
NGC 3353	13.47	22.4	9.9E+03	36.0	4.1E+04	0.24	-18.3
NGC 3395	12.46	36.0	4.1E+04	92.2	6.9E+05	0.06	-20.3
NGC 3432	11.94	12.3	1.7E+03	40.1	5.7E+04	0.03	-18.5
1049+2003	14.20	18.0	5.2E+03	20.7	7.8E+03	0.66	-17.1
NGC 3448	12.42	31.7	2.8E+04	82.5	5.0E+05	0.06	-20.1
1052+4959	14.00	32.4	3.0E+04	40.8	6.0E+04	0.50	-18.6
1058+4555	14.10	154.1	3.2E+06	185.3	5.6E+06	0.58	-21.8
NGC 3516	12.86	52.2	1.3E+05	111.2	1.2E+06	0.10	-20.7

Table 3–5. (cont.)

Object	m_{zw}	D_{obs} (Mpc)	V_{obs} (km/sec)	D_{max} (Mpc)	V_{max} (km/sec)	$\frac{V}{V_{max}}$	M_{zw}
1104+4400	14.40	16.2	3.8E+03	17.0	4.4E+03	0.87	-16.7
IC 691	14.20	28.8	2.1E+04	33.1	3.2E+04	0.66	-18.1
IC 694	12.60	61.5	2.1E+05	147.6	2.8E+06	0.07	-21.3
NGC 3741	14.20	6.8	2.7E+02	7.8	4.2E+02	0.66	-15.0
NGC 3769	12.71	17.1	4.4E+03	39.0	5.3E+04	0.08	-18.5
NGC 3786	13.50	55.2	1.5E+05	87.5	5.9E+05	0.25	-20.2
NGC 3879	13.50	32.5	3.0E+04	51.4	1.2E+05	0.25	-19.1
NGC 3982	12.45	22.4	9.9E+03	57.5	1.7E+05	0.06	-19.3
1154+5327	14.10	25.6	1.5E+04	30.7	2.6E+04	0.58	-17.9
NGC 3991	13.83	63.3	2.2E+05	86.2	5.7E+05	0.40	-20.2
IC 755*	13.90	18.7	5.8E+03	24.7	1.3E+04	0.44	-17.5
IC 755*	13.90	28.2	2.0E+04	37.2	4.6E+04	0.44	-18.4
IC 755*	13.90	37.5	4.7E+04	49.5	1.1E+05	0.44	-19.0
NGC 4051	11.23	14.6	2.8E+03	66.0	2.6E+05	0.01	-19.6
1202+3127	14.00	133.8	2.1E+06	168.4	4.2E+06	0.50	-21.6
NGC 4108B	14.50	52.1	1.3E+05	52.1	1.3E+05	1.00	-19.1
NGC 4151	11.48	19.0	6.1E+03	76.2	3.9E+05	0.02	-19.9
NGC 4173	13.70	17.7	4.9E+03	25.6	1.5E+04	0.33	-17.5
1212+3614	14.20	18.0	5.2E+03	20.7	7.8E+03	0.66	-17.1
NGC 4214	10.38	6.8	2.7E+02	45.1	8.2E+04	0.00	-18.8
NGC 4235*	12.86	24.7	1.3E+04	52.6	1.3E+05	0.10	-19.1
NGC 4235*	12.86	26.7	1.7E+04	56.8	1.6E+05	0.10	-19.3
NGC 4235*	12.86	47.4	9.4E+04	100.8	9.1E+05	0.10	-20.5
NGC 4253	13.70	73.5	3.5E+05	106.3	1.1E+06	0.33	-20.6
1216+0408*	14.50	20.1	7.1E+03	20.1	7.1E+03	1.00	-17.0
1216+0408*	14.50	27.8	1.9E+04	27.8	1.9E+04	1.00	-17.7
1216+0408*	14.50	38.1	4.9E+04	38.1	4.9E+04	1.00	-18.4
1219+7535	14.50	362.1	4.2E+07	362.1	4.2E+07	1.00	-23.3
NGC 4388*	12.69	24.0	1.2E+04	55.3	1.5E+05	0.08	-19.2
NGC 4388*	12.69	28.4	2.0E+04	65.3	2.5E+05	0.08	-19.6
NGC 4388*	12.69	51.1	1.2E+05	117.7	1.4E+06	0.08	-20.9
1229+4007	13.90	13.5	2.2E+03	17.8	5.0E+03	0.44	-16.8
NGC 4509	14.10	14.8	2.9E+03	17.7	5.0E+03	0.58	-16.7
1241+5510	14.50	90.8	6.6E+05	90.8	6.6E+05	1.00	-20.3
NGC 4656	11.18	11.5	1.3E+03	53.0	1.3E+05	0.01	-19.1
NGC 4670	13.44	16.9	4.3E+03	27.5	1.8E+04	0.23	-17.7
NGC 4765	12.90	8.3	5.1E+02	17.4	4.6E+03	0.11	-16.7
1254+5709	14.10	212.6	8.5E+06	255.7	1.5E+07	0.58	-22.5
NGC 4861	13.16	15.0	3.0E+03	27.8	1.9E+04	0.16	-17.7

Table 3–5. (cont.)

Object	m_{zw}	D_{obs} (Mpc)	V_{obs} (km/sec)	D_{max} (Mpc)	V_{max} (km/sec)	$\frac{V}{V_{max}}$	M_{zw}
NGC 5033	10.85	16.8	4.2E+03	90.0	6.5E+05	0.01	-20.3
NGC 5109	13.60	45.5	8.4E+04	68.9	2.9E+05	0.29	-19.7
NGC 5107	13.70	19.8	6.8E+03	28.6	2.1E+04	0.33	-17.8
1329+1122	14.50	169.3	4.3E+06	169.3	4.3E+06	1.00	-21.6
NGC 5238	14.20	8.0	4.5E+02	9.1	6.8E+02	0.66	-15.3
1333+6215	14.10	61.8	2.1E+05	74.3	3.6E+05	0.58	-19.9
1335+3925	14.20	110.6	1.2E+06	127.0	1.8E+06	0.66	-21.0
NGC 5252	14.50	125.1	1.7E+06	125.1	1.7E+06	1.00	-21.0
NGC 5256	14.10	148.4	2.9E+06	178.4	5.0E+06	0.58	-21.8
NGC 5283	14.30	54.4	1.4E+05	59.7	1.9E+05	0.76	-19.4
NGC 5273	12.71	22.8	1.0E+04	51.9	1.2E+05	0.08	-19.1
1345+3424	14.50	91.4	6.8E+05	91.4	6.8E+05	1.00	-20.3
1351+6933	14.50	160.6	3.7E+06	160.6	3.7E+06	1.00	-21.5
1407+4916	14.40	43.4	7.2E+04	45.4	8.3E+04	0.87	-18.8
IC 4397	14.20	83.9	5.2E+05	96.3	7.9E+05	0.66	-20.4
NGC 5548	13.54	94.1	7.4E+05	146.4	2.8E+06	0.27	-21.3
NGC 5674	13.70	134.4	2.2E+06	194.2	6.5E+06	0.33	-21.9
1434+5901	14.30	164.8	4.0E+06	180.7	5.2E+06	0.76	-21.8
NGC 5695	13.90	80.6	4.6E+05	106.2	1.1E+06	0.44	-20.6
1448+3547	14.50	27.8	1.9E+04	27.8	1.9E+04	1.00	-17.7
NGC 5789	13.90	39.8	5.6E+04	52.5	1.3E+05	0.44	-19.1
1501+1038	14.00	191.3	6.2E+06	240.9	1.2E+07	0.50	-22.4
NGC 5899	12.79	52.8	1.3E+05	116.1	1.4E+06	0.09	-20.8
NGC 5929	14.00	52.2	1.3E+05	65.7	2.5E+05	0.50	-19.6
NGC 5940	14.30	178.9	5.1E+06	196.1	6.7E+06	0.76	-22.0
1604+4129	13.60	42.6	6.9E+04	64.5	2.4E+05	0.29	-19.5
NGC 6104	14.10	148.7	2.9E+06	178.7	5.1E+06	0.58	-21.8
NGC 7077	14.30	21.9	9.3E+03	24.0	1.2E+04	0.76	-17.4
NGC 7241	13.80	26.9	1.7E+04	37.2	4.6E+04	0.38	-18.4
2237+0747	14.30	127.2	1.8E+06	139.4	2.4E+06	0.76	-21.2
NGC 7464	14.50	31.7	2.8E+04	31.7	2.8E+04	1.00	-18.0
NGC 7468	14.00	36.9	4.5E+04	46.5	8.9E+04	0.50	-18.8
NGC 7469	13.00	82.6	5.0E+05	164.8	4.0E+06	0.13	-21.6
NGC 7603	14.40	148.7	2.9E+06	155.7	3.3E+06	0.87	-21.5
NGC 7674	13.60	146.0	2.8E+06	221.0	9.6E+06	0.29	-22.2
NGC 7682	14.30	87.1	5.9E+05	95.5	7.7E+05	0.76	-20.4
NGC 7714	13.10	47.2	9.3E+04	90.0	6.5E+05	0.14	-20.3
2354+1633	14.50	30.3	2.5E+04	30.3	2.5E+04	1.00	-17.9
NGC 7800	13.40	29.7	2.3E+04	49.3	1.1E+05	0.22	-19.0

List of Figures for Chapter 3.

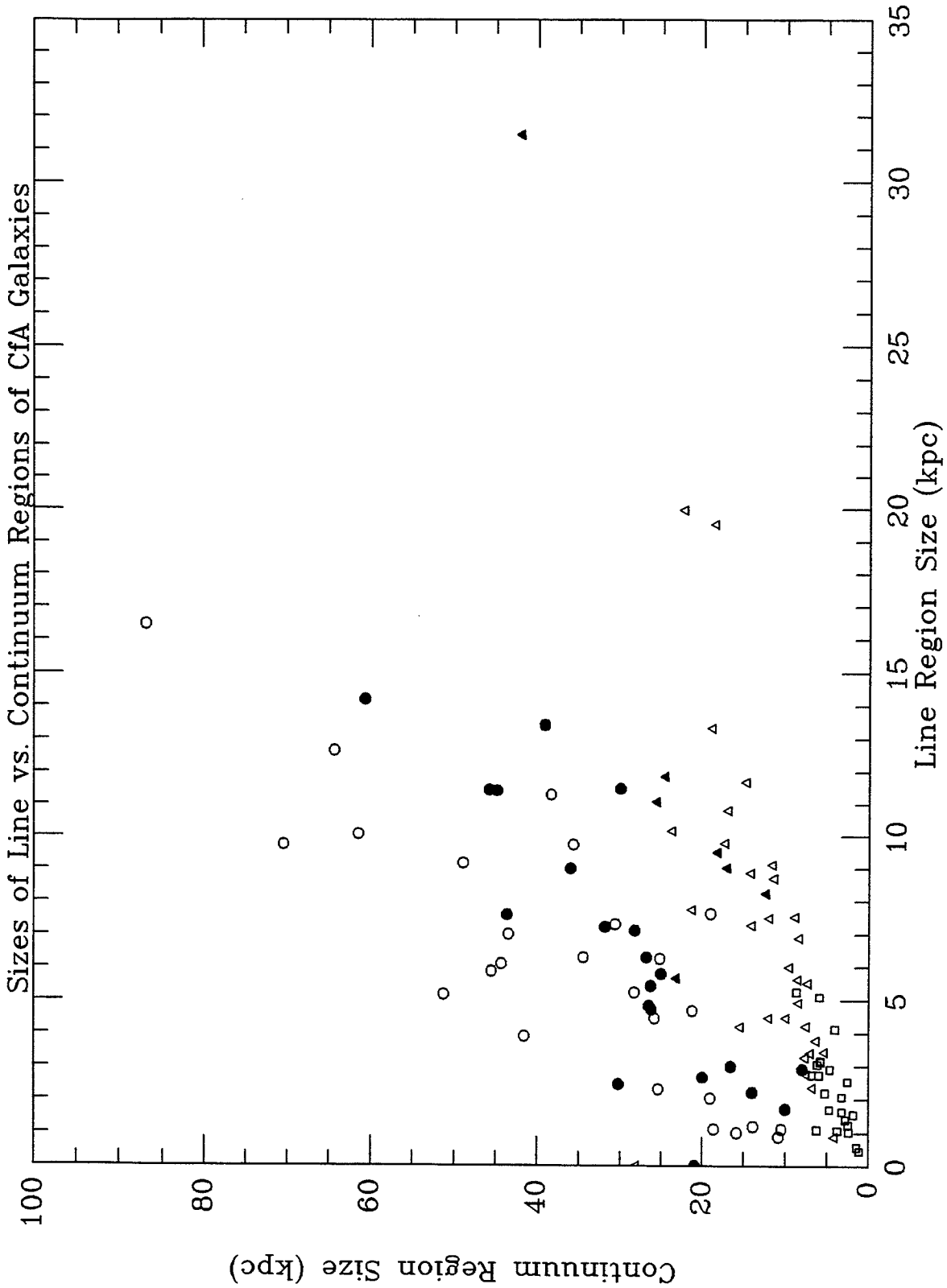
Sizes of Line vs. Continuum Regions of CfA Galaxies
Continuum Region Size (kpc)
Line Region Size (kpc)
0
20
40
60
80
100
0
5
10
15
20
25
30
35

Figure 3–1

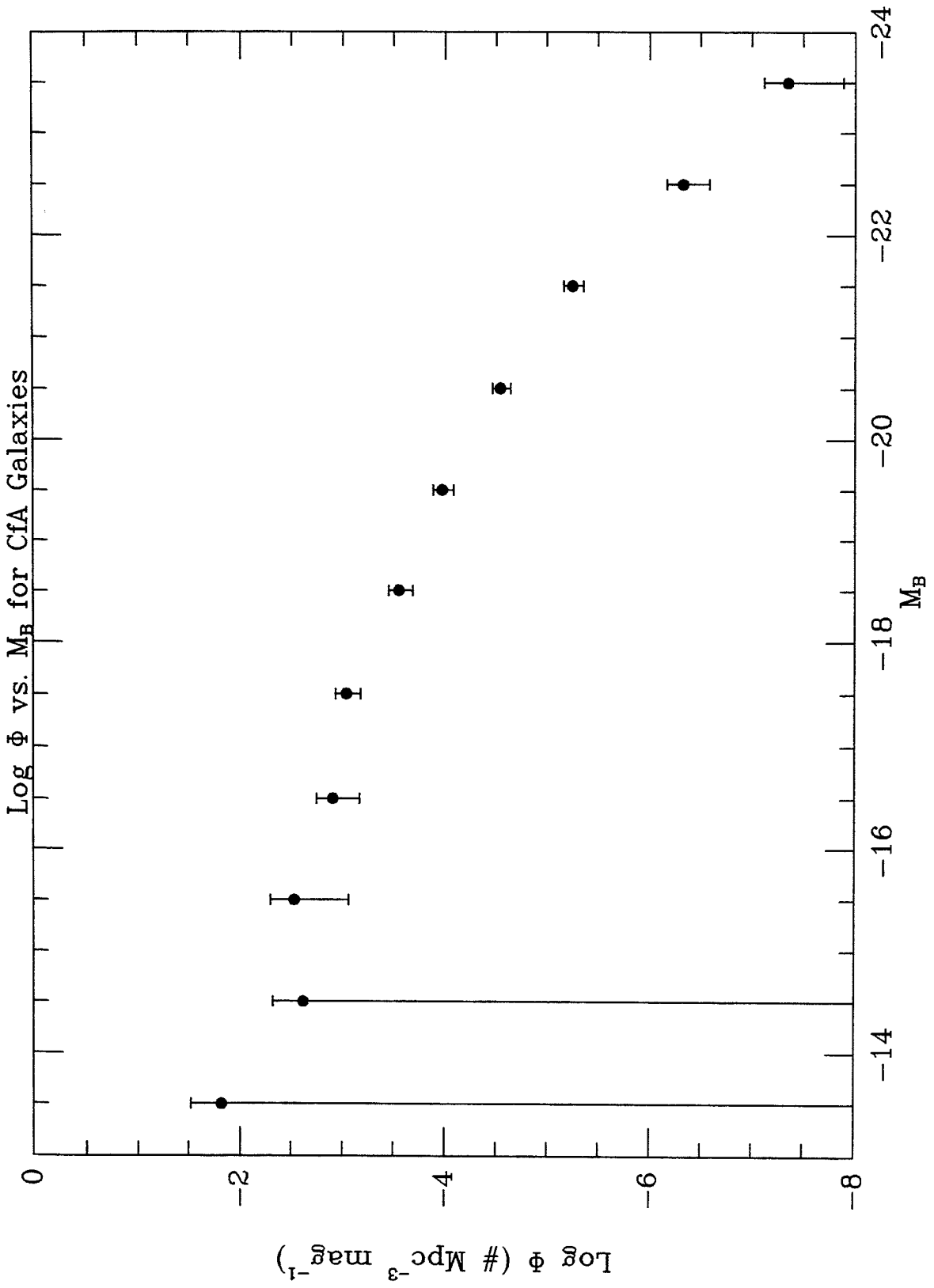
Log Φ vs. M_B for CfA Galaxies
Log Φ (# Mpc^{-3} mag^{-1})
M_B
0
-2
-4
-6
-8
-14
-16
-18
-20
-22
-24

Figure 3–2

Line Ratio Diagnostics for CfA Galaxies

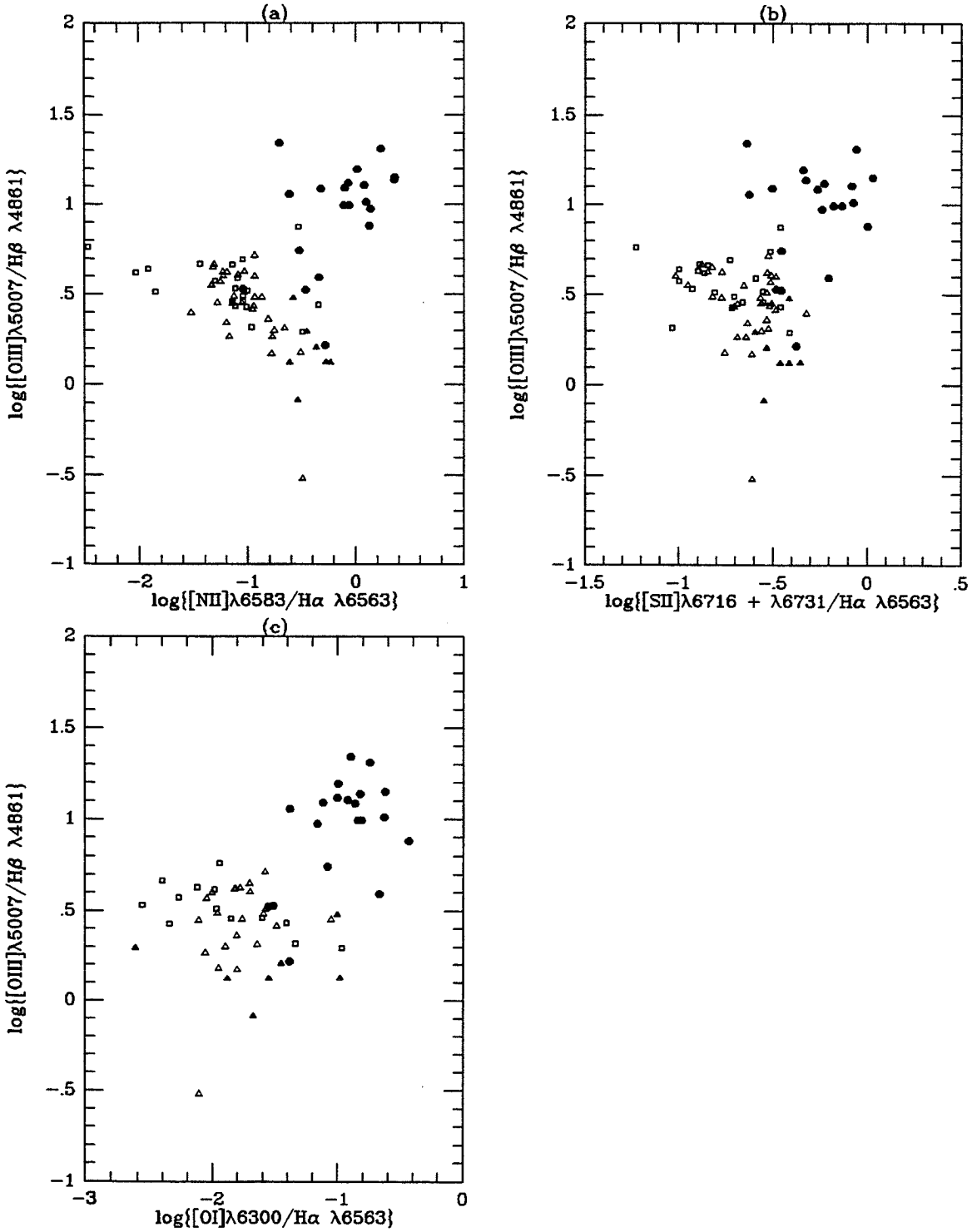

Figure 3–3(a)-(c)

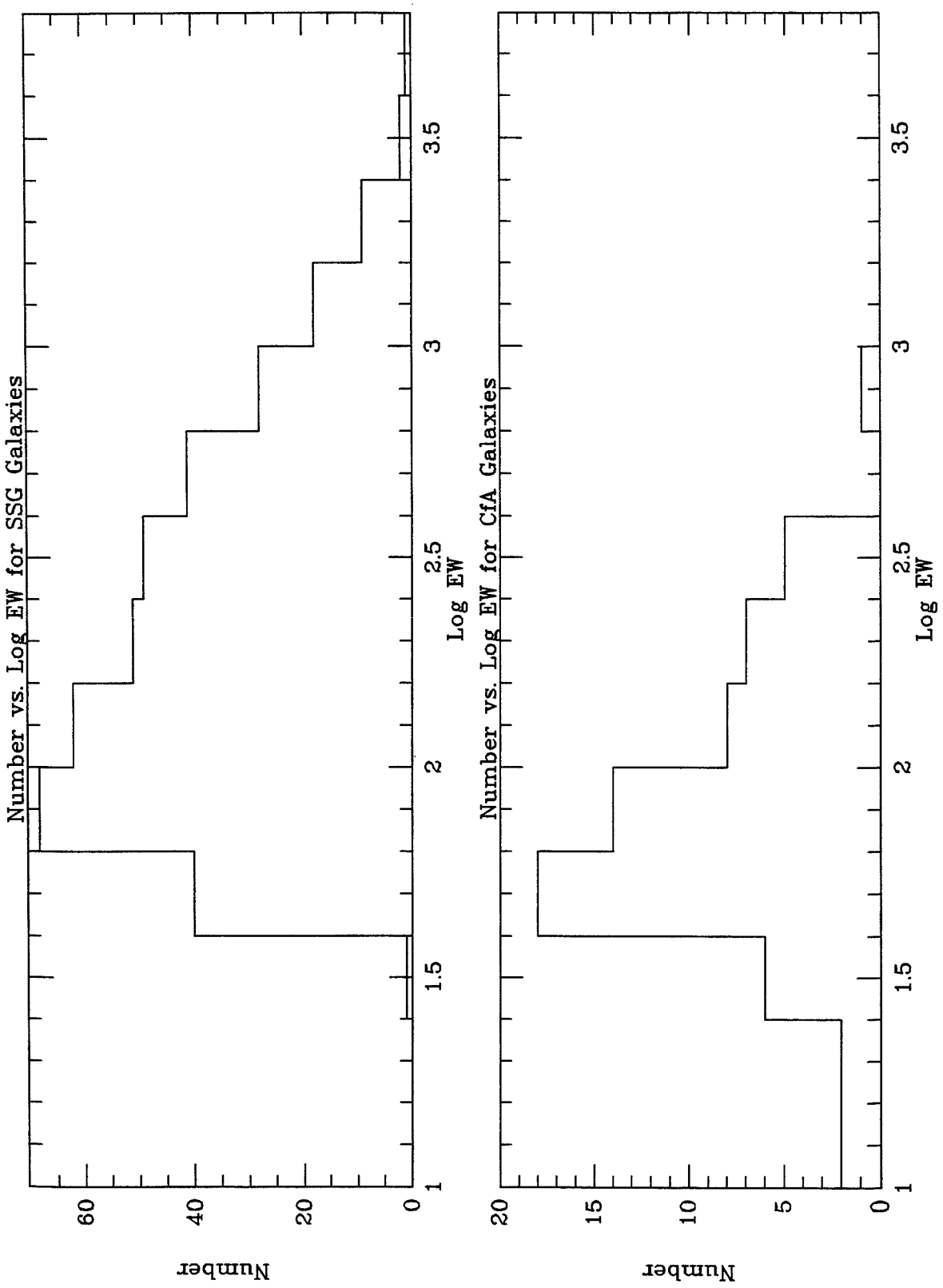
Number vs. Log EW for SSG Galaxies
Number
Log EW
0
20
40
60
1
1.5
2
2.5
3
3.5
Number vs. Log EW for CfA Galaxies
Number
Log EW
0
5
10
15
20
1
1.5
2
2.5
3
3.5

Figure 3–4

Chapter 4
Analysis of the CfA Data

4.1 Introduction

The basic premise that has been followed for analyzing the data from the CfA galaxies has been to compare how the measured line fluxes and equivalent widths for each galaxy would vary as a function of redshift as observed by the grism survey. Since the grism survey involves "slitless" spectroscopy, the spatial light distribution of a galaxy represents an important feature of the selection criteria for the distant sample. Therefore, the analysis proceeds by first modelling how a given CfA galaxy appears on the plane of the sky as a function of wavelength, using all of the data that is available from each pair of spectra that were taken for that galaxy. Then, this "model" of the galaxy's light distribution is moved through redshift space in an attempt to determine the maximum redshift to which the emission line would be detectable in each of the distant surveys. At each test redshift, several convolutions are performed in order to convert the pair of long-slit, over-resolved spectra into the equivalent spectrum that would be observed by the grism survey. This spectrum is then searched for the presence of an emission feature near the expected wavelength for that redshift using the algorithm employed by DPS to analyze the grism survey data, and the line flux and equivalent width are measured and compared to the survey criteria.

This procedure has been developed for the analysis in order to mimic the grism observations, rather than to simply determine the luminosity function (LF) of those

CfA galaxies that fulfill the transit survey selection criteria and then comparing this LF to the observed LF for the distant sample. The reasoning behind this is that, since its angular size would decrease at greater redshifts, an increasing amount of the galaxy's emission would be detectable by the fixed aperture used in the grism survey. Since the emission lines and continuum of the galaxy are generally not co-spatial, one effect of this is that there would be a redshift dependence to the measured equivalent widths. Meanwhile, the line fluxes would tend to diminish at a rate which is slower than $\frac{1}{D^2}$, since more emission would enter the "effective aperture" of the grism survey at a greater redshift. In addition, a convolution of the data in the direction parallel to the dispersion of the grism will give different results as a function of redshift, due to the changing spatial and spectral scales.

4.1.1 Definition of Terminology

In this chapter, I will be using a number of terms which are specifically defined for this work. In order to minimize confusion, I shall define each of these terms in this section.

- The **major axis** of a galaxy is defined to either be the major axis given by the UGC Catalog (Nilsson, 1971) or, if the catalog has no entry, by a position angle of 45°.
- The **minor axis** of a galaxy is defined to be the major axis ±90°.
- A **spatial cut** is created from the CCD spectrum by extracting the entire observed spectrum along the slit. It is indicative of the spatial profile of the galaxy along a given axis integrated over all observed wavelengths.
- A **centroid spectrum** is the spectrum of a galaxy measured at the centroid of its spatial cut. It is used for normalizing the secondary spectra as well as for measuring the line fluxes used for the line ratio diagnostics of each galaxy.
- The **primary spectrum** consists of a fully reduced spectrum, which has been

flux- and wavelength-calibrated. This spectrum contains both the spatial as well as the spectral information for the galaxy along that axis. Mathematically, this can be represented as $I_\theta(x-x_0,\lambda)$, where I is the measured flux density at position angle θ for the slit and x_0 is the location of the centroid along the slit.

- The **secondary spectrum** is a fully reduced spectrum that has been normalized by dividing it by the centroid spectrum created in the analysis. It therefore is indicative of the spatial profiles along a given axis as a function of wavelength. This can be represented by $\frac{I_\theta(x-x_0,\lambda)}{I_\theta(0,\lambda)}$.
- An **axis pair** consists of two fully reduced spectra, one of which is a primary spectrum, the other of which is a secondary spectrum. One of the two spectra comes from the major axis of the galaxy, while the other is from the minor axis. For every galaxy, all axis pairs of {Major,Minor} and {Primary,Secondary} are utilized in the analysis. A given galaxy will have an even multiple of axis pairs.
- Since the galaxies in the transit survey are randomly oriented on the sky, and since the grism dispersion "imposes" a particular orientation on the data, there are two different cases that are examined in the analysis. **Case A** analyzes the axis pair with the primary spectrum perpendicular to the direction of dispersion of the grism survey while **Case B** analyzes the axis pair with the primary spectrum parallel to the direction of dispersion. These are chosen since they represent the extreme range of possible position angles for a given galaxy, and thus should effectively bracket the potential range of limiting redshifts.

For a number of galaxies, there exists more than one spectrum from a particular axis, and thus there would be more than one pair of spectra for those galaxies. For each axis pair of a galaxy, first the major axis spectrum is denoted as the primary spectrum and then the minor axis spectrum becomes the primary spectrum. This is done so as to avoid any *a priori* biases with regards to the quality of the data for a given axis.

The analysis that follows will move this axis pair out in redshift and calculate the spatial and spectral convolutions that would occur with the grism survey, measuring at each redshift whether or not the galaxy would be observable in a particular survey based on the methods developed by DPS to analyze the grism data (see Chapter 2.). For each of the two cases, a limiting redshift is determined to which that galaxy would be observable. This pair of limiting redshifts then serves as the range of maximum redshifts to which that particular galaxy with that particular axis pair would be observable in that particular grism sub-survey. In addition, the measured equivalent width at each test redshift is compared to the survey limit of 50Å in order to ensure that the CfA galaxy would be detectable by the transit survey. For some of the CfA galaxies, the most important consideration ends up being the measured equivalent widths at each test redshift, as for a number of objects this quantity "straddles" the 50Å line, with values at some test redshifts which are in excess of 50Å while at other test redshifts, the value is below 50Å. In general, in these cases, I attempted to give the widest latitude in the range of maximum redshifts, to take this into account.

4.1.2 Data Quality Considerations

When all axis pairs of a particular galaxy have been analyzed for a specific sub-survey using the following procedure, a determination based on issues of data quality is made on the choice of limiting redshifts. In general, it is readily apparent which values to use when there is a substantial difference in the resulting maximum redshifts, as can be seen from the plots in Appendix B. This is based on an examination of the original input spectra for each galaxy, where one spectrum is chosen as the "best" spectrum and the maximum redshift derived when this spectrum is the primary spectrum is utilized.

First and foremost, it is possible that differences in axial ratios or an asymmetric light distribution can lead to differences between the measured line fluxes and equivalent widths for the major and minor axes of a given axis pair.

In Appendix B, a graphical representation of the data for each galaxy is given. The differences that are apparent in these figures between different axis pairs or between the major and minor axis of a given axis pair are generally due to one or more of the following difficulties that occurred at the telescope.

The greatest difficulty came about as a result of the inaccurate (uncertainty ~1') positions for each CfA galaxy prior to the publication of the RC3 (deVaucouleurs et al. 1991). A number of the observations taken in 1990 and 1991 have been made with the slit of the spectrograph misaligned relative to the nucleus of the galaxy. As a result, the CfA galaxies, which are too faint to be visible on the guide camera at the P60, have been located by measuring offsets on finder charts from bright nearby stars of known position. However, with a slit that is only 1.″3 wide, this frequently leaves the nucleus off of the slit. Since one of the central assumption in the data analysis in Chapter 4 is that the slit for the two axes intersect on each galaxy's nucleus, this misalignment will cause an underestimate to the measured spectral energy distribution.

A test was performed utilizing one of the axis pairs for which a good signal was observed in both spectra (the pair for NGC 4151). This test was designed to determine what would occur had one or both of those spectra been "off-nuclear." The procedure for this test was as follows: First, the two input spectra were modified to "remove" their central nuclear peaks, and then I redid the analysis (as described below) for each combination of axis pairs (using both "on-nuclear" and "off-nuclear") in order to determine what effects, if any, an "off-nuclear" spectrum would have on these results. If one spectrum was "on-nuclear" and one "off-nuclear," the results would tend to overestimate the predicted maximum redshift, since the spatial profiles of the secondary, "off-nuclear" spectrum would be broadened out, thus leading to an overestimate in the predicted line flux. This result is demonstrated most effectively in the plot for NGC 1068 (Figure B–13). If both spectra were "off-nuclear," then the results would tend to parallel the case where both were "on-nuclear," except

that the maximum observable redshift would tend to be underestimated, since the overall line flux would be diminished. How these problems would affect the overall result is mixed. Clearly, if the maximum observable redshift for a CfA galaxy is underestimated, that would result in an underestimate for the predicted number counts for that galaxy in the distant sample, and vice versa. Therefore, cases where both spectra are "off-nuclear" would result in an underestimate to the predicted number counts for that galaxy, while cases with one spectrum "on-nuclear" and one "off-nuclear" would tend to lead to an overestimate in the predicted counts. It is difficult to know, *a posteriori*, which spectra are "on-nuclear" and which are "off-nuclear," but the overall effect, assuming that it is more likely to miss the nucleus on both axes, would be to underestimate the predicted counts, which as is shown in the next chapter, would tend to increase the discrepancy between the predictions from the CfA sample and the observations of the SSG sample.

An additional minor problem deals with the guiding of the P60 telescope. Since the galaxies are often not visible on the guider, whenever an object lacked bright, nearby stars on which to guide, the exposures have been made with no guiding. Over the course of a typical 1200 second exposure, this could lead to a shift of several arcseconds by the slit. This, in turn, could lead to some uncertainty in the absolute photometric calibration for that spectrum.

A third concern deals with the photometric stability of some of the data, which have not all been taken under strictly photometric conditions. In general, non-photometric data tend to be of lesser quality, and are either ignored or minimally utilized in the data analysis. However, for some objects, non-photometric data has been used in the analysis, due to a lack of a second spectrum of that axis taken under better conditions.

The last concern about data quality deals with the differences in seeing between the data taken for a given galaxy if done on separate nights (which is generally the

case). By combining good seeing data with poor seeing data in the analysis, one result will overestimate the observed line fluxes while the other will underestimate this quantity, sinilar to what occurs in the above description for "off-nuclear" spectra. This is due to the method of analysis which follows, in which the secondary spectrum is used to provide the spatial information perpendicular to the primary spectrum. If the primary spectrum is taken under good seeing conditions while the secondary is taken under poor seeing conditions, the extended profiles from that spectrum will overestimate the light from the primary spectrum. In the reverse case, the constricted profiles from good data will underestimate the emission from the galaxy.

4.2 Analysis Procedure

4.2.1 Sky Subtraction and Gaussian Fit to Spatial Profile

The first step in preparing an axis pair for analysis is the removal of the sky background. This is accomplished by first extracting a spatial cut of the spectrum. Sky regions are picked out through a visual examination of this cut. These regions are chosen to avoid any obvious defects in the image, as well as to avoid the emission from the object itself. The sky regions are extracted, summed together and normalized to a single row and this sky spectrum is then subtracted off of the image row-by-row.

Each image is next examined to see if there are any obvious remaining defects (cosmic rays, bad columns/rows, etc.), which are then corrected by interpolating the data in surrounding pixels. In addition, any night sky lines which are not completely removed by the sky subtraction are cleaned up at this point.

Once again, a spatial cut is extracted, to which a gaussian profile is fit so as to determine both the centroid and width of the spectrum of that axis of the galaxy. These quantities are needed for other parts of the analysis as described below. The gaussian fit is of the form

$$f(x) = Ae^{-(x-x_0)^2/2\sigma^2} + B$$

where A is the amplitude, B is the residual background level, x_0 is the centroid and σ is the width.

Although the mean sky background is now ~ 0, there is still residual sky noise in regions beyond the maximum extent of the galaxy. It is therefore necessary to determine the maximum spatial extent of each primary spectrum using the spatial cuts, beyond which the data would be set to zero. This is done in order to minimize the propagation of this noise, which frequently overwhelms the signal, particularly for faint spectra, at later stages of the analysis. This extent is determined using an automatic routine and then through a visual confirmation of those positions with the spatial cut. The visual inspection is intended to prevent errors by the routine due to noise spikes in the spatial cut. First, we determine the first "zero-crossing" of these cuts from the centroid outwards in both directions. The program would then calculate the standard deviation of the data values from the location of that point outward to the edge of the cut and then recalculate a position where the data first fall below a set number of σ (typically 5σ), again from the centroid outwards. This gives four positions for each spatial cut, two each (at 0σ and 5σ) for the two directions outwards from the centroid of the cut. The outer (0σ) points represent the interior bounds of the region beyond which all of the data will be set to zero during the redshift search. The inner (5σ) points represent the interior bounds for the regions where the observed spectral data is retained but for which any extrapolation of the spectrum to cover the appropriate wavelength range of the grism surveys, is set to zero (see discussion of the redshift search below for a description of this extrapolation). For the region between the two 5σ points, all of the data, including in the extrapolated regions, is utilized. See Figure 4–1 for a pictorial representation of these regions. The vertical lines in the plot signify the locations of the 0σ and 5σ cutoffs.

4.2.2 Creation of Centroid Spectrum and Secondary Spectrum

The next step is creating the centroid spectrum. This is accomplished by first

examining both the spatial cut as well as the fitted gaussian to select the range of rows over which to extract a spectrum. An attempt is made to choose this range over which the spatial cut is roughly equivalent to the fitted gaussian. Next, this extracted spectrum is normalized to the centroid of the gaussian by calculating the correction factor in the following manner. First, at a particular wavelength, λ, the measured flux density at a position, x, is given approximately by:

$$f(x - x_0, \lambda) \simeq A(\lambda) e^{-(x-x_0)^2/2\sigma^2}$$

where $A(\lambda)$ is the desired centroid flux density. The sum of these flux densities over the spatial range given above (i.e., the extracted spectrum at that wavelength) would be:

$$\sum_{x=x_1}^{x_2} f(x - x_0, \lambda) \simeq \int_{x_1}^{x_2} f(x - x_0, \lambda) dx \simeq A(\lambda) \int_{x_1}^{x_2} e^{-(x-x_0)^2/2\sigma^2} dx.$$

Solving for the centroid amplitude, we find:

$$A(\lambda) \simeq \frac{\sum_{x=x_1}^{x_2} f(x - x_0, \lambda)}{\int_{x_1}^{x_2} e^{-(x-x_0)^2/2\sigma^2} dx}.$$

The numerator in this expression is given by the above extracted spectrum and the denominator can be numerically calculated.

The full centroid spectrum needs to be corrected for bad pixels on either end (a result of the data scrunching in Chapter 3), as well as for any values that fall below zero flux level (which are set to a value consistent with the spectrum at that wavelength). This condition only occurs for a few values in spectra with poor signal-to-noise.

The secondary spectrum is then created by dividing the primary spectrum by this centroid spectrum row-by-row. This creates the 1-D spatial profiles of the galaxy along one axis while the data along the perpendicular axis consists of both spatial and spectral information. This pair of images is used during the search in redshift space.

4.2.3 Redshift Search Routine

The FIGARO program that performs the search, proceeds along the following lines: First, taking as input the above axis pair, the observed heliocentric redshift of the object (from the CfA list), cosmological parameters like H_0 and q_0, the flux limit data from one of the transit sub-surveys and a redshift from which to begin the search, the axis pair is "redshifted" from its observed redshift to the first test redshift. When moving the axis pair from z_{obs} to z_{test}, a number of changes need to be made to the data. If the wavelength at z_{obs} is given by λ_1, then at z_{test} that wavelength is changed to $\lambda_2 = \Delta_1\lambda_1$ where $\Delta_1 = \frac{(1+z_{test})}{(1+z_{obs})}$ is the metric term. For a point along the axis that is a particular distance in kiloparsecs from the nucleus of the galaxy at z_{obs}, which corresponds to a particular angular extent on the plane of the sky of x_1-x_0, it would have an angular extent of x_2-x_0=$\Delta_1^2\Delta_2(x_1 - x_0)$ at z_{test} where $\Delta_2 = \frac{A(z_{obs})}{A(z_{test})}$. The intensity measured at a particular wavelength and distance in Kpc from the nucleus at z_{obs}, $I_1(x_1\text{-}x_0, \lambda_1)$, is changed to $I_2(x_2 - x_0, \lambda_2) = \Delta_1\Delta_2^2 I_1(x_1 - x_0, \lambda_1)$ at z_{test}.

A two-dimensional convolution is then performed to determine what the grism survey would observe. First, we determine the spatial extent perpendicular to the dispersion that the grism survey would include. According to DPS, this extent is 1.2× the seeing FWHM of a given survey (see Table 2–1 for these values). For Case A, the primary spectrum is perpendicular to the dispersion direction, so the extraction is performed on this data array (for Case B, it is performed on the secondary spectrum data array). Starting from the above measured centroid for the appropriate axis, the data are extracted in a swath running between $x_0 - 0.6\times$ FWHM to $x_0 + 0.6\times$ FWHM with a linear interpolation between fractional pixels. This 1-D extracted spectrum is then multiplied, row-by-row, with the data from the other axis. The resulting spectrum is indicative of the one-dimensional spectrum in the direction parallel to the grism dispersion.

At z_{test} the wavelength coverage of this spectrum, is from λ_1=4350Å $\times\Delta_1$ to

λ_n=7200Å $\times\Delta_1$. Since the grism surveys are sensitive to a wavelength coverage from about 4250Å to 7500Å, it is necessary to extrapolate this spectrum from the wavelength coverage at the test redshift to the wavelength coverage of the grism survey using template spectra of the different types of emission line galaxies. These templates were created by averaging the slit spectra from the sample of galaxies discovered by the transit survey. To perform this extrapolation, the template spectrum is first redshifted to the test redshift. Then, for those rows in the extracted spectrum that fall between the 5σ cutoffs, the template spectrum amplitude is matched to the first few non-zero data values on the blue edge of the spectrum. For the rows that fall outside of these cutoffs, the extrapolated values are all set to zero. This results in an output spectrum being properly normalized and having the proper wavelength coverage for the transit survey. It is assumed that since the 4-Shooter is insensitive to wavelengths shortward of the blue limit of the survey (about 4250Å) and since there was a filter that blocked out emission beyond the red limit (about 7500Å), data beyond these wavelength ranges, at the test redshift, can be removed.

The next step is the second spatial convolution of the spectrum. This is done in the direction parallel to the dispersion. Utilizing a scale of 77.5Å/arcsec for the 4-Shooter in grism mode, together with the spatial and spectral scales at the test redshift, the spectrum is shifted and summed, row-by-row, in order to build up the "grism" spectrum, which is what would be observed by the transit survey for that object. Each row, x, is shifted relative to the object centroid by an amount:

$$\Delta = \frac{77.5\text{Å}}{\text{arcsec}} \times \left[\frac{(x - x_0)\Delta r}{\Delta\lambda}\right] \text{ pixels},$$

where Δr is the spatial scale in arcsec/pixel and $\Delta\lambda$ is the wavelength scale in Å /pixel. Following this, the spectrum is convolved to the resolution of the transit survey, utilizing a gaussian of width:

$$\sigma(\text{Å}) = \frac{77.5\text{Å}}{\text{arcsec}} \times \frac{FWHM('')}{2\ln 2}.$$

This convolved spectrum is then rebinned to the same binsize as the transit survey (either 51.67Å/pixel for double-binned surveys or 77.5Å/pixel for tripled-binned surveys). Figure 4–2 shows an example of each of these steps using the actual data from the galaxy NGC 1068.

Lastly, this rebinned spectrum is searched near the expected wavelength for the [OIII]$\lambda\lambda$4959, 5007 and Hβ λ4861 lines for a possible emission feature that would be detectable to the transit survey. This search examines the five wavelength bins most likely to contain the emission lines at the test redshift. For each bin, the program first determines which points to use in calculating the continuum by selecting the ten bins on either side of the line beyond a specified linewidth and then fits a $2^{\underline{nd}}$ order polynomial to those points. This continuum fit is subtracted off of the rebinned spectrum and then the gaussian amplitude of the remainder is fit at the bin wavelength. For a fixed width, this amplitude corresponds to an area for the gaussian, which is proportional to the product of the line flux and the wavelength squared. The program proceeds to calculate the ratio of amplitude to λ^2 for each of the five wavelength bins, and selects the one which maximizes this value. With this value and the appropriate continuum fit, both the expected line flux and the equivalent widths are calculated and returned to the main program.

The resulting values of the test redshift, the observed line flux, the limiting line flux and the equivalent width are output to a file. The limiting redshift corresponding to the limiting line flux for a particular sub-survey or the equivalent width limit of 50Å was derived by iterating the above procedure. For each axis pair, this analysis is performed independently using the flux limits from each of the six grism sub-surveys, as is shown in Appendix B.

4.2.4 Effects of Sparse Spatial Sampling of CfA Galaxies

It is difficult to get a quantitative measure on the effects caused by the sparse spatial sampling of the CfA data, due to the usage of a narrow slit along the two

principle axes of each galaxy. Since the distant survey utilizes a slitless grism, and thus is sensitive to the spatial light distribution within D. P. Schneider's aperture, this issue is one that needs to be addressed.

For the two observed position angles, the slits expose roughly 1% of the 6'x 6' square area, and while most emission tends to be concentrated in the nuclear region, there is, on occasion, substantial off-nuclear emission, which, if it falls along one of the two principle axes of the galaxy, could lead to an overestimate in the predicted maximum redshift, or if it was not observed on the slit, it would underestimate the total line flux and thus the maximum observable redshift. How this effect would affect the results of this thesis is not readily apparent using the existing data set. With the assumption that position angle should be a random quantity relative to the spatial light distribution of a given galaxy (i.e., that galactic HII regions don't cluster or avoid the major and minor axes of a galaxy), then the overall effect should tend to cancel out if the data sample is sufficiently large or else it might lead to a slight underestimate in the predicted counts, as off-nuclear sources are less likely to have been observed, leading to an underestimate in the total measure line flux. This would, of course, drive the results in the next chapter even further away from demonstrating positive evolution. Other factors to consider are the spatial extent and orientation of any such "off-nuclear" emission, whether it subtends a substantial azimuthal angle or is more like a point source or a radial source as well as the rejection by SSG of sub-galactic candidates, based on their visual inspection of the finding charts (i.e., obvious galactic HII regions were rejected by SSG in their survey).

List of Figures for Chapter 4.

- Figure 4–1: Plot of a spatial cut denoting the different regions utilized as described in the text. In the central region (denoted with dashed lines), the data at the blue edge of the spectrum is extended using the template spectrum for each object type, as the galaxy is moved to higher redshifts. The regions within the dotted lines uses all of the observed spectral data but does not extrapolate into the blue spectral region, due to the lower signal-to-noise of this data. The regions exterior to the dotted lines (denoted with large zeros), is ignored completely, as it is a source of solely sky noise.
- Figure 4–2: 1-dimensional plots of how a typical galaxy, in this case NGC 1068, would appear in the transit survey if it were observed at a redshift of z=0.2. The first plot shows the spectrum at the full resolution of the input data set. The next plot shows the spectrum convolved to the resolution of the transit survey. The third plot shows the spectrum rebinned to the size of the wavelength bins of the transit survey. The final plot shows the fitted continuum based on the algorithm provided by Dr. D. P. Schneider.

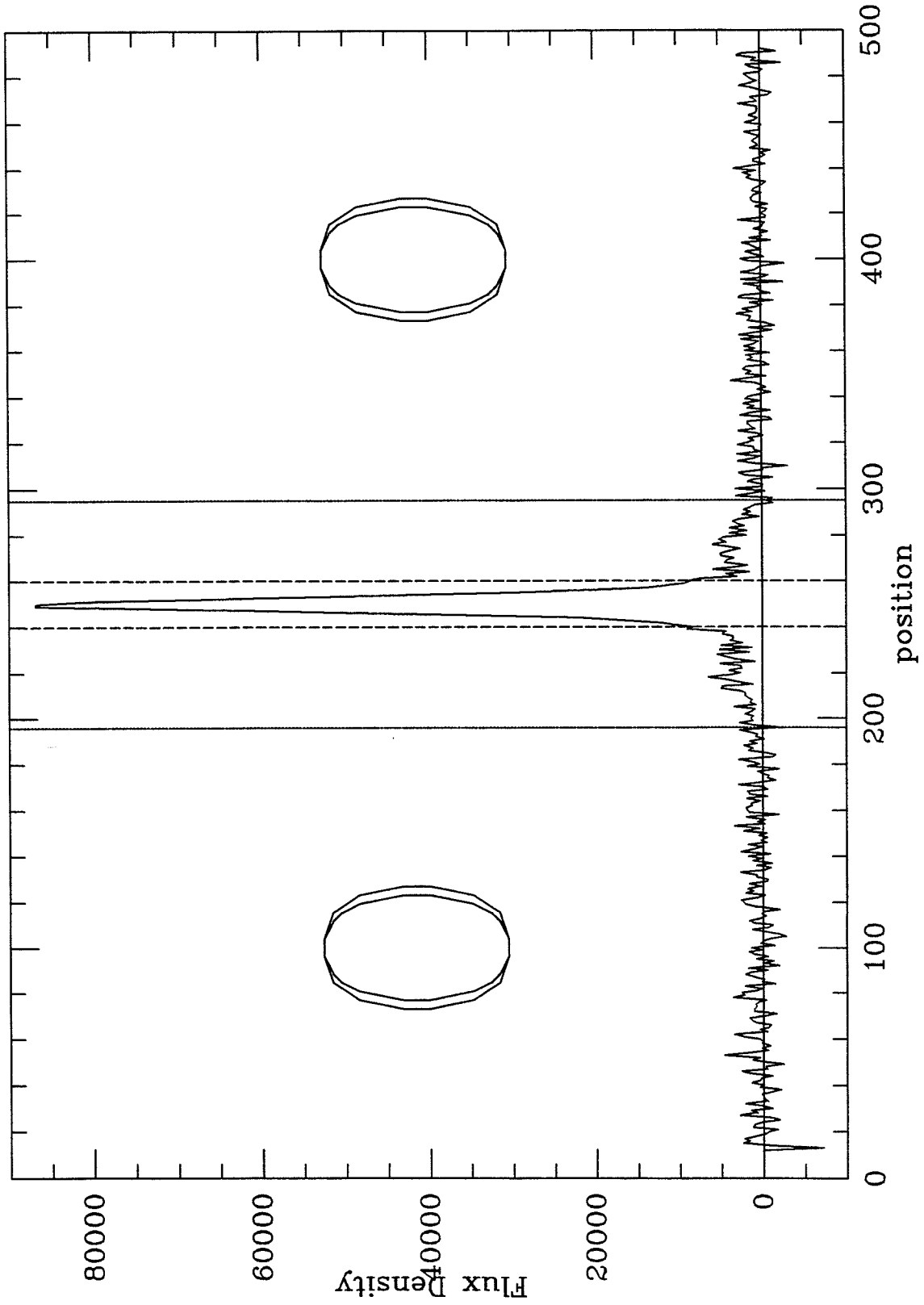
Flux Density
80000
60000
40000
20000
0
0
100
200
300
400
500
position

Figure 4–1

NGC 1068 @ z=0.2

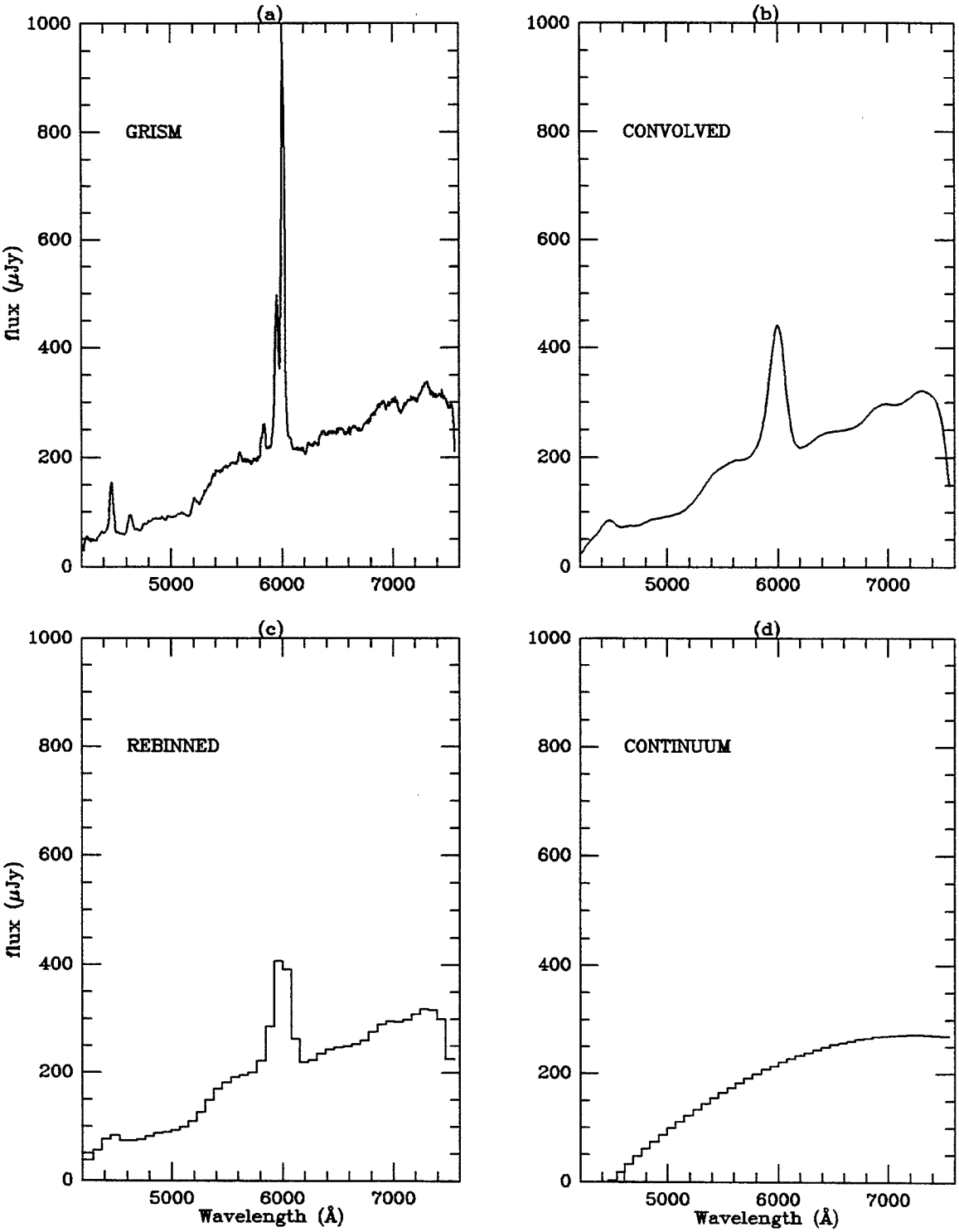

Figure 4–2

Chapter 5
Conclusions

From the analysis performed for each CfA galaxy, a pair of maximum redshifts are determined to which that galaxy would be observable in each of the six grism sub-surveys. The reason for choosing two maximum redshifts is to take into account differences due to orientation effects as well as to account for the equivalent width criterion in the grism survey. These maximum redshifts are translated into accessible volumes using the equation from Chapter 2, and these volumes are compared to the maximum volume accessible to each CfA galaxy in the CfA survey (see Chapter 3). This ratio gives an estimate of the number of galaxies that would be observable in the grism survey for each galaxy in the CfA sample.

5.1 Completeness of Burg's Subsample

We have used as a basis for this thesis, Richard Burg's analysis of the spectra of 1948 CfA galaxies. This represents 81% of the total number of all galaxies in the CfA survey. His analysis catagorizes the objects based upon their Hubble types, from early type ellipticals to late type spirals and irregulars. The completeness within any given sub-group varies from a high of 90% for the ellipticals to a low of 73% for Scdm spirals. The range of completeness as a function of Hubble type is given in Table 5–1 (from Burg's Table 3.3). Each of the 81 galaxies from Burg's list are corrected by the appropriate factor based upon their Hubble type. This is the first of two completeness corrections that must be made to the sample provided by Burg.

The other correction deals with the lower limit of the [OIII]$\lambda\lambda 4959, 5007$ equiva-

lent width of 23.75Å for the CfA galaxies provided by Burg. Assuming that the 81 galaxies from that sample represent an ensemble average of the spatial distribution of the light profiles in the [OIII]$\lambda\lambda$4959, 5007 emission line for all 2401 CfA galaxies, we can use the measured equivalent widths of these 81 galaxies from the transit survey analysis (see Chapter 4) to estimate how many galaxies with Burg's equivalent width below 23.75Å would have an equivalent width in excess of 50Å when observed in the grism transit survey. For each CfA galaxy, a range of equivalent widths are determined at different redshifts as well as for different axis pairs and orientations by the algorithm in Chapter 4. To determine the equivalent width used for this completeness correction, first the median equivalent width from each search in redshift is determined. Then, each series of median equivalent widths are plotted in order to determine whether any values should be discarded based on data quality considerations (see Section 4.1.1). Finally, the average value of the surviving median equivalent widths for a given galaxy is calculated to determine the transit survey equivalent width used in this analysis.

If we imagine decreasing the [OIII]$\lambda\lambda$4959, 5007 emission uniformly across the galaxy, then both the Burg equivalent width as well as the transit survey equivalent width would decrease monotonically. A plot of the Burg equivalent width vs. the transit survey equivalent width for each galaxy (Figure 5–1) shows that for the thirteen objects which fall above the line that passes through the origin and the point that represents the limits for the two surveys (23.75,50), that each of these galaxies would have been detectable in the transit survey sample had their Burg equivalent width been below 23.75Å. To compute the correction factor for each of these galaxies, we first calculate the value of the Burg equivalent width for which that galaxy would have an equivalent width of 50Å in the transit survey analysis. Then, utilizing the number distribution of [OIII]$\lambda\lambda$4959, 5007 equivalent widths from Burg's total sample, the total number of galaxies with Burg's equivalent width greater than this

minimum value are determined. Since each of these galaxies represents one out of 81 galaxies in the total sample, and since this sample is assumed to represent an ensemble average of the full CfA survey, it follows that $\frac{1}{81}$ of the above number of galaxies represents the correction factor to be applied to that particular galaxy. For those galaxies that fall below the line in Figure 5–2, their equivalent width correction is unity, as they represent those galaxies which would not pass the equivalent width criterion had their Burg equivalent width been less than 23.75Å. As an example, the galaxy NGC 7468 has an equivalent width of 31.13Å according to Burg, while the transit survey analysis shows it to have a typical equivalent width of 182.37Å. This would therefore correspond to an equivalent width of 50Å in the transit survey analysis if it had a Burg equivalent width of 8.53Å. By summing up the total number of galaxies from Burg with [OIII]$\lambda\lambda$4959, 5007 equivalent widths between 8.53Å and 23.75Å(200), the correction factor is determined to be 2.47 and is applied to the predicted counts for NGC 7468. Table 5–2 provides the equivalent width correction for the 13 galaxies to which it has been applied.

5.2 Overdensity of CfA Survey

In order to compare the nearby and distant samples of emission line galaxies, it is necessary to correct the nearby sample from the CfA survey for the perceived overdensity of this survey over the average density of galaxies in the observable universe. According to Santiago and Strauss (1992), the overdensity of the CfA can be calculated as a function of redshift and galaxy type (E/S0, spirals, irregulars), relative to the mean density of that type in the CfA survey out to 8000 km sec^{-1} (4000 km sec^{-1} for the irregulars). For each of the galaxies in the nearby sample, the correction for the CfA overdensity is determined by first calculating the maximum redshift to which that galaxy would be observable in the CfA survey, and then averaging the data from Santiago and Strauss out to that redshift to estimate this correction. Figure 5–2 gives

this overdensity correction as a function of redshift (and was kindly provided by Dr. Santiago). This represents the cumulative overdensity within the plotted redshift, which is the value that has been utilized in this exercise for the CfA overdensity, rather than the overdensity measured at that particular redshift shell.

5.3 Discussion of the Results

This thesis has attempted to measure the extent to which evolution is discernable between two samples of emission line galaxies by measuring the maximum observable redshifts for galaxies in the nearby sample by the criteria of both the nearby and the distant samples and comparing the resulting available volumes to predict number counts in the distant sample. In tables 5–3 and 5–4, the total pre-correction predicted number counts are provided for each Seyfert galaxy in the CfA sample which is observable in the distant survey (i.e., has an EW > 50Å), along with each of the above correction factors and the resulting predicted counts. Tables 5–5 through 5–10 give the comparable information for LINERs, Starbursts and HII galaxies, respectively. These number counts are then compared to what is actually observed in the distant sample in order to make the determination of the role played by galaxy evolution for these objects.

In addition, if we examine the results using a power-law for density evolution of the form:

$$\rho(z) = \frac{dN(z)}{dV(z)} = \rho_0(1+z)^n = \frac{1}{V_{CfA}}(1+z)^n$$

where the volume element is given by (see Chapter 2):

$$dV(z) = \omega\left(\frac{c}{H_0}\right)A^2(z)(1+z)^{-3}(1+2q_0z)^{-1/2}dz$$

and the luminosity distance by:

$$A(z) = \frac{2c}{H_0}\left\{1 + \frac{z}{\sqrt{1+2q_0z}+1}\right\}\left\{\frac{z}{\sqrt{1+2q_0z}+1}\right\},$$

which gives:

$$dN(z) = \frac{4\omega}{V_{CfA}}\left(\frac{c}{H_0}\right)^3 f_n(z)dz$$

where

$$f_n(z) = \frac{(1+z)^{n-3}}{(1+2q_0z)^{1/2}}\left\{1 + \frac{z}{(1+2q_0z)^{1/2}+1}\right\}^2\left\{\frac{z}{(1+2q_0z)^{1/2}+1}\right\}^2.$$

This leads to a prediction for the number counts of an arbitrary density law index, n, of:

$$N_{pred} = \frac{4\omega}{V_{CfA}}\left(\frac{c}{H_0}\right)^3 \int_0^z f_n(z')dz'.$$

For the case where $q_0 = 0.5$, the integrand can be simplified to the following expression:

$$f_n(z) = (1+z)^{n-5/2}\left[(1+z)^{1/2} - 1\right]^2.$$

This is directly integrable for all values of the power-law index. The solutions for the above integral are as follows:

$$\int_0^z f_n(z')dz' = \left\{(1+z)^n\left[\frac{1}{(1+z)^{3/2}} + \frac{3-2n}{(n-1)(1+z)} + \frac{2n-3}{(2n-1)(1+z)^{1/2}}\right] - \frac{1}{(n-1)(2n-1)}\right\}\left(\frac{2}{2n-3}\right); \quad n \neq \frac{1}{2}, 1, \frac{3}{2}$$

$$\int_0^z f_{1/2}(z')dz' = \left\{\frac{1}{3}(1+z) - 2(1+z)^{1/2} + \frac{8}{3}(1+z)^{1/4} - 1\right\}\left(\frac{1}{1+z}\right)^{1/4}; \quad n = \frac{1}{2}$$

$$\int_0^z f_1(z')dz' = (1+z)^{1/2} - \ln(1+z) - \frac{1}{(1+z)^{1/2}}; \quad n = 1$$

$$\int_0^z f_{3/2}(z')dz' = 4(1+z)^{1/2}\left[(1+z)^{1/2} - 1\right] + \ln(1+z) - 3z; \quad n = \frac{3}{2}$$

The results for each class of object are summarized in Table 5–11, in which a range of predicted counts, based on the two maximum redshifts derived for each CfA galaxy are compared to the observed counts. Table 5–12 gives a summary for different values of the density power law from $n = 0$ to $n = 4$. An analysis of what is found for each class is given below:

- **Seyfert galaxies**: The Seyfert galaxies appear to be either a non-evolving population or perhaps even a negatively evolving population, as there were 136 total observed objects in the distant sample while the predictions based on the CfA sample are in excess of 200 galaxies that should have been detected in the distant sample. If one discounts the above corrections factors, the numbers for Seyferts are more in line with the predicted counts. This is due to the effect of the CfA overdensity having an "inflating" effect on the predicted counts, since most of the Seyfert galaxies are bright enough to be seen out beyond the local overdense region (see Figure 5–2). If the overdensity correction is lacking for this group (many are observable beyond the 8000 km/sec limit of the Santiago and Strauss data), then these predicted numbers are liable to be decreased. When one includes possible density evolution, the differences between the two samples are further exasperated. It would be very difficult to reconcile these results with the results obtained by Lonsdale and Chokshi (1993), who found evidence for strong density evolution ($n = 4 \pm 2$) in faint galaxy samples taken in both the blue and far-infrared, though clearly the unique selection criteria for this work makes a direct comparison with the results of Lonsdale and Chokshi and others, very difficult.

- **LINERs**: LINERs appear in both samples in very small numbers, and thus any statistical arguments on their evolution will not carry much weight. Only 8 CfA galaxies are classified as LINERs, while only 9 of the SSG galaxies are so classified. This is primarily due to the fact that LINERs are a class defined as having weak [OIII]$\lambda\lambda 4959, 5007$ emission, and thus are not likely to appear in great numbers in a sample that is based on [OIII]$\lambda\lambda 4959, 5007$ line flux. Regardless, the predicted and observed number counts are at least consistent with a non-evolving population, though they are not inconsistent with a range of density evolution scenarios.

- **Starburst galaxies**: Depending on where one places the magnitude limit between luminous and dwarf star-forming galaxies, the results for both the Starbursts as well as the HII galaxies do show dramatic changes. In part, this is due to the presence of a single object in the CfA sample, NGC 4861, which has an M_B ~-17.8, and for which the predicted counts in the distance sample are quite substantial. The reason this one galaxy has such a large effect is due to the strength of its [OIII]$\lambda\lambda$4959, 5007 emission line, with an equivalent width of nearly 1000Å. This causes the galaxy to be observable to large redshifts in the line-selected grism survey, while it can be seen only to modest distances in the continuum-selected CfA survey. As for the Starburst galaxies, using a continuum magnitude cutoff of -18 (and thus ignoring the effect of NGC 4861 for this class), we find that the predicted counts are consistent with a non-evolving population, similar to the results of Boroson, Salzer and Trotter (1993; see Chapter 1) and these results do not support the conclusions of BES and LDSS that there exists a substantial population of star-forming galaxies to explain the excess blue galaxy counts. As shown in Table 5–11, the median redshift for the sample of Starburst galaxies is 0.129, and we therefore should detect some sign of evolution in these objects (excess observed counts) if the model of BES is correct. However, it is also apparent that the low end of the predicted counts remains within 1σ of the observed counts for indices $n \leq 4$.

- **HII galaxies**: With NGC 4861, the HII galaxies predictions far exceed the observed counts and are not consistent with an evolving population of dwarf star-forming galaxies. Even when NGC 4861 is removed from the sample, the numbers are still consistent with the non-evolving model, and thus there is no evidence for evolution amongst these objects, though the numbers are not inconsistent up to an $n = 4$ power law. However, the median redshift of this sample is only 0.026, and only 6% of the HII galaxies have redshifts above 0.1, and thus it is conceiv-

able that the grism survey does not observe deep enough for this class of object to determine whether or not evolution begins to have an effect at cosmologically interesting redshifts.

This thesis has attempted to address the issue of the evolution of emission line galaxies out to redshifts of $\sim$0.5. To accomplish this task, I have utilized two samples of emission line galaxies, one nearby from the CfA survey, and a distant sample from the grism survey. The comparison has involved observing the nearby sample using the P60 Echelle spectrograph in a low-resolution, long slit mode, and then using these spectra to model the spatial and spectral light distributions of each CfA galaxy and how those distributions would appear to the grism survey as a function of redshift. By determining maximum redshifts for each CfA galaxy for both the CfA survey as well as in each grism sub-survey, predicted number counts for each type of emission line galaxy could be made and compared to the observed counts from the grism survey. These number counts have shown that for each class of emission line galaxy observed (Seyferts, LINERs, Starbursts and HII galaxies), the results are consistent with a no-evolution model. For Seyfert galaxies, they are generally inconsistent with models requiring substantial evolution over modest redshift ranges.

References

DeLapparent, V., Geller, M. and Huchra, J., 1989, *Ap. J.*, **343**, 1

deVaucouleurs, G., deVaucouleurs, A., Corwin, H.G., Buta, R.J., Paturel, G. and Fouqué, P., 1991, *Third Reference Catalog of Bright Galaxies*, Springer-Verlag, New York

Lonsdale, C. and Chokshi, A., 1993, *A. J.*, **105**, 1333

Table 5–1. Completeness of CfA Sample by Hubble Type (from Burg 1987)

Type	$N_{observed}$	N_{total}	Completeness
Ell	243	270	0.90
S0	516	613	0.84
Sab	658	792	0.83
Scdm	460	630	0.73
Irr	69	91	0.76

Table 5–2. Equivalent Width Corrections to CfA Galaxies

OBJECT	EW_{obs} (Burg)	EW_{obs} (SSG)	EW_{min} (Burg)	$N(>EW_{min})$ (Burg)	Correction Factor
NGC 7468	31.13	182.37	8.53	200	2.47
NGC 3310	27.25	107.37	12.69	145	1.79
NGC 3991	24.22	94.16	12.86	145	1.79
NGC 4509	55.05	211.07	13.04	145	1.79
NGC 5548	30.05	113.88	13.19	142	1.75
NGC 1068	49.53	178.24	13.89	137	1.69
NGC 5238	36.69	105.36	17.41	109	1.35
NGC 5107	41.05	115.15	17.82	106	1.31
1052+4959	98.23	253.55	19.37	100	1.23
NGC 7241	66.15	147.62	22.41	88	1.09
IC 694	24.33	53.33	22.81	87	1.07
1501+1038	52.20	110.76	23.57	82	1.01
NGC 4214	86.88	183.31	23.70	81	1.00

Table 5–3. Pre- and Post-corrected Predictions for Seyferts.

Object	Pre-corrected Predictions	Complete Correct	CfA Overdens	EW Correct	Post-corrected Predictions
0003+1955	4.66 – 4.77	1.00	1.00	1.00	4.66 – 4.77
0141+0206	22.07 – 22.13	1.19	0.65	1.00	40.52 – 40.62
NGC 863	3.02 – 3.02	1.00	1.00	1.00	3.02 – 3.02
NGC 1068	9.73 – 10.72	1.20	1.00	1.69	19.80 – 21.80
NGC 3227	0.10 – 0.90	1.20	1.04	1.00	0.11 – 1.04
1058+4555	2.51 – 2.62	1.20	1.00	1.00	3.02 – 3.16
NGC 3786	0.11 – 0.12	1.00	0.88	1.00	0.13 – 0.14
NGC 3982	0.00 – 0.08	1.00	1.42	1.00	0.00 – 0.06
NGC 4051	0.00 – 0.05	1.20	1.18	1.00	0.00 – 0.05
1202+3127	1.50 – 6.83	1.19	1.00	1.00	1.78 – 8.12
NGC 4151	35.43 – 35.43	1.20	1.00	1.00	42.66 – 42.66
NGC 4253	7.12 – 7.68	1.20	0.86	1.00	9.93 – 10.71
1219+7535	1.46 – 1.47	1.00	1.00	1.00	1.46 – 1.47
NGC 4388*	3.43 – 3.97	1.20	0.86	1.00	4.81 – 5.54
NGC 4388*	20.14 – 23.30	1.20	1.19	1.00	20.31 – 23.50
NGC 4388*	33.08 – 38.27	1.20	1.50	1.00	26.46 – 30.62
NGC 5252	8.86 – 9.33	1.19	0.76	1.00	13.90 – 14.63
NGC 5283	0.51 – 5.09	1.19	0.75	1.00	0.81 – 8.01
1351+6933	16.13 – 16.28	1.00	0.92	1.00	17.56 – 17.72
NGC 5548	7.01 – 7.14	1.19	1.00	1.75	14.63 – 14.91
1434+5901	4.22 – 5.00	1.00	1.00	1.00	4.22 – 5.00
1501+1038	4.00 – 4.01	1.11	1.00	1.01	4.49 – 4.50
2237+0747	1.89 – 2.28	1.20	1.01	1.00	2.25 – 2.71
NGC 7469	5.18 – 8.67	1.20	1.00	1.00	6.23 – 10.44
NGC 7674	3.27 – 3.89	1.20	1.00	1.00	3.94 – 4.68
NGC 7682	4.08 – 4.44	1.20	0.84	1.00	5.86 – 6.37

Table 5–4. Predicted vs. Observed Number Counts of Seyfert Galaxies.

Survey	Predicted Counts	Observed Counts
GH	41.1±14.0 – 51.0±15.5	17
IJ	13.1± 4.4 – 15.7± 4.9	8
KL	23.0± 7.5 – 27.8± 8.3	10
MN	27.7±10.4 – 37.3±11.6	41
OP	51.2±17.3 – 63.9±19.4	26
QR	49.8±16.4 – 61.5±18.8	32
Totals	205.8±69.8 – 257.2±78.4	136

Table 5–5. Pre- and Post-corrected Predictions for LINERs.

Object	Pre-corrected Predictions	Complete Correct	CfA Overdens	EW Correct	Post-corrected Predictions
NGC 3310	4.26 – 4.58	1.20	0.87	1.79	10.58 – 11.39
NGC 3395	0.20 – 0.35	1.37	0.85	1.00	0.32 – 0.57
IC 694	0.57 – 1.11	1.37	1.00	1.07	0.83 – 1.63
NGC 5256	0.33 – 3.44	1.20	1.00	1.00	0.40 – 4.14

Table 5–6. Predicted vs. Observed Number Counts of LINER's.

Survey	Predicted Counts	Observed Counts
GH	1.9± 1.9 – 3.6± 2.4	2
IJ	0.8± 0.7 – 1.4± 0.8	0
KL	2.1± 1.3 – 2.4± 1.4	0
MN	1.5± 1.5 – 1.5± 1.5	2
OP	3.0± 2.6 – 4.6± 3.2	3
QR	2.8± 2.8 – 4.3± 3.1	2
Totals	12.1±10.6 – 17.7±12.2	9

Table 5–7. Pre- and Post-corrected Predictions for Starbursts.

Object	Pre-corrected Predictions	Complete Correct	CfA Overdens	EW Correct	Post-corrected Predictions
0109+0104	0.00 – 0.14	1.32	1.00	1.00	0.00 – 0.18
0157+2103	0.00 – 4.61	1.19	1.36	1.00	0.00 – 4.01
0940+0943	0.14 – 0.90	1.32	1.00	1.00	0.19 – 1.18
0954+1553	3.55 – 3.82	1.20	0.85	1.00	5.01 – 5.40
NGC 3239	0.00 – 1.77	1.32	1.98	1.00	0.00 – 1.18
1029+5439	2.32 – 2.42	1.32	1.43	1.00	2.15 – 2.24
NGC 3353	32.67 – 33.63	1.32	2.63	1.00	16.36 – 16.84
NGC 3432	0.08 – 0.30	1.37	1.94	1.00	0.06 – 0.21
NGC 3448	0.00 – 0.62	1.19	1.00	1.00	0.00 – 0.73
1052+4959	5.70 – 8.05	1.32	1.90	1.23	4.86 – 6.86
IC 691	7.21 – 8.02	1.19	2.07	1.00	4.14 – 4.60
NGC 3769	0.00 – 0.04	1.20	1.96	1.00	0.00 – 0.03
NGC 3991	6.26 – 7.21	1.32	1.00	1.79	14.78 – 17.02
NGC 4214	0.49 – 0.53	1.32	1.65	1.00	0.39 – 0.42
1216+0408*	7.07 – 8.17	1.11	1.58	1.00	4.96 – 5.74
NGC 4656	0.38 – 1.48	1.37	1.35	1.00	0.38 – 1.50
NGC 5109	0.47 – 1.35	1.37	1.14	1.00	0.56 – 1.62
1407+4916	0.10 – 1.51	1.37	1.90	1.00	0.08 – 1.09
NGC 5789	35.70 – 40.47	1.37	1.34	1.00	36.47 – 41.34
1604+4129	8.77 – 10.99	1.37	1.21	1.00	9.95 – 12.48
NGC 7241	51.46 – 68.48	1.20	2.50	1.09	26.98 – 35.91
NGC 7468	9.02 – 38.07	1.11	1.16	2.47	21.32 – 89.97
NGC 7714	5.69 – 7.35	1.20	0.86	1.00	7.92 – 10.24
NGC 7800	0.00 – 0.12	1.32	1.38	1.00	0.00 – 0.12

Table 5–8. Predicted vs. Observed Number Counts of Starburst Galaxies.

Survey	Predicted Counts	Observed Counts
GH	30.7±11.2 – 51.2± 22.6	23
IJ	10.7± 3.8 – 16.8± 7.2	7
KL	16.7± 6.1 – 28.3± 11.8	14
MN	19.9± 7.3 – 33.0± 14.8	45
OP	41.5±15.0 – 65.2± 27.6	15
QR	37.0±13.8 – 60.5± 26.0	47
Totals	151.6±56.8 – 255.2±109.8	149

Table 5–9. Pre- and Post-corrected Predictions for HII Galaxies.

Object	Pre-corrected Predictions	Complete Correct	CfA Overdens	EW Correct	Post-corrected Predictions
0948+0804	3.01 – 8.00	1.32	2.00	1.00	1.98 – 5.27
1004+1036	3.63 – 6.38	1.19	2.60	1.00	1.66 – 2.91
NGC 3264	9.17 – 18.61	1.37	3.17	1.00	3.97 – 8.05
NGC 4173	0.00 – 0.02	1.37	3.06	1.00	0.00 – 0.01
1216+0408*	18.21 – 21.02	1.11	2.58	1.00	7.83 – 9.04
1216+0408*	48.46 – 55.94	1.11	3.95	1.00	13.62 – 15.72
NGC 4509	43.99 – 45.36	1.32	4.82	1.79	21.55 – 22.22
NGC 4670	24.64 – 24.64	1.19	2.63	1.00	11.15 – 11.15
NGC 4861	187.53 – 188.74	1.37	2.81	1.00	91.31 – 91.90
NGC 5107	7.78 – 10.38	1.37	2.69	1.31	5.19 – 6.93
NGC 5238	0.04 – 0.75	1.37	2.01	1.35	0.03 – 0.69
1448+3547	12.71 – 12.81	1.32	2.81	1.00	5.98 – 6.02
2354+1633	0.00 – 3.34	1.32	2.37	1.00	0.00 – 1.86

Table 5–10. Predicted vs. Observed Number Counts of HII Galaxies.

Survey	Predicted Counts	Observed Counts
GH	30.0±20.1 – 36.2±20.5	14
IJ	9.4± 6.1 – 11.5± 6.3	9
KL	14.3± 9.6 – 17.4± 9.9	6
MN	19.7±13.4 – 23.5±13.8	21
OP	35.6±23.8 – 43.8±24.3	8
QR	33.9±22.0 – 40.4±22.7	16
Totals	150.6±95.3 – 172.7±97.5	74

Table 5–11. Summary of Results for each Object Type

Object Type	Pre-corrected Predictions	Post-corrected Predictions	Observed Number	z_{med}
Seyferts	146± 49 – 200± 64	206±70 – 257± 78	136	0.285 (Sy1)
				0.192 (Sy2)
LINERs	5± 4 – 9± 6	12±11 – 18± 12	9	0.205
Starbursts	170± 73 – 242± 97	152±57 – 255±110	149	0.129
HII Galaxies	311±196 – 375±205	151±95 – 173± 98	74	0.026
HII (w/o NGC 4861)	123± 57 – 186± 81	59±27 – 81± 33		

Table 5–12. Results for each Object Type as a Function of the Power Law Index

n	HII Galaxies	Starbursts	LINERs	Seyfert Galaxies
#obs	74	149	9	136
0	143± 95–173± 97	156±57–255±110	12± 11– 18± 12	206± 70–257± 78
1	155±105–187±108	171±63–282±122	14± 12– 20± 14	252± 85–312± 95
2	169±117–202±119	188±70–313±136	15± 14– 23± 16	310±105–382±116
3	185±130–219±132	206±77–347±152	17± 15– 27± 18	383±130–469±143
4	202±144–238±147	226±85–385±169	20± 17– 31± 21	476±162–580±177

List of Figures for Chapter 5.

SSG Equivalent Widths vs. Burg Equivalent Widths

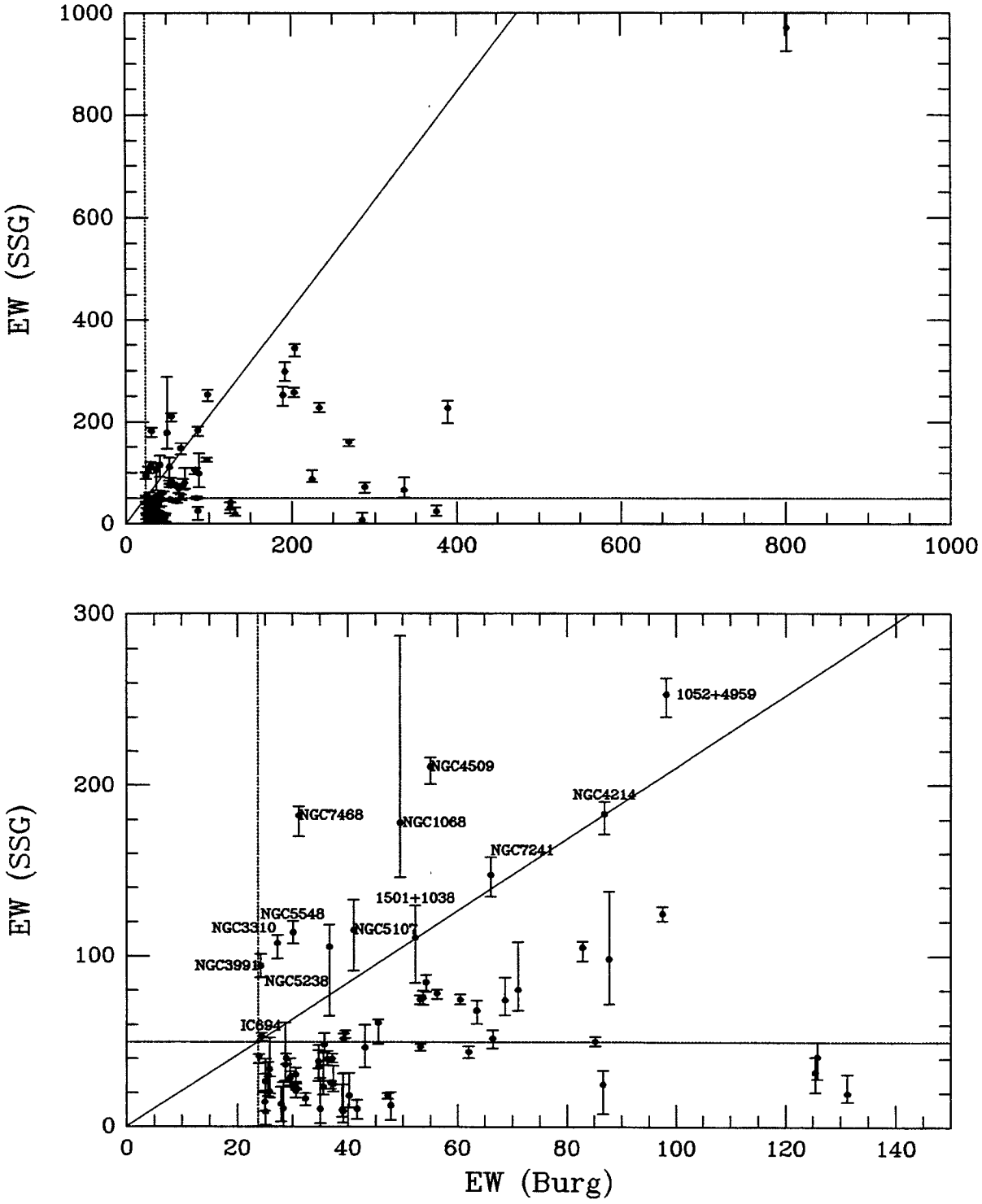

Figure 5–1(a)-(b)

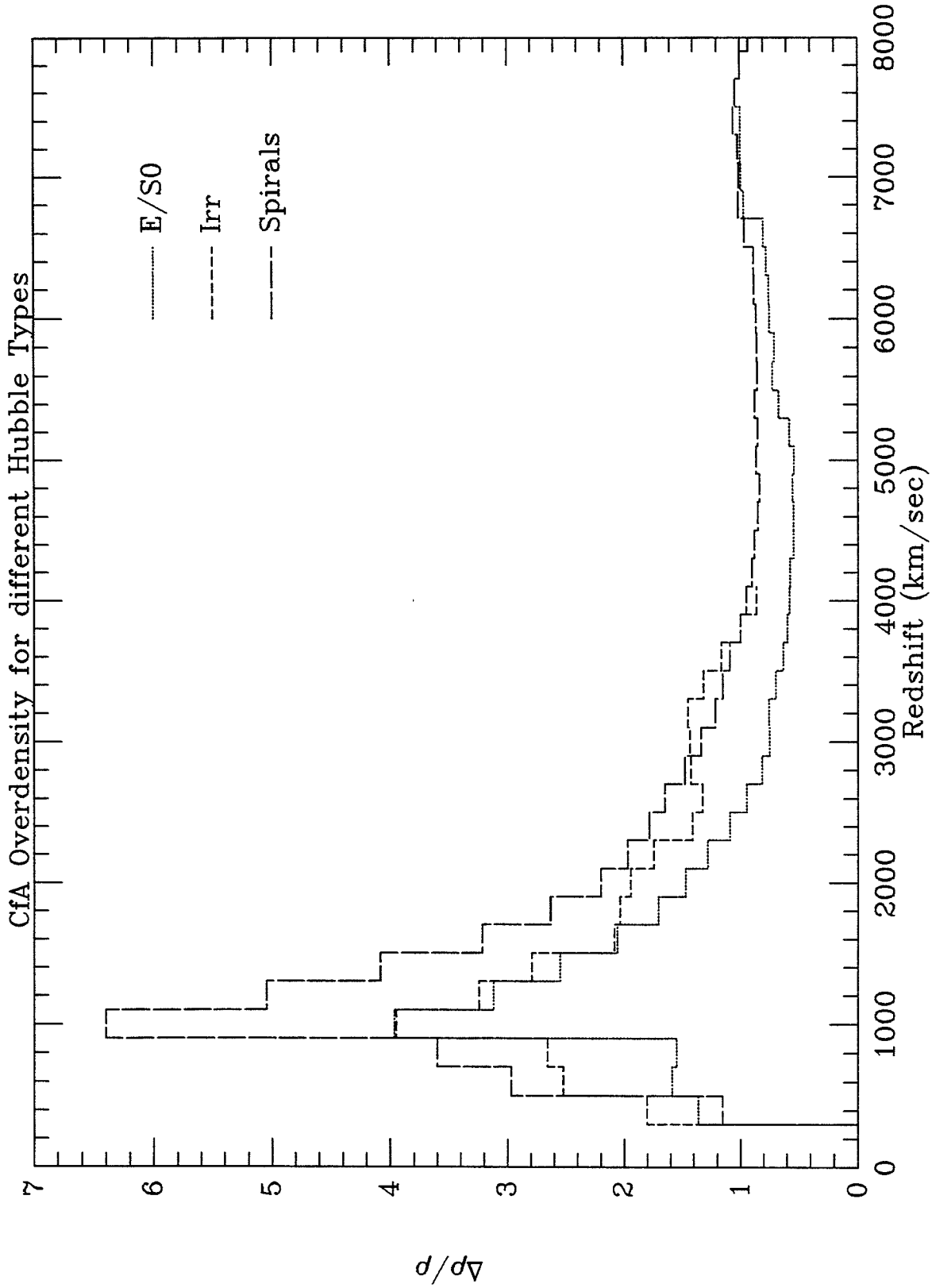
CfA Overdensity for different Hubble Types
E/S0
Irr
Spirals
Redshift (km/sec)
0
1000
2000
3000
4000
5000
6000
7000
8000
0
1
2
3
4
5
6
7
Δρ/ρ

Figure 5–2

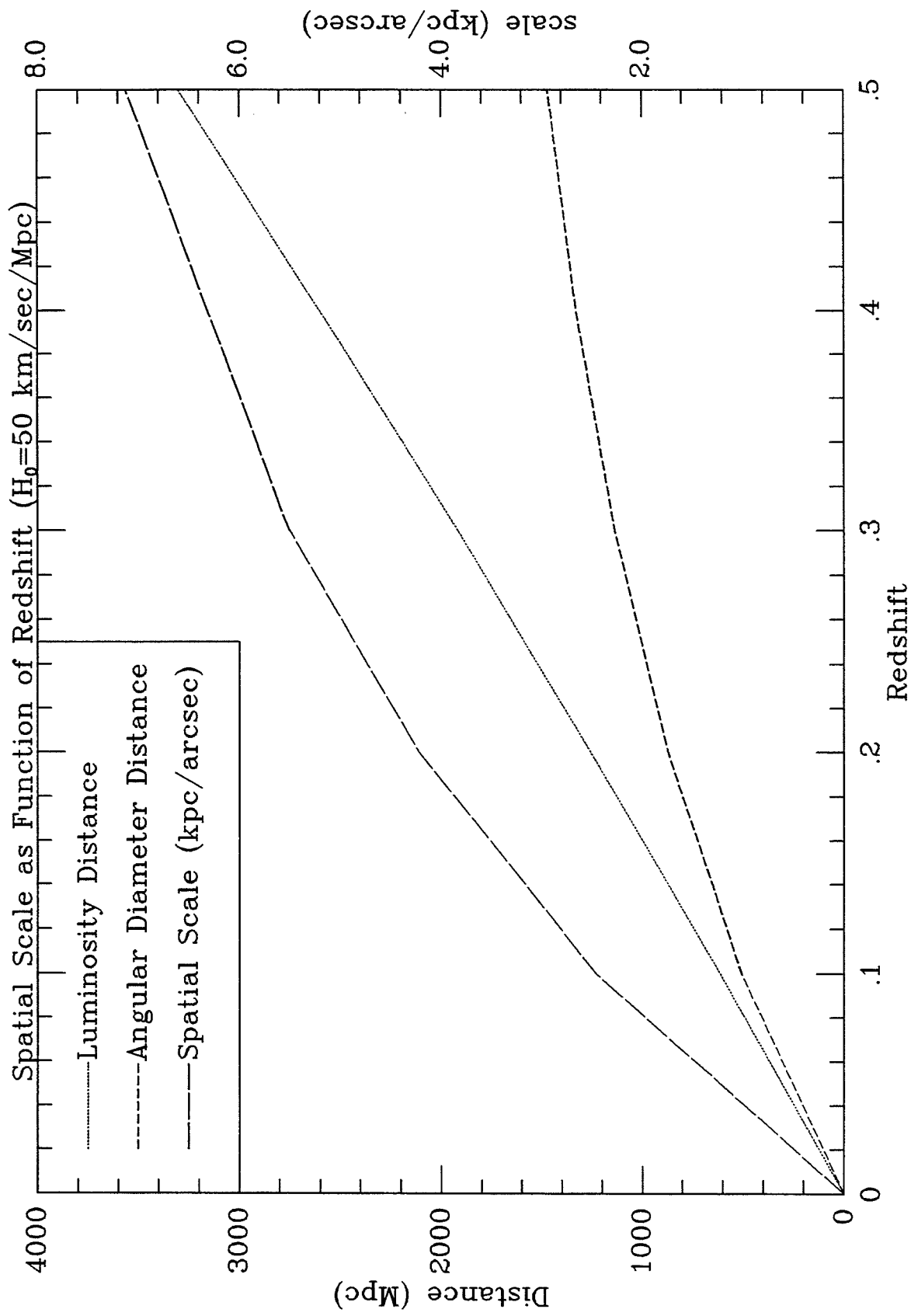
Spatial Scale as Function of Redshift (H_0=50 km/sec/Mpc)
Luminosity Distance
Angular Diameter Distance
Spatial Scale (kpc/arcsec)
Distance (Mpc)
scale (kpc/arcsec)
Redshift
0
1000
2000
3000
4000
2.0
4.0
6.0
8.0
.1
.2
.3
.4
.5

Figure 5–3

Appendix A
P60 ECHELLE GRATING MODE OBSERVERS' HELPFUL HINTS MANUAL

INTRODUCTION

This manual is intended to serve as a supplement to the P60 ECHELLE SPECTROGRAPH OBSERVING MANUAL (McCarthy, 1990) and is meant to assist users of the long slit grating mode (g-mode) in setting up and observing with the instrument in the most efficient manner possible. This manual is based on the experiences of the author in using the g-mode of the P60 Echelle and should hopefully explain all of the problems that have occurred in setting up the instrument so that they can be easily avoided in the future. If any user of the instrument encounters a problem not covered in this document (or the aforementioned echelle observing manual), please bring it to the attention of the author (ih@deimos.caltech.edu) so that it may be included in future revisions of this document.

A. LOGGING ONTO THE MICROVAX

1. log on as CCD
    a. type "DIR" to make sure that the previous observer has removed all of his or her files
    b. use the "DCLEAR" command to remove any remaining files (but only after checking with the previous observer!)
2. type "CAMERAS" at the prompt– answer the questions
    a. the telescope is 60 (default)

b. the number of CCD cameras in use is 1 (default)

c. the number of the CCD port to use is 0 (default)

d. the CCD dewar number is 9 (for the P60 Echelle CCD dewar)

e. you may decide to change certain readout parameters from the following list. I would suggest that you change the following:

i. #5 to no (this results in faster readout of the chip as well as less memory usage for each image);

ii. #6 to the first value of x that is imaged by a flat field exposure using the internal lamps and long slits (need to determine this);

iii. #7 to 500 (the number of pixels that are imaged by the long slit in the x direction); and

f. make sure that #13 is set to S (for the spectroscopic tables, you must do this!).

3. type "NIGHT" and give it a night number (usually starting at 1 for the first night of the run, but determined by the individual observer)

4. type "FRAME" and give it a frame number for the SNAP command (you can also set the frame number for the FOCUS command)

5. type "ANGLES" and give the relevant information concerning the grating that you will be using (# lines/mm and the tilt angle relative to the collimator axis)

6. type "SWITCHTAB" and confirm that the filter wheel positions are given by the slit names (and are not the names of photometric filters)

7. type "ECHZERO" to send the slit wheel assembly to its home position (which should be ALONG5). Make sure that the names of the different slits are given in their proper positions (this should be the case if the filter names were correct above)

8. type "ECHMOVE" to go to the pinhole slit (FHOLE0) for focusing the in-

strument

9. type "CWON" for continuous readout of the chip during the instrument setup (requires two carriage returns)

B. INITIAL INSTRUMENT SETUP

1. Make certain that the prism mount has been rotated out of the path of the beam. The instructions in the Echelle Observing Manual are quite good, however I would like to point out that the prism elevation clamp is located in a position which is extremely difficult to reach on top of the spectrograph near the guider camera. The best way to loosen this clamp is to reach in from both sides with your hands and rotate clockwise.

2. installation of the grating into the grating mount and the mount into the spectrograph is well covered in the P60 Echelle Observing Manual. A few points I would like to make on the subject include:

   a. use only gratings that are clearly marked as having been reversed in their cells for use with the echelle spectrograph. These gratings were originally used with the P200 Digital Spectrograph which had followed the same optical orientation as used in the old P60 Spectrograph. This orientation is opposite in direction to the P60 Echelle spectrograph.

   b. when inserting the grating mount into the instrument, it may be necessary to search around until the mounting pin is firmly placed in its socket. If you experience difficulty in doing this, I would suggest removing the entire grating mount from inside the instrument and trying again.

   c. Jim McCarthy has written a Figaro routine which calculates the desired grating tilt angle for a given grating and central wavelength. The program is called g_mode. It requires the grating name and central wavelength as input. It outputs the value for the grating tilt angle based on the formula given in the observing manual. It is fairly simple to run, as it

will prompt you for the various parameters. You should still check that this is the correct tilt angle for the wavelength range you wish to cover by taking an arc exposure and fitting the lines using ARC. You may find that small modifications to this angle are needed to get the proper wavelength coverage.

3. The rotation of the CCD dewar is determined by a micrometer located on the side of the instrument. Since the echelle slits are rotated relative to the long slits (see McCarthy's thesis) it is necessary to rotate the CCD dewar between the e-mode and g-mode in order to minimize the misalignment of the spectrum with the rows and columns of the CCD. In the best of all worlds, there would be a certain rotation of the dewar which would simultaneously image the slits along the rows and image in the dispersion direction parallel to the columns. This however requires a precise alignment of the long slits in the slit wheel assembly which is quite difficult to achieve. Since there does exist software routines which can take misaligned spectra and align them (in FIGARO these routines are IARC and ISCRUNCH), it should suffice to simply align the dispersion along the columns. To accomplish this, take a 1 second test image of the internal flat lamps using the pinhole slit (FHOLE0). Align the resulting spectrum along a single column by rotating the dewar. It may be helpful to expand the image by a factor of 5 in the x direction and display the central 100 columns around the image. The method for rotating the dewar is described in the Echelle Observing Manual. Be careful not to use the micrometer to push the dewar, as it is more likely to slip against its set screw. Rather, you should first move the dewar away from the micrometer, set the micrometer to the desired value and finally rotate the dewar against the end of the micrometer and bolt it in place.

C. FOCUSING THE INSTRUMENT

1. Depress ON button on camera lens focus digital micrometer (located on side of Echelle) and note current position. If the readout is weak (or non-existent) this is probably due to a low charge on the battery. In this event, it will be necessary to plug in the battery charger so that you can continue. If so, it is strongly recommended that observers ask the Palomar support staff for assistance in this endeavor.
2. Loosen the two brass knobs located underneath the Echelle (these clamp down the camera lens)
3. Type "CWOFF" on the keyboard (again with two carraige returns)
4. Take a test exposure with the pinhole slit (FHOLE0) using the internal flat field lamps (turn both lamps on, and expose for 1 second). You may wish to change the display parameters such that they clearly show the image of the pinhole and you can monitor the changes that occur when you change the lens focus. I have found that displaying the 100 pixels (in x) that surround the slit image, expanded by a factor of 5, is adequate for the job. This is also a good way to measure the CCD dewar rotation, and make certain that the dispersion is parallel to the columns.
5. By iterating in steps of 0.250 on the micrometer, it should be possible to locate a focus with a FWHM of 2 pixels or less in the spatial direction through out the spectrum. Having reached this focus, I would suggest that you turn on the helium arc (or neon if you're working mainly beyond 7000) and test the focus in the dispersion direction. You should get images of the arcs that have a 2 pixel FWHM in both the spatial and spectral directions. If the images show evidence of astigmatism then it may be necessary to collimate the beam.
6. Insert slit BLONG4 and take an arc exposure. Do not be alarmed if the arc lines do not fall parallel to the rows of the CCD, as this effect can be taken out using software (see above discussion of IARC and ISCRUNCH). In addition,

you may notice that the arcs are not uniform from one end of the chip to the other. This is due to the fact that the source lamps (both arcs and flat field lamps) do not uniformly illuminate the long slits. This does not present a problem with the arcs (since they are used solely for wavelength calibration, and night sky lines can be used near the edges if necessary) but they make using the internal flat lamps completely useless for anything but instrumental focus. I will outline below the preferred method for flat fielding your spectra.

7. Having found an acceptable focus, tighten the two brass knobs underneath the Echelle. If it was necessary to insert the battery charger during the focusing operation, then request that the mountain staff remove the charger plug and seal up the instrument body.

8. If it proves necessary to change the collimator focus, follow the instructions in the observing manual.

D. CALIBRATIONS

1. There are four different types of calibration frames that are required to reduce your data: flat fields; arcs; flux standards; and B-star standards (optional if $\lambda_{max} < 6800\mathring{A}$).

2. Flat Fields–since the calibration source lamps do not uniformly illuminate the slit, I have found that using dome flats gives an adequate calibration. This requires removing the mirror cover and turning on the flat lamp. You should set the counter on the lamp to 660. If you are working at short wavelengths ($\lambda < 4500\mathring{A}$), you may also wish to take some twilight sky flats, as the dome flat lamp is quite red. A typical exposure with the $1.''3$ slit (BLONG4) covering from $4350\mathring{A} < \lambda < 7200\mathring{A}$ with the 300 lines/mm grating ($\lambda_B = 5000\mathring{A}$) is 900 seconds. I would suggest that you take a test exposure in order to determine the best exposure time for the flat fields. There is a command for taking a series of exposures without spawning off a sub-process.

I recommend using it for taking flat fields during dinner. The command file should look something like this (starting with the slit ALONG5):

```
$ SET VERIFY
$ FIGARO
$ I=0
$ LOOP:
$       ECHNAP CAM=0 TIME=300 WAIT NODISPLAY NOCURSOR
             NAME=''DOME FLAT'' \
$       I=I+1
$ IF I.LT.4 GOTO LOOP
$ ECHMOVE
BLONG4
$ J=0
$ LOOP:
$       ECHNAP CAM=0 TIME=900 WAIT NODISPLAY NOCURSOR
             NAME=''DOME FLAT'' \
$       J=J+1
$ IF J.LT.4 GOTO LOOP
$ END
```

To submit it, just type @filename at the prompt. This will create four exposures of 300 seconds each for the wide slit and four exposures of 900 seconds each for the narrow slit (which are typical exposures for the 300 lines/mm grating).

3. Arcs

   a. The only comment concerning arcs that I would like to make is that you should take test exposures prior to actual images in order to determine the best exposure time. I have found that for neon arcs, exposures as short as 0.1 seconds will give well exposed spectra longward of 5800Å, while for argon, an exposure time of 0.5 second is good beyond 6800Å. If your spectra are entirely blueward of these wavelengths, the exposure times would increase, due to a lack of strong arc lines. For helium, I have found that a 30 second exposure is adequate (note all exposures are for the 300 lines/mm grating). Since arcs are used solely for wavelength calibration, the fact that the shutter may not uniformly open on short timescales is not of any concern.

   b. If any frames of the arcs are not well-exposed, there is a possibility that

the lamp is getting too weak. The helium arc lamp was replaced because of this. If there is a problem, please consult with the mountain staff.

4. Flux Standards

   a. The list of calibrating flux standards (Oke and Gunn) is in the P60 control room. When observing a flux standard, you should use the wide slit (ALONG5) so that there is no light lost due to vignetting by the slit. Typical exposures range from 10–60 sec, depending on the magnitude of the star and the wavelength range (again for the 300 lines/mm grating). I would again suggest that you take a test exposure to determine the best exposure time for your standards.

5. B-star Standards

   a. B-star standards can be located in the current edition of the Astronomical Almanac in the Bright Star lists. I would suggest locating a B star on the main sequence (Luminosity Class V) that is not in a double star system. This should be your first object of a night, and you should use this star for focussing the telescope. To focus, take a series of test exposures of this star, changing the telescope focus between each test by 20mm. Locate the position where the best focus is achieved. You may need to wait until the mirror has reached equilibrium with the outside air.

   b. If your spectra go beyond 6700Å, it may prove necessary to remove the effects of atmospheric absorption from the "A" and "B" bands. For this, you require an object with a relatively flat spectrum (no emission lines). B-stars serve this purpose well, as the only lines apparent are due to Hydrogen and Helium, and are not superimposed on the atmospheric features. A well exposed B-star spectrum can be used to correct for these bands.

   c. In order to fully rectify your spectra in the dispersion direction, it is also

useful to have a well exposed stellar spectrum with each long slit used during the night. The FIGARO routines SDIST and CDIST are then used to rectify the spectrum in this direction.

E. OBSERVATIONAL HINTS

1. When rotating the echelle, remember to rotate the counterweights to positions aligned with the letter E on the cass ring. Also remember to rotate the instrument such that the dewar will be beneath the instrument when the telescope is pointing at your object (to prevent LN2 spillage).
2. To use the autoguider, set to mode 2 and set the ring angle to 90+ the value from the cass ring measured on the side opposite the position of the guider camera (diagram exists in the guider manual). So if the echelle is rotated to the angle 000 (as read on the ring) then set the counter to 090 and the telescope will properly autoguide on a bright star.
3. The current guide camera has very poor optics and it is frequently difficult to see a faint object on the monitor. I would suggest that you measure offsets from bright stars in the field, set those stars on the slit and then move to the position of your object if you can't locate it in the finder.
4. If you decide to change the long slits in the filter wheel, please ask the mountain staff to assist you. This is a very delicate operation, and observers are strongly advised not to attempt this on their own!

Appendix B
Graphical Results of Redshift Search for each CfA Galaxy

The graphical results of the redshift search of the 175 axis pairs of the galaxies observed for this thesis are presented in this appendix. They are plotted as Figures B–1.a through B–107.b. Each figure consists of 6 pairs of plots, which are for the six separate sub-surveys in the SSG transit survey. In each pair of plots, the top plot shows how the measured flux in the emission line changes as a function of redshift. For instances in which the algorithm presented in Chapter 4 fails to measure a positive line flux, the data are set to log Flux = -15.0, a value which is clearly below the minimum observable flux for the SSG survey at all wavelengths. The bottom plot shows how the equivalent width changes as a function of redshift. Each axis pair is displayed with four curves, which represent the two possible orientations of the primary spectrum with respect to the direction of dispersion of the transit survey (Case A and Case B) when the major axis is analyzed as the primary spectrum as well as when the minor axis is analyzed as the primary spectrum. In addition, on each line flux vs. redshift plot, there is a curve which represents the limiting line flux as a function of redshift for that particular sub-survey, and should be utilized to determine the maximum redshift that the galaxy would be observable in that particular sub-survey.

For each axis pair, in a particular sub-survey, the first criterion to consider is whether or not the equivalent width is in excess of the survey limit of 50Å. If it is not, then that galaxy would not be observable in the transit survey. If it is above 50Å at all redshifts, then the maximum redshift is determined by examining the line flux

plot and determining at which point the line flux falls below the survey limit. If the equivalent width is above 50Å at some redshifts and below 50Å at other redshifts, then greater care is required in interpreting the results.

Below is a legend for use in interpreting the plots in this appendix.

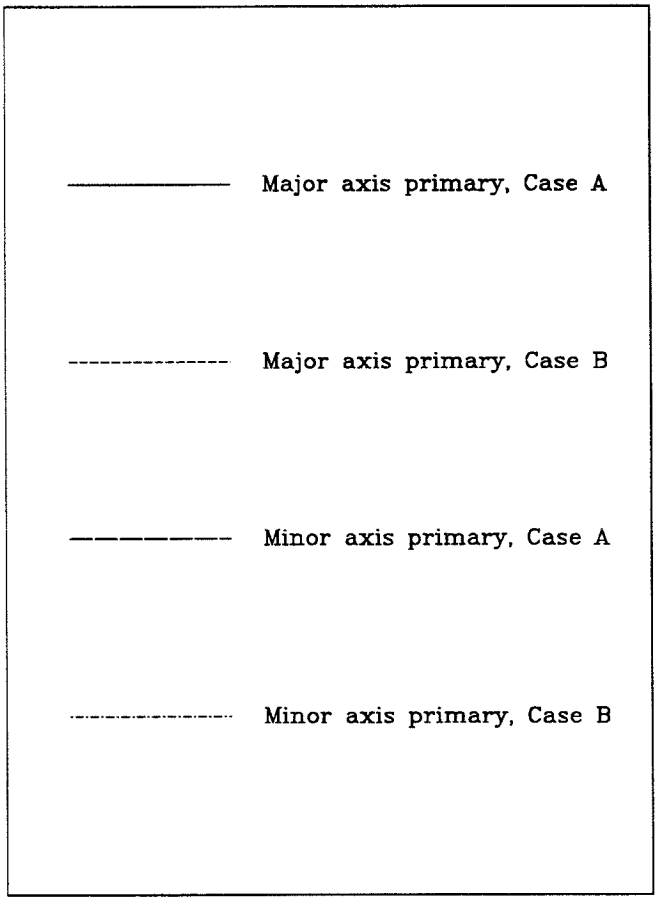

0000+2141 MAJA/MIN

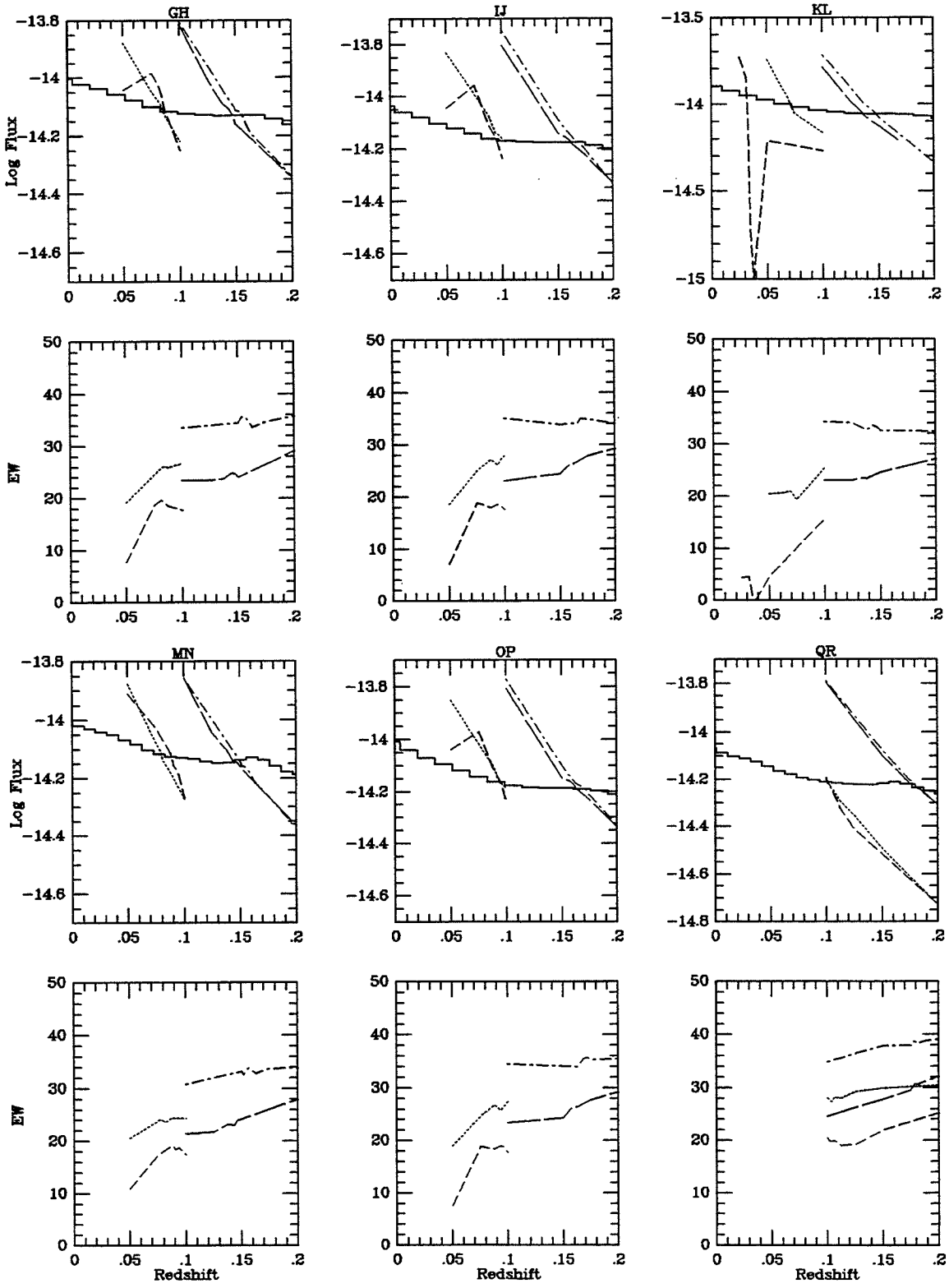

Figure B–1.a

0000+2141 MAJB/MIN

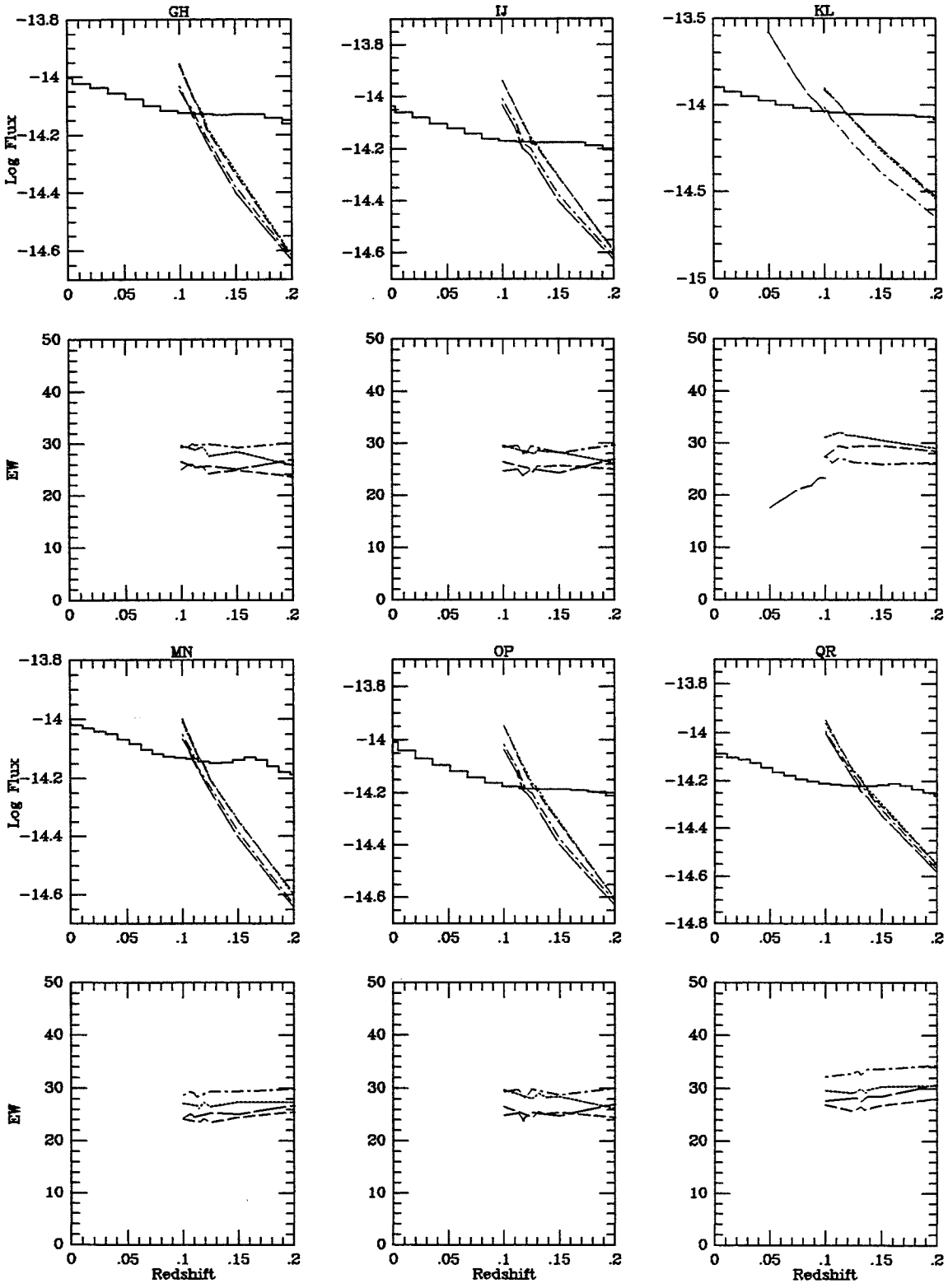

Figure B–1.b

0003+1955 MAJ/MIN

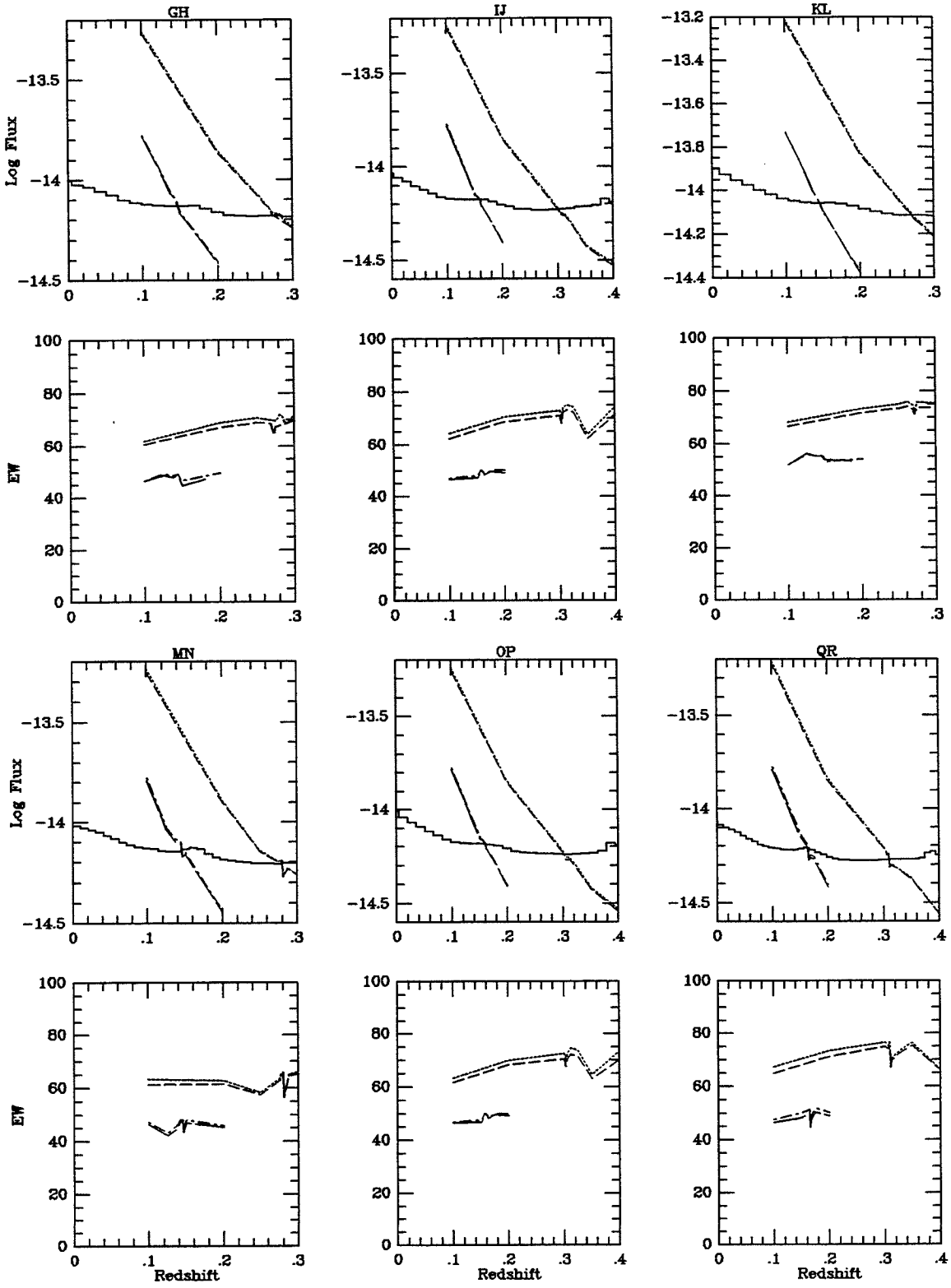

Figure B–2.

0048+2908 MAJ/MINA

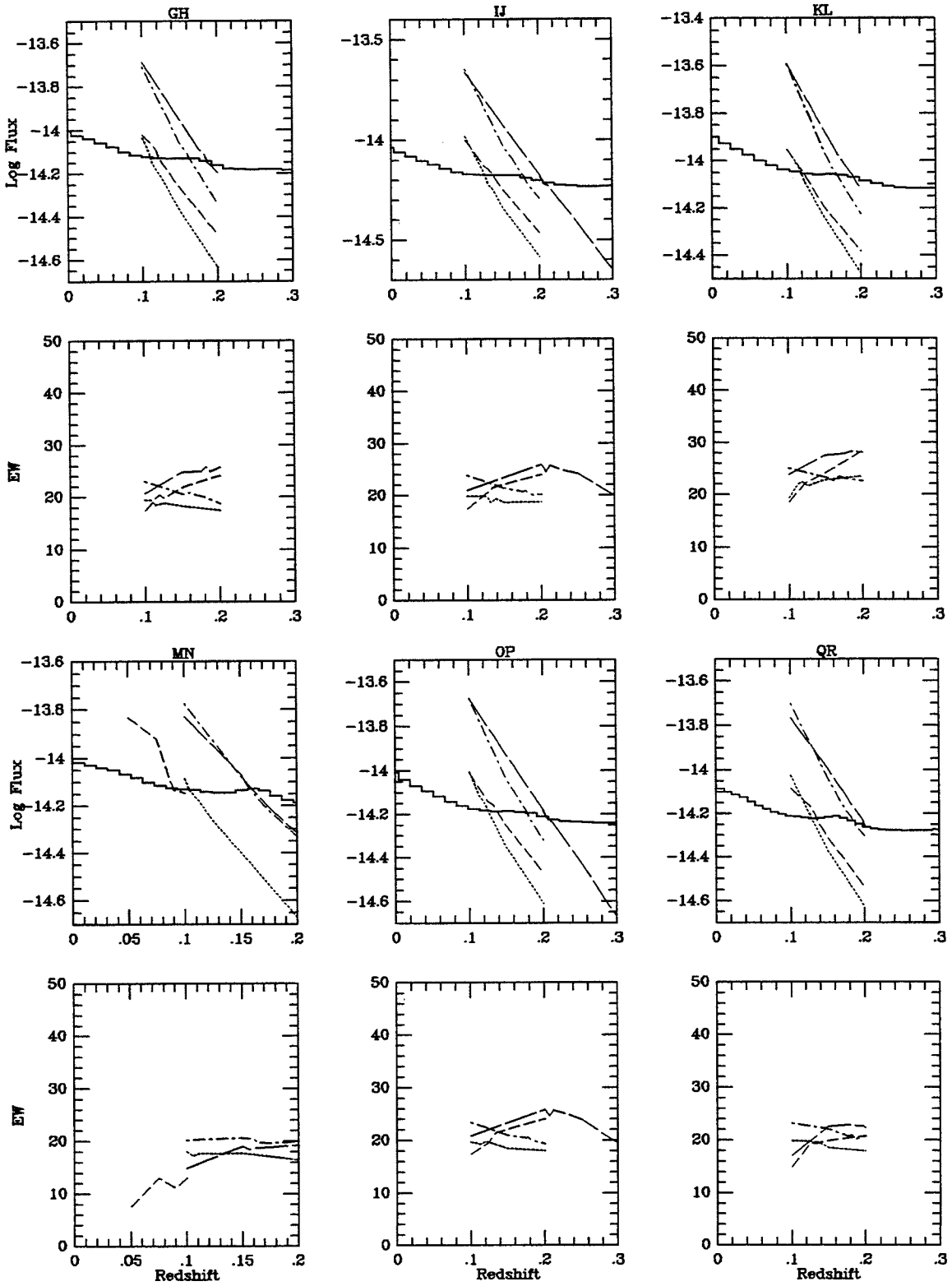

Figure B–3.a

0048+2908 MAJ/MINB

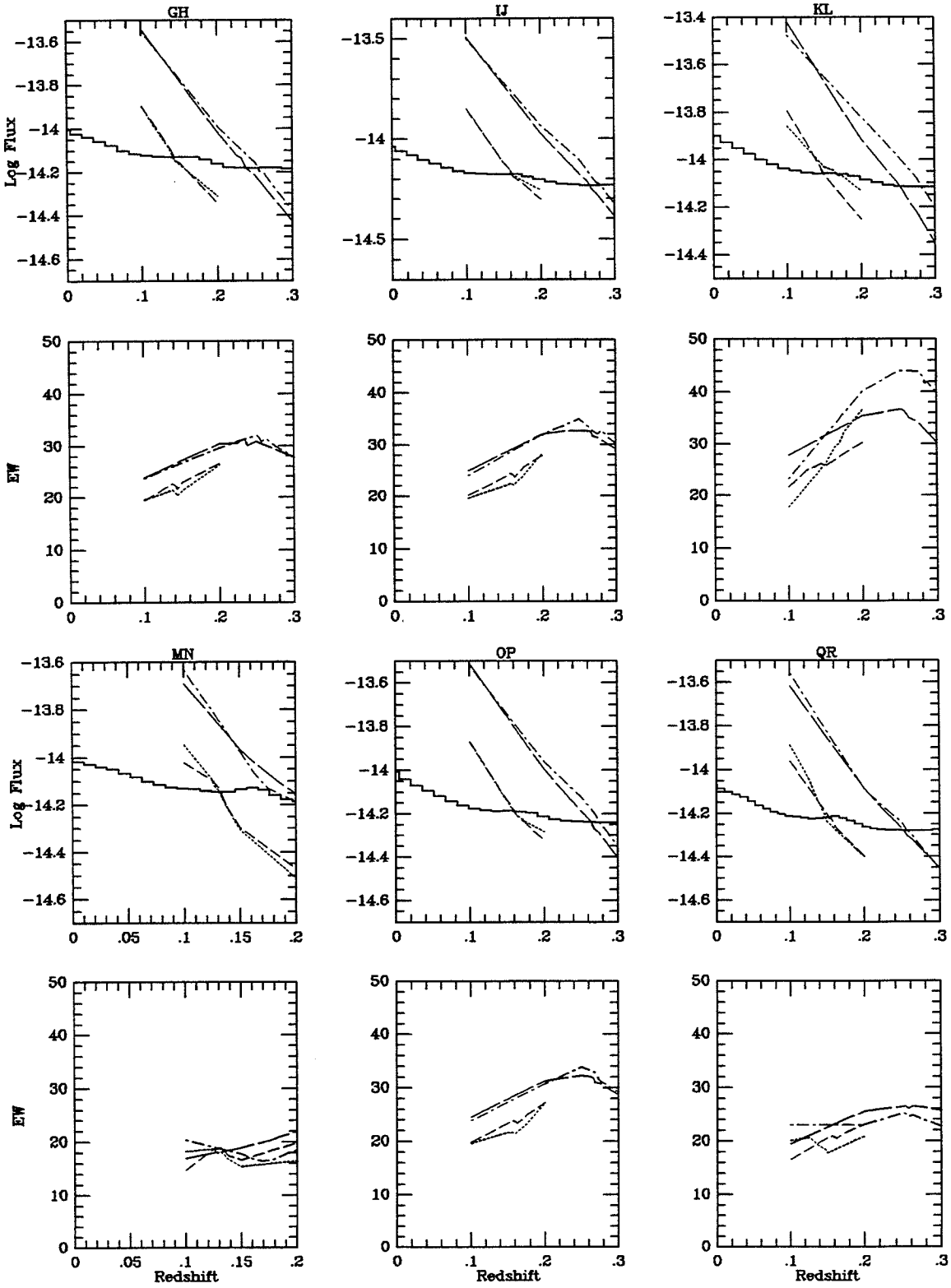

Figure B–3.b

0051+1225 MAJ/MIN

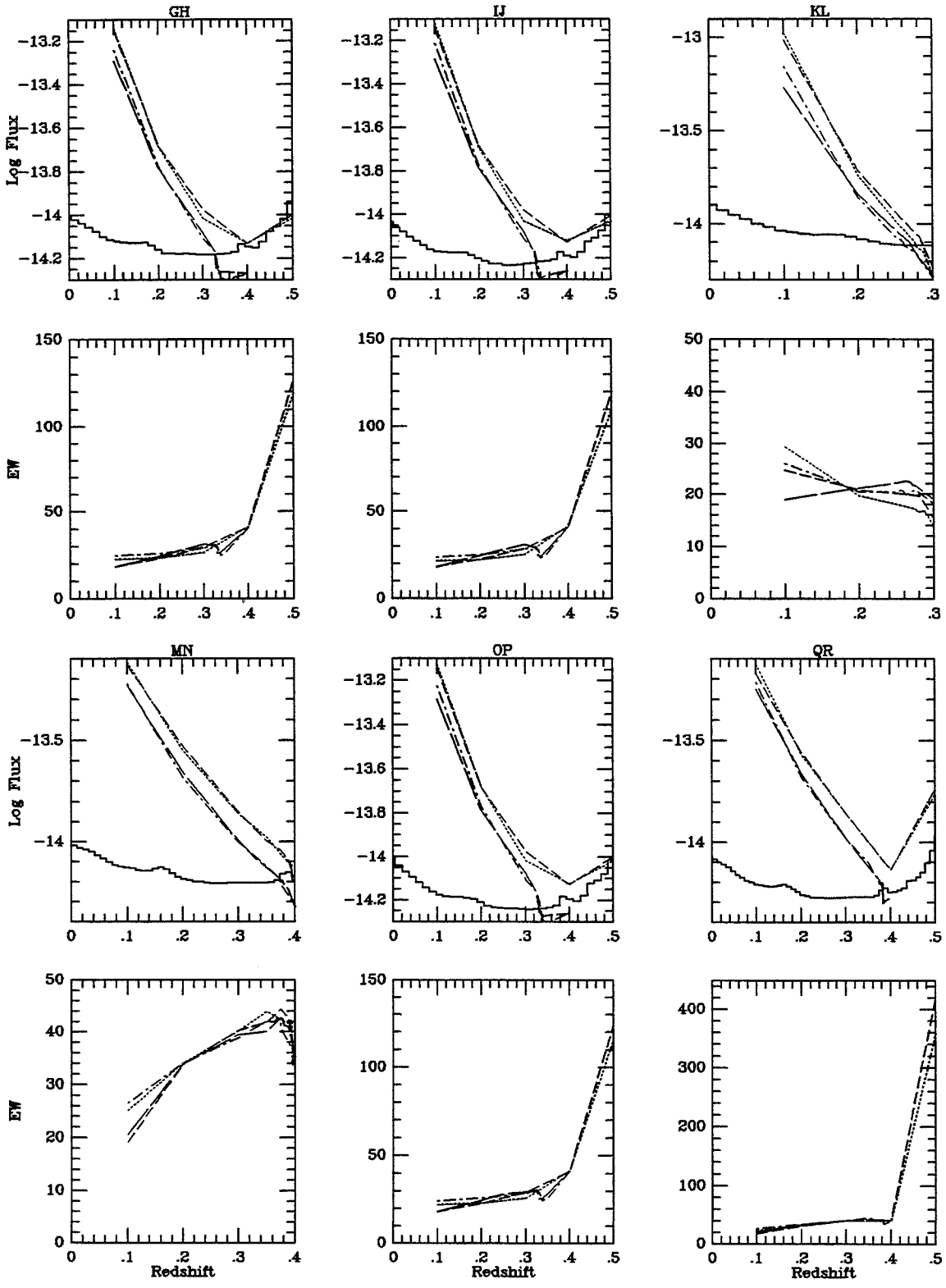

Figure B–4.

0104+1625 MAJA/MINA

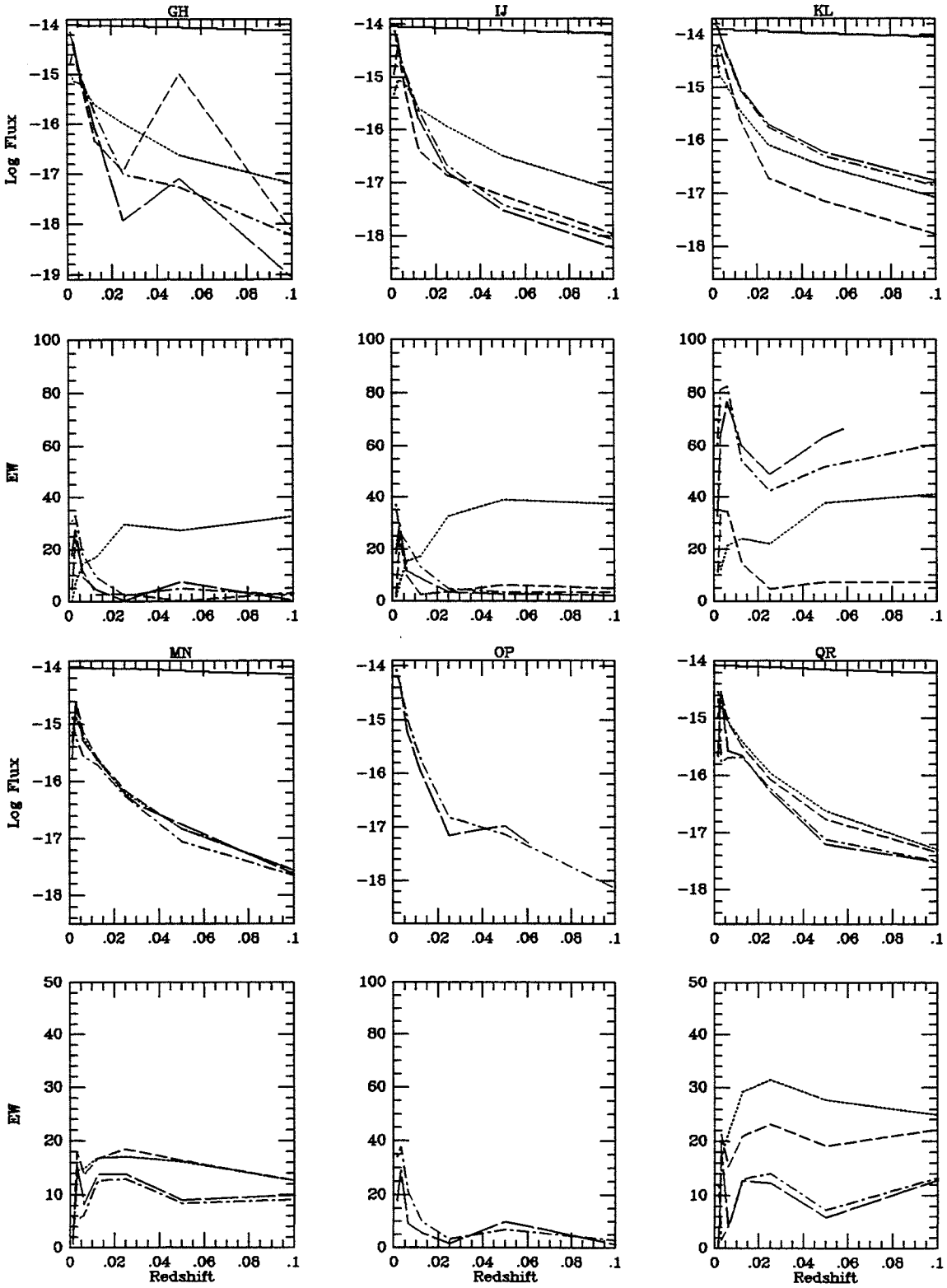

Figure B–5.aa

0104+1625 MAJA/MINB

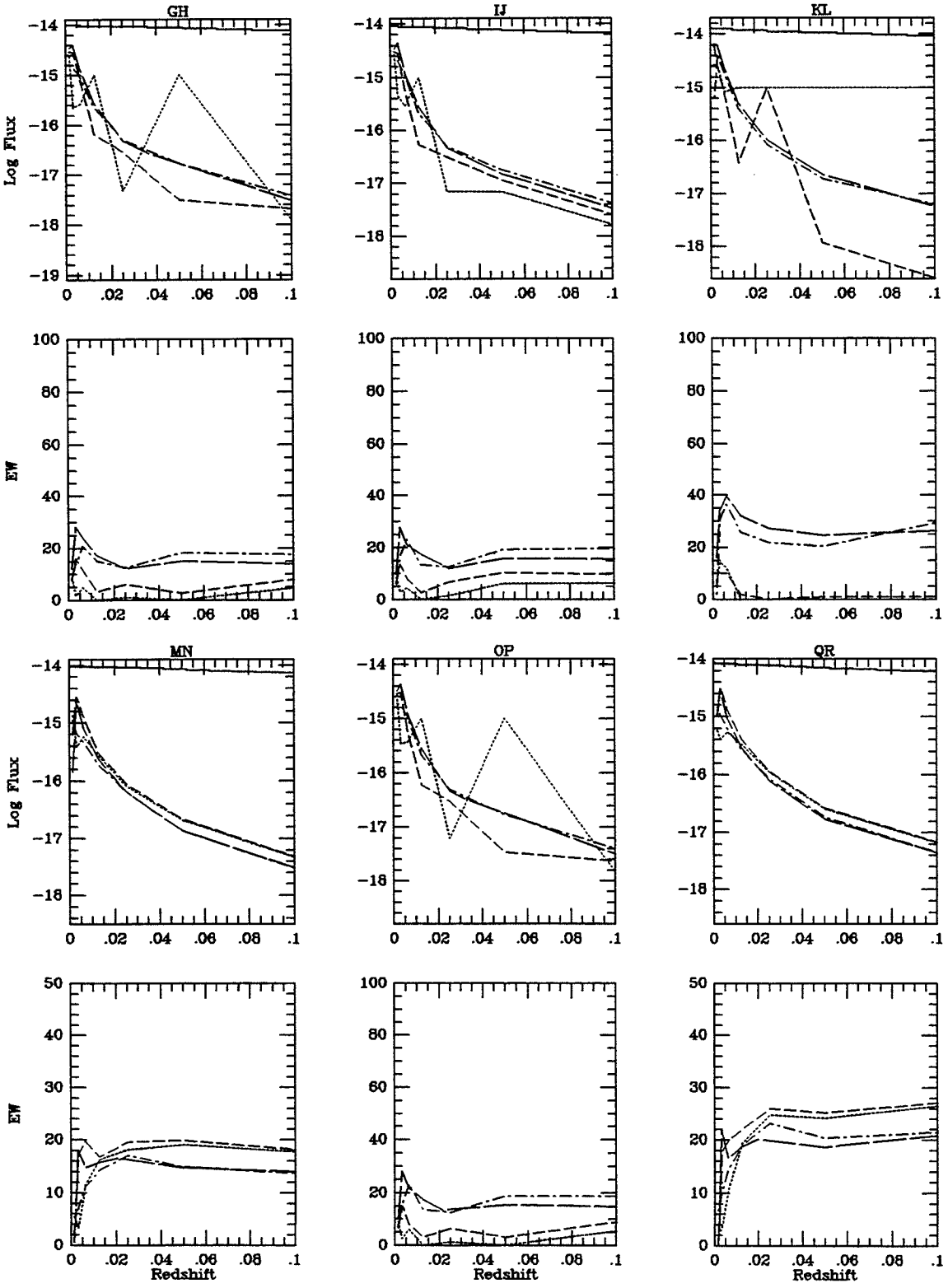

Figure B–5.ab

0104+1625 MAJB/MINA

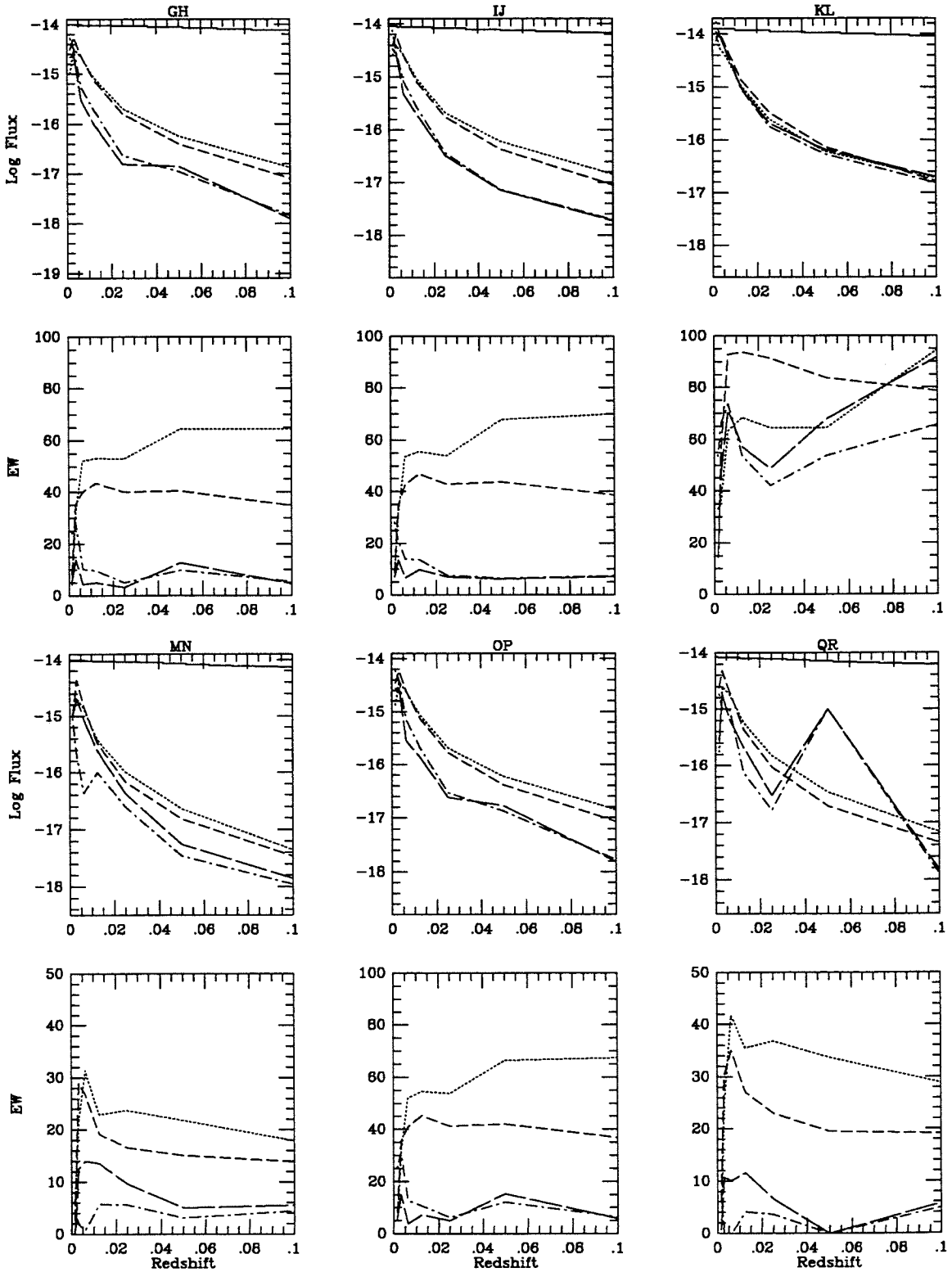

Figure B-5.ba

0104+1625 MAJB/MINB

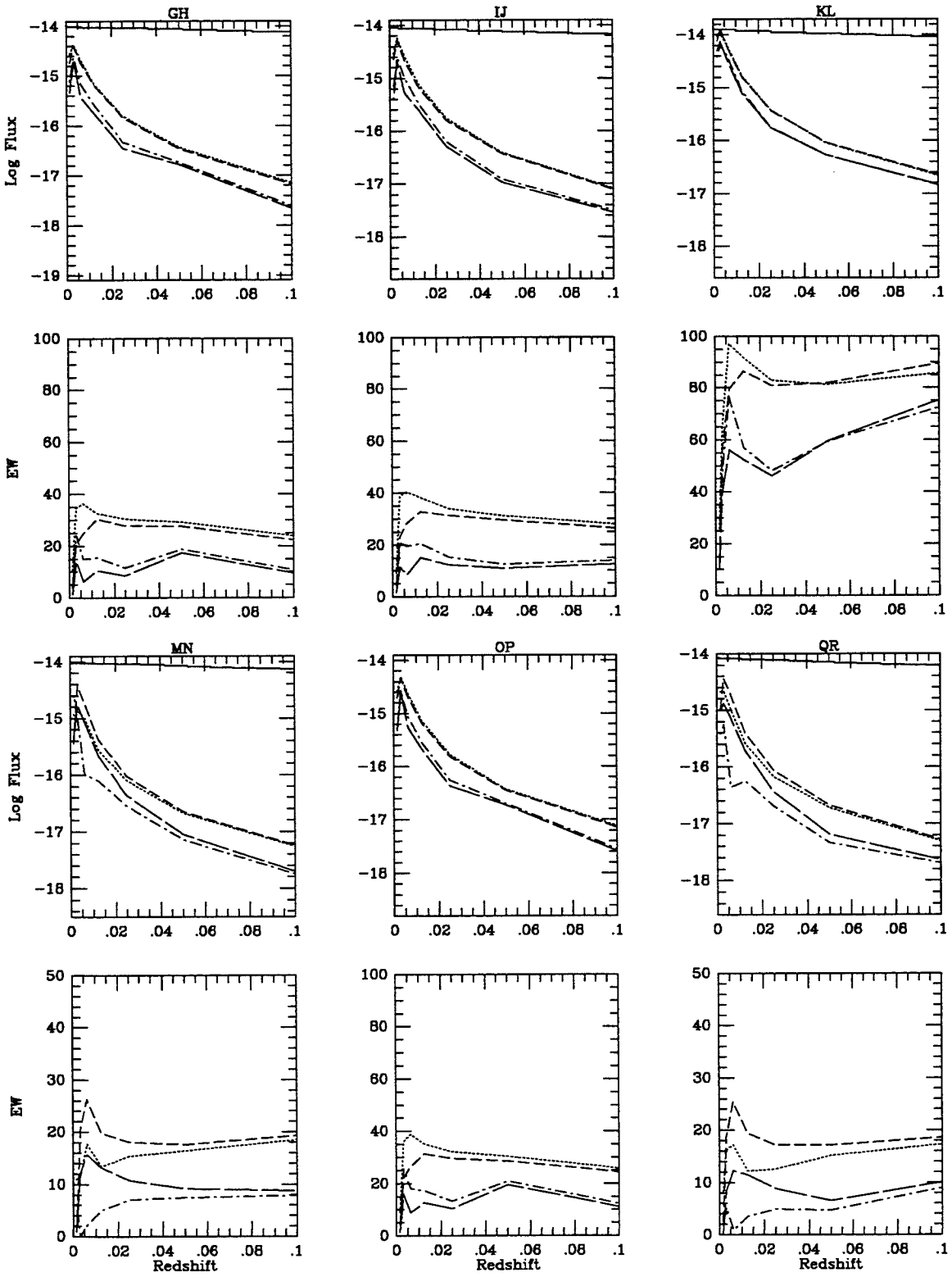

Figure B-5.bb

0104+1625 MAJC/MINA

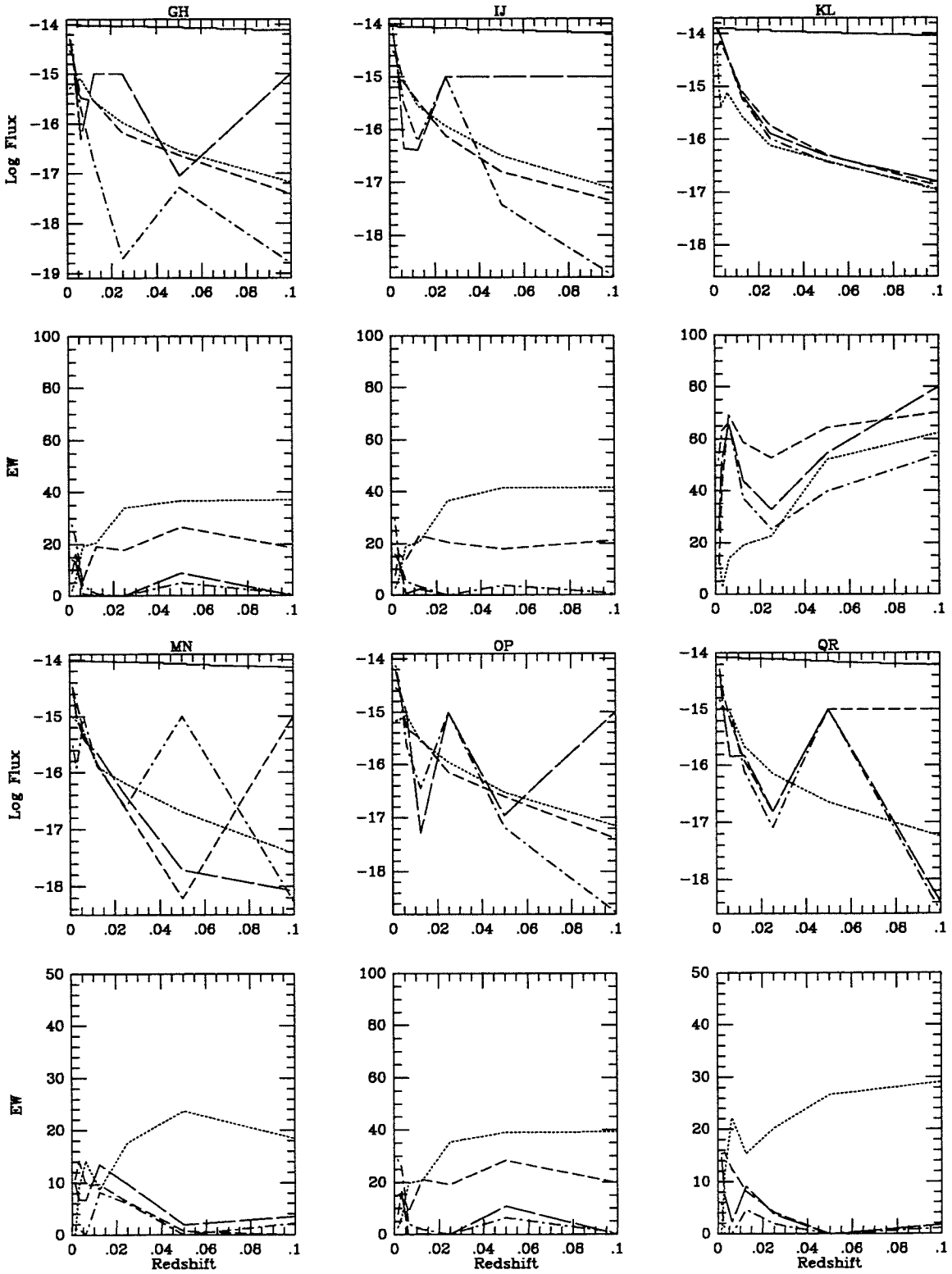

Figure B-5.ca

0104+1625 MAJC/MINB

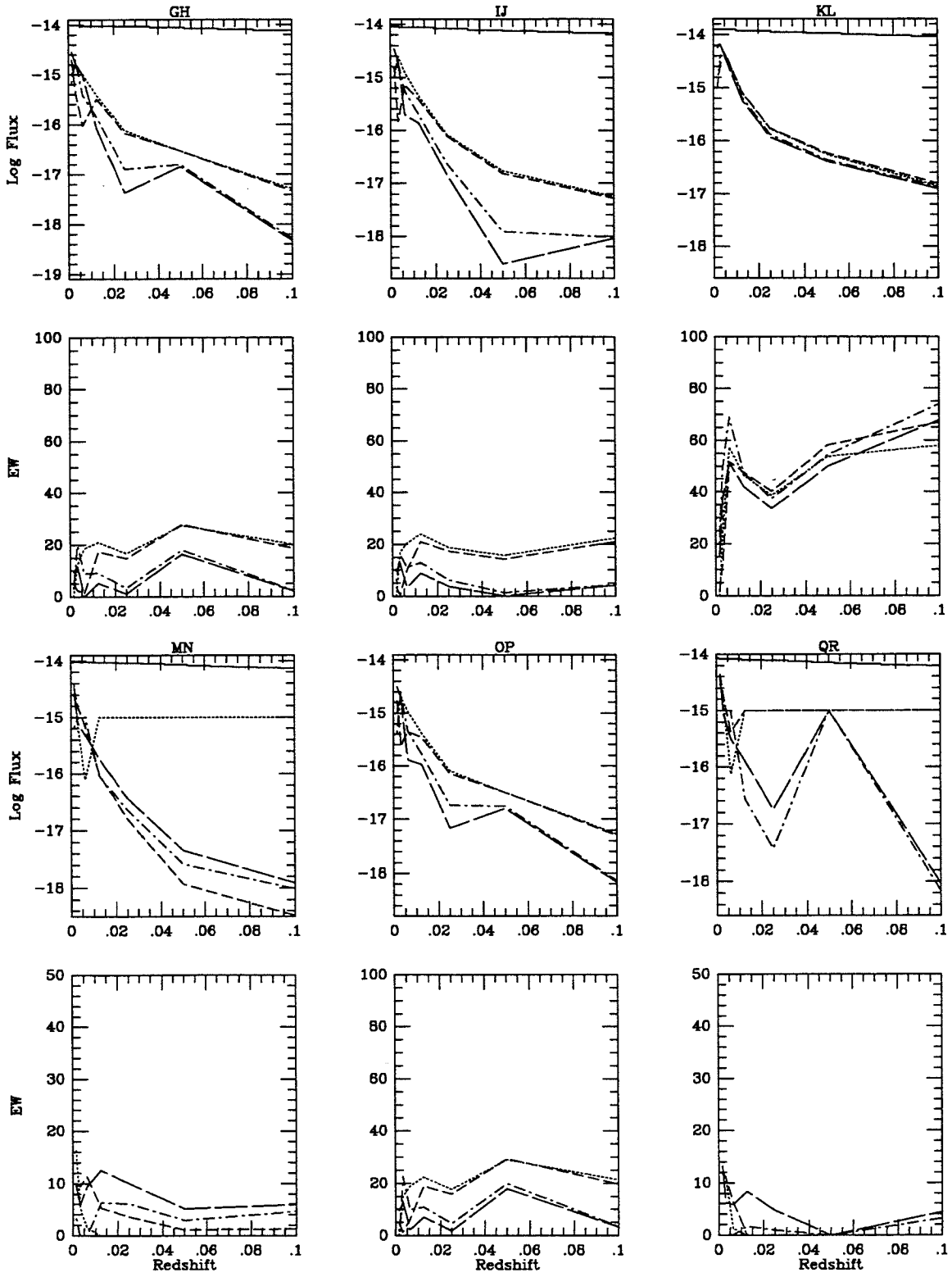

Figure B–5.cb

0109+0104 MAJ/MIN

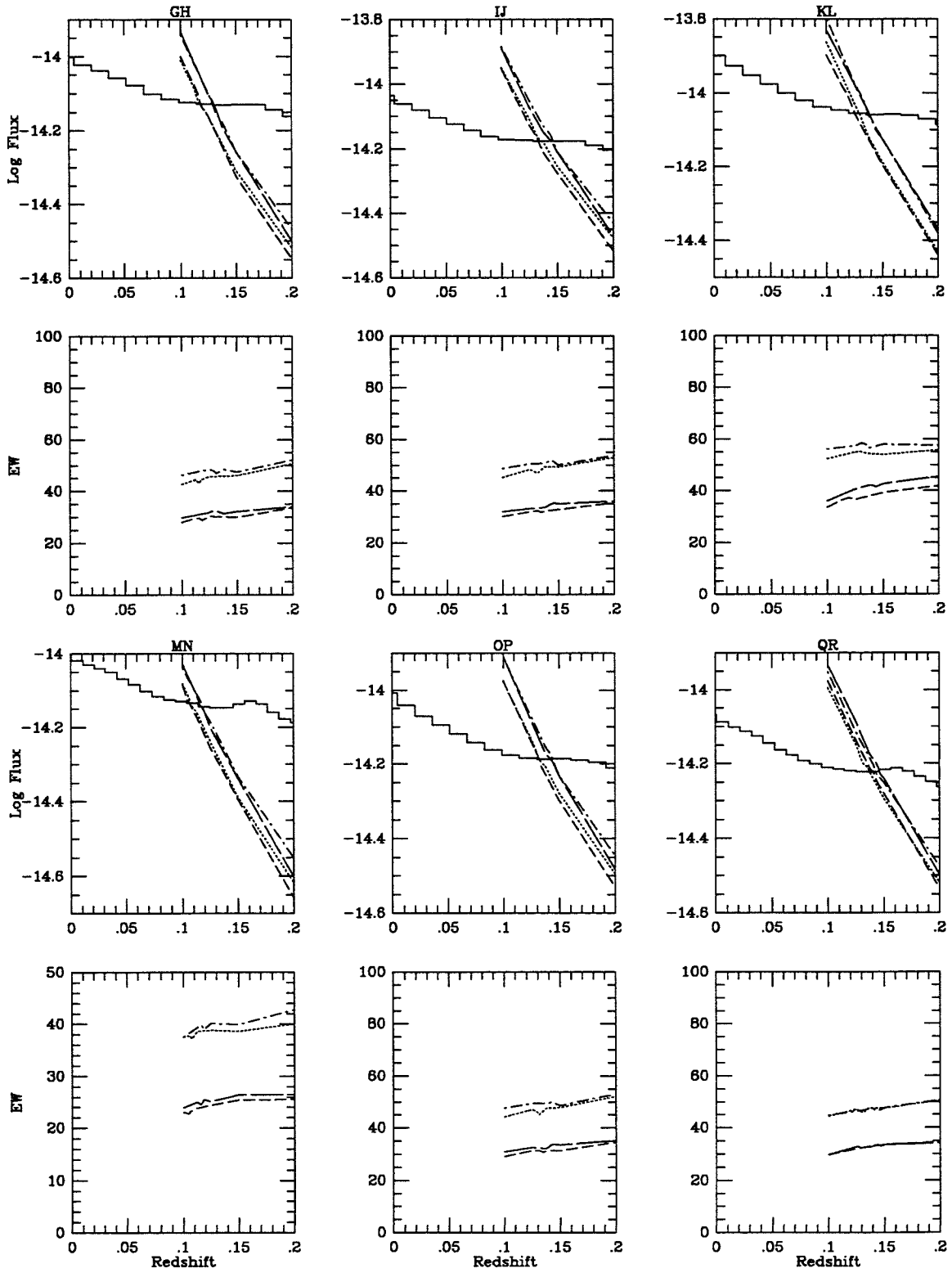

Figure B-6.

0122+3153 MAJA/MINA

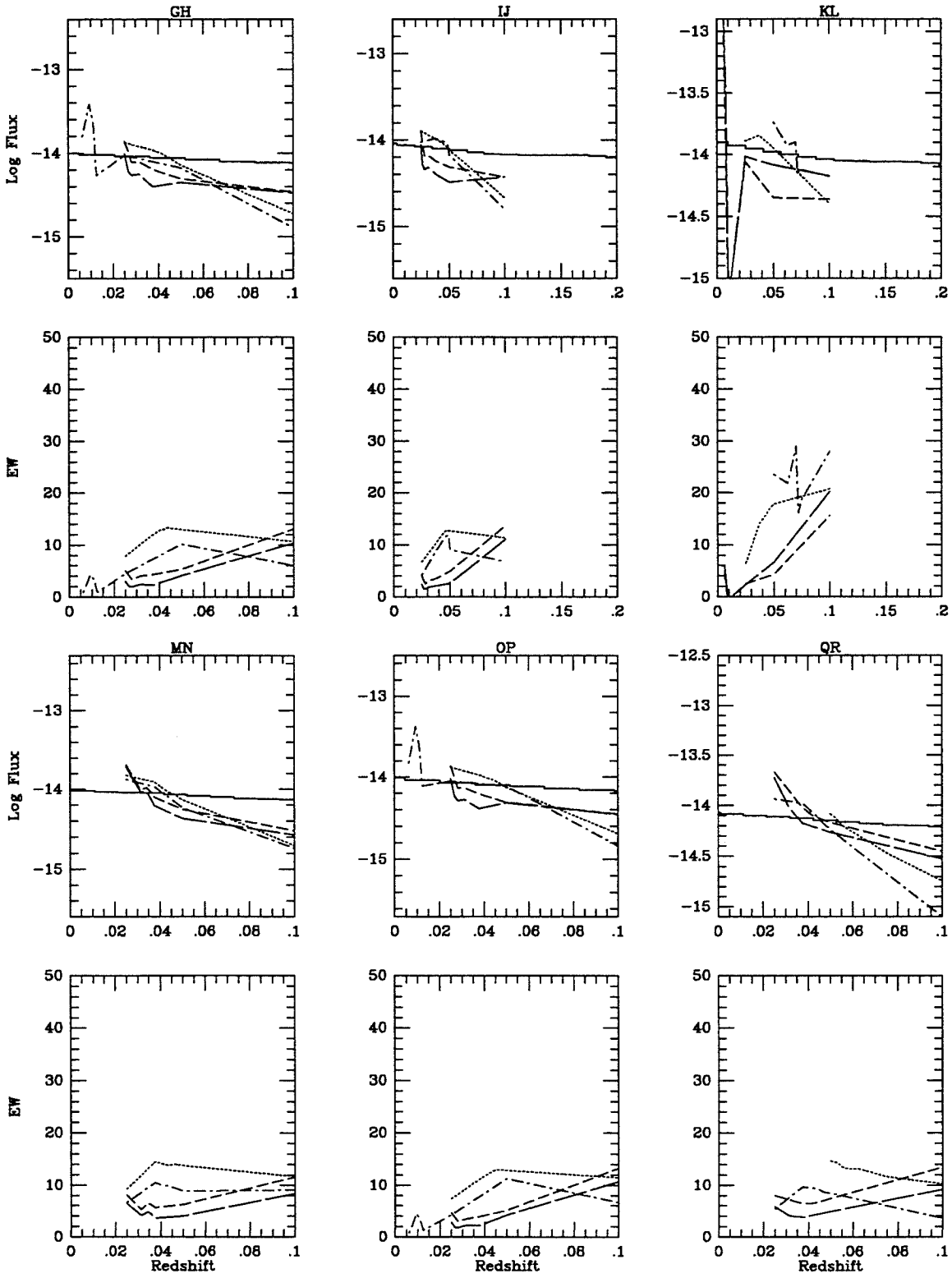

Figure B–7.aa

0122+3153 MAJA/MINB

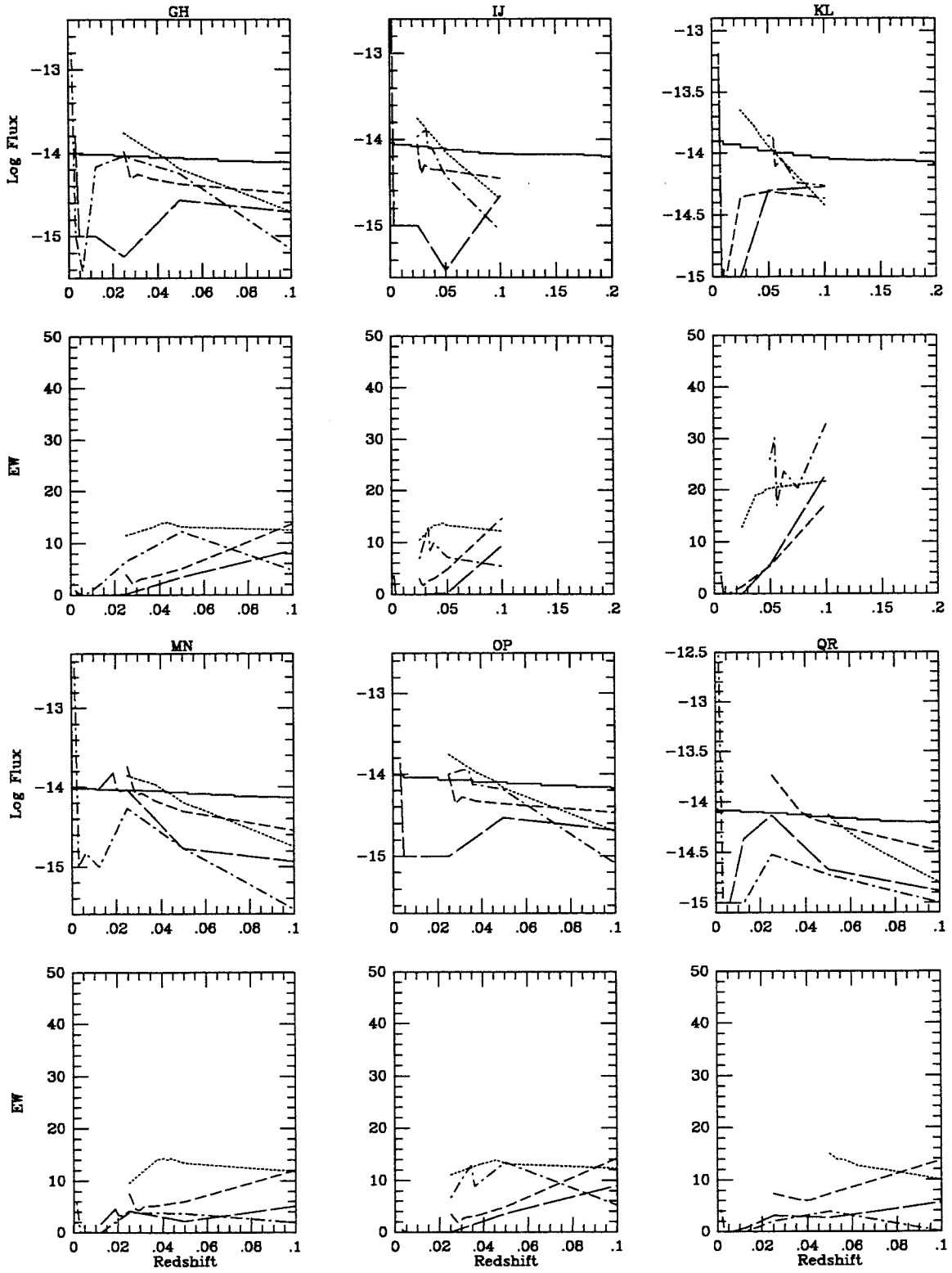

Figure B-7.ab

0122+3153 MAJB/MINA

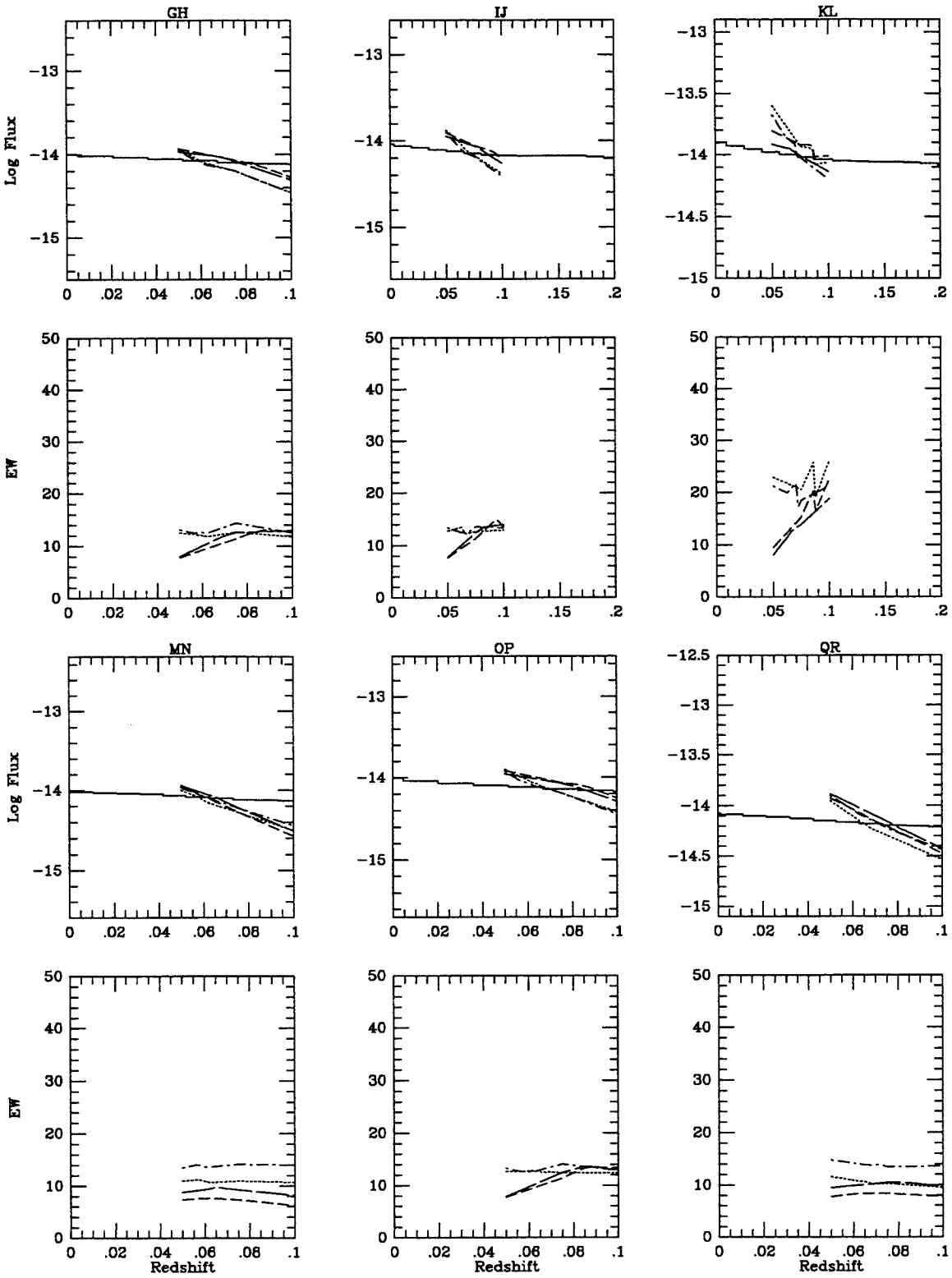

Figure B-7.ba

0122+3153 MAJB/MINB

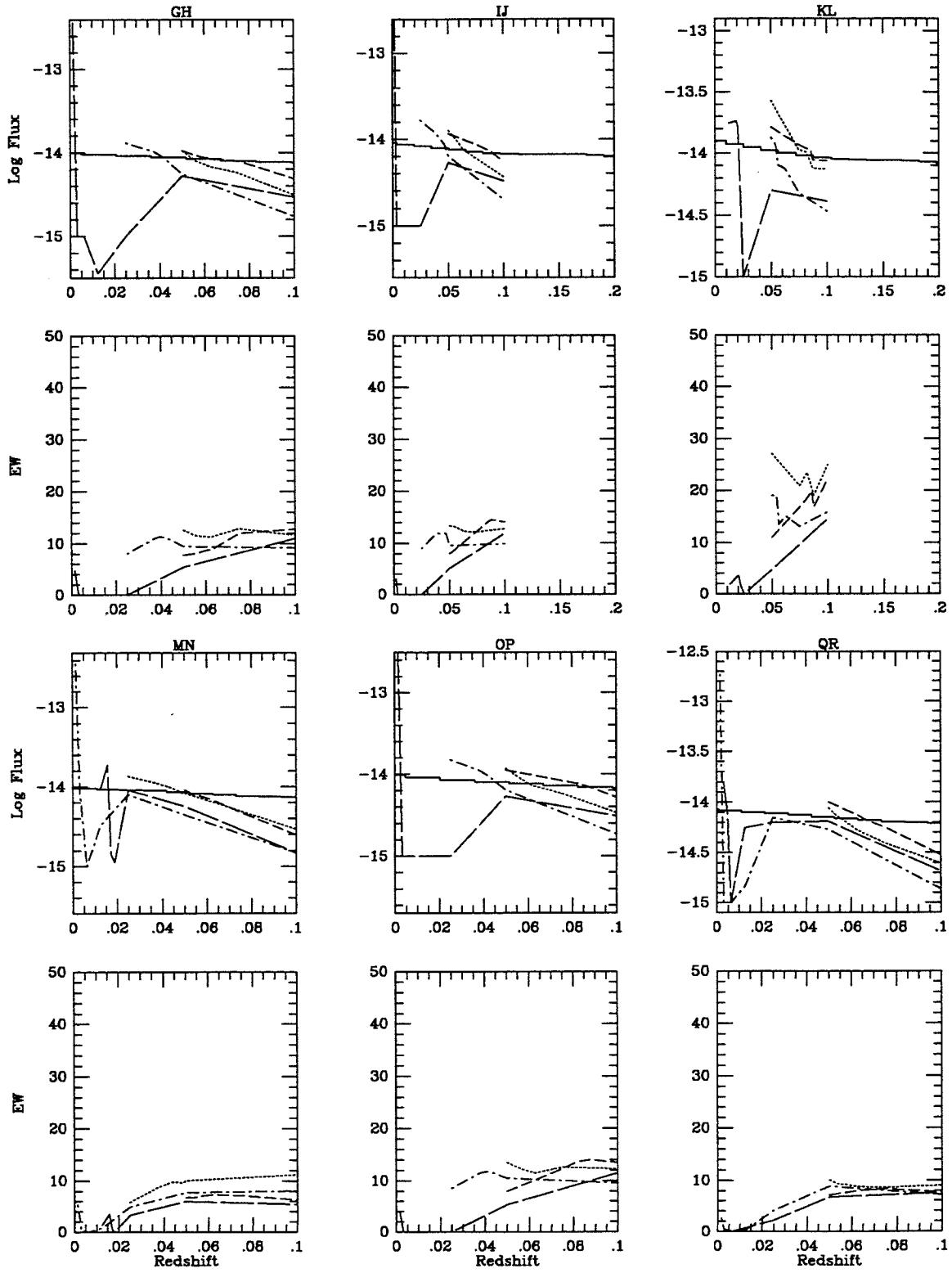

Figure B–7.bb

0122+3153 MAJC/MINA

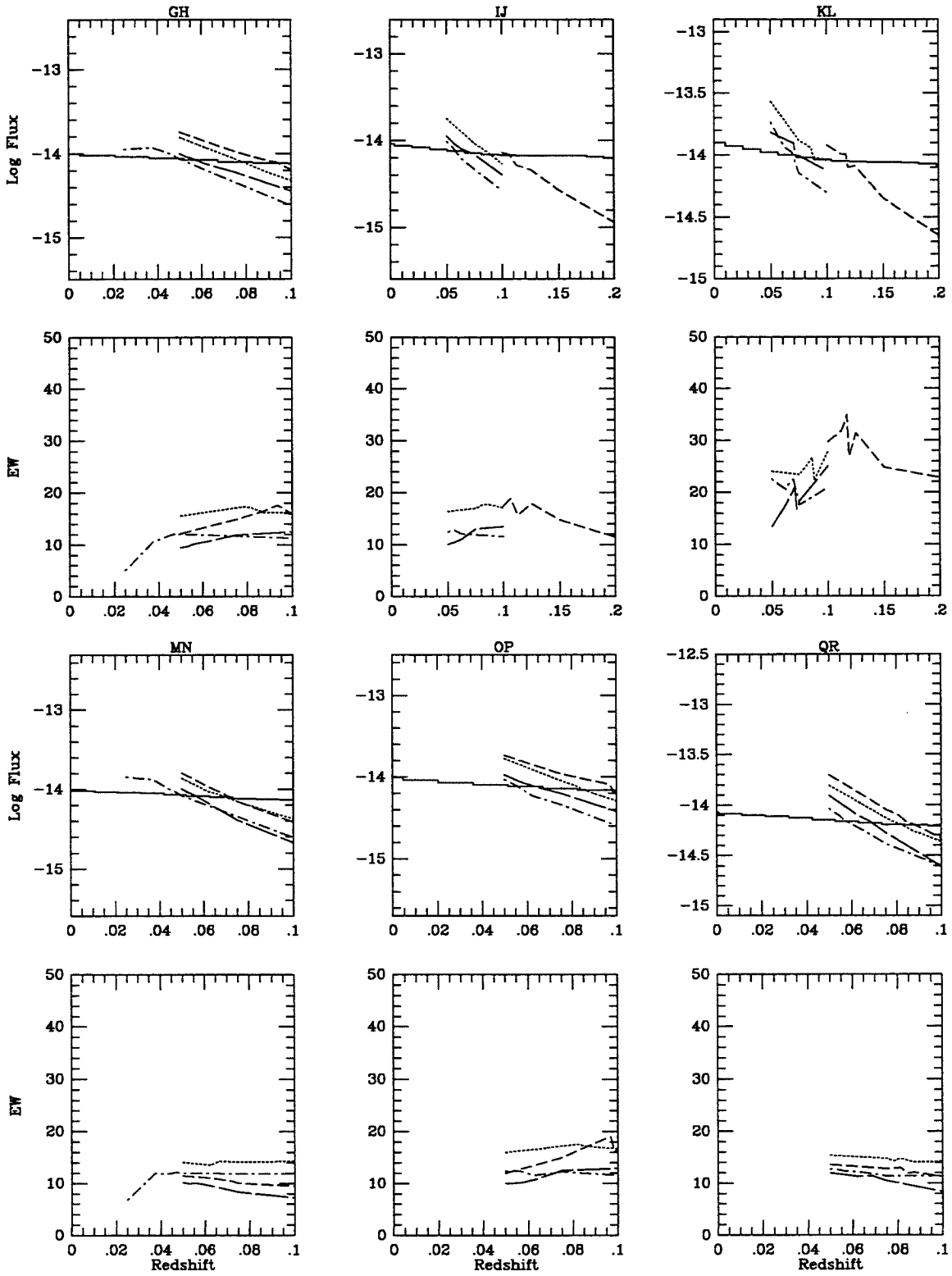

Figure B-7.ca

0122+3153 MAJC/MINB

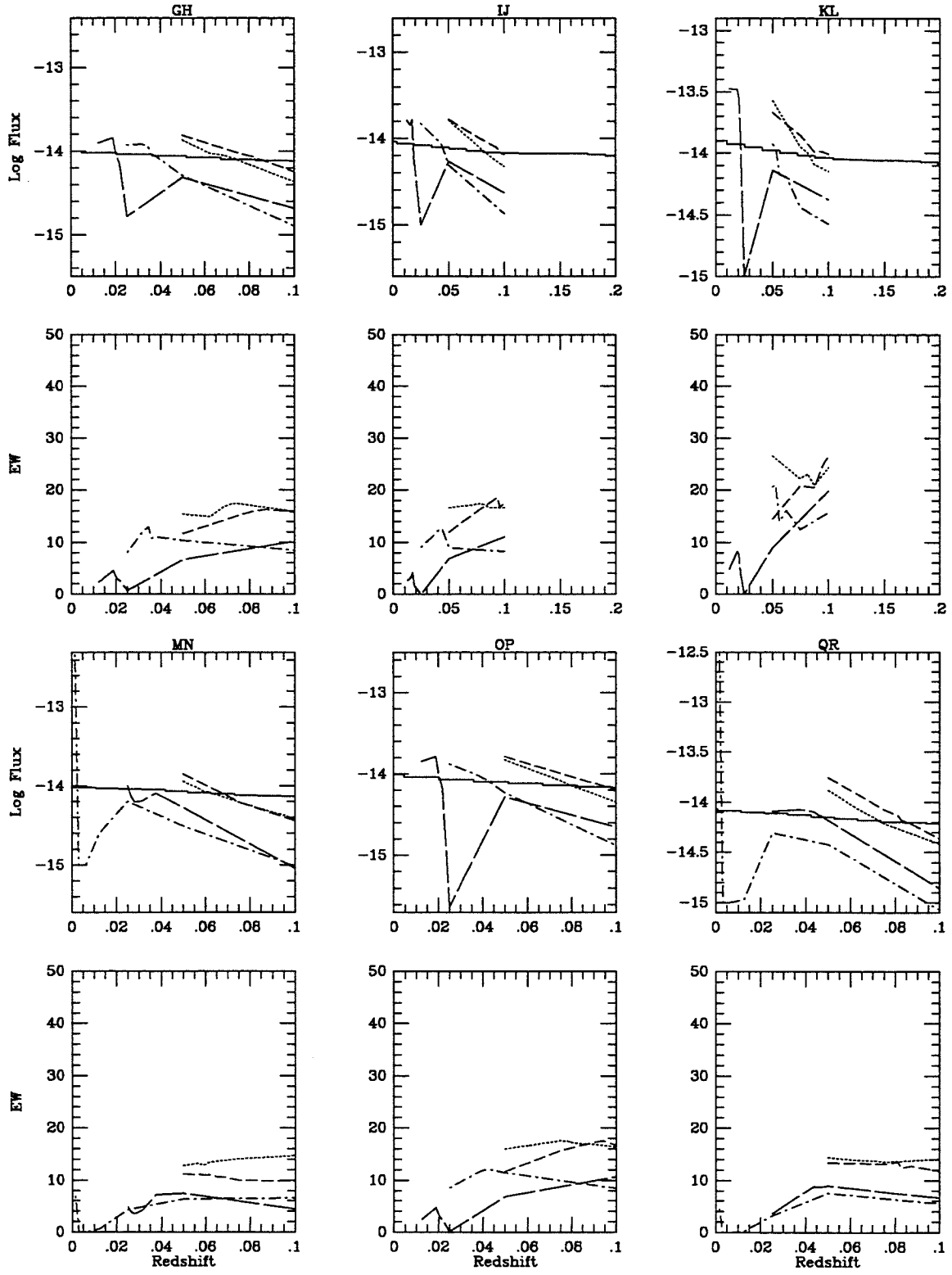

Figure B–7.cb

0141+0206 MAJ/MIN

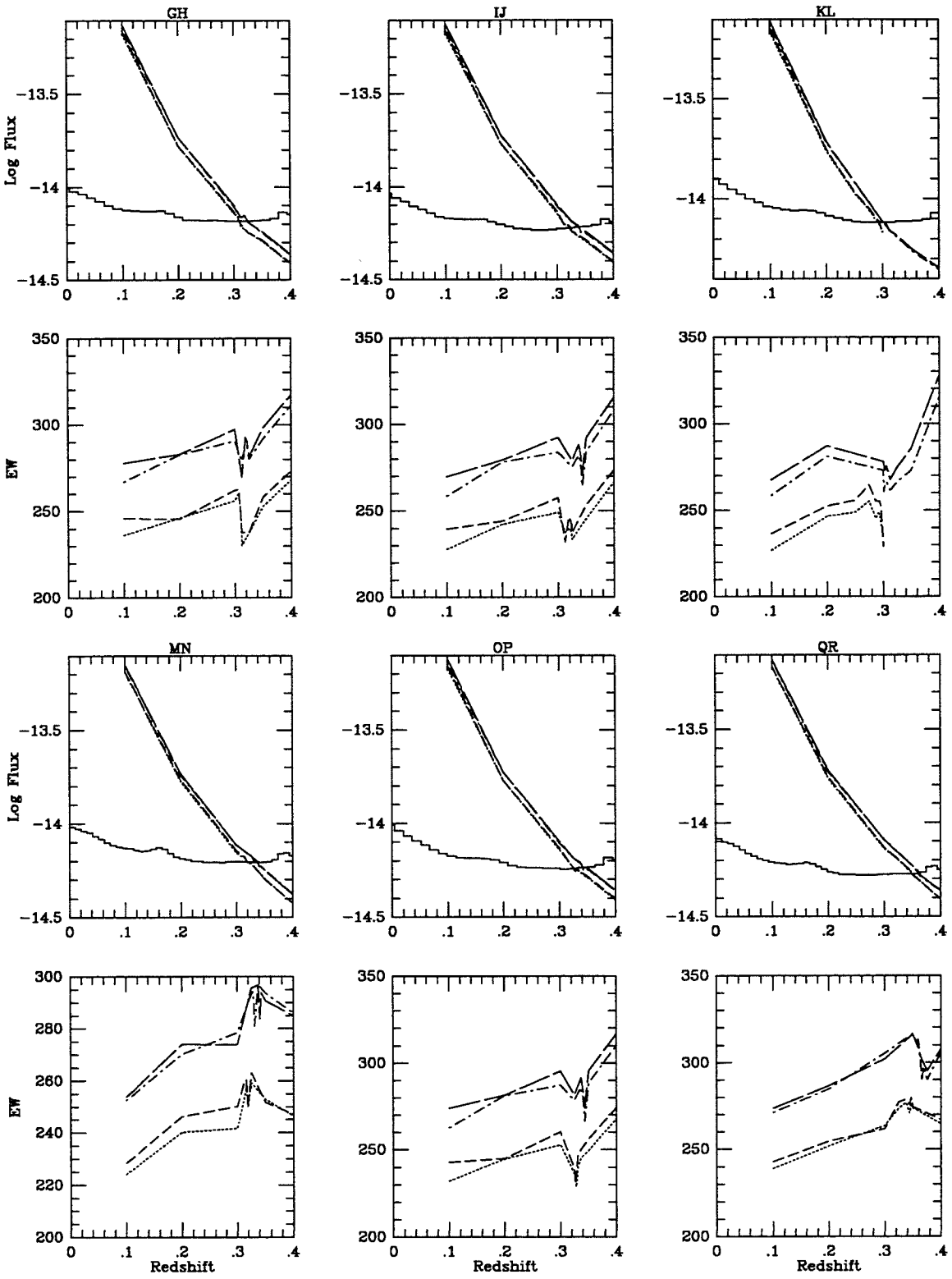

Figure B–8.

0152+0621 MAJ/MIN

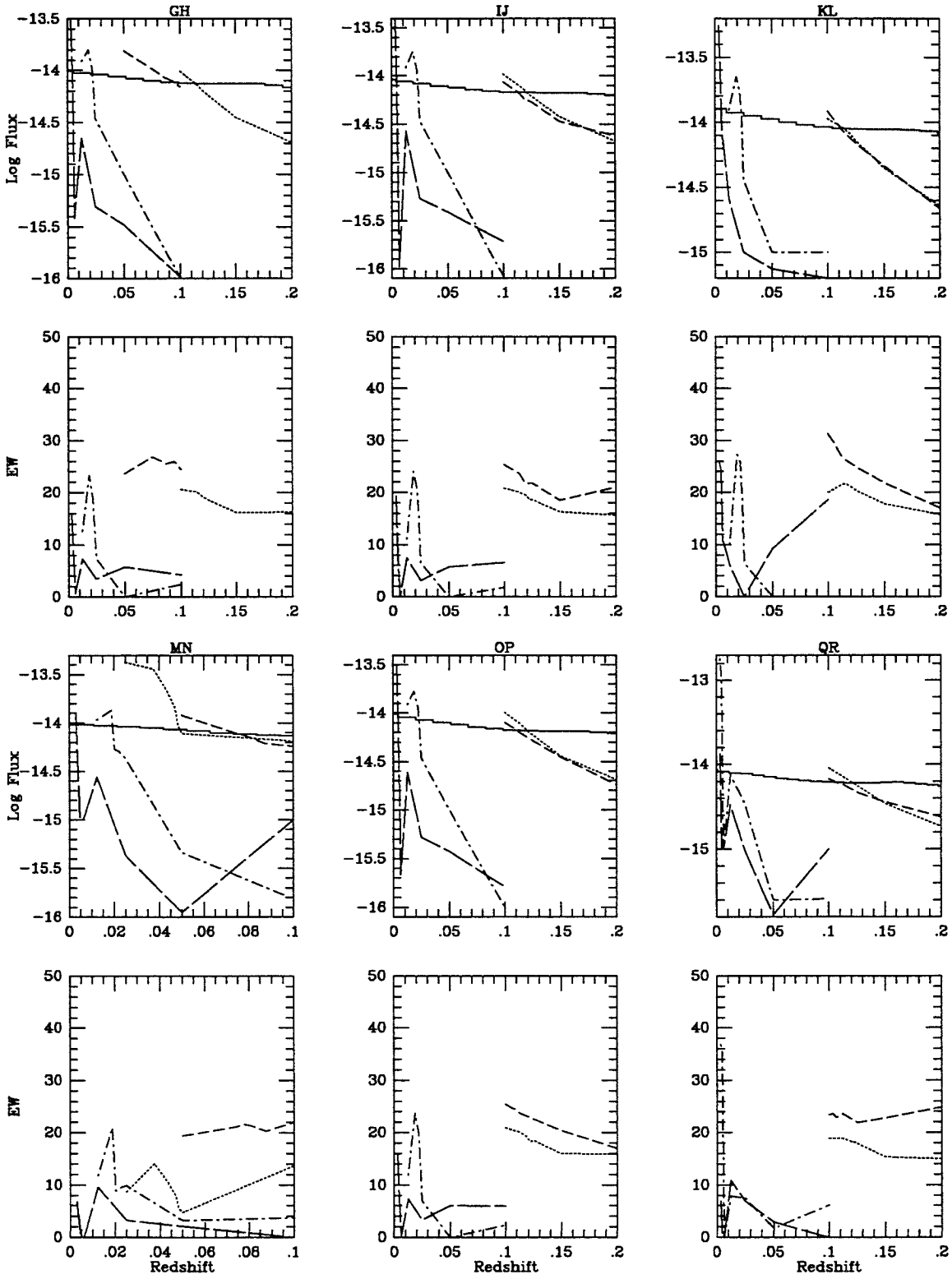

Figure B–9.

0157+2103 MAJ/MINA

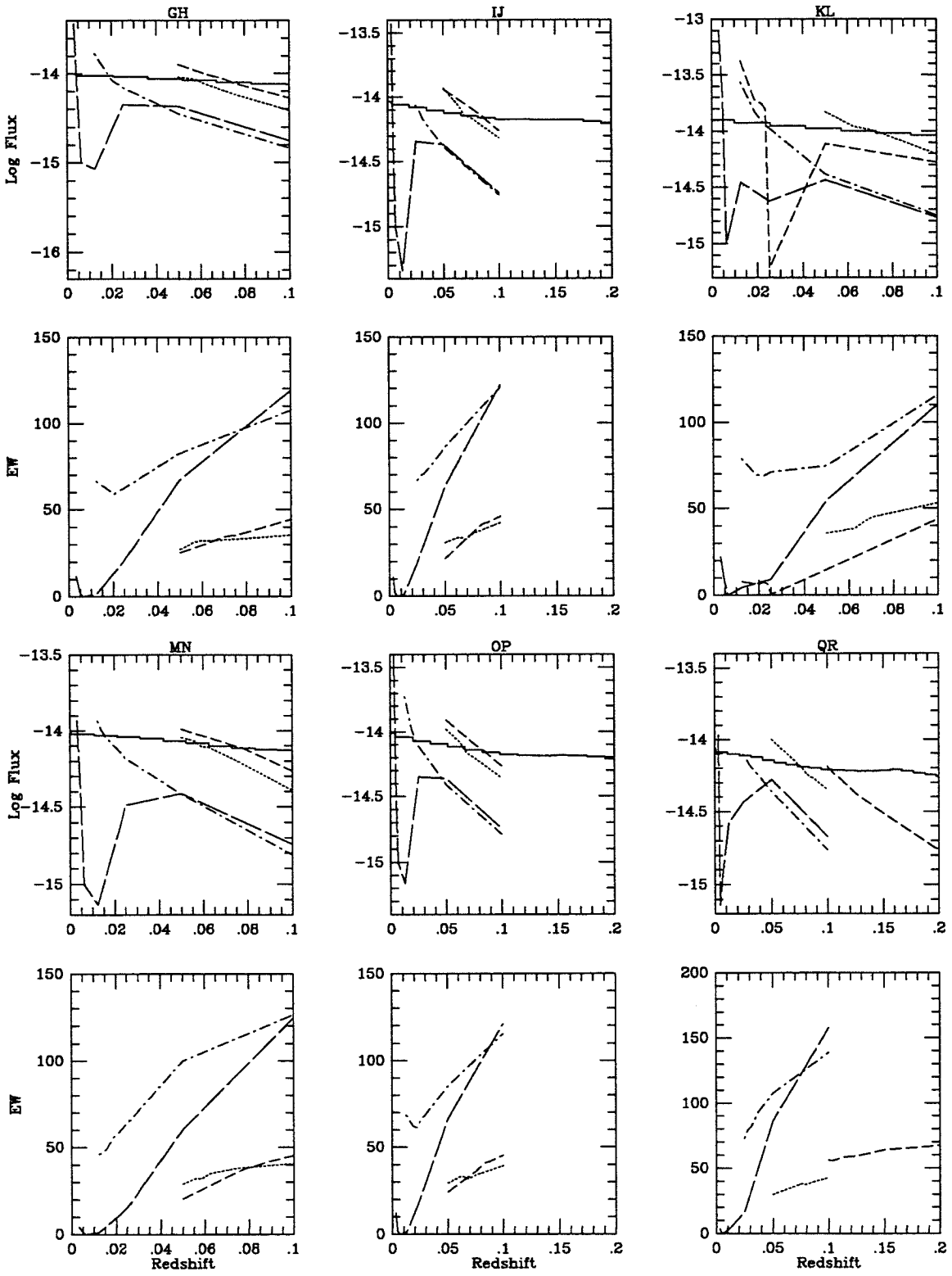

Figure B–10.a

0157+2103 MAJ/MINB

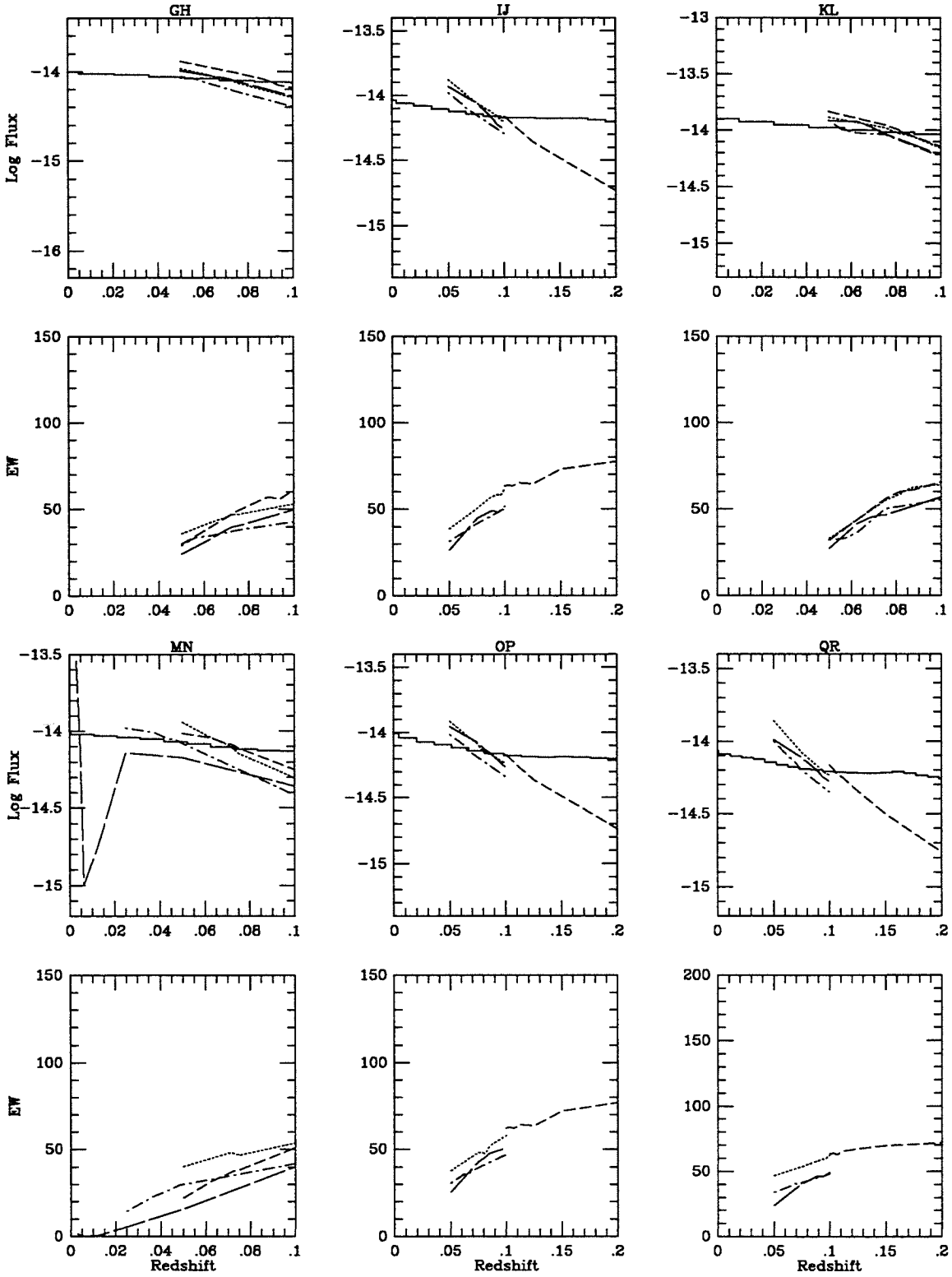

Figure B-10.b

0157+2103 MAJ/MINC

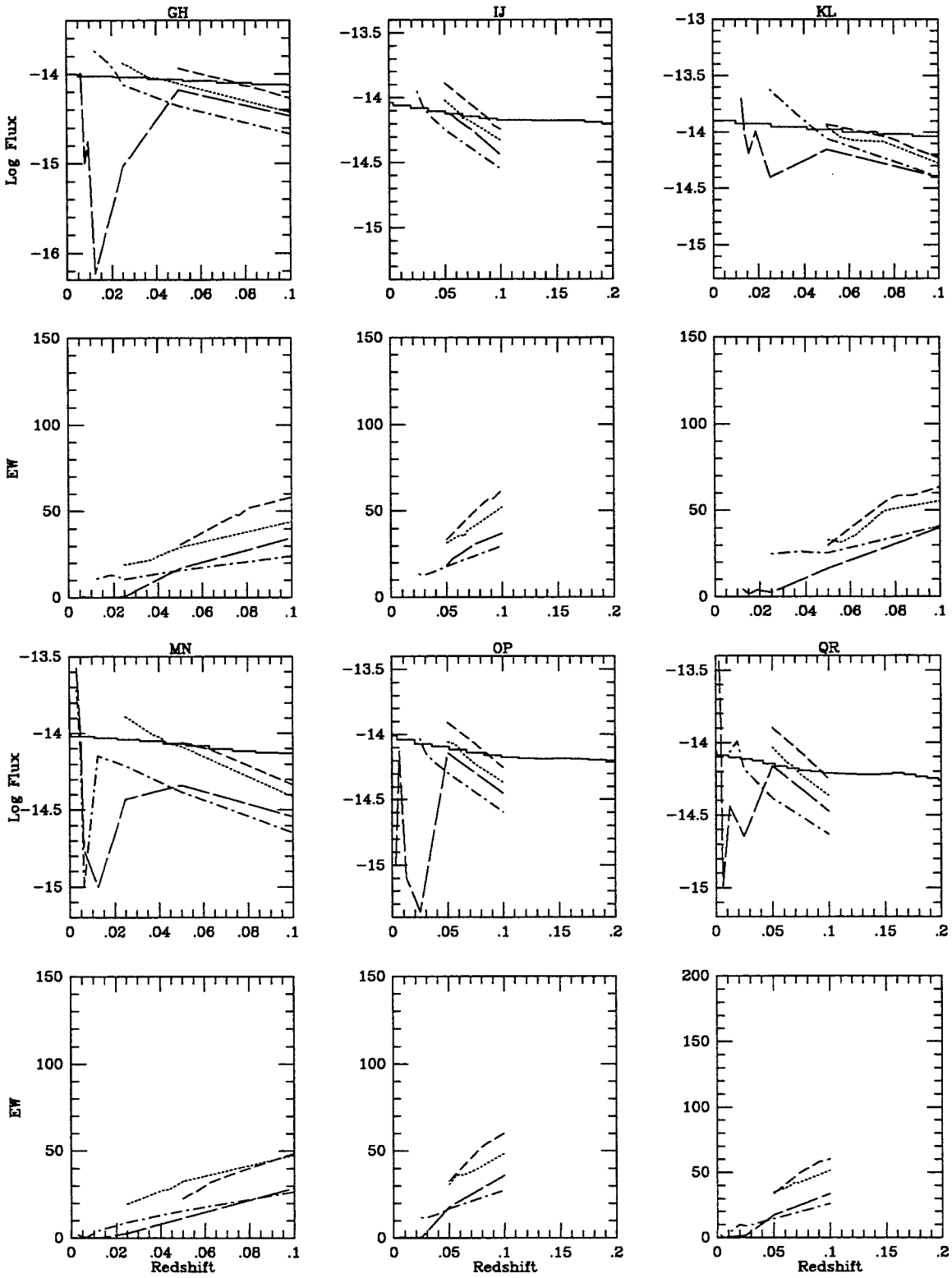

Figure B-10.c

NGC 863 MAJ/MIN

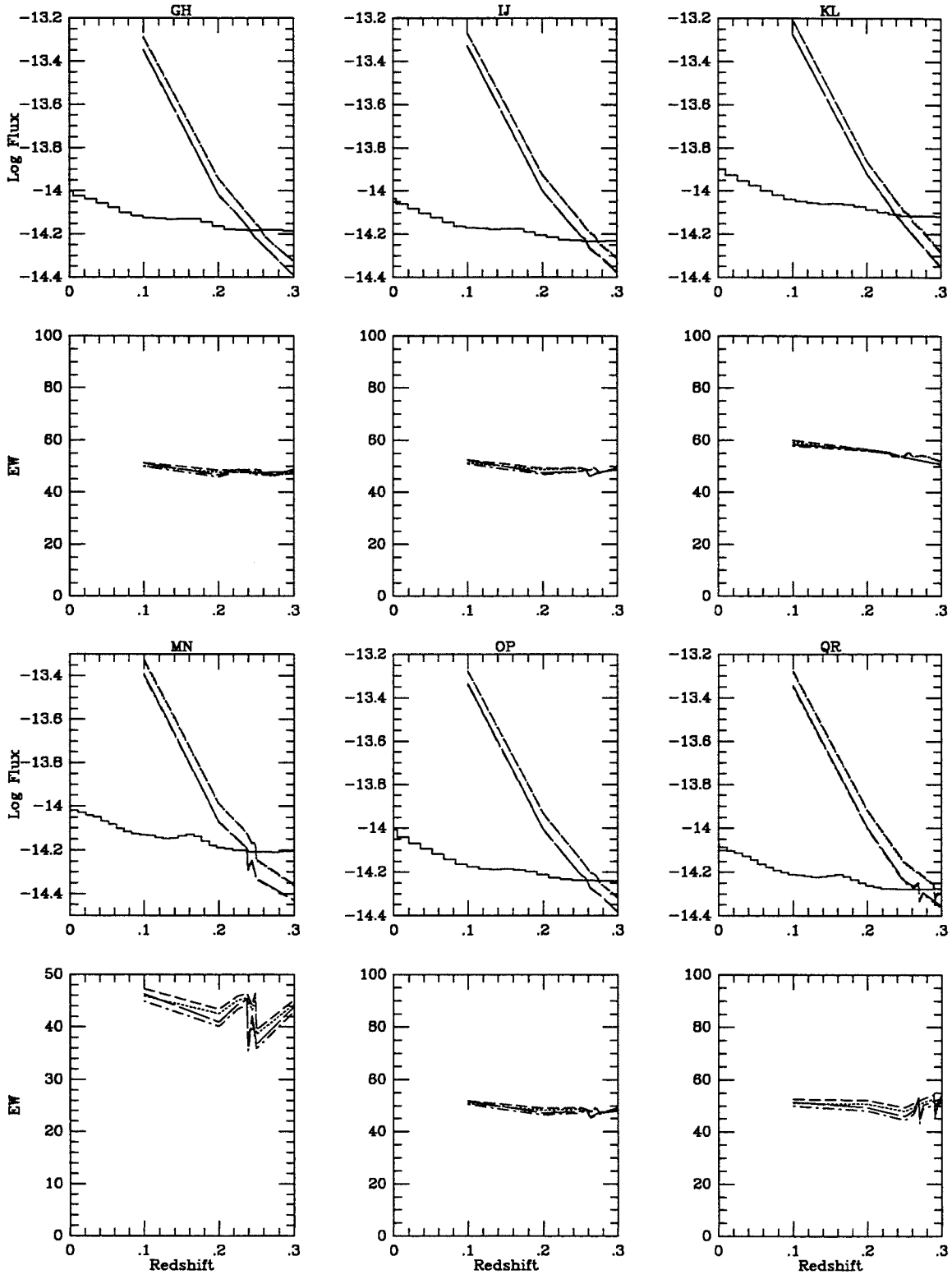

Figure B–11.

NGC 1036 MAJ/MIN

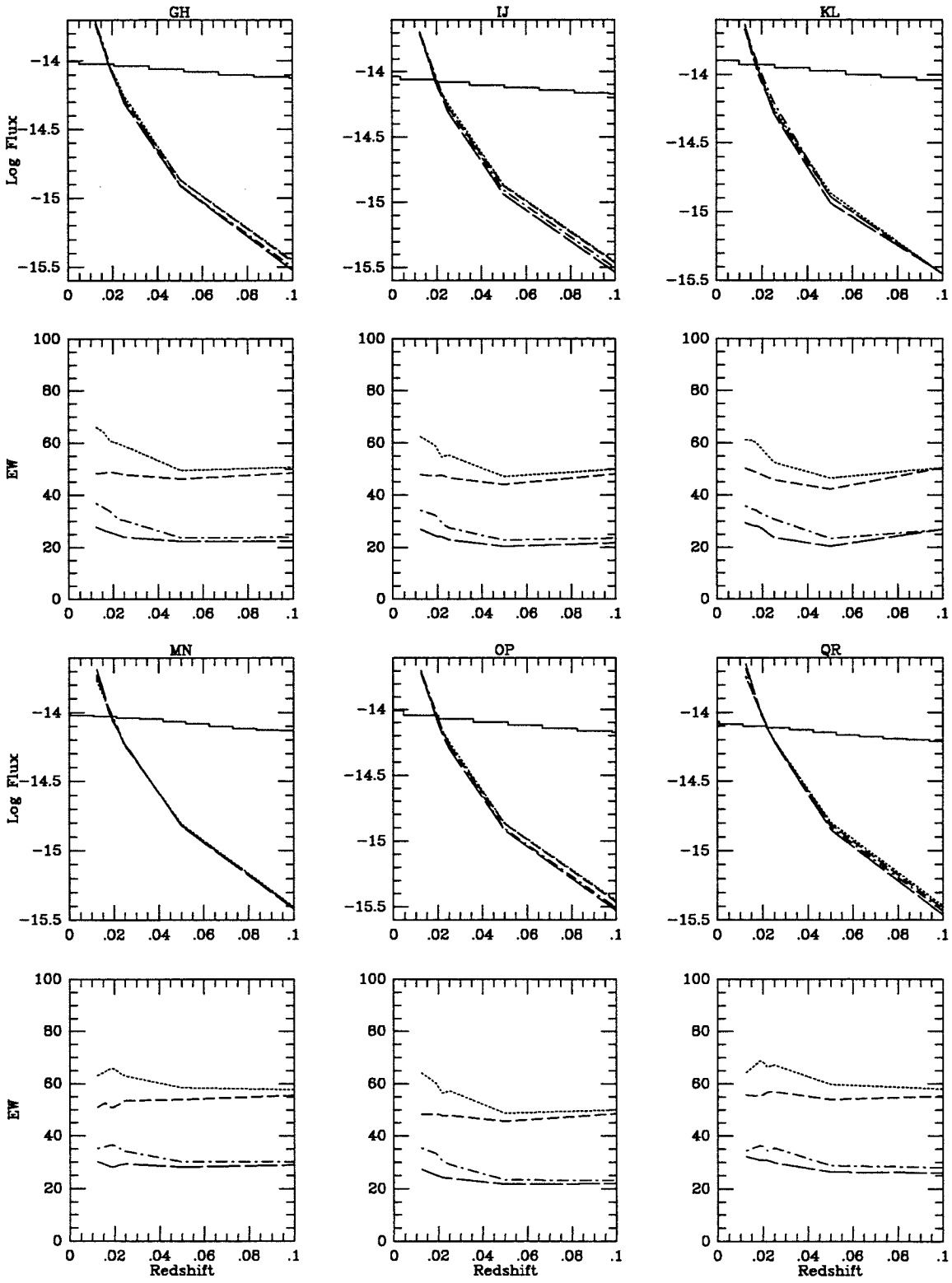

Figure B-12.

NGC 1068 MAJ/MIN

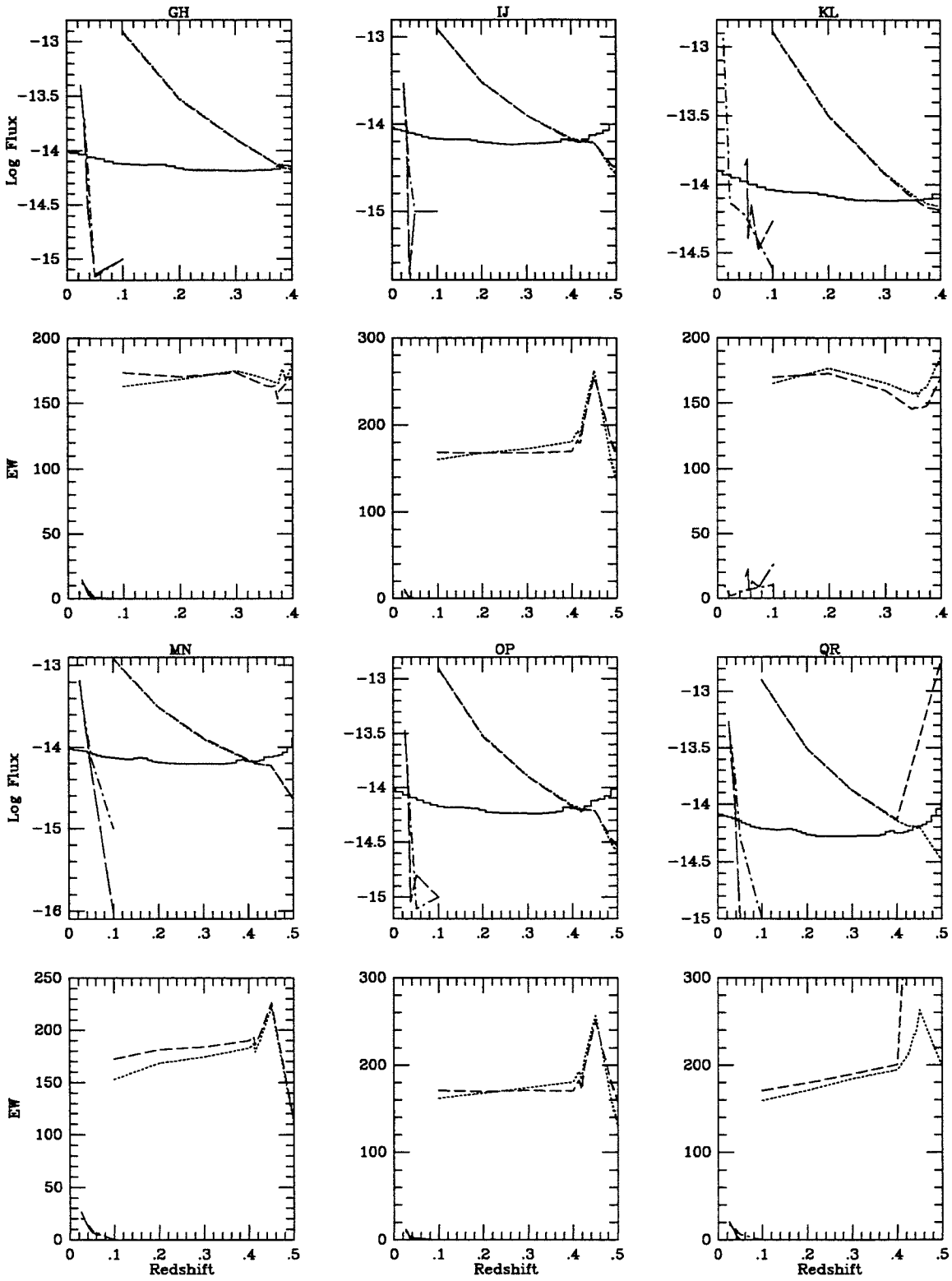

Figure B-13.

NGC 1144 MAJ/MINA

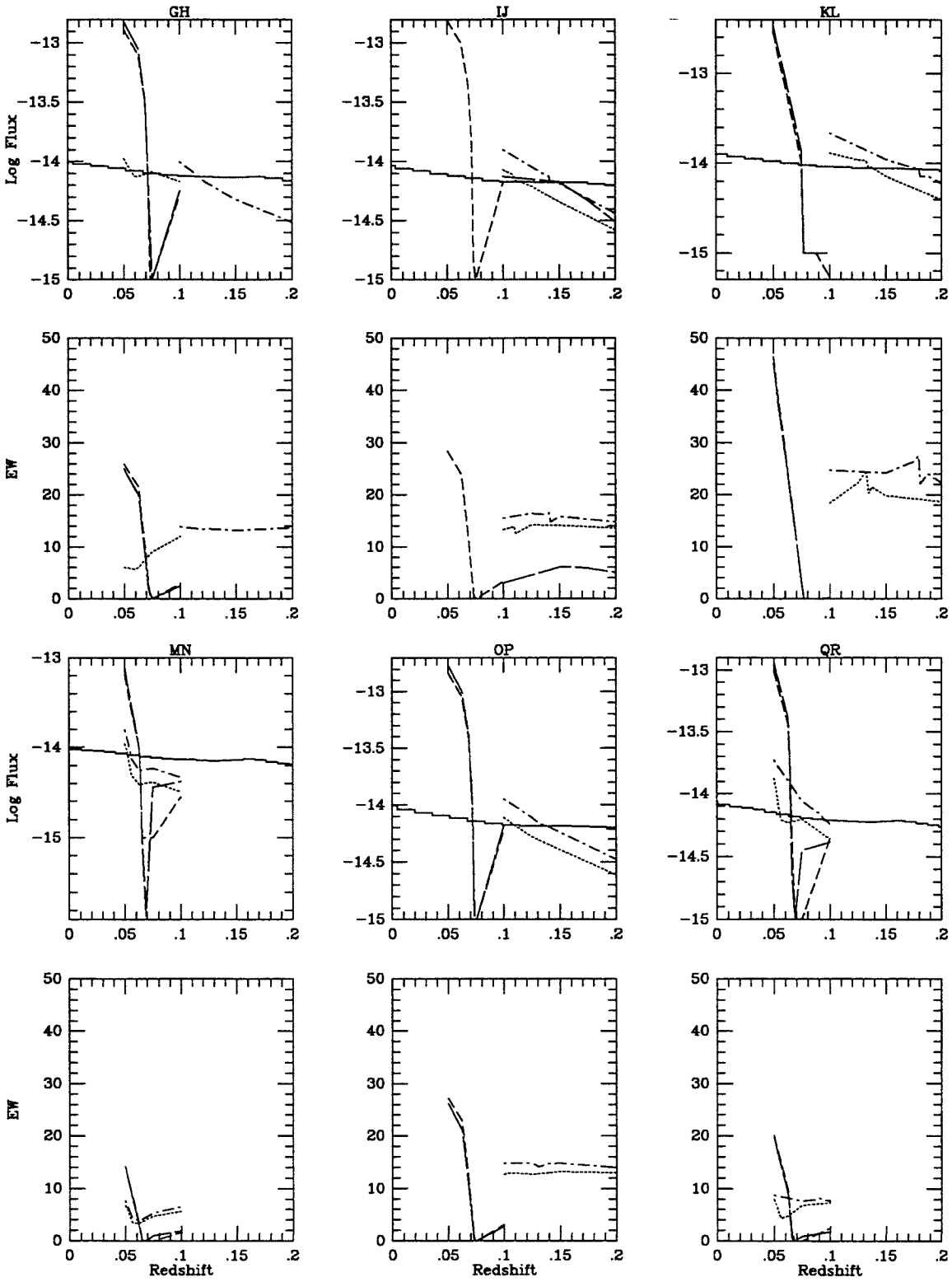

Figure B–14.a

NGC 1144 MAJ/MINB

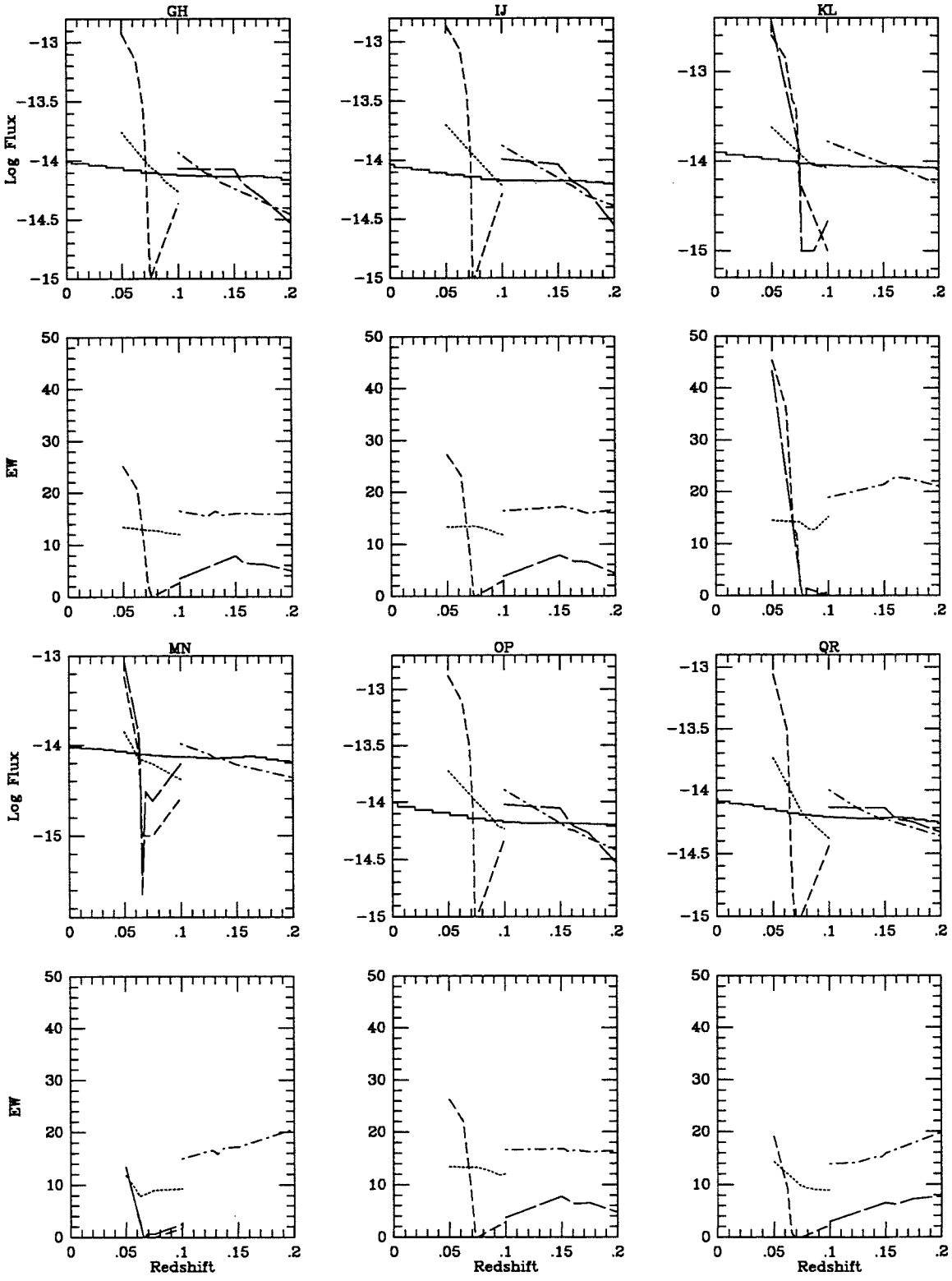

Figure B–14.b

NGC 2719A MAJ/MIN

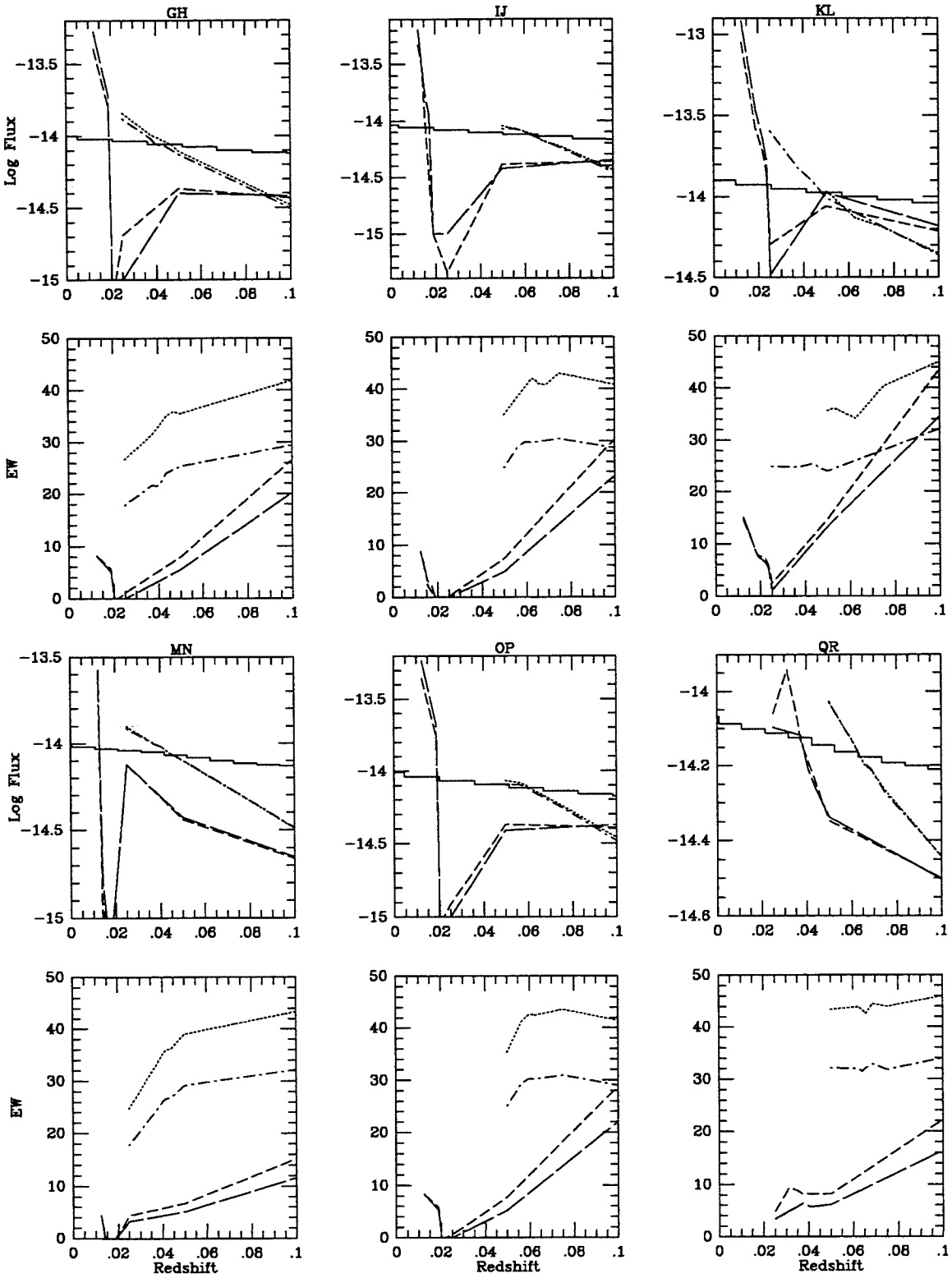

Figure B-15.

NGC 2820 MAJ/MINA

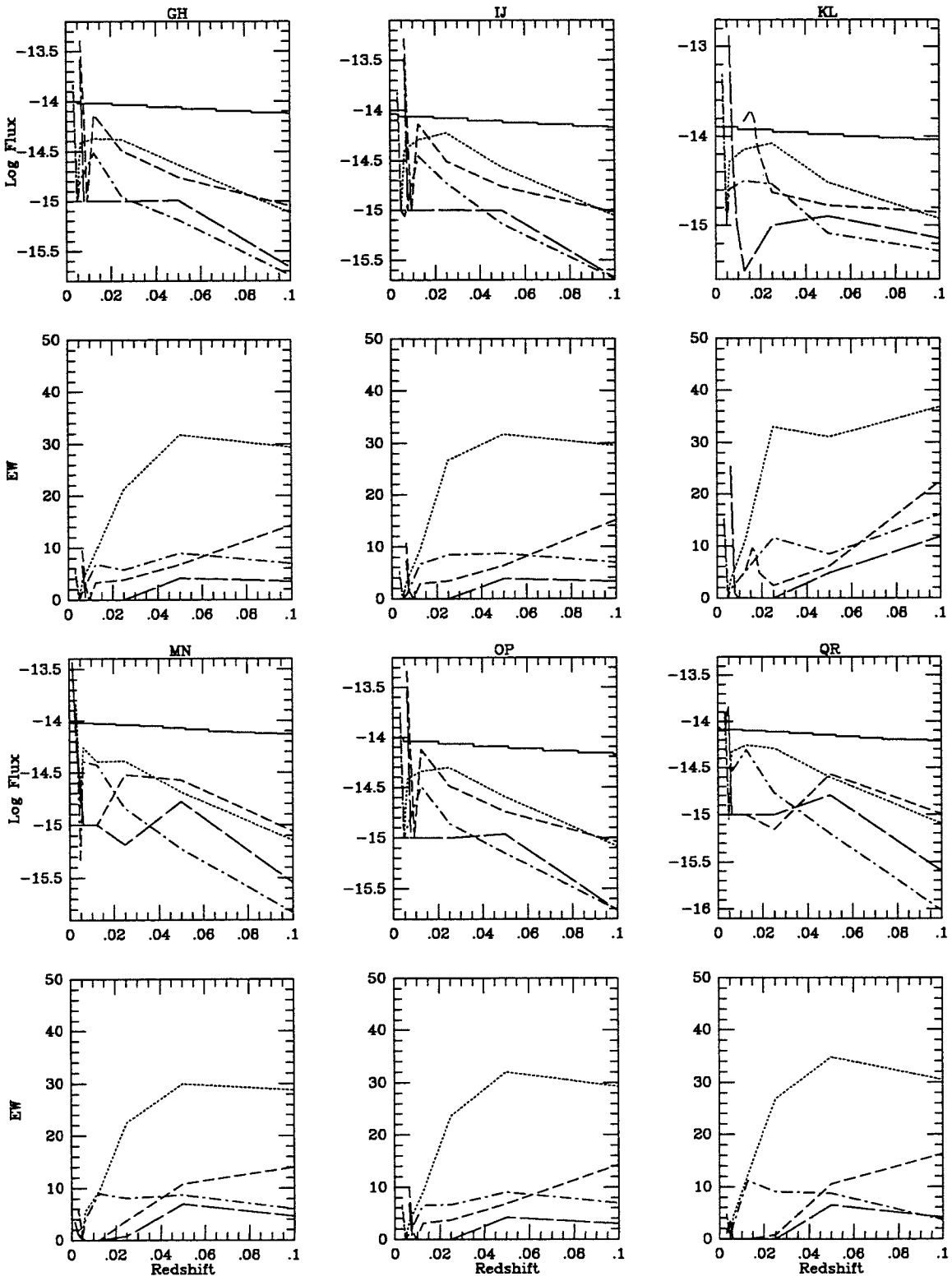

Figure B-16.a

NGC 2820 MAJ/MINB

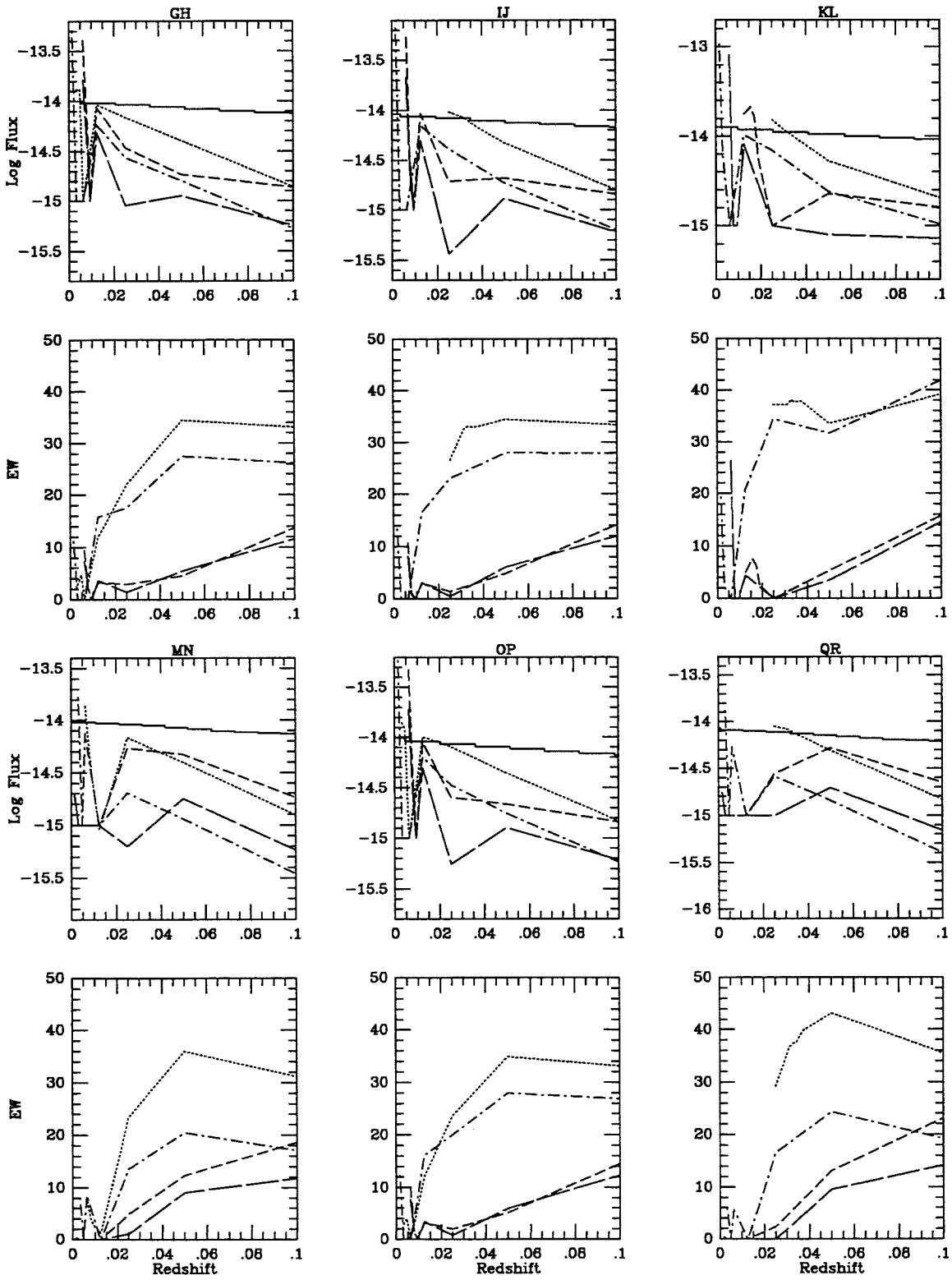

Figure B–16.b

NGC 2820 MAJ/MINC

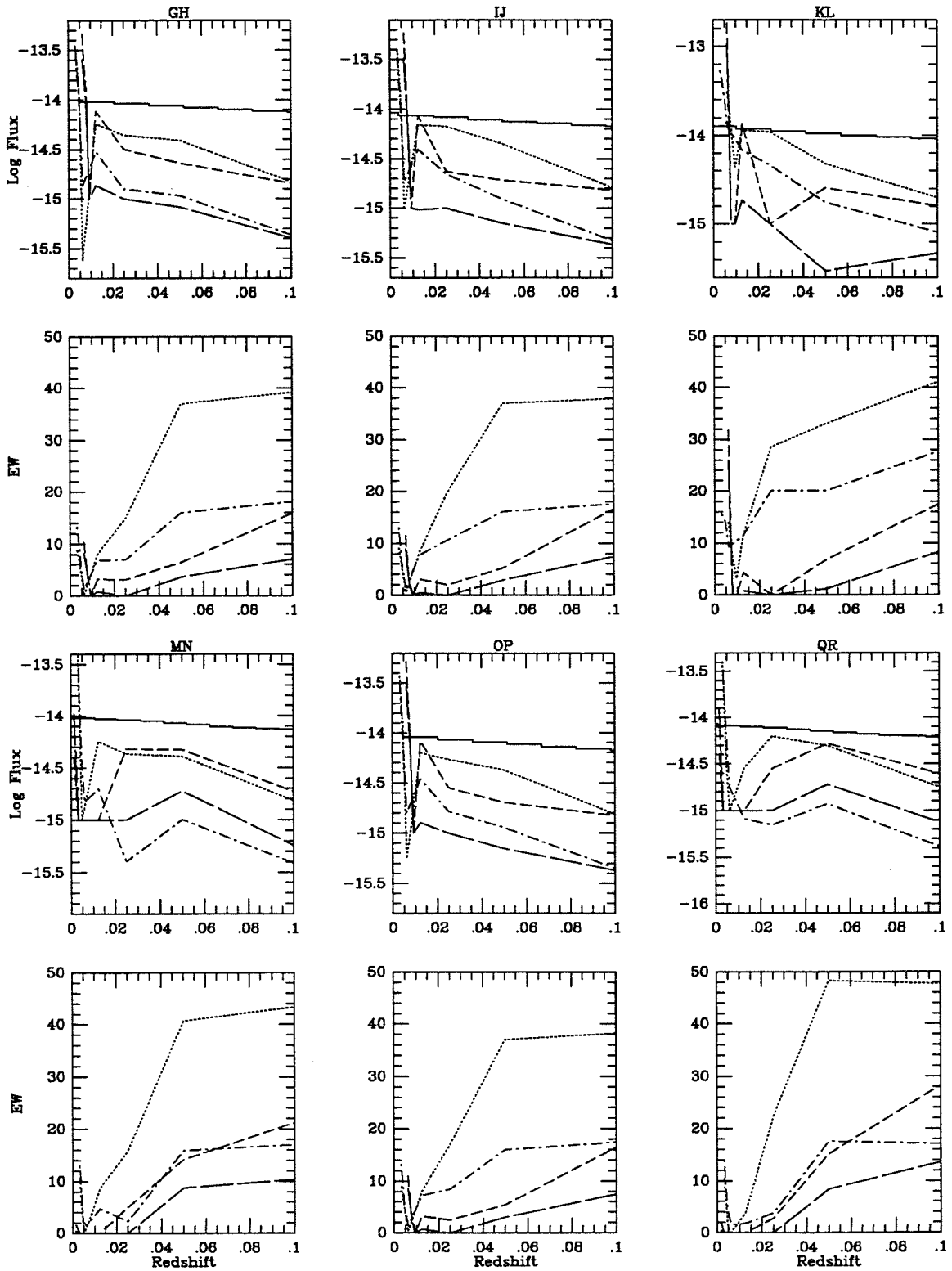

Figure B–16.c

0940+0943 MAJ/MIN

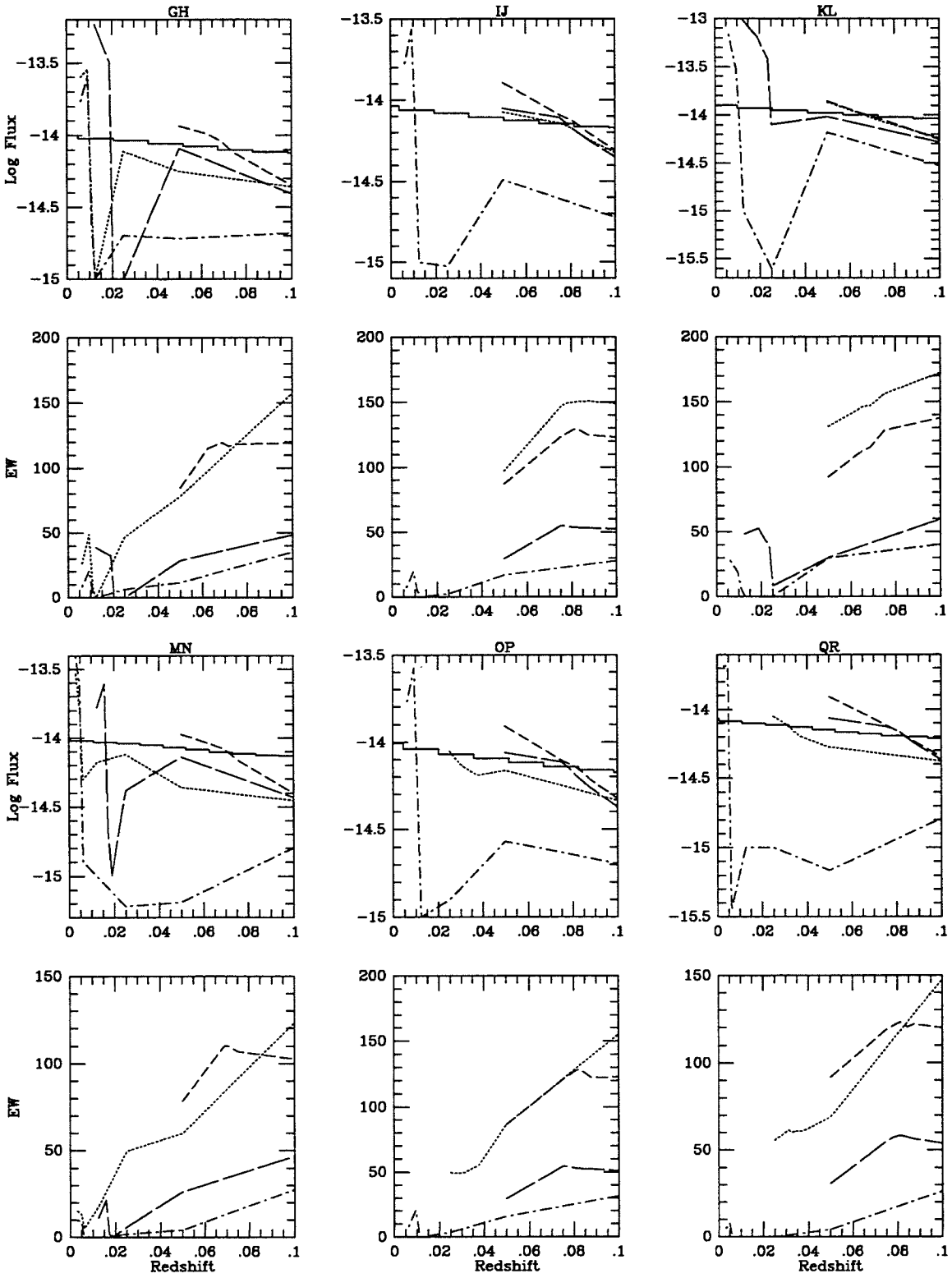

Figure B–17.

0948+0804 MAJ/MIN

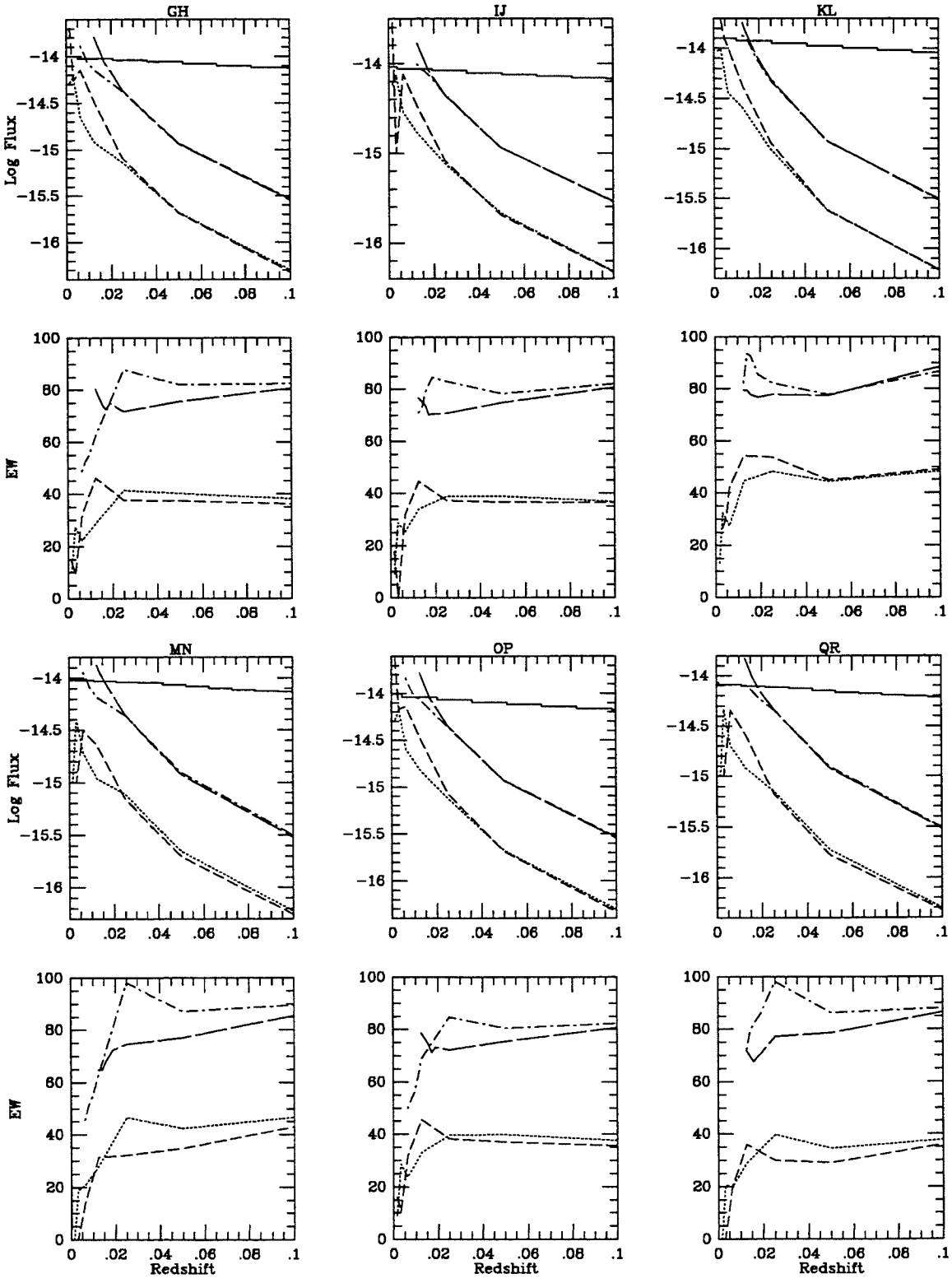

Figure B-18.

0954+1553 MAJ/MIN

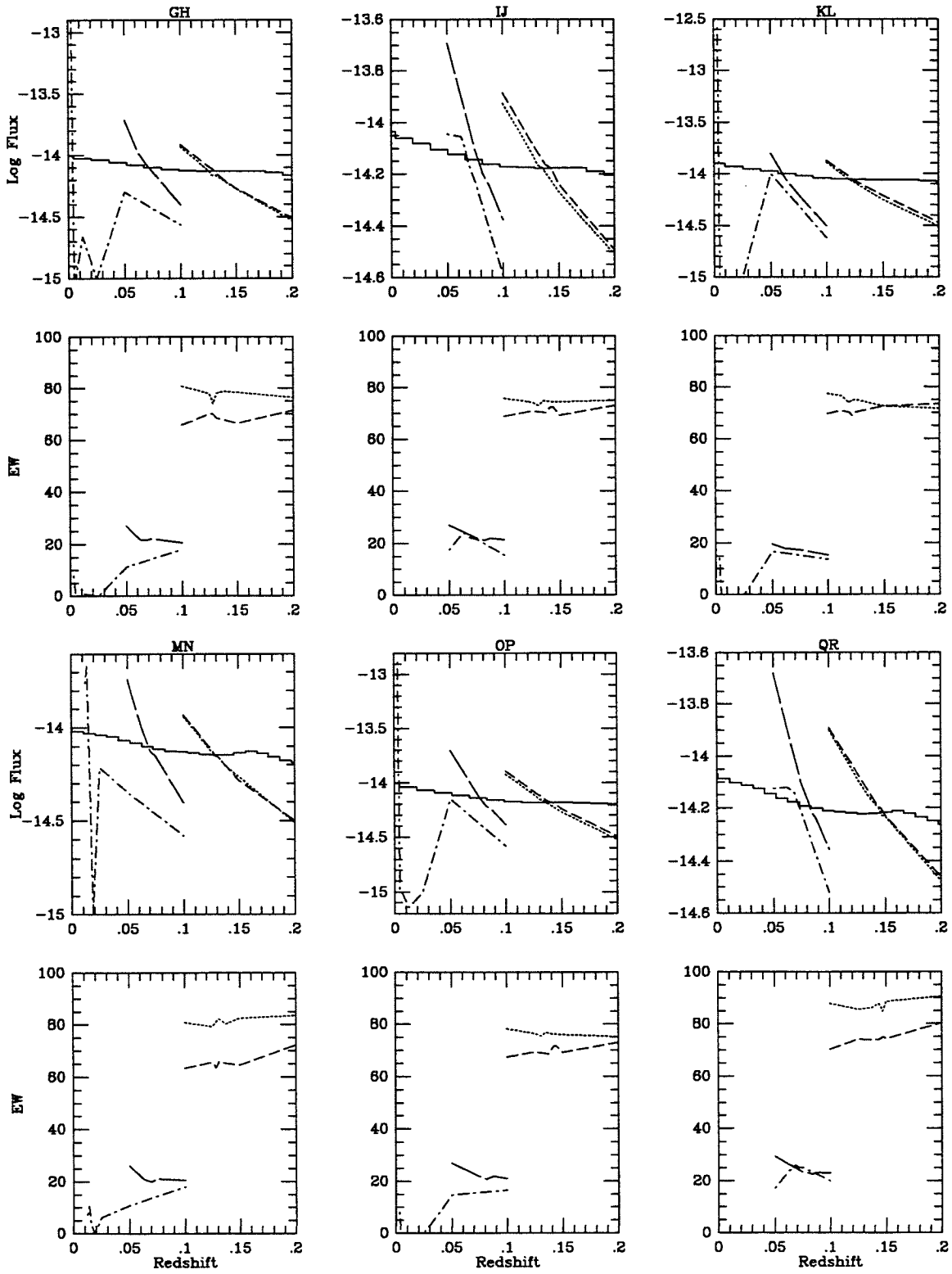

Figure B–19.

NGC 3080 MAJA/MIN

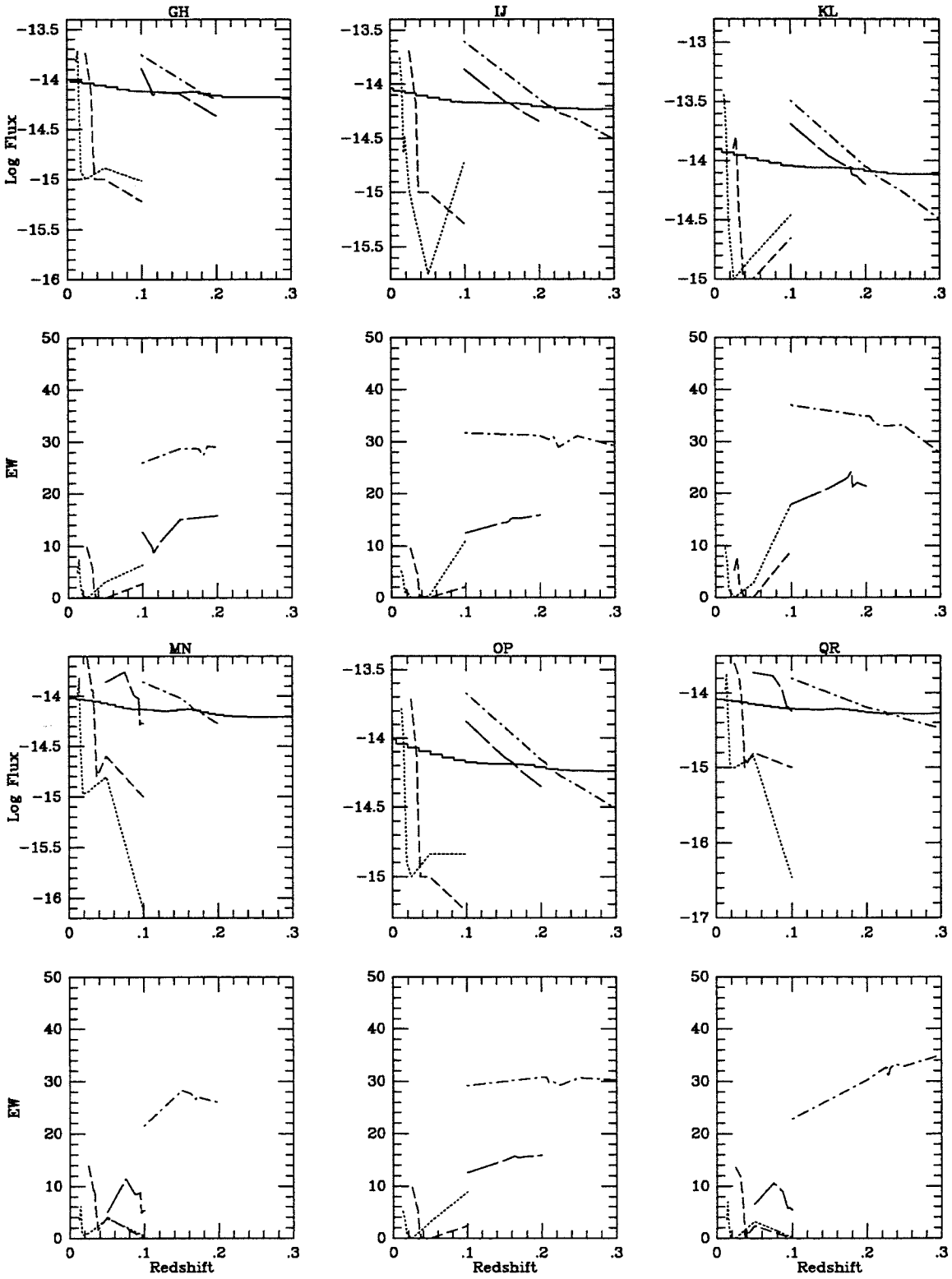

Figure B-20.a

NGC 3080 MAJB/MIN

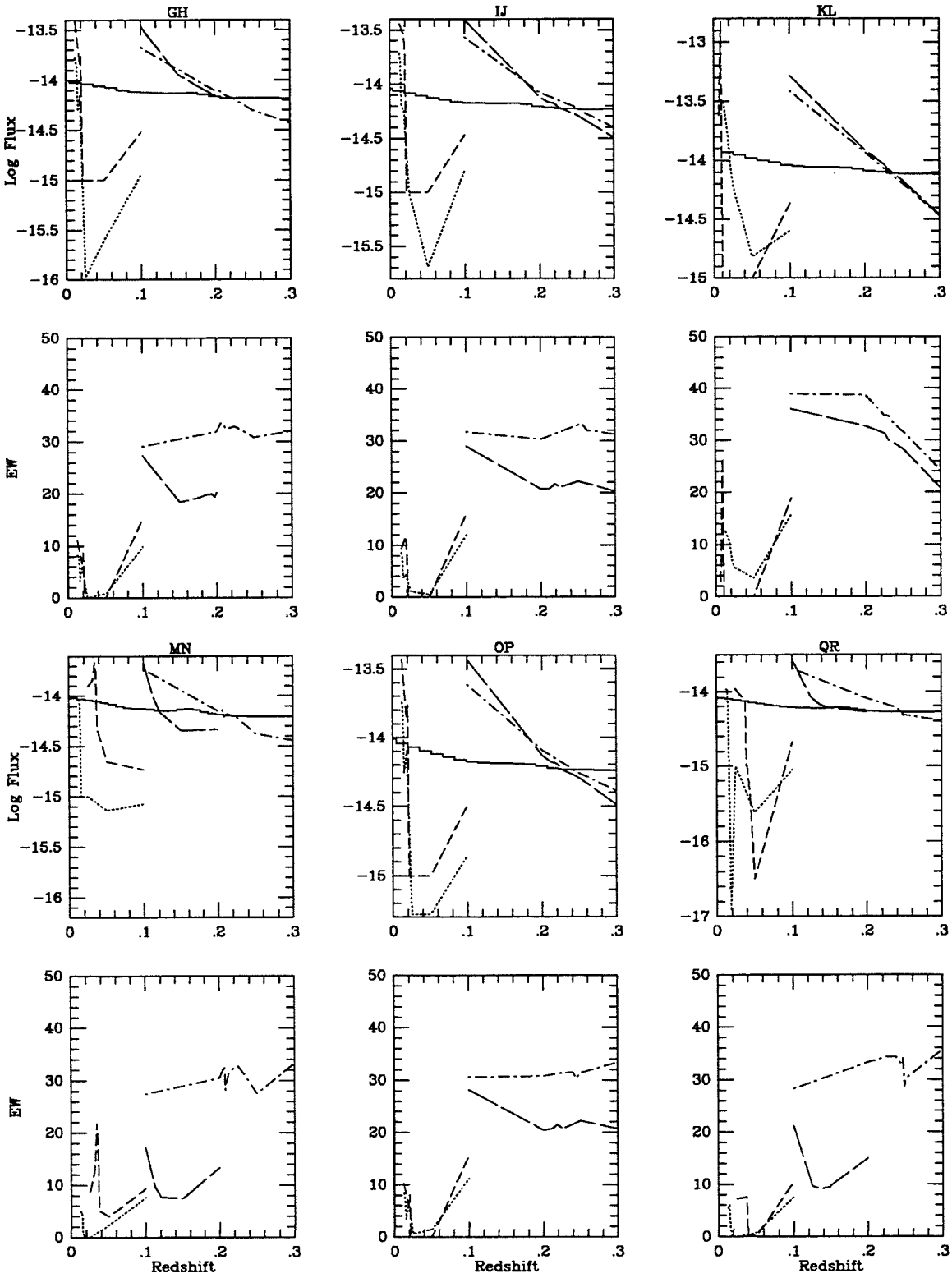

Figure B–20.b

NGC 3079 MAJ/MIN

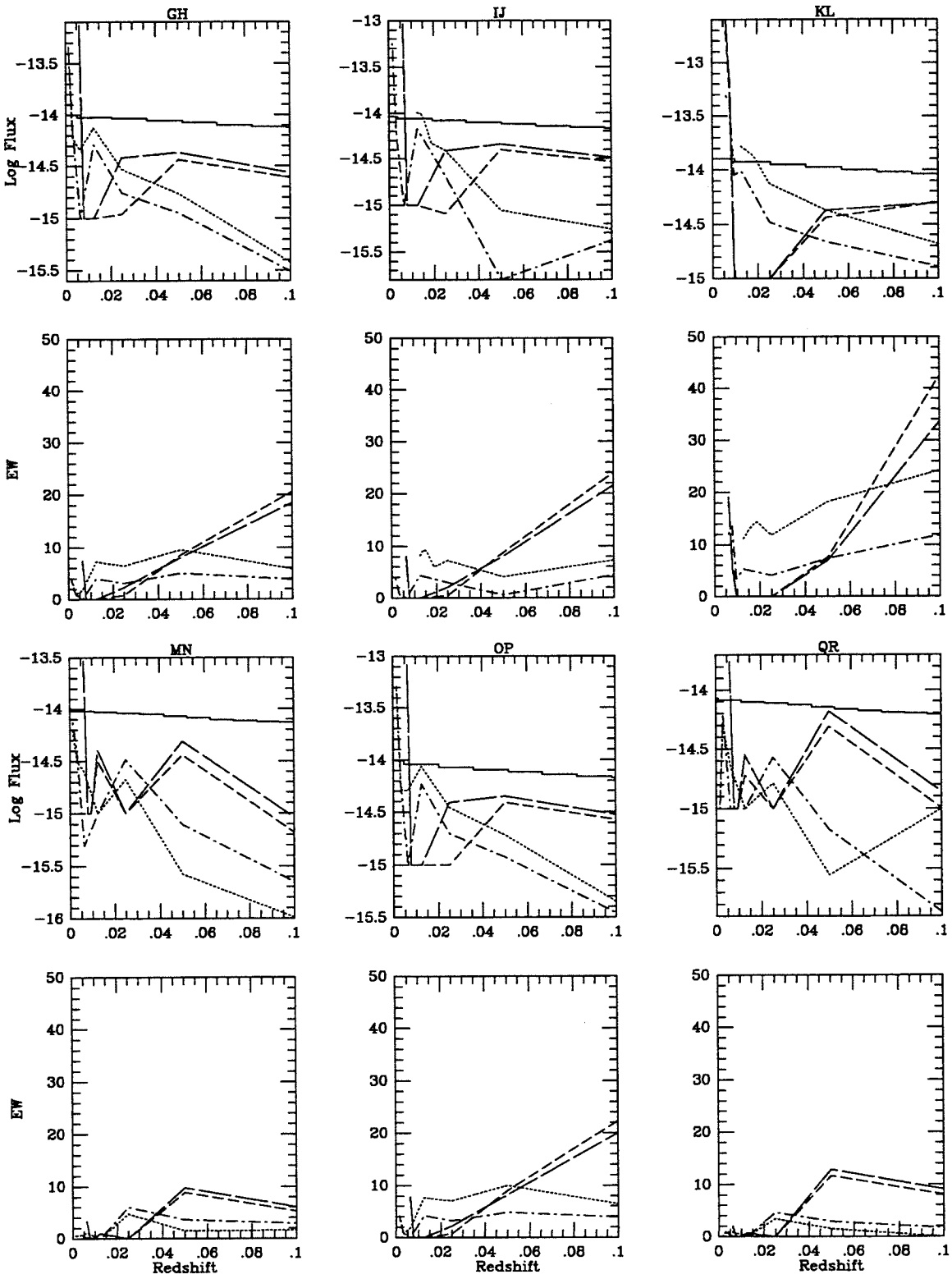

Figure B–21.

1004+1036 MAJ/MIN

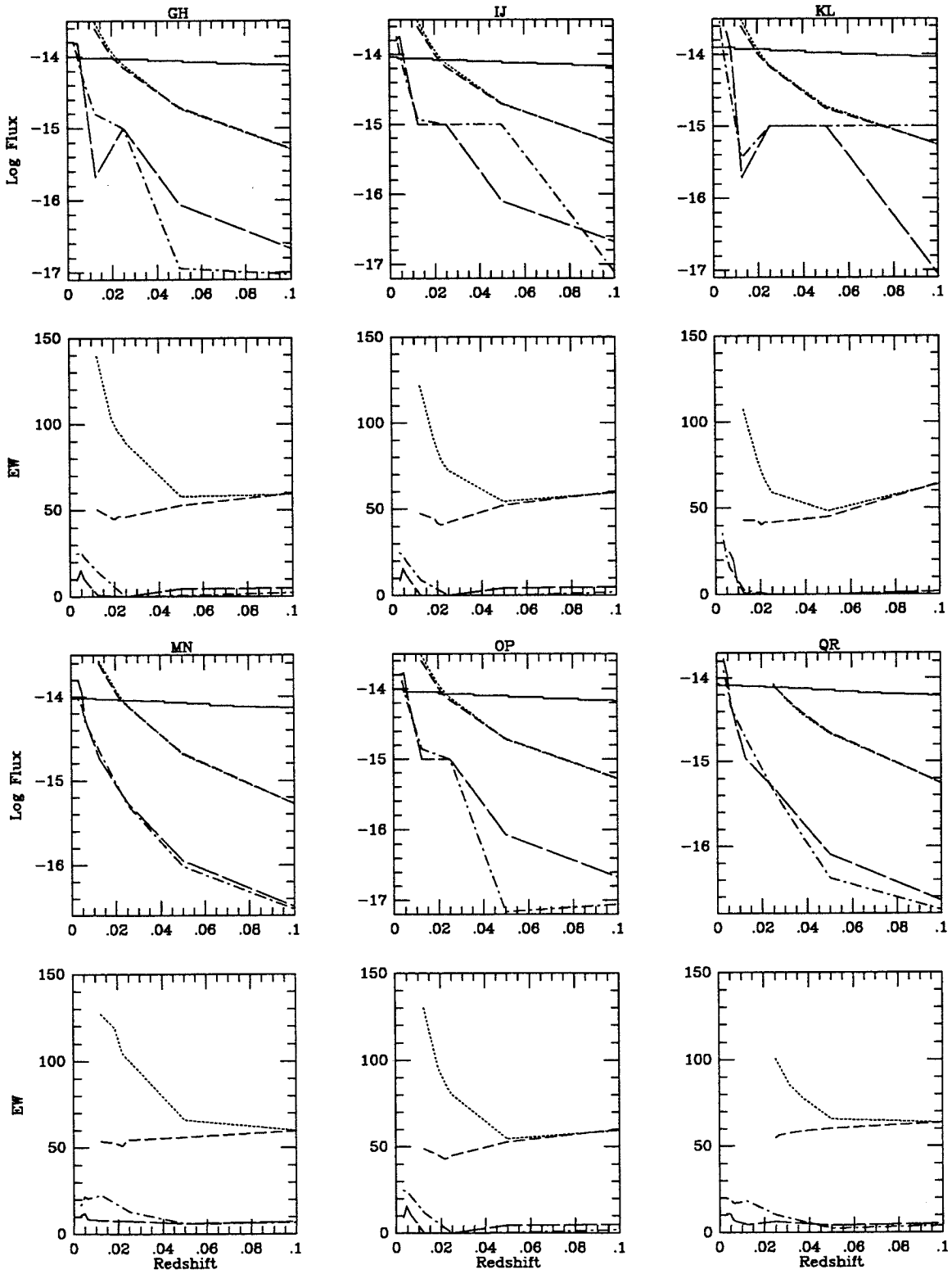

Figure B–22.

NGC 3227 MAJ/MIN

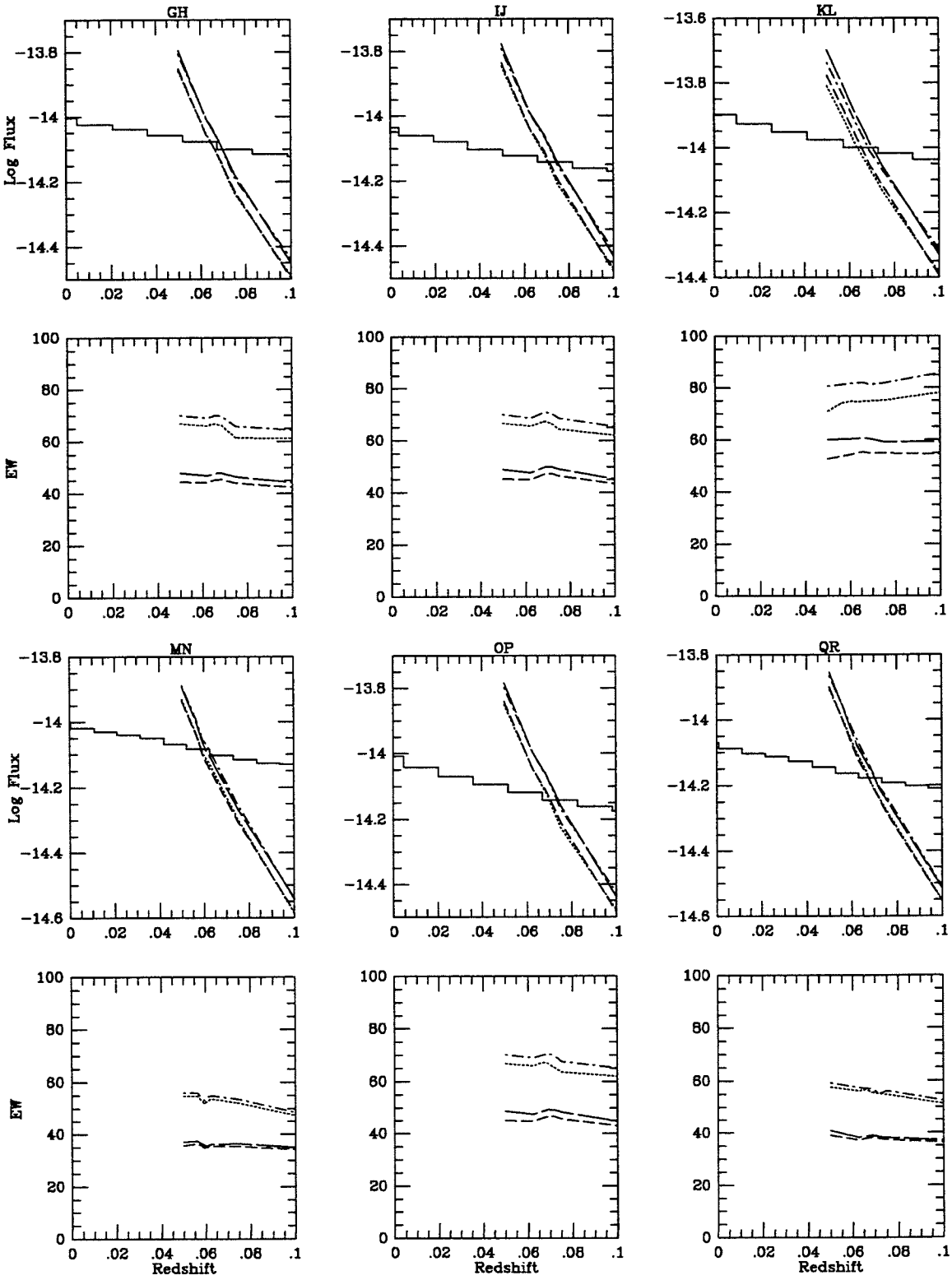

Figure B–23.

NGC 3239 MAJ/MIN

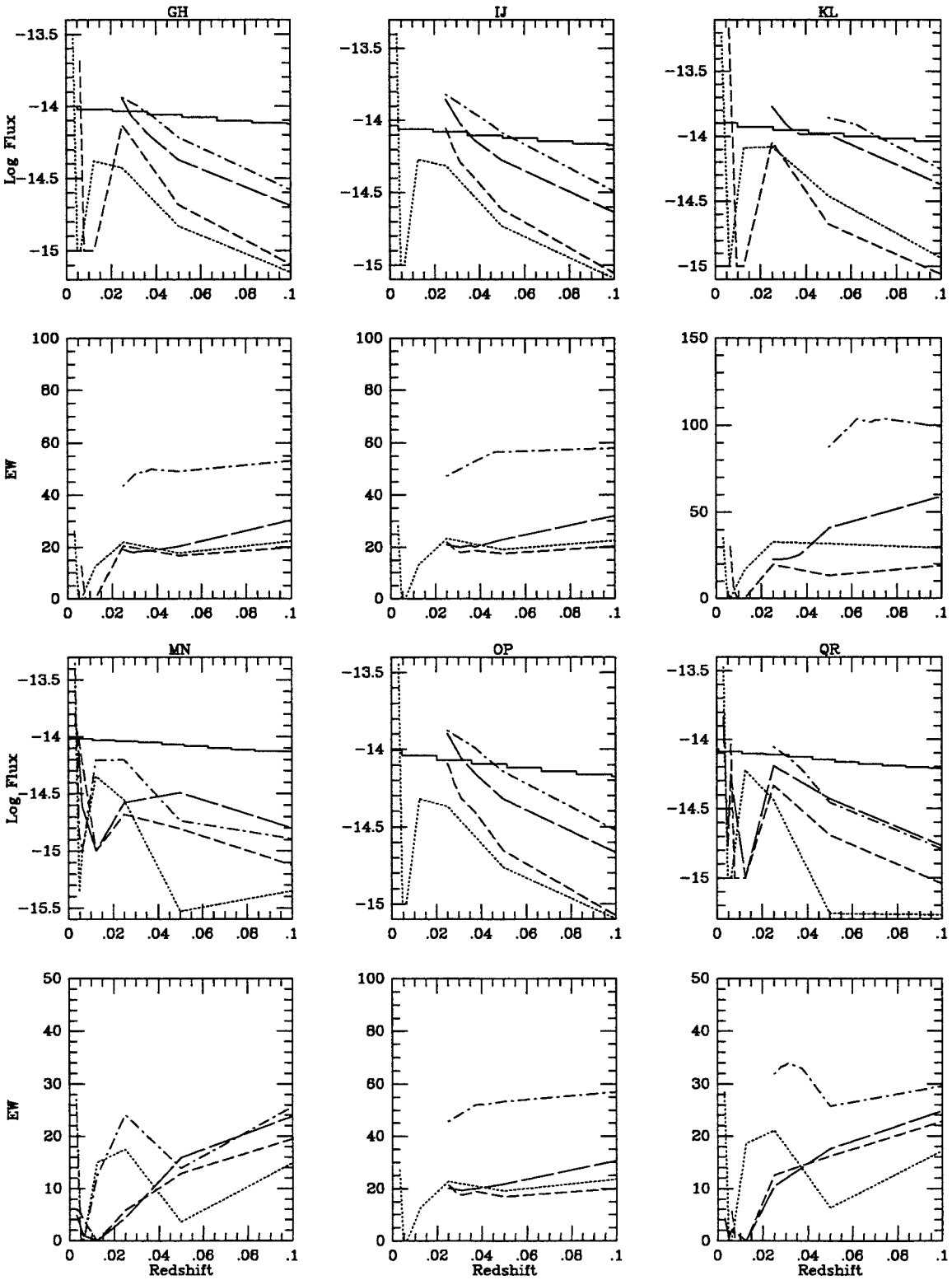

Figure B–24.

NGC 3264 MAJ/MINA

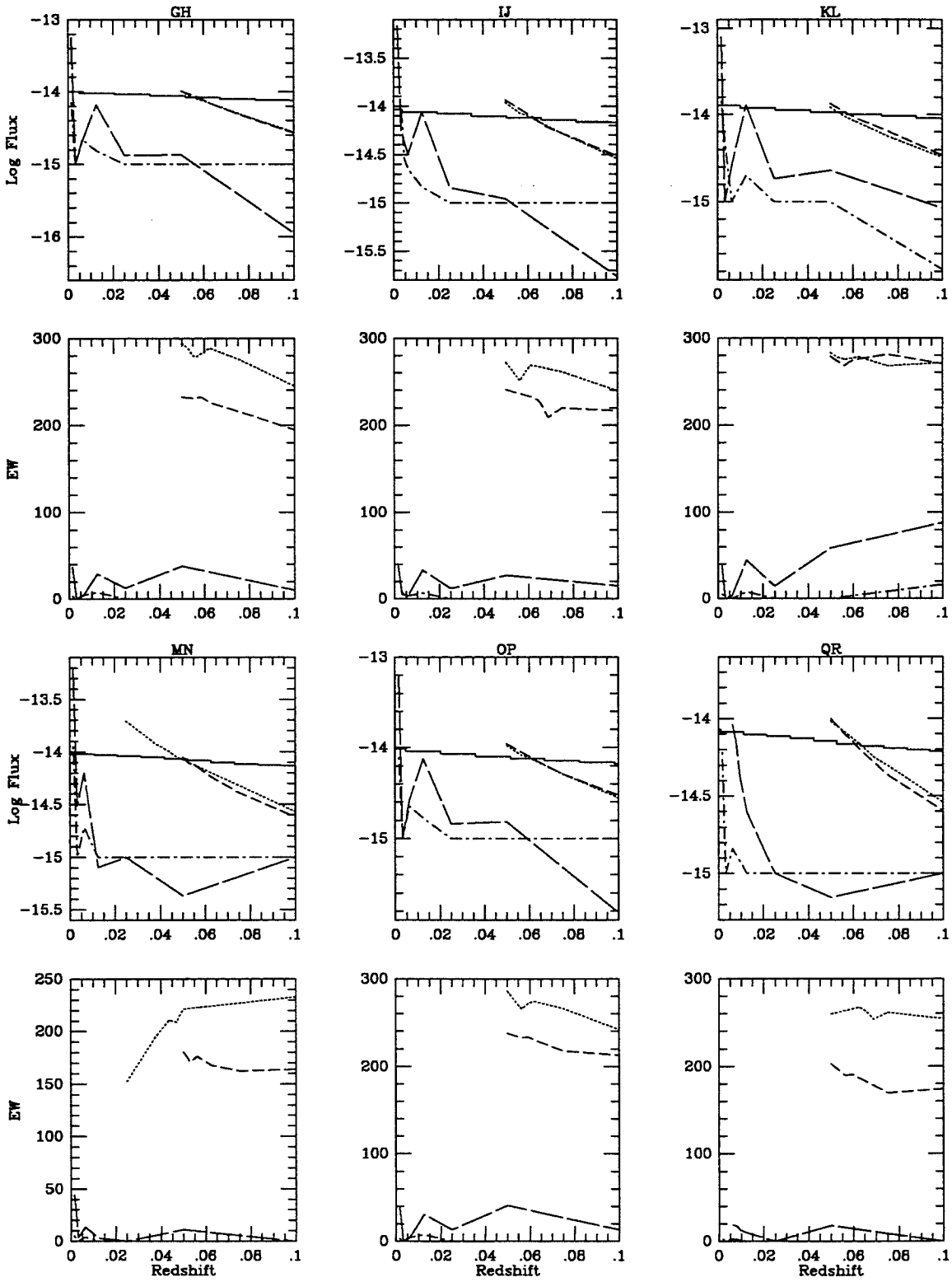

Figure B–25.a

NGC 3264 MAJ/MINB

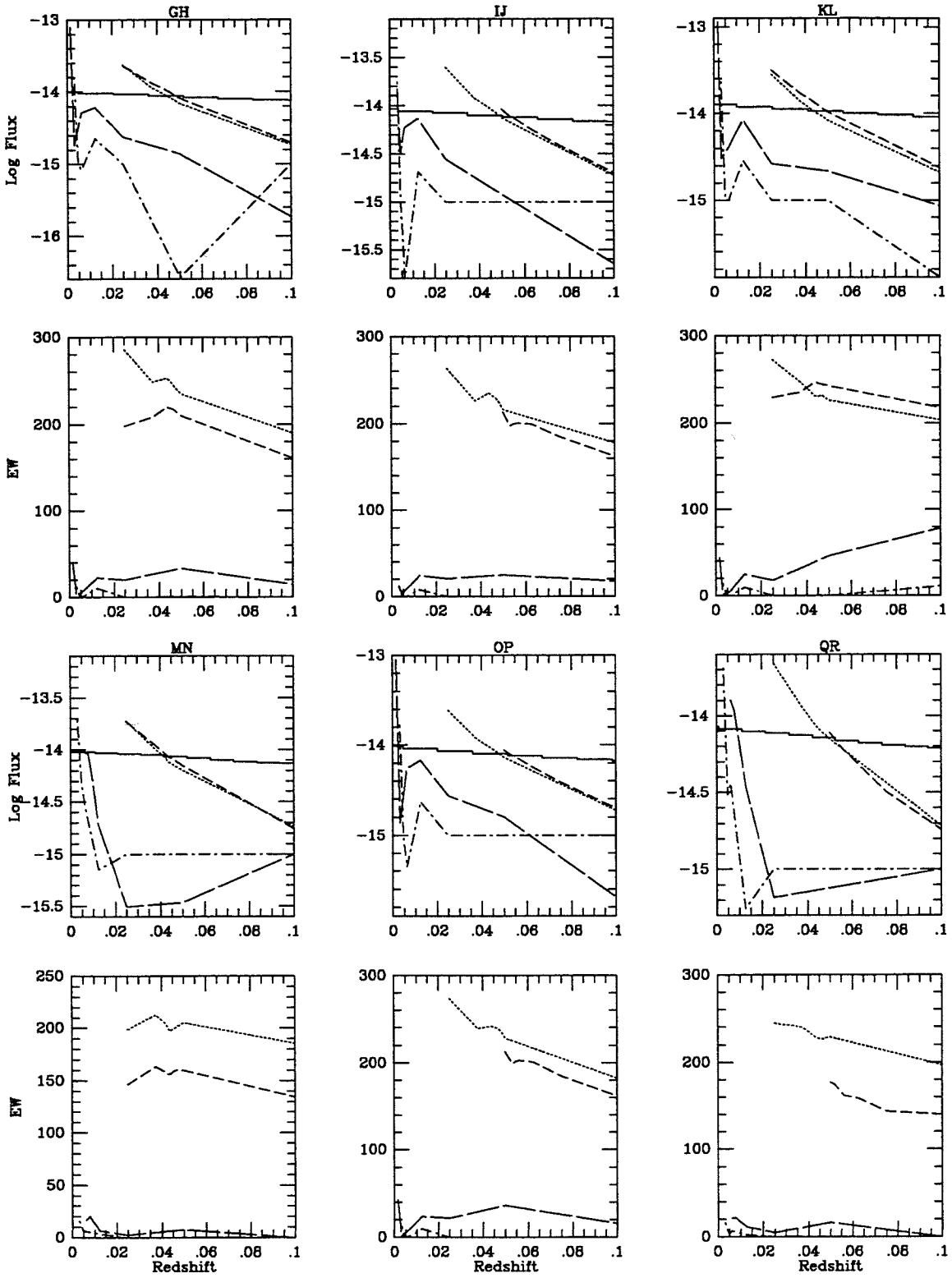

Figure B–25.b

1029+5439 MAJ/MIN

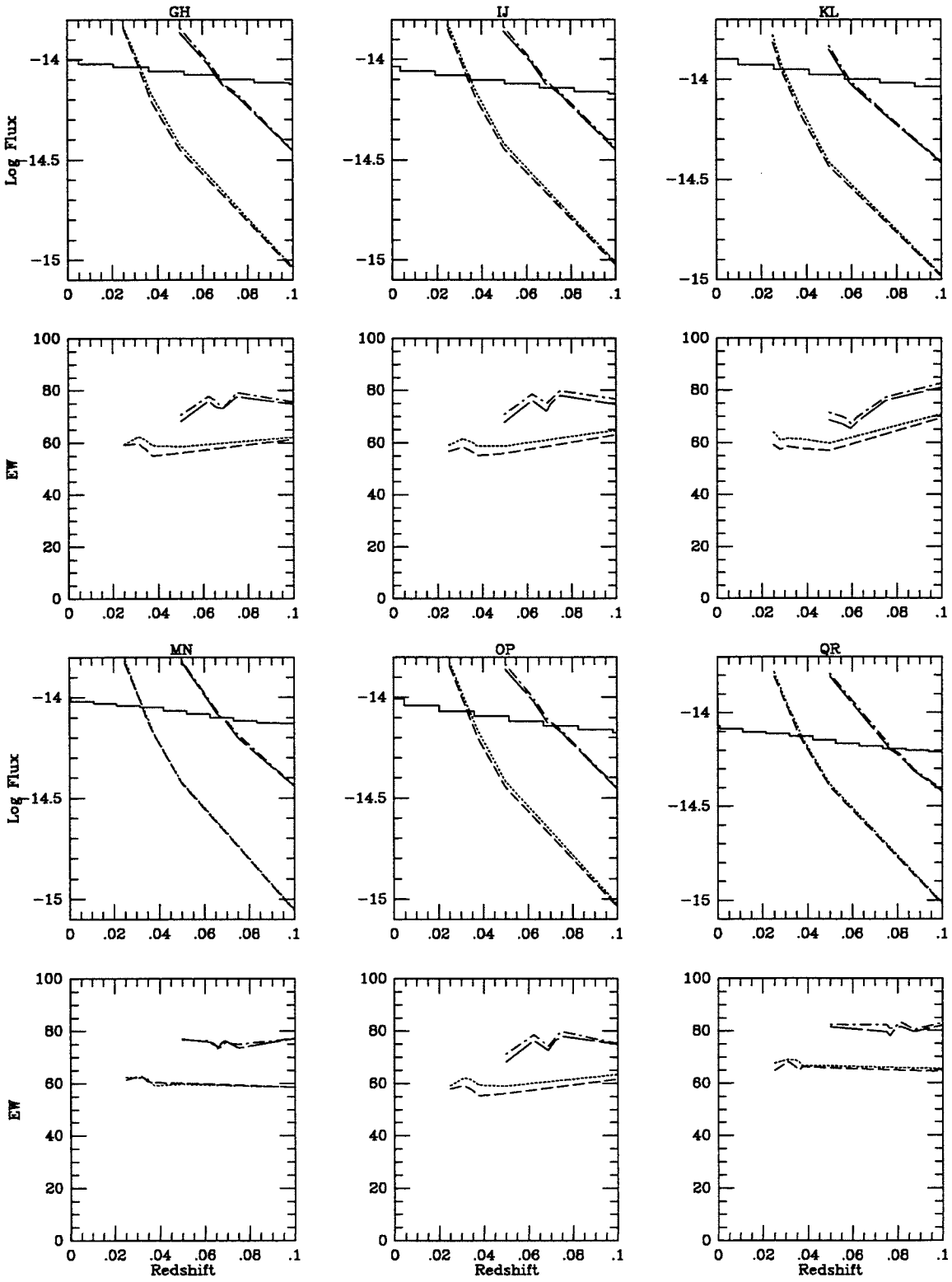

Figure B–26.

NGC 3310 MAJ/MIN

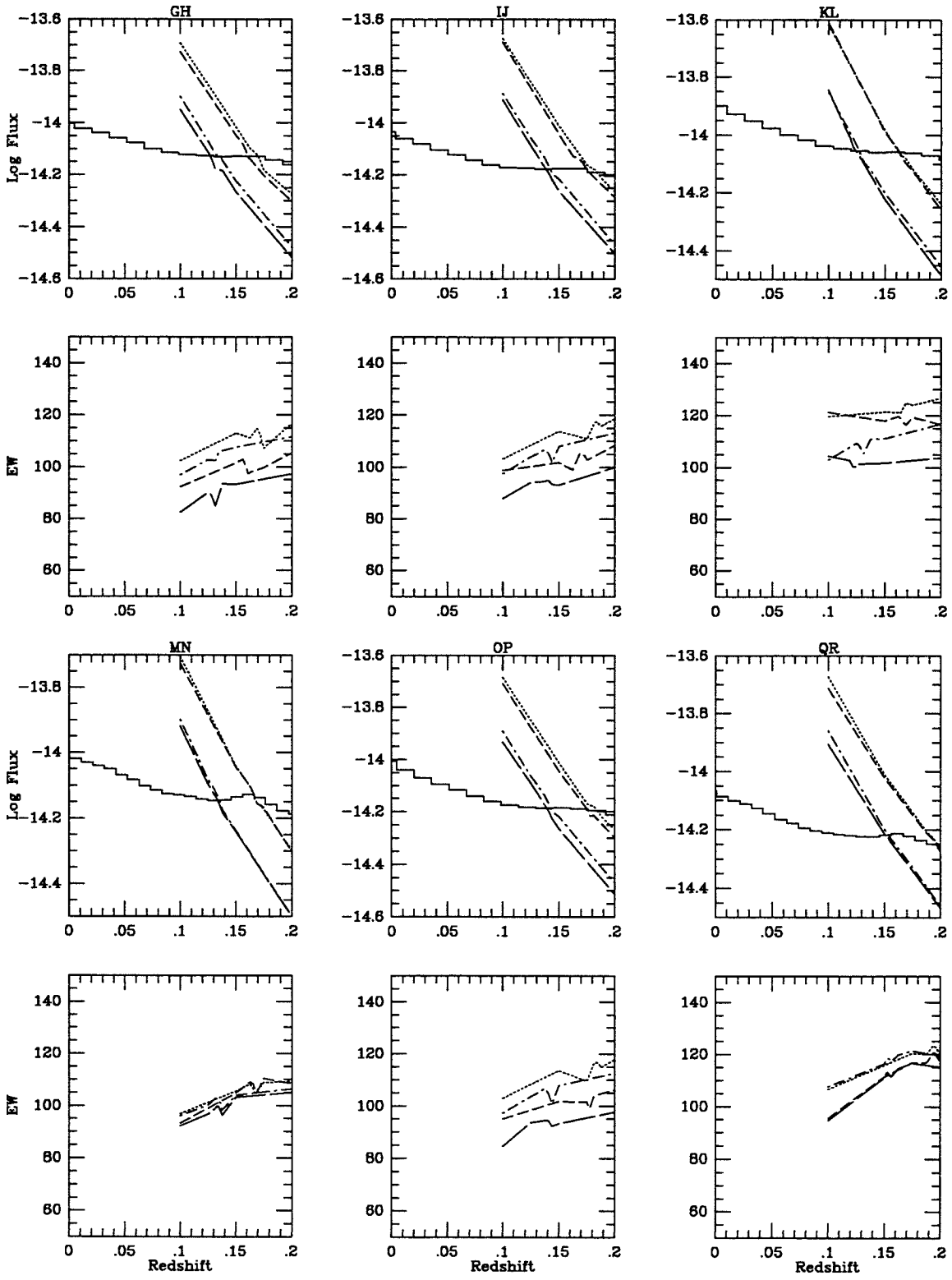

Figure B–27.

1036+4811 MAJ/MINA

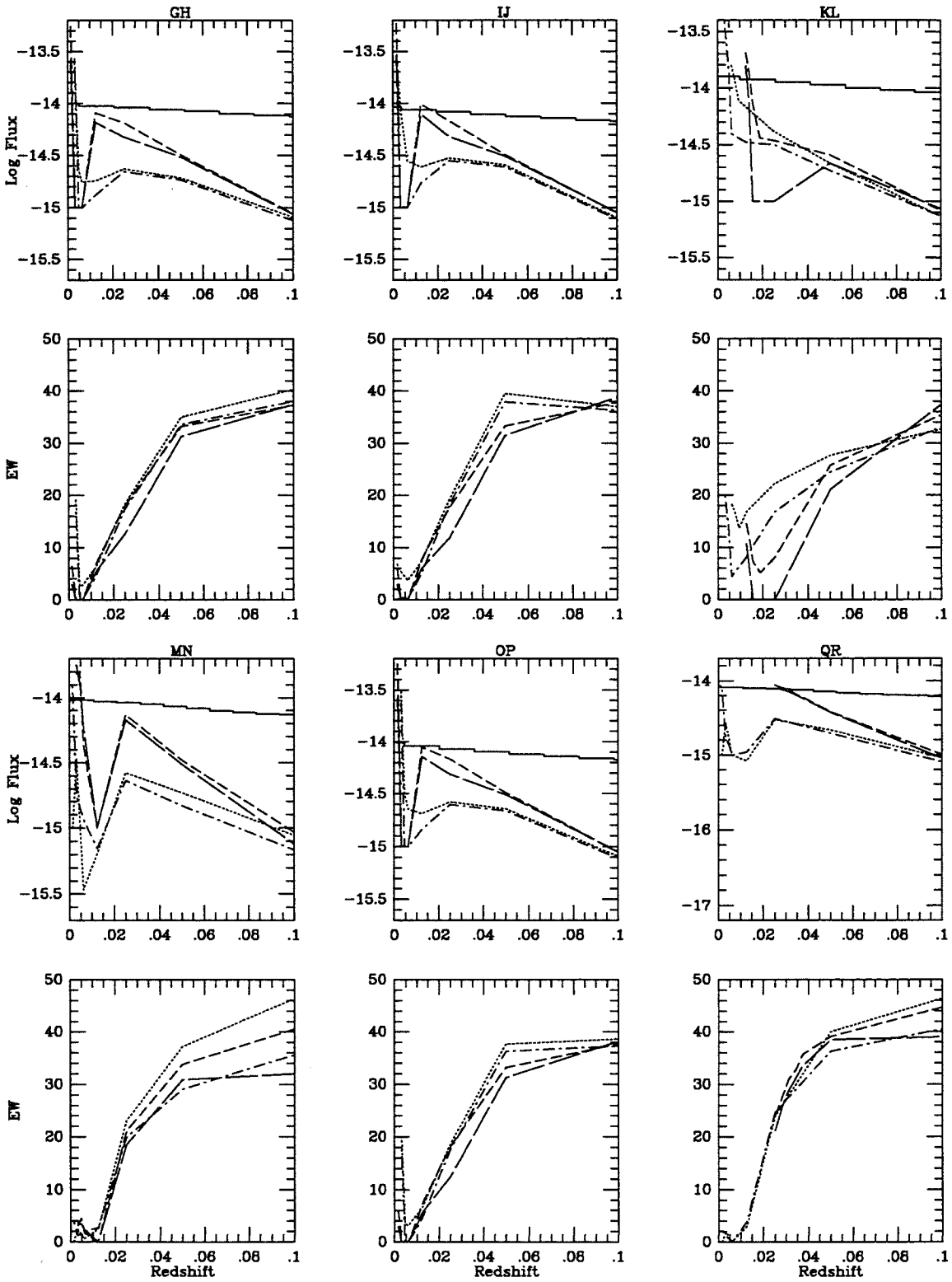

Figure B-28.a

1036+4811 MAJ/MINB

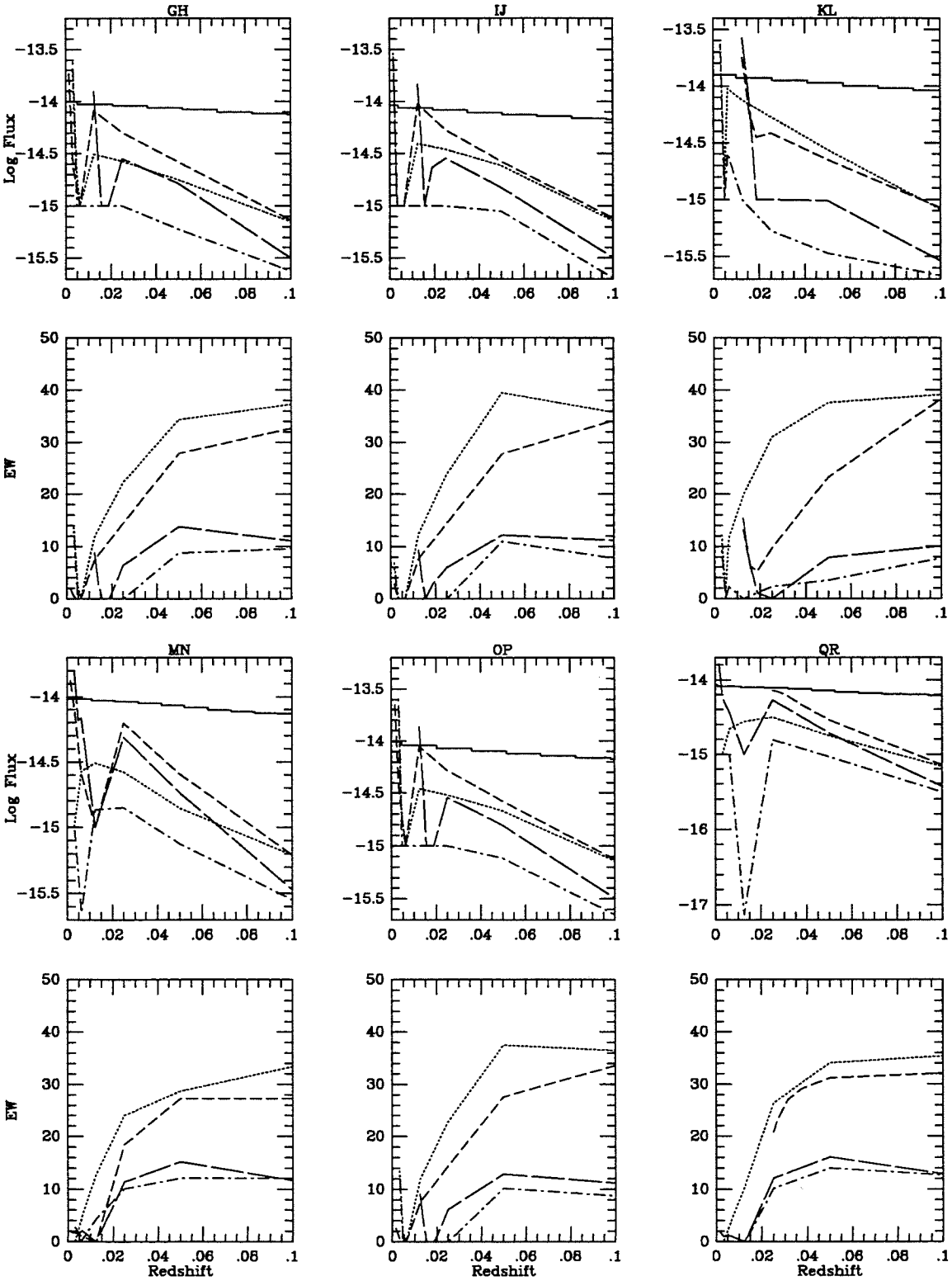

Figure B–28.b

NGC 3362 MAJ/MIN

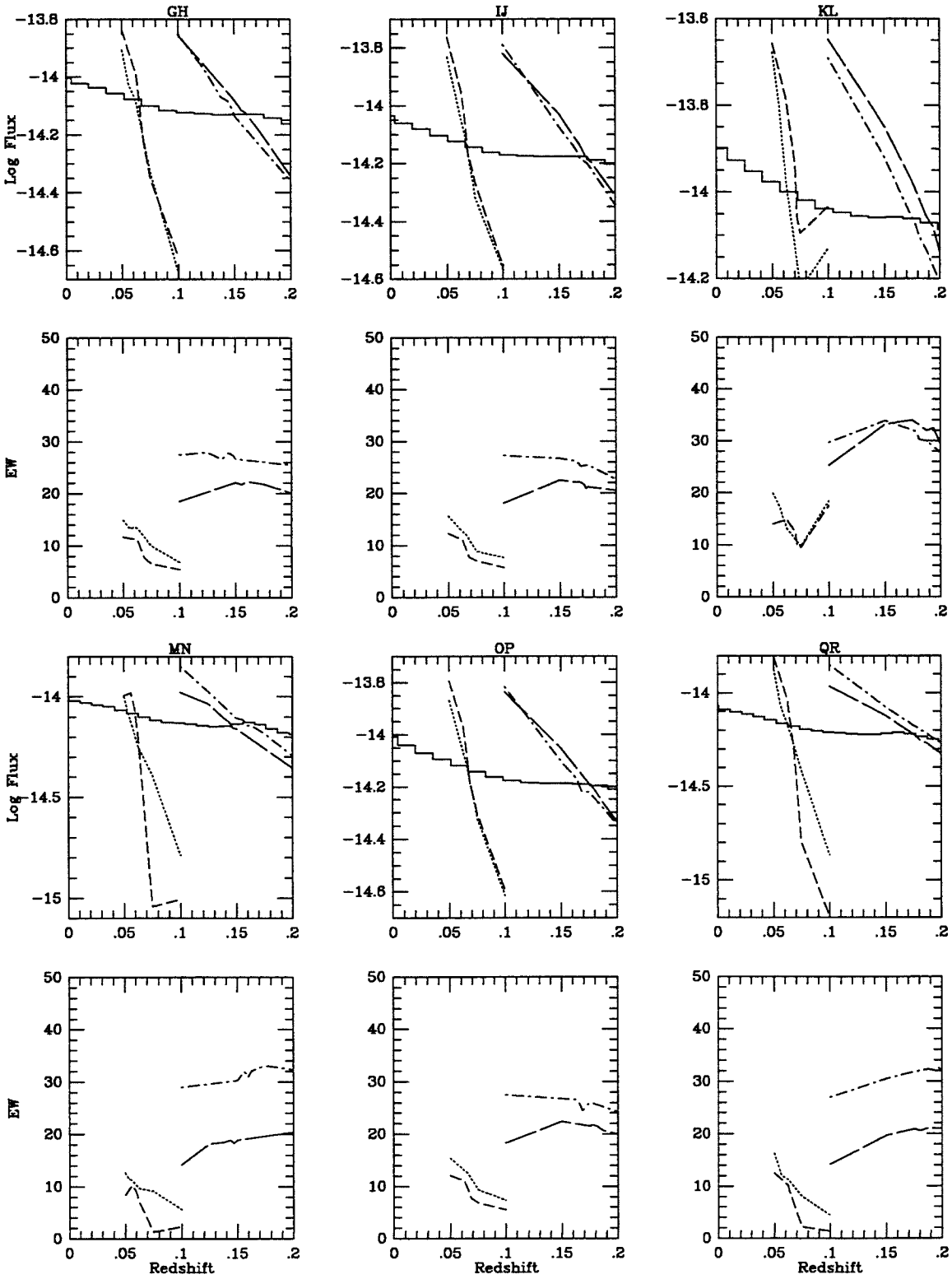

Figure B–29.

NGC 3353 MAJ/MIN

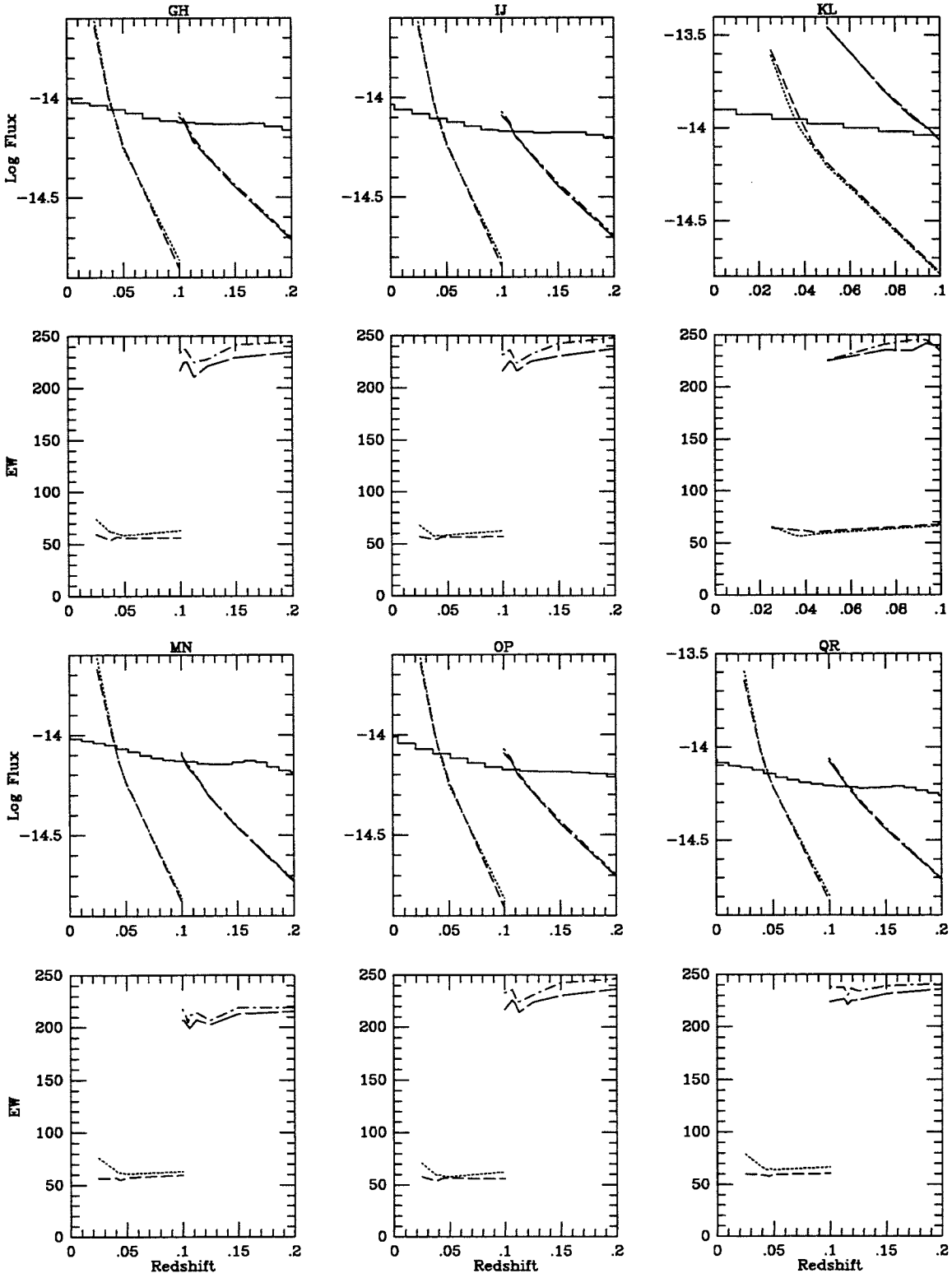

Figure B-30.

NGC 3395 MAJ/MIN

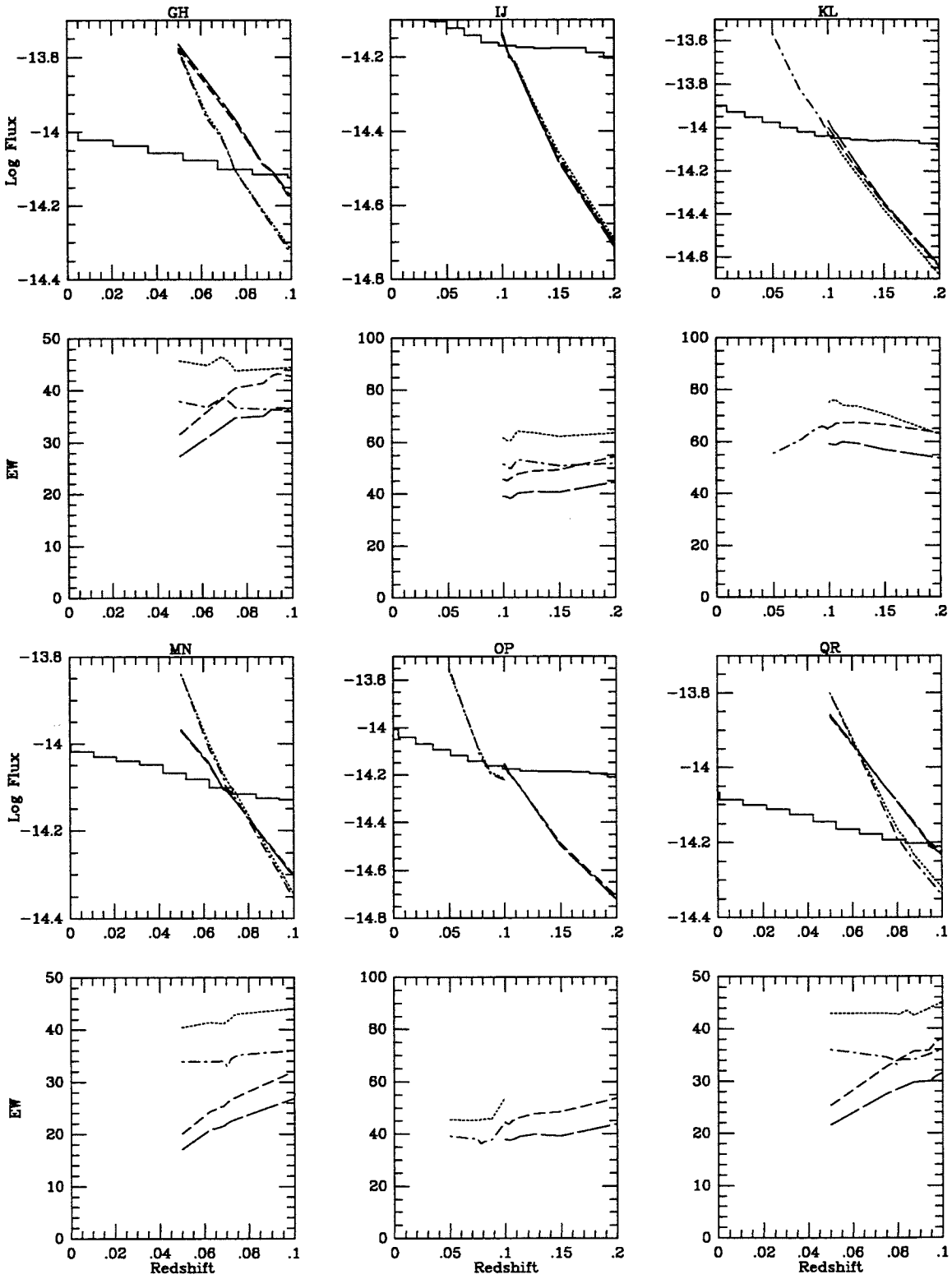

Figure B–31.

NGC 3432 MAJ/MIN

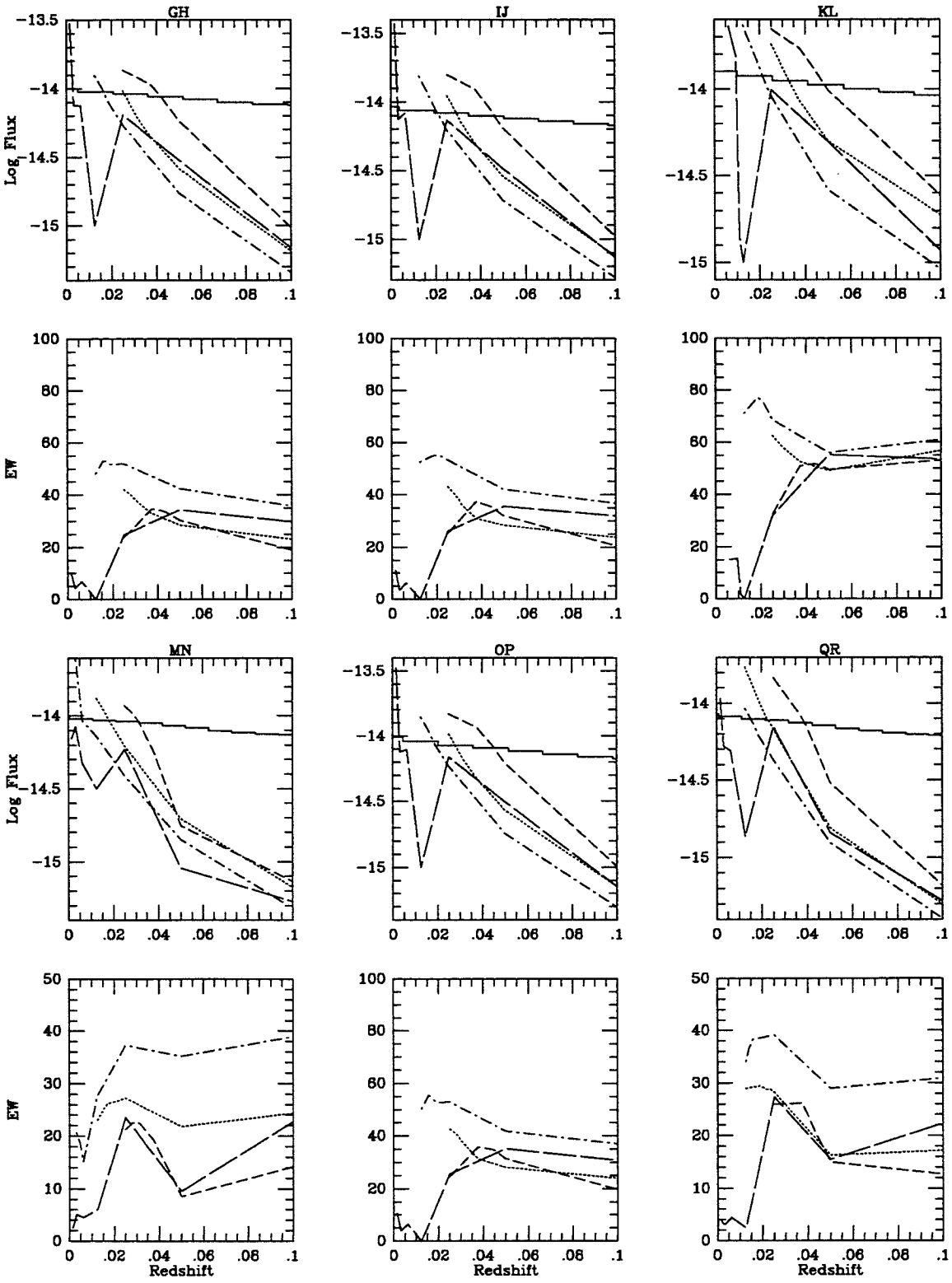

Figure B-32.

1049+2003 MAJ/MIN

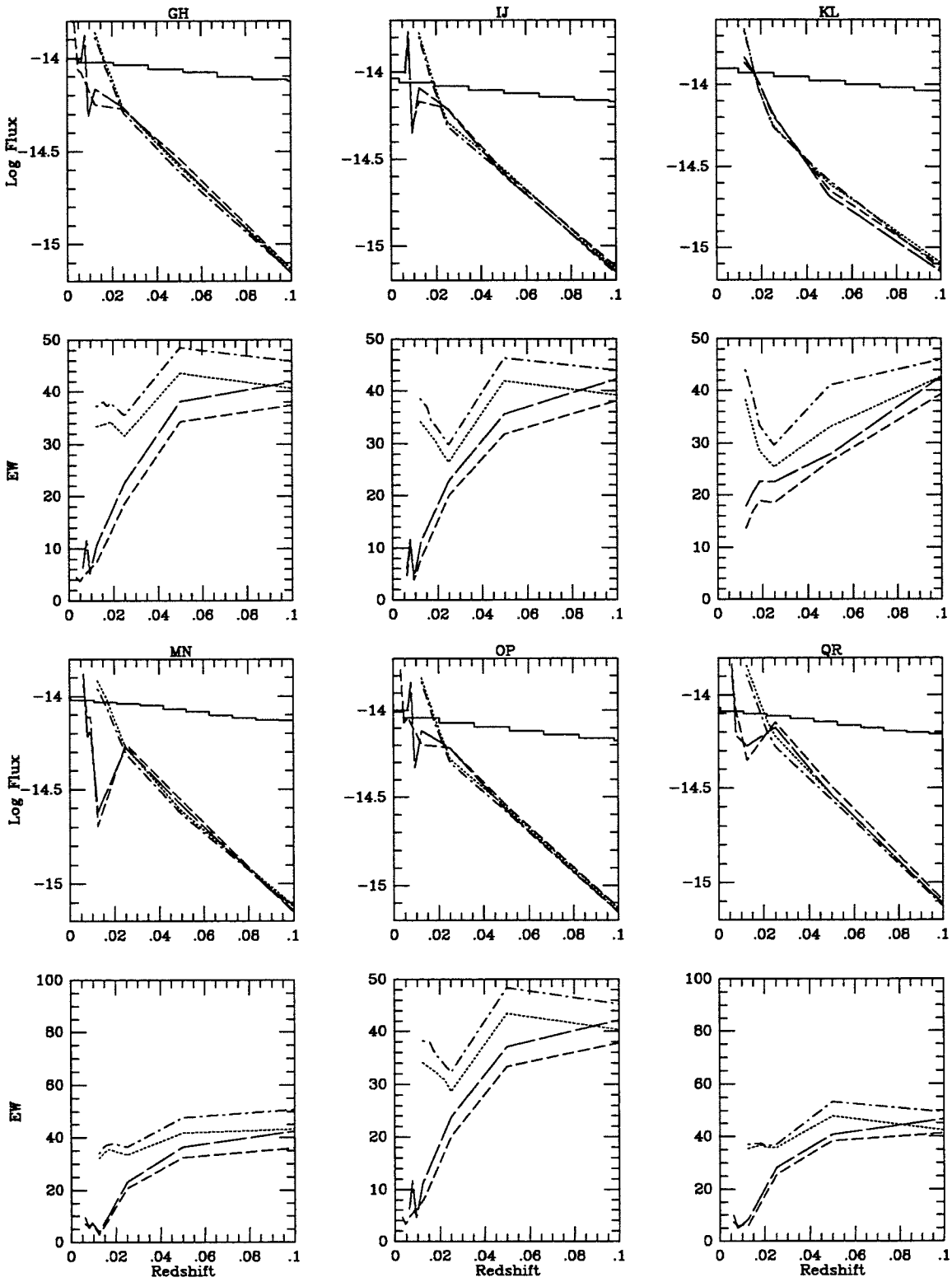

Figure B–33.

NGC 3448 MAJ/MIN

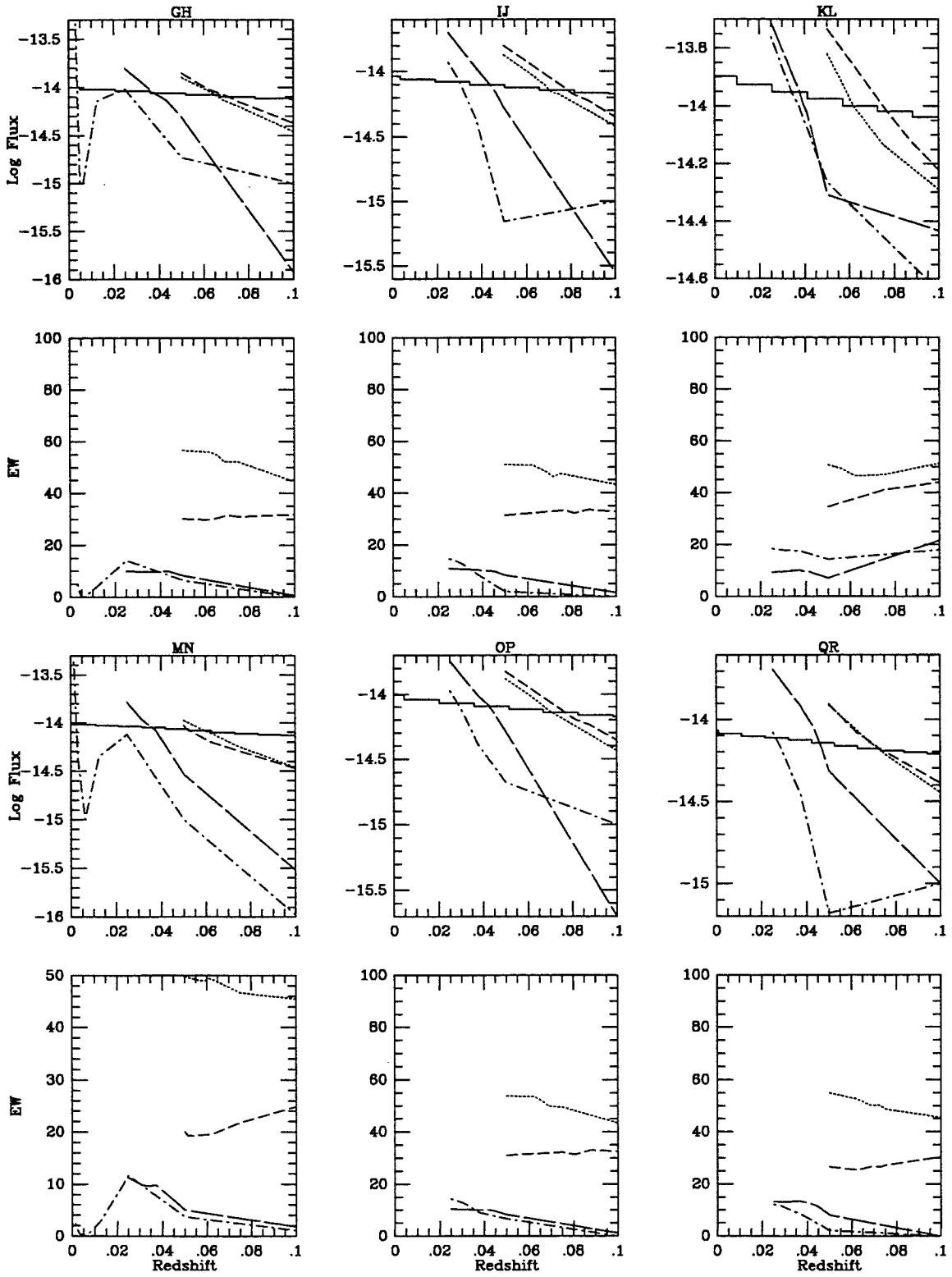

Figure B–34.

1052+4959 MAJA/MIN

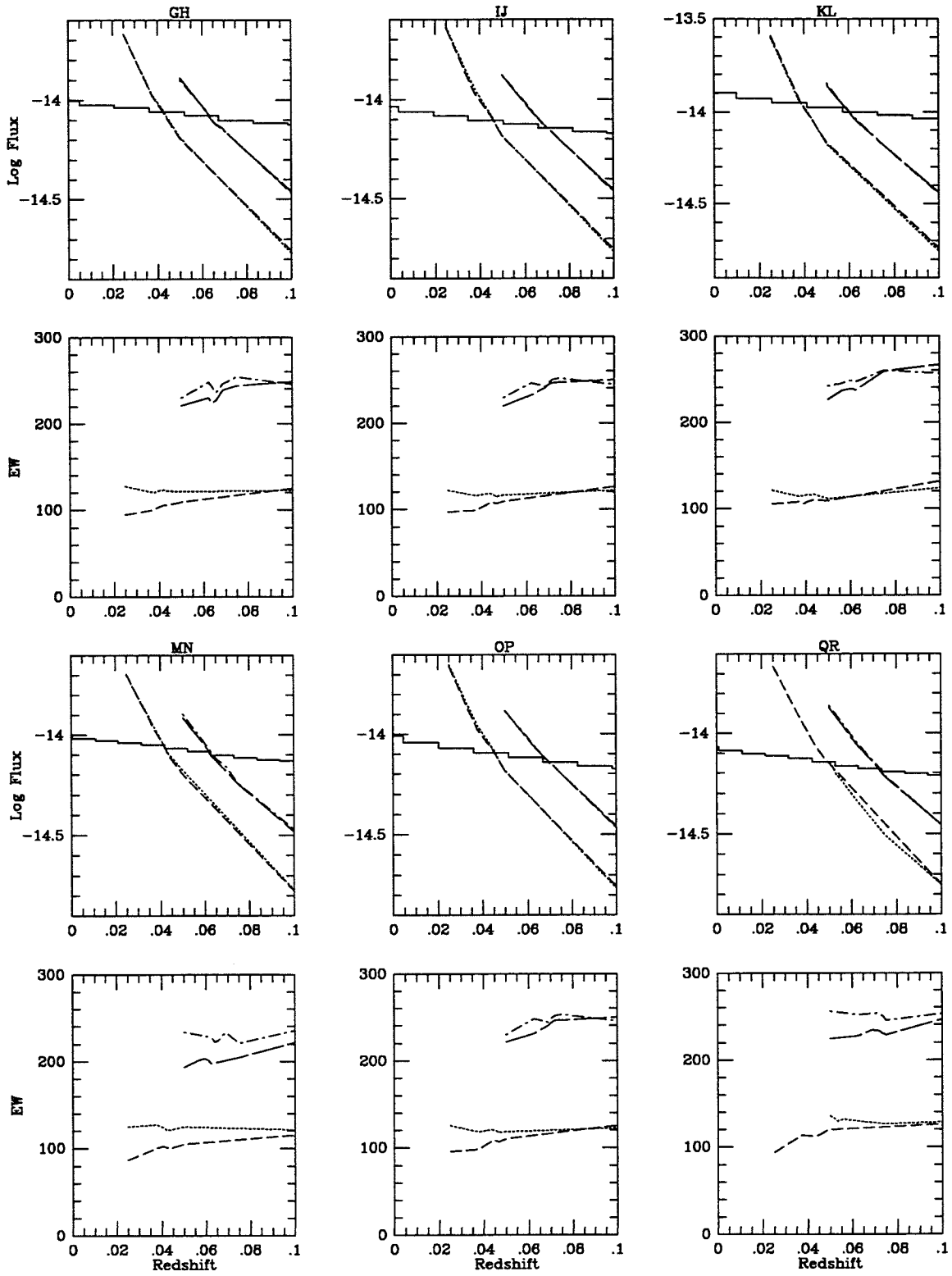

Figure B-35.a

1052+4959 MAJB/MIN

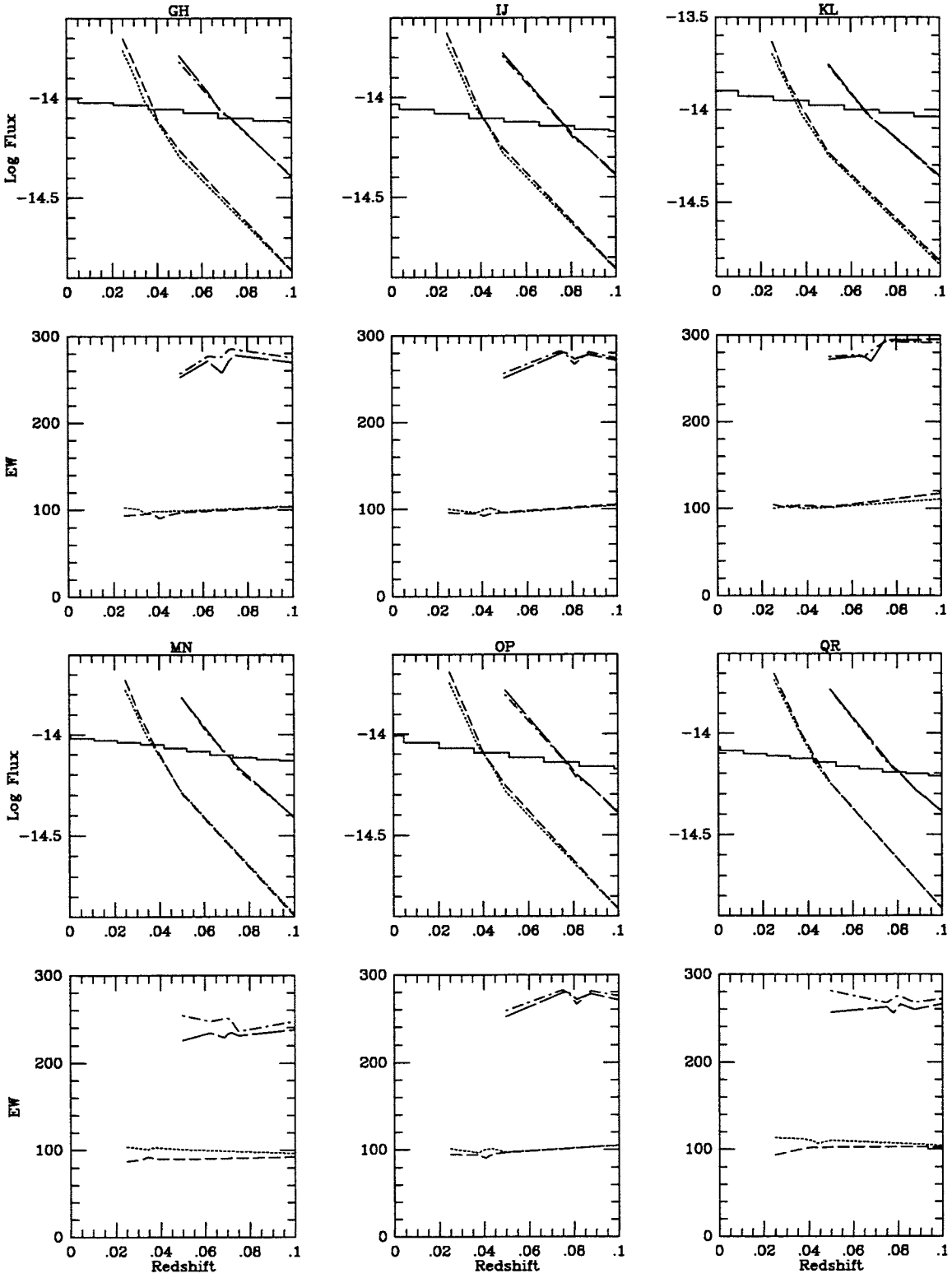

Figure B-35.b

1058+4555 MAJ/MIN

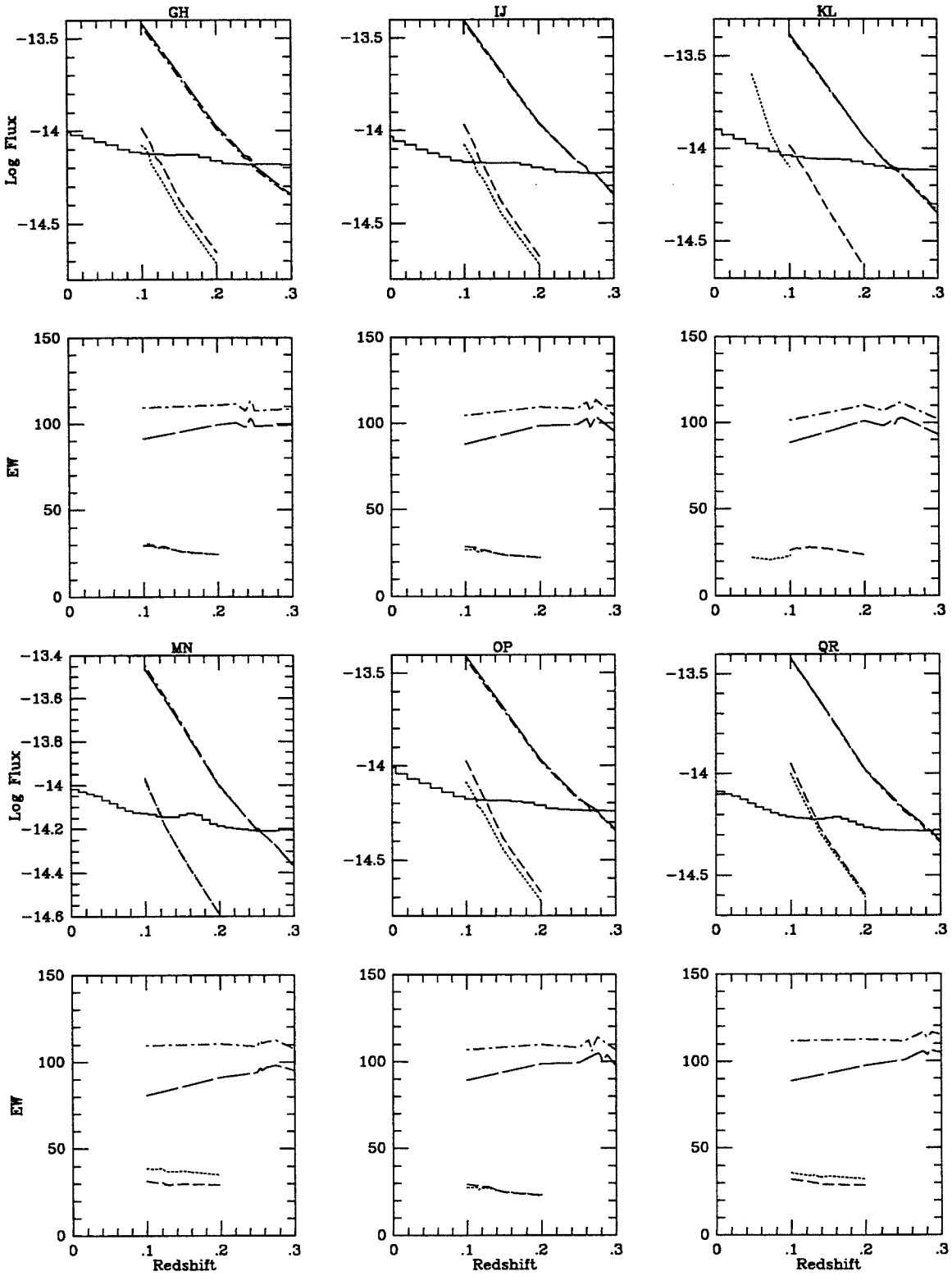

Figure B-36.

NGC 3516 MAJ/MIN

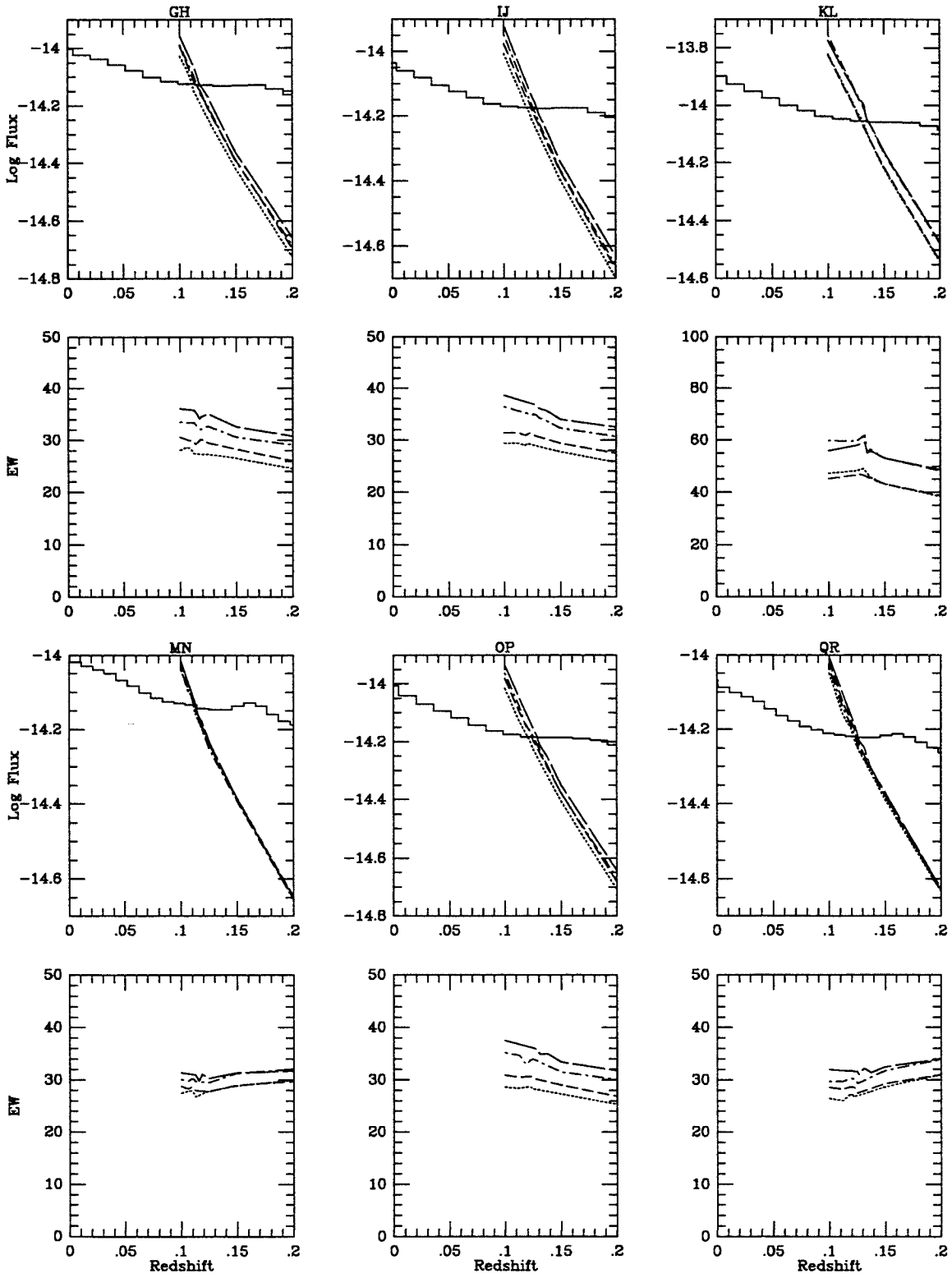

Figure B–37.

1104+4400 MAJ/MINA

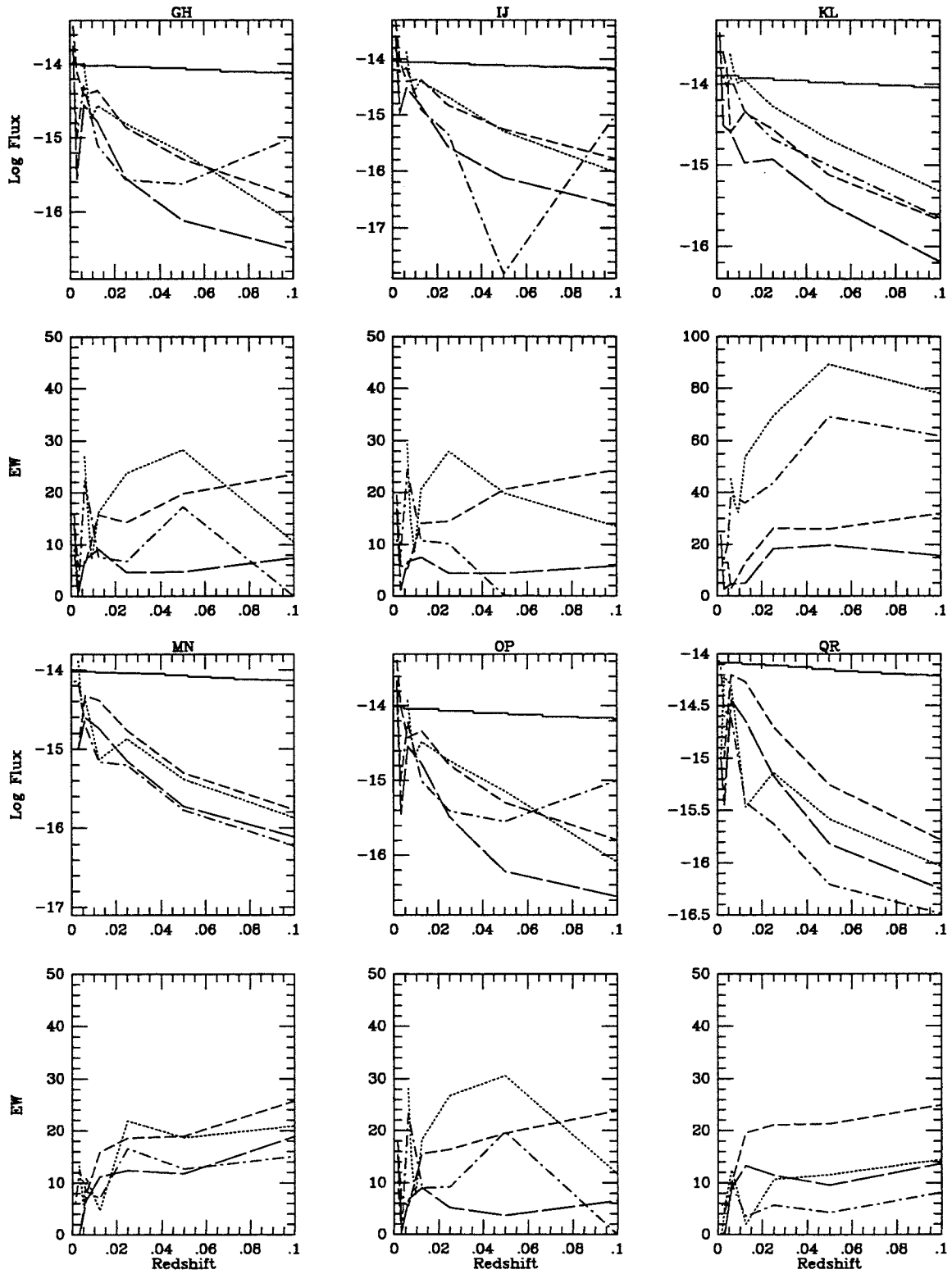

Figure B-38.a

1104+4400 MAJ/MINB

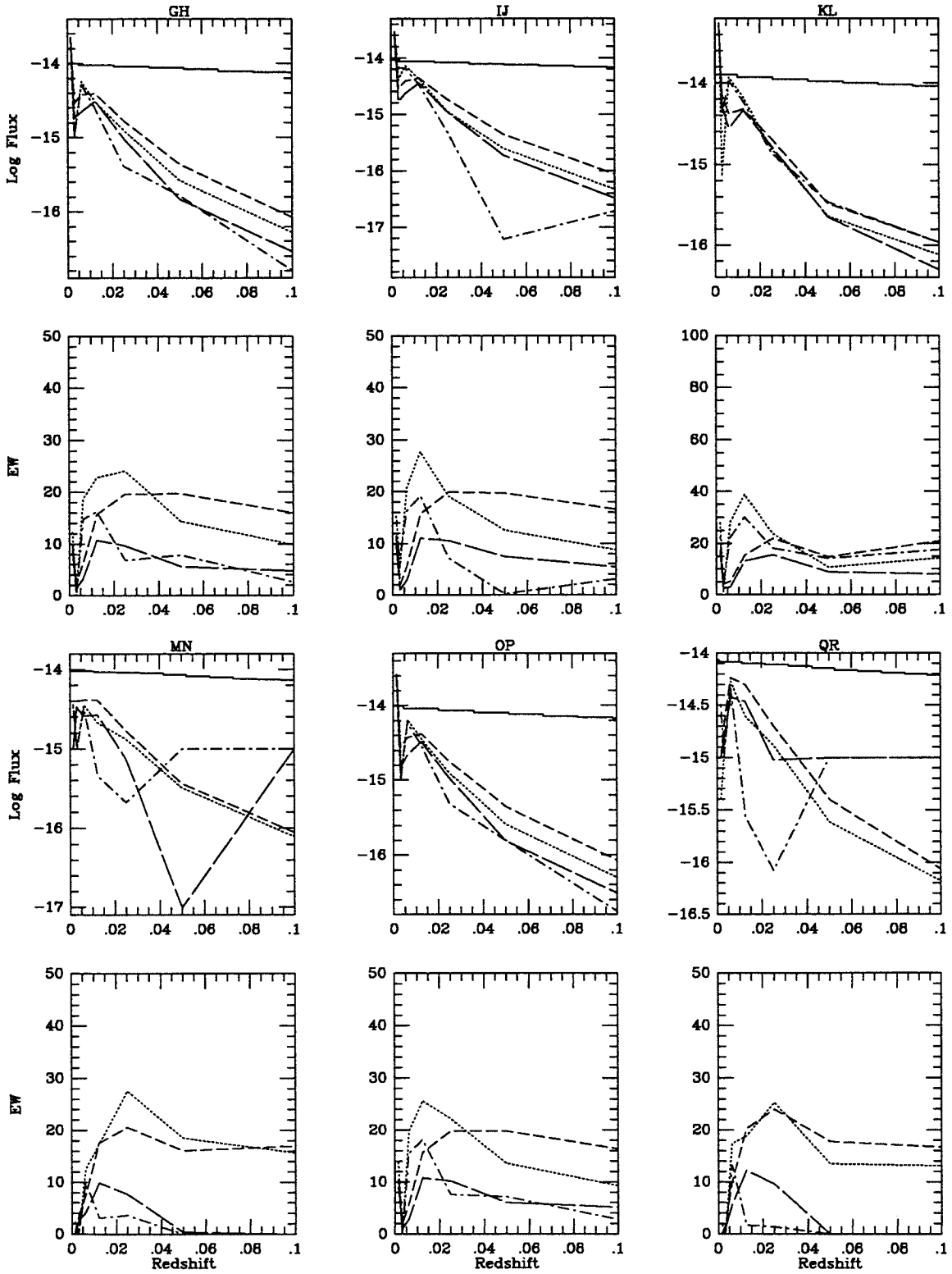

Figure B-38.b

IC 691 MAJ/MIN

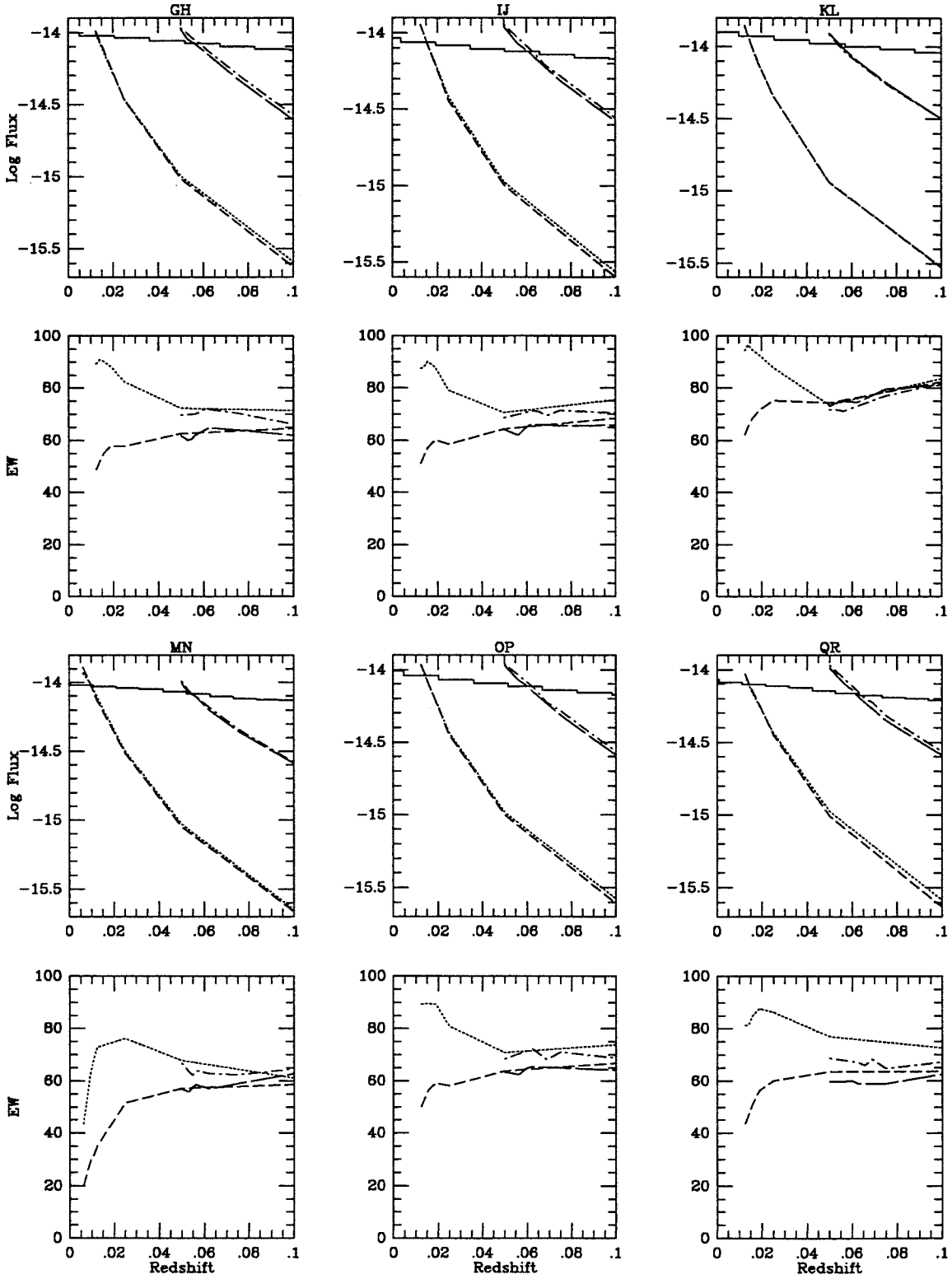

Figure B–39.

IC 694 MAJ/MIN

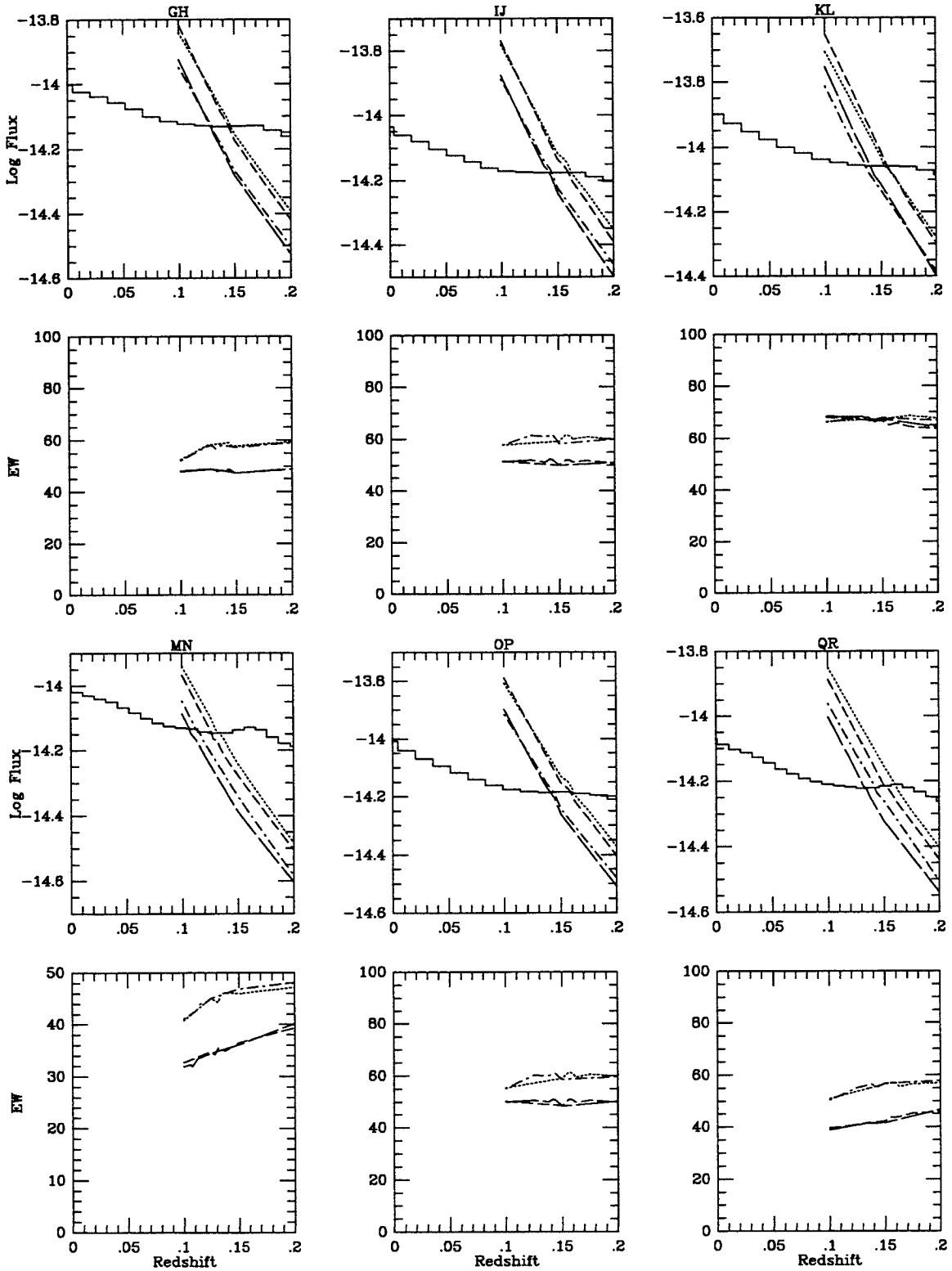

Figure B–40.

NGC 3741 MAJA/MINA

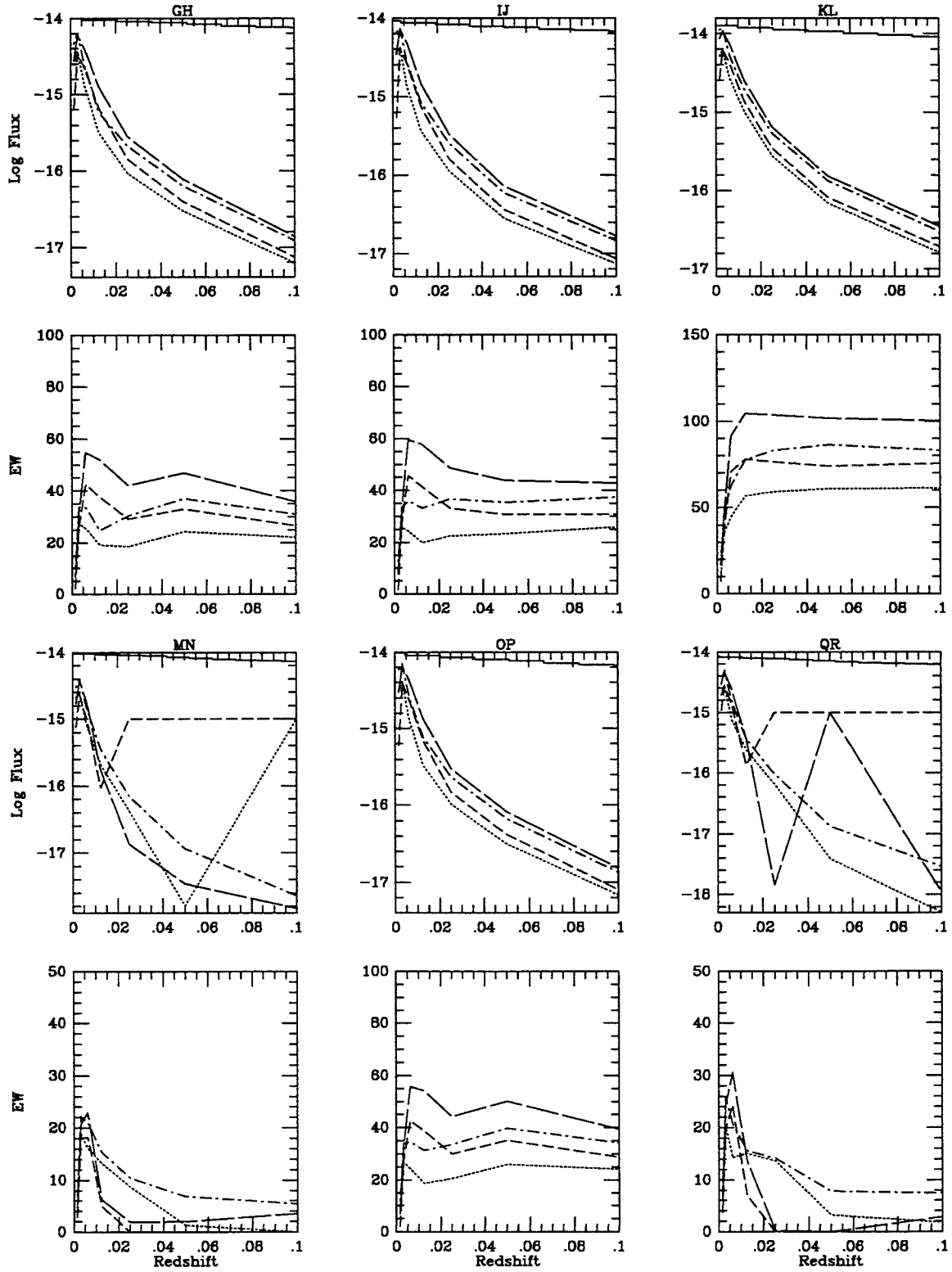

Figure B–41.aa

NGC 3741 MAJA/MINB

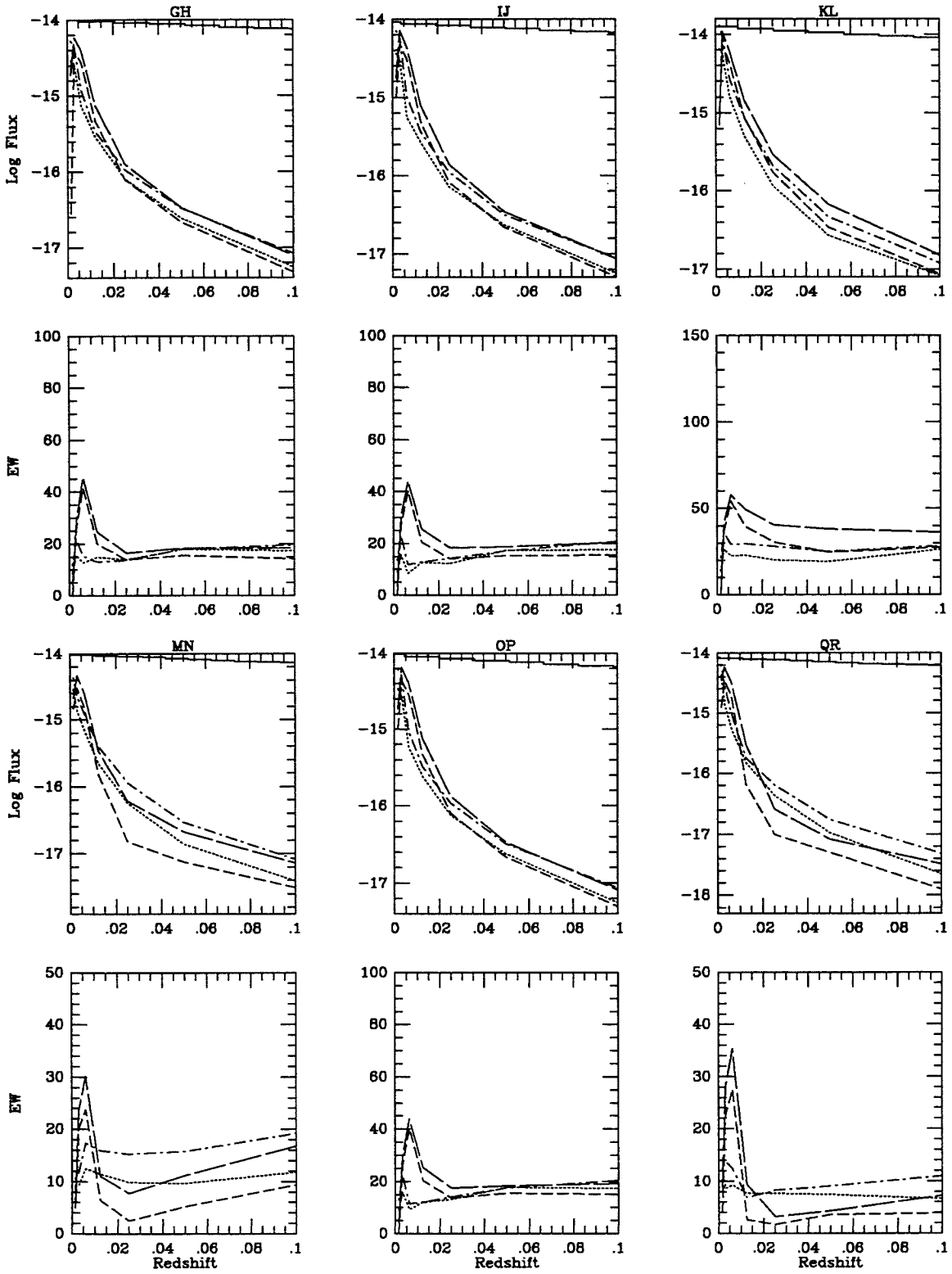

Figure B–41.ab

NGC 3741 MAJB/MINA

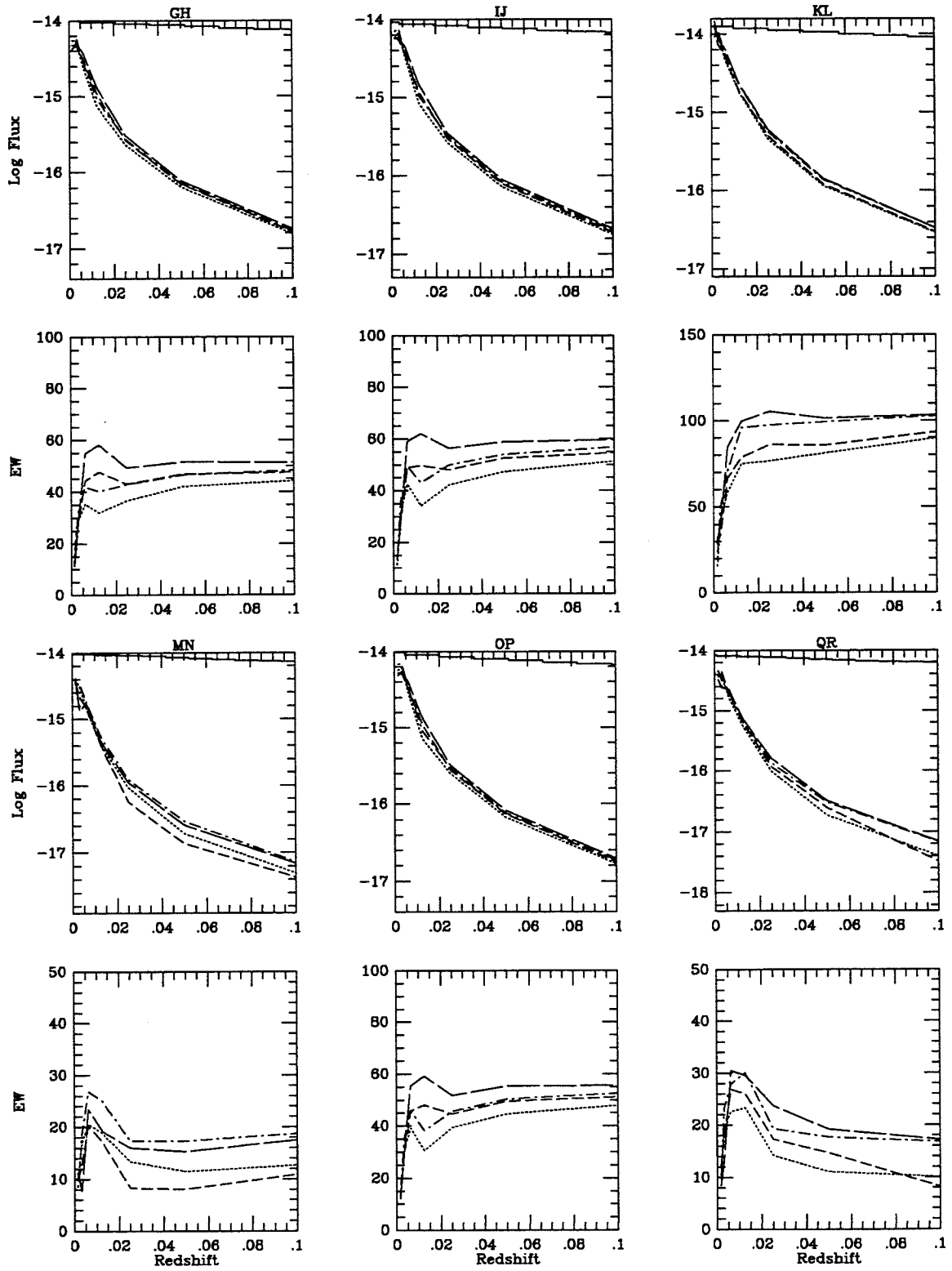

Figure B–41.ba

NGC 3741 MAJB/MINB

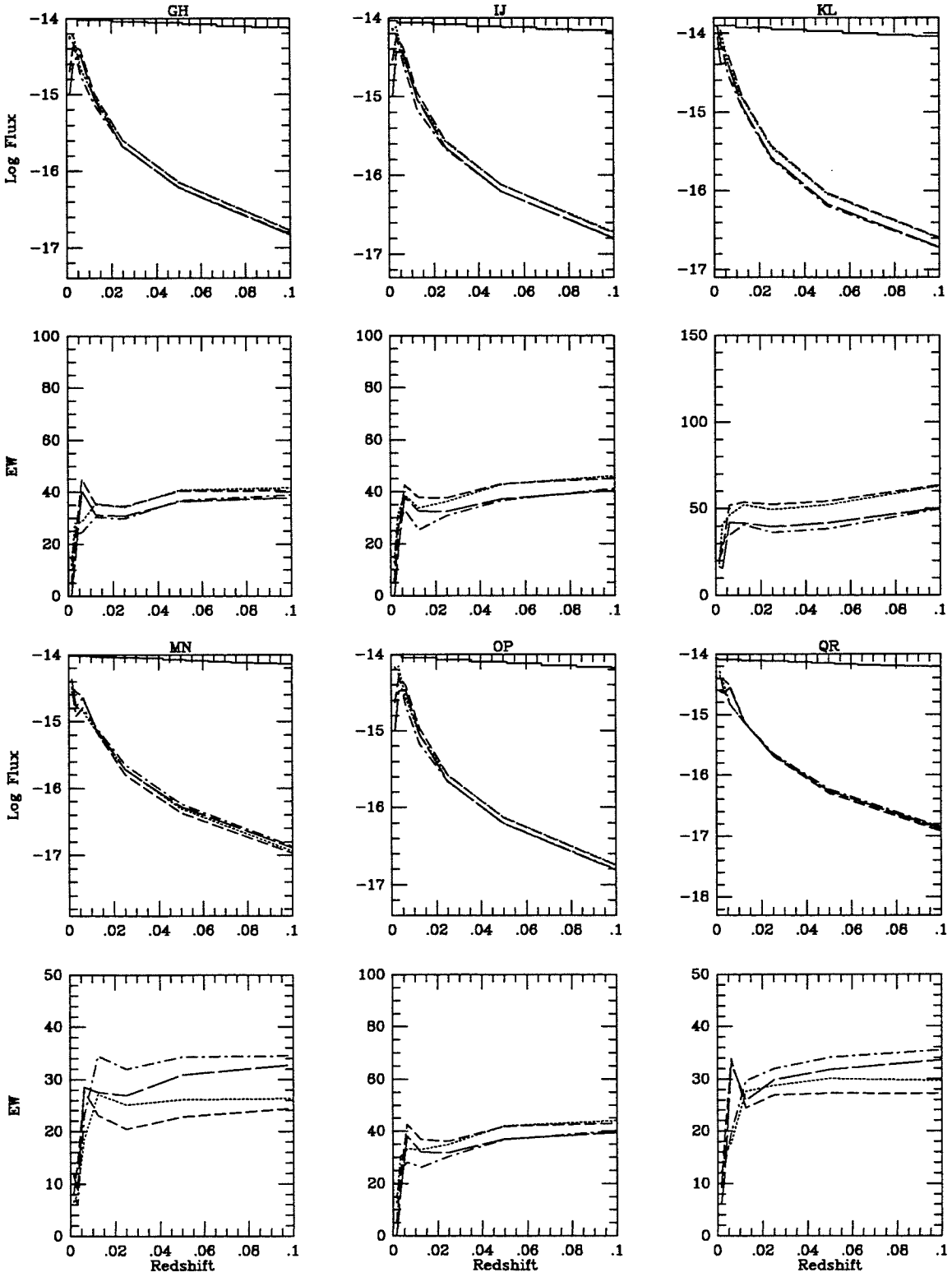

Figure B–41.bb

NGC 3769 MAJ/MIN

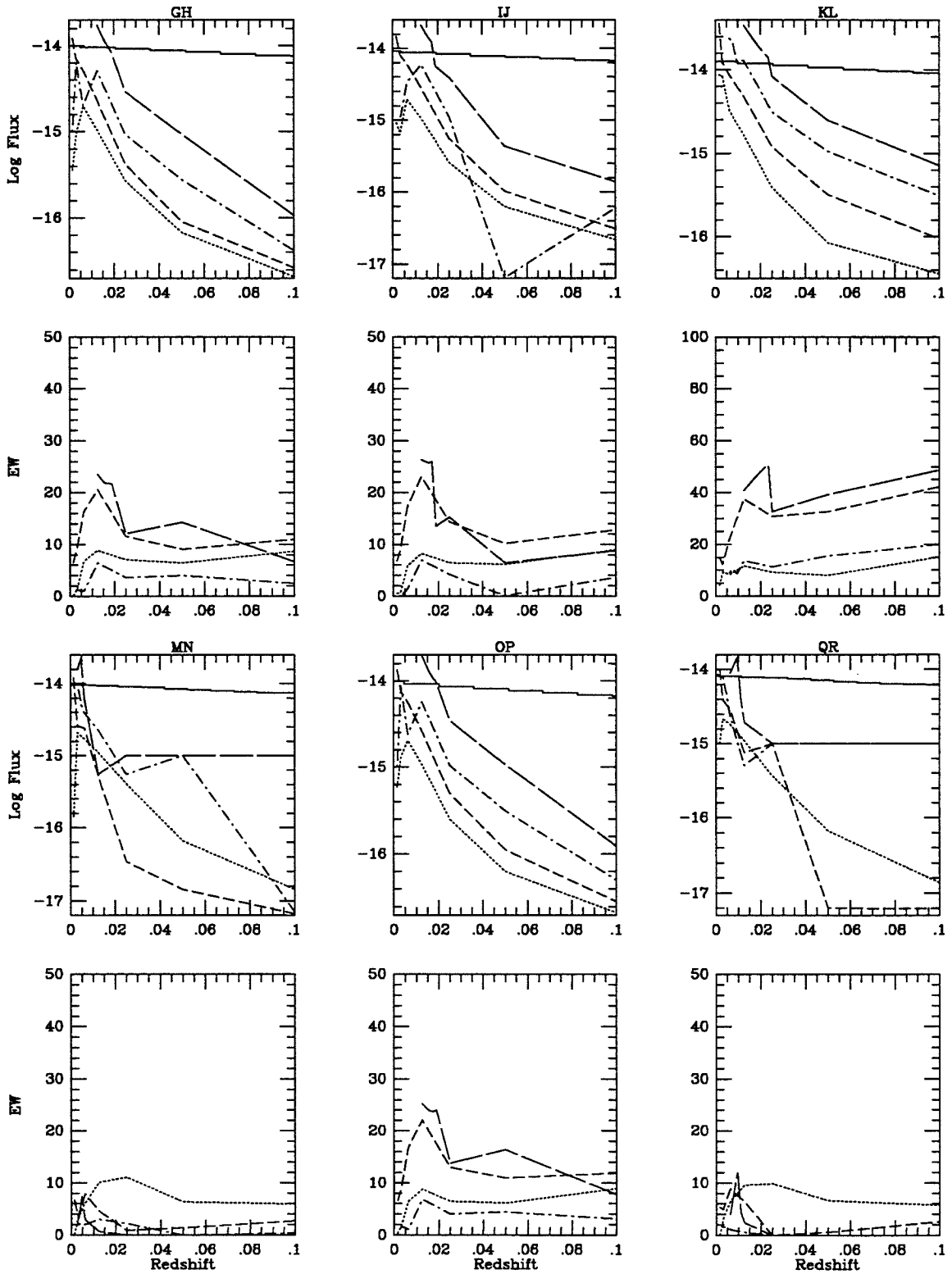

Figure B–42.

NGC 3786 MAJ/MIN

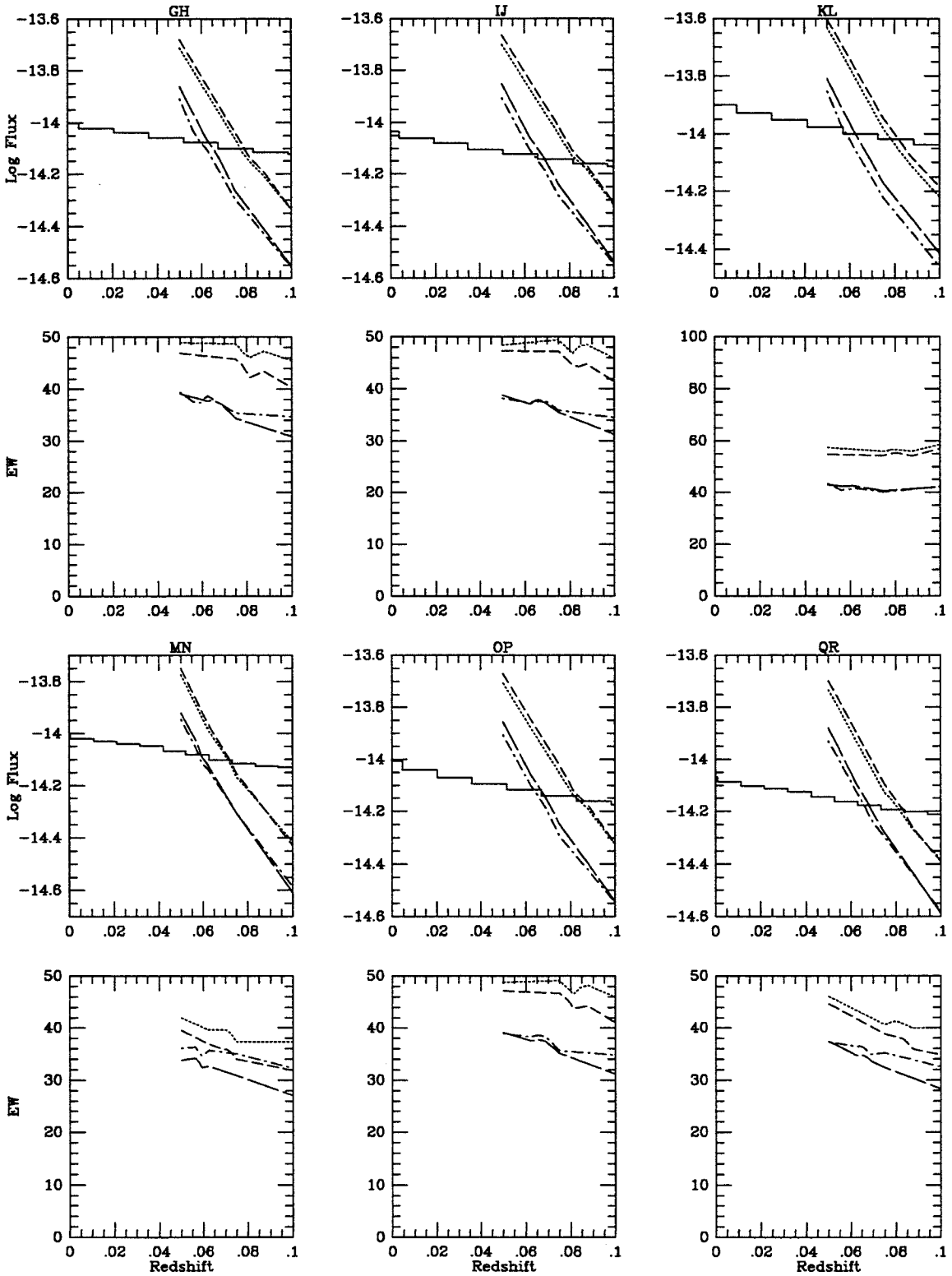

Figure B–43.

NGC 3879 MAJ/MINA

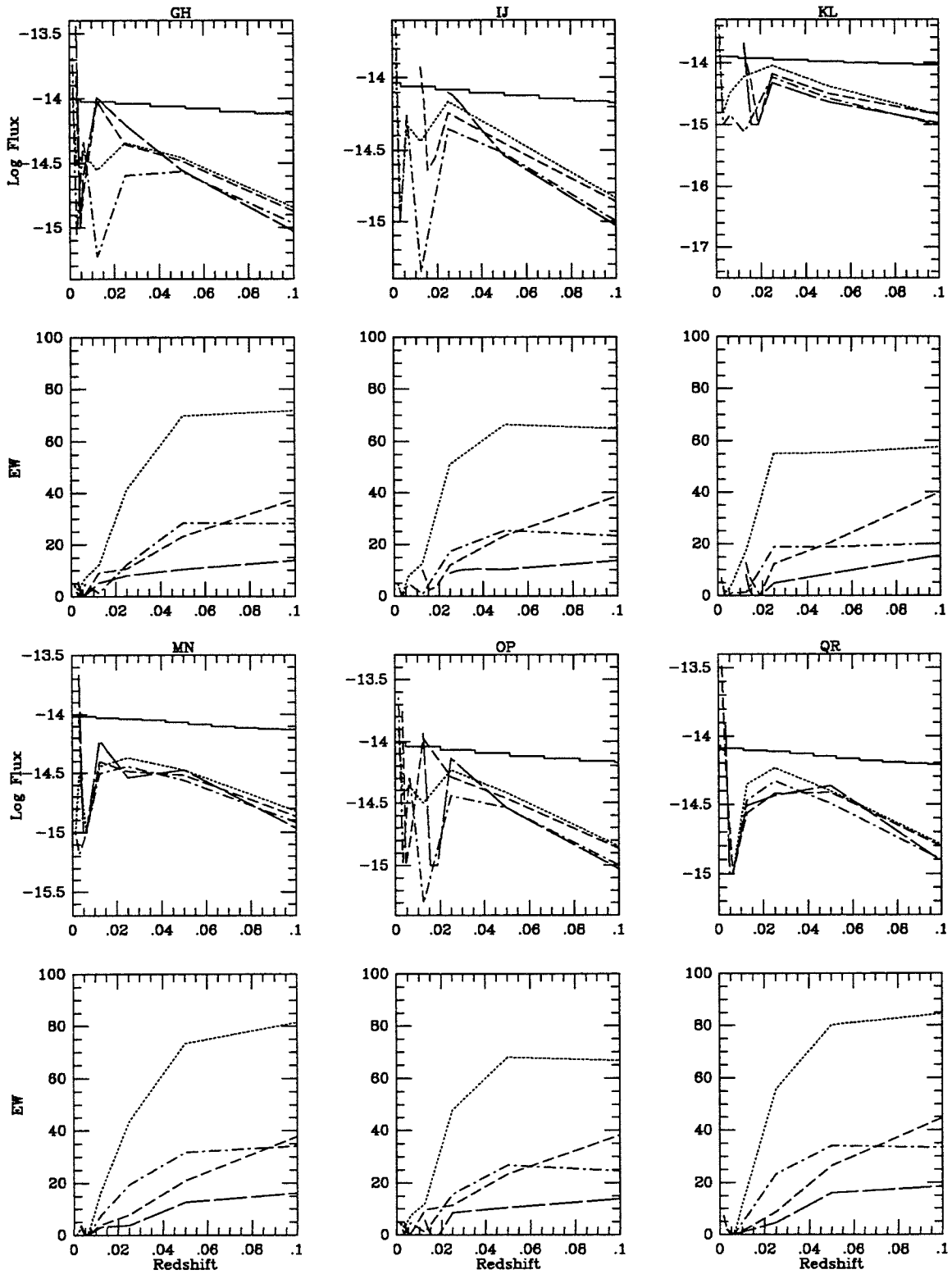

Figure B-44.a

NGC 3879 MAJ/MINB

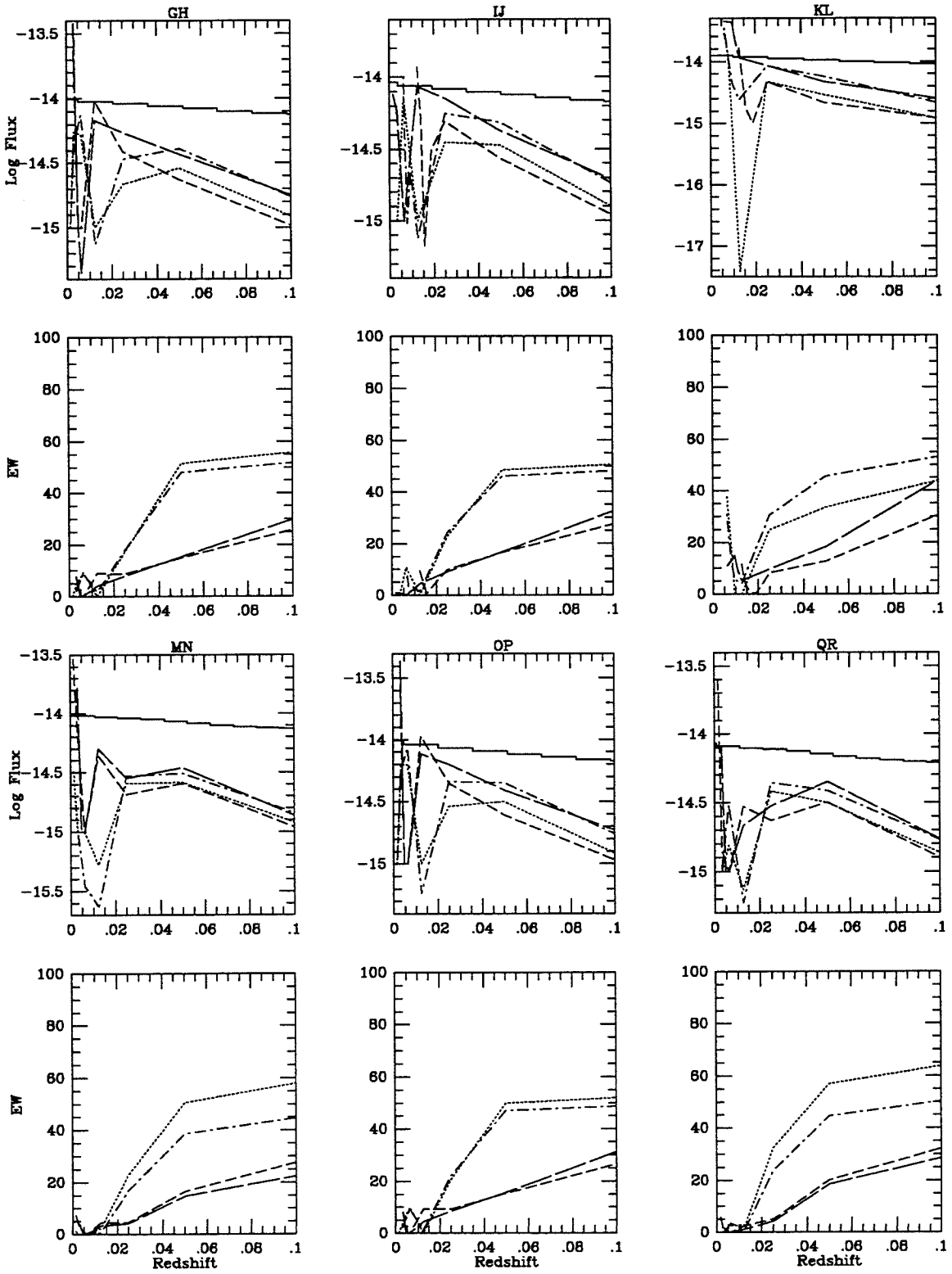

Figure B-44.b

NGC 3982 MAJ/MIN

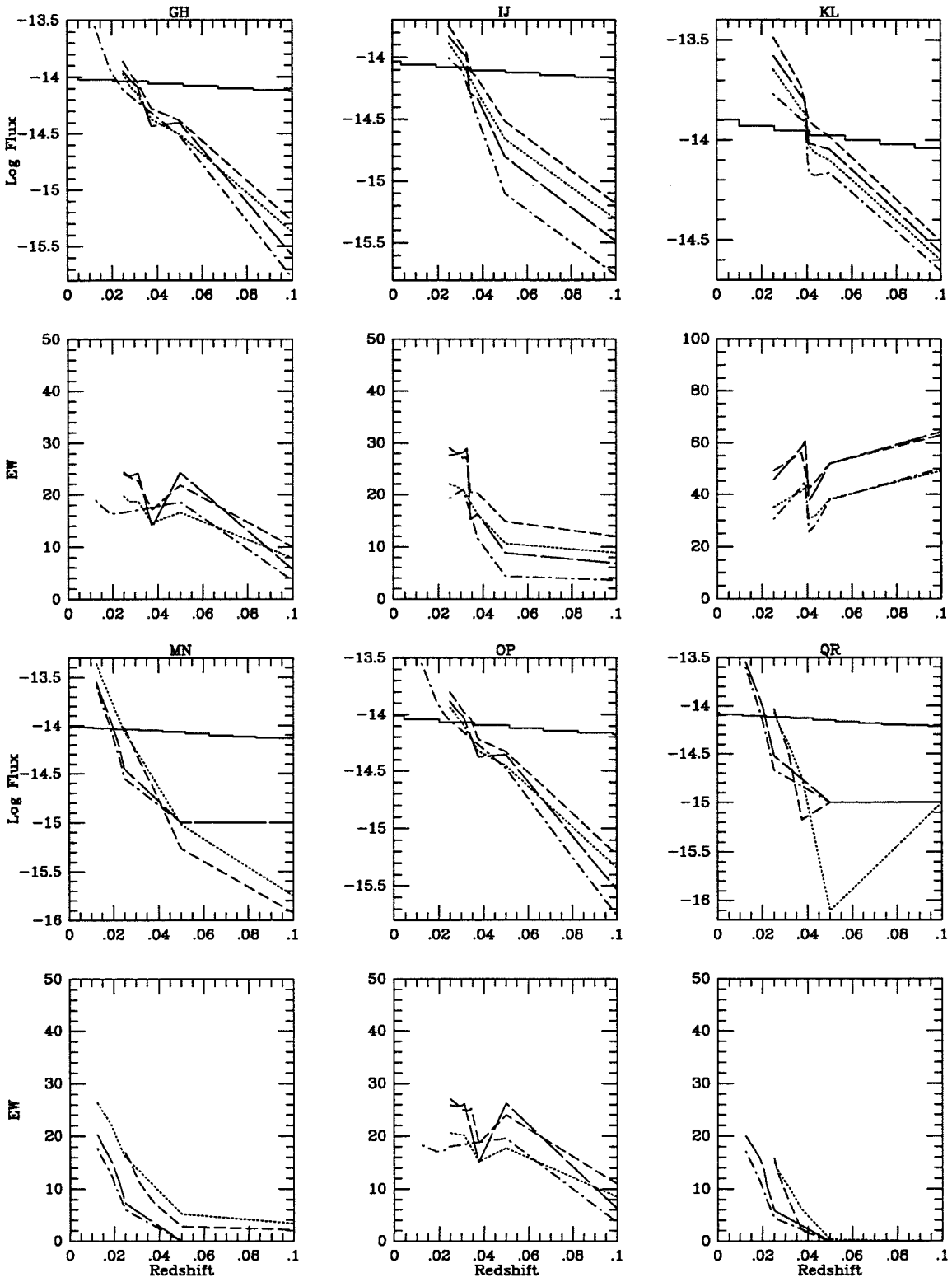

Figure B–45.

1154+5327 MAJ/MIN

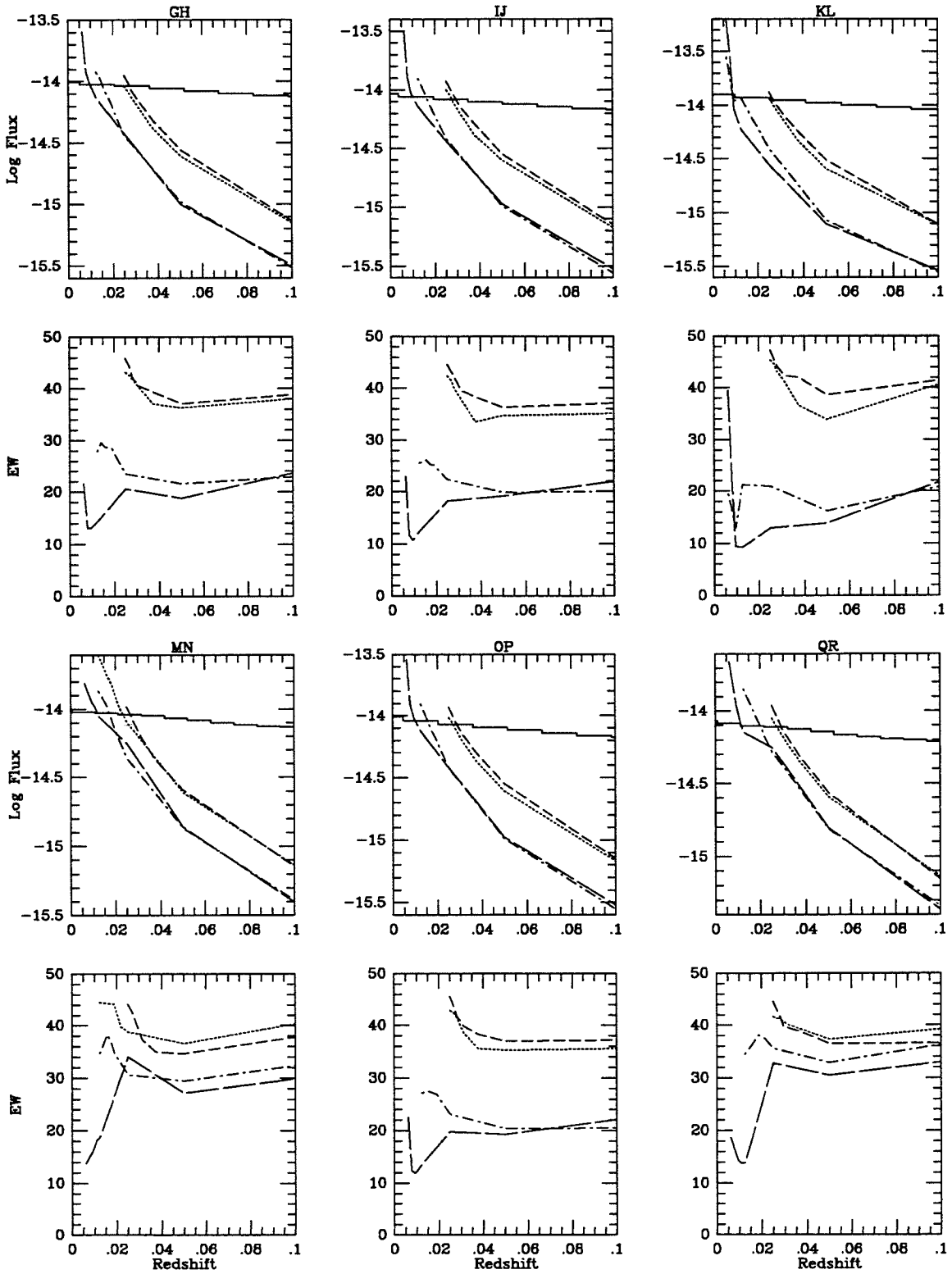

Figure B–46.

NGC 3991 MAJ/MIN

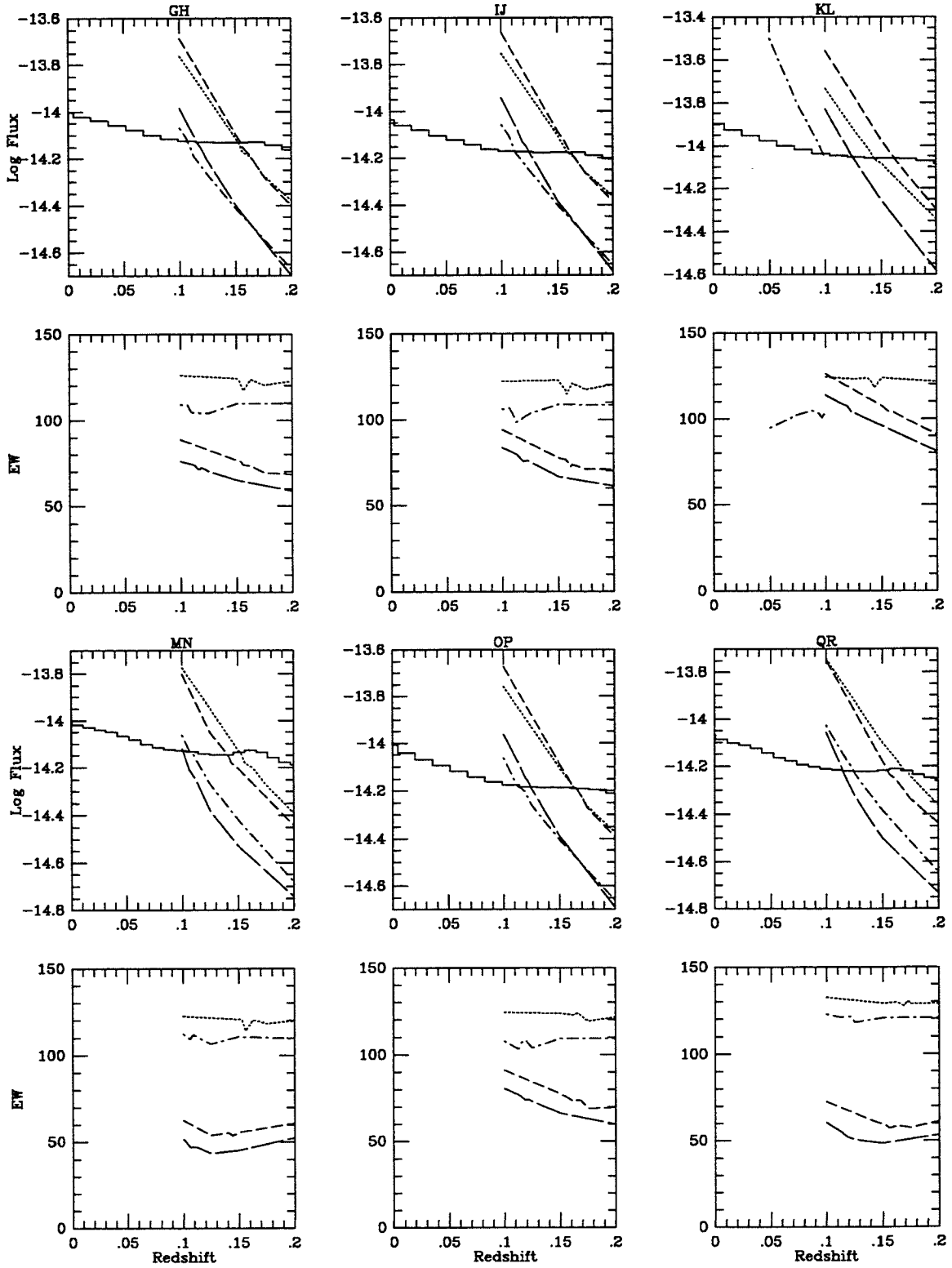

Figure B-47.

IC 755 MAJ/MIN

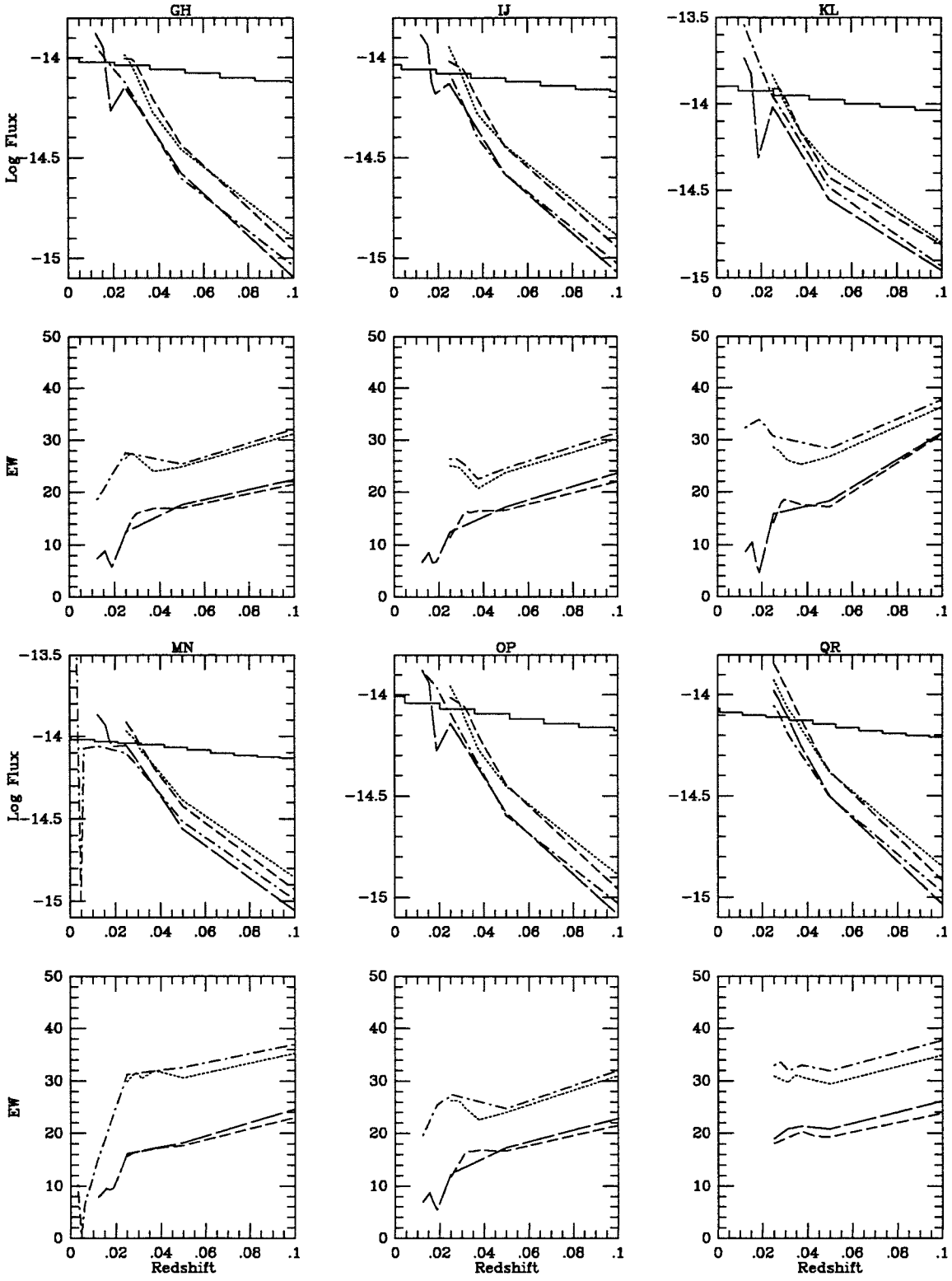

Figure B–48.

NGC 4051 MAJA/MIN

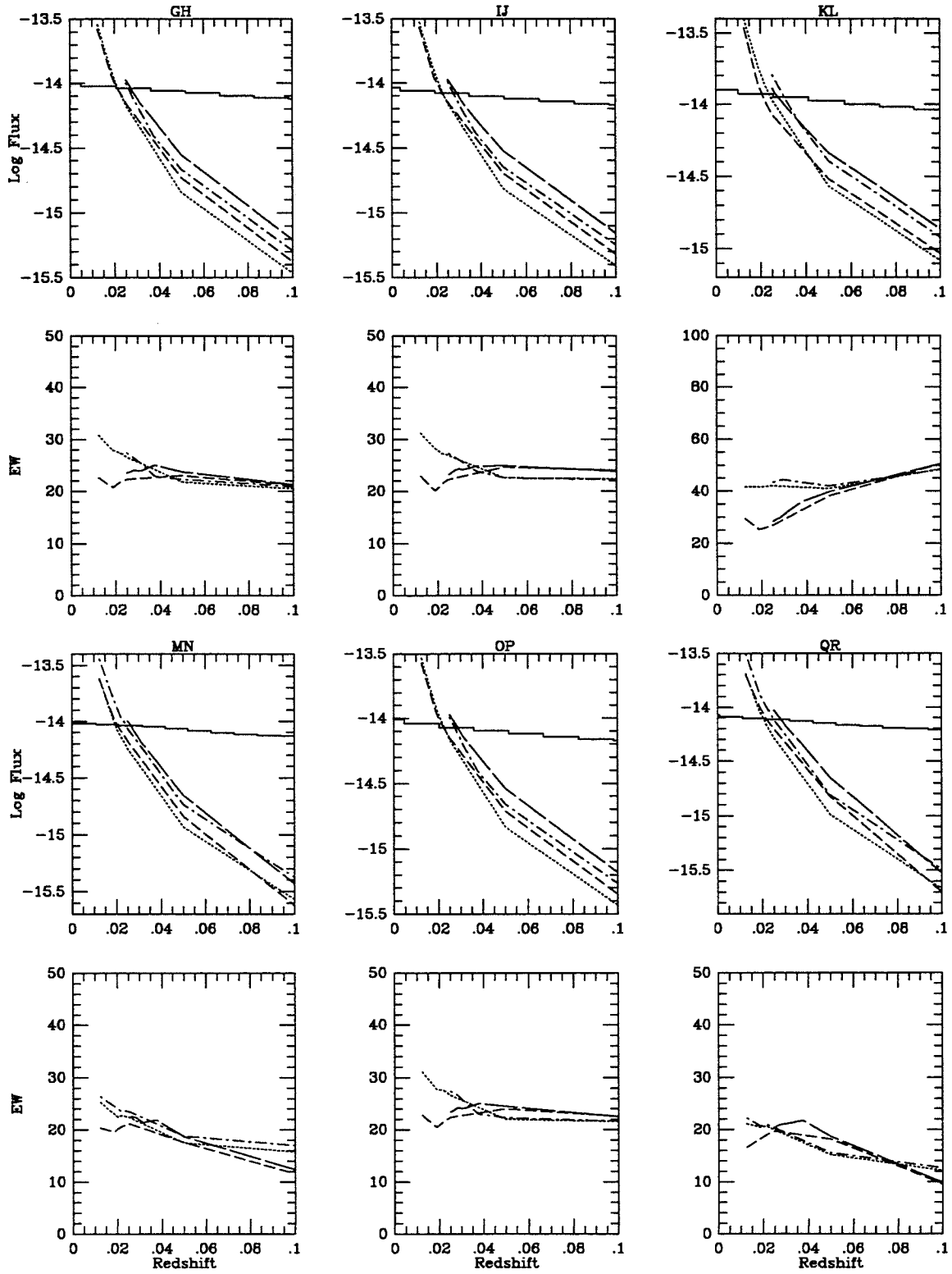

Figure B–49.a

NGC 4051 MAJB/MIN

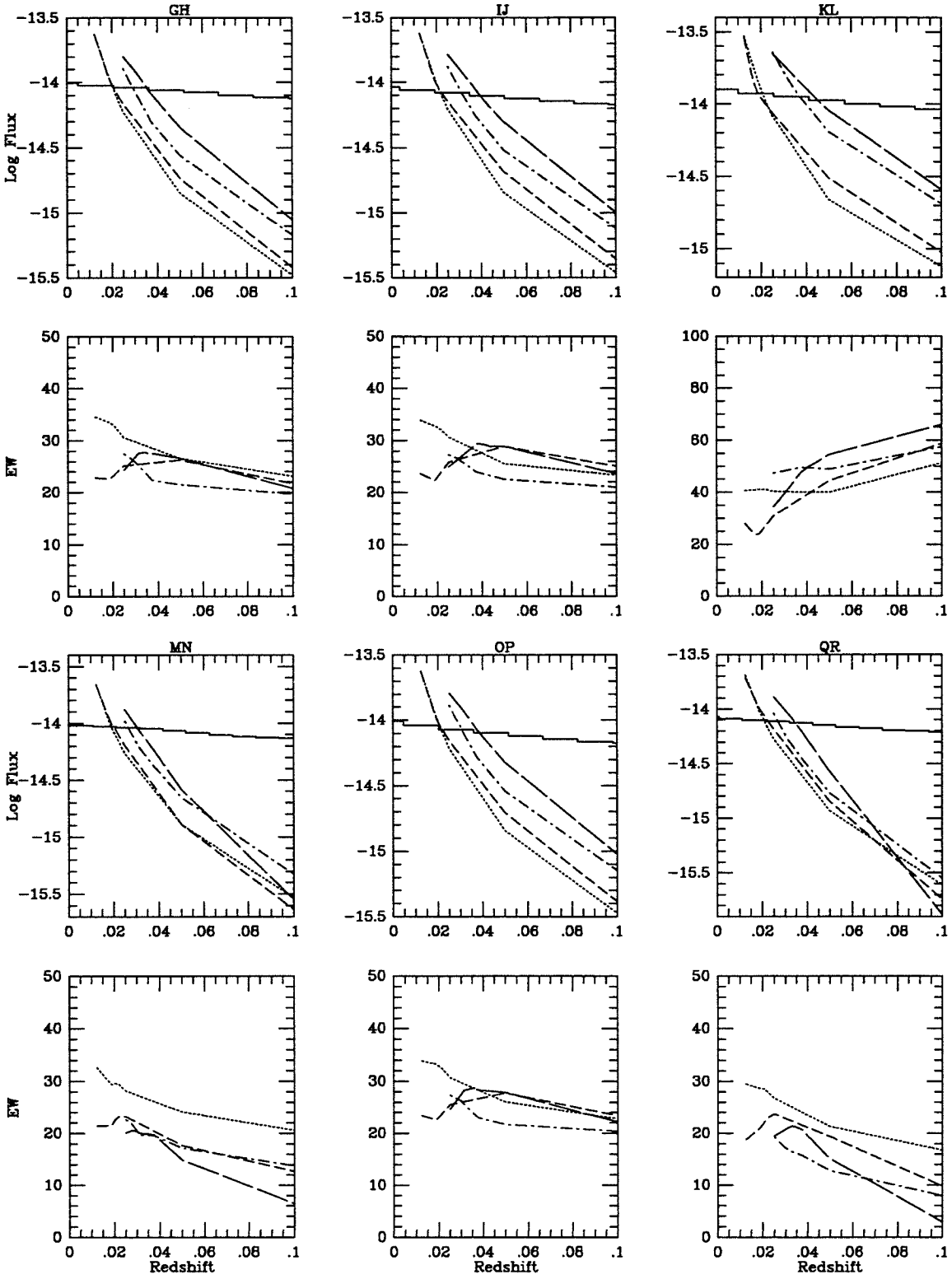

Figure B–49.b

1202+3127 MAJA/MIN

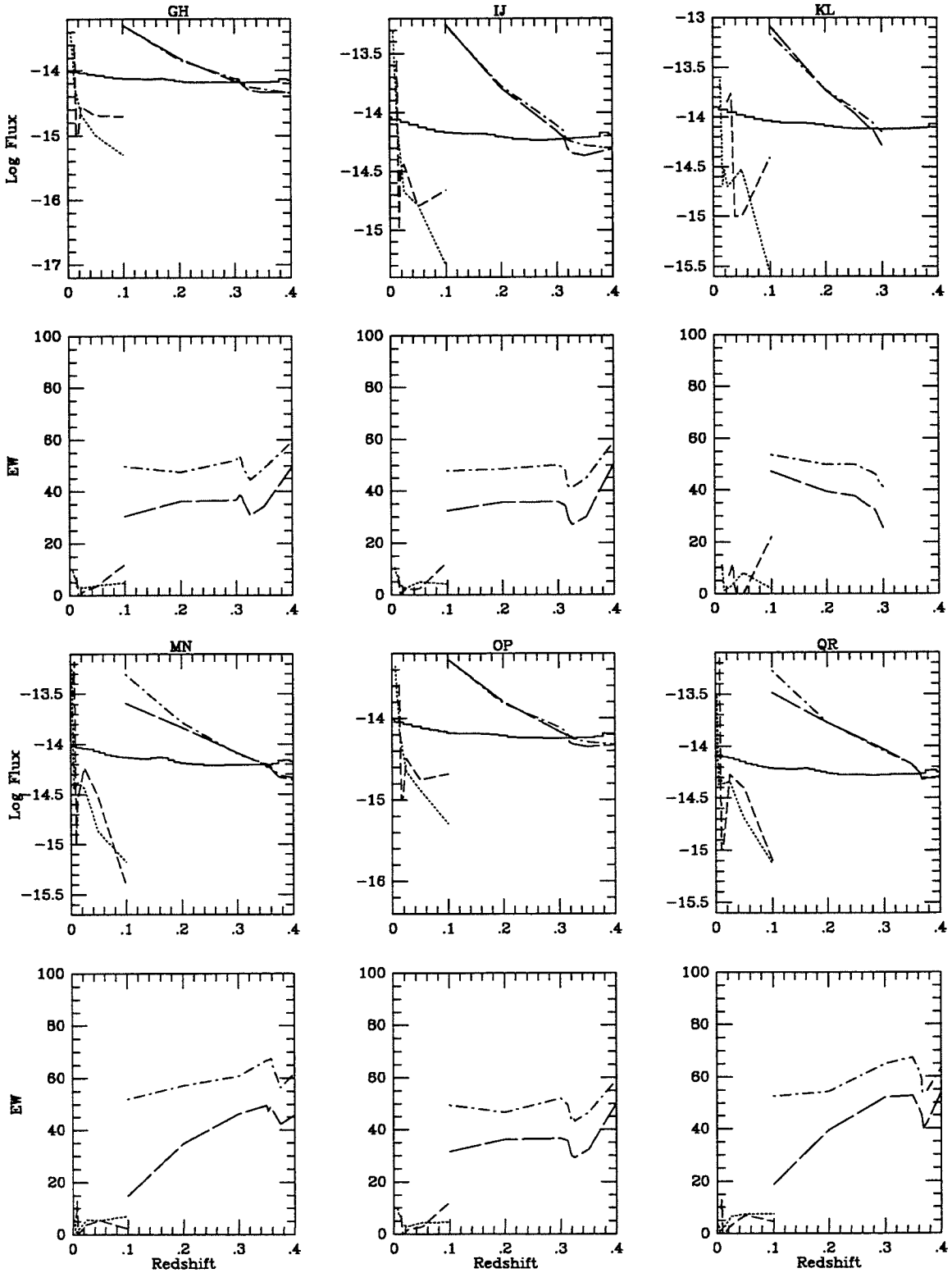

Figure B–50.a

1202+3127 MAJB/MIN

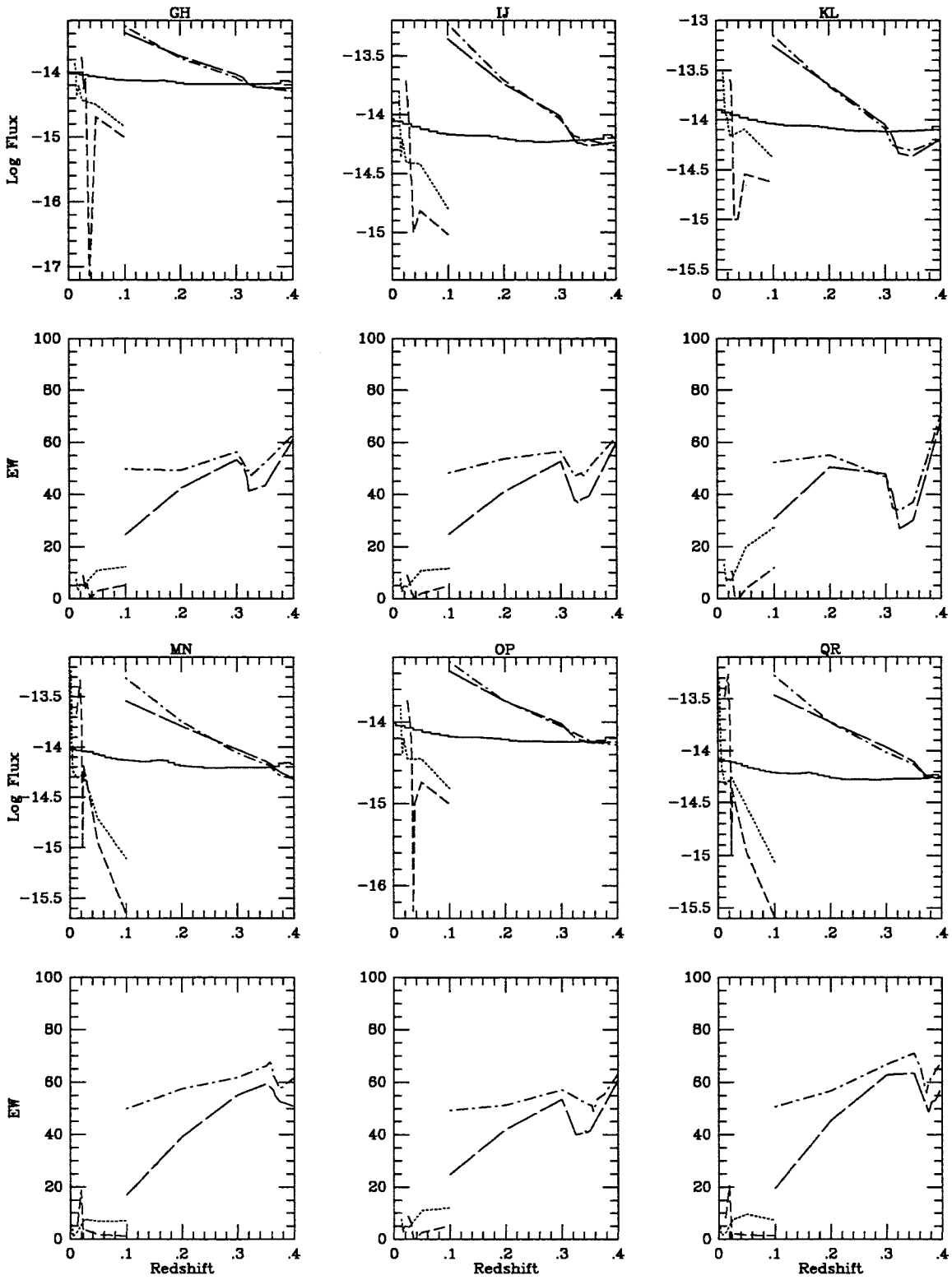

Figure B-50.b

NGC 4108B MAJ/MIN

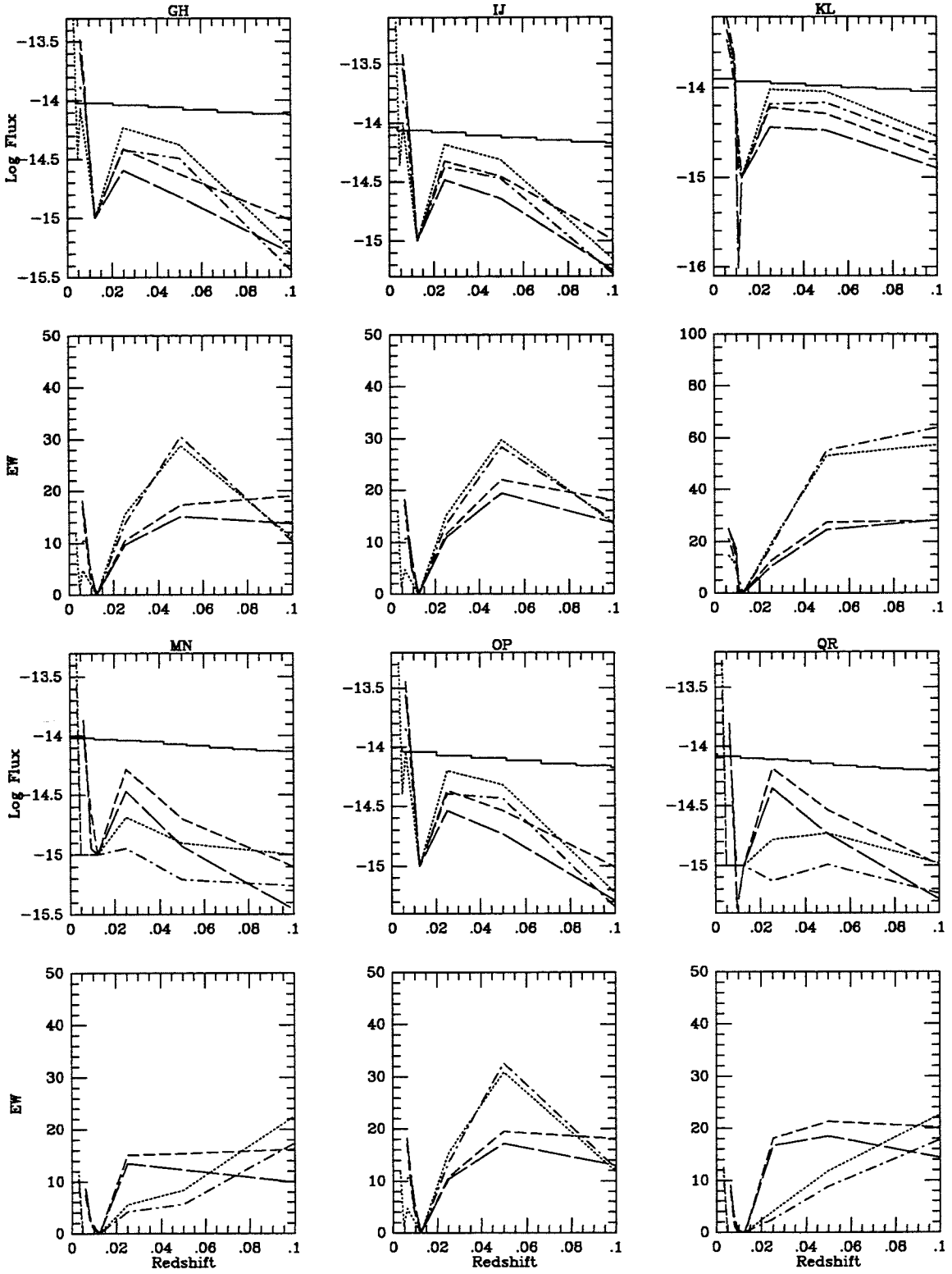

Figure B-51.

NGC 4151 MAJ/MIN

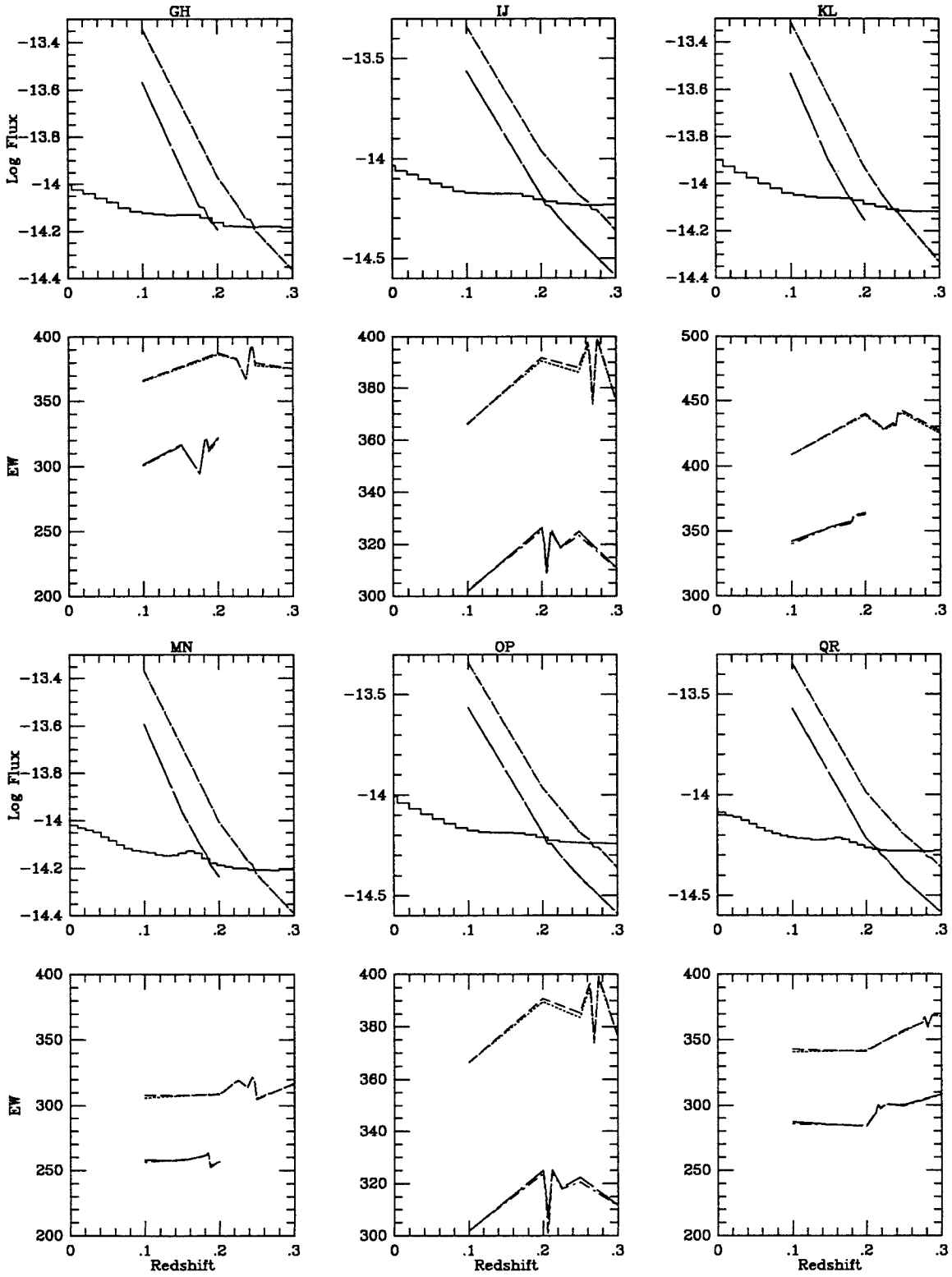

Figure B–52.

NGC 4173 MAJA/MINA

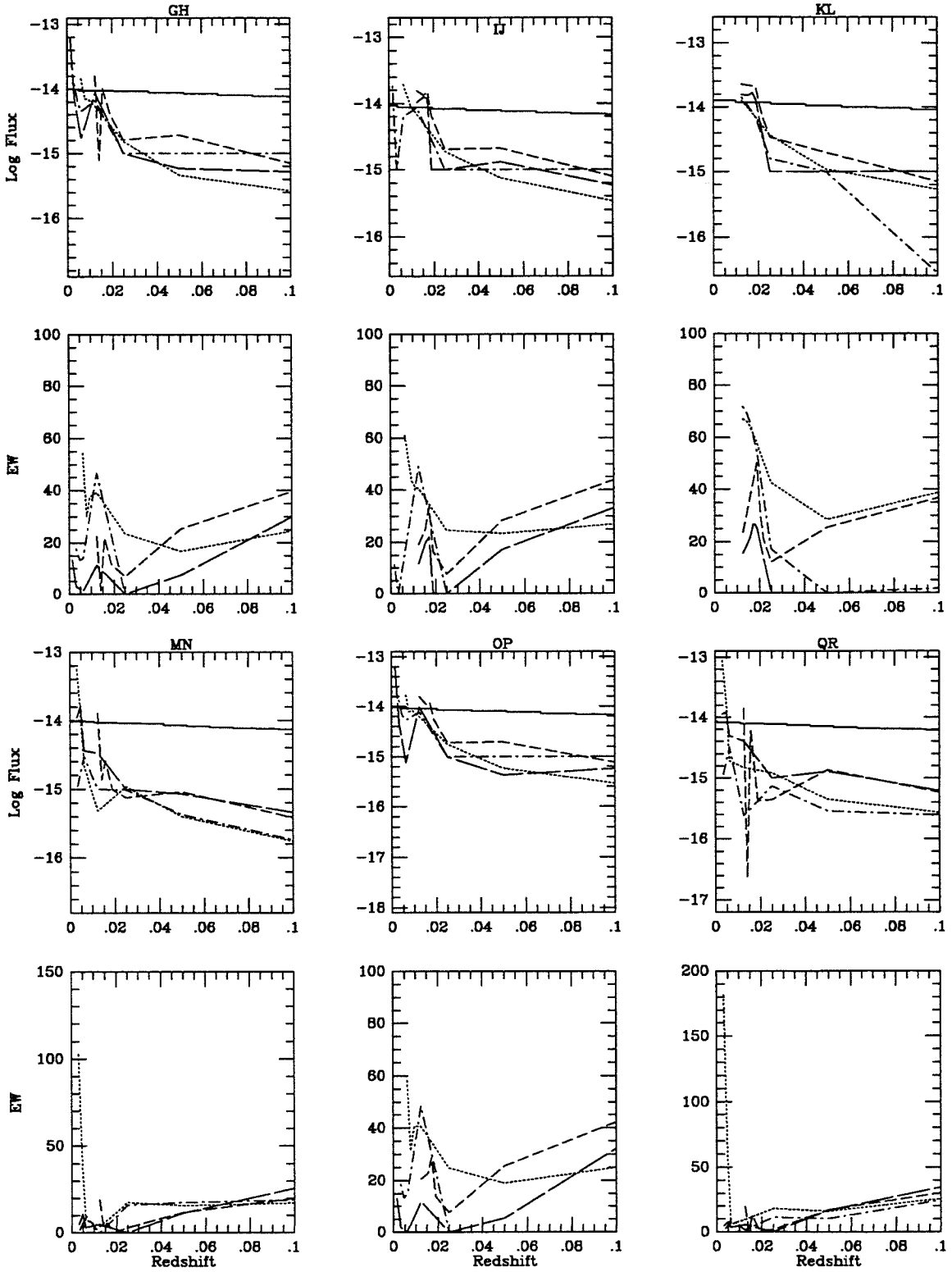

Figure B-53.aa

NGC 4173 MAJA/MINB

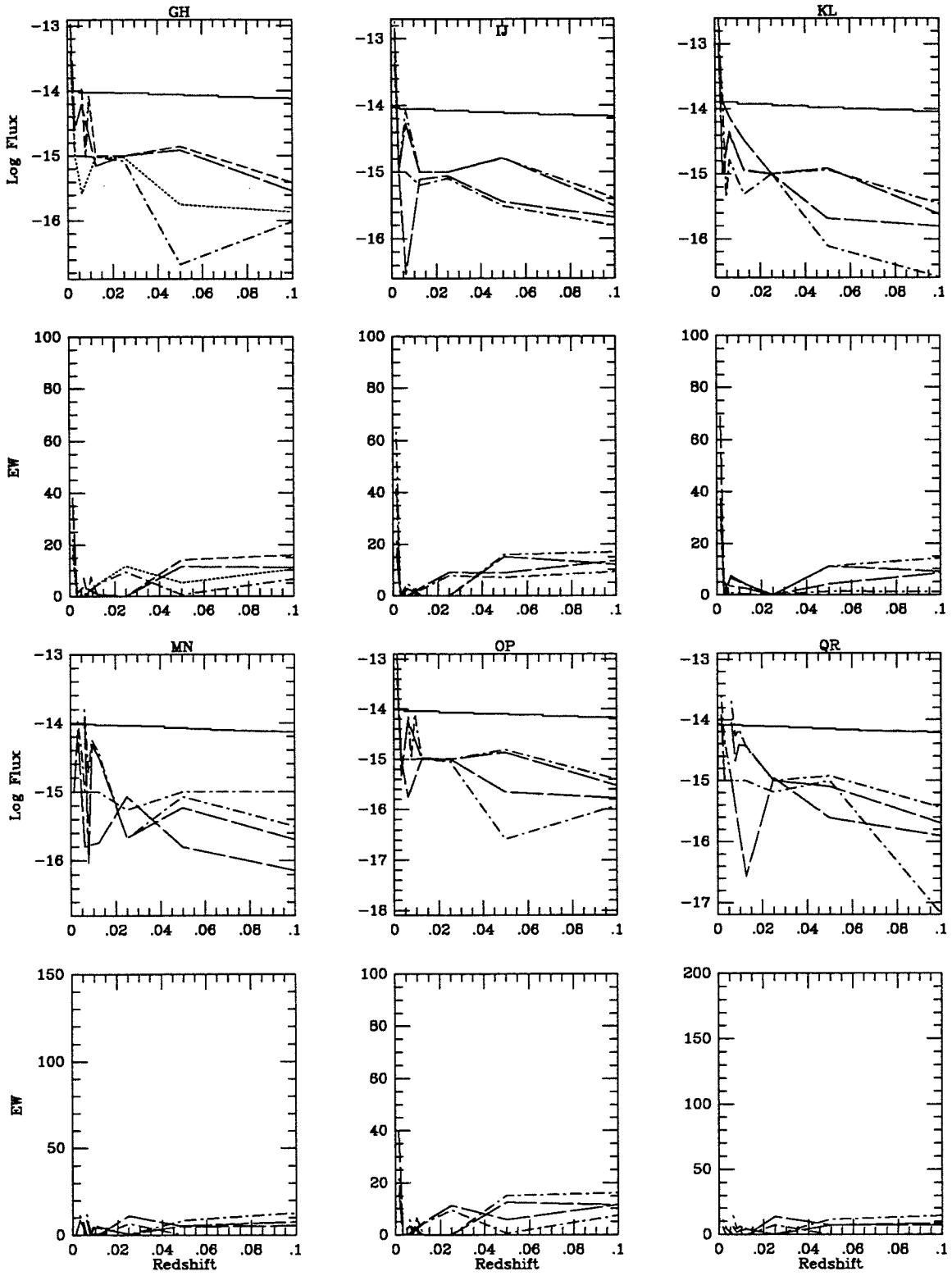

Figure B-53.ab

NGC 4173 MAJA/MINC

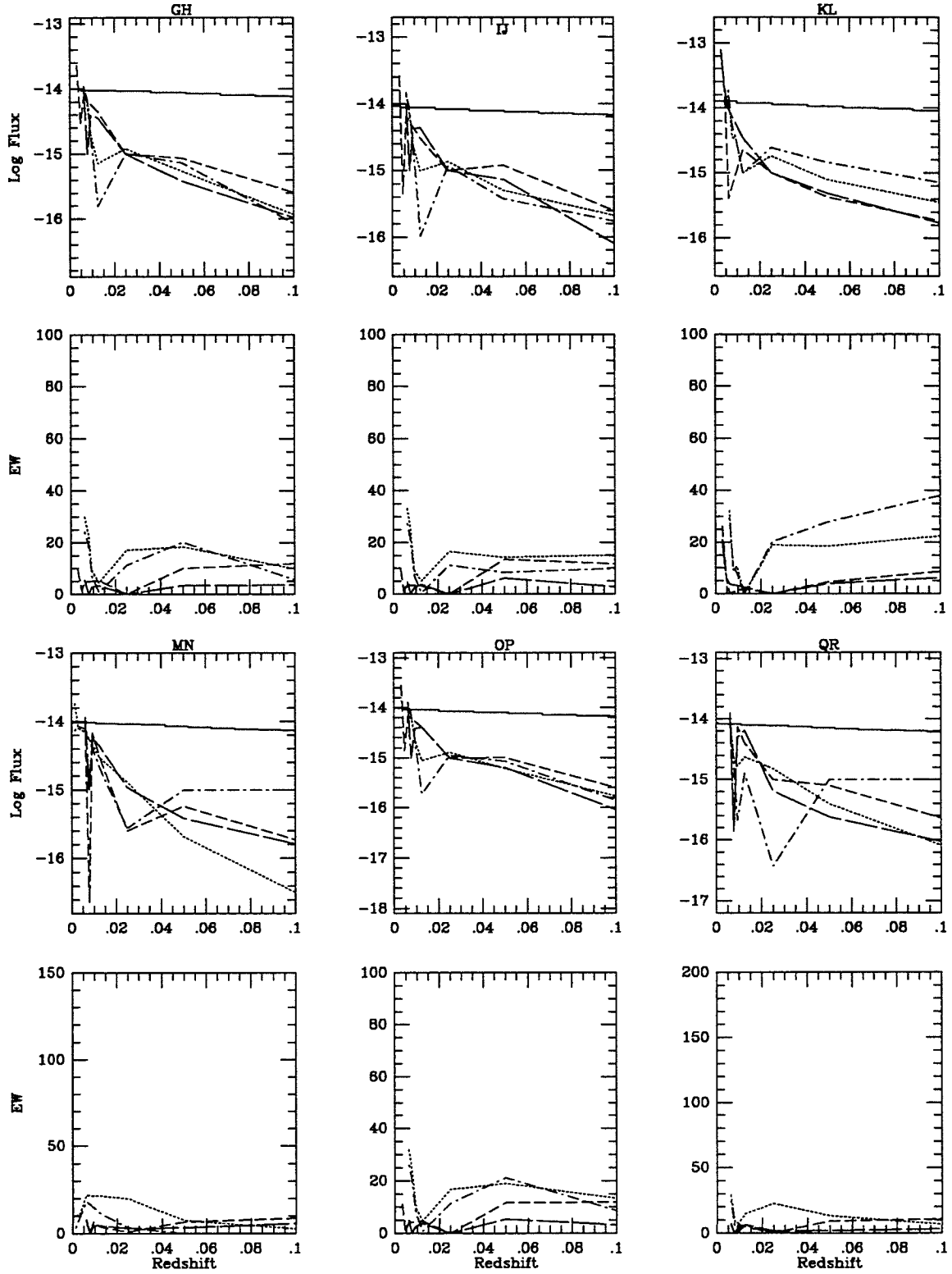

Figure B–53.ac

NGC 4173 MAJB/MINA

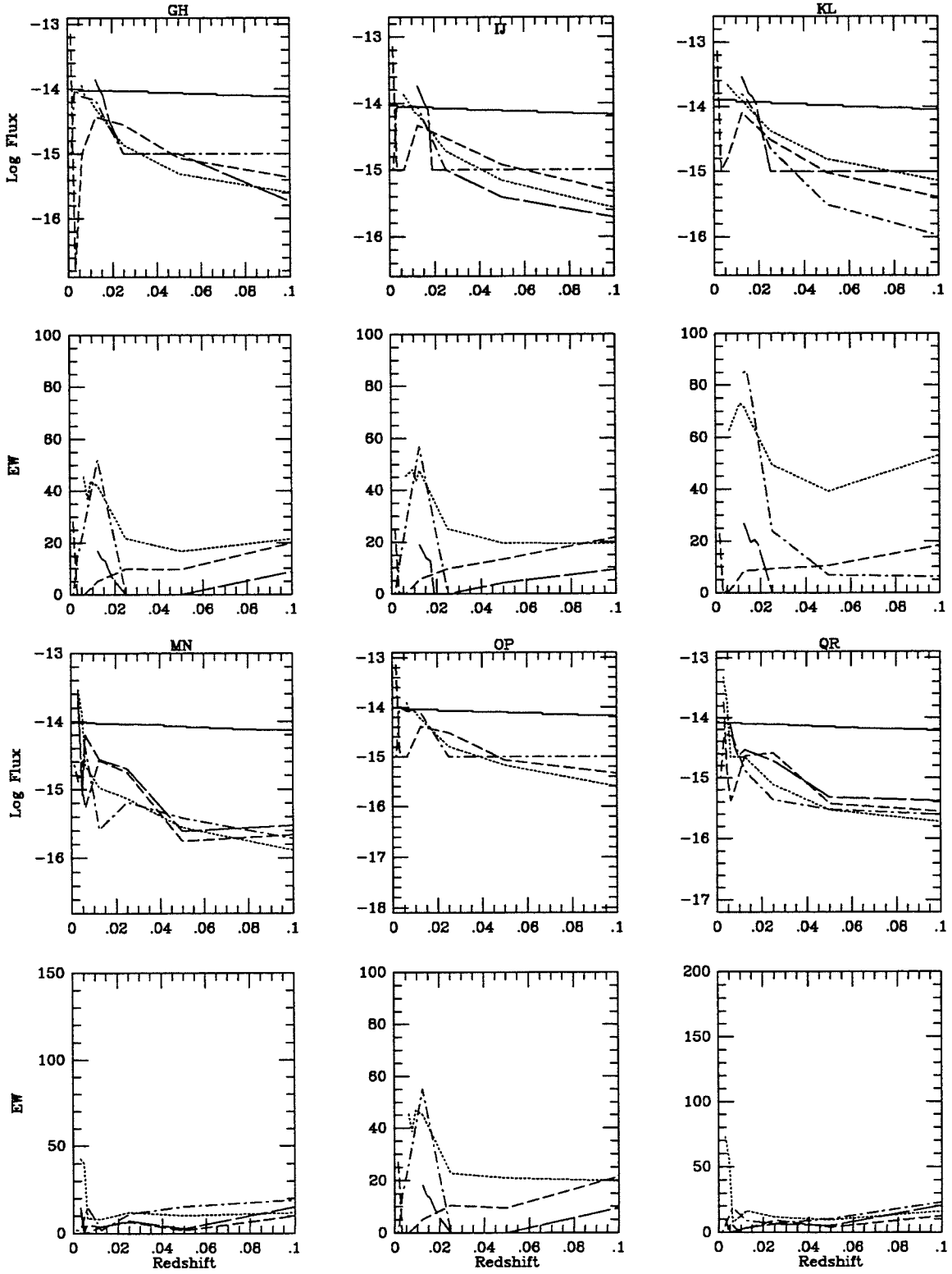

Figure B-53.ba

NGC 4173 MAJB/MINB

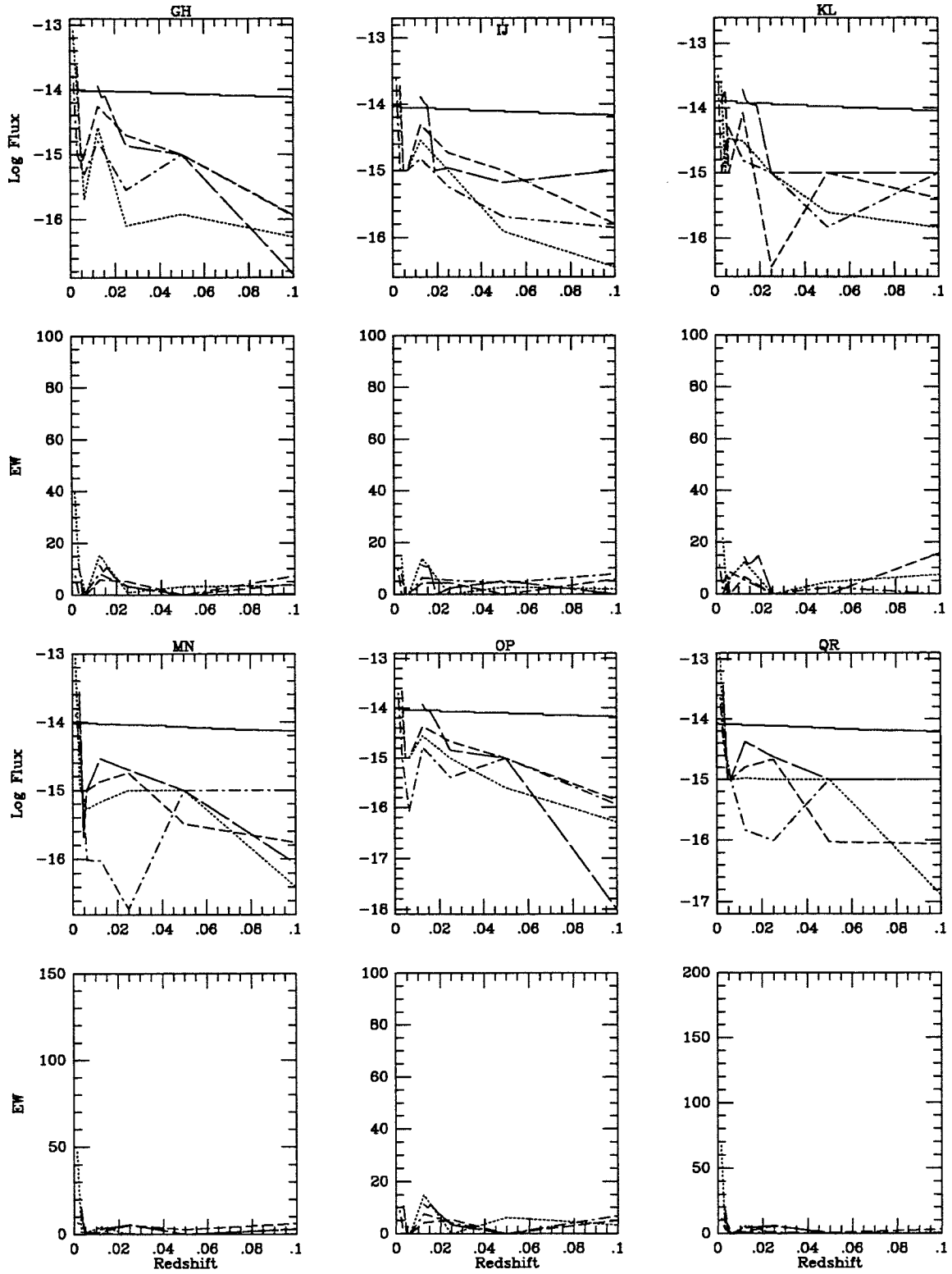

Figure B–53.bb

NGC 4173 MAJB/MINC

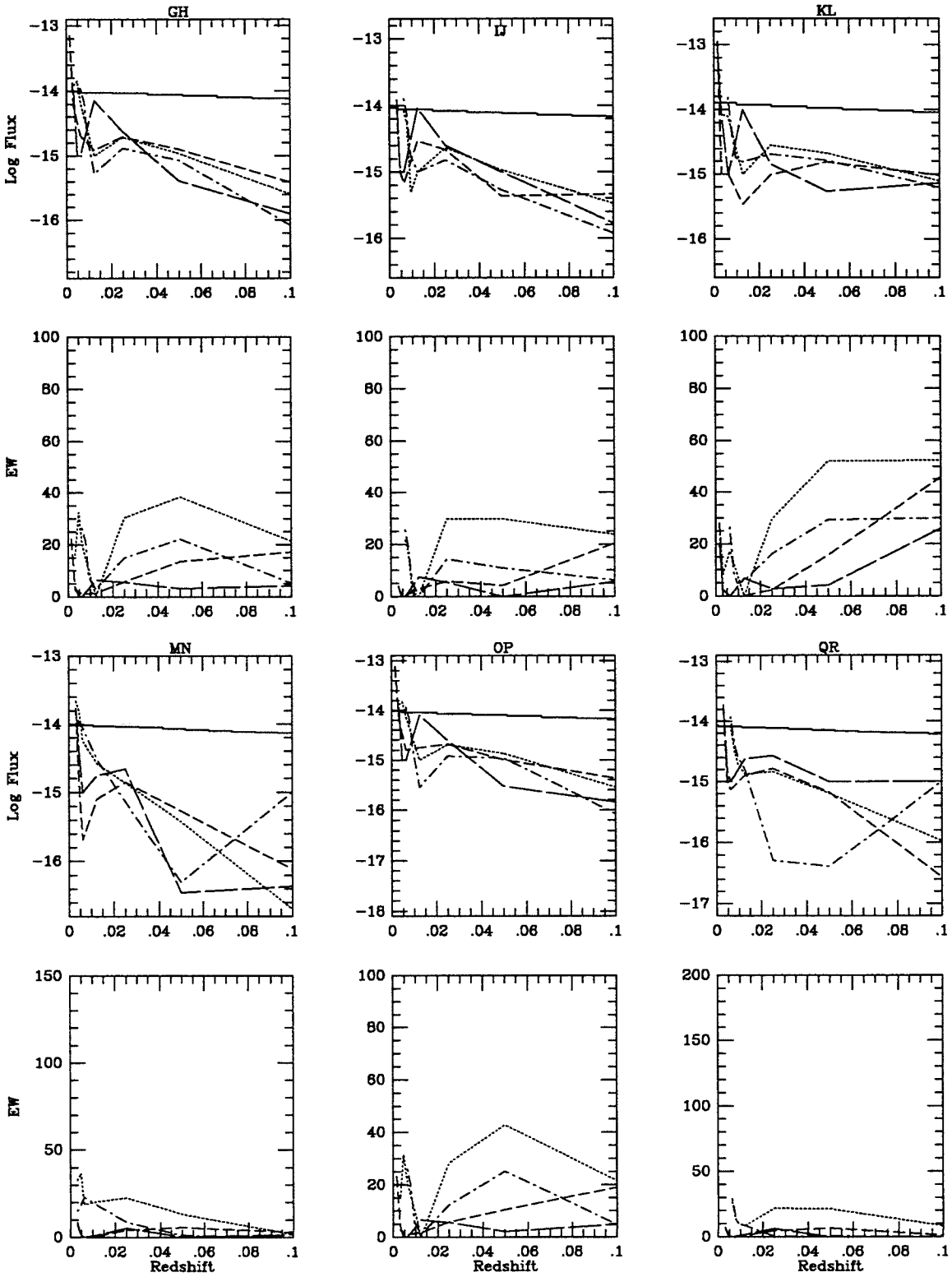

Figure B-53.bc

1212+3614 MAJ/MIN

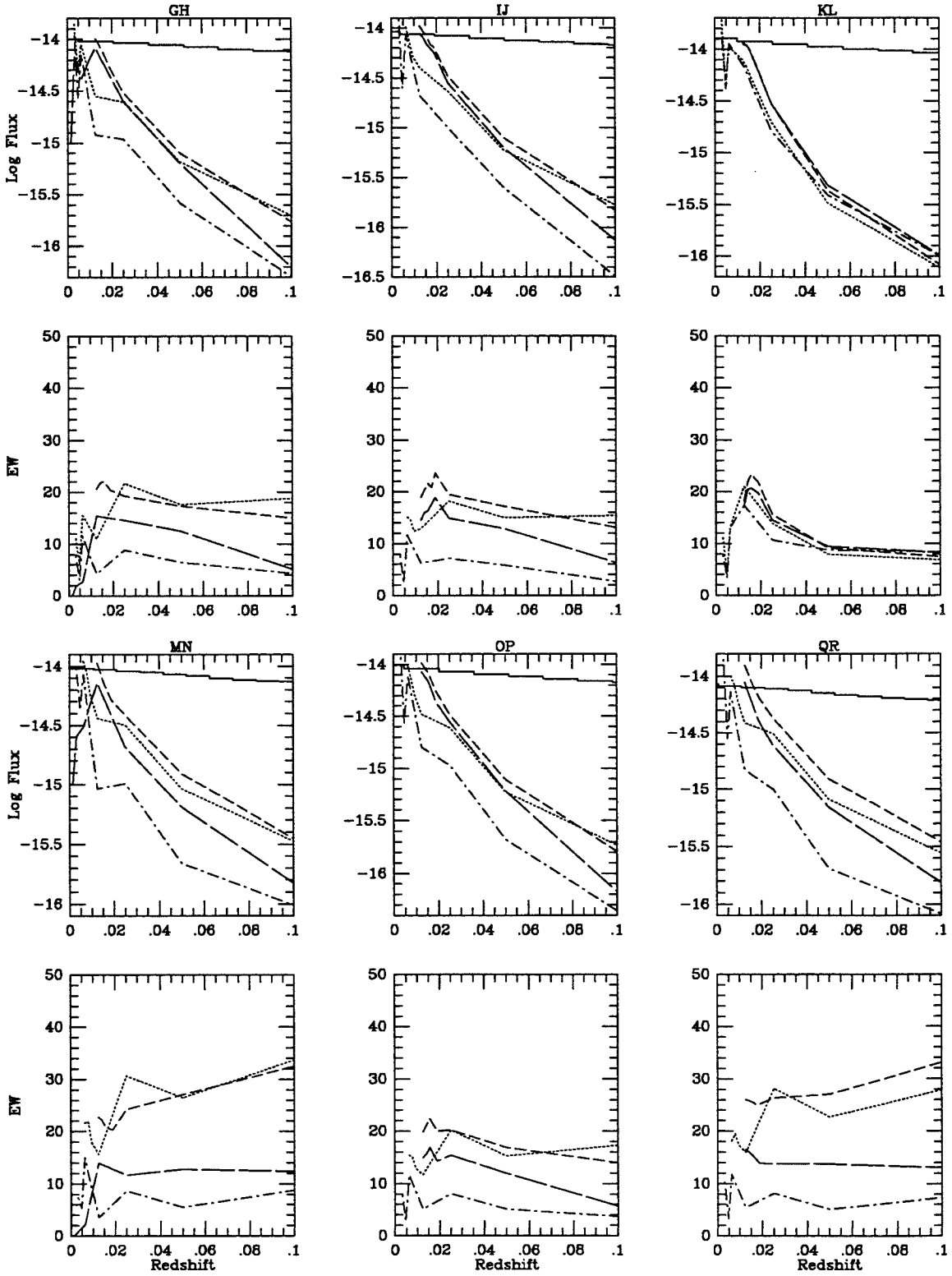

Figure B–54.

NGC 4214 MAJ/MIN

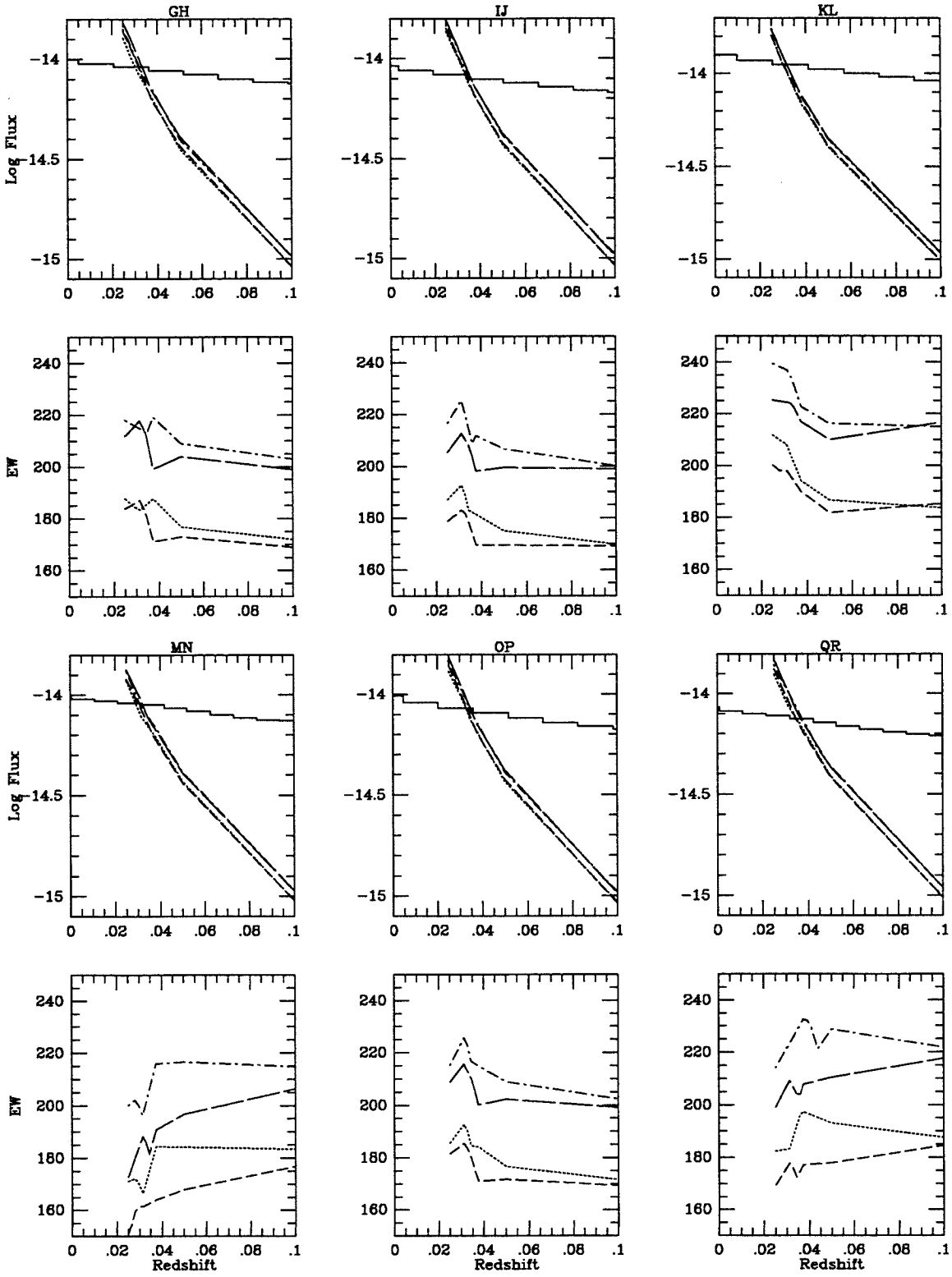

Figure B–55.

NGC 4235 MAJ/MIN

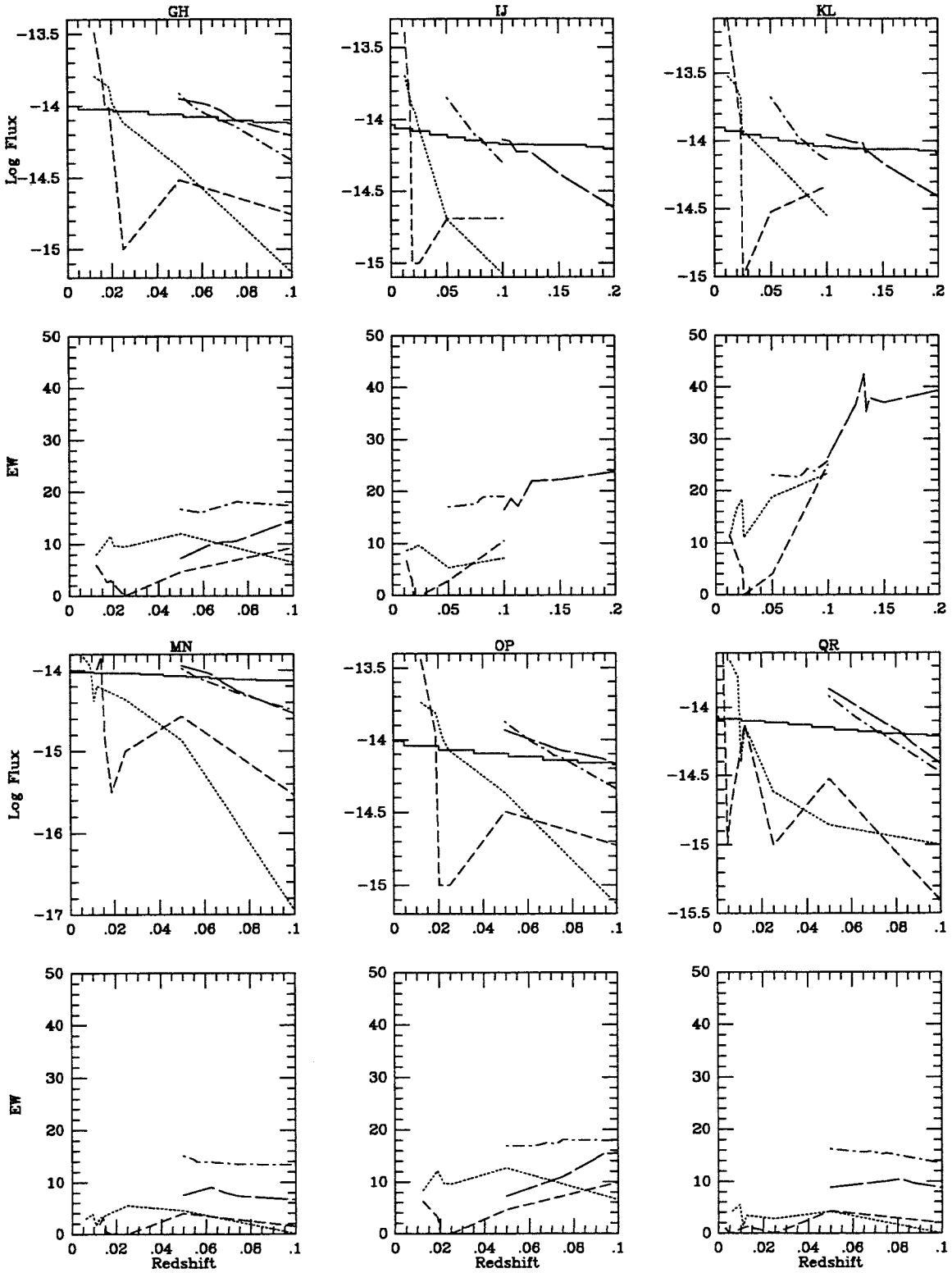

Figure B-56.

NGC 4253 MAJ/MIN

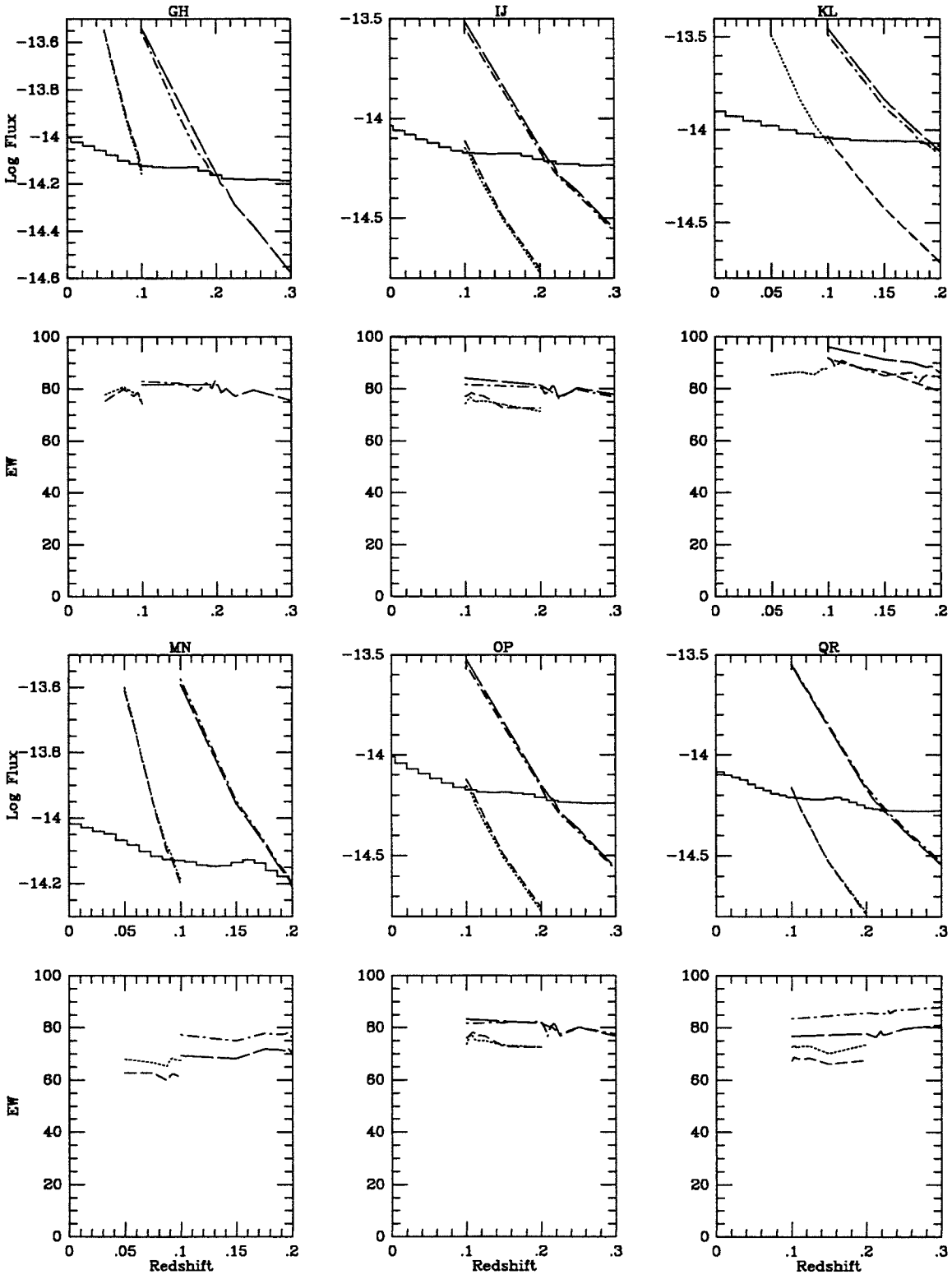

Figure B–57.

1216+0408 MAJ/MIN

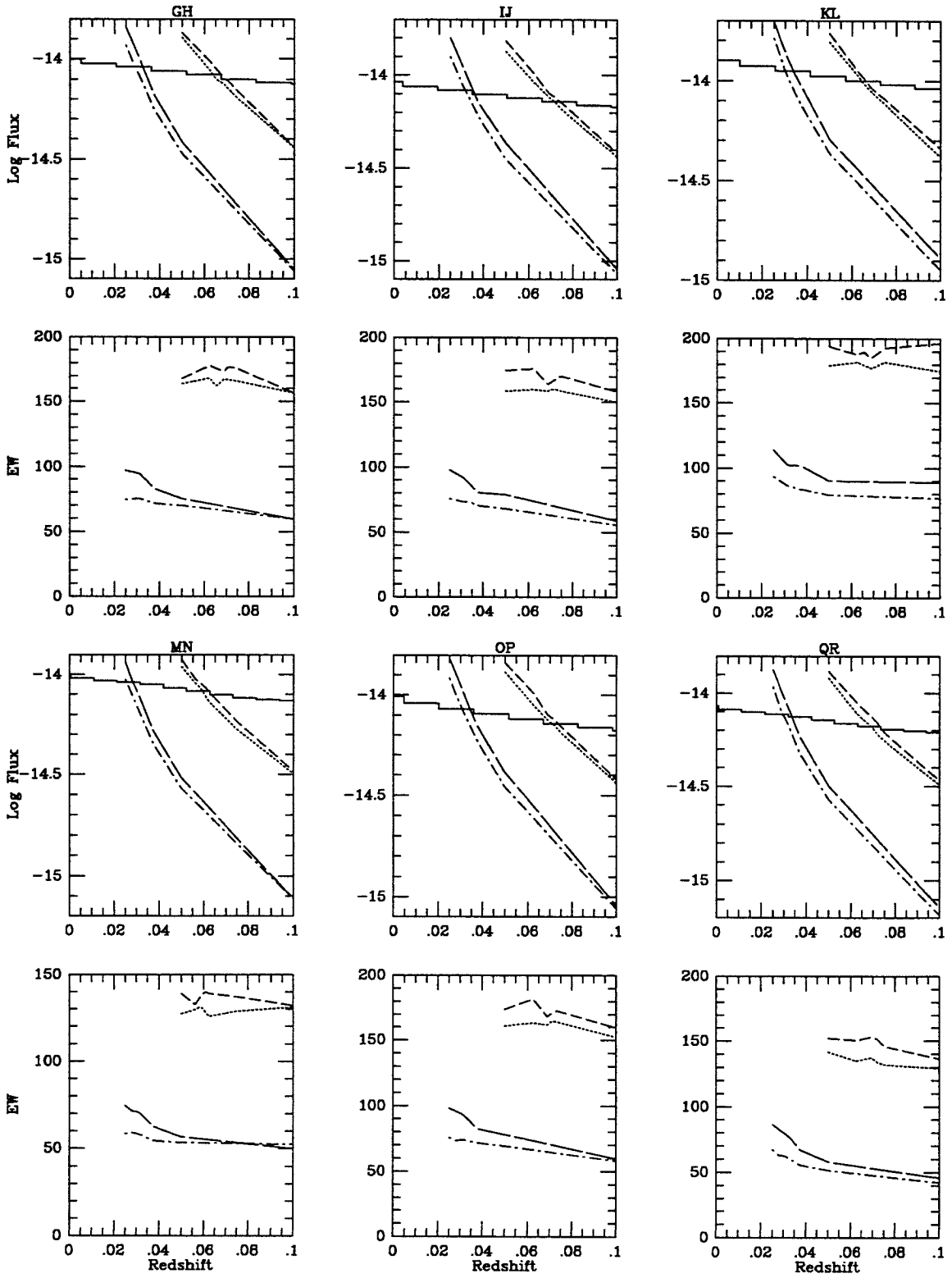

Figure B-58.

1219+7535 MAJ/MIN

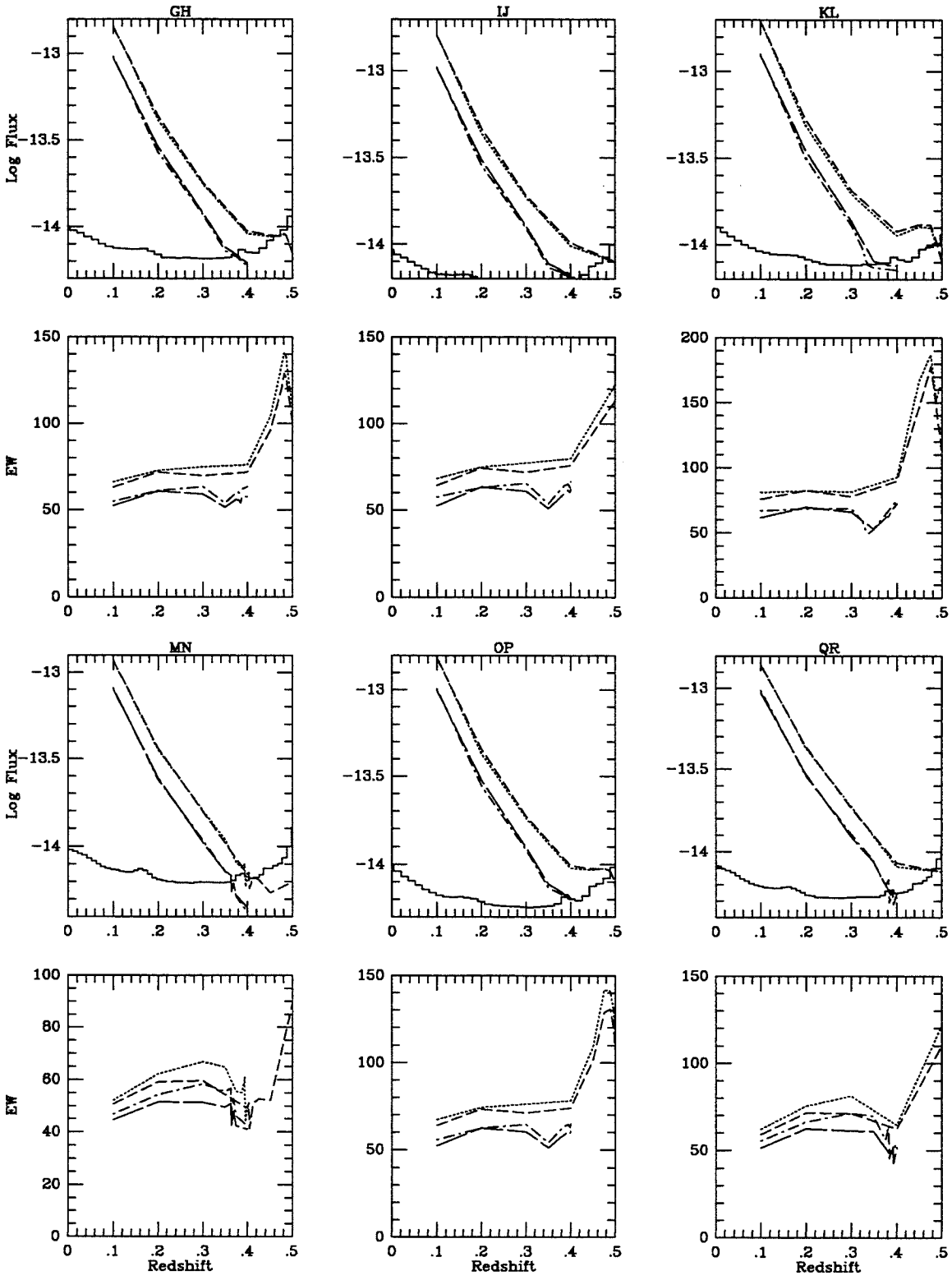

Figure B-59.

NGC 4388 MAJ/MIN

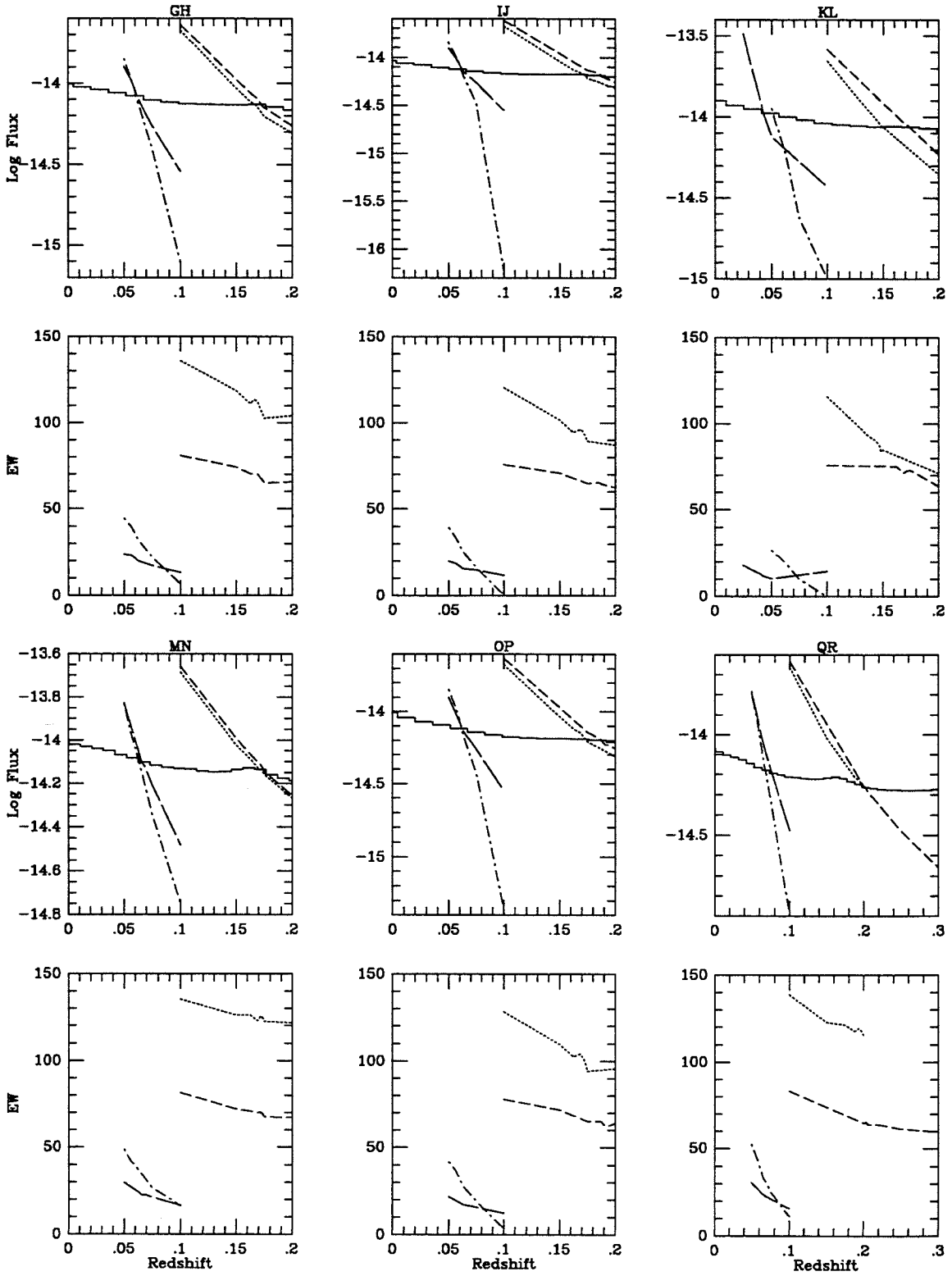

Figure B-60.

1229+4007 MAJ/MIN

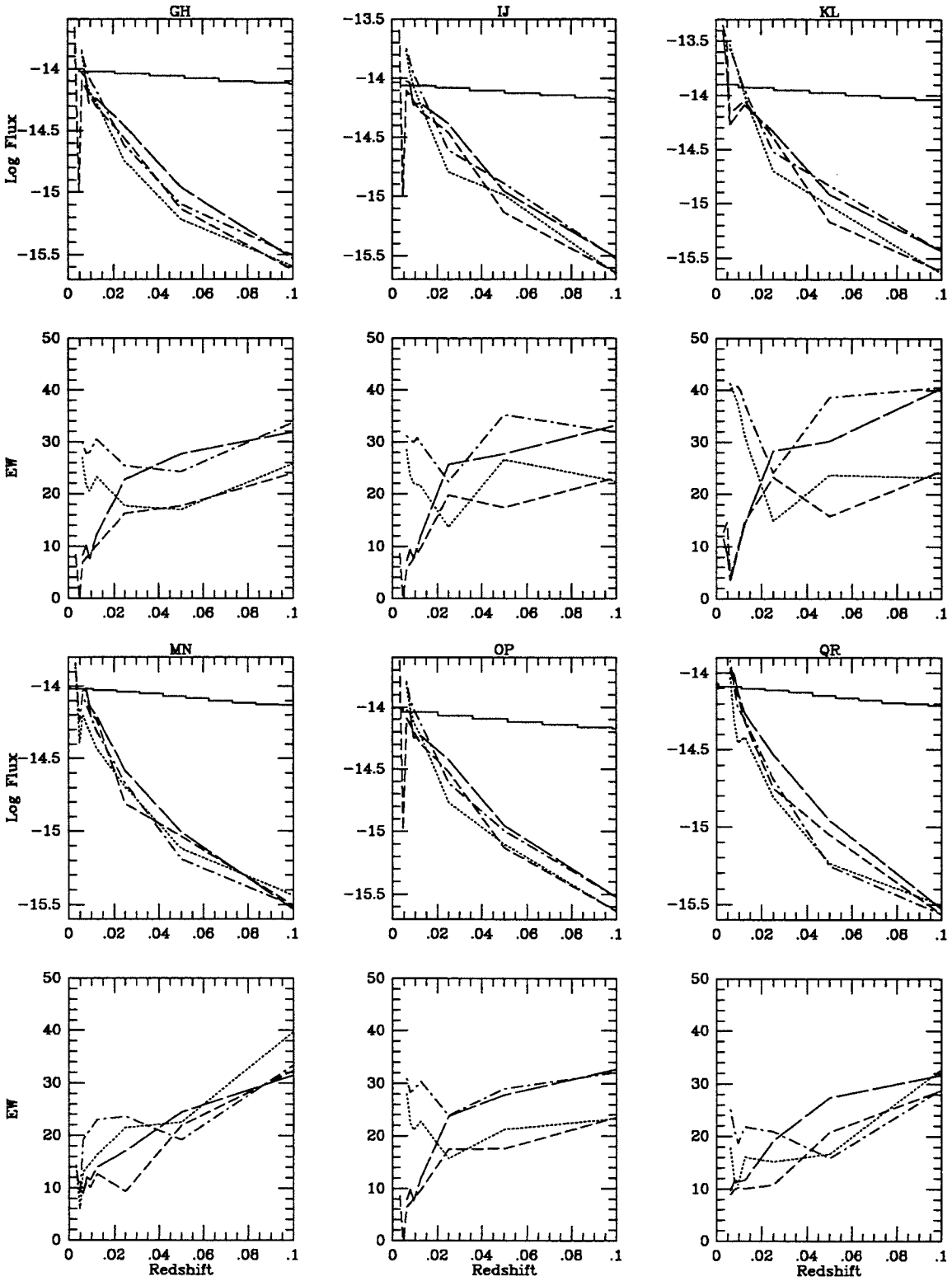

Figure B–61.

NGC 4509 MAJ/MIN

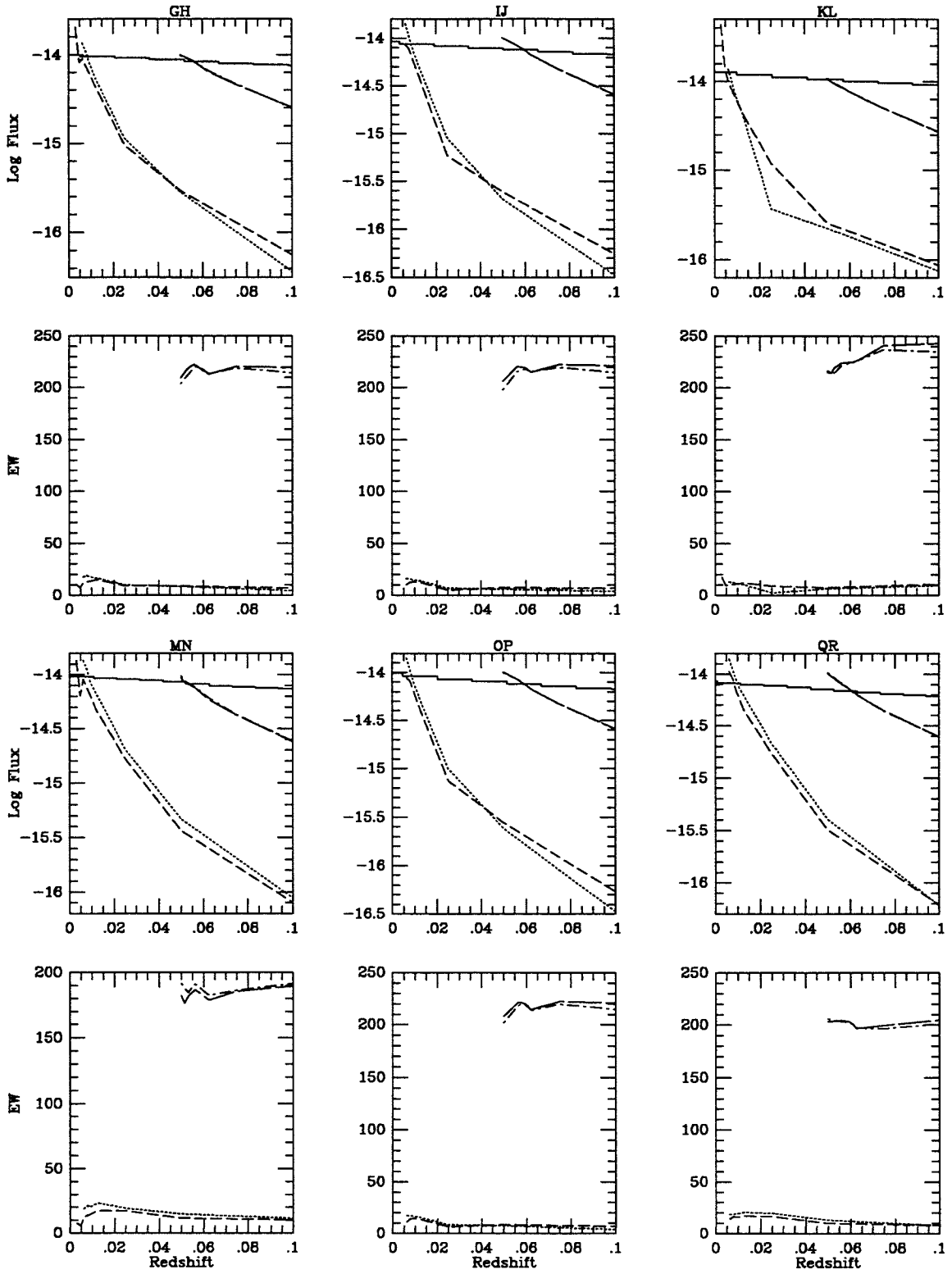

Figure B-62.

1241+5510 MAJ/MIN

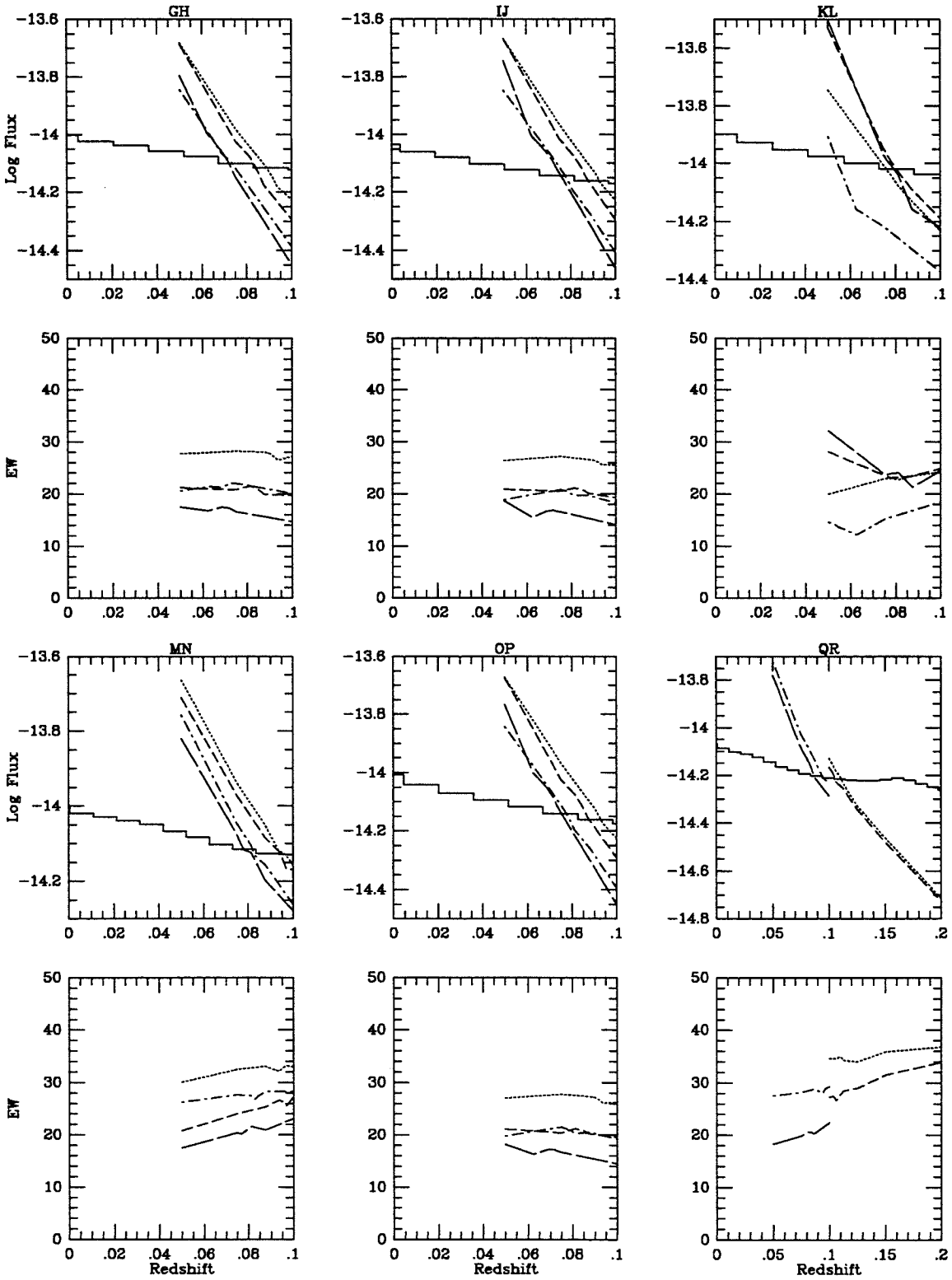

Figure B–63.

NGC 4656 MAJ/MIN

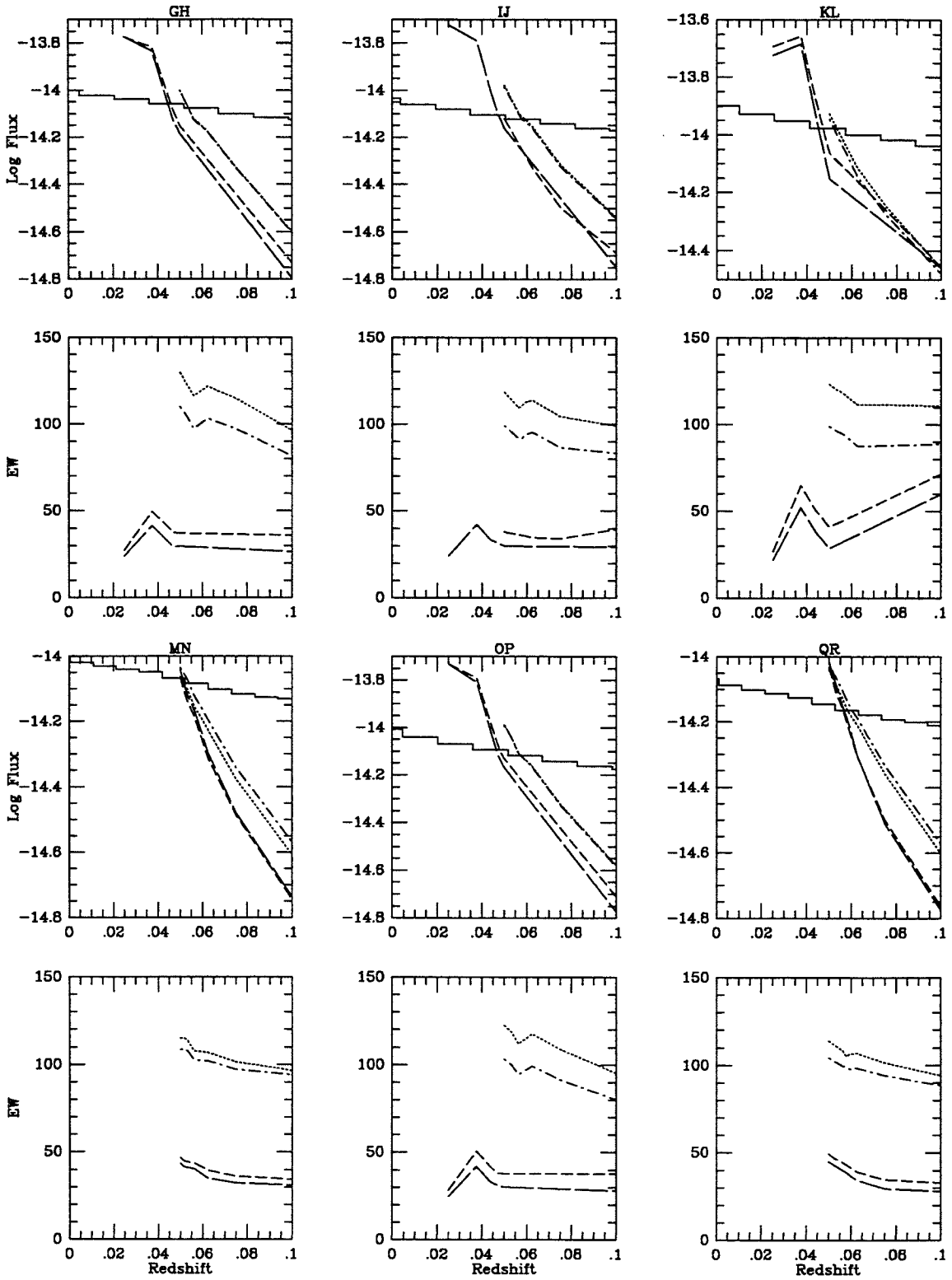

Figure B-64.

NGC 4670 MAJ/MIN

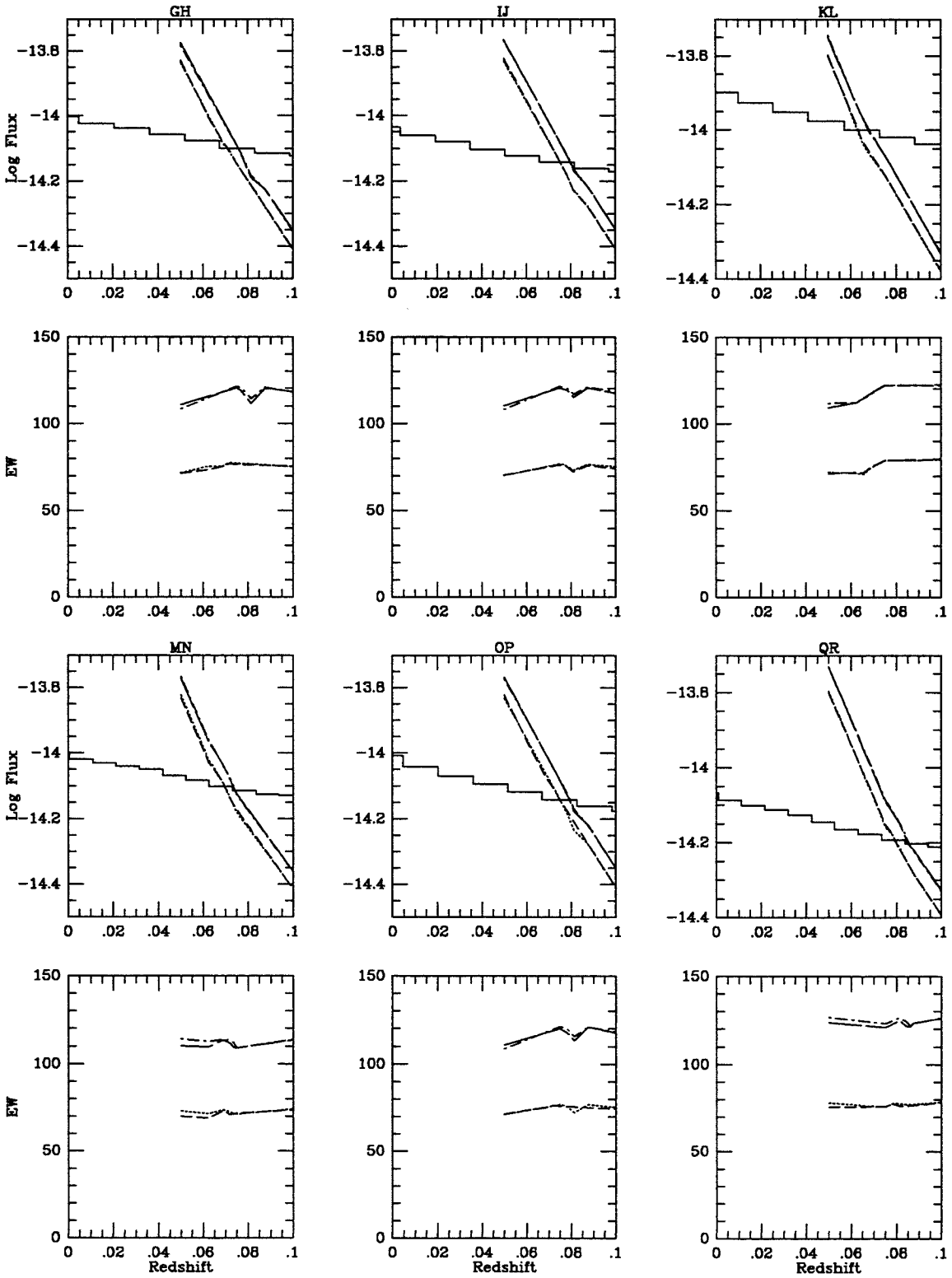

Figure B–65.

NGC 4765 MAJ/MIN

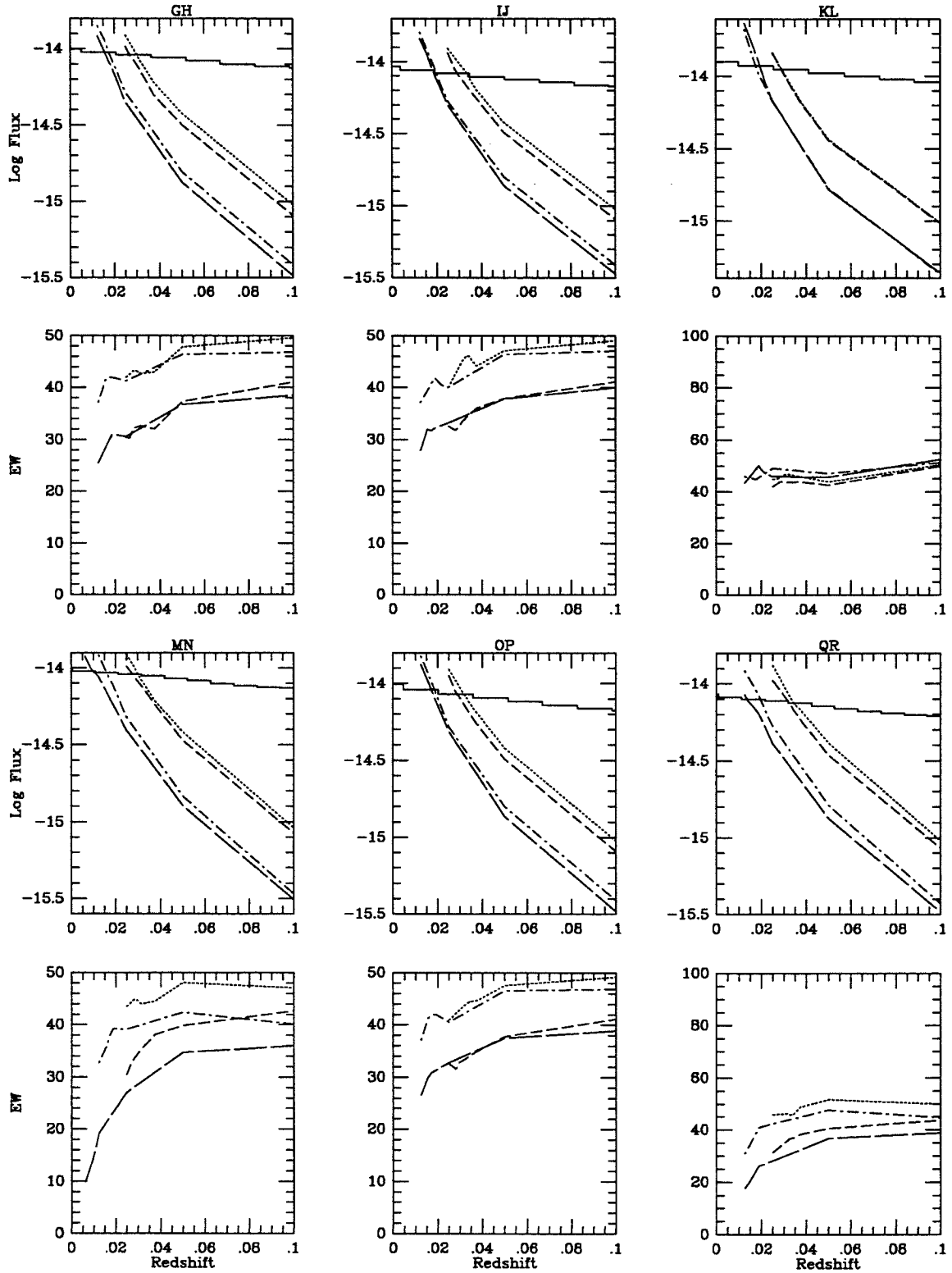

Figure B-66.

1254+5709 MAJ/MIN

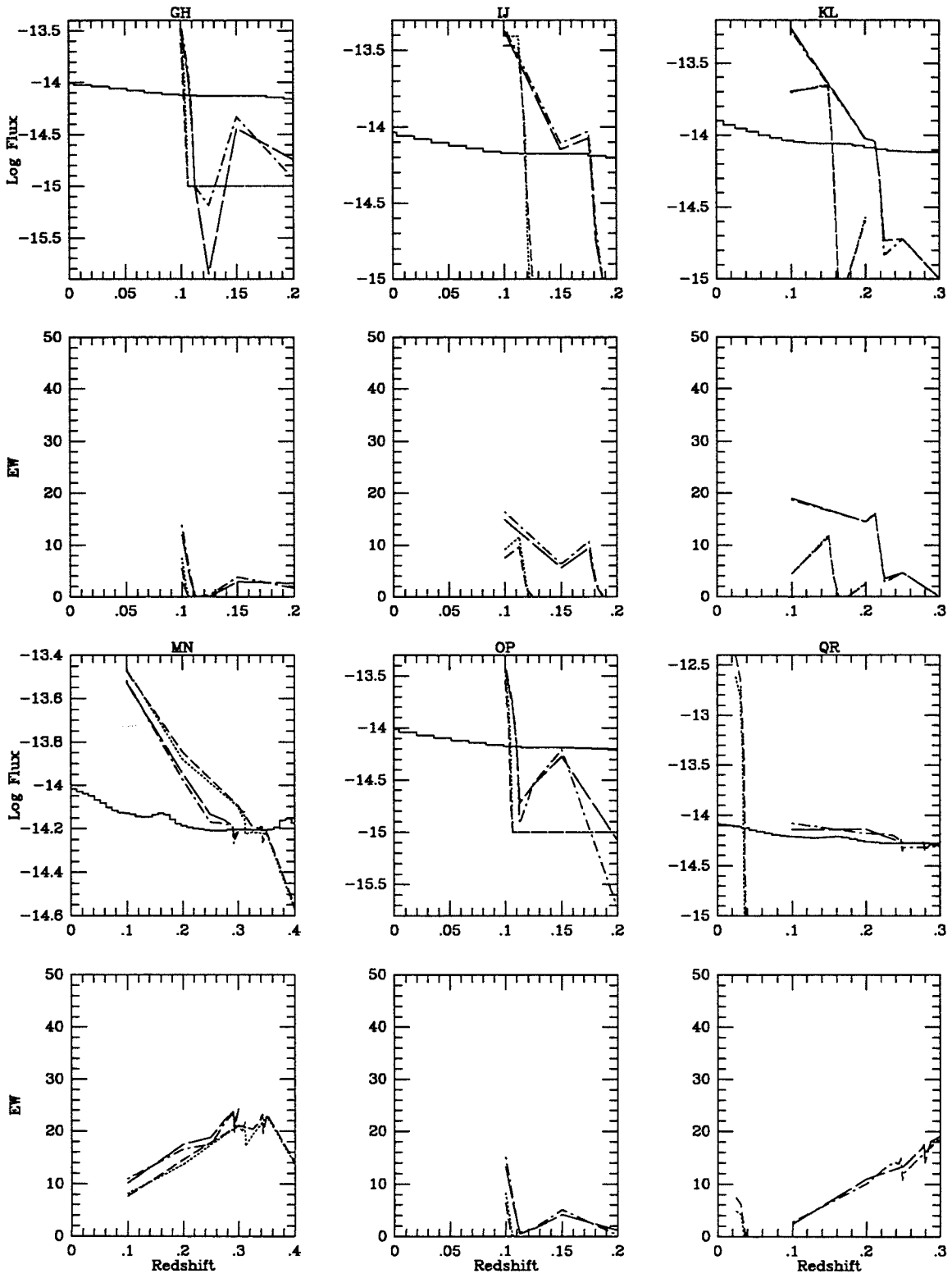

Figure B-67.

NGC 4861 MAJ/MIN

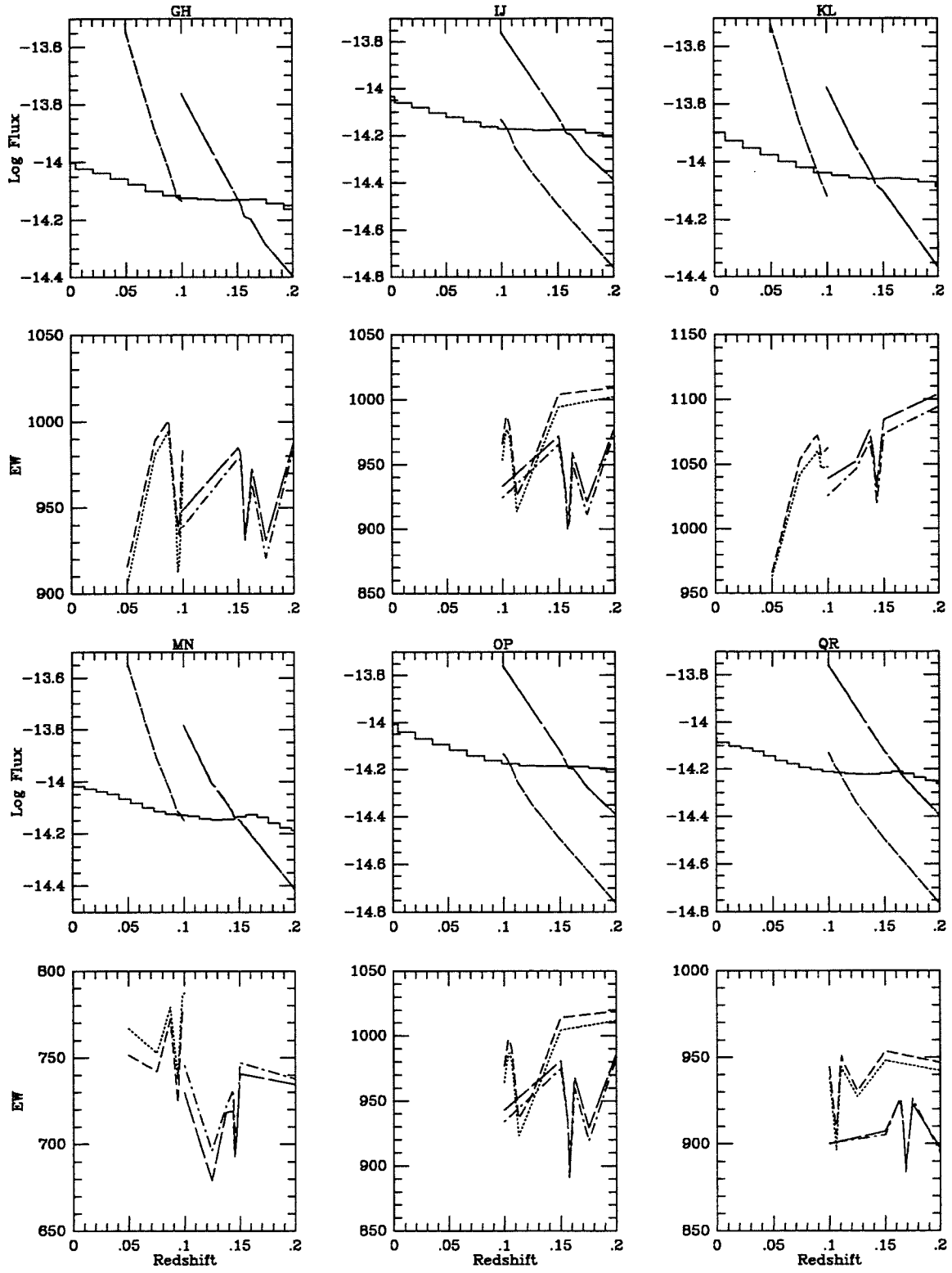

Figure B–68.

NGC 5033 MAJ/MIN

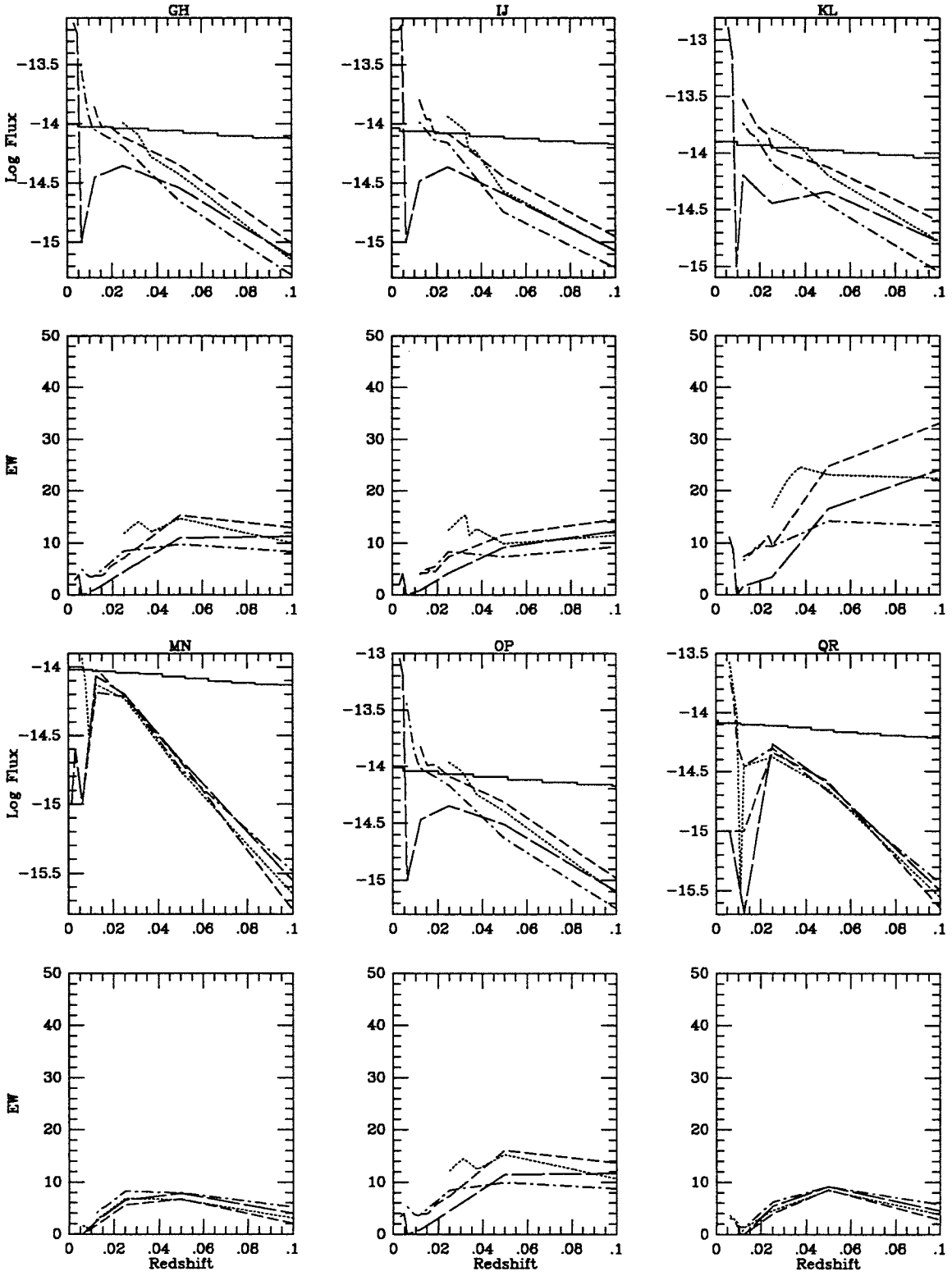

Figure B-69.

NGC 5109 MAJ/MIN

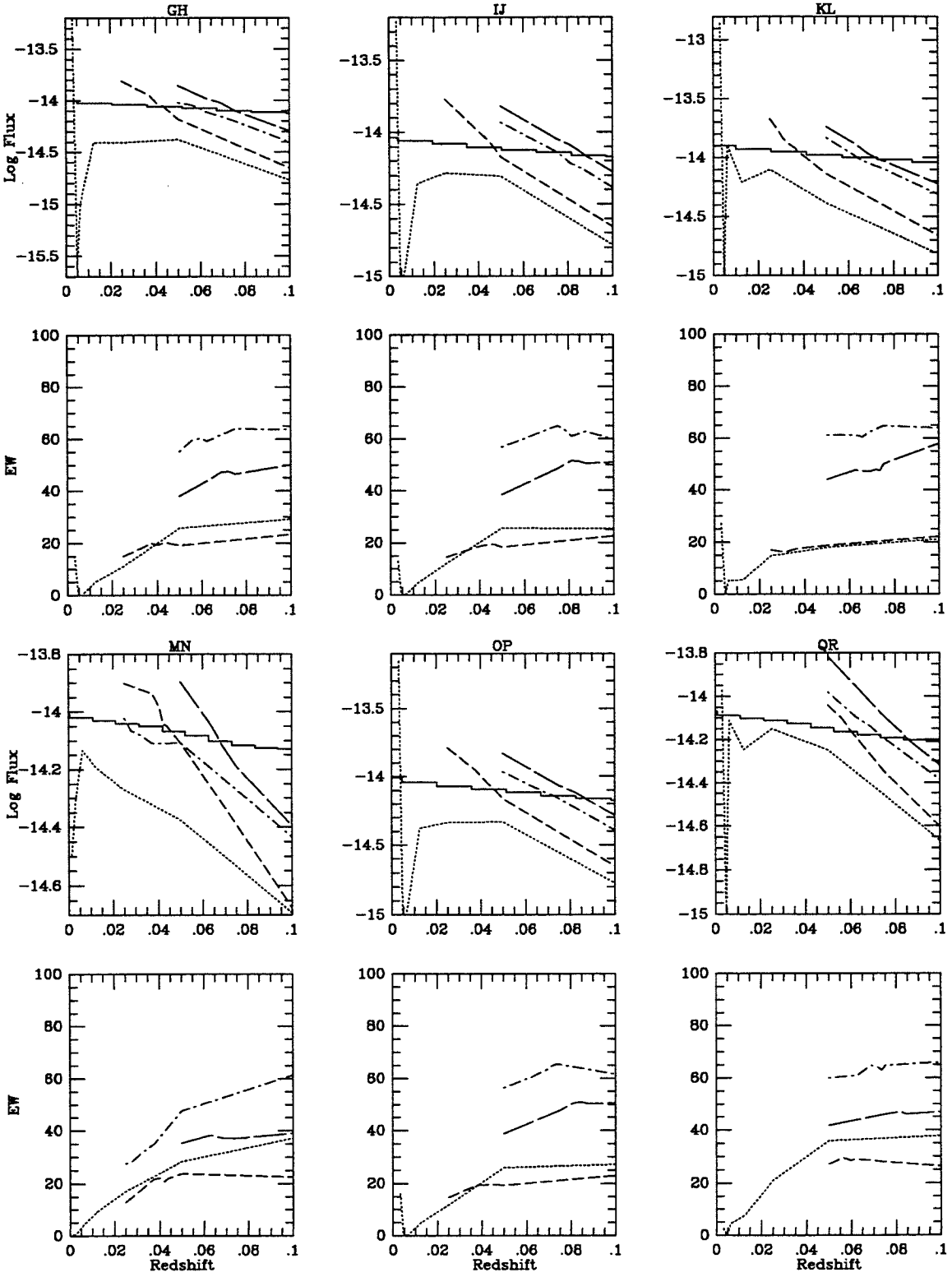

Figure B-70.

NGC 5107 MAJ/MINA

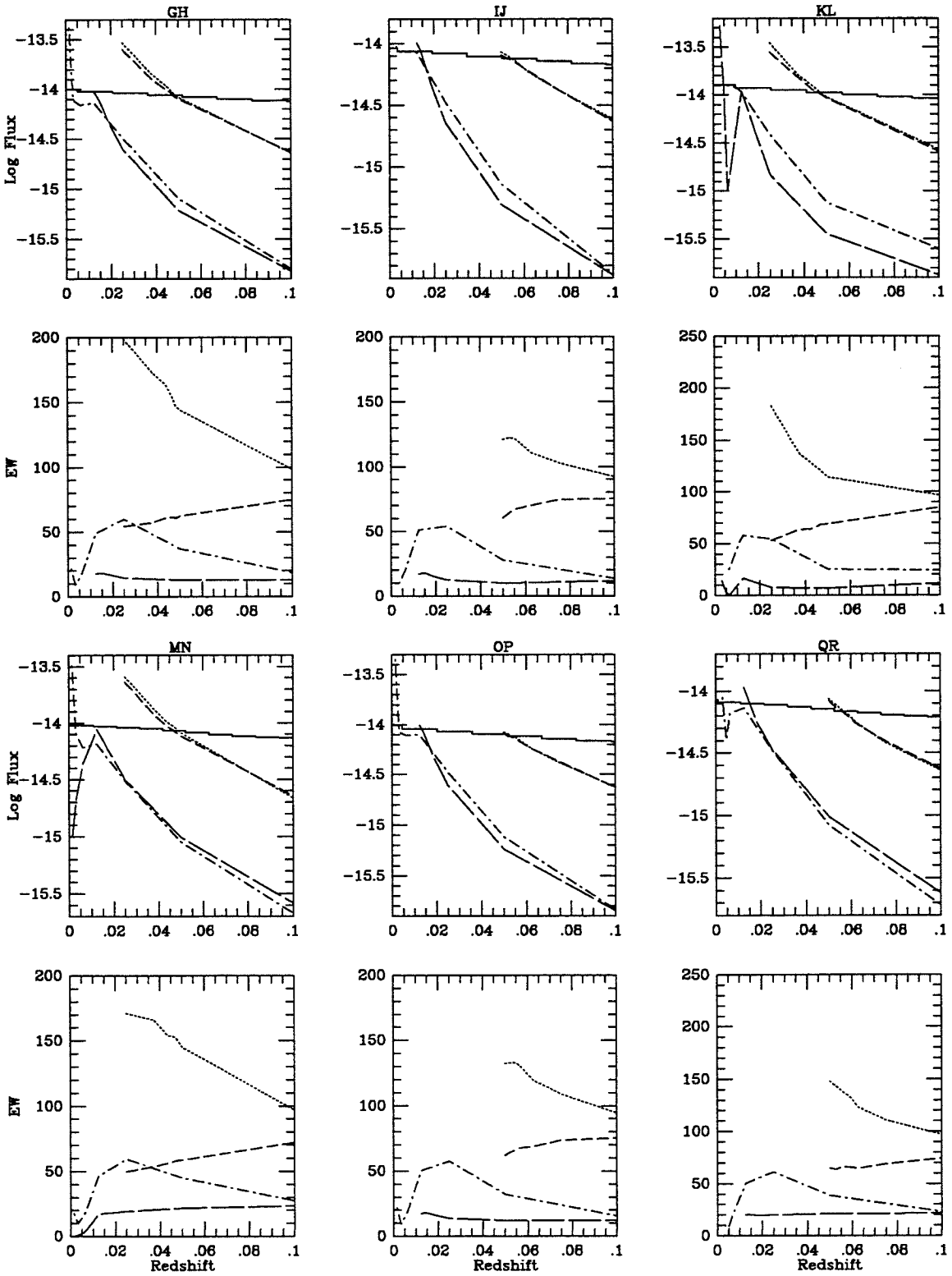

Figure B–71.a

NGC 5107 MAJ/MINB

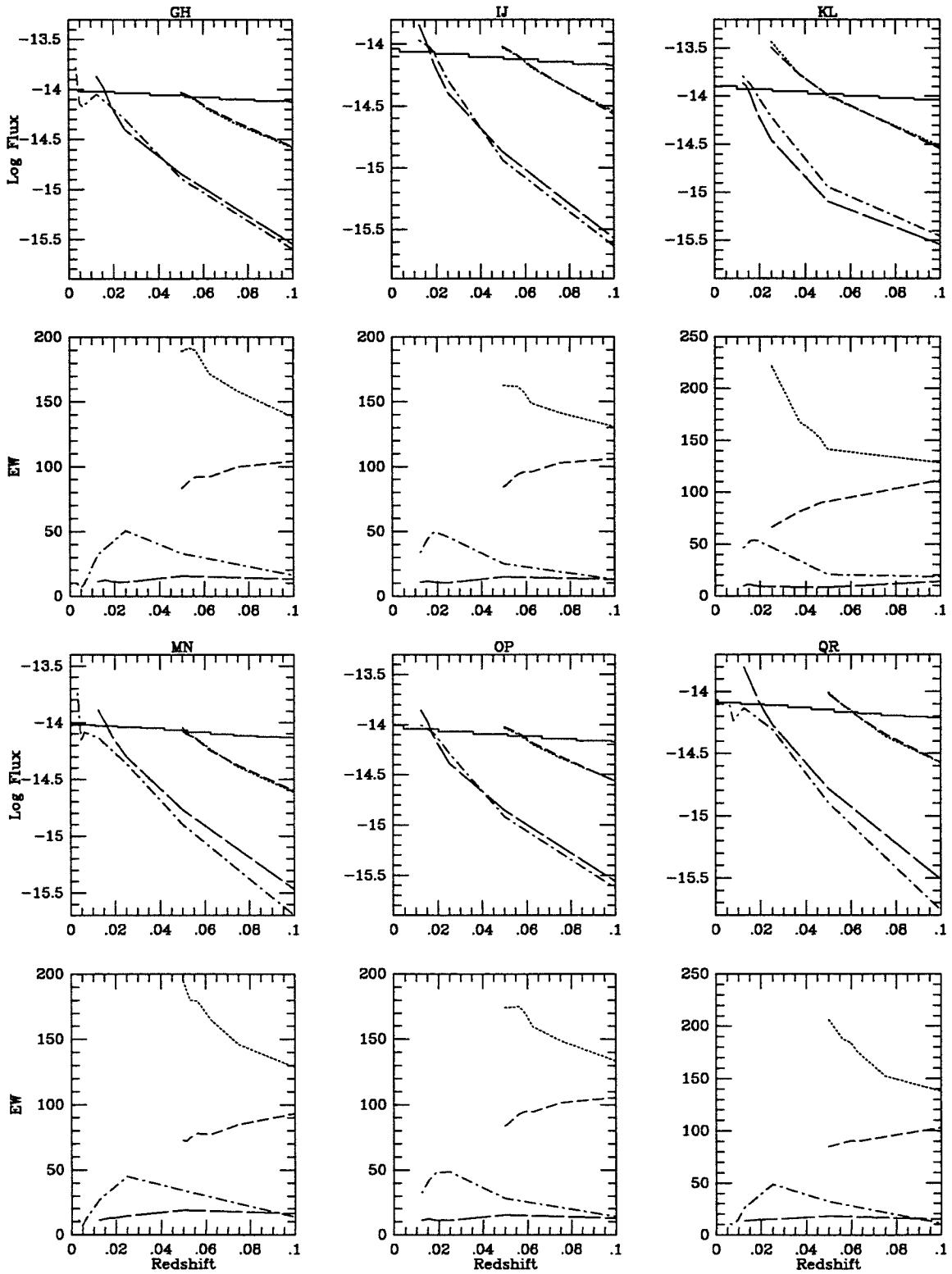

Figure B–71.b

1329+1122 MAJ/MIN

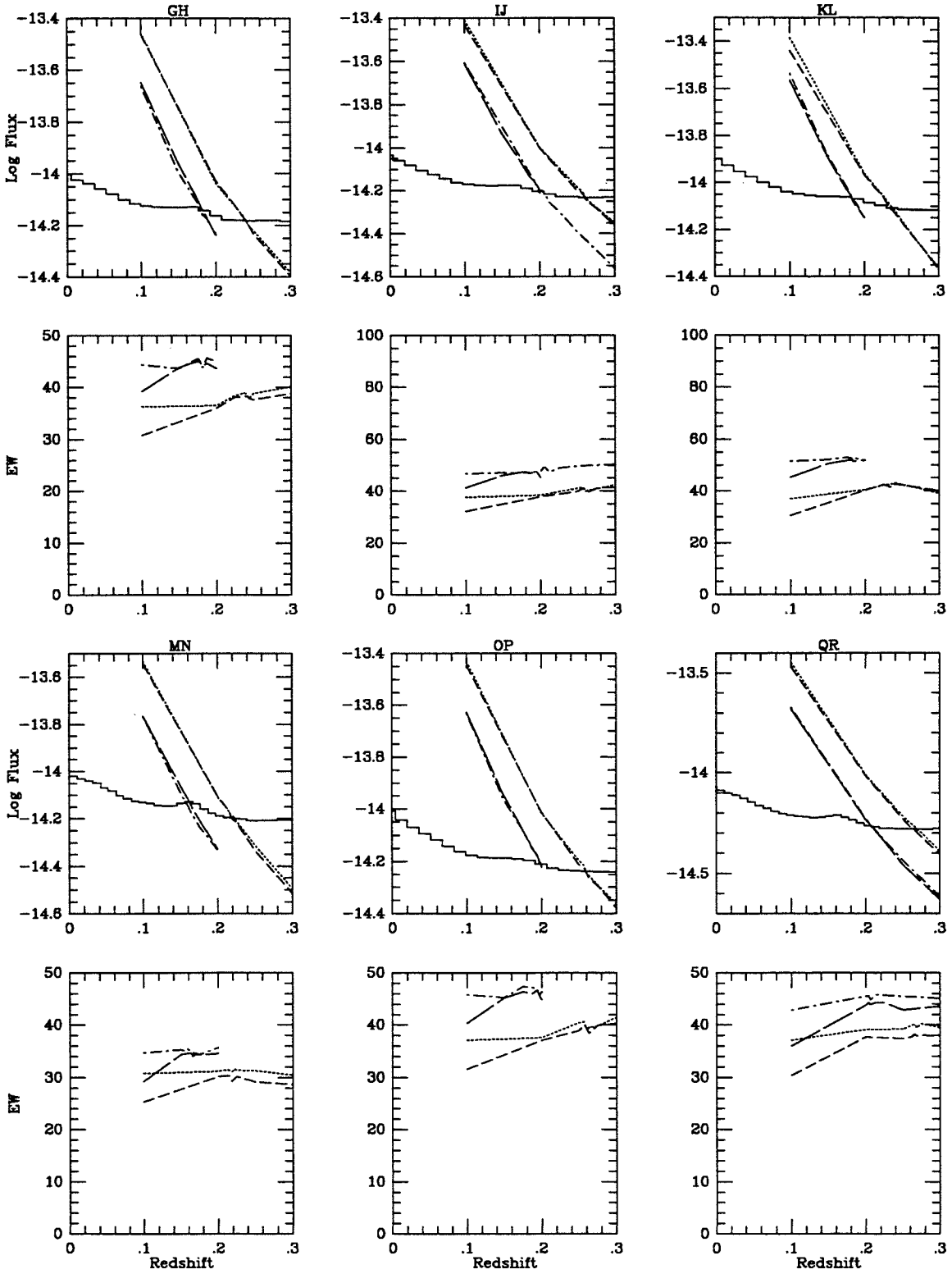

Figure B–72.

NGC 5238 MAJ/MINA

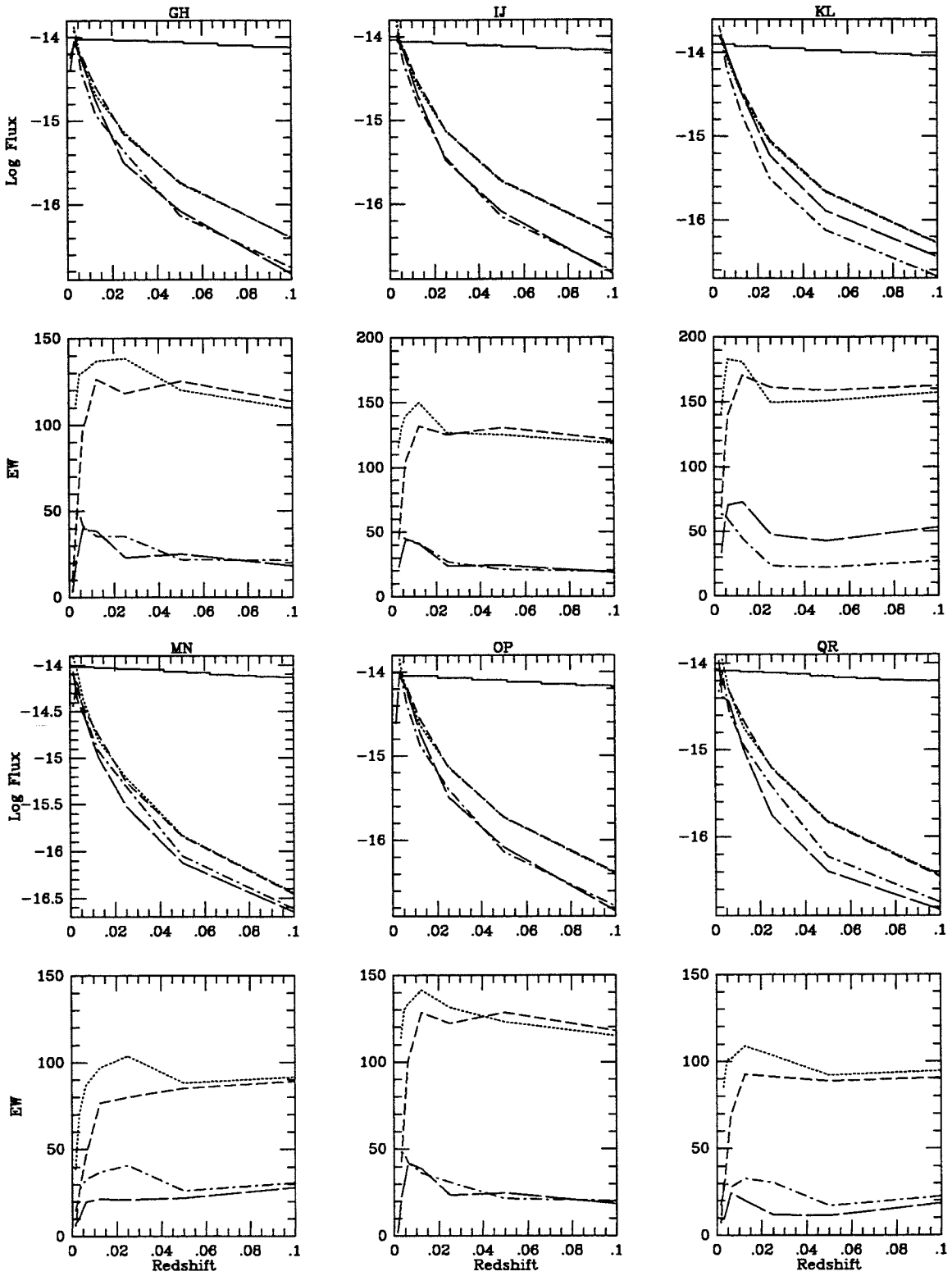

Figure B–73.a

NGC 5238 MAJ/MINB

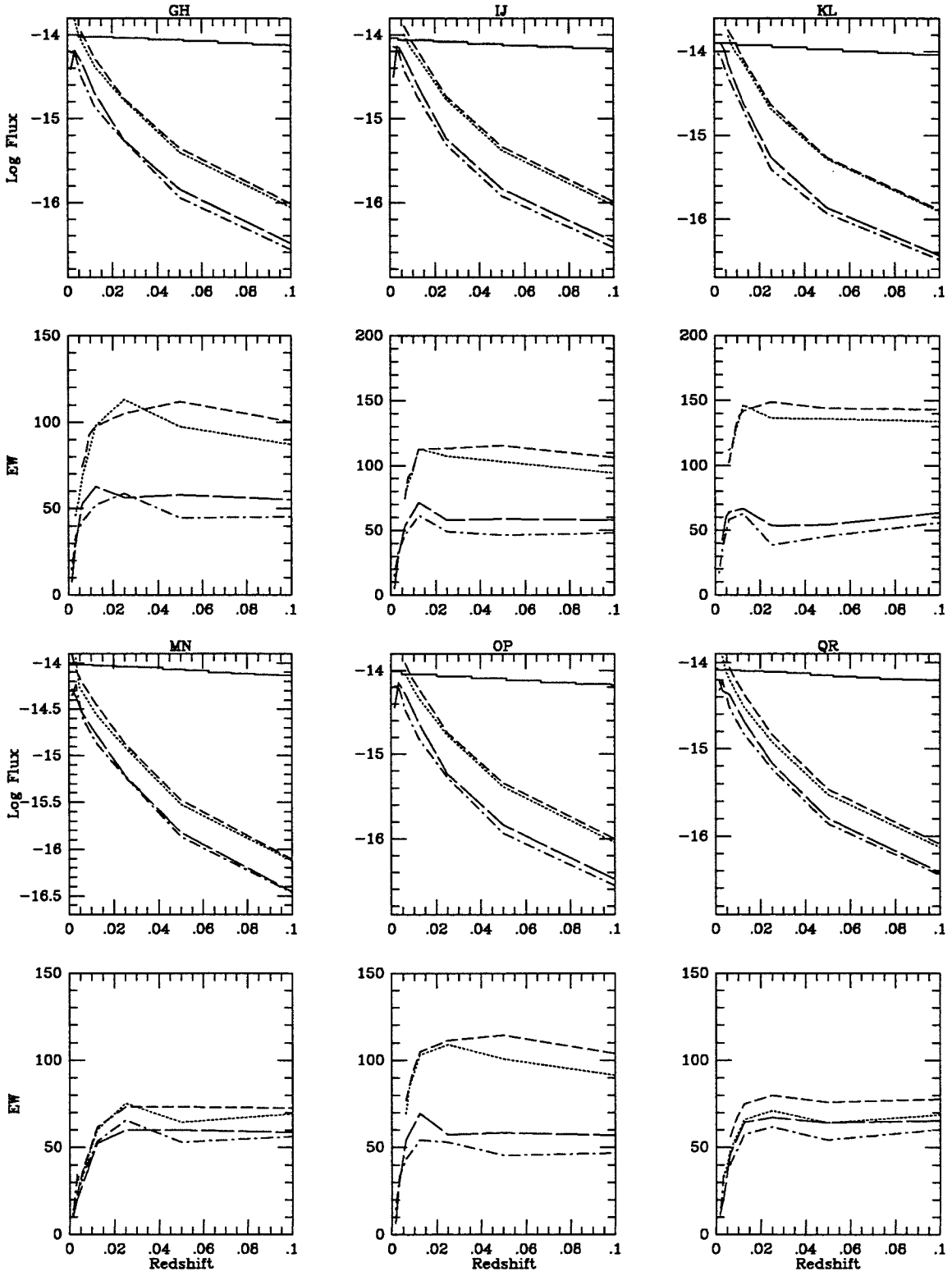

Figure B–73.b

1333+6215 MAJ/MIN

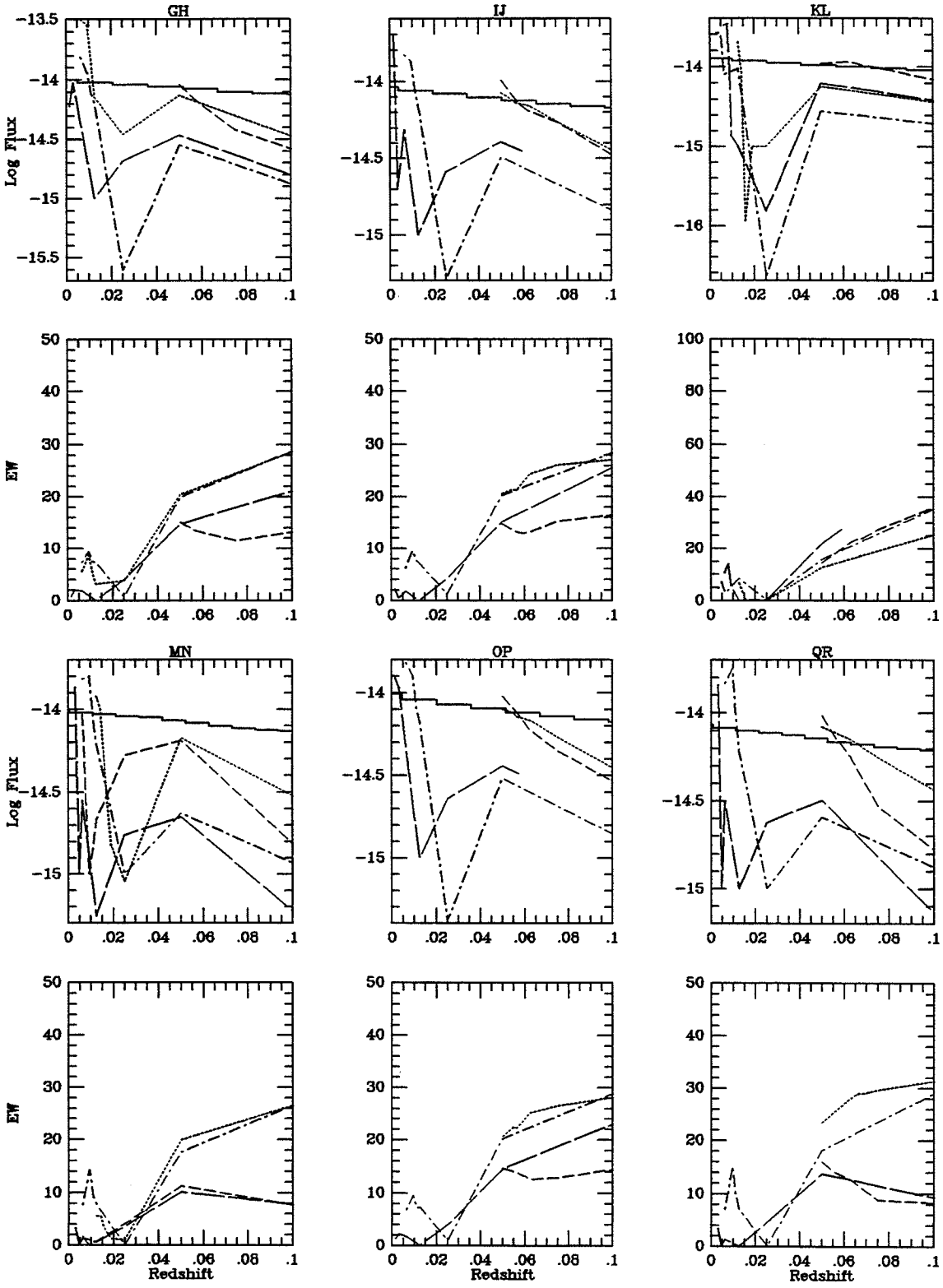

Figure B–74.

1335+3925 MAJ/MIN

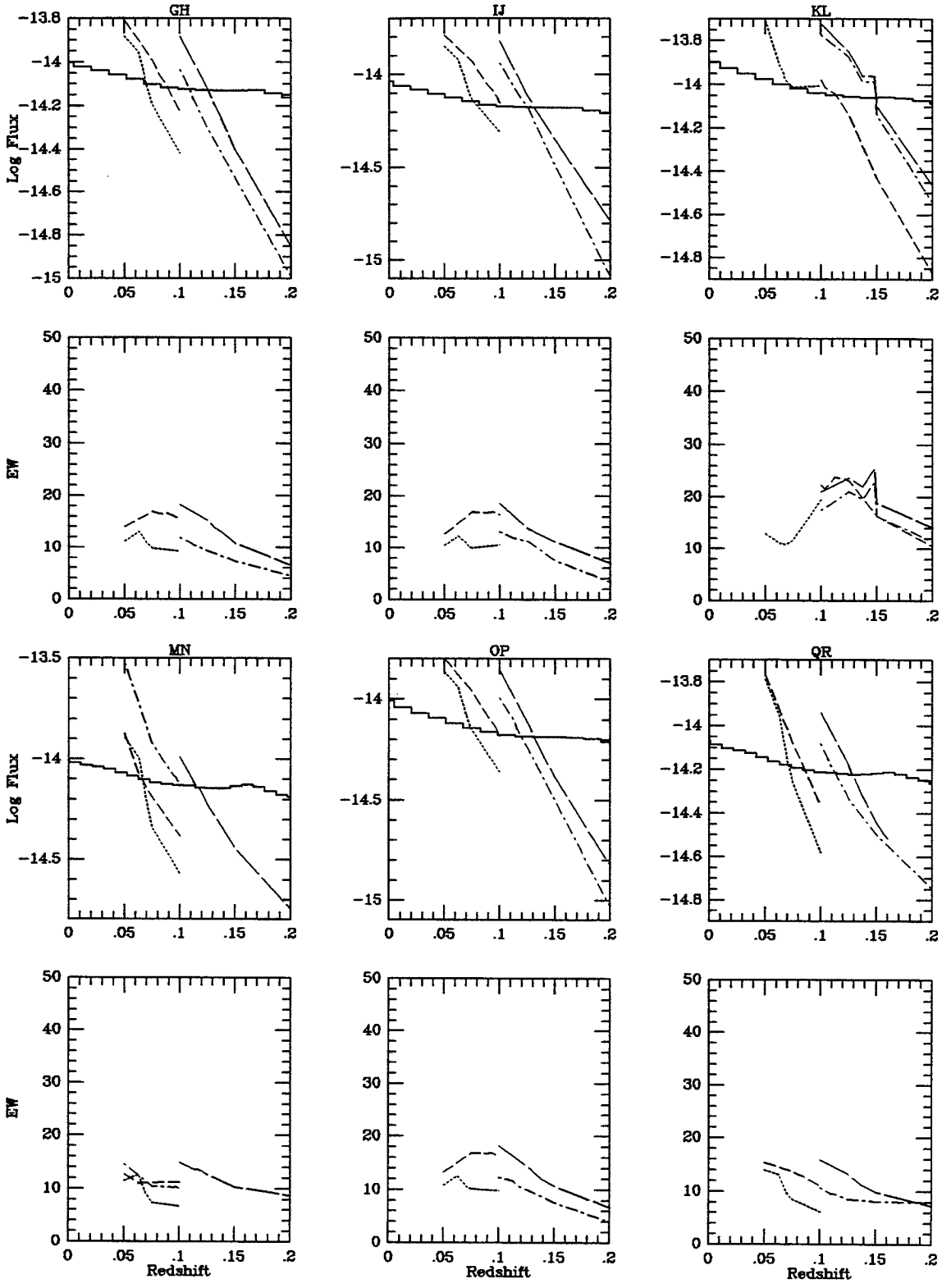

Figure B–75.

NGC 5252 MAJ/MIN

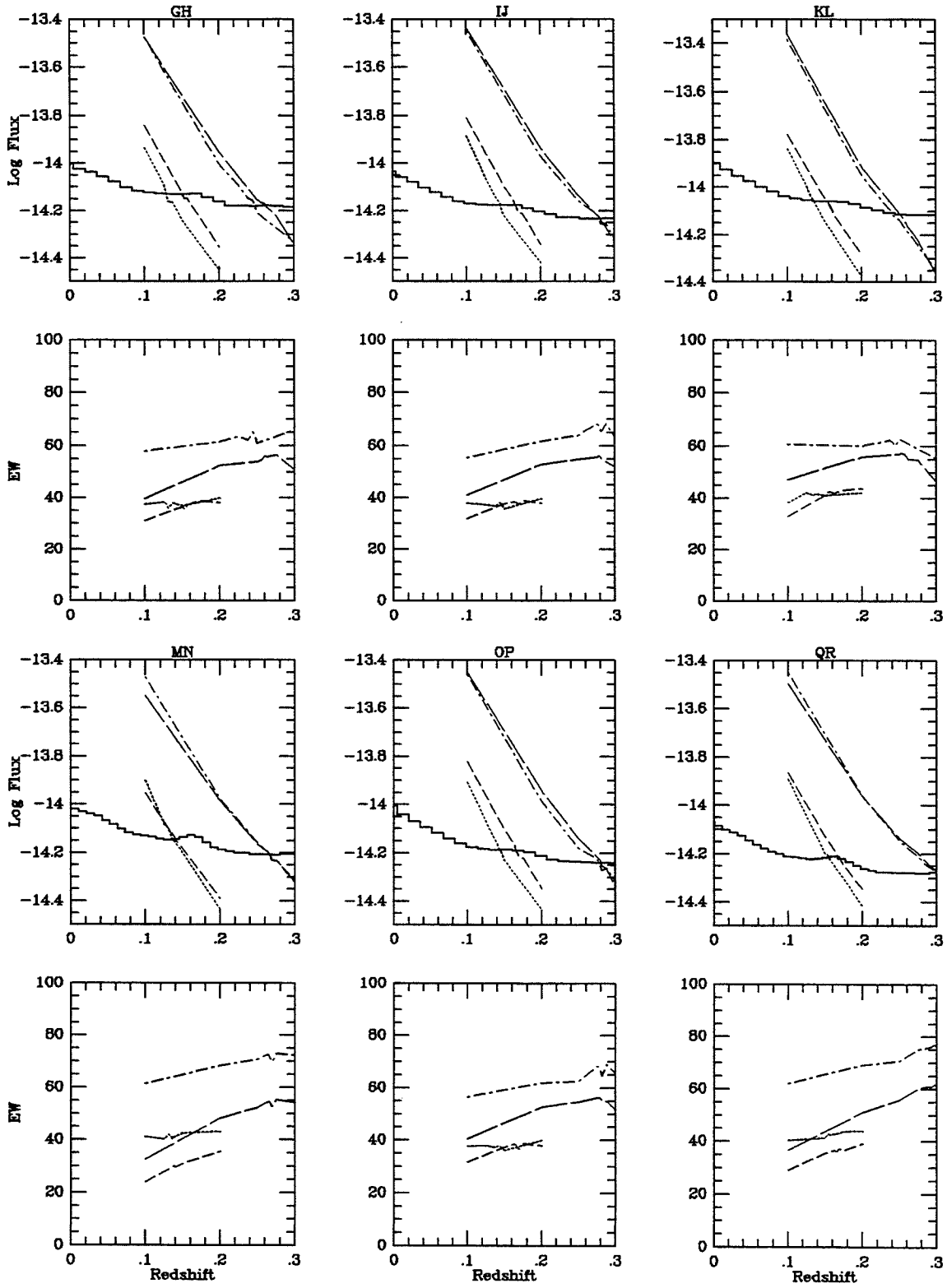

Figure B–76.

NGC 5256 MAJA/MIN

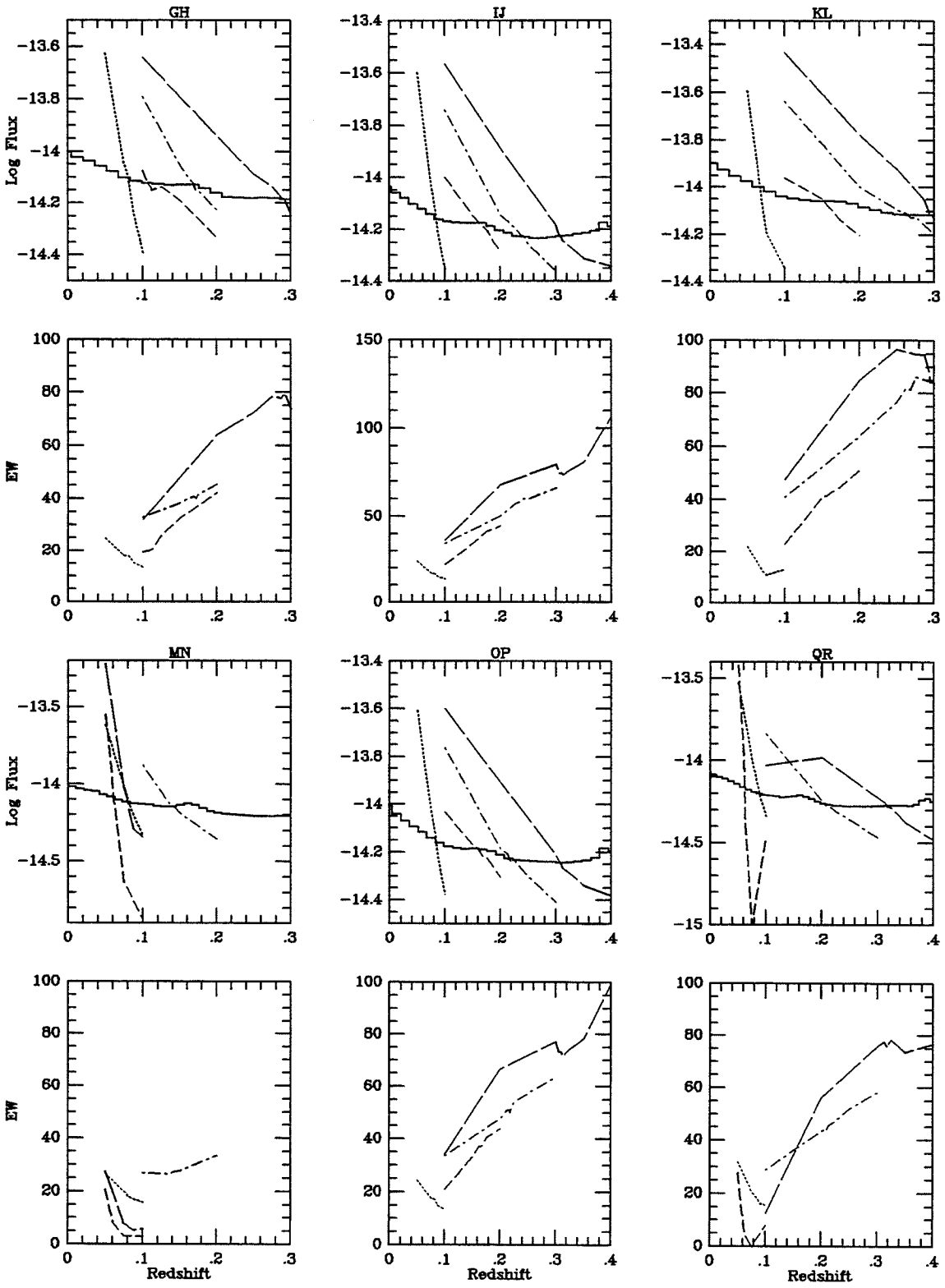

Figure B-77.a

NGC 5256 MAJB/MIN

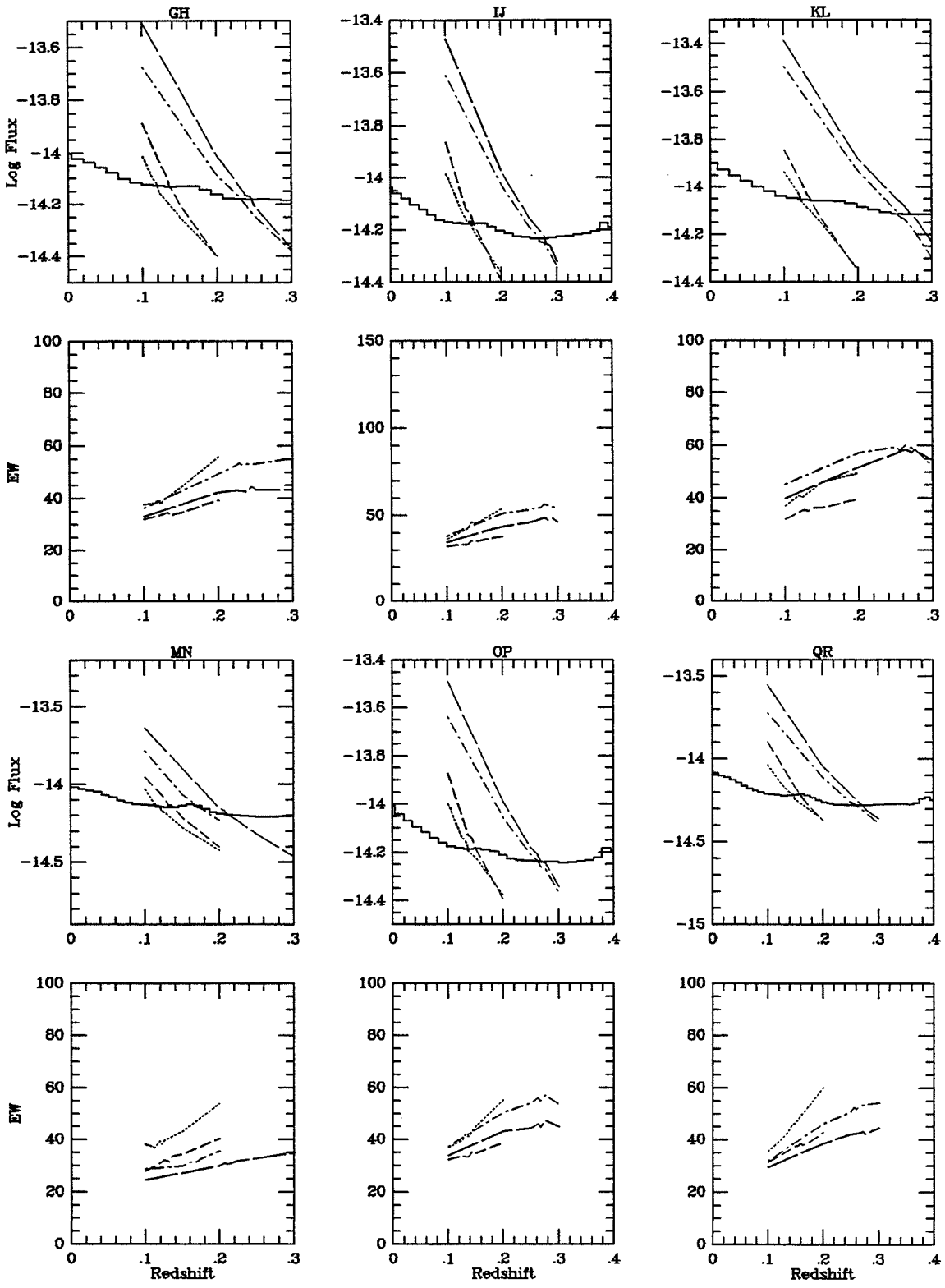

Figure B–77.b

NGC 5283 MAJ/MIN

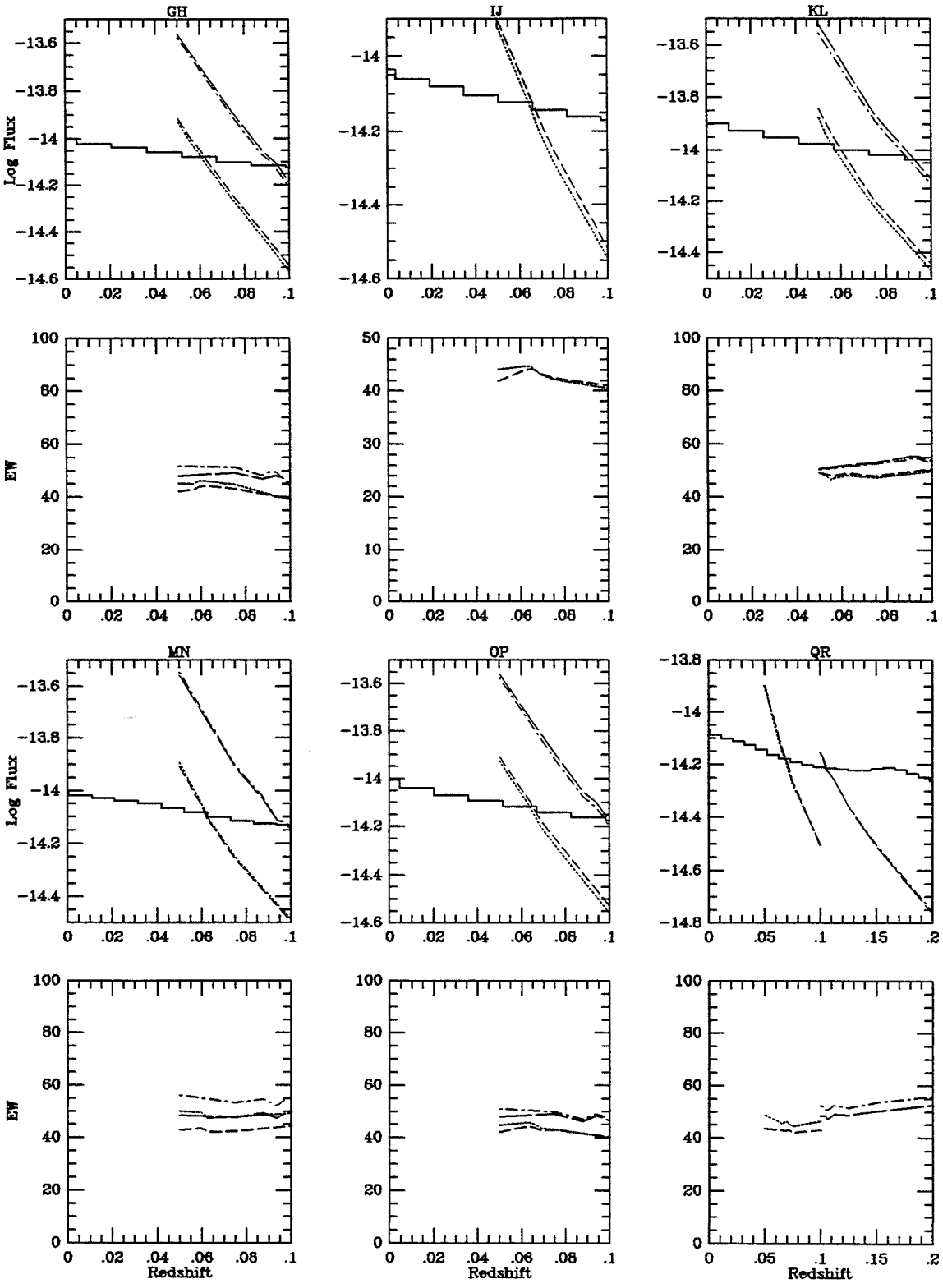

Figure B–78.

NGC 5273 MAJ/MIN

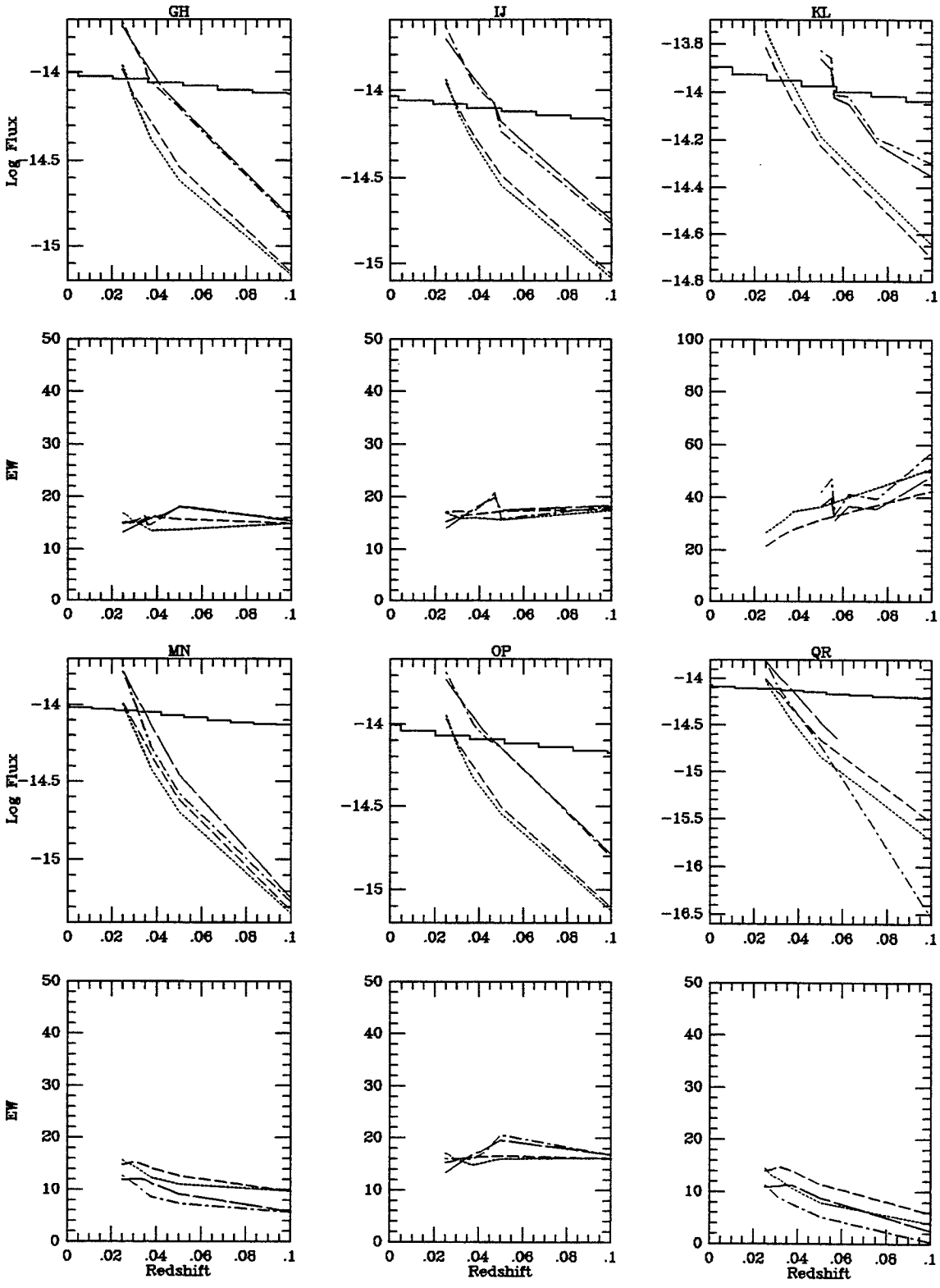

Figure B–79.

1345+3424 MAJ/MIN

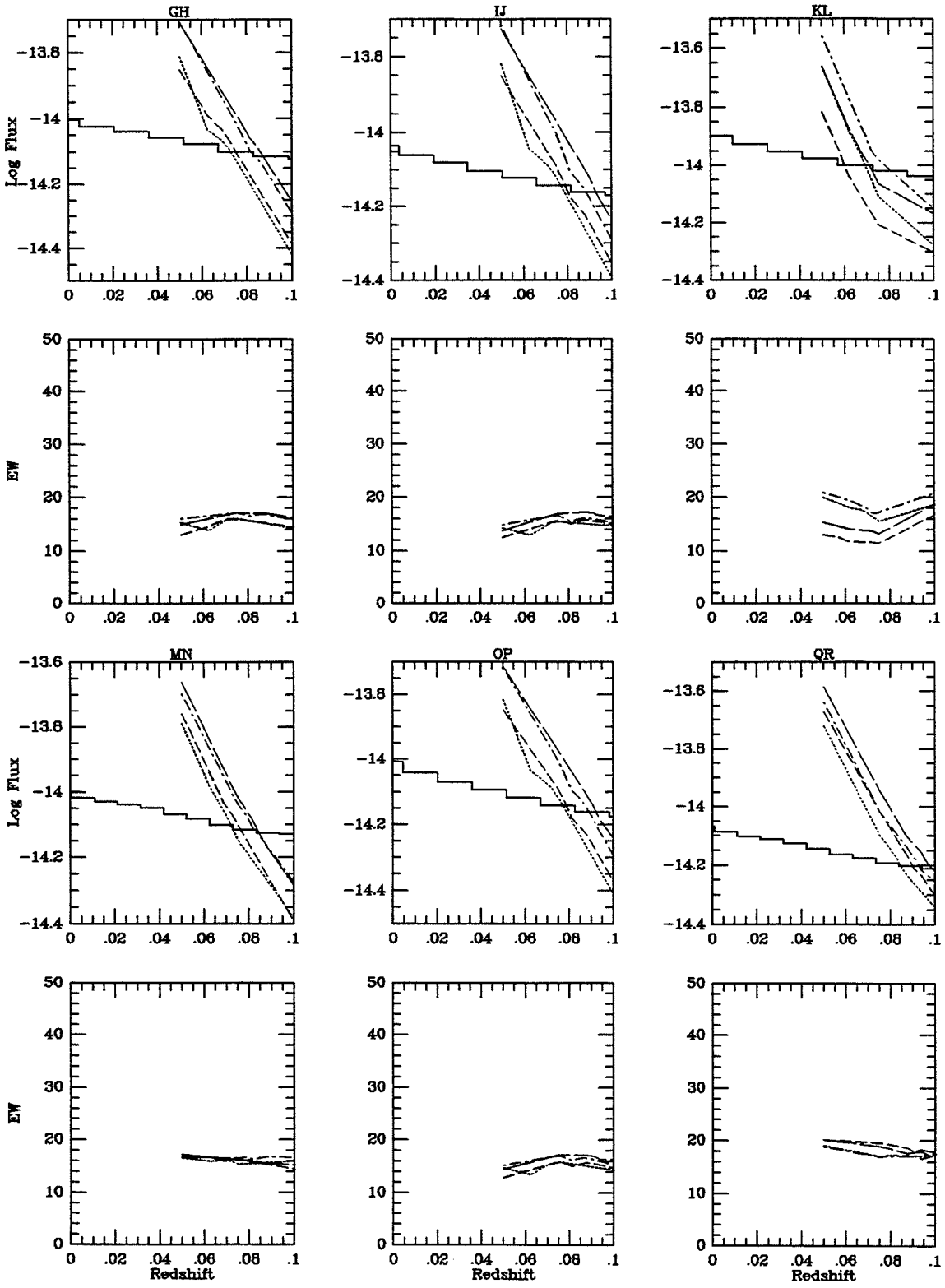

Figure B–80.

1351+6933 MAJ/MIN

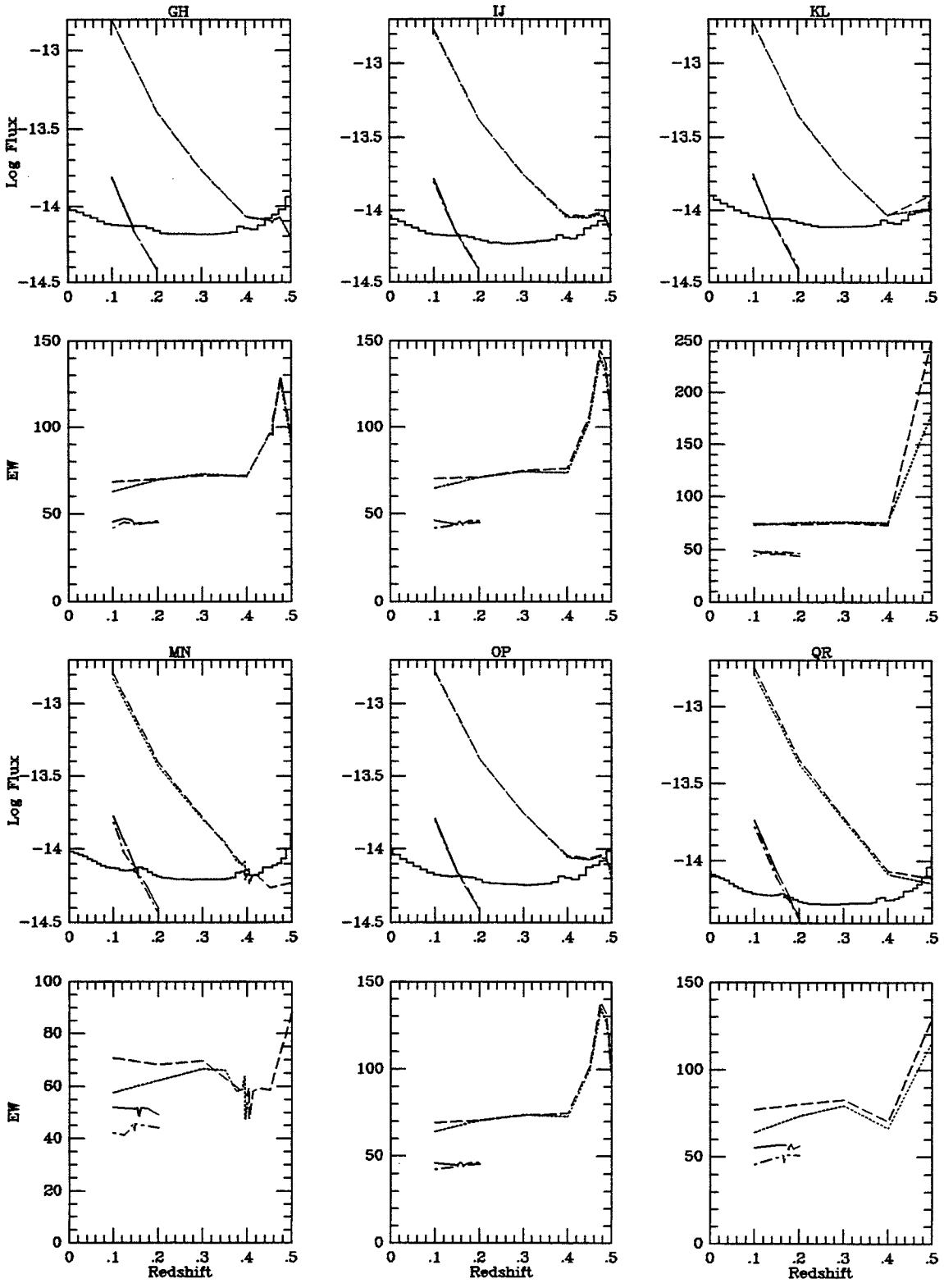

Figure B–81.

1407+4916 MAJ/MIN

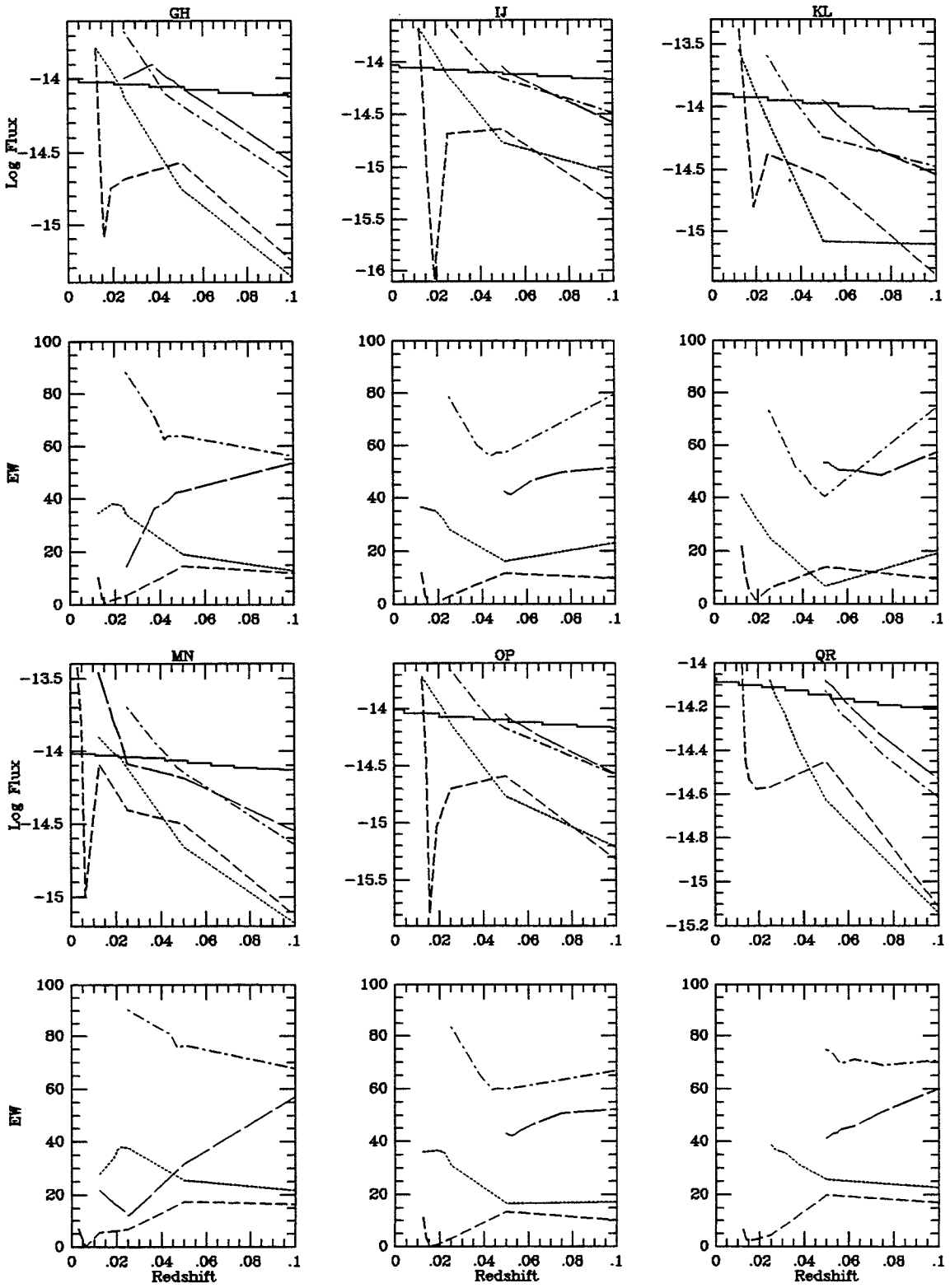

Figure B–82.

IC 4397 MAJ/MIN

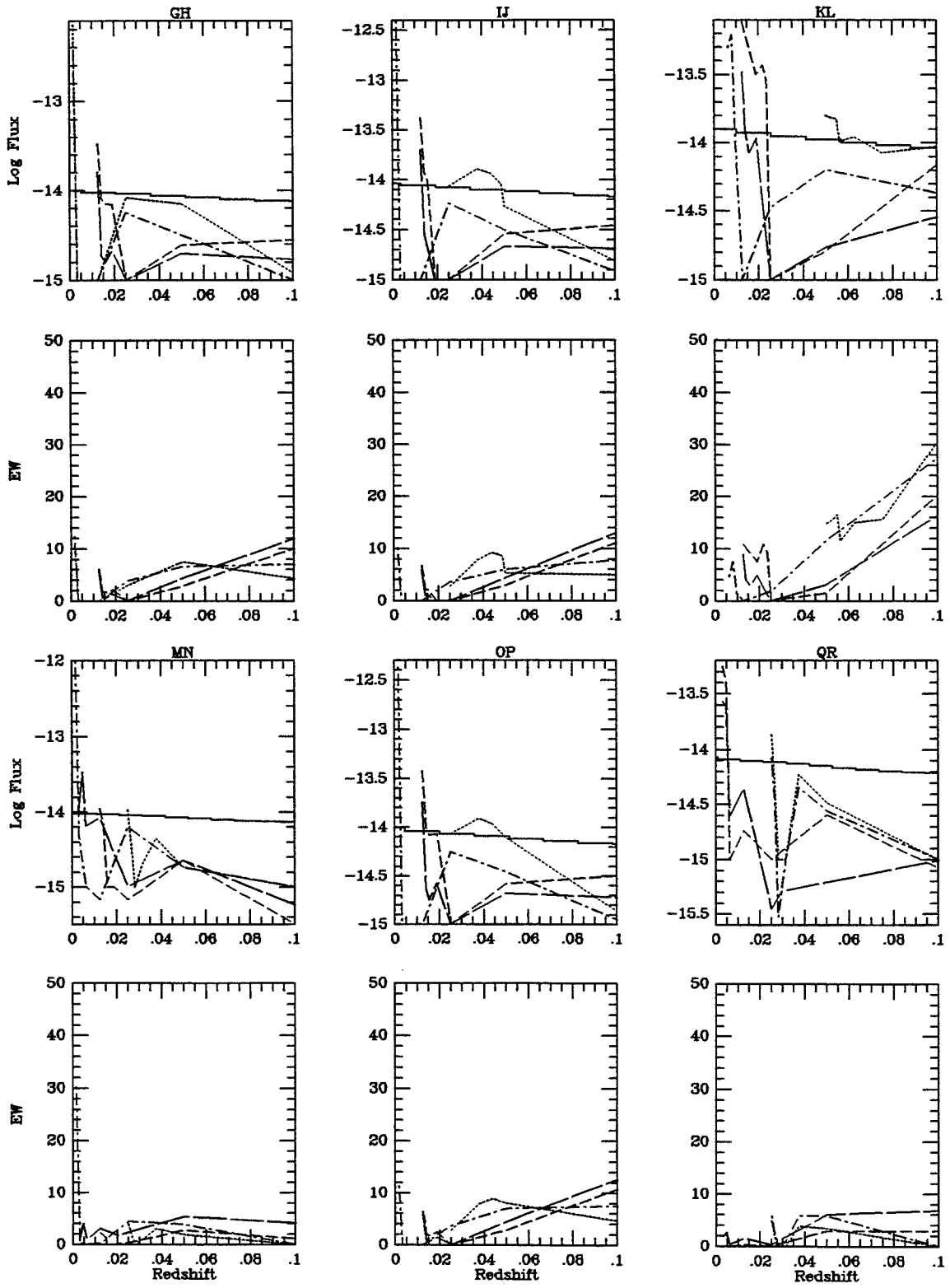

Figure B-83.

NGC 5548 MAJ/MIN

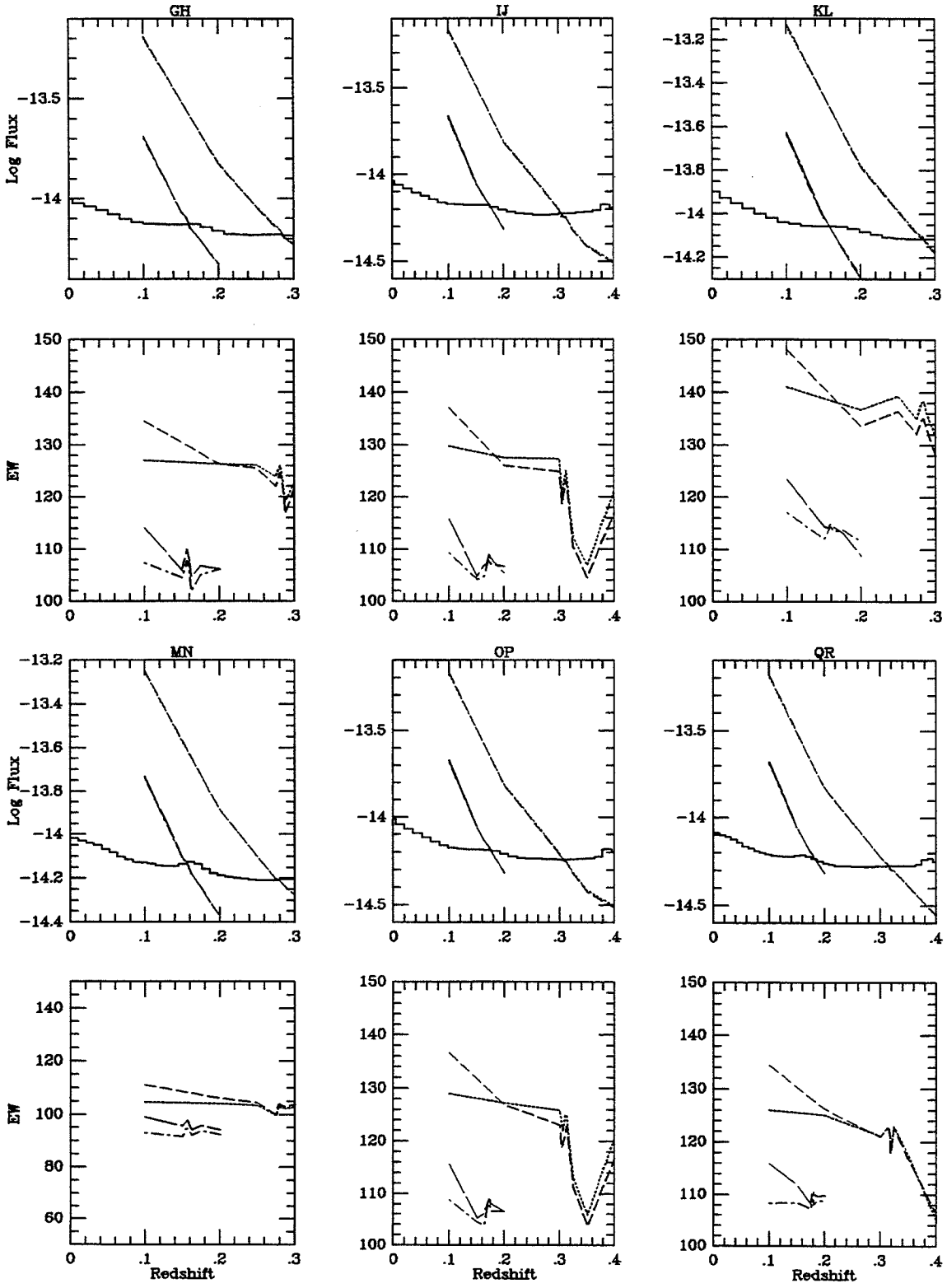

Figure B–84.

NGC 5674 MAJA/MIN

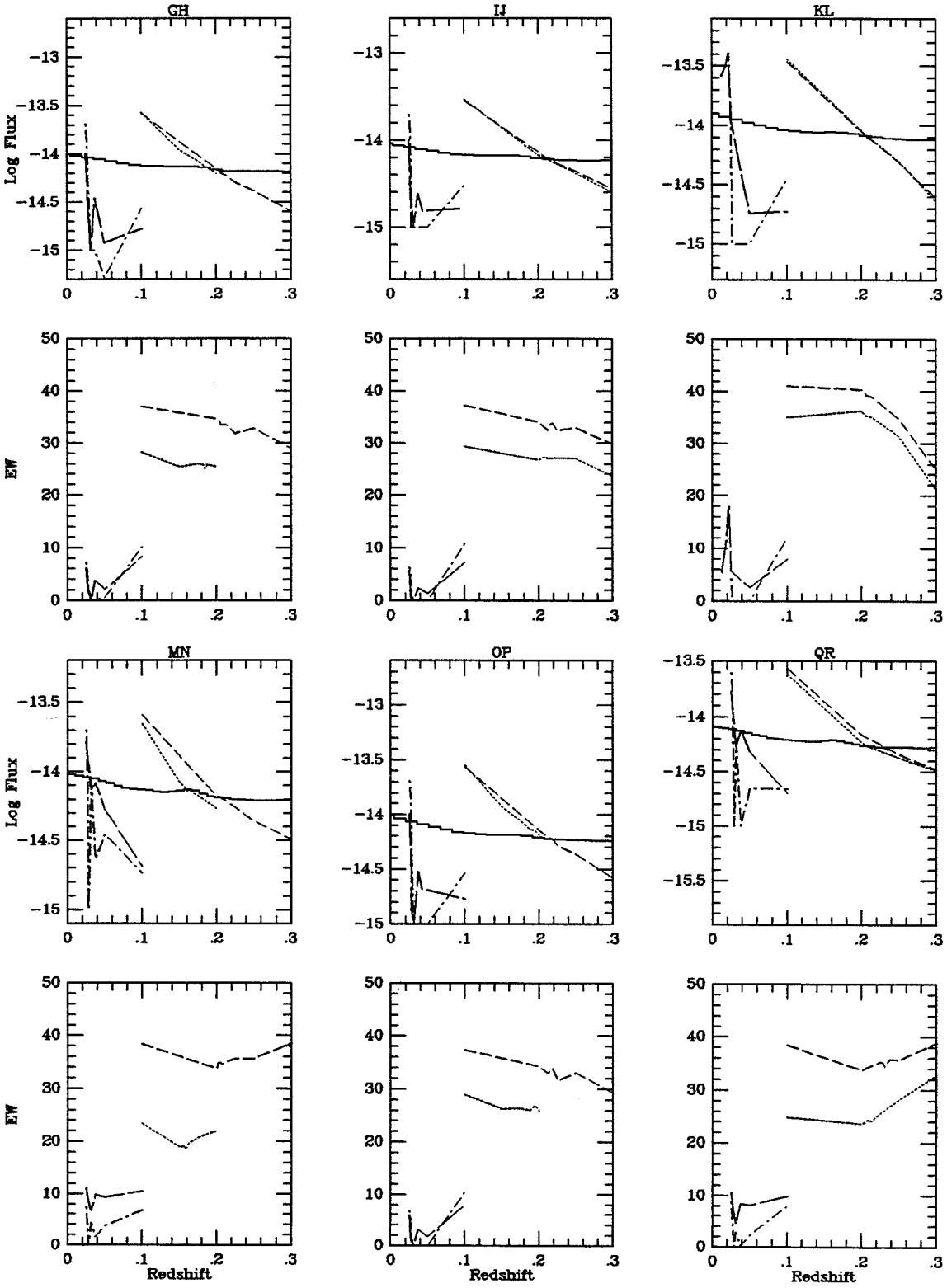

Figure B–85.a

NGC 5674 MAJB/MIN

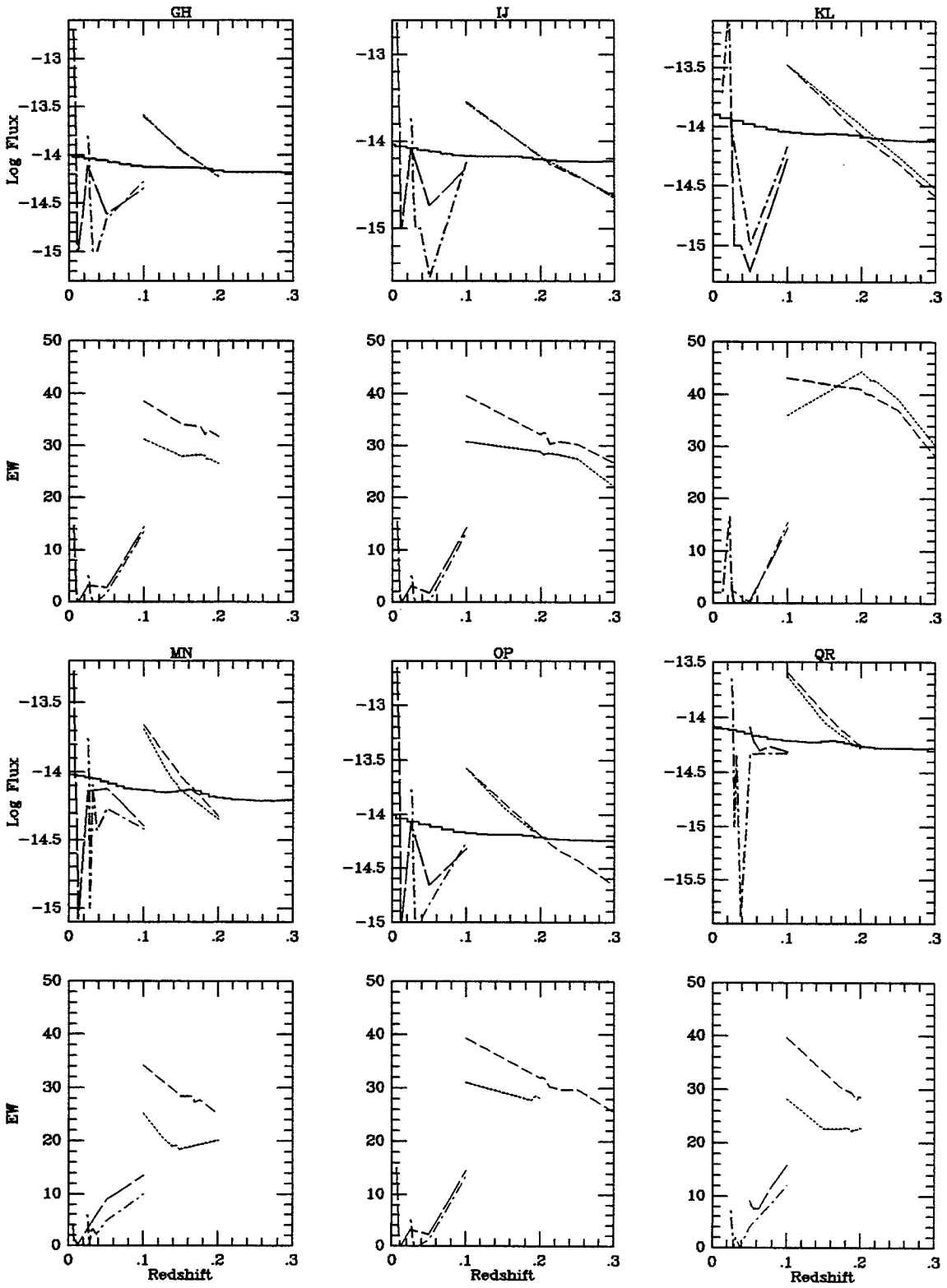

Figure B–85.b

1434+5901 MAJ/MIN

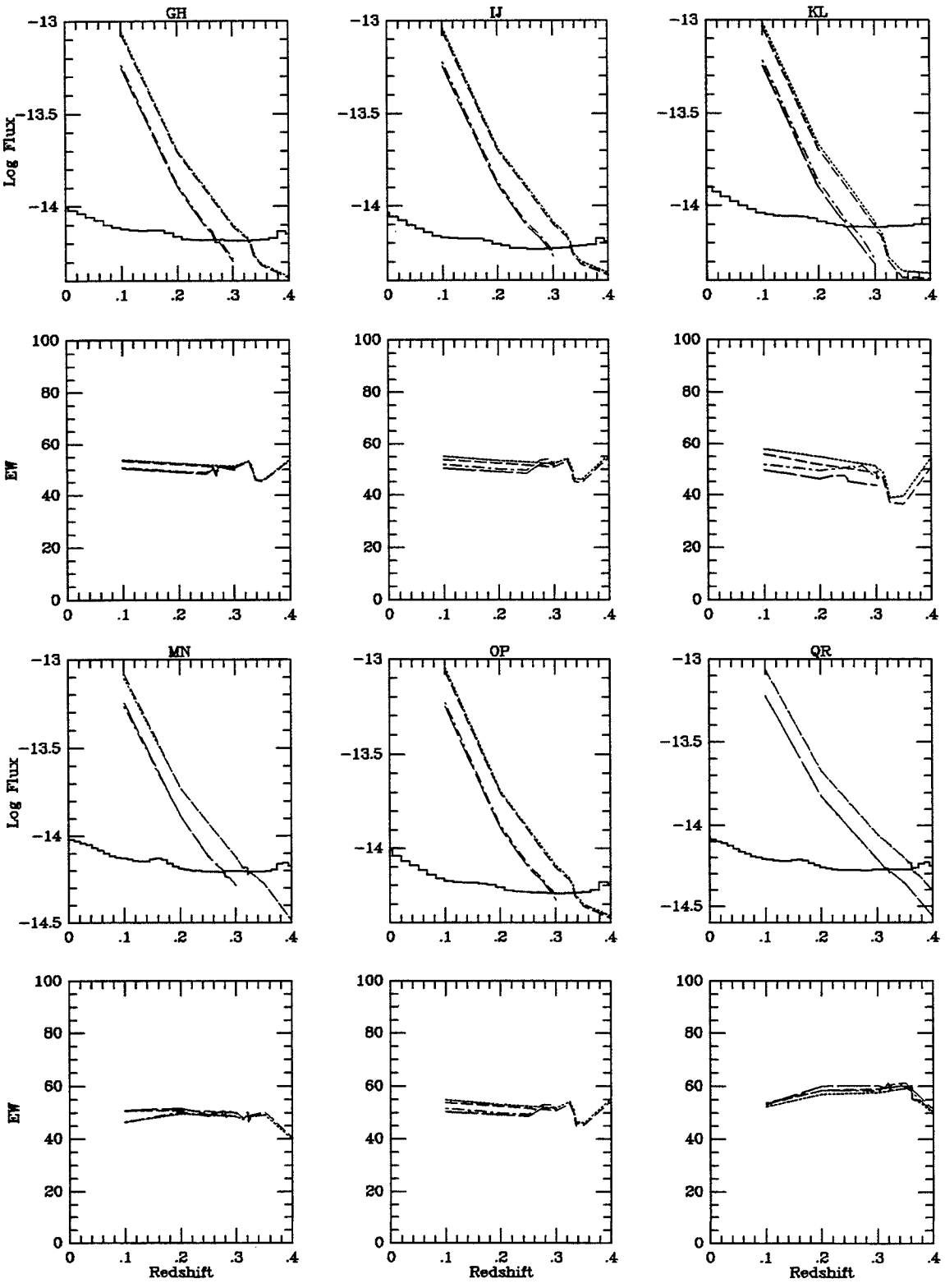

Figure B–86.

NGC 5695 MAJA/MIN

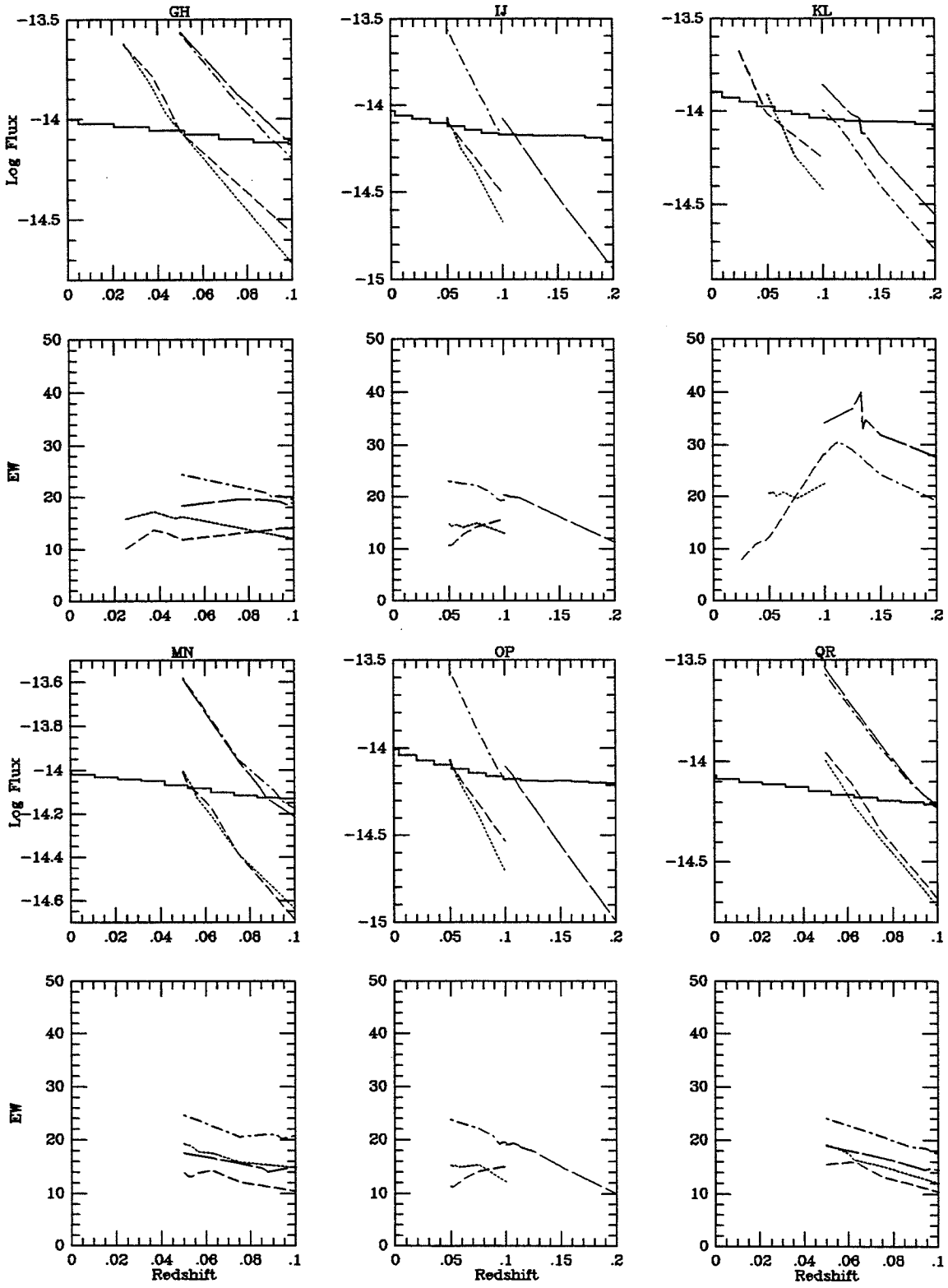

Figure B–87.a

NGC 5695 MAJB/MIN

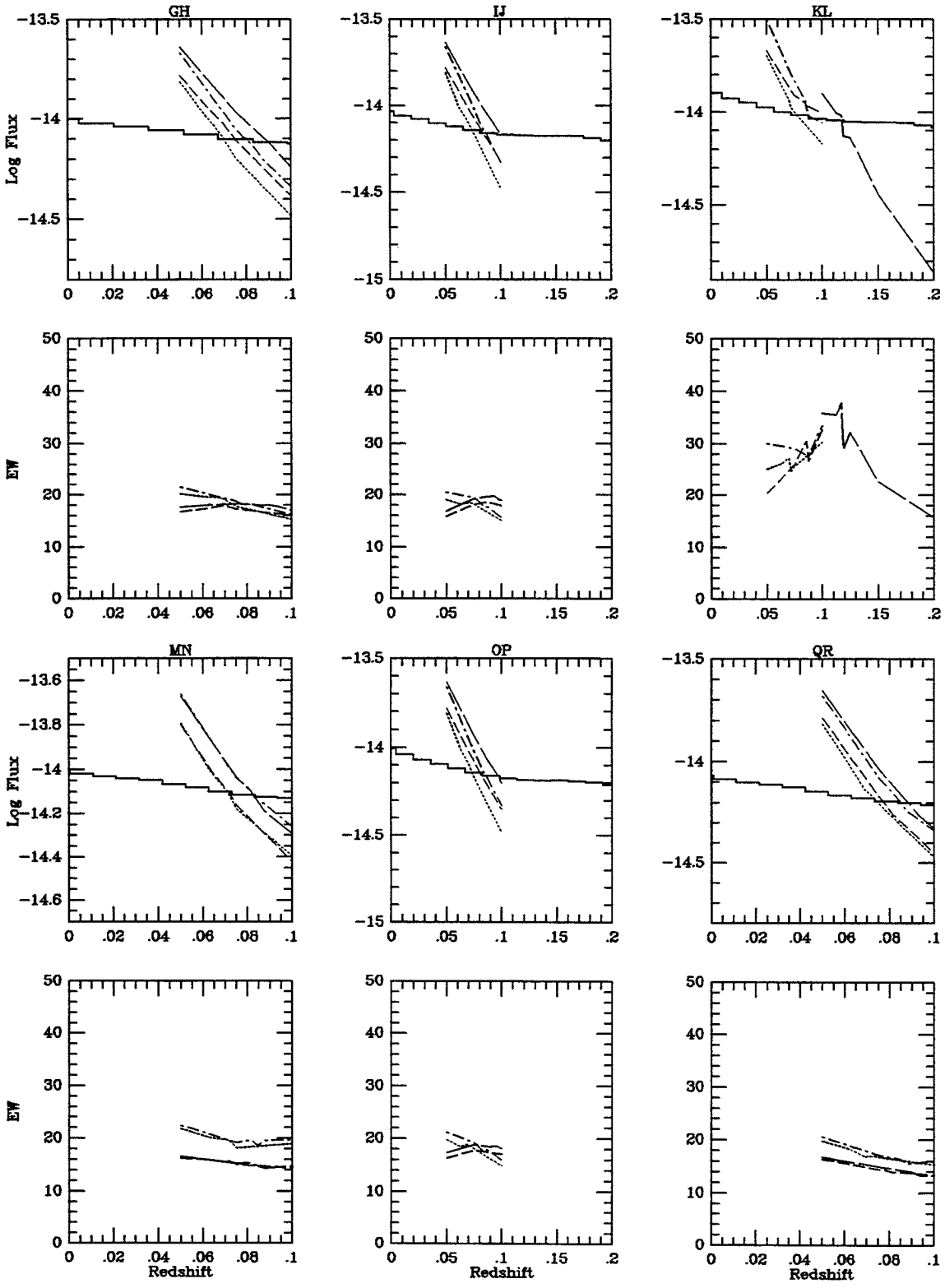

Figure B–87.b

1448+3547 MAJ/MIN

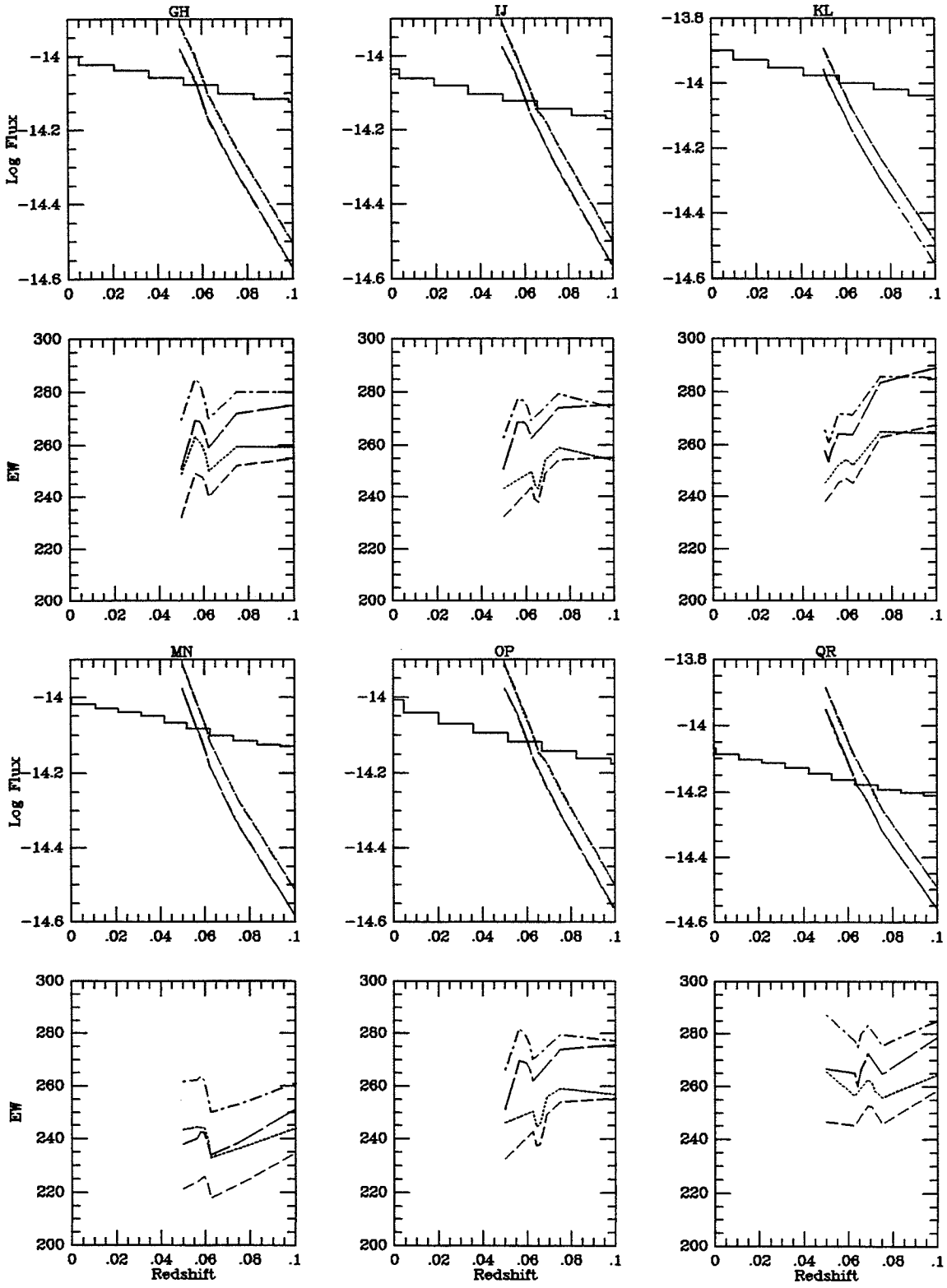

Figure B-88.

NGC 5789 MAJ/MINA

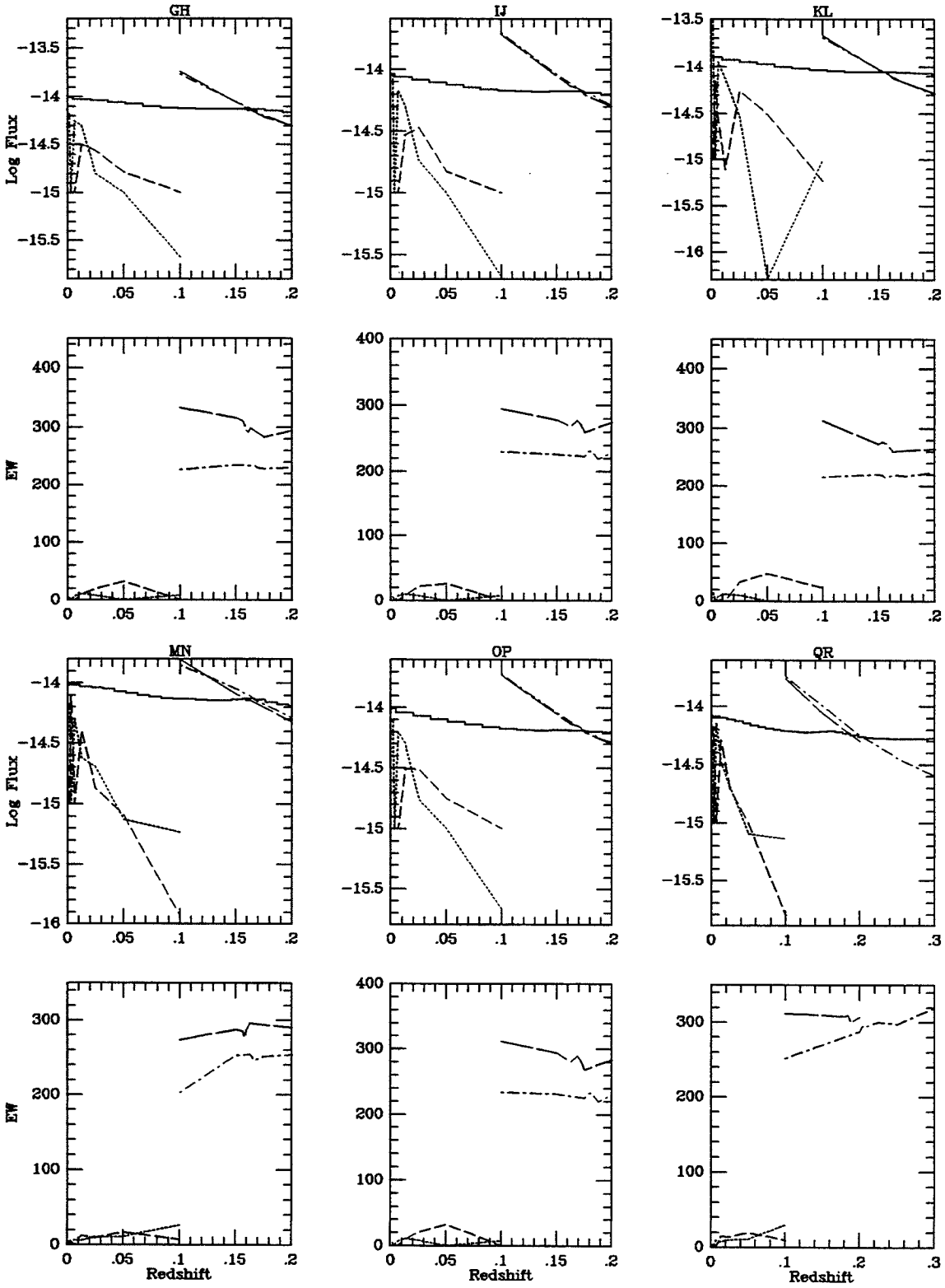

Figure B–89.a

NGC 5789 MAJ/MINB

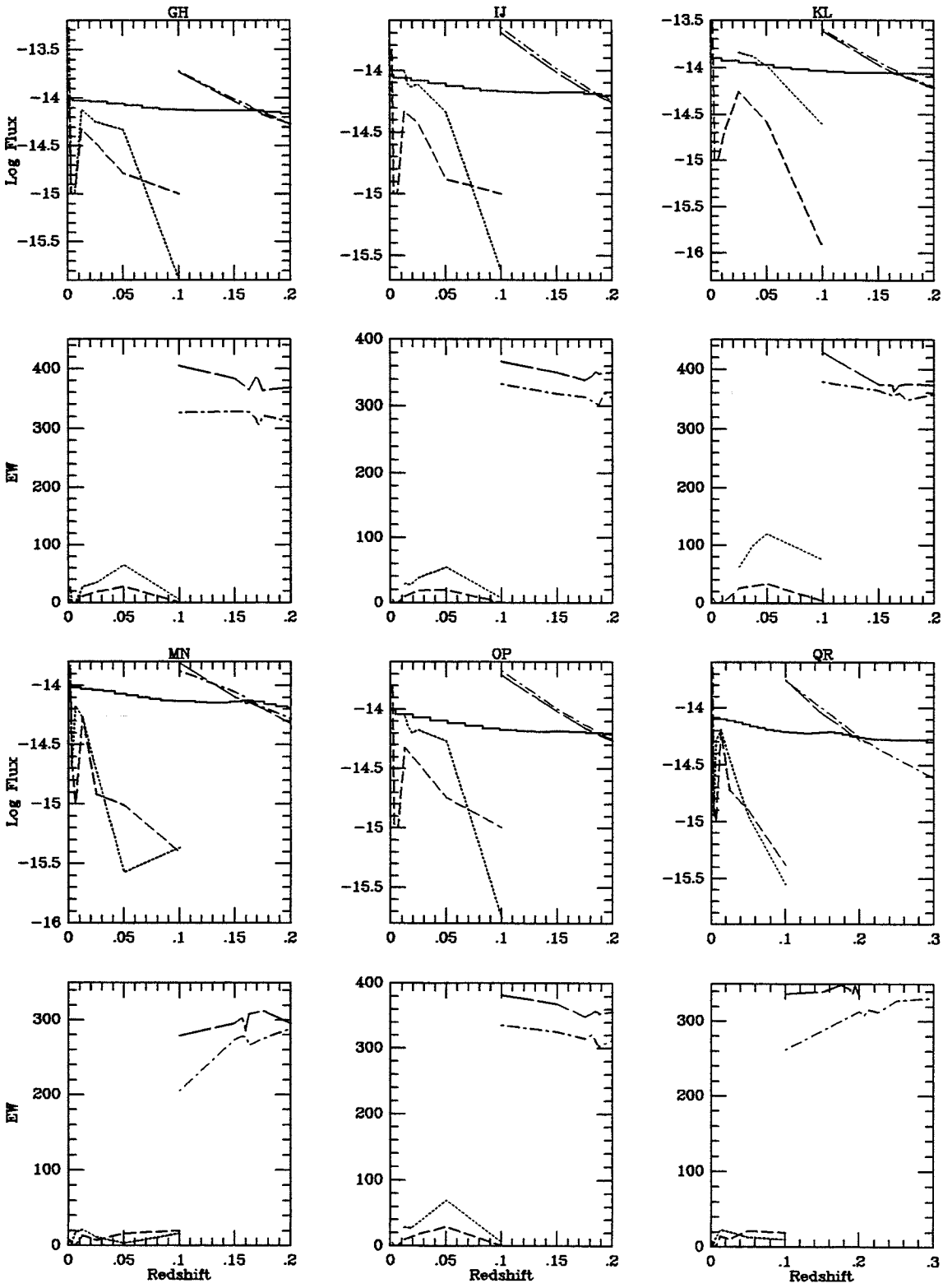

Figure B–89.b

1501+1038 MAJA/MIN

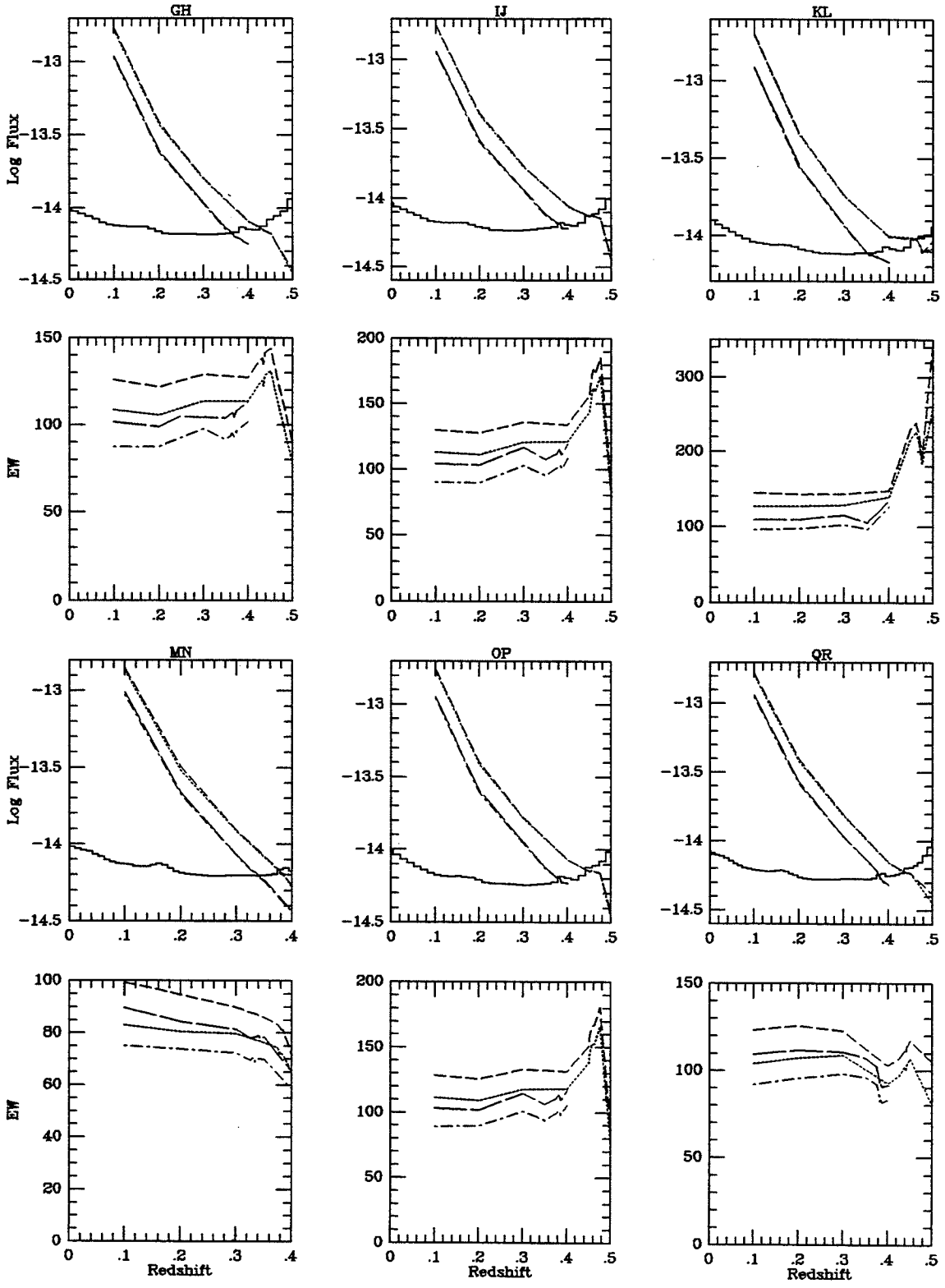

Figure B-90.a

1501+1038 MAJB/MIN

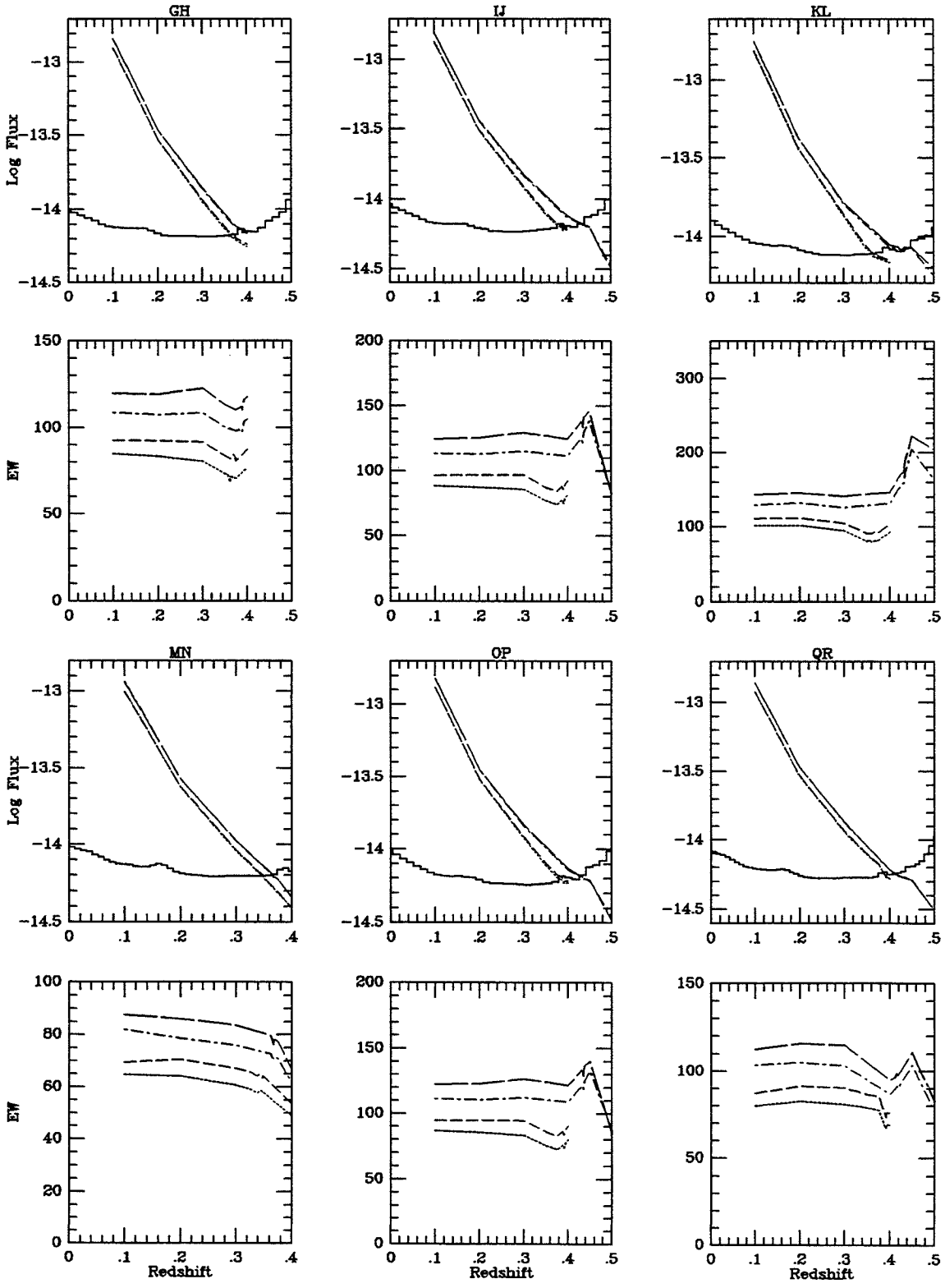

Figure B–90.b

1501+1038 MAJC/MIN

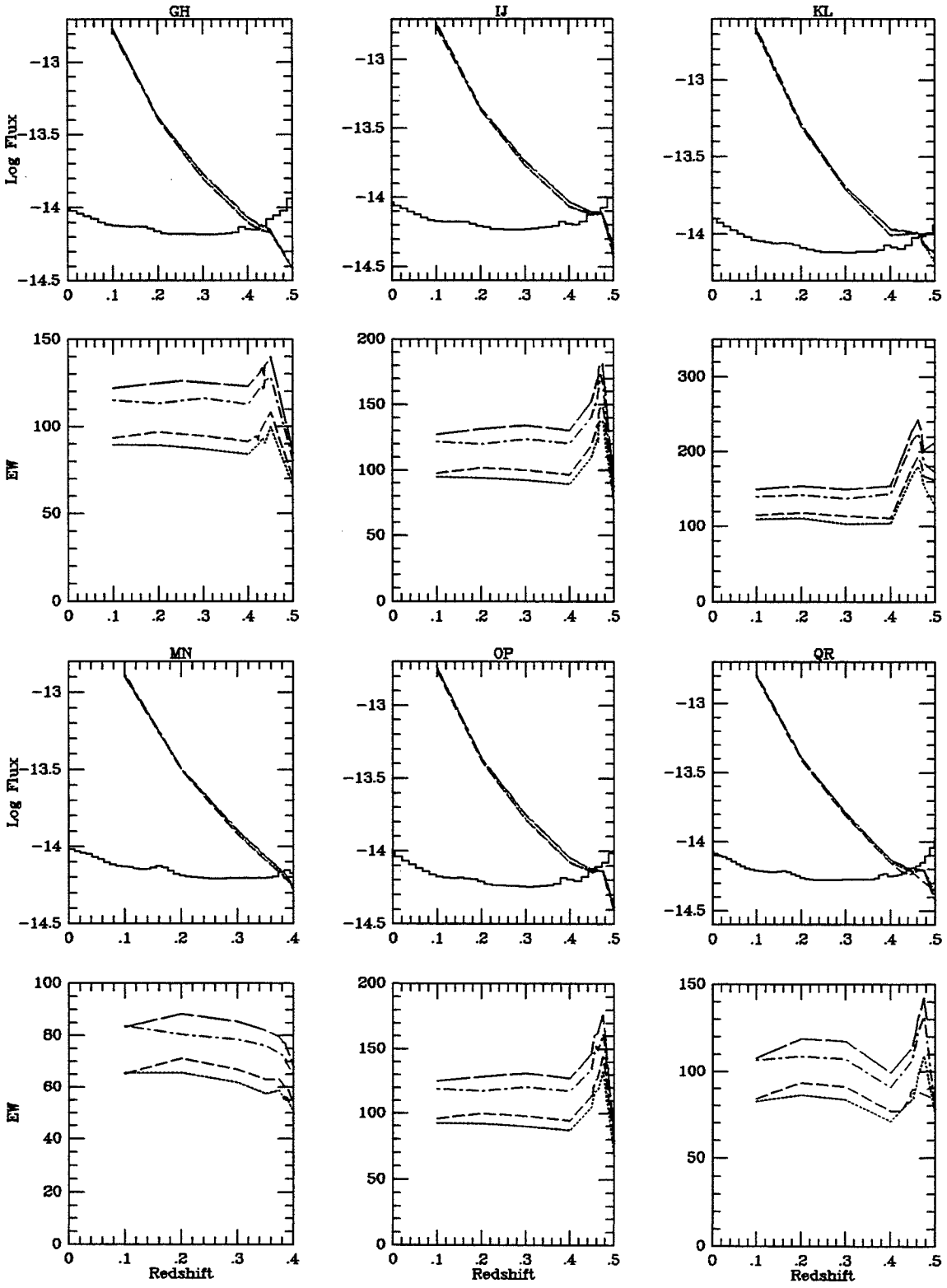

Figure B–90.c

NGC 5899 MAJ/MINA

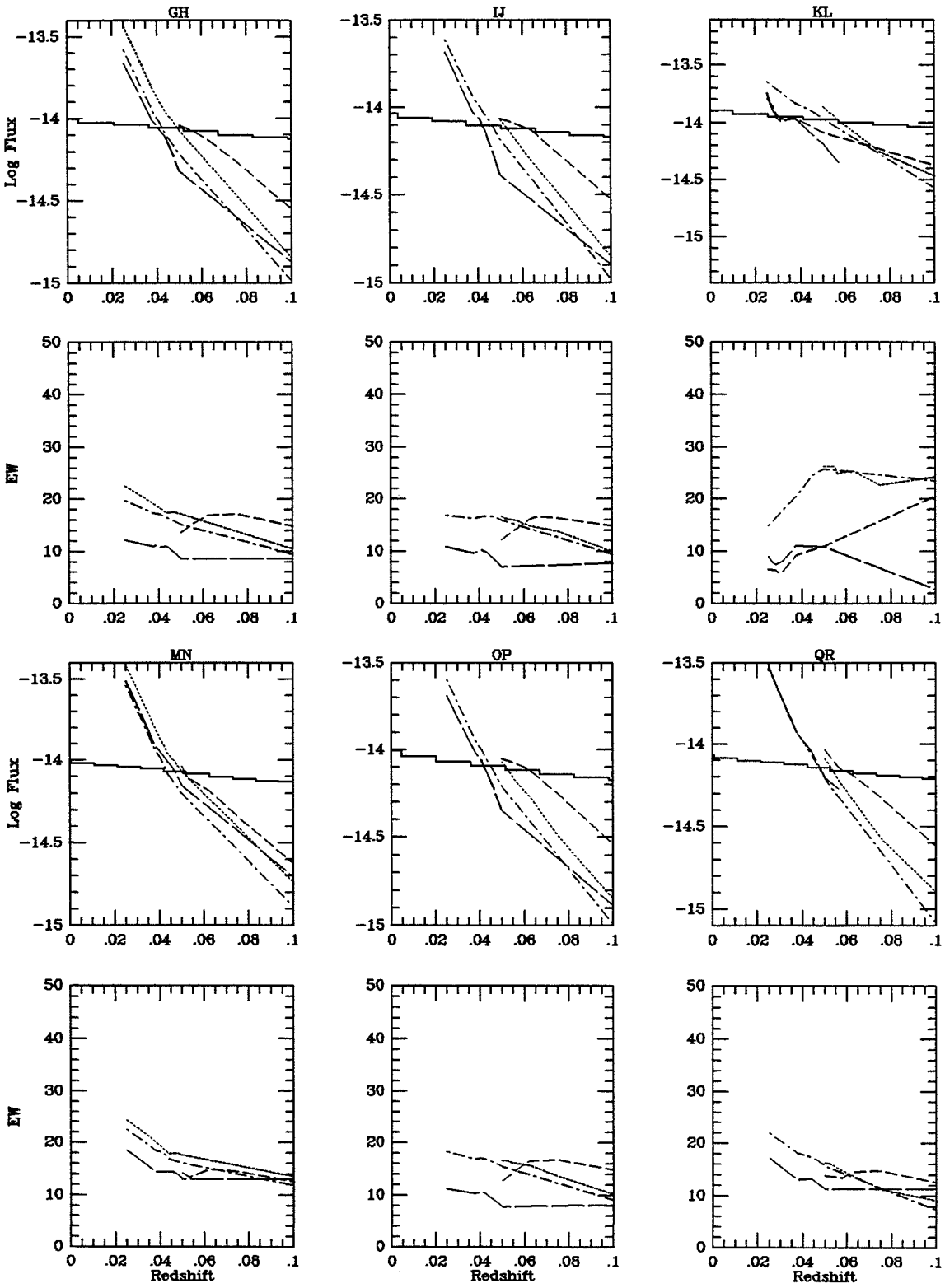

Figure B–91.a

NGC 5899 MAJ/MINB

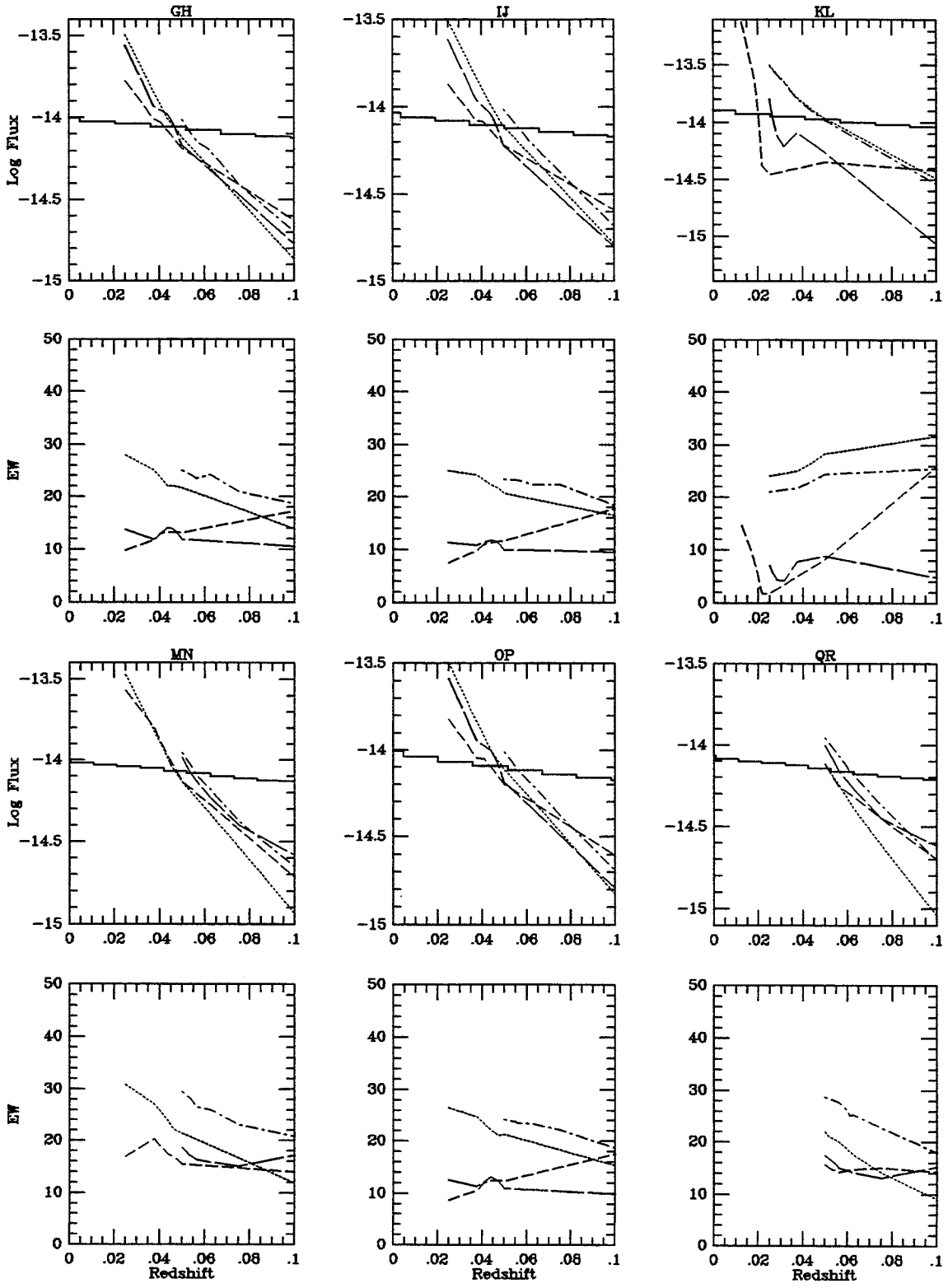

Figure B–91.b

NGC 5929 MAJ/MIN

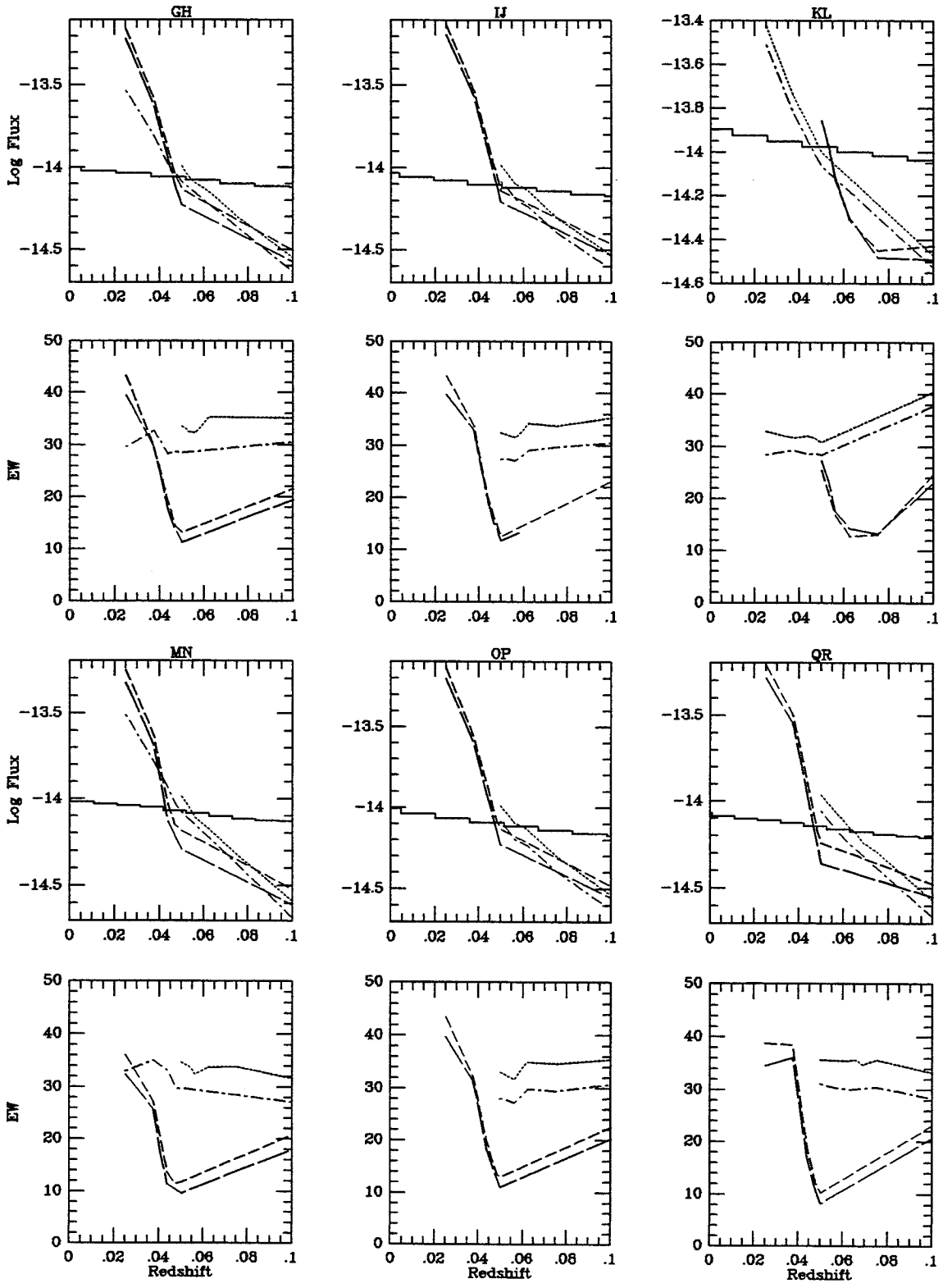

Figure B-92.

NGC 5940 MAJ/MIN

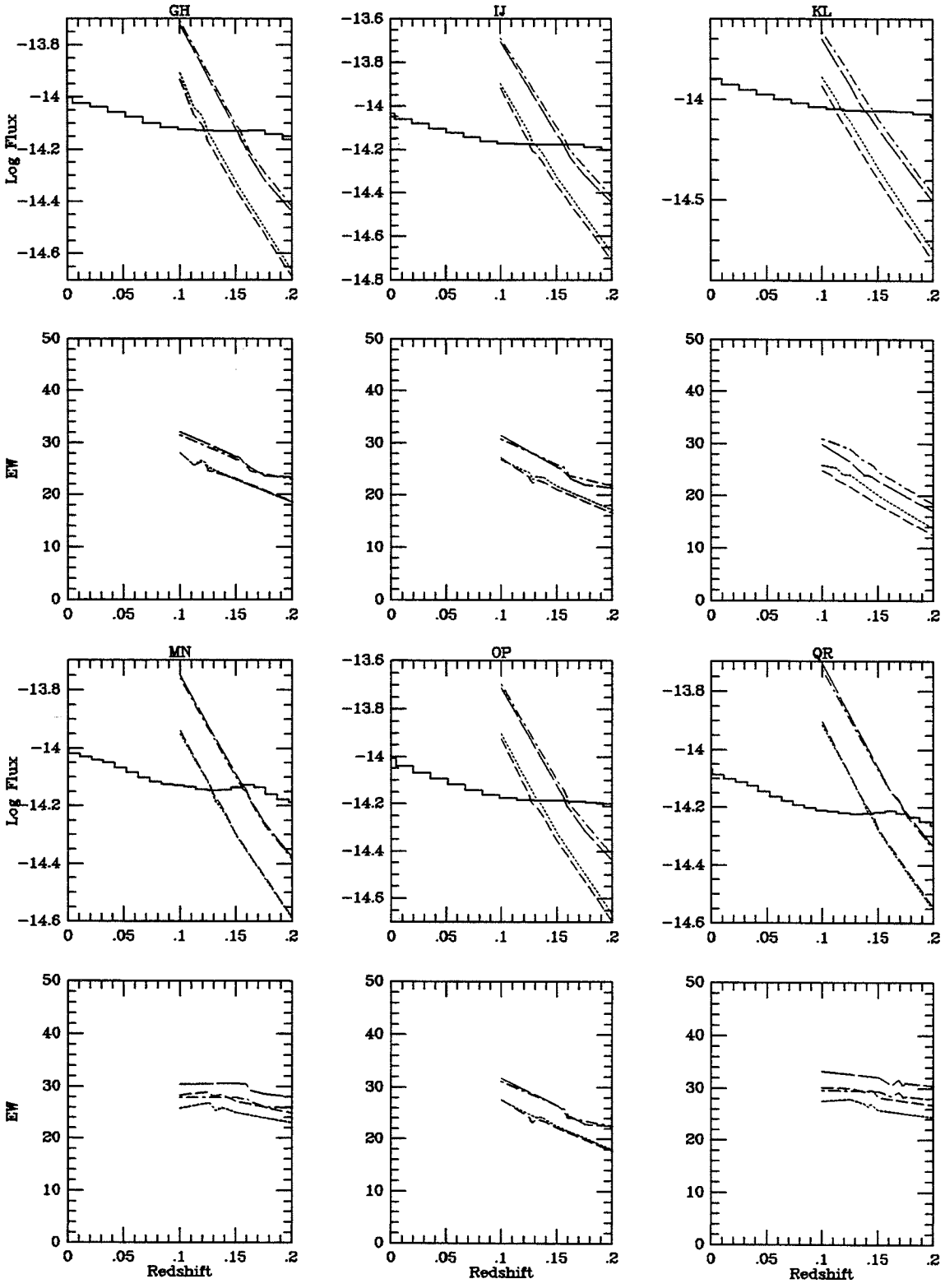

Figure B–93.

1604+4129 MAJA/MINA

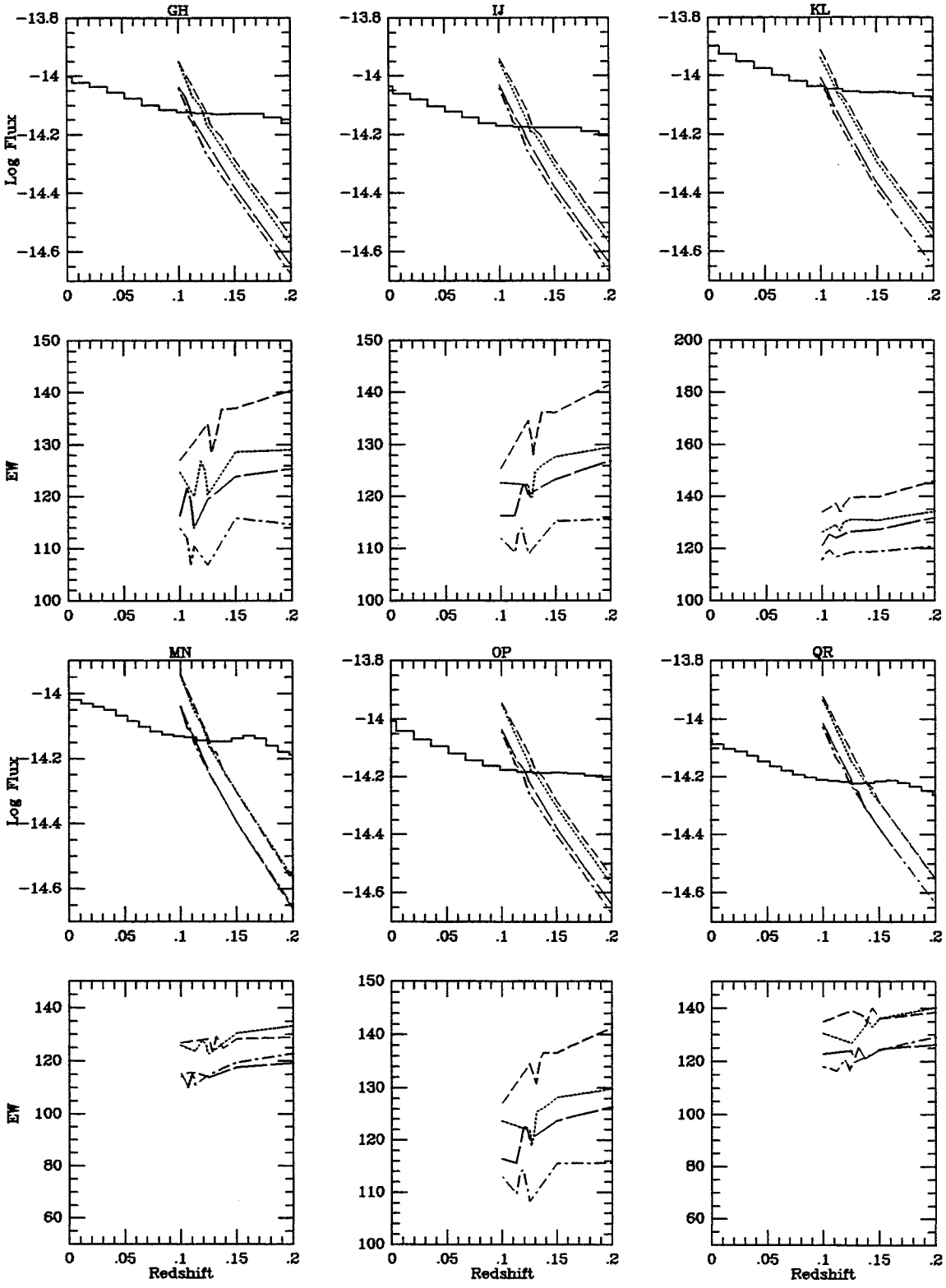

Figure B-94.aa

1604+4129 MAJA/MINB

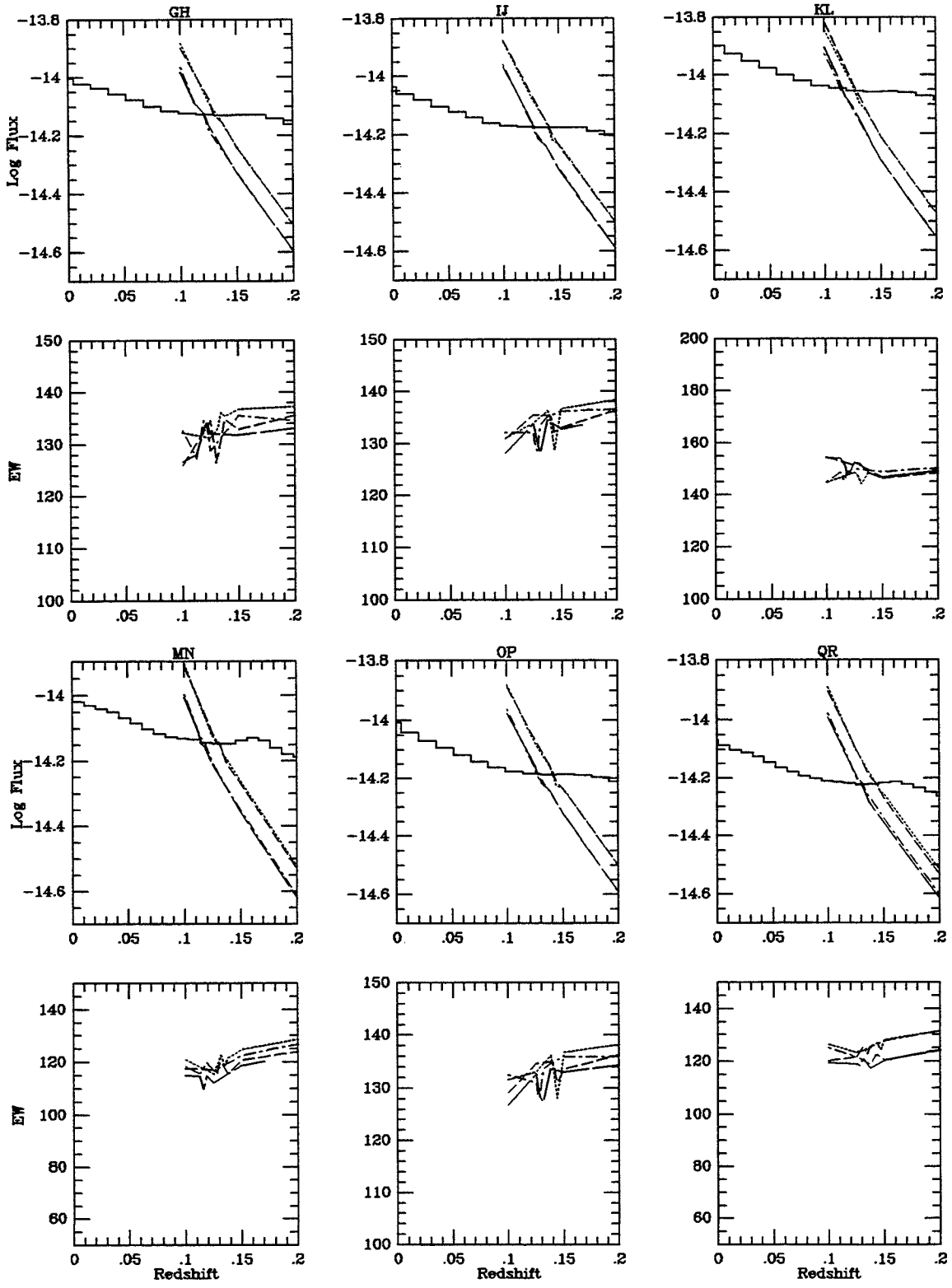

Figure B–94.ab

1604+4129 MAJB/MINA

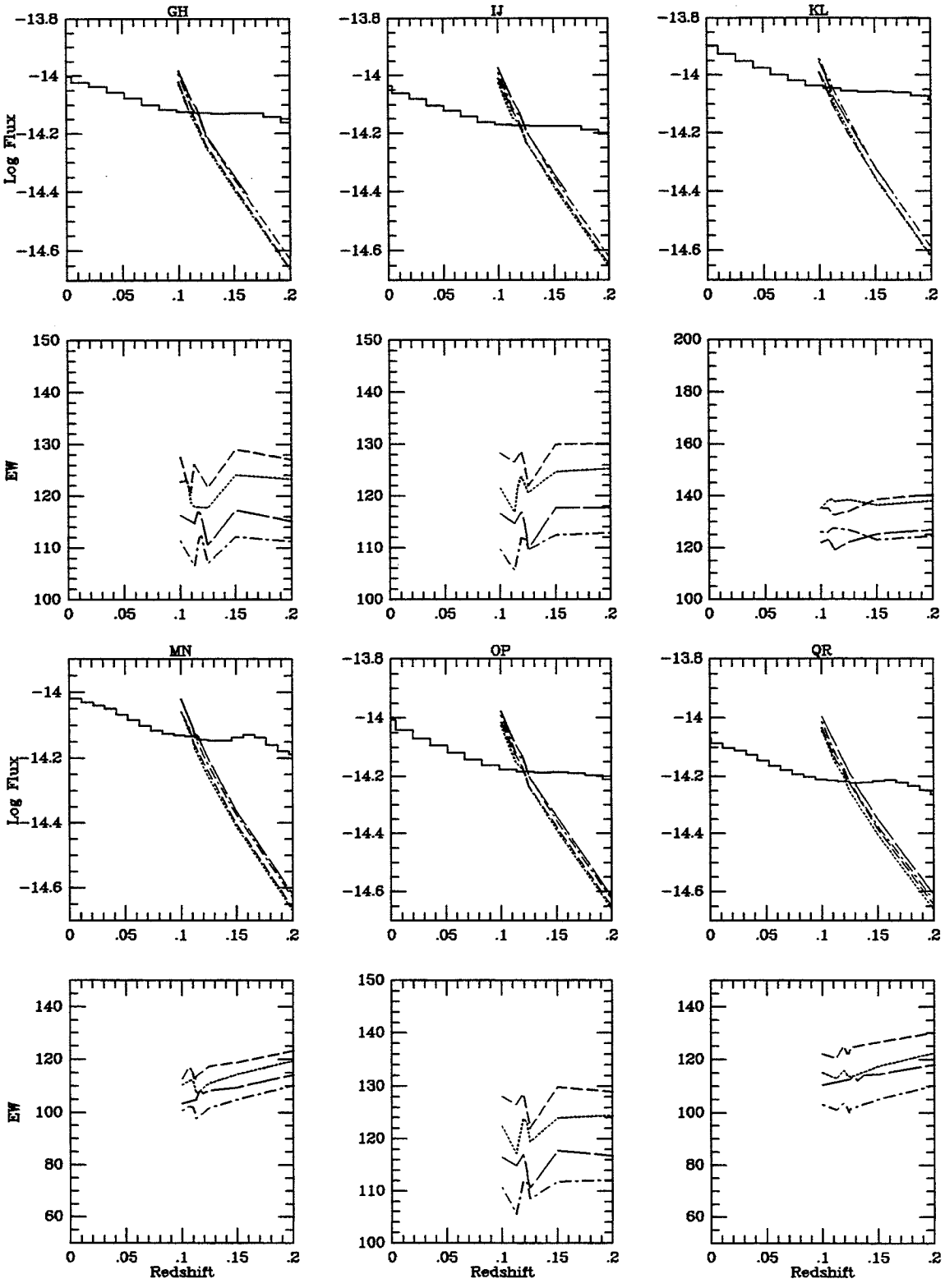

Figure B–94.ba

1604+4129 MAJB/MINB

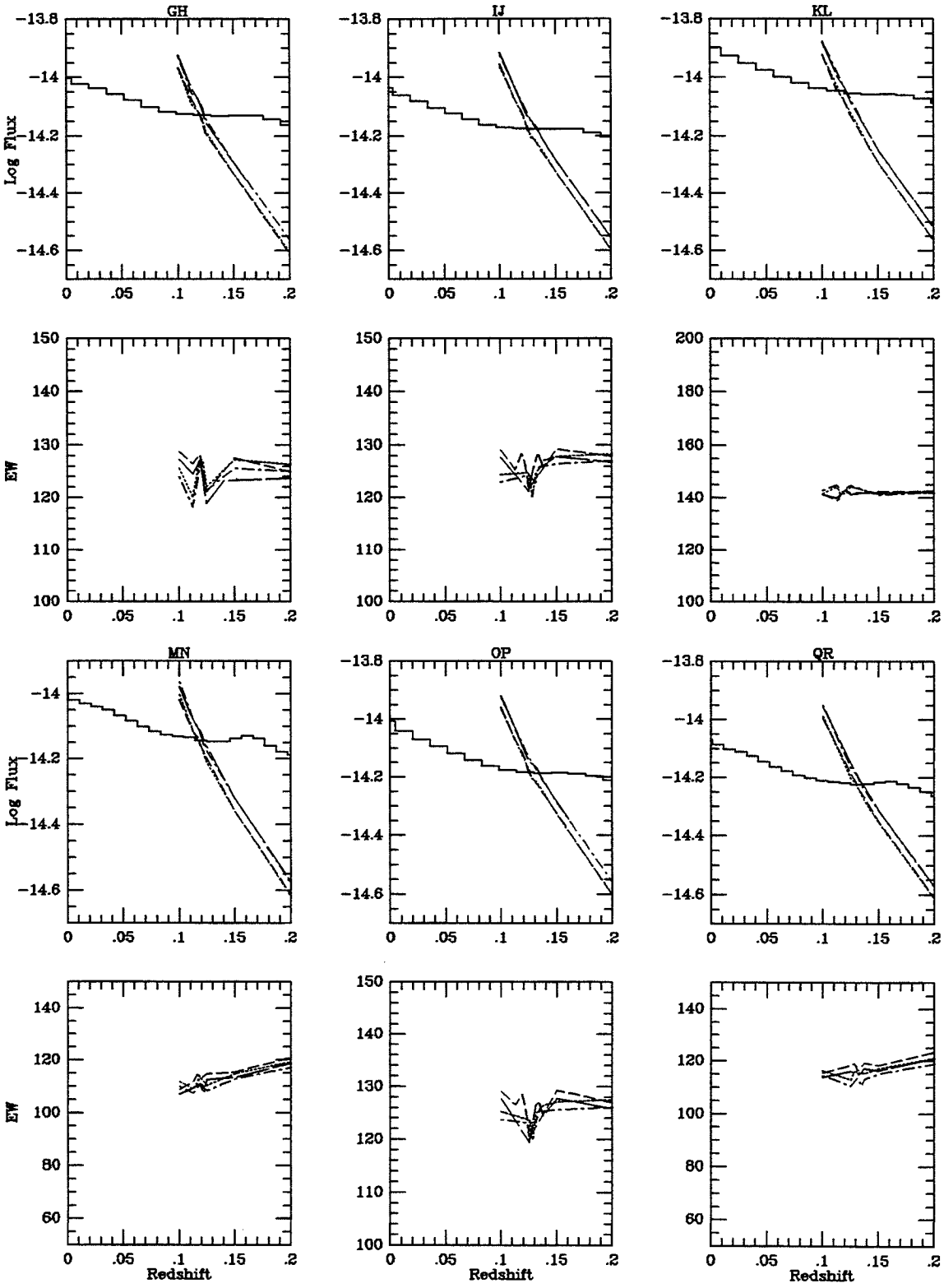

Figure B–94.bb

NGC 6104 MAJ/MIN

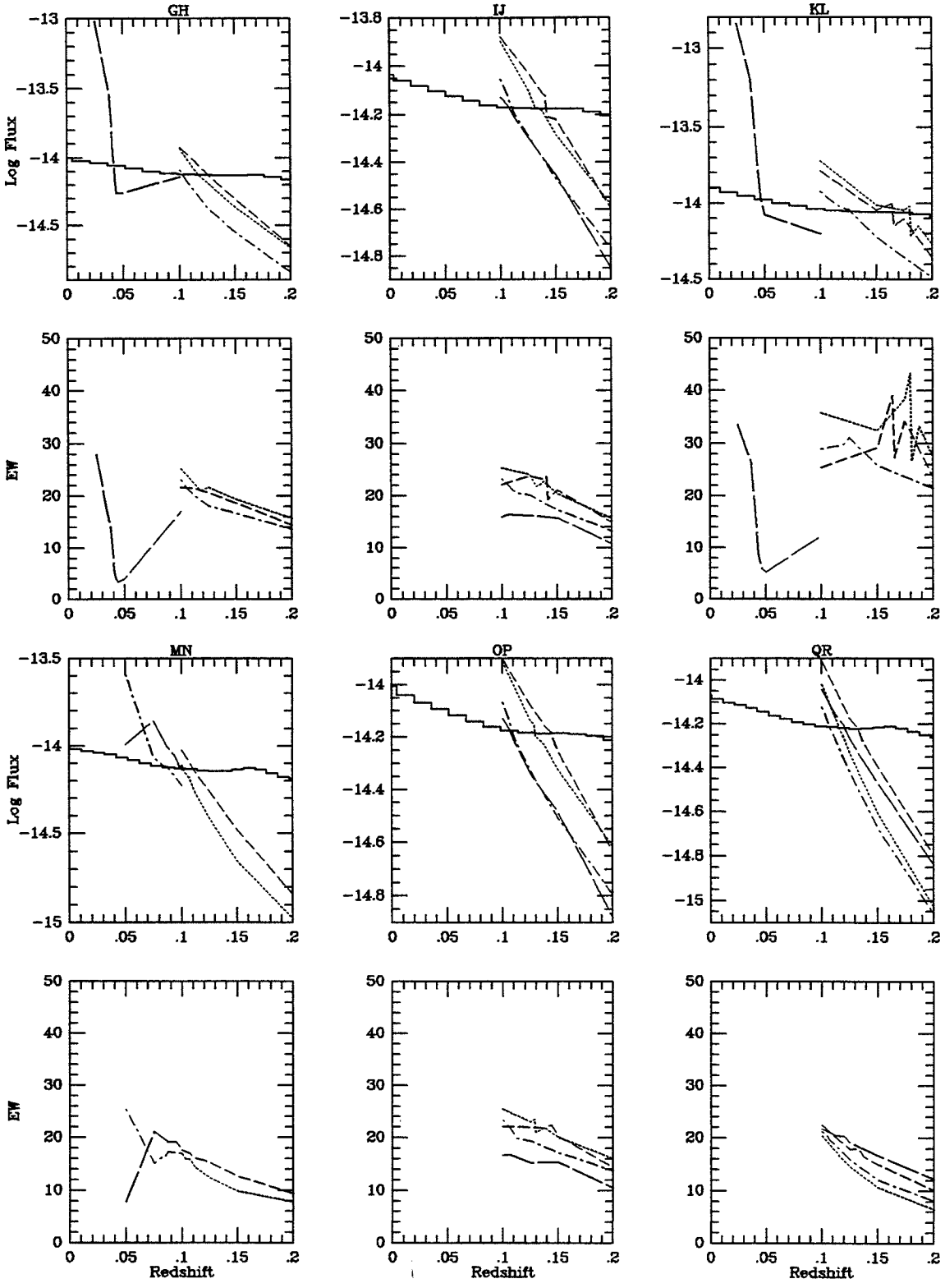

Figure B–95.

NGC 7077 MAJ/MIN

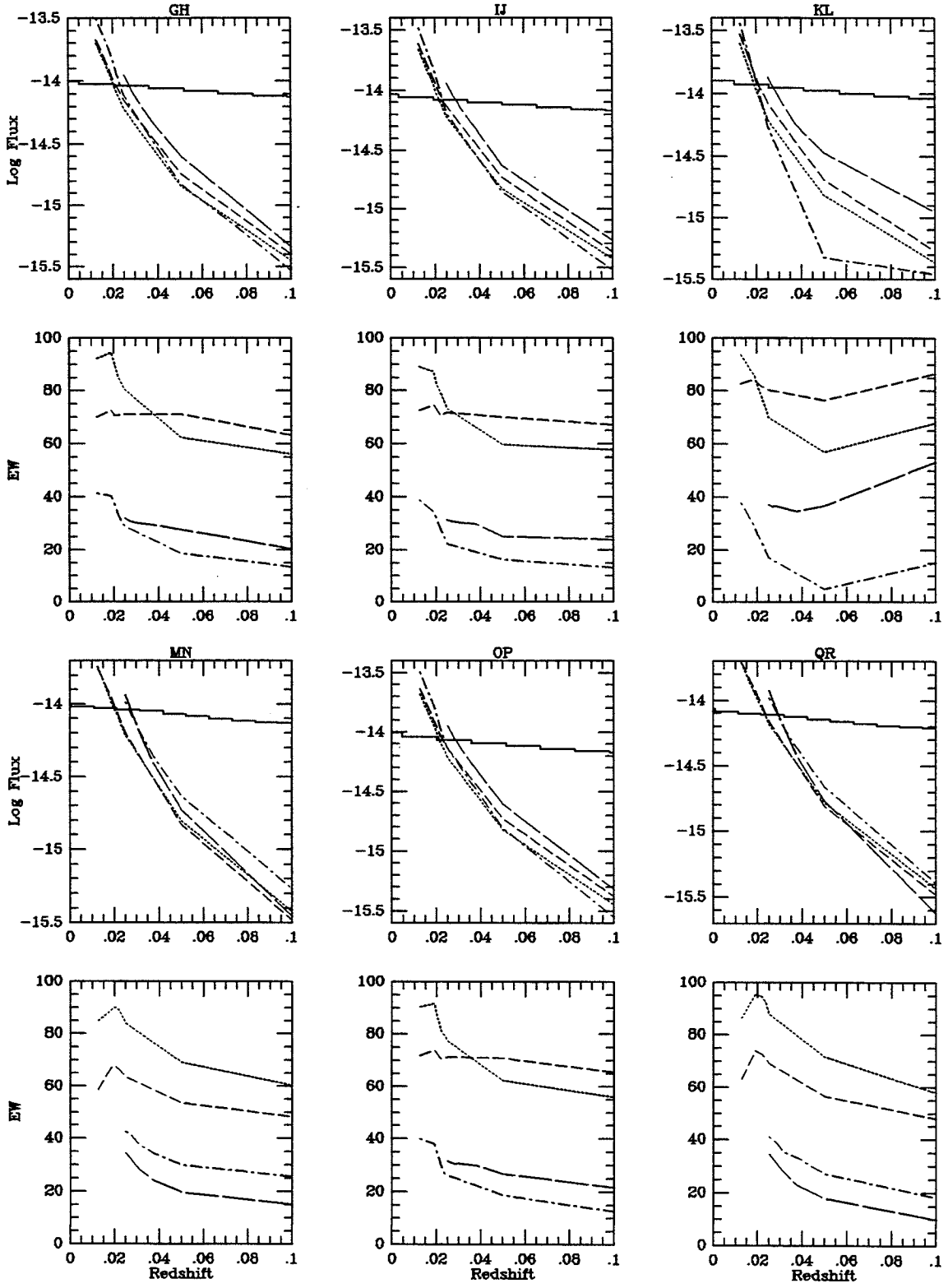

Figure B–96.

NGC 7241 MAJ/MINA

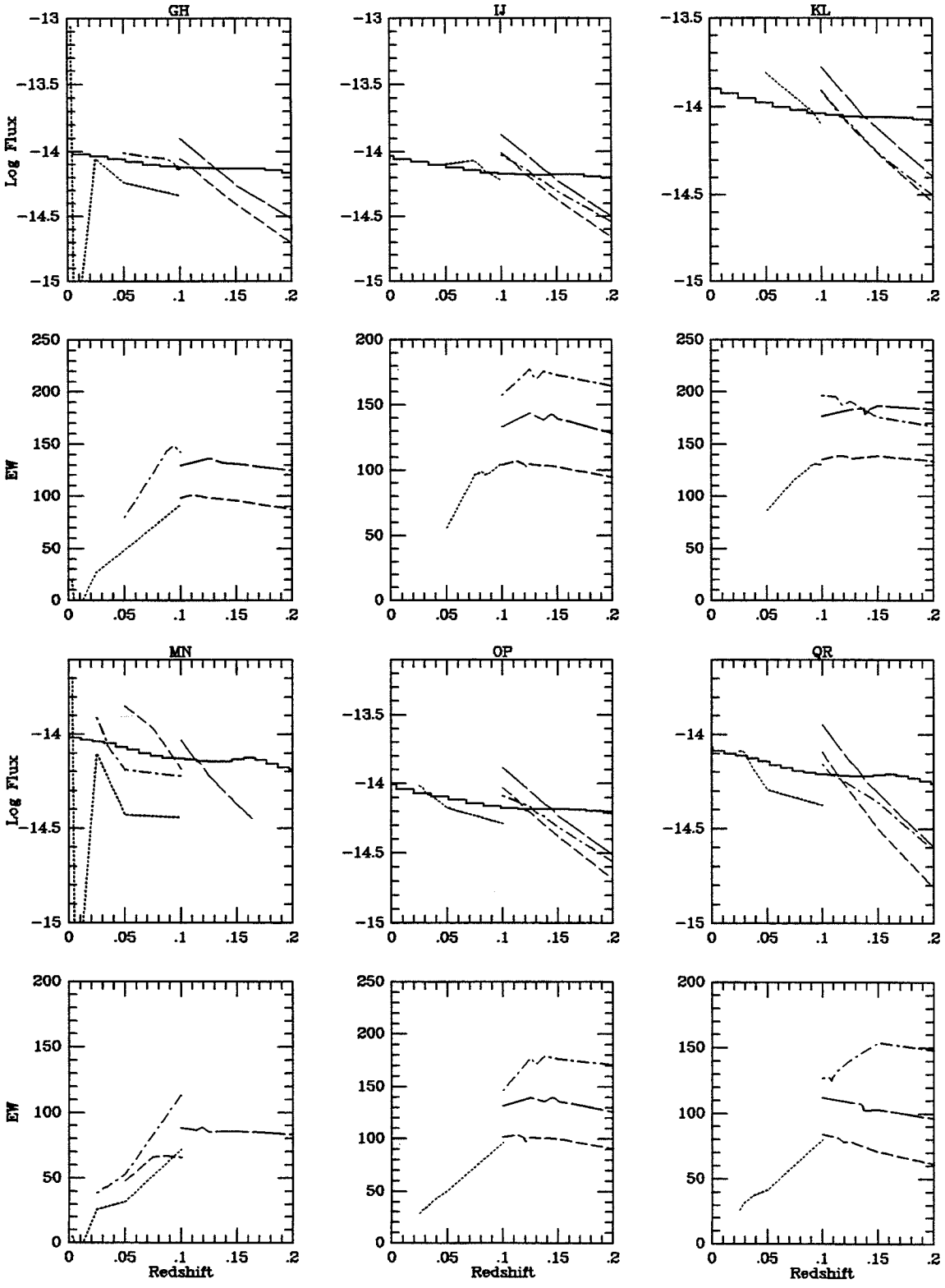

Figure B-97.a

NGC 7241 MAJ/MINB

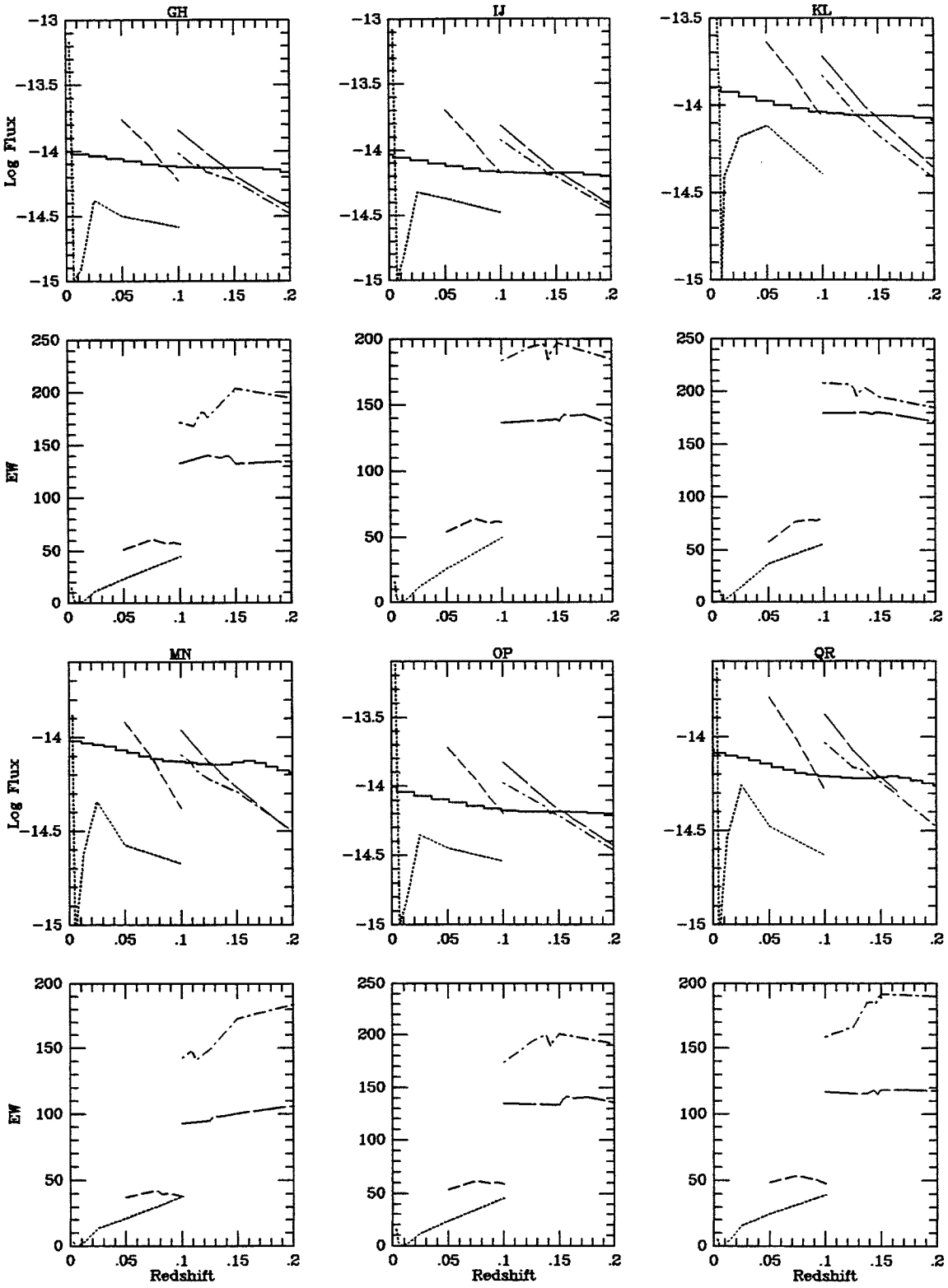

Figure B–97.b

2237+0747 MAJ/MIN

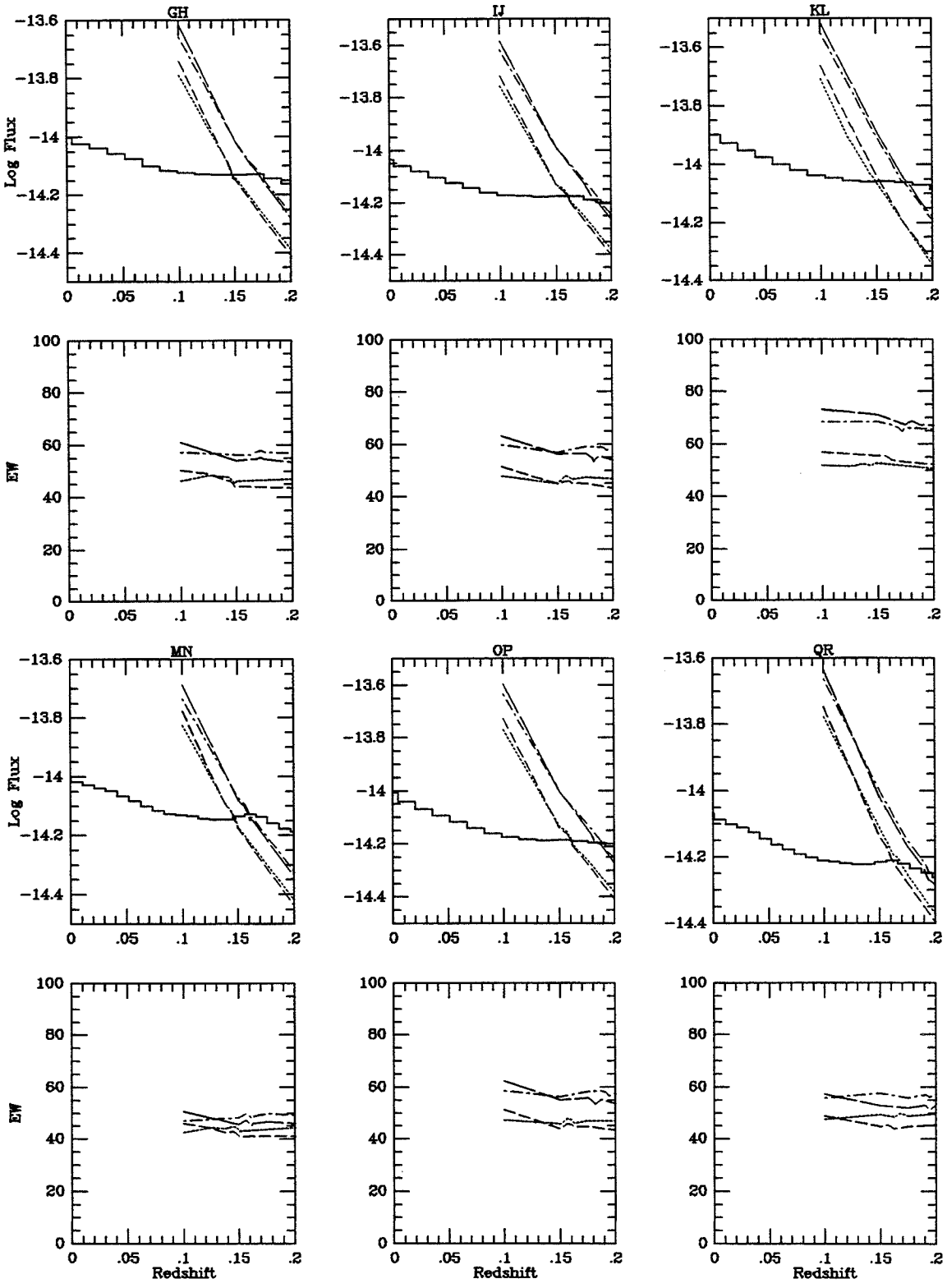

Figure B-98.

NGC 7464 MAJ/MINA

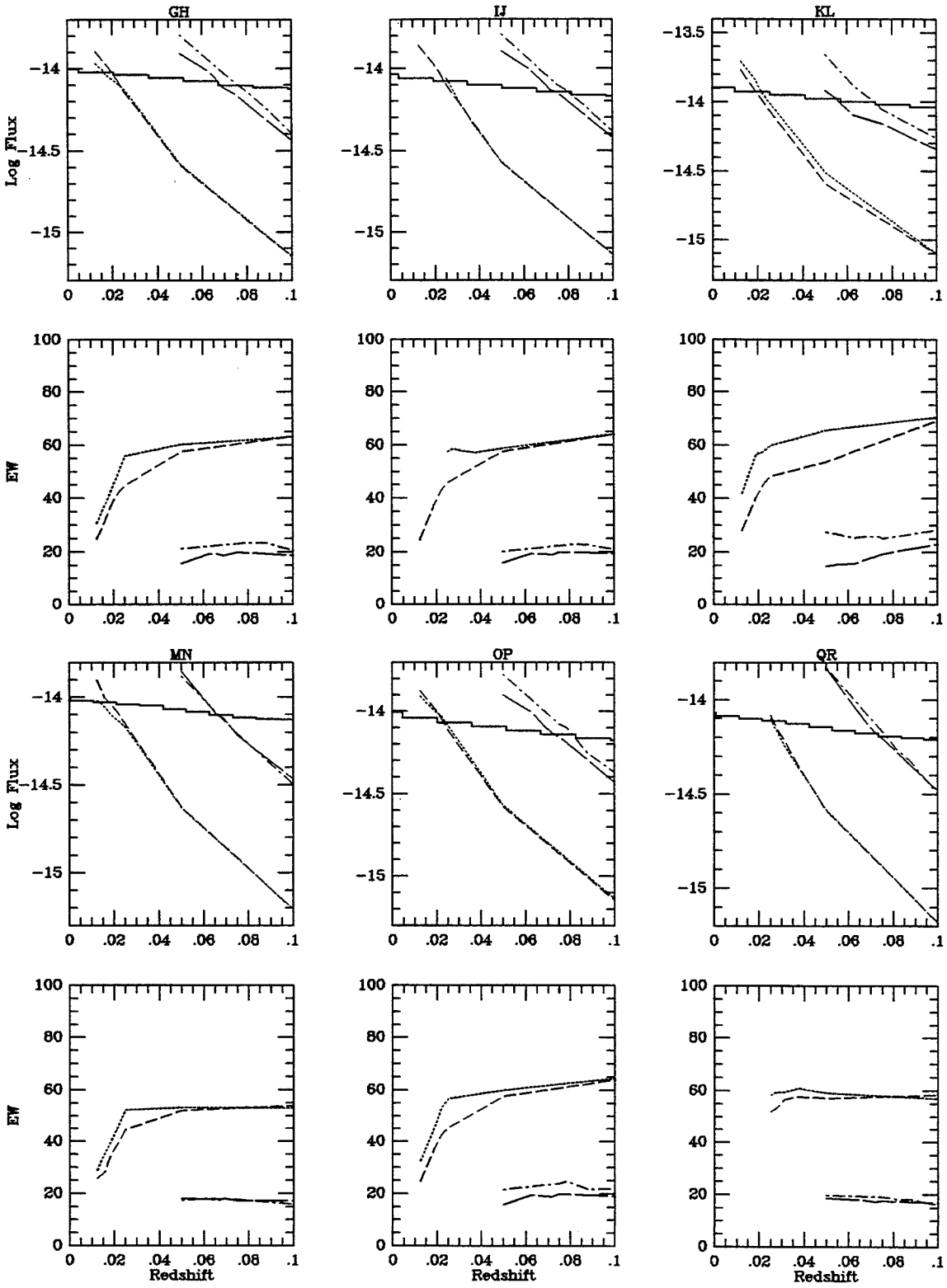

Figure B-99.a

NGC 7464 MAJ/MINB

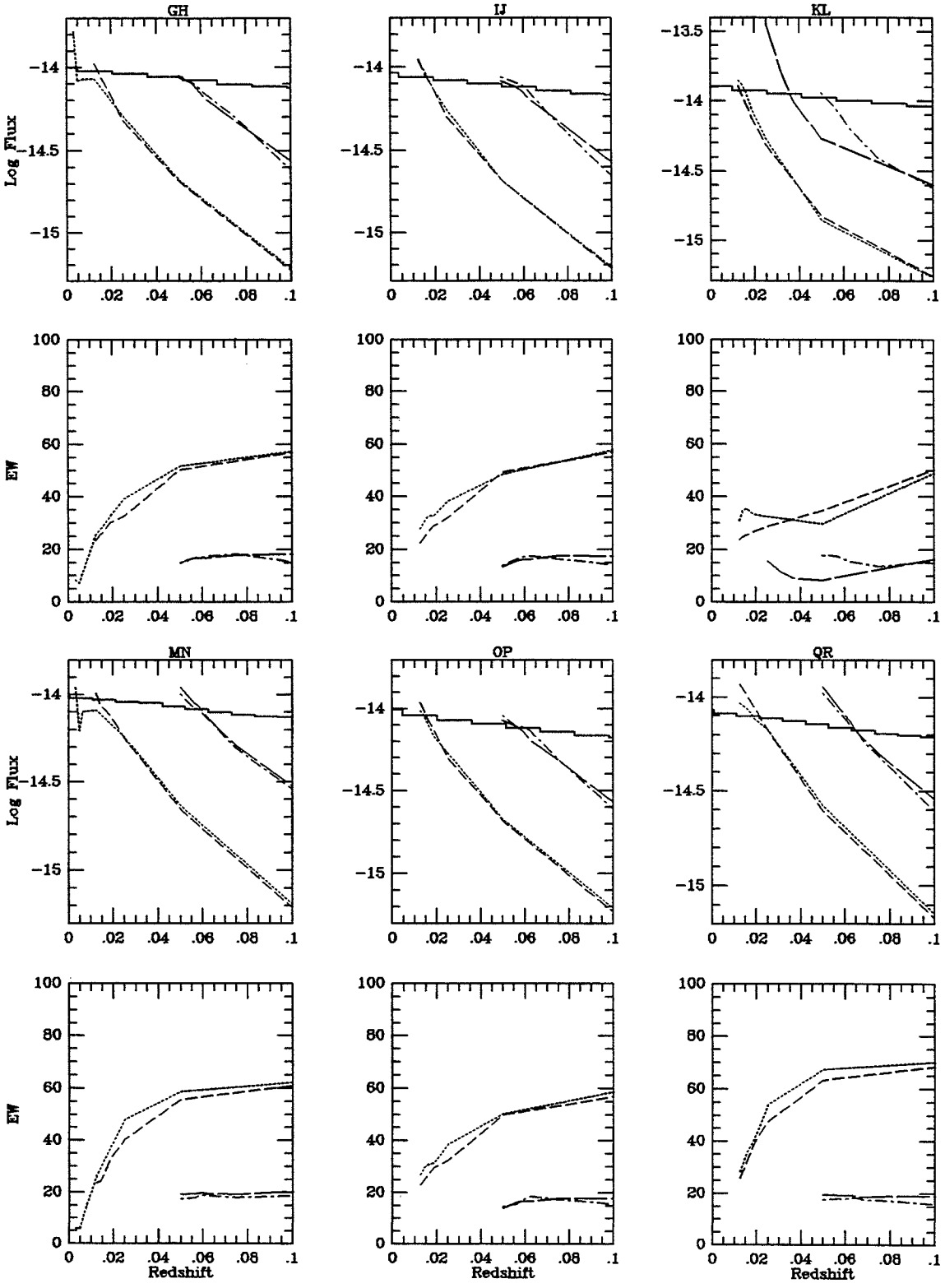

Figure B-99.b

NGC 7468 MAJ/MINA

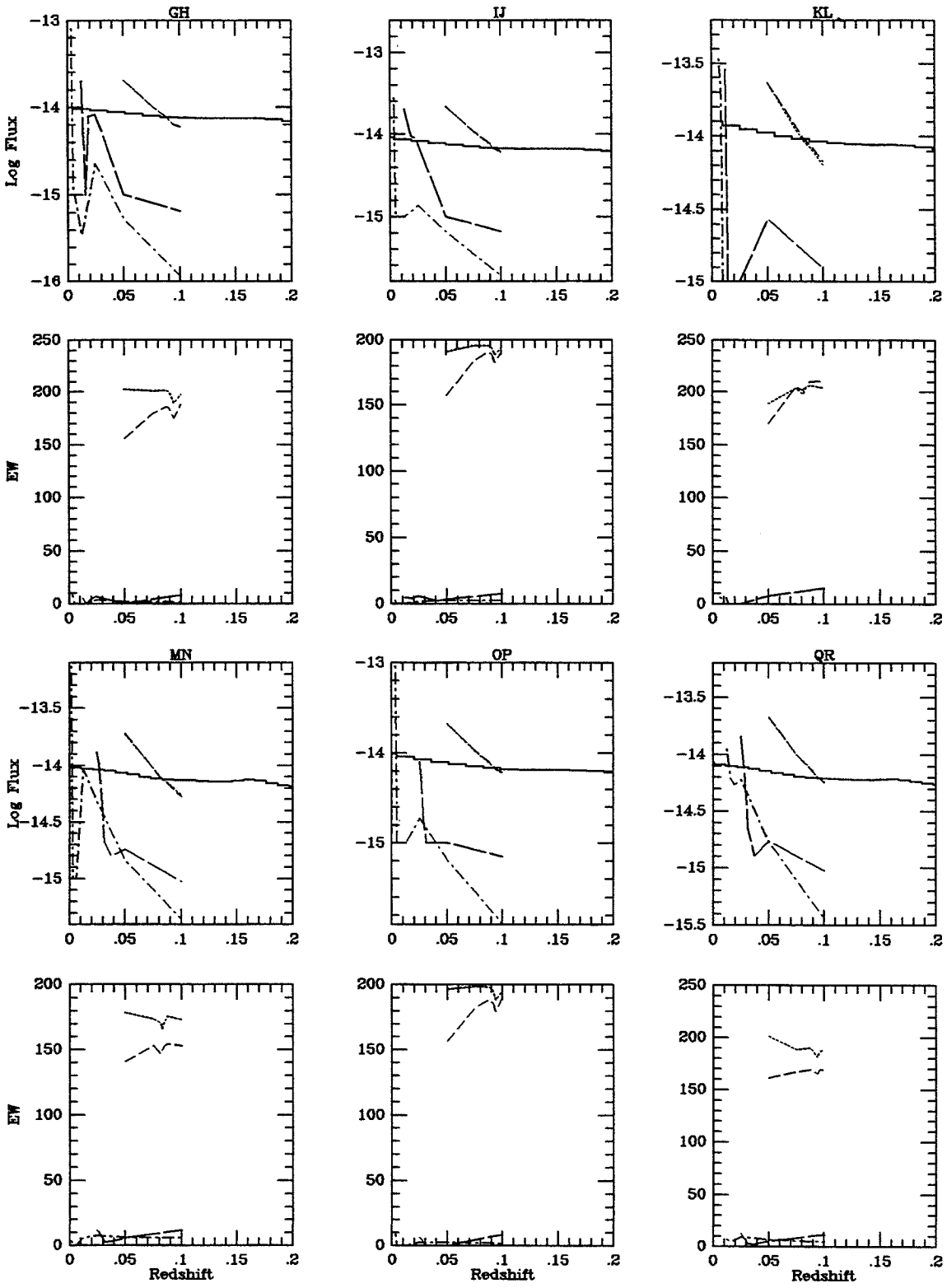

Figure B-100.a

NGC 7468 MAJ/MINB

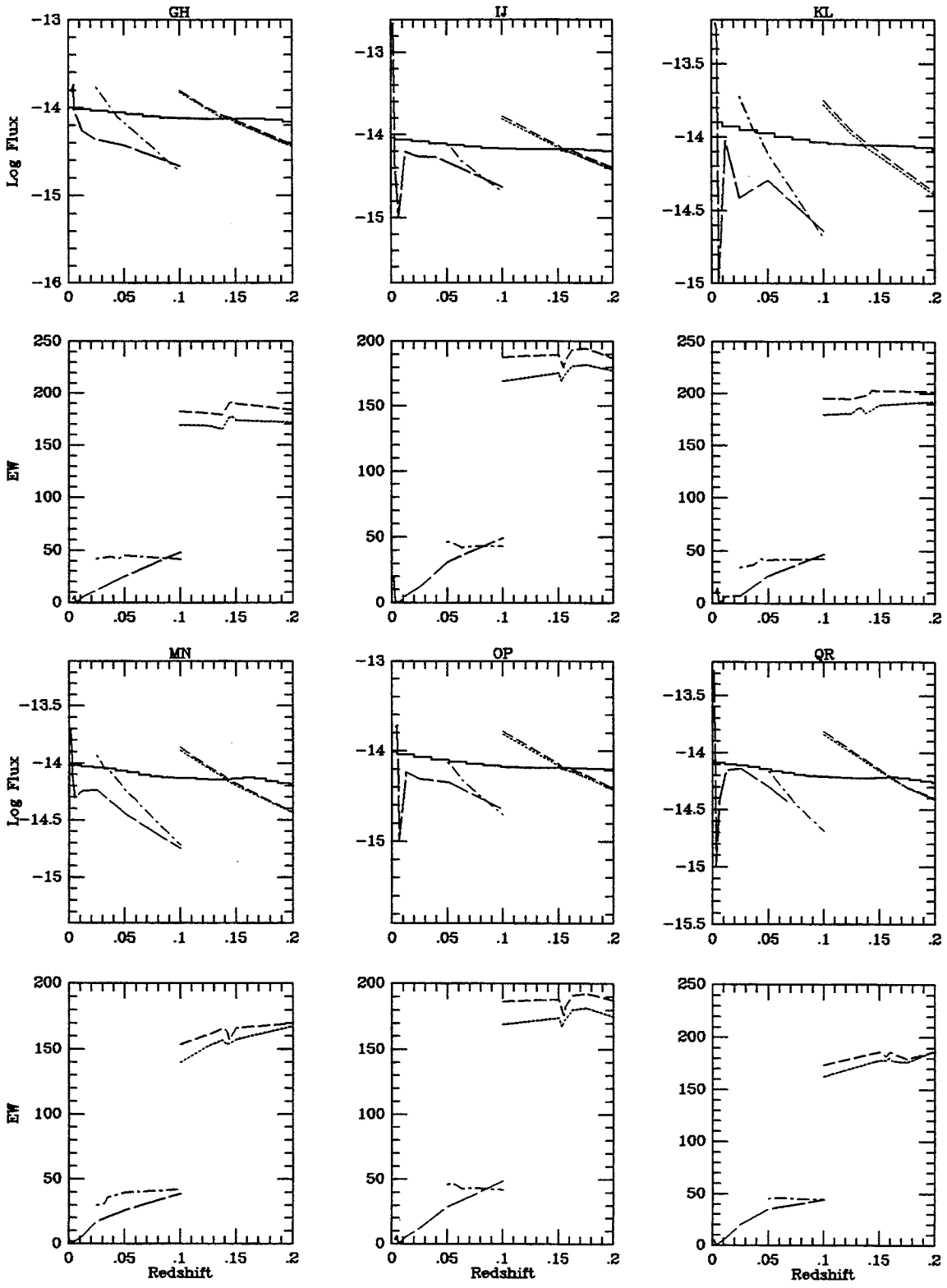

Figure B–100.b

NGC 7469 MAJA/MINA

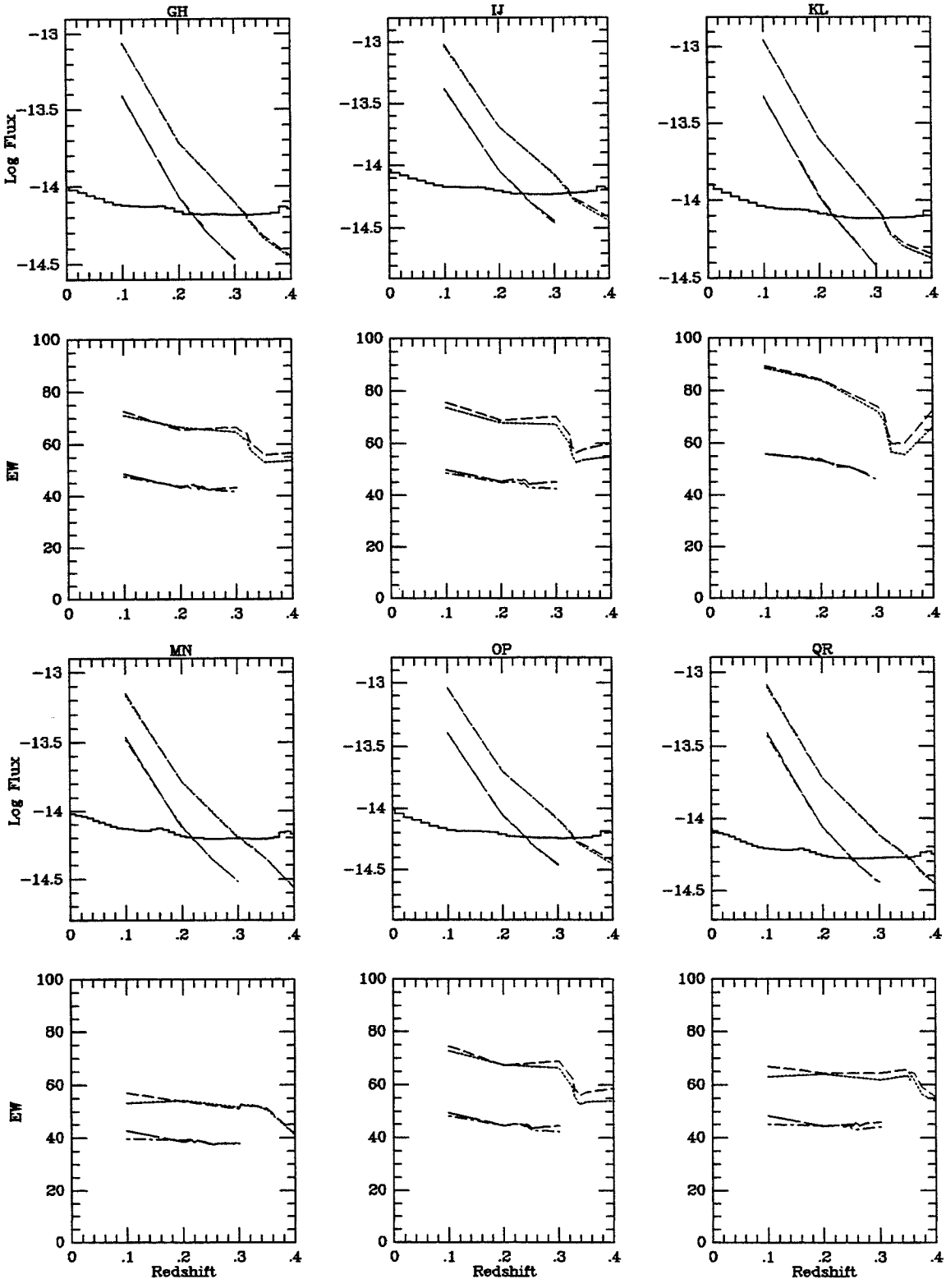

Figure B-101.aa

NGC 7469 MAJA/MINB

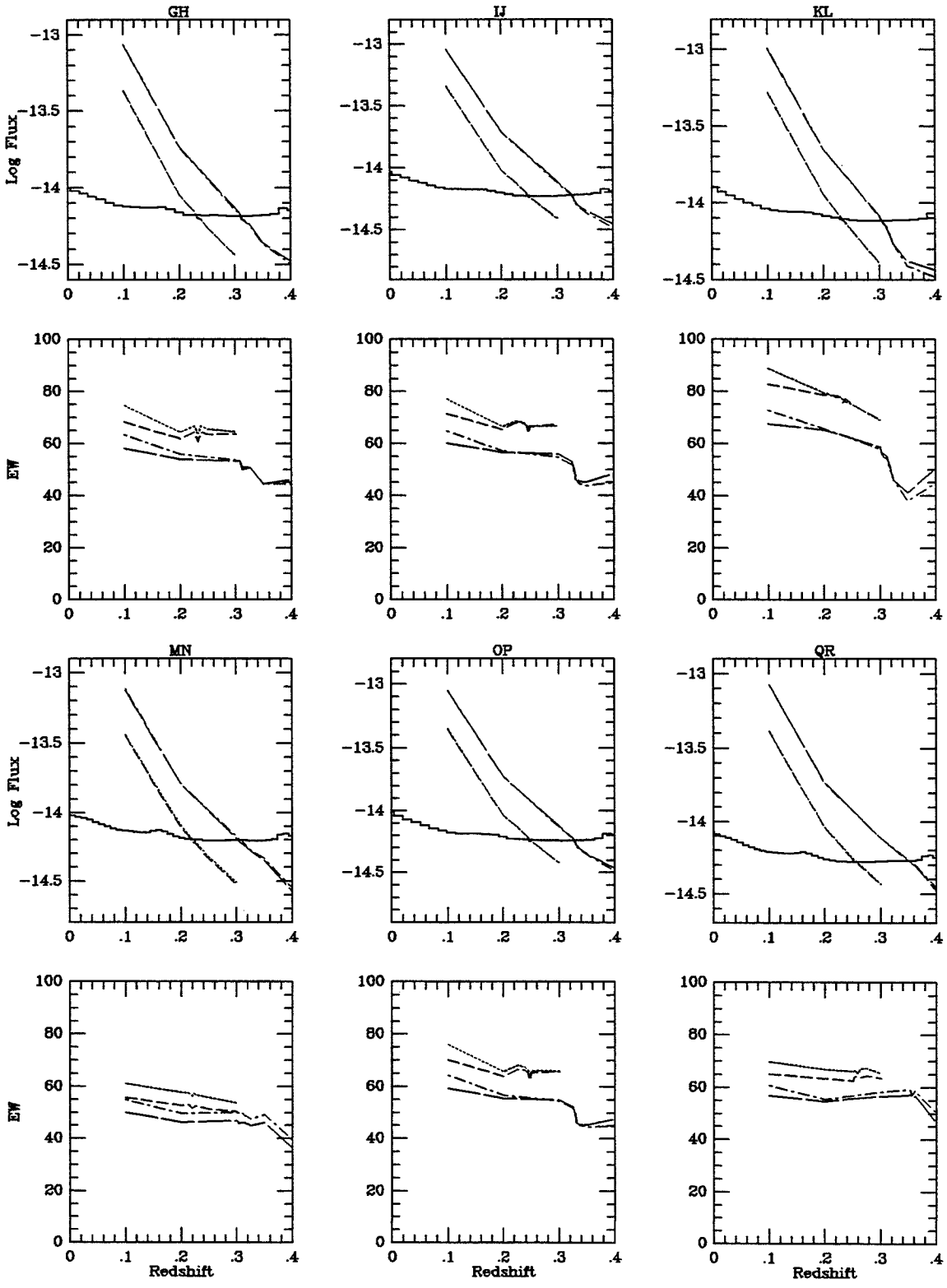

Figure B–101.ab

NGC 7469 MAJB/MINA

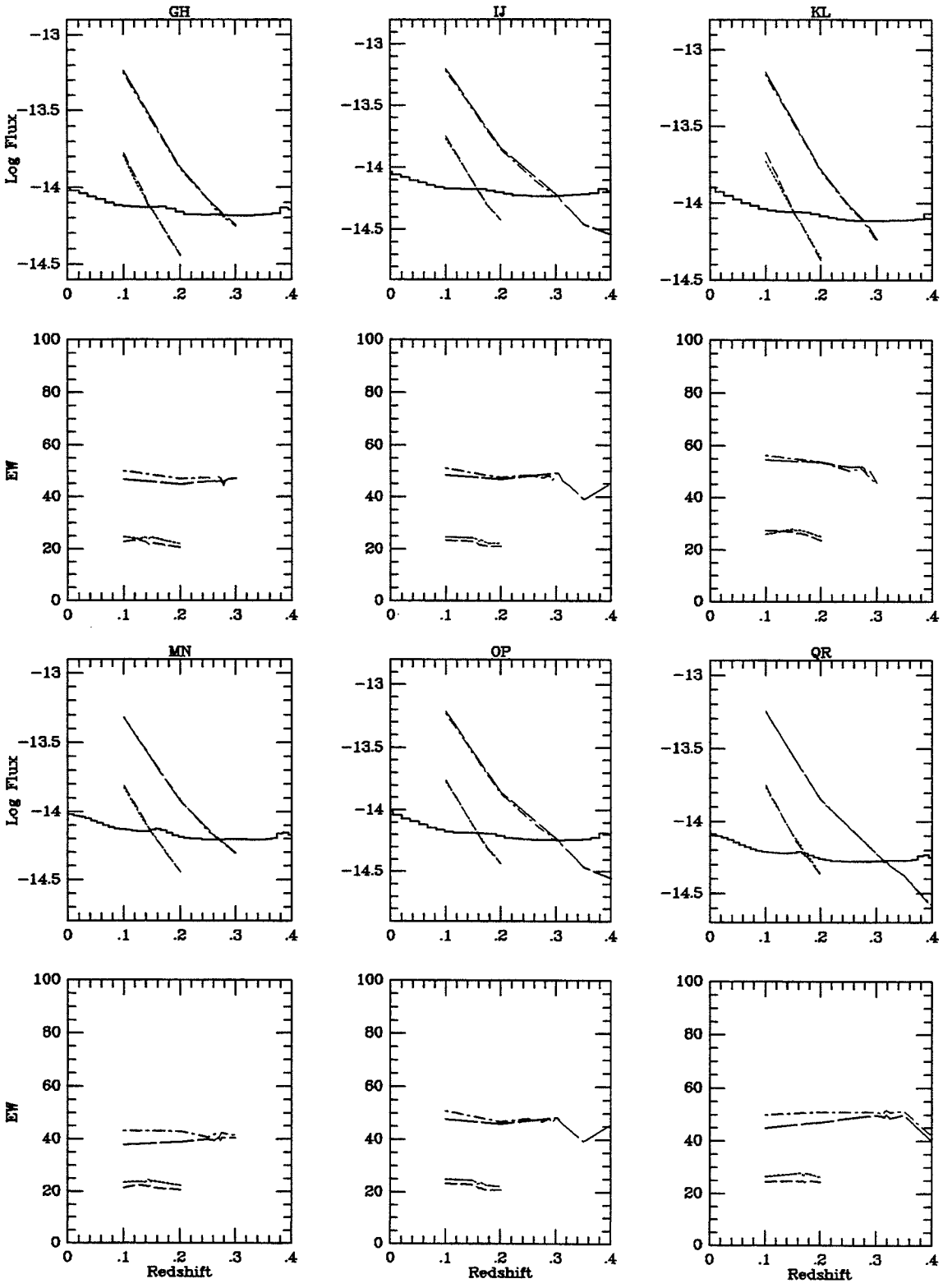

Figure B–101.ba

NGC 7469 MAJB/MINB

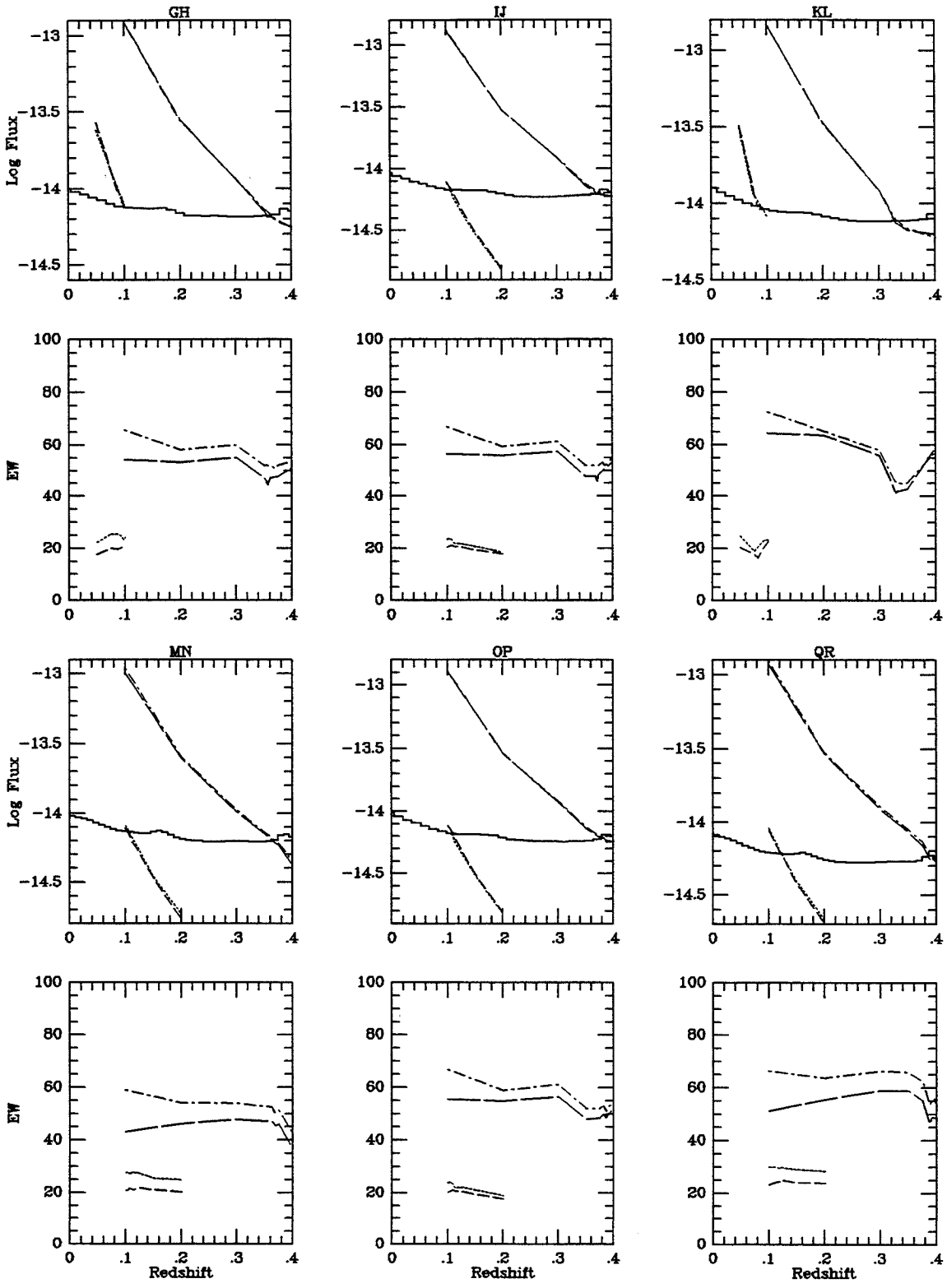

Figure B–101.bb

NGC 7603 MAJ/MINA

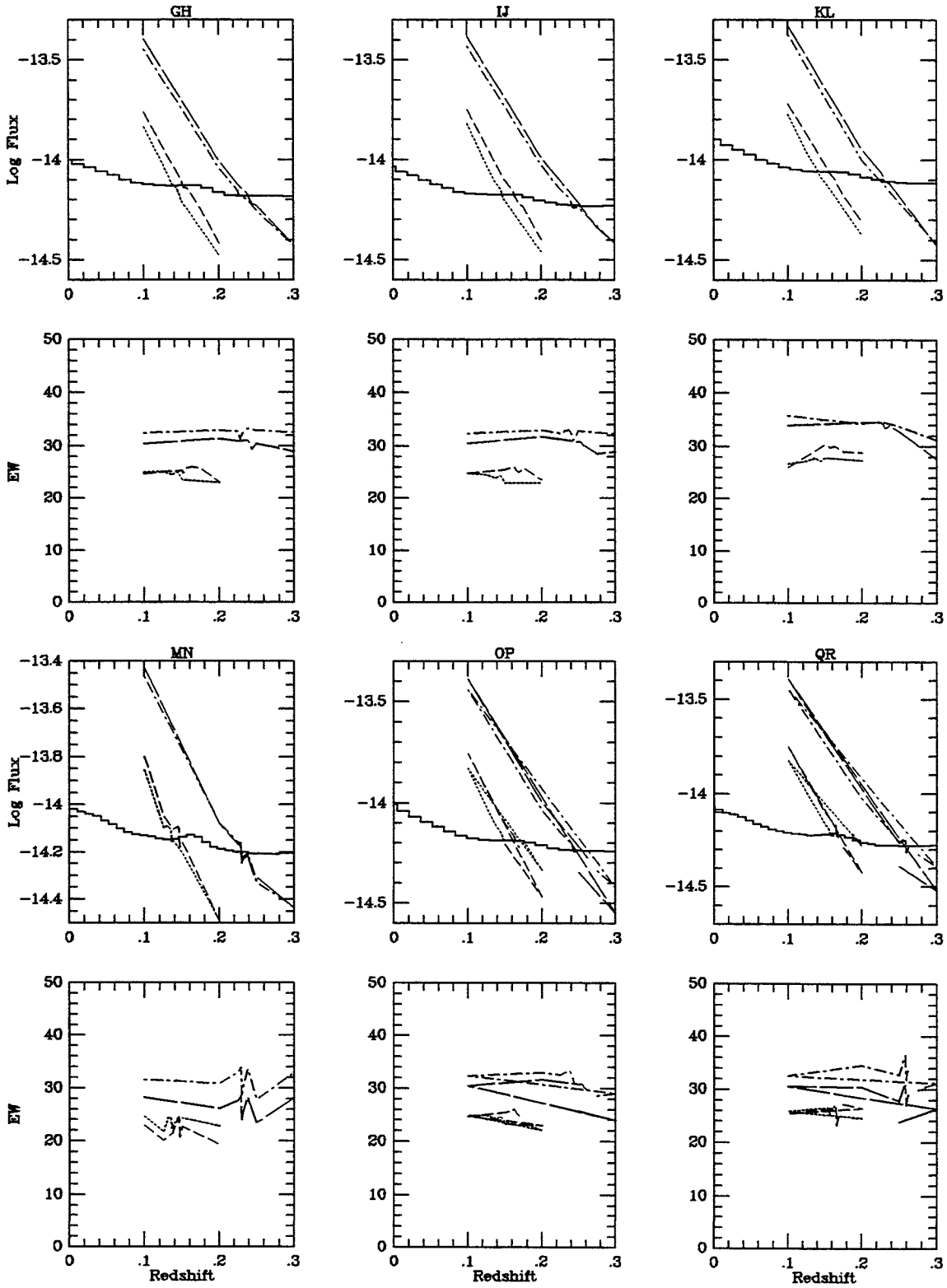

Figure B-102.a

NGC 7603 MAJ/MINB

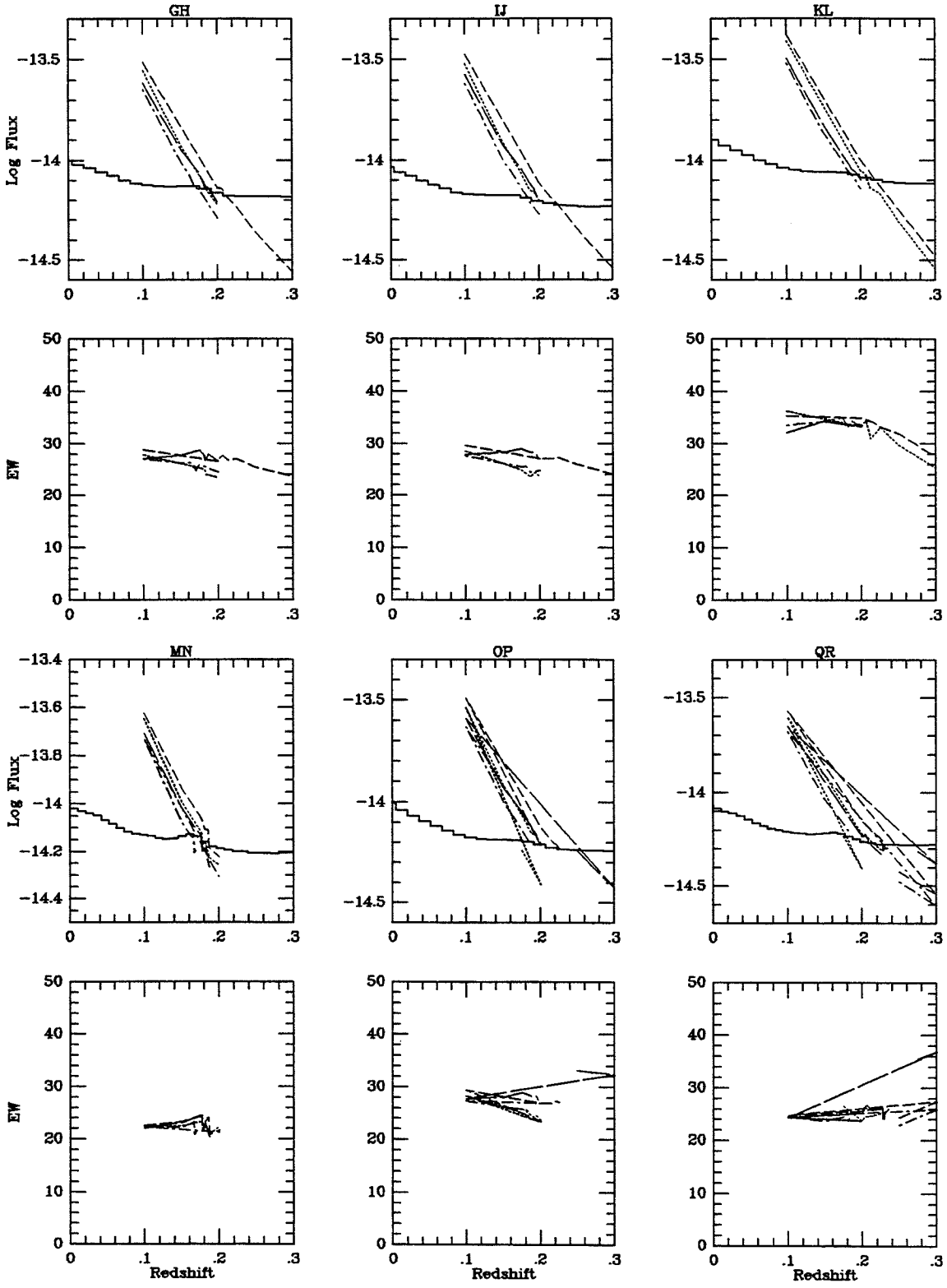

Figure B-102.b

NGC 7674 MAJ/MIN

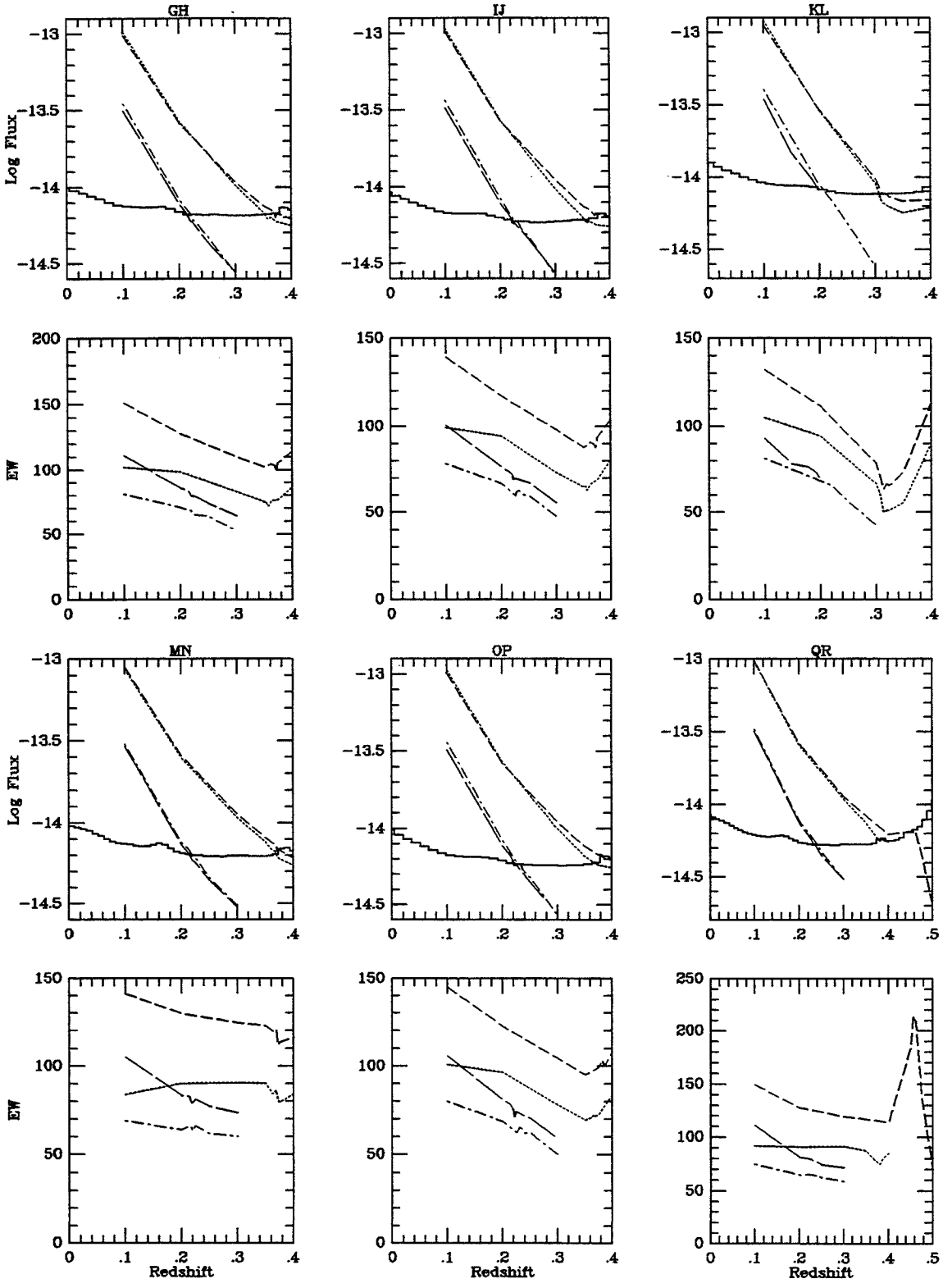

Figure B–103.

NGC 7682 MAJA/MIN

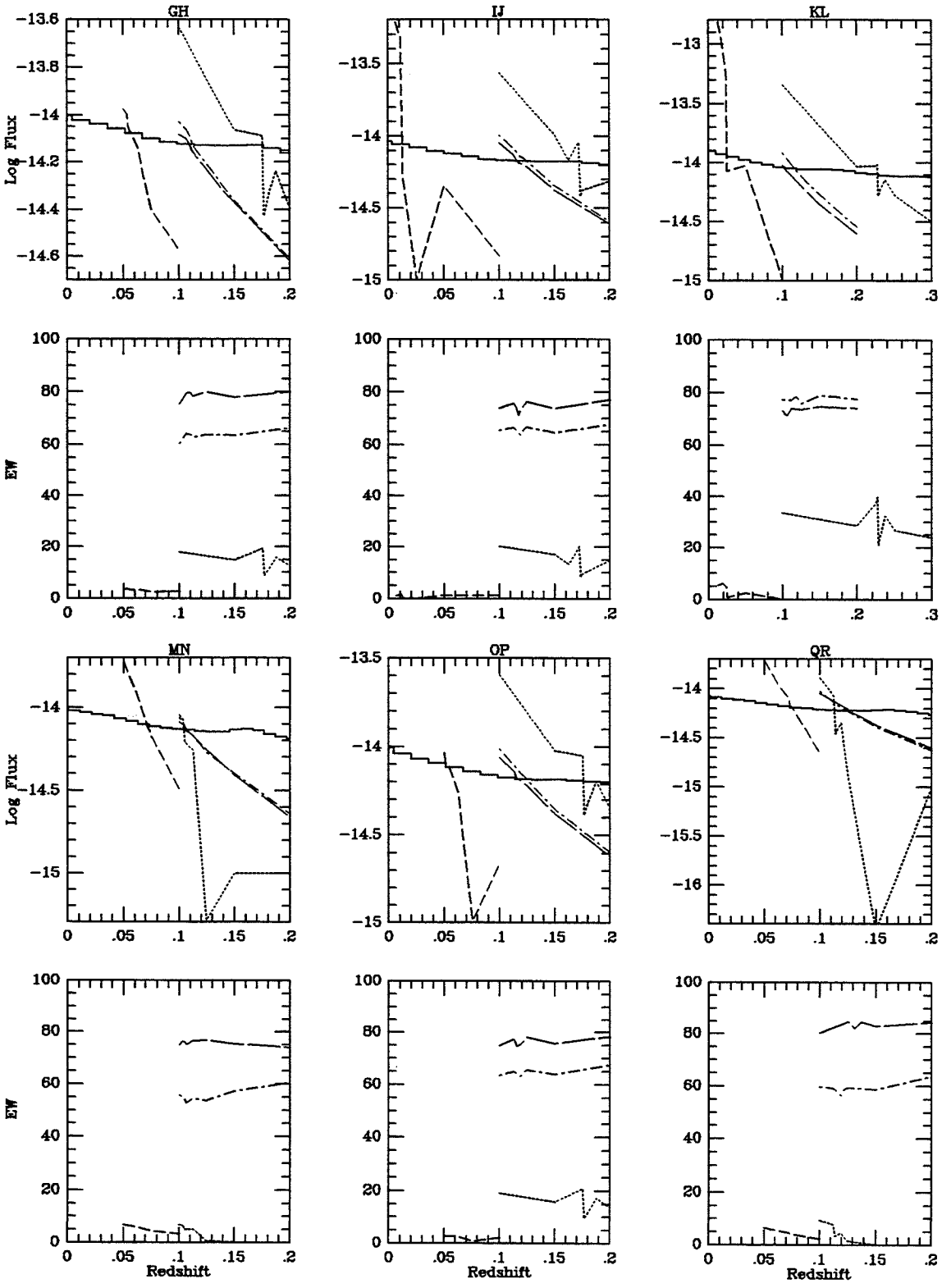

Figure B–104.a

NGC 7682 MAJB/MIN

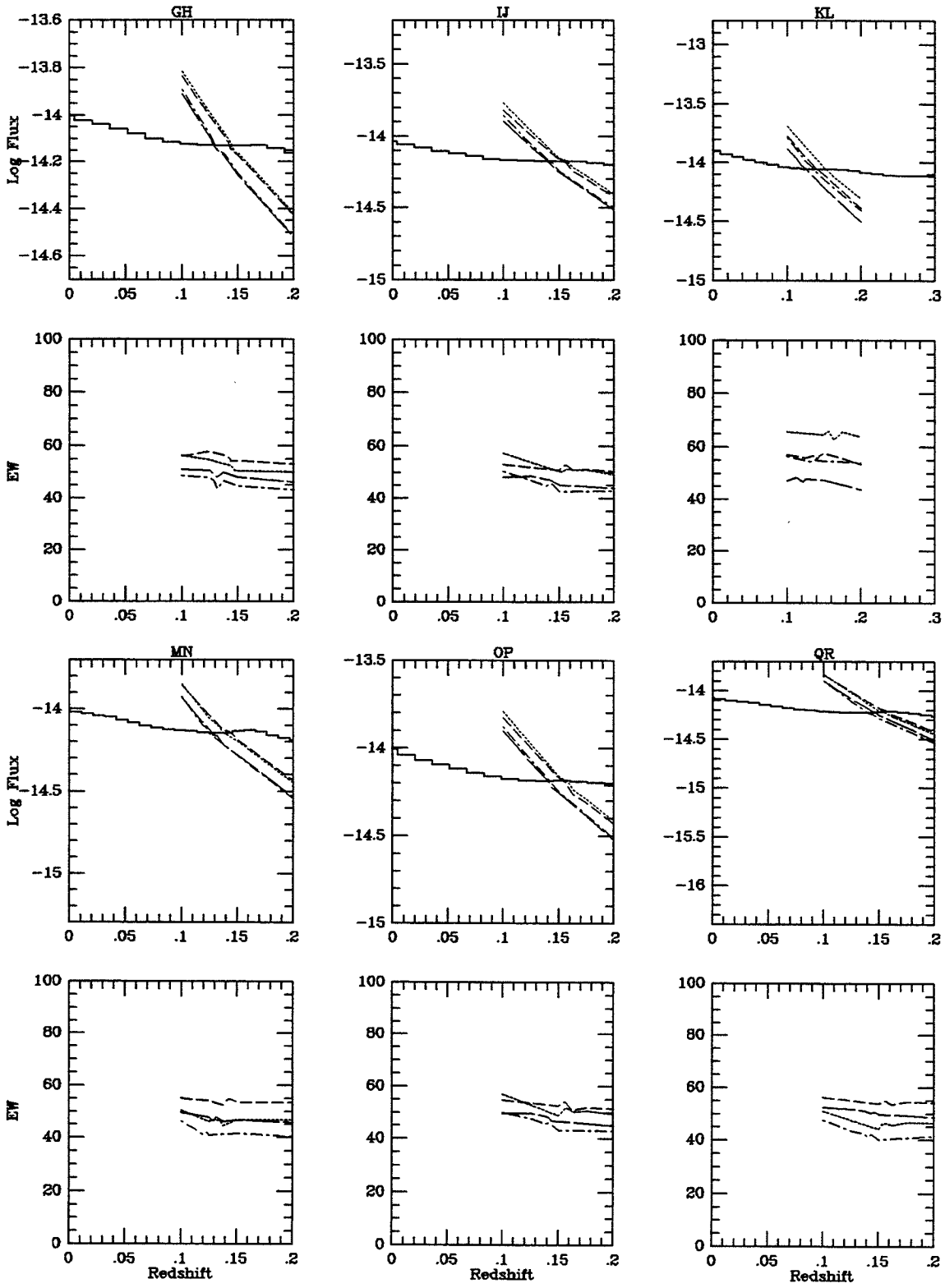

Figure B-104.b

NGC 7682 MAJC/MIN

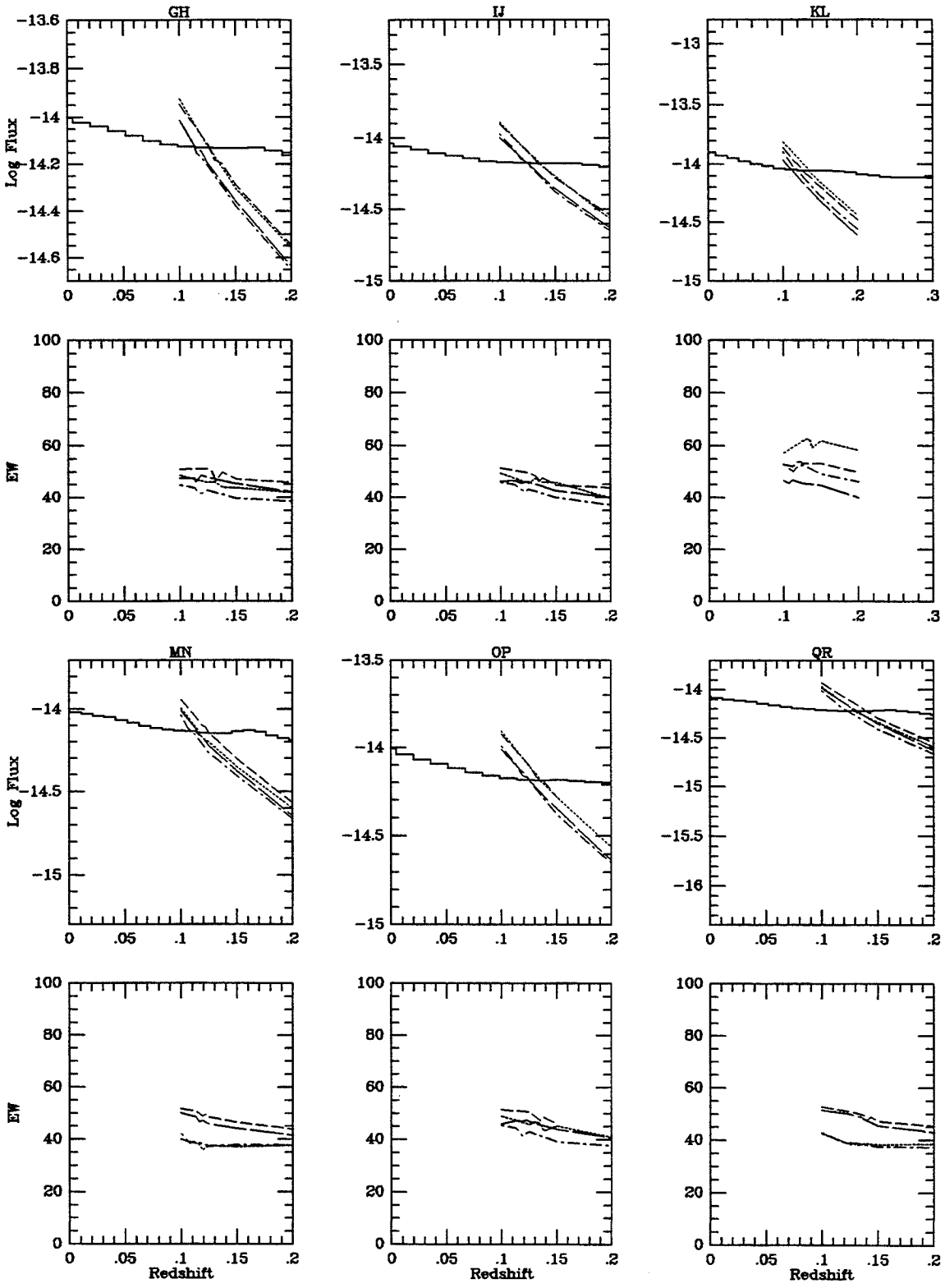

Figure B–104.c

NGC 7714 MAJA/MINA

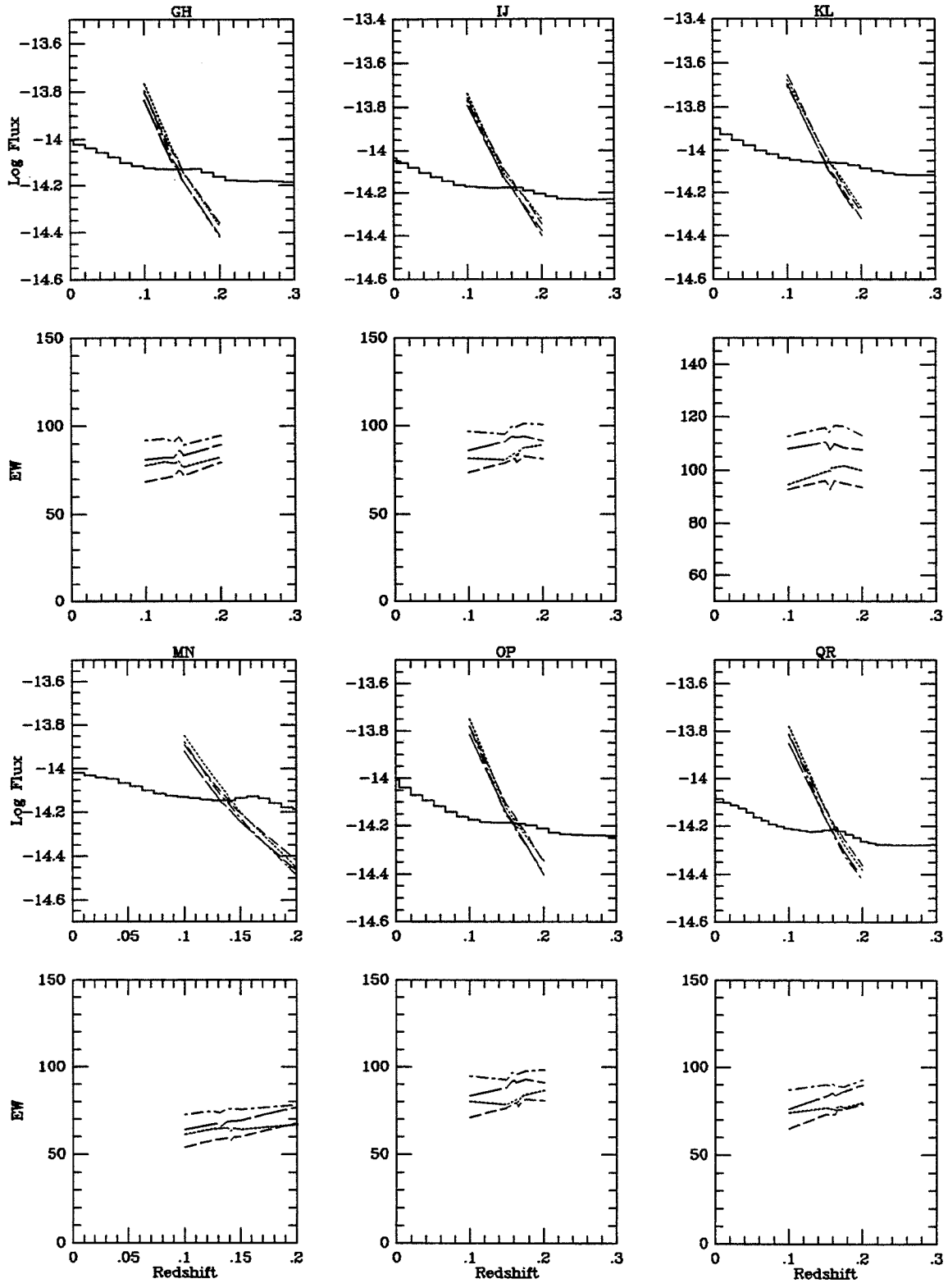

Figure B-105.aa

NGC 7714 MAJA/MINB

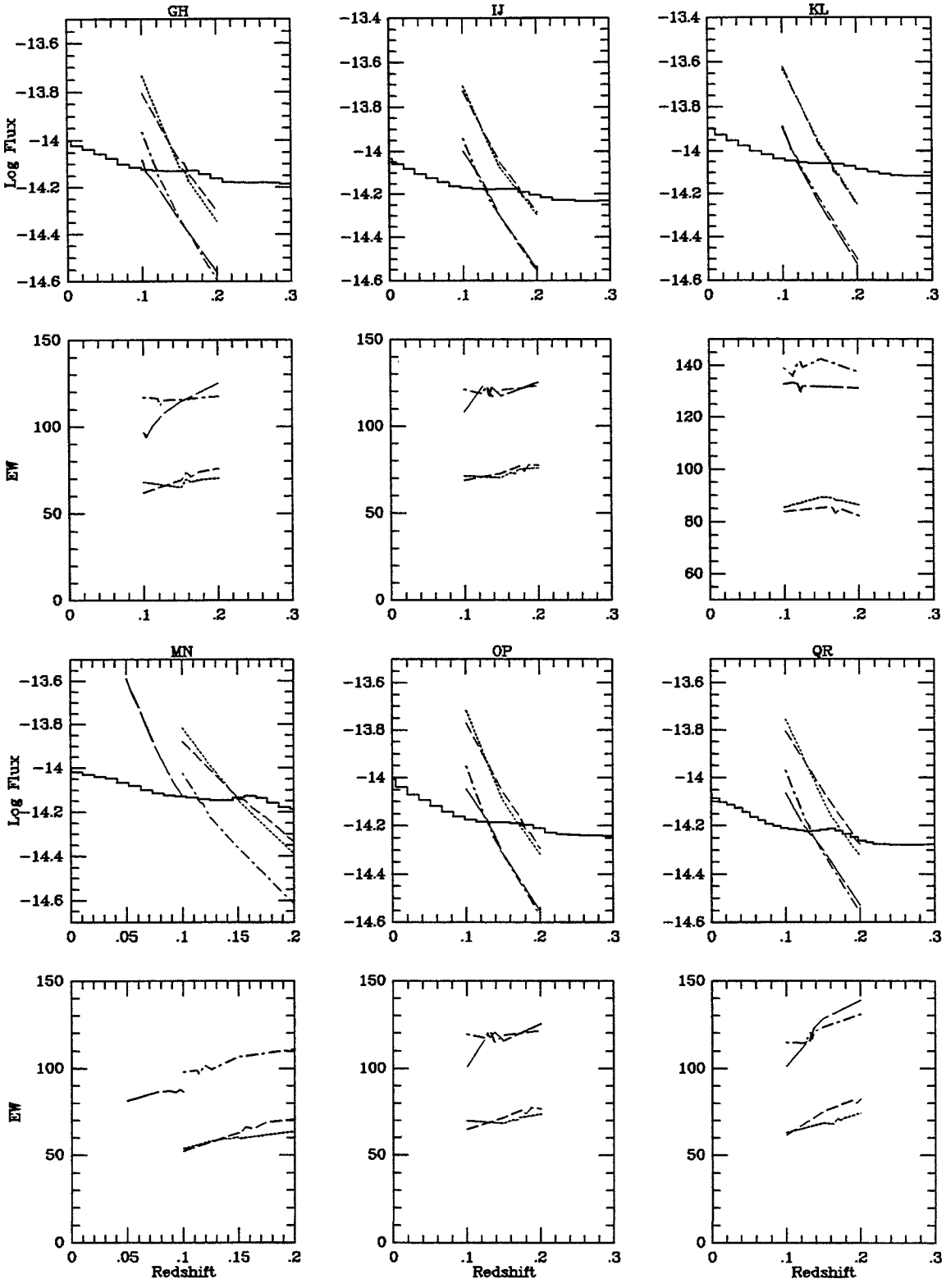

Figure B–105.ab

NGC 7714 MAJB/MINA

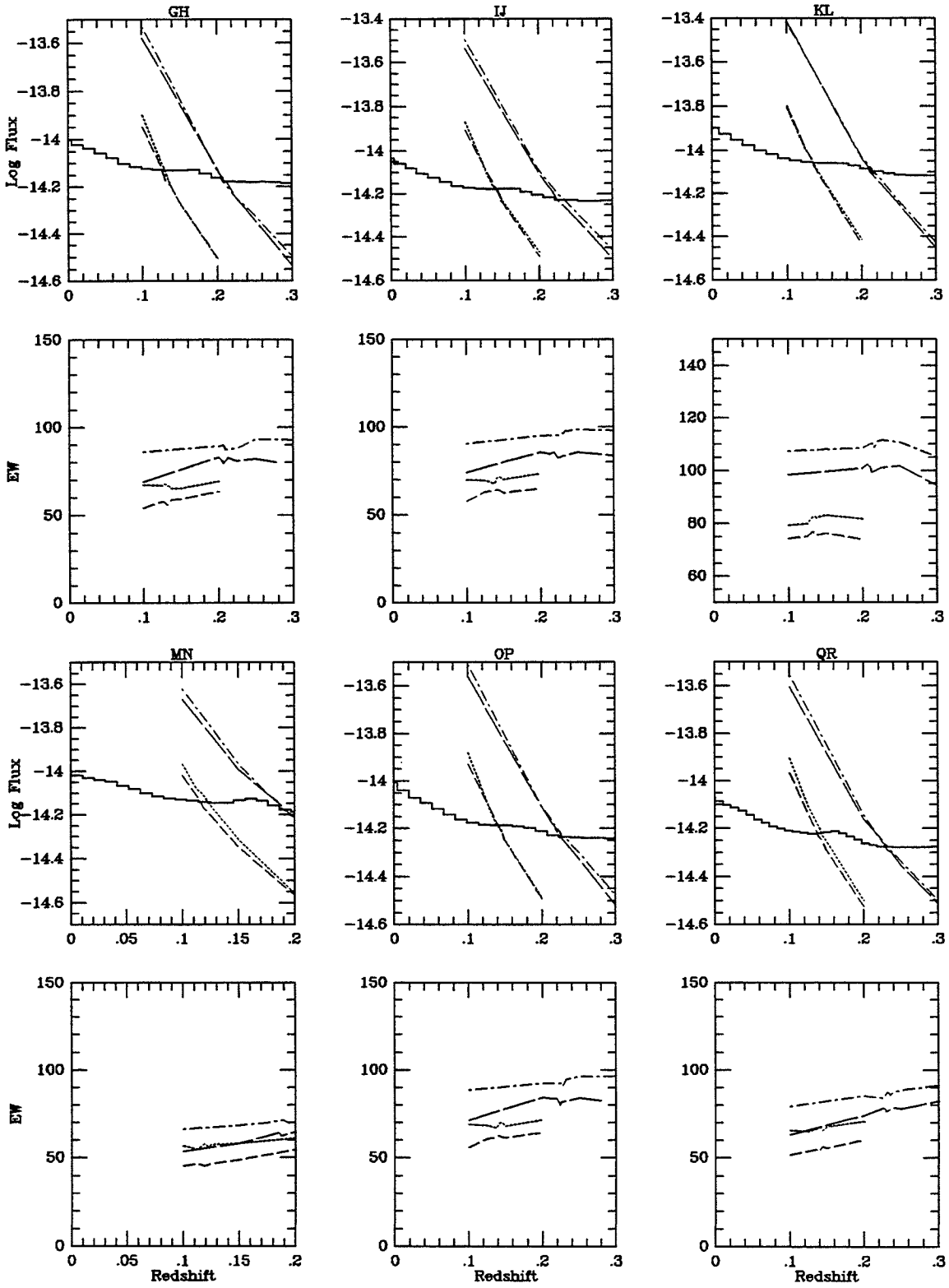

Figure B-105.ba

NGC 7714 MAJB/MINB

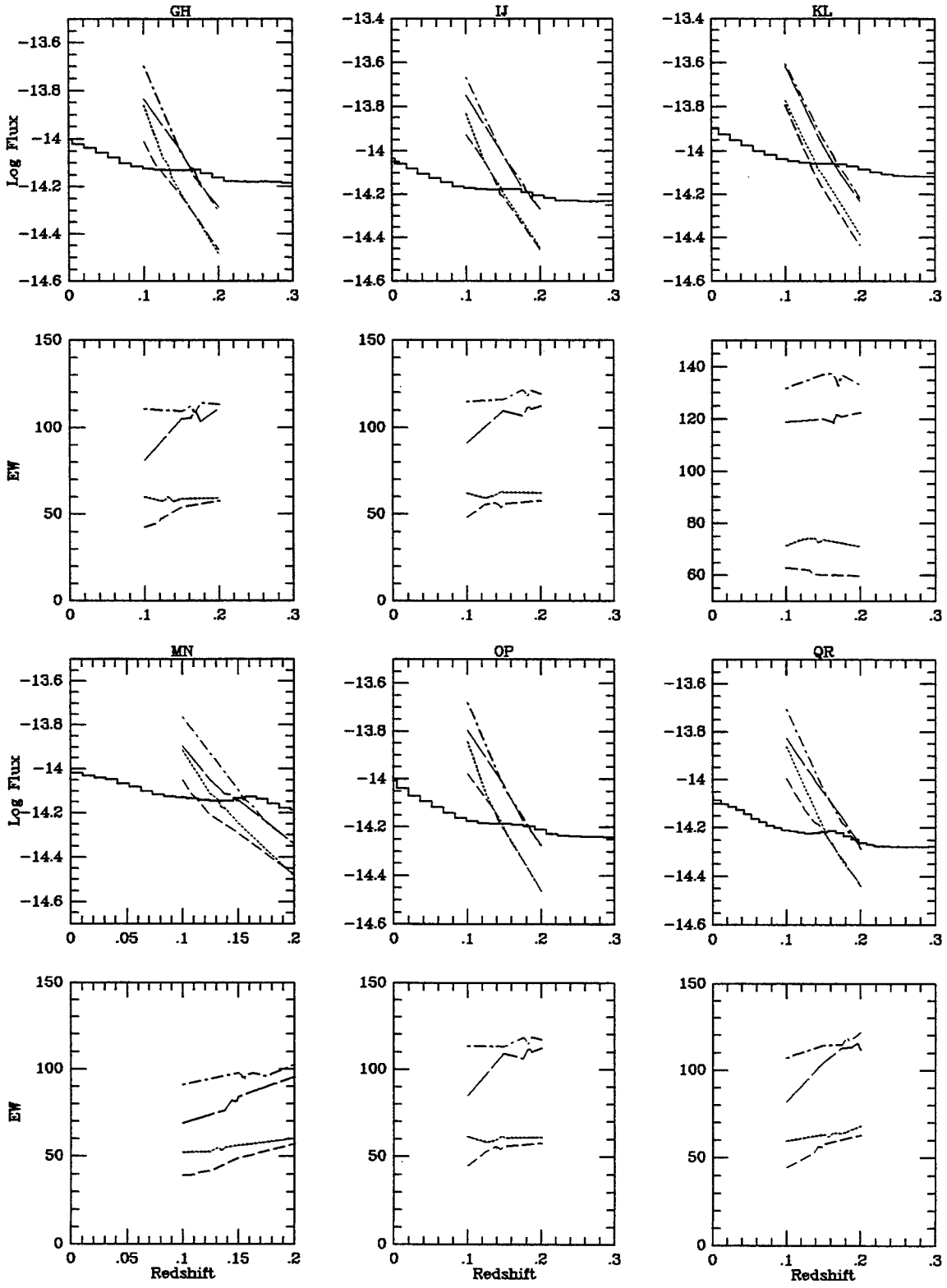

Figure B-105.bb

NGC 7714 MAJC/MINA

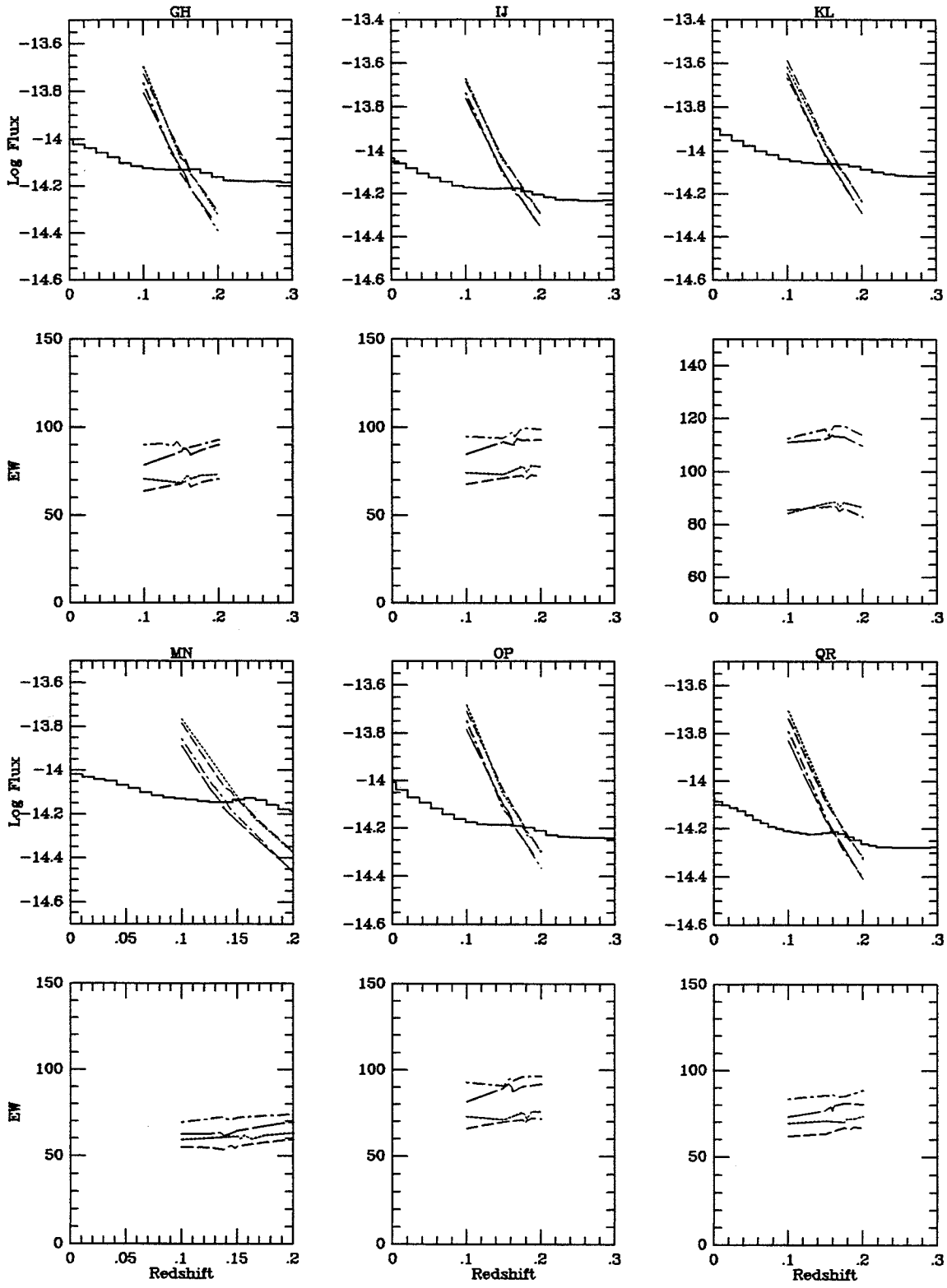

Figure B–105.ca

NGC 7714 MAJC/MINB

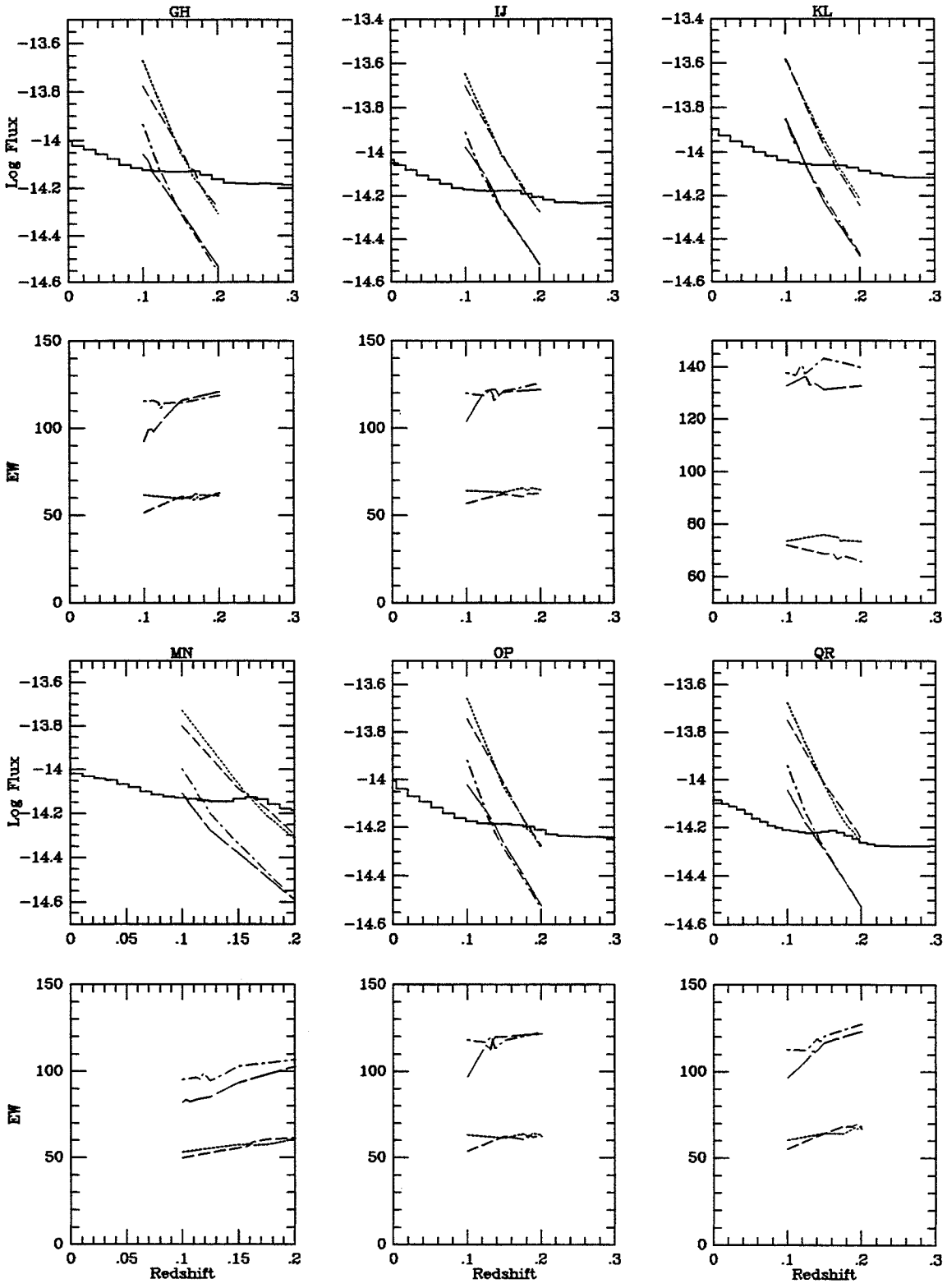

Figure B–105.cb

2354+1633 MAJA/MINA

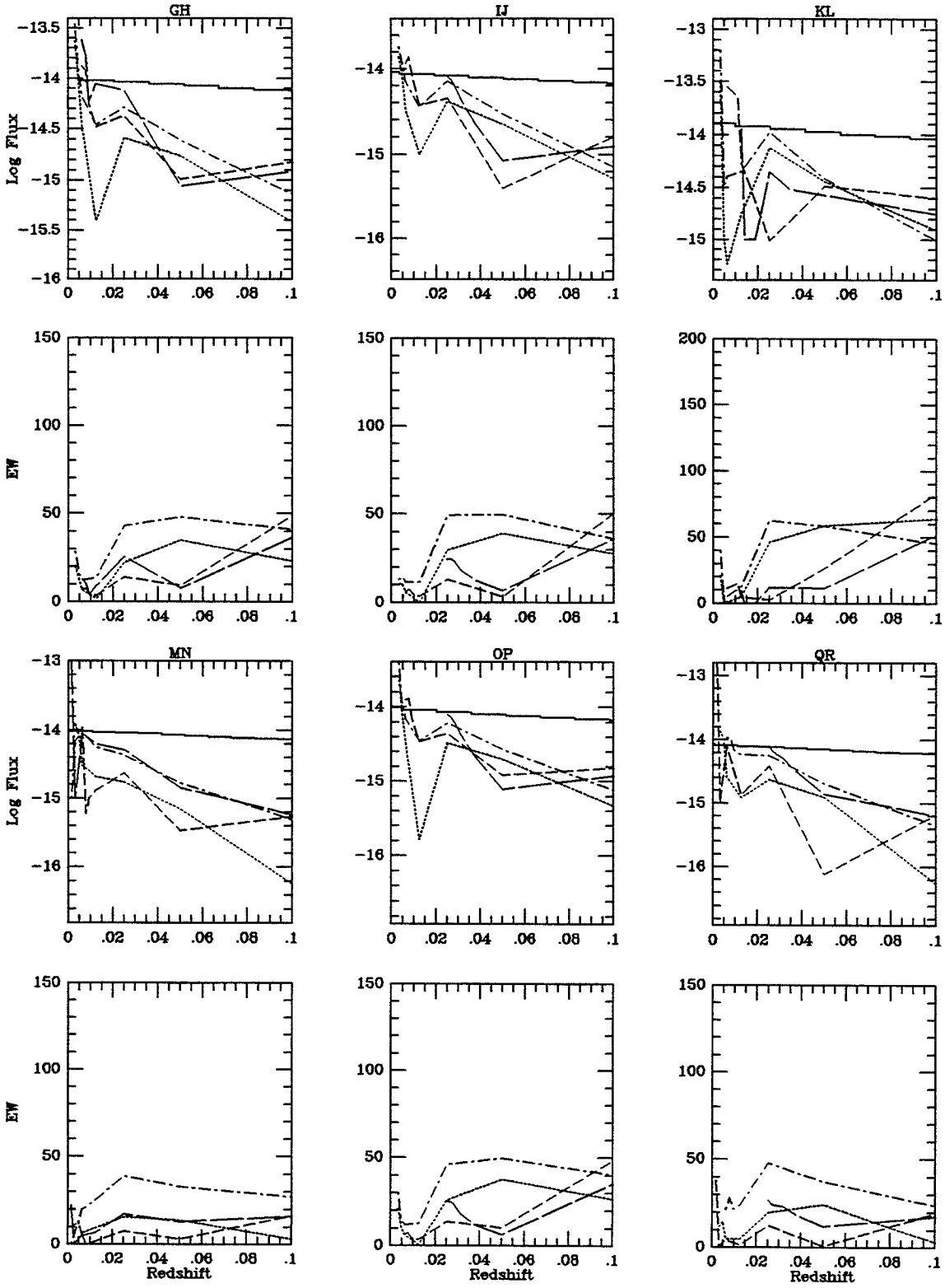

Figure B-106.aa

2354+1633 MAJA/MINB

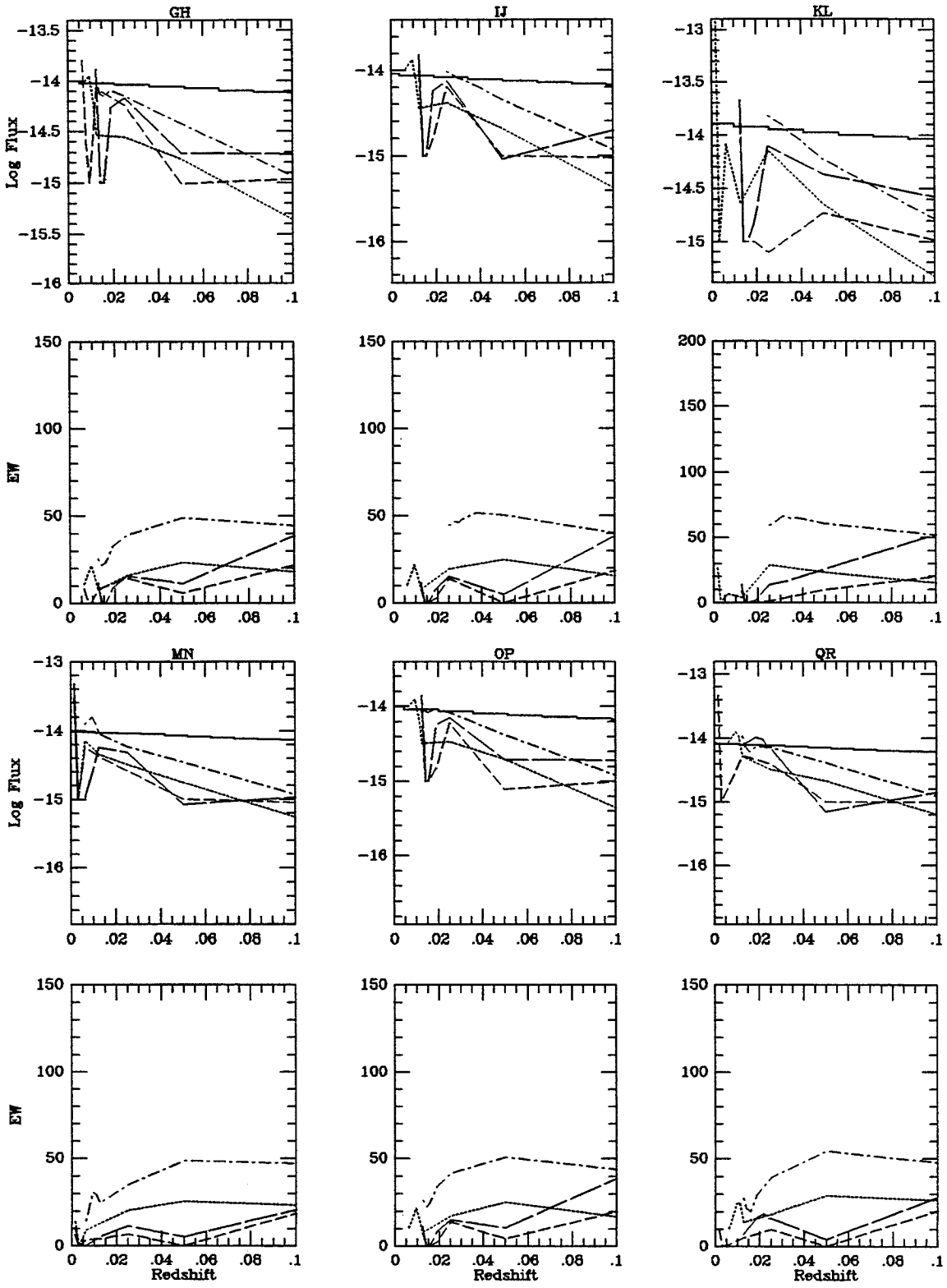

Figure B-106.ab

2354+1633 MAJA/MINC

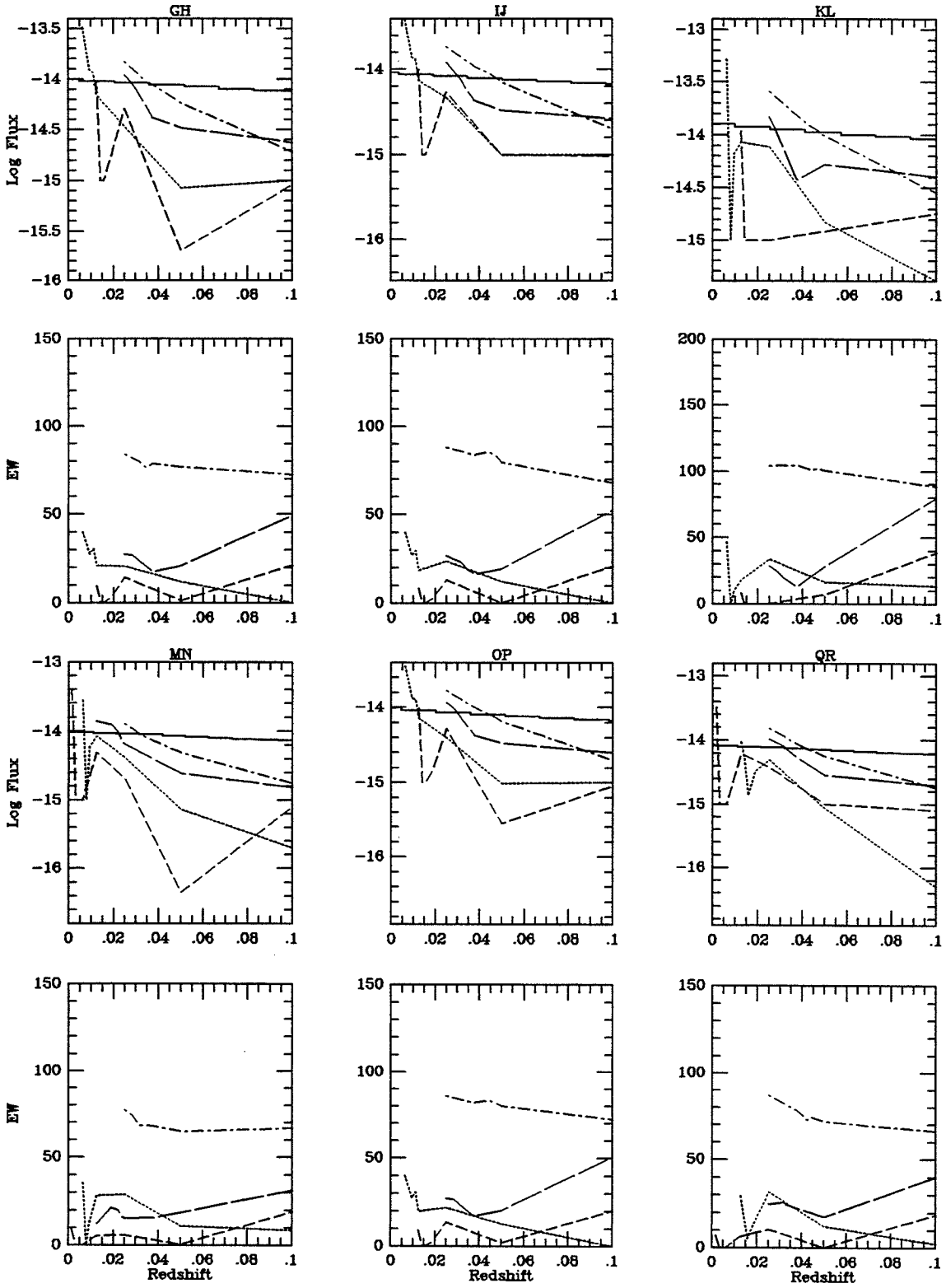

Figure B–106.ac

2354+1633 MAJB/MINA

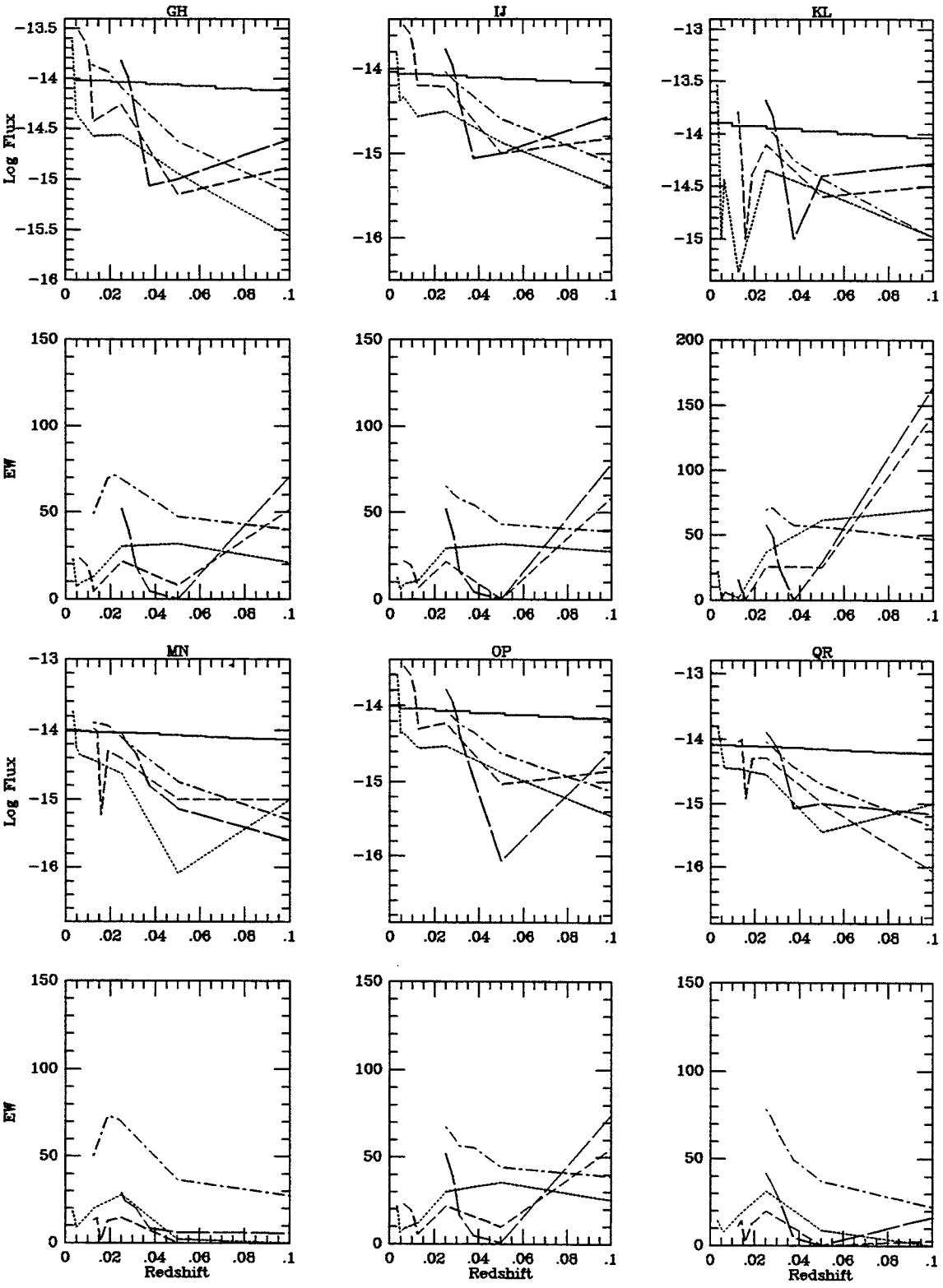

Figure B-106.ba

2354+1633 MAJB/MINB

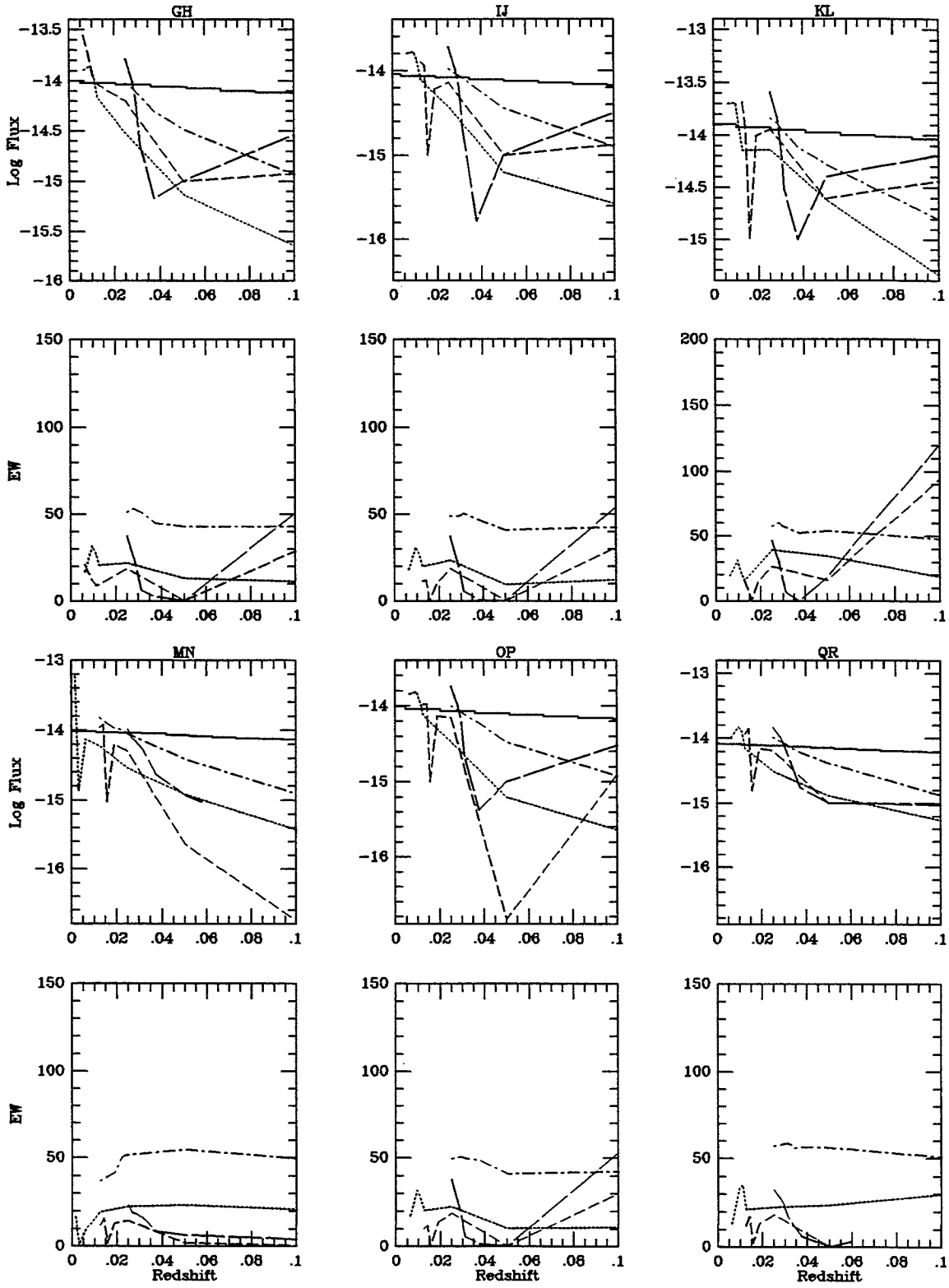

Figure B-106.bb

2354+1633 MAJB/MINC

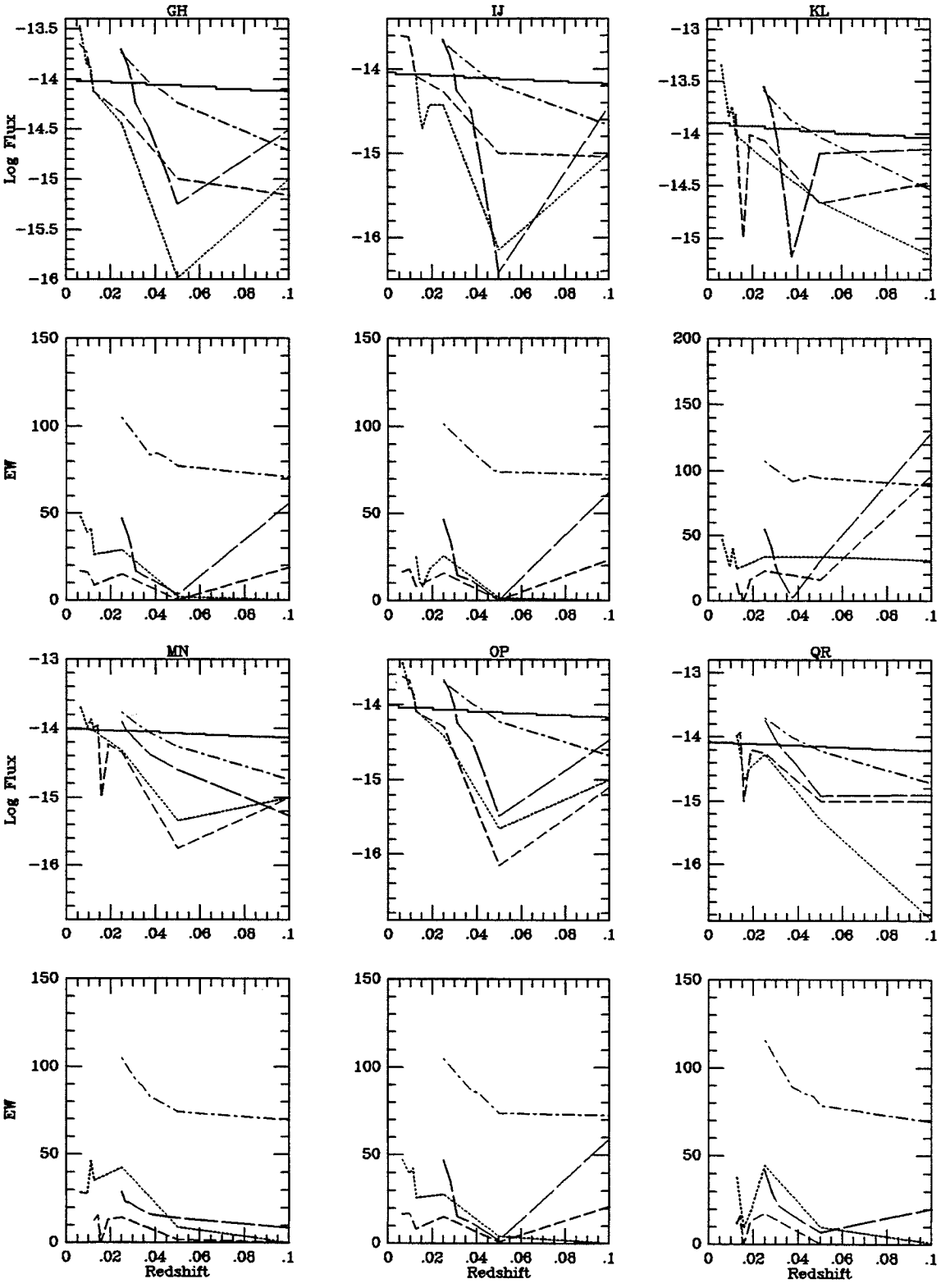

Figure B–106.bc

2354+1633 MAJC/MINA

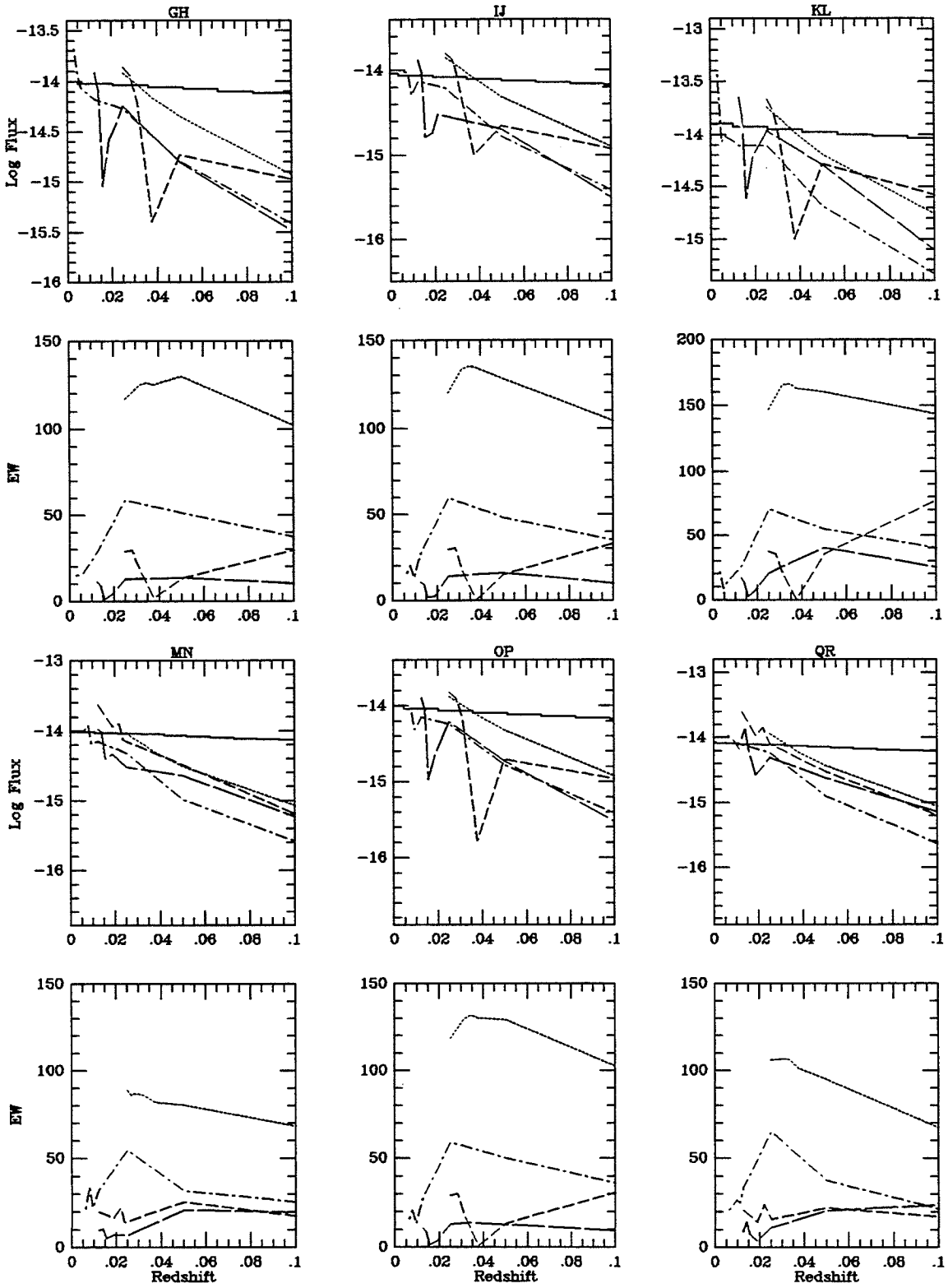

Figure B–106.ca

2354+1633 MAJC/MINB

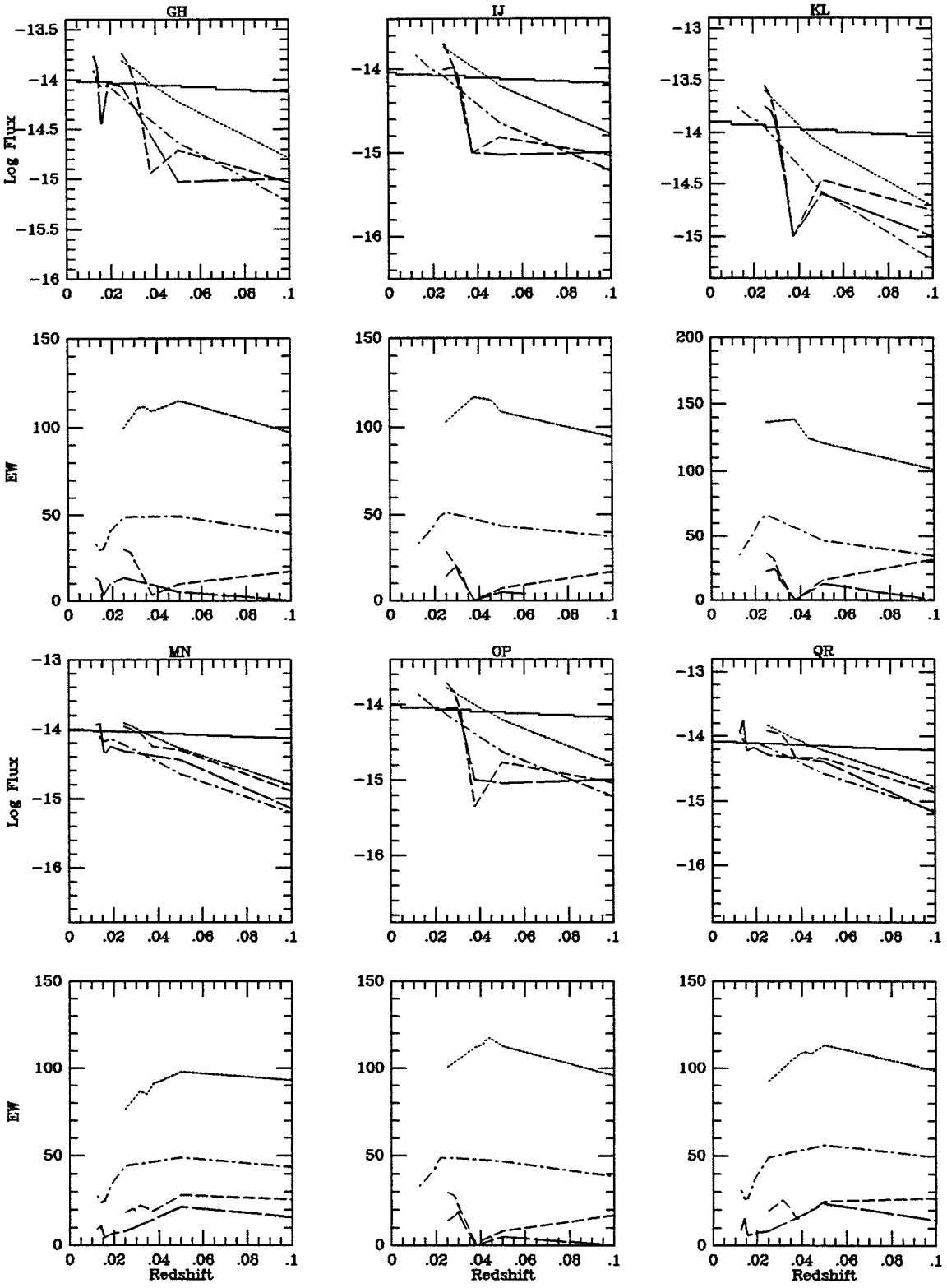

Figure B–106.cb

2354+1633 MAJC/MINC

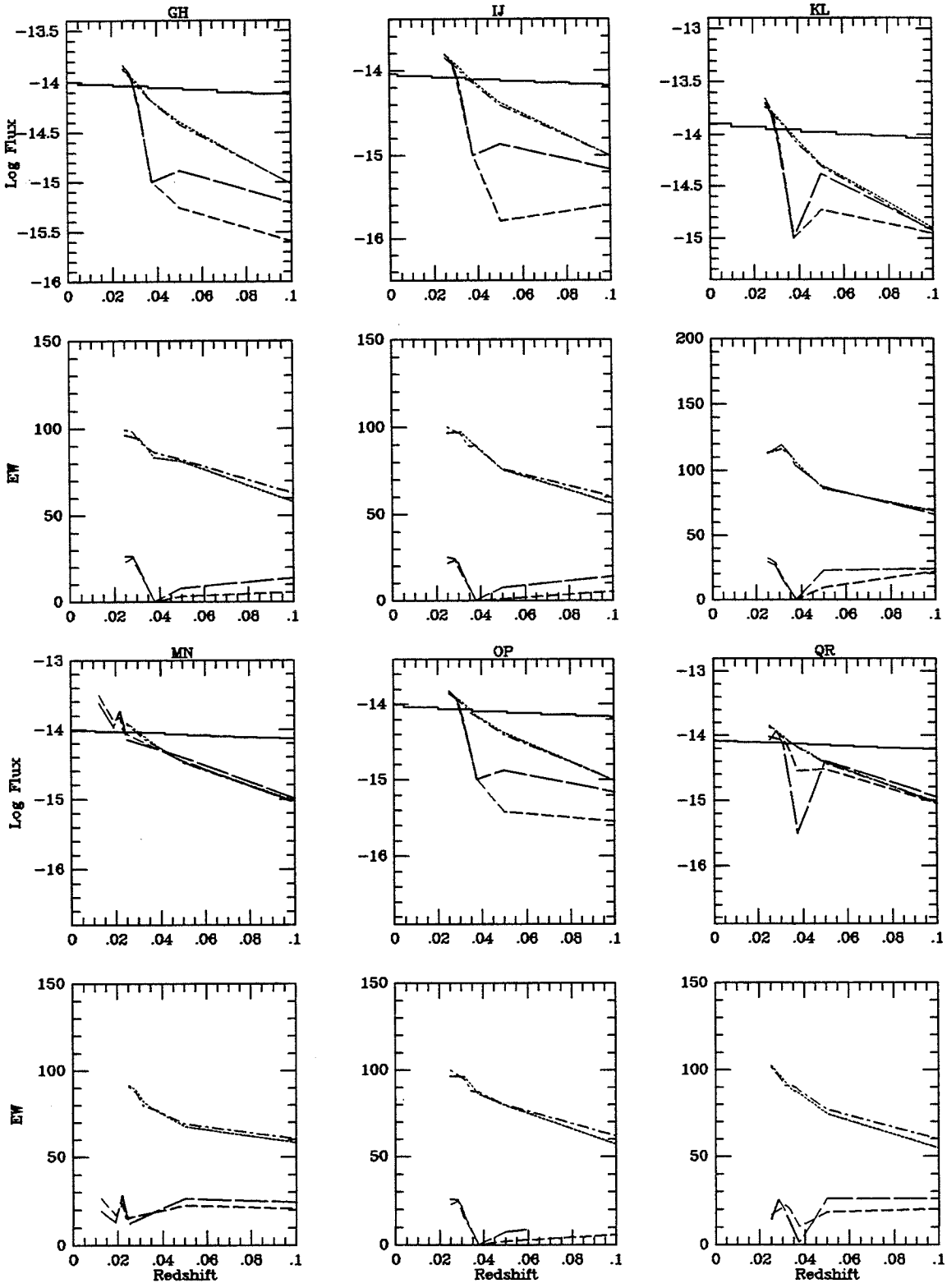

Figure B–106.cc

NGC 7800 MAJ/MINA

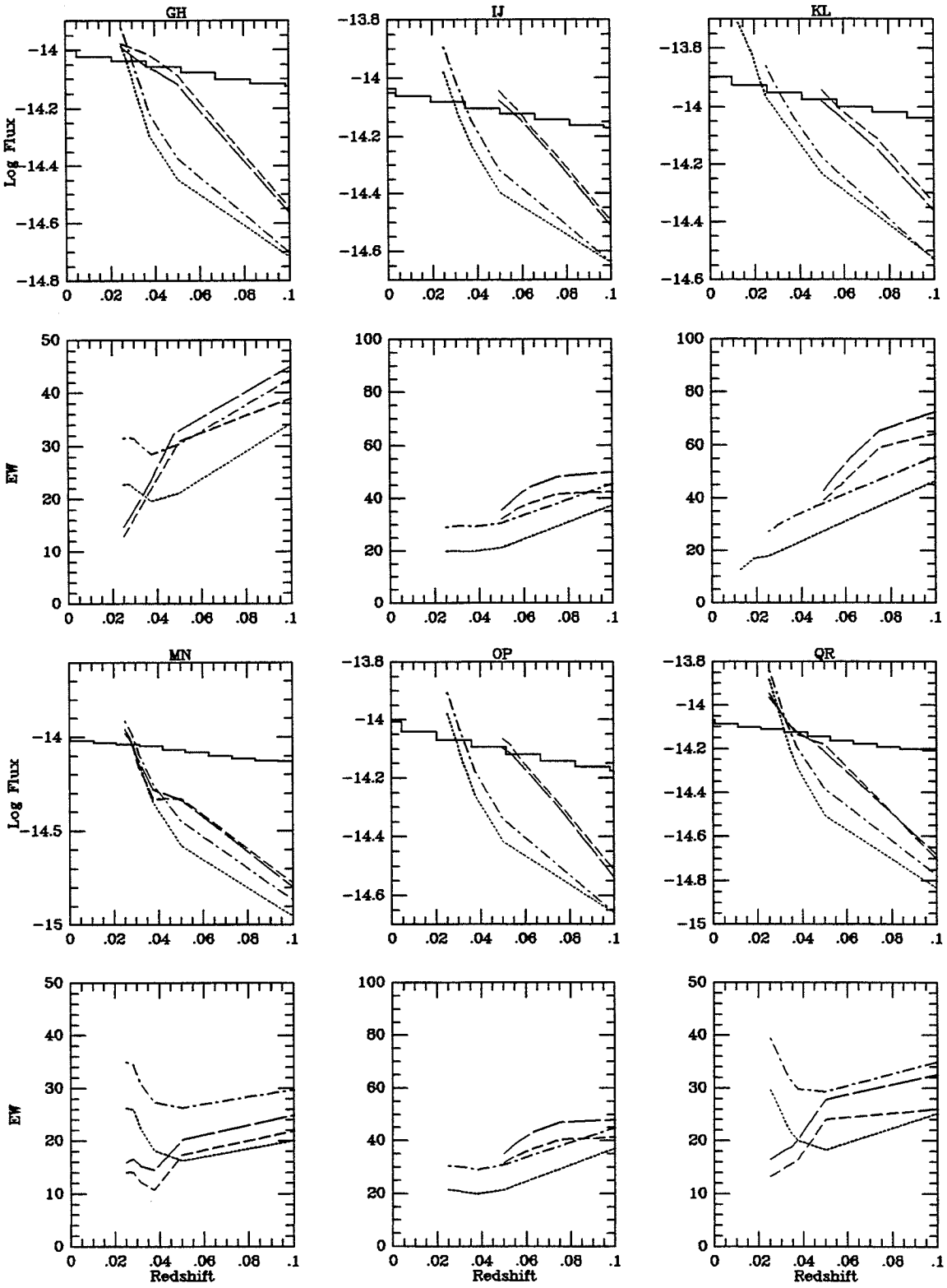

Figure B–107.a

NGC 7800 MAJ/MINB

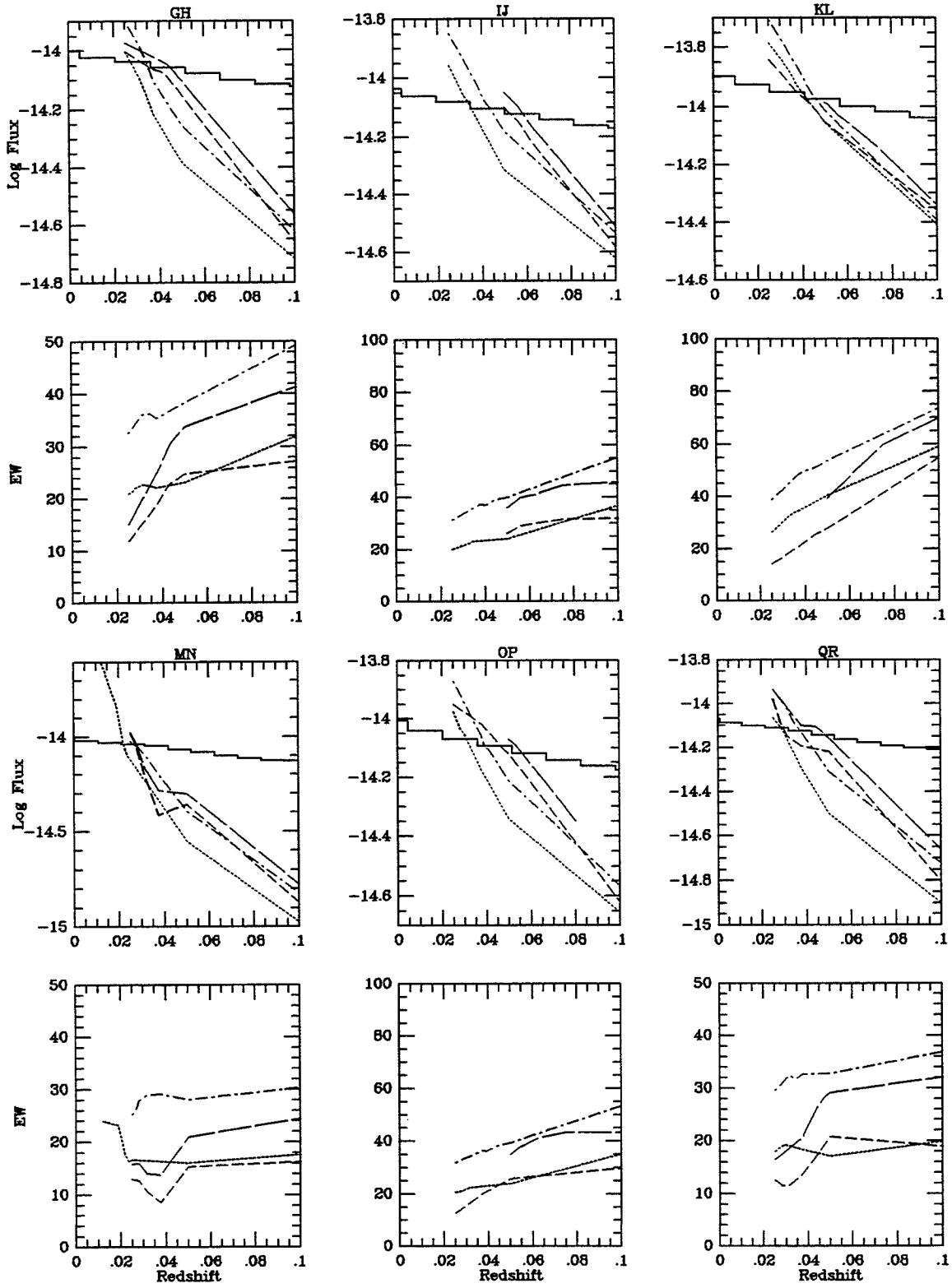

Figure B–107.b